THE UNIVERSITY *of* EDINBURGH

Evaluation of the Nordland Group overburden as an effective seal for the Sleipner CO_2 storage site (offshore Norway) using analytical and stochastic modelling techniques – Grant Douglas Nicoll

Abstract:

Saline aquifers and depleted hydrocarbon fields situated beneath the North Sea are currently being proposed as storage repositories for anthropogenic CO_2 captured from point source emitters in the UK and mainland Europe. Two experimental sites are already operating successfully offshore Norway: Sleipner since 1996 and Snøhvit since 2007, collectively storing several million tonnes of CO_2/year in the sub-surface. Despite the apparent success of these current projects, one of the major public and scientific concerns is the ability of storage sites to retain CO_2 on the millennial timescales required for CO_2 plume stabilisation and dissolution. Some areas of the North Sea are also known to contain palaeo-gas seepage pathways within overburden sediments that overlie deeper hydrocarbon reservoirs (e.g. Witch Ground Graben). These areas either need to be avoided for CO_2 storage or rigorously assessed in terms of leakage risk. Since the Sleipner storage site lies within such a province, this thesis delivers a detailed evaluation of the Nordland Group overburden and a critical assessment of its long-term sealing capability for CO_2.

From interpretation and detailed mapping of a baseline 3D seismic dataset (acquired before CO_2 injection operations commenced in 1996), we identified numerous palaeo-migration pathways and high-amplitude seismic anomalies within the Nordland Group overburden sediments deposited above the Sleipner CO_2 storage site. We attributed these features to thermogenic or biogenic gas migration, accumulation and bio-degradation over geological time. We also mapped a complex network of sand-filled, glacial channels and tunnel valleys distributed within a few hundred metres below seabed and highlighted their significance as potential fluid migration networks and/or secondary storage containment for leaking CO_2. Of further significance, we confirmed that these overburden features also create spatial density variations that impact on the accuracy of seismic time-depth conversions, resulting in the probability of topographic distortions being propagated into seismic interpretations and models. To the best of our knowledge no such detailed mapping of the Nordland Group overburden at Sleipner has been undertaken previously.

To determine whether the top layer of the CO_2 plume at Sleipner might encounter these relict pathways as it ascended and migrated laterally beneath the caprock, we evaluated the critical column heights required for a CO_2 accumulation to enter such a pathway under a range of storage conditions for a CH_4/CO_2/brine system; assuming that these pathways currently contain methane gas. Risking scenarios were based on a range of phase saturation, pressure, temperature, density, viscosity, interfacial tension and wettability conditions likely to be encountered at depths commensurate with the caprock at Sleipner. We concluded that given certain conditions at the caprock, CO_2 could leak more easily into palaeo-migration pathways than CH_4 (i.e. at lower entry pressures and therefore smaller column heights), assuming that brine densities and, most importantly, pore radii have not changed significantly over geological time (i.e. no cementation or dissolution has taken place).

To further understand the dynamic significance of these palaeo-migration pathways, channels and tunnel valleys, including their ability to form inter-connected leakage/migration networks, we constructed a series of high-resolution 3D models of the Sleipner storage site and overburden, then used stochastic basin modelling and simulation techniques to investigate the processes involved during the introduction of CO_2 into the storage site over a prolonged time period. Models were populated with geological, stratigraphic and structural information derived from our seismic interpretation. Flow simulations were calibrated to published data and matched to the present-day plume distribution. The absence of observational reservoir pressure and temperature data from Sleipner introduces significant uncertainty to model outcomes with respect to CO_2 density and column height estimates and to surmount this difficulty we constrained the caprock temperature to CO_2 density estimates obtained from the most recent gravity data observations at Sleipner. We concluded that the overburden heterogeneity is significant and palaeo-migration pathways, high-permeability channels and tunnel valleys at Sleipner may become potential migration pathways for CO_2 as the plume continues to spread laterally over the coming decade, but the possible storage response is difficult to quantify given the absence of sufficient overburden rock property information and accurate pressure and temperature data for the storage site.

The overall conclusion from this work is that insufficient information was collected within the Sleipner area prior to storage site development and too many significant studies which should have been performed as a pre-requisite (e.g. obtaining a caprock sample for laboratory testing of potential seal capacity), were actually performed some years after CO_2 injection operations had already commenced. The pressure and temperature conditions at the caprock depth for the Sleipner storage site are also marginal in terms of maintaining CO_2 above critical point conditions in dense phase and thus maximising storage efficiency. Most significantly, no rigorous overburden mapping and risking was performed for Sleipner (such as the work we describe in this thesis), thus the fact that no leakage has been detected at Sleipner is more due to good fortune than following best practices. Hopefully, our work has highlighted these key deficiencies so that future CO_2 storage site feasibility and development studies will be performed more diligently.

Evaluation of the Nordland Group overburden as an effective seal for the Sleipner CO_2 storage site (offshore Norway) using analytical and stochastic modelling techniques

Grant Douglas Nicoll

Thesis submitted in fulfilment of
the requirements for the degree of
Doctor of Philosophy

School of Geosciences
University of Edinburgh

2011

Declaration:

I declare that this thesis is my own work, except where otherwise acknowledged and it has not been submitted, in whole or part, to any previous application for a degree at this or any other university.

Grant Douglas Nicoll 23rd. November, 2011

Dedication:

I dedicate this thesis to Anne Roberts (Nicoll), who continued to believe in me throughout the whole arduous process – you are my shining star!

Anne on Suilven 2008

Abstract:

Saline aquifers and depleted hydrocarbon fields situated beneath the North Sea are currently being proposed as storage repositories for anthropogenic CO_2 captured from point source emitters in the UK and mainland Europe. Two experimental sites are already operating successfully offshore Norway: Sleipner since 1996 and Snøhvit since 2007, collectively storing several million tonnes of CO_2/year in the sub-surface. Despite the apparent success of these current projects, one of the major public and scientific concerns is the ability of storage sites to retain CO_2 on the millennial timescales required for CO_2 plume stabilisation and dissolution. Some areas of the North Sea are also known to contain palaeo-gas seepage pathways within overburden sediments that overlie deeper hydrocarbon reservoirs (e.g. Witch Ground Graben). These areas either need to be avoided for CO_2 storage or rigorously assessed in terms of leakage risk. Since the Sleipner storage site lies within such a province, this thesis delivers a detailed evaluation of the Nordland Group overburden and a critical assessment of its long-term sealing capability for CO_2.

From interpretation and detailed mapping of a baseline 3D seismic dataset (acquired before CO_2 injection operations commenced in 1996), we have identified numerous palaeo-migration pathways and high-amplitude seismic anomalies within the Nordland Group overburden sediments deposited above the Sleipner CO_2 storage site. We attributed these features to thermogenic or biogenic gas migration, accumulation and bio-degradation over geological time. We also mapped a complex network of sand-filled, glacial channels and tunnel valleys distributed within a few hundred metres below seabed and highlighted their significance as potential fluid migration networks and/or secondary storage containment for leaking CO_2. Of further significance, we confirmed that these overburden features also create spatial density variations that impact on the accuracy of seismic time-depth conversions, resulting in the probability of topographic distortions being propagated into seismic interpretations and models. To the best of our knowledge no such detailed mapping of the Nordland Group overburden at Sleipner has been undertaken previously.

To determine whether the top layer of the CO_2 plume at Sleipner might encounter these relict pathways as it ascends and migrates laterally beneath the caprock, we evaluated the critical column heights required for a CO_2 accumulation to enter such a pathway under a range of storage conditions for a CH_4/CO_2/brine system; assuming that these pathways currently contain methane gas. Risking scenarios were based on a range of phase saturation, pressure, temperature, density, viscosity, interfacial tension and wettability conditions likely to be encountered at depths commensurate with the caprock at Sleipner. We concluded that given certain conditions at the caprock, CO_2 could leak more easily into palaeo-migration pathways than CH_4 (i.e. at lower entry pressures and therefore smaller column heights), assuming that brine densities and, most importantly, pore radii have not changed significantly over geological time (i.e. no cementation or dissolution has taken place).

To further understand the dynamic significance of these palaeo-migration pathways, channels and tunnel valleys, including their ability to form inter-connected leakage/migration networks, we constructed a series of high-resolution 3D models of the Sleipner storage site and overburden, then used stochastic basin modelling and simulation techniques to investigate the processes involved during the introduction of CO_2 into the storage site over a prolonged time period. Models were populated with geological, stratigraphic and structural information derived from our seismic interpretation. Flow simulations were calibrated to published data and matched to the present-day plume distribution. The absence of observational reservoir pressure and temperature data from Sleipner introduces significant uncertainty to model outcomes with respect to CO_2 density and column height estimates and to surmount this difficulty we constrained the caprock temperature to CO_2 density estimates obtained from the most recent gravity data observations at Sleipner. We concluded that the overburden heterogeneity is significant and palaeo-migration pathways, high-permeability channels and tunnel valleys at Sleipner may become potential migration pathways for CO_2 as the plume continues to spread laterally over the coming decade, but the possible storage response is difficult to quantify given the absence of sufficient overburden rock property information and accurate pressure and temperature data for the storage site.

The overall conclusion from this work is that insufficient information was collected within the Sleipner area prior to storage site development and too many significant studies which should have been performed as a pre-requisite (e.g. obtaining a caprock sample for laboratory testing of potential seal capacity), were actually performed some years after CO_2 injection operations had already commenced. The pressure and temperature conditions at the caprock depth for the Sleipner storage site are also marginal in terms of maintaining CO_2 above critical point conditions in dense phase and thus maximising storage efficiency. Most significantly, no rigorous overburden mapping and risking was performed for Sleipner (such as the work described in this thesis), thus the fact that no leakage has been detected at Sleipner is more due to good fortune than following best practices. Hopefully, our work has highlighted these key deficiencies so that future CO_2 storage site feasibility and development studies will be performed more diligently.

Acknowledgements:

"Knowledge is in the end based on acknowledgements…"

Ludwig Wittgenstein (1889-1951)

I would like to thank my supervisory team and fellow collaborators:
Stuart Haszeldine at The University of Edinburgh for offering me the project and organising the funding. Special thanks to Sebastian Geiger at Heriot-Watt University, Andrew Cavanagh at The Permedia Research Group Inc., Ottawa, Canada and Mark Naylor at The University of Edinburgh for their continued encouragement, technical support and feedback throughout the good and the bad times!

I thank the Natural Environment Research Council (NERC) and the various consortium members associated with Scottish Carbon Capture and Storage (SCCS), for funding this project through 2007 to 2011.

For software provision and support I thank Aaron Brown, Dan Carruthers, Andrew Cavanagh, David Kennedy and Scott Toelly at The Permedia Research Group Inc. (now part of the Halliburton Group), Ottawa, Canada, for their help and generosity during my visit to Ottawa in February 2008 and for giving up their valuable time to deal with my technical support issues. Thanks also to Schlumberger for providing Petrel software and to Chris Place and the IT support teams at The University of Edinburgh and Heriot-Watt University for problem solving computer/software issues and keeping things running smoothly.

For help with seismic data acquisition and interpretation, discussions, feedback and provision of useful advice I would also like to thank Andrew Curtis, Stuart Gilfillan, John Underhill, Mark Wilkinson and Andy Wright at The University of Edinburgh; Gillian Pickup and Simon Stewart at Heriot-Watt; Joe Bulat, Tom Bradwell, Joana Gafeira, David Long, Brighid O' Dochartaigh and Martyn Stoker at the British Geological Survey (BGS), Edinburgh; Chris Jackson and Margaret Stewart at Imperial College, London; Ingunn Gjertson, John Norman and Atul Solanki at Landmark-Halliburton; Joe Cartwright at Cardiff University; Mads Huuse at Manchester University; Allan Mathieson and David Roberts (consultants).

On a personal level there are many work colleagues to thank for helping to preserve a degree of sanity (and occasional moments of insanity!) during the long haul. Firstly my cell mates in Room 401 since 2007, including Damien Carson, Mohammed Desaye, Niklas Heinemann, Rudra Kapila, Rachel Kilgallon, David Lee, Jen Roberts and Tom Russon. Also the other Crew, Grant and Drummond stalwarts such as Alex Kaye, Andy Rutherford, Craig Duguid, Gillian McCay, James Howie, Matt Booth, Matt Brolly, Nick Johnson, Rosie Jones, Simon Haunch, Simon King, Steve Gourlay and many others who shared the journey. Thank you all for your generosity, friendship, lunchtime banter, pub nights and spontaneous motorcycle trips!

To Mike Wood OBE, my former geography lecturer at The University of Aberdeen, I give thanks for reminding me that the Introduction should consider both sides of the climate change argument.

I also thank my current employers Senergy and particularly my line manager Don Morrison in the Edinburgh office for allowing me some free time to finish this thesis. Also to Iain Morrison in the Aberdeen office for supplying the Prosper® data in Appendix 5.4 used to generate Figure 5.2.

Finally, I give special thanks to Anne for her love, encouragement and support over the years, also to our cats Loki and Pinkie for providing lap warmth, inspiration and a calming influence on those otherwise wearisome "home office" days!

Table of Contents:

List of Figures:

Chapter 4:

Chapter 5:

List of Tables:

Chapter 4:

Chapter 5:

Copyright and Trademark Details:

Chapter 1:
Introduction

"I'd like to share a revelation that I've had during my time here. It came to me when I tried to classify your species and I realized that you're not actually mammals. Every mammal on this planet instinctively develops a natural equilibrium with the surrounding environment but you humans do not. You move to an area and you multiply and multiply until every natural resource is consumed and the only way you can survive is to spread to another area. There is another organism on this planet that follows the same pattern. Do you know what it is? A virus. Human beings are a disease, a cancer of this planet. You're a plague and we are the cure."

Agent Smith's speech to Morpheus (The Matrix, 1999)

The Triumph of Death by Pieter Bruegel the Elder (circa 1562)

1.1 Perceived Environmental Impact of Anthropogenic CO_2

A body of international scientists believe that increased greenhouse gas emissions from industrial processes are responsible for a significant increase in global temperatures over the past few hundred years, thus there is a direct correlation between the two phenomena (IPCC, 2001, 2002, 2005, 2007). These scientists further suggest that if such emissions are allowed to continue unabated this will have a detrimental impact on the biosphere and oceans. The three main gases deemed to be responsible for this enhanced greenhouse gas effect are carbon dioxide (CO_2), methane (CH_4) and nitrous oxide (NO). Although the latter two gases have a greater potential for atmospheric warming, CO_2 is far more abundant in terms of atmospheric concentration and is cited as being responsible for over 60% of the proposed warming effect (Gale, 2004; Maslin, 2004).

Atmospheric concentrations of CO_2 have risen from 280 ppmv (parts per million by volume) in the pre-industrial 1700s to levels exceeding 390 ppmv in 2011 (NASA, 2011; NOAA, 2011) as a direct result of the industrial revolution and increasing use of the various fossil fuels from which most of this CO_2 is derived. This represents a CO_2 increase of 160 billion tonnes; a 30% increase over pre-industrial concentrations (Maslin, 2004). As illustrated below for the year 2000 (Figure 1.1), almost 70% of these anthropogenic CO_2 emissions are produced from power generation, various industrial processes (e.g. cement manufacturing, metal/chemical/petroleum refining, distilling/brewing) and transportation; all of which involve fossil fuel combustion.

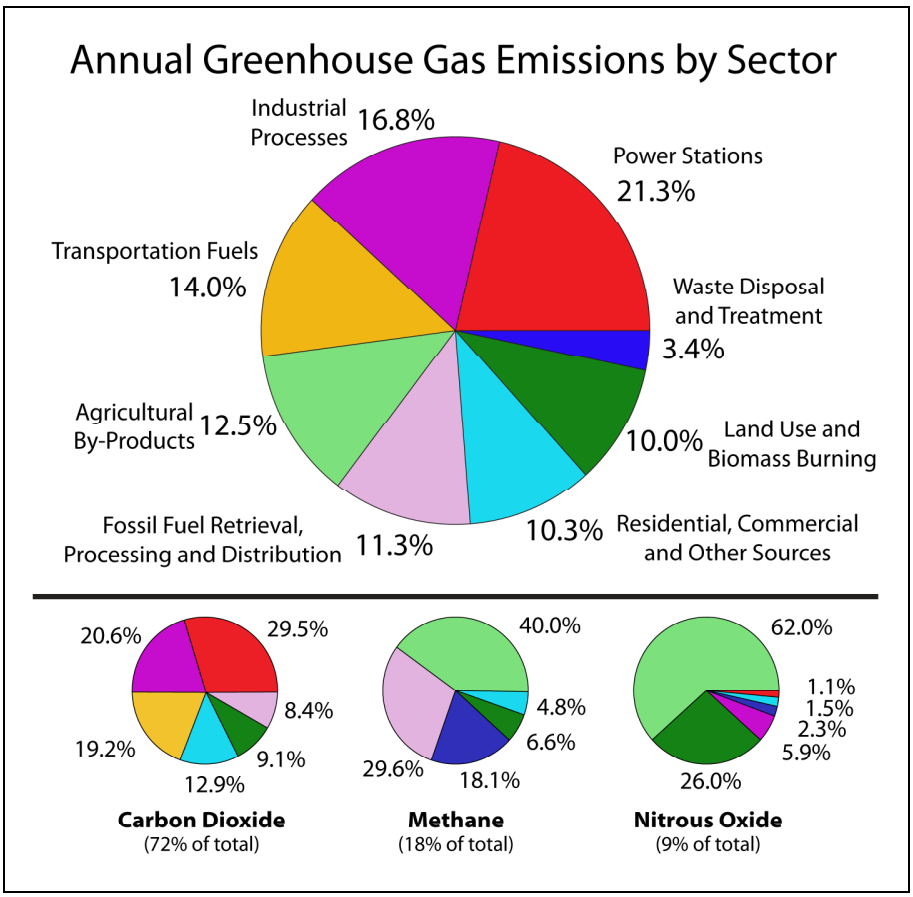

Figure 1.1 – The relative fraction of anthropogenic greenhouse gases for the year 2000 produced by eight source categories, as estimated by the Emission Database for Global Atmospheric Research version 3.2, fast track 2000 project.

***Note:** The upper diagram shows the combined sum of all greenhouse gases, weighted by their global warming potential over the next 100 years. This consists of 72% carbon dioxide, 18% methane, 8% nitrous oxide and 1% other gases. The lower three diagrams show the comparable separate information for each of these three primary greenhouse gases, with the same colouring of sectors as used in the top chart. Segments with less than 1% fraction are not labelled (images and text reproduced from Rohde, 2000).*

Although levels of CO_2 from natural processes such as volcanic eruptions have led to higher levels of atmospheric CO_2 in the geologic past, some of these episodes, such as the end Permian 251 Ma ago have been linked with global warming and mass extinctions of marine and terrestrial fauna (Knoll *et al.*, 2007; Fraiser & Bottjer, 2007; Doney *et al.,* 2009). The recent evidence for a link between increased anthropogenic CO_2 emissions and global warming is summarised by the following observations (Stuiver, 1984; IPCC, 2001, 2002, 2005, 2007; Maslin, 2004; Henderson, 2006; NASA, 2011; NOAA, 2011):

- Annual increases of atmospheric CO_2 concentrations measured at the Mauna Loa Observatory, Hawaii since 1958 (refer to Figure 1.2). Additional atmospheric evidence also indicates higher levels of CO_2 in the northern hemisphere, compared to the southern hemisphere, consistent with the distribution of industrialised nations, the main sources of anthropogenic pollution,
- Elevated CO_2 concentrations in shallow (post-industrial) layers of ice cores from polar regions, in comparison to measurements acquired from deeper (pre-industrial) layers (refer to Figure 1.2),
- Reduced pH levels in the world's oceans and noticeable damage to the carbonate skeletons of marine organisms, indicating that the ocean's buffering capacity for CO_2 is being overwhelmed, leading to rising oceanic acidity levels,
- Melting of polar ice sheets, glaciers and associated sea level rise,
- Decreasing C^{13}/C^{12} carbon isotope ratio from tree rings, ice cores and shells of marine organisms, indicating a dilution effect due to increased levels of organic C^{12} derived from the burning of fossil fuels,
- A divergence over the past 50 years between observed surface temperatures (global mean) and predicted climate model temperatures based on natural forcings (i.e. volcanic activity and solar variation), yet convergence between predicted climate model temperatures based on anthropogenic forcings (i.e. greenhouse gases).

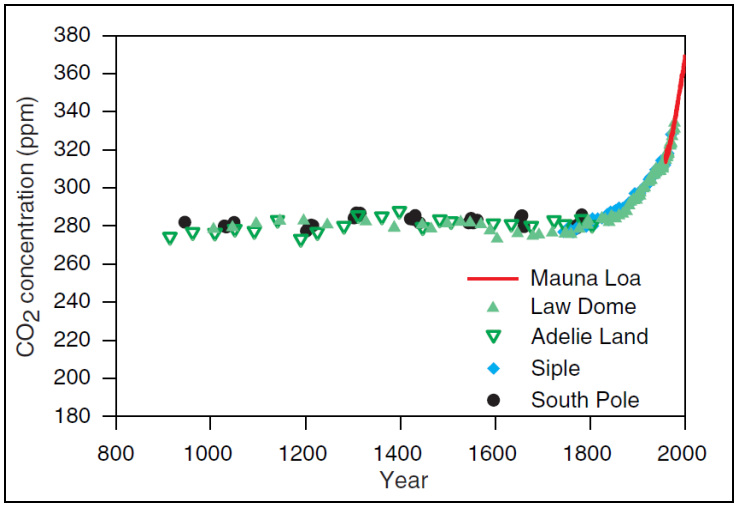

Figure 1.2 – CO_2 concentrations from Antarctic ice cores and atmospheric data (reproduced from IPCC, 2001)

Following the establishment of the Intergovernmental Panel on Climate Change (IPCC) in 1988 to investigate these lines of evidence, reduction of greenhouse gas emissions has now become a major priority for industrialised countries bound by international treaties such as the Kyoto Protocol of 1998. In the past ten years, most of the IPCC emphasis has been placed on persuading established industrialised countries such as the USA and emergent developing countries such as China and India to reduce their CO_2 emissions to "acceptable levels" and to develop technology for the capture, transport and storage of anthropogenic CO_2 (Gale, 2004; Maslin, 2004; IPCC, 2005).

The increasing globalisation of the world economy and transfer of manufacturing to developing countries has resulted in an alarming CO_2 emissions growth sector as illustrated in Figure 1.3 for global anthropogenic CO_2 emissions between 1751-2010 (Boden *et al.*, 2010) and Table 1.1 for the main CO_2 emitting countries during the period 1994-2004 (Environment Department – The World Bank, 2007).

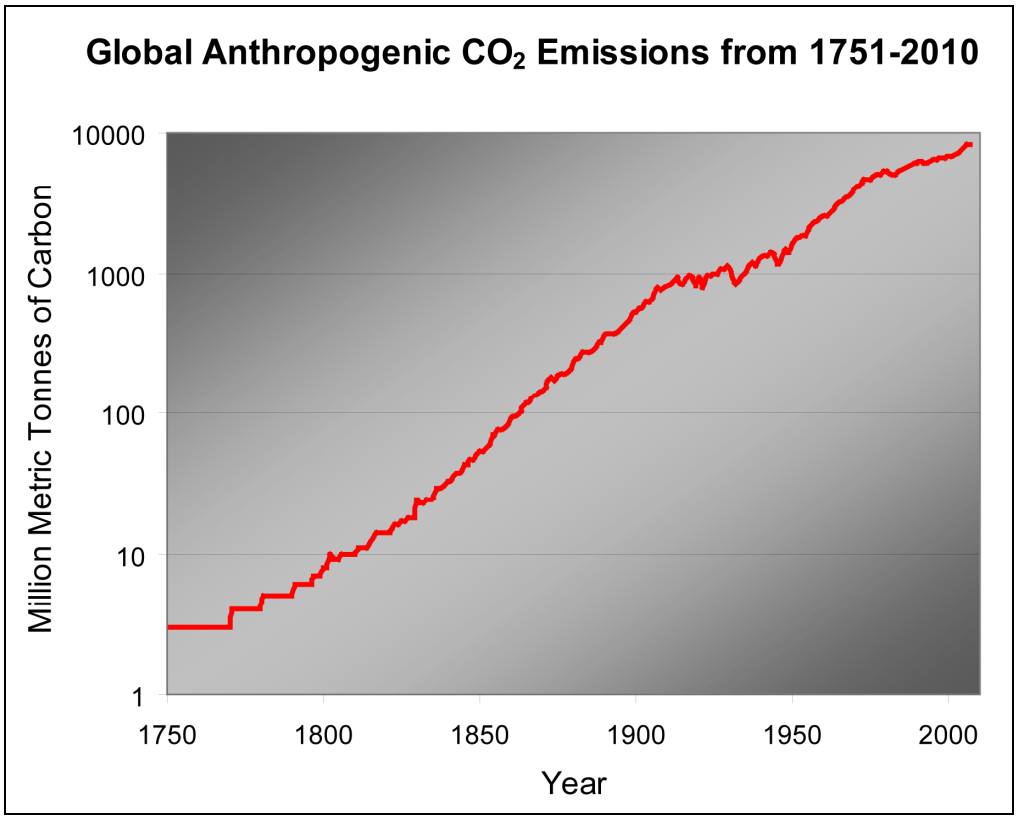

Figure 1.3: Global anthropogenic CO_2 emissions from 1751-2010 (Boden et al., 2010)

Country	Total CO_2 emissions in 2004 from fossil fuel combustion (million metric tonnes)	Increase since 1994 (million metric tonnes)	% increase since 1994
United States	5912	674	13
Peoples Rep. of China	4707	1911	68
Russian Federation	1685	-5	0
Japan	1262	174	16
India	1113	384	53
Germany	862	-5	-1
Canada	588	95	19
United Kingdom	580	12	2
Rep. of Korea	497	143	40
Italy	485	85	21
South Africa	430	86	25
France	406	46	13
Iran	402	153	62
Australia	386	107	38
Mexico	385	52	15
Saudi Arabia	365	127	53
Ukraine	364	-76	-17
Spain	362	128	55
Brazil	337	69	26
Indonesia	308	99	48

Table 1.1 – Top 20 CO_2 emitters 2004 - highest percentage increases highlighted in pink (extract from Environment Department – The World Bank, 2007)

In a 2007 British newspaper article, the Netherlands Environmental Assessment Agency stated that China produced 6,200 million tonnes of CO_2 during 2006, compared with 5,800 million tonnes from the USA and 600 million tonnes from Britain over the same period, thus it would appear that China has subsequently overtaken the USA as the leading emitter of anthropogenic CO_2. Large increases in electricity generation from coal burning power stations and cement production were cited as the main causes for this large increase (Vidal & Adam, 2007).

1.2 The Sceptical Viewpoint on Climate Change:

Whilst it is not disputed by scientists that increasing the concentration of CO_2 in the atmosphere creates a greenhouse effect (Arrhenius, 1896), a contradictory body of scientific opinion suggests that a direct correlation between anthropogenic CO_2 emissions and climatic changes of the past few hundred years is still unproven. Counter arguments are usually centred on the following points:

- The global ice age or "Snowball Earth" of the Neoproterozoic occurred at a period when atmospheric CO_2 levels were 10-200 times greater than the present day (Kaufman & Xiao, 2003),
- The record cold winters of 1940s-1970s, that followed World War 2 and a period of intense industrial activity and atmospheric pollution (IPCC, 2007),
- Neither the Medieval Warm Period (~800-1300) nor the Little Ice Age (~1400-1900) appear to have been associated with significant changes in atmospheric CO_2 concentrations (Cronin *et al.,* 2003),
- Compared to CO_2, water (in the form of clouds) has a much higher atmospheric abundance and greenhouse gas potential, notwithstanding that clouds have a high albedo that can reflect incoming solar radiation back to space yet also act as a blanket for retaining a proportion of the Earth's radiative energy (IPCC, 2007),
- Significant time-lag of several hundred to a thousand years between a global temperature increase and increasing CO_2 concentrations revealed by ice core data (Monnin *et al*., 2001),
- A number of researchers (e.g. Soon & Baliunas, 2003; McIntyre & McKitrick, 2003) have questioned the reliability of various proxies (e.g. dendrochronology and ice cores) and statistical methodology used to produce the CO_2-temperature correlation and infamous "hockey stick" graph (Mann *et al.,* 1998),
- The questionable selection of particular temperature measuring stations, given the urban heat island effect and growing influence of urbanisation (Wood, 1988),
- Some evidence suggests a better correlation of climatic variation with solar activity (Helama *et al.*, 2010),
- The moderation of climate science terminology from "global warming" to "climate change" and an increasing emphasis on ocean acidification as a justification for mitigation action, which suggests the original argument for a global warming effect may actually be a weak one.

Climate sceptics have frequently made accusations of data manipulation and abuse of the peer-review process, particularly after the publication of leaked emails from the Climate Research Group at East Anglia in 2009, which suggested "significant irregularities" in the scientific research approach (Pearce, 2010). Similarly, the climate change lobby have accused the sceptics via the popular press and Internet of being sponsored by hydrocarbon companies, even though many of these same companies now actively promote carbon capture and storage projects.

If vested interests and the climate argument are set aside, it is probably more relevant to think of CO_2 emissions as part of a greater environmental pollution problem. If a historical comparison is made between atmospheric conditions in major world cities before and after environmental legislation was introduced (e.g. Victorian versus present-day London), it is clear that many health problems such as bronchitis and high infant mortality have traditionally been associated with air pollution (i.e. primarily CO_2, SO_2, and particulate matter) created by burning fossil fuels, predominantly coal. Thus, even a hardened climate sceptic would surely agree that continuing to emit anthropogenic pollutants of any kind into the atmosphere in vast quantities and allowing them to accumulate and dissolve into the oceans is not acceptable or very sensible from an environmental and health perspective. Considering that CO_2 is by far the largest pollutant in terms of atmospheric concentration (Figure 1.1), it appears to be the prime candidate for any pollution mitigation strategy.

1.3 Proposed Emissions Reduction Solutions:

Various solutions have been proposed for the reduction of CO_2 emissions, including:

- Use of alternative green energy sources (e.g. wind, tidal, fuel cells, recycled CO_2, synthetic fuels), to replace fossil fuel power plants (Pacala & Socolow, 2004; Johnston, 2007; Graham-Rowe, 2008). Whilst seemingly attractive, some of this technology is still in its infancy and generation efficiencies cannot yet match conventional energy sources.
- Nuclear power, which offers higher efficiency, but with attendant toxic waste disposal problems (World Nuclear Association).
- Improving the combustion efficiency of existing and proposed fossil fuel power stations will help in the short term, but ultimately CO_2 will still be generated to some extent (Pacala & Socolow, 2004; Gibbins *et al.*, 2006).
- Capture of CO_2 at point source, followed by transportation and storage/sequestration in non-atmospheric sinks, including:
    - The deep ocean environment (Teng *et al.*, 1996)
    - The terrestrial biosphere, including forests and soils (Gale, 2004)
    - Carbonate mineralisation at surface (Lackner, 2002; IPCC, 2005)
    - Deep geological formations including depleted oil and gas reservoirs, saline aquifers, coal and oil shale beds, methane hydrate deposits and salt caverns (Baines & Worden, 2004; Gale, 2004; Holloway, 2001, 2006; IPCC, 2005; Jadhawar *et al.*, 2006).

These options are most attractive if the CO_2 can be captured and transported economically to the sink (i.e. there is an existing infrastructure in place and/or source and sink are in close proximity). However, in the case of the first three options there are concerns about the permanence of CO_2 storage and sequestration in the longer term (Gale, 2004). Deep ocean storage may also have detrimental effects on ocean circulation patterns, acidity levels and marine organisms (Gale, 2004; Henderson, 2006). Deep geological formations appear to offer the best storage/sequestration alternative in terms of permanence, storage potential and financial upsides from Enhanced Oil Recovery (EOR) or methane recovery from hydrocarbon reserves. Global storage capacities are presented in Table 1.2 for some of these geological storage options (Gale, 2004).

Global Capacity		
Storage Option	**Gt CO_2**	**% of Emissions to 2050**
Depleted Oil and Gas Fields	920	45
Deep Saline Aquifers	400-10,000	20-500
Unminable Coal Seams	20	< 2

Table 1.2 – Global Capacity of Potential Geological Storage for CO_2 (Gale, 2004)

Saline aquifers and depleted hydrocarbon reservoirs appear to offer the largest potential storage capacity of the three options considered. Sorption of CO_2 onto organic material is the storage mechanism in coals and oil shales (Holloway, 2001; Bachu *et al.*, 2007), with subsequent methane displacement offering some recovery upsides, but as Table 1.2 shows, the global storage potential is much smaller. Methane hydrate deposits and salt caverns are considered to present a greater storage risk given the inherent instabilities of the storage media (Bachu & Rothenburg, 2003; Klerkx *et al.*, 2006).

1.4 Storage Mechanisms:

Given the favourable capacity and economic arguments for storage in saline aquifers and depleted hydrocarbon reservoirs, the different mechanisms for trapping injected CO_2 within this type of geological media need to be considered in detail from a modelling perspective (IPCC, 2005; Bachu *et al.*, 2007). Storage mechanisms are classified into two categories:

- **Physical** - where CO_2 is stored as a (high density) supercritical fluid and/or (low density) free gas phase:
  - Migrating slowly upwards and laterally, displacing resident pore fluids. In some literature this is often referred to as hydrodynamic trapping although strictly this requires dynamic interaction with an active aquifer to disperse and mix CO_2 and resident formation fluids. This is a drainage process with CO_2 displacing formation fluids.
  - Static in structural and stratigraphic traps, enclosed by a low permeability sealing formation.
  - Residual trapping in pore space at S_{girr}. This is of greater significance after the CO_2 injection and migration process has ceased and formation fluids start to reoccupy pore spaces in an imbibition process.

- **Chemical** – where CO_2 is stored and/or sequestered by dissolution and reaction to form stable compounds:
  - Solubility in water/brine (CO_{2aq}).
  - Ionic trapping as dissolved species (HCO_3^-, CO_3^{2-}).
  - Reaction with resident minerals (e.g. feldspar) and aqueous metallic species (e.g. Ca^{2+}, Fe^{2+}), to form new carbonate and silicate minerals (e.g. calcite, siderite and dawsonite).
  - Adsorption onto organic compounds in rocks (e.g. shales, coals).

With reference to Figure 1.4, physical trapping is believed to be most significant mechanism for short-term storage security (i.e. 100's of years), with chemical trapping becoming more significant in the long-term (i.e. 1000's of years). This thesis will concentrate on the physical trapping processes.

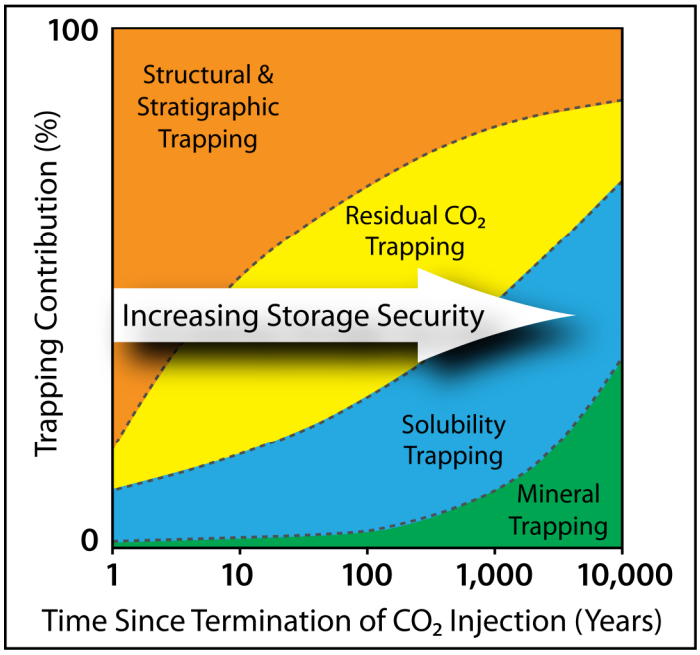

Figure 1.4 - Significance of Different Trapping Mechanisms Post-Injection (after Bachu et al., 2007)

1.5 Depleted Hydrocarbon Reservoirs Versus Saline Aquifers:

Both of these storage candidates have positive and negative aspects that must be evaluated for specific storage locations:

<u>Depleted Hydrocarbon Reservoirs</u>:

- ✓ These offer the economic benefits of an existing transport and processing infrastructure. There may be further economic benefits from Enhanced Oil Recovery (EOR) and Carbon Tax savings (Pearce, 1994).

- ✓ Reservoirs should be well-characterised in terms of structure, storage capacity, sealing capability, petrophysical properties, PVT and fluid flow behaviour; existing basin models may also be suitable for CO_2 injection and fluid migration modelling (Cawley *et al.*, 2005).

- × The reservoir may have suffered overpressure or compaction effects during hydrocarbon depletion. This could have a critical impact on reservoir and/or seal integrity (Bachu *et al.*, 2007).

- × CO_2 will have a different behaviour to hydrocarbons formerly contained in the reservoir (e.g. higher acidity, different wettability characteristics, higher mobility and a greater interaction between reservoir rock/pore fluids), so there is no guarantee that sealing formations will contain CO_2 as securely as hydrocarbons (Li *et al.*, 2006; Chiquet *et al.*, 2007a; Chalbaud *et al.,* 2009).

- × Existing well penetrations into the reservoir could provide potential leakage paths; internally via leaking wellbore seals/plugs or externally via degraded annular cement (Celia & Bachu, 2003 and Cawley *et al.*, 2005).

Saline Aquifers:

- ✓ These offer a greater storage potential than depleted hydrocarbon reservoirs.

- ✓ Generally, there should be no previous well penetrations (assuming the chosen site is located some distance away from a hydrocarbon exploration province), so sealing integrity should be higher.

- ✓ Substantial Carbon Tax savings may be available (Pearce, 1994).

- × A dedicated transport, processing and injection infrastructure will be required and there will be no EOR benefits (assuming the site is not located near a CO_2 point source that could be adapted to CCS use).

- × Characterisation relies on interpolation from adjacent wells/logs (where available) and geophysics; remote monitoring of reservoir layers and fluid migration lacks the desired resolution for accurate modelling.

- × Not all saline aquifers may be suitable for CO_2 storage. They may be too deep or too shallow, have unfavourable porosity/permeability characteristics, poor sealing potential or they may be too saline for adequate dissolution of CO_2 (i.e. salting-out effect, described by Koschel *et al.*, 2006) or to maintain long-term injectivity. They may also be compromised by remnant or post-injection high-permeability structures located or subsequently developed within the aquifer, seal/caprock and overburden that allow CO_2 to migrate out of the storage facility.

This thesis seeks to address some of these negative aspects as described in the following sections.

1.6 Thesis Aims and Objectives:

The main aims of this thesis are:

- To analyse known sites of CO_2 and CH_4 accumulation and leakage as analogues for modelling and predicting CO_2 retention for a storage period of millennia. We focus on data rich areas such as the North Sea, where comparable seismic interpretation, modelling and 4D monitoring work has been performed on the Sleipner CO_2 storage site (Alnes *et al*., 2008, 2011; Arts *et al*., 2008; Bickle *et al*., 2007; Chadwick *et al*., 2005, 2009a/b; Chadwick & Noy, 2010; Grimstad *et al*., 2009; Lindeberg *et al*., 2001, 2009; Nooner *et al*., 2007).

- To identify, investigate and quantify areas of current uncertainty in existing models, including retention, migration and leakage processes, rates and spatial pathways affecting the upward migration of CO_2 from a storage reservoir, through overlying sediments to the seabed or surface. We investigate seismic anomalies that may be reliable indicators of leakage potential, particularly in the overburden formations above the seal and reservoir. This is an area often neglected in modelling studies that tend to concentrate on the CO_2 reservoir capacity and seal/caprock integrity, in line with conventional hydrocarbon industry practices. Seismic anomalies associated with hydrocarbon and CO_2 seeps have been reported from many areas of the world including extensive areas of the North Sea (Andreassen, 2007; Cartwright, 1994; Cartwright *et al*., 2007; Gay *et al*., 2006; Heggland, 2005; Hurst *et al*., 2003; Judd & Hovland, 2007; Ligtenberg, 2003, 2005; Nunn & Meulbroek, 2002; Walraven, 2005; Xie *et al*., 2003). The sub-seabed geology of the North Sea province has also been subjected to tectonic forces and ice loading/unloading processes over geological time that probably contributed to, or further enhanced the formation of fluid migration pathways.

- To improve the understanding of CO_2 flow modelling in the sub-surface and provide more accurate predictions for future basin modelling and simulation work. We create high resolution 3D models of Sleipner for a range of plausible scenarios, populate with relevant geological and structural information, test the effects of the prevailing transport mechanisms and develop a screening methodology that could be adopted for future feasibility/development studies.

To achieve these aims, the research objectives are outlined as follows:

- Examine technical literature to gain an understanding of the physical and chemical processes relating to CO_2/fluid/rock interactions, how these affect fluid migration processes and the ability to accurately model CO_2 flow and retention in the sub-surface.
- Assess existing CO_2 basin models and data held at The University of Edinburgh, identify any shortcomings and improve as required with additional data if available and relevant.
- Use high-resolution basin modelling software (Petrel® and MPath®) in conjunction with seismic interpretations and petrophysical data from Sleipner to create and populate the models respectively, calibrate then investigate/quantify migration and leakage processes (e.g. to simulate a leaking storage facility).
- Test the conceptual models, history match against existing data and compare with other models (sensitivity analysis). Garner information about processes and physical parameters (e.g. PVT), to calibrate and validate future models.
- Re-iterate the process as required to develop stable models and a robust screening methodology. Results will hopefully improve prediction accuracy and public confidence in future storage facilities. With specific reference to the Sleipner CO_2 storage facility, Nooner *et al.* (2007) suggest that robust modelling simulations must be able to:
    - Accurately reproduce CO_2 plume/layer morphologies observed on seismic monitoring data,
    - Match injected volumes of CO_2,
    - Match measured seismic and gravity anomalies.

  In monitored areas, it is proposed that any leakage past a seal/caprock should be detected by retarded growth or shrinkage of the uppermost CO_2 layers (Neufeld *et al.*, 2009; Chadwick & Noy, 2010) and the formation of gas chimneys in the overburden; both of these processes should be detected by seismic and gravity monitoring.

1.7 Thesis Structure:

This thesis is comprised of five chapters, with an introductory chapter, three chapters compiled as separate technical papers and a final chapter incorporating a summary, research conclusions and proposals for future work. The contents of the three technical papers (chapters 2-4) are briefly described as follows:

- Chapter 2 begins with a description of the regional geology and stratigraphy in the Sleipner CO_2 storage site vicinity, situated in the South Viking Graben area of the North Sea (Block 15/9 of the Norwegian sector). Using a 3D seismic dataset (acquired prior to CO_2 injection) correlated with well logs and drilling reports, we describe our seismic interpretation methodology and use of Petrel® for this phase of the research. We demonstrate that the Sleipner overburden contains a complex "plumbing" network, with evidence of palaeo-gas migration structures at various levels, in addition to sand-filled glacial tunnel valleys and channels within a few hundred metres of the seabed. Collectively, these features may form potential migration pathways or provide secondary storage for CO_2 if it leaks from the storage formation. We suggest that overburden formations above the storage site have leaked natural gas over geological time, thus if migrating CO_2 within the storage site encounters and re-uses any of these relict pathways, there is a risk of CO_2 leakage into the overburden,
- Chapter 3 defines what is meant by a palaeo-gas migration pathway and describes how these features could adversely affect successful long-term CO_2 storage in the sub-surface below the North Sea. We assess whether it is possible for migrating supercritical and gaseous CO_2 to re-use palaeo-gas migration pathways as preferential bypass routes through the caprock and overburden using Sleipner as a case study. We further consider the effects of parameter uncertainty on the CO_2 migration process using a series of risking scenarios. These are based on phase saturations, pressure, temperature, density, viscosity, interfacial tension (IFT) and wettability conditions likely to be encountered at depths commensurate with the Sleipner caprock. Finally, using end-point column height scenarios we evaluate the critical column heights required for capillary entry into these pathways under a range of storage conditions for both a CH_4/brine and CO_2/brine system (assuming the original pathways predominantly contain methane gas),

- Chapter 4 describes the process by which we constructed high-resolution 3D models of the Sleipner storage site and overburden. These range in complexity from simple "layer-cake" models, to heterogeneous lithological models populated with geological, stratigraphic and structural information derived from the earlier seismic interpretation work (previously described in Chapter 2). We demonstrate the sensitivity of CO_2 migration below the caprock to structural influences that can be distorted by incorrect time/depth conversions using a simple "fill-spill" analysis. A series of 3D flow simulations performed in MPath® are then calibrated to published data and matched to the present-day plume distribution. This provides a base case scenario for modelling whether the trapped CO_2 plume may encounter the identified palaeo-gas migration pathways and to evaluate the potential for flow along these pathways.

Chapter 2:

Overburden architecture and palaeo-fluid migration indicators above the Sleipner CO_2 storage site

Grant Nicoll[1], Andrew Cavanagh[2], Sebastian Geiger[3] and Stuart Haszeldine[1]

[1]The University of Edinburgh, Edinburgh, Scotland.
[2]The Permedia Research Group Inc., Ottawa, Canada,
[3]Heriot-Watt University, Riccarton, Edinburgh, Scotland.

"While you're strolling down the fairway showing no remorse
Glowing from the poisons they've sprayed on your golf course
While you're busy sinking birdies and keeping your scorecard
The devil's been busy in your back yard

Steaming down the highway with your trucks of toxic waste
Where you gonna hide it in the outer space?
You don't know what you're doing or what you have to guard
The devil's been busy in your back yard

Sometimes you think you're crazy but you know you're only mad
Sometimes you're better off not knowing how much you've been had…"

Extract from "The Devil's Been Busy in Your Back Yard" (The Travelling Wilburys, 1990)

2.1 Introduction:

The Sleipner CO_2 storage site is situated in Norwegian Block 15/9 of the North Sea and contains ~12 Mt of CO_2 separated from natural gas extraction at the Sleipner Vest (West) hydrocarbon field (Figure 2.1). Supercritical CO_2 has been injected since 1996 at a rate of approximately 1 Mt (1 x 10^6 tonnes) per annum (equivalent to 2,750 tonnes/day or 32 kg/sec) into the Utsira Formation at a depth of 1012 m via a highly-deviated well 15/9-A-16, drilled from the Sleipner A facility (Korbøl & Kaddour; 1995; Baklid *et al.*, 1996; Hansen *et al.*, 2005).

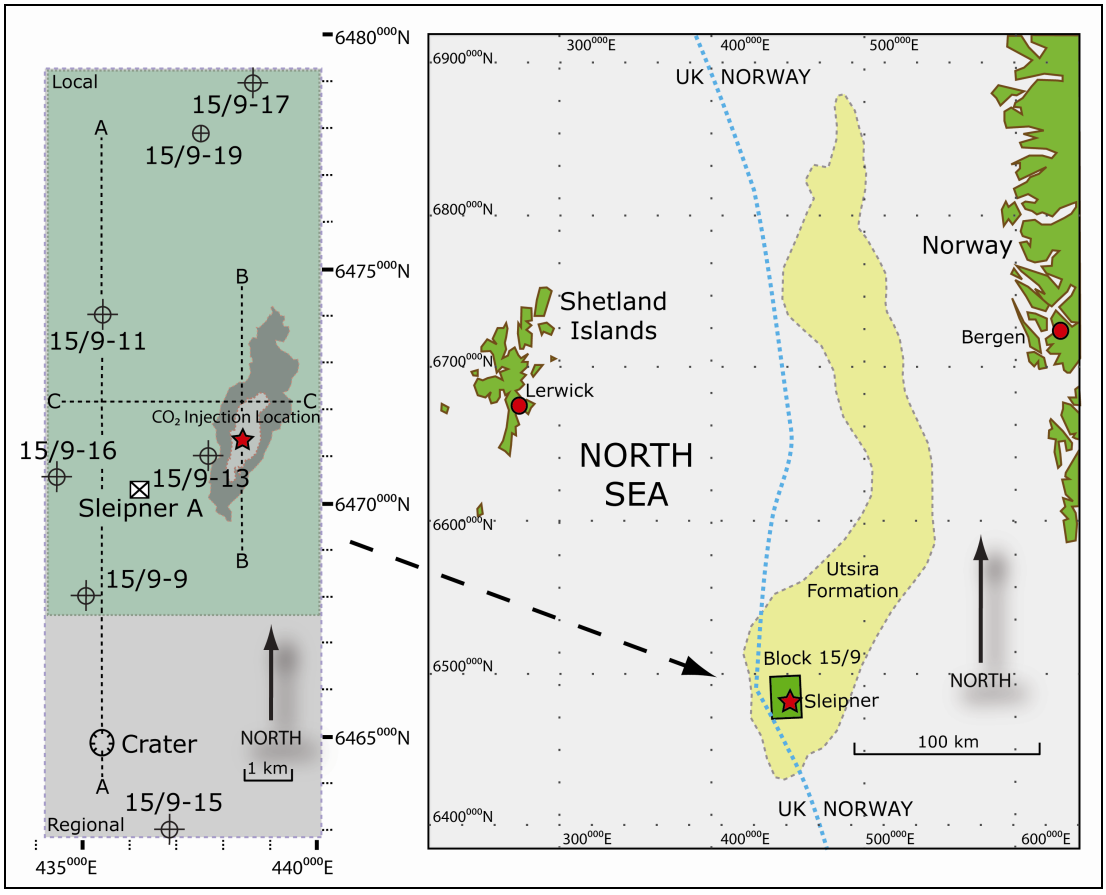

Figure 2.1: Location map for the Sleipner storage site, offshore Norway (right) with the sub-seabed areal extent of the Utsira Formation depicted by orange shading. Inset (left) shows the 3D seismic data coverage for the regional (grey) and local (green) study areas and locations of cross-sections, wells, the Sleipner A facility and a seabed crater described in this chapter. The areal extent and continued growth of the CO_2 plume is also depicted for 1999 (light grey) and 2008 (dark grey) - modified after Hermanrud et al. (2010).

Seismic data reveals evidence of palaeo-fluid migration structures, tunnel valleys and glacial channelling within sedimentary sequences overlying the Utsira Formation. To investigate these features and their potential as CO_2 migration pathways above the Sleipner storage site we correlate 3D seismic survey data of 1994 vintage (i.e. acquired prior to CO_2 injection) with well logs, drilling reports and related studies from the Sleipner area.

This study of the Hordaland and Nordland sedimentary sequences at the Sleipner storage site includes a regional (16.5 x 5.7 km) overview using a time to depth converted 3D seismic cube (from the ST9407 survey) supplied by the British Geological Survey (BGS). A local (11.5 x 5.6 km) focussed investigation was also performed encompassing the CO_2 plume, exploration wells 15/9-9, 15/9-11, 15/9-13, 15/9-16, 15/9-17, 15/9-19 and the injection location for the CO_2 injection well 15/9-A-16 (Figure 2.1). Seismic interpretations were performed using Petrel® software. Mapped surfaces were verified against drilling reports and well log data from the Norwegian Petroleum Directorate (NPD, 2010) and published horizon depths and seismic characteristics (Lothe & Zweigel, 1999; Zweigel *et al*., 2000; Carlsen *et al*., 2001).

Well log motifs and symbols used in figures are based on the Shell Exploration & Production Standard Legend (1995). Similarly, unless explicitly stated otherwise, all depths referred to in the text, figures and tables are Total Vertical Depth Below Mean Sea Surface (TVDSS).

2.2 Geological Setting and Stratigraphic Framework:

The Neogene and Quaternary geology and stratigraphy for the Sleipner area are extensively documented by a number of authors (Sejrup *et al.*, 1987, 1991; Isaksen & Tonstad, 1989; Gregersen *et al.*, 1997; Eidvin & Rundberg, 2001, 2007; Bauer & Fichler, 2002; Galloway, 2002; Fichler *et al.*, 2005; Chadwick *et al.*, 2004; Head *et al*., 2004; Zweigel *et al.*, 2004a; Gregersen & Johannessen, 2007). The Sleipner area is proximal to the UK/Norway median line, thus reference to published material from the UK sector is also useful from a regional perspective (Johnson *et al.*, 1993; Carr *et al.,* 2006; Graham *et al*., 2007; BGS Map Sheet 58N 00 Fladen (Quaternary), 1988).

NOTE: a reclassification of the Pliocene to Pleistocene boundary (affecting **all** of this cited material) was accepted by the International Commission on Stratigraphy during 2009/2010, by which the Gelasian stage (formerly in the late Pliocene) was reclassified as early Pleistocene (details are outlined in Gibbard & Head, 2010). This is particularly significant for this study since the overburden formations at Sleipner (formerly regarded as late Pliocene to Holocene) are now revised as Pleistocene to Holocene in age.

The Utsira Formation (Figure 2.1) is a regionally extensive saline aquifer deposited as a shallow marine sand with interbedded muds during the Miocene to late Pliocene, forming a 200-300 m thick sequence at the storage site (Head *et al*., 2004; Zweigel *et al*., 2004a). Mudstone-dominated sediments of the Hordaland Group (Eocene to late Miocene) underlie the Utsira Formation. Top Hordaland Group is interpreted as a regional unconformity (Løseth *et al*., 2003). Overlying marine and glacial sediments of the Nordland Group were deposited in a deep to shallow marine transitional environment (Pleistocene to Holocene) and form the overburden (Head *et al*., 2004).

The overburden is categorised as three seismic stratigraphic units in the Sleipner area (Gregersen & Johannessen, 2007), with further sub-divisions suggested by Heggland (1997) and Bøe & Zweigel (2001); we employ all of these stratigraphic units in our interpretation (Figure 2.2). Additional units are included for the shallower Pleistocene to Holocene sequences to capture anomaly-rich horizons, glacial channelling and inter-glacial depositional sequences.

Seismic stratigraphy is based on regional interpretations from the UK and Norwegian sectors (Boe & Zweigel, 2001; Bauer & Fichler, 2002; Fichler *et al*., 2005; Graham *et al*., 2007; Stewart *et al*., 2007), correlated against well logs and drilling reports (NPD, 2010).

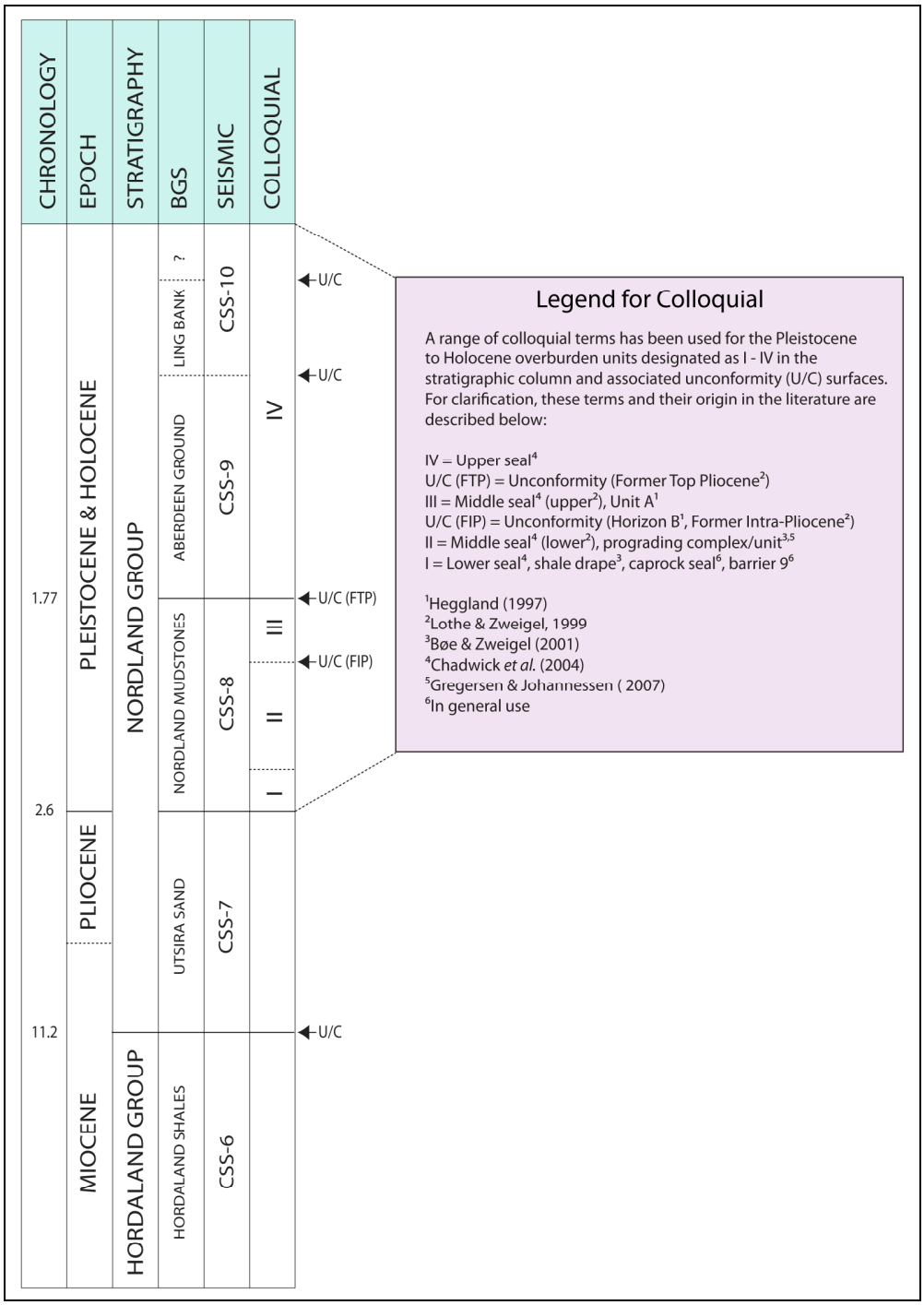

Figure 2.2: Neogene and Quaternary stratigraphy and chronology (Ma) for the Sleipner area (after Jordt et al., 1995; Head et al., 2004; Gibbard and Head, 2010).

2.2.1: Detailed Stratigraphy for the Sleipner Area:

The mid-Miocene Hordland Group Shales (~12-15.5 Ma) underlie the Utsira Formation and are characterised by polygonal faulting, soft sediment deformation and mud diapirism, similar to the features described by Cartwright (1994); Berndt *et al.* (2003); Stuevold *et al.* (2003) and Jackson & Stoddart (2005), for contemporaneous North Sea formations offshore Norway. Mud diapirs up to 100 metres high and ~1-2 km in diameter in the Sleipner vicinity are onlapped by the Utsira Formation, creating thickness variations on a local scale; there is also evidence of erosion prior to deposition of the Utsira Formation and the Hordland/Nordland interface is generally regarded as a regional unconformity (Løseth *et al*., 2003; Chadwick *et al.*, 2004; Zweigel *et al.*, 2004a; Jackson & Stoddart, 2005).

The late mid-Miocene to late Pliocene Utsira Sand (~2.5-12 Ma) is described as the main seismically resolvable sand unit within the Utsira Formation in the Sleipner area (Head *et al*., 2004). It is generally defined as a basin-restricted sand of marine origin, interbedded with over 10 thin shale units of average thickness ~1.3 m, interpreted from gamma-ray log peaks (Lothe & Zweigel, 1999; Zweigel *et al.*, 2000; Galloway, 2002). Sleipner is located at the main depocentre, where the formation thickness varies between 200-300 metres (Chadwick *et al*., 2004; Gregersen & Johannessen, 2007).

Near the top Utsira Formation a larger regional gamma-ray log peak has been correlated to a thicker shale unit described in the literature as the 5.0, 6.5 or 7.0 metre shale (Chadwick *et al.*, 2004; Zweigel *et al*., 2004a). The top of the Utsira Formation was originally thought to correspond to the base of this shale unit, but this interpretation was subsequently revised to account for a “sand wedge”, initially interpreted as a separate sand body disposed stratigraphically higher than the Utsira Formation, but now thought to be a younger, progradational intercalation of the Utsira Sand (Figure 2.3), according to Hamborg *et al.* (2003).

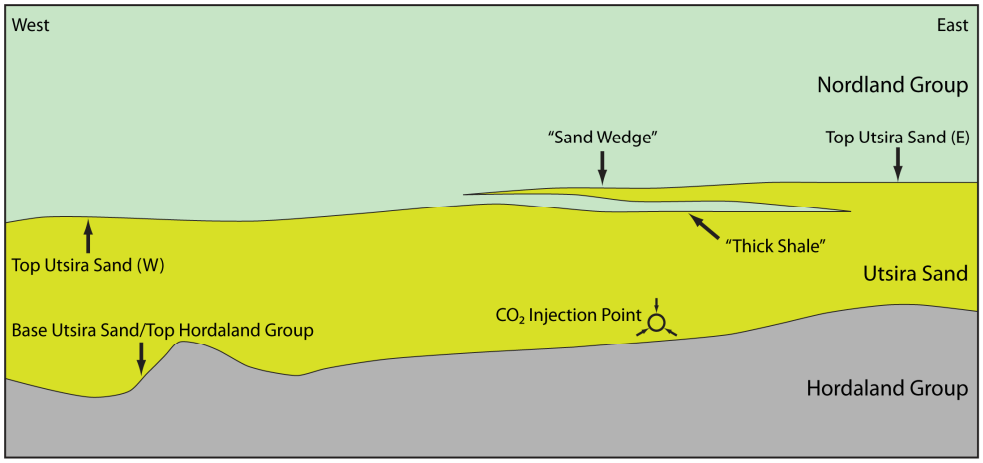

Figure 2.3 – Revised cross-sectional model (West to East) for the upper Utsira Sand (not to scale - modified after Hamborg et al., 2003).

The overlying Pleistocene (Gelasian) to Holocene sequence of Nordland Group Mudstones (~2.5-0 Ma) represents a deep water, transitional environment (Head *et al*., 2004). These sequences have been sub-divided stratigraphically into three seismic units for the southern depocentre around Sleipner by Gregersen & Johannessen (2007):

- The Shale Drape (or Lower Seal of Chadwick *et al*., 2004) is considered to be a basal surface for downlapping clinoforms from an overlying prograding sequence. It is described as a shaly unit between 50-150 metres thick, overlying the Utsira Formation and forming an overlap to the east and west (Chadwick *et al*., 2004; Zweigel *et al*., 2004a). In the Sleipner area this unit is 50 metres thick where the Sand Wedge is absent, but thins to less than 25 metres eastward where the Sand Wedge is present (Bøe & Zweigel, 2001). Based on marine palynomorphs and forminifera from well 15/9-A11, Head *et al.* (2004) date this unit to ~1.8-2.5 Ma (Gelasian) and consider it to represent a maximum flooding surface, deposited during a warm to cool transitional climatic phase,

- The Prograding Unit/Complex (or Middle Seal of Chadwick *et al*., 2004) is described as a series of clinoform units prograding from east to west into the basin centre and from within the basin towards the north. Shaly sediments dominate within the basin centre, but coarsen upwards and laterally into sandier facies towards the basin margins. Tectonic uplift of Scandinavia during the Neogene and sea-level decline due to glacio-eustatic processes are suggested as some of the major controls on progradation and increased sediment input during the mid-late Pliocene* (Gregersen *et al.*, 1997; Faleide *et al.*, 2002; Gregersen & Johannessen, 2007).

  (*Given the recent stratigraphic reclassification of Gibbard & Head (2010), this should now be regarded as Pleistocene – refer to earlier note on page 22).

  These clinoforms are considered to be potential migration pathways for CO_2, in the event of a seal failure, particularly within the sandier facies towards the basin margins (Bøe & Zweigel, 2001). This unit is further sub-divided by Heggland (1997) and Bøe & Zweigel (2001) into a lower unit (containing clinoforms) which is 100-150 metres thick in the Sleipner area, and an upper basin-restricted unit characterised by high amplitude seismic anomalies and higher velocity, density and resistivity log measurements compared to overlying and underlying units; this upper unit is 70-100 metres thick in the Sleipner area, but locally varies up to 129 metres thick (Figure 2.4),

- The remaining Pleistocene to Holocene unit (or Upper Seal of Chadwick *et al.*, 2004) forms a basal regional unconformity, truncating the surface of the Prograding Complex/Unit and is predominantly comprised of glacial tills and glacio-marine clays, which show evidence of extensive channelling within a few hundred metres of the present day seabed (Bauer & Fichler, 2002; Fichler *et al*., 2005; Graham *et al.*, 2007). Attempts have been made by Sejrup *et al.* (1987, 1991) and Carr *et al.* (2006), to correlate this unit across the UK/Norway median line by matching 2D seismic data lines to geotechnical borehole data from the BGS Fladen core (200 m) 81/26 (UK) and Sleipner core (120 m) B2001 (Norway).

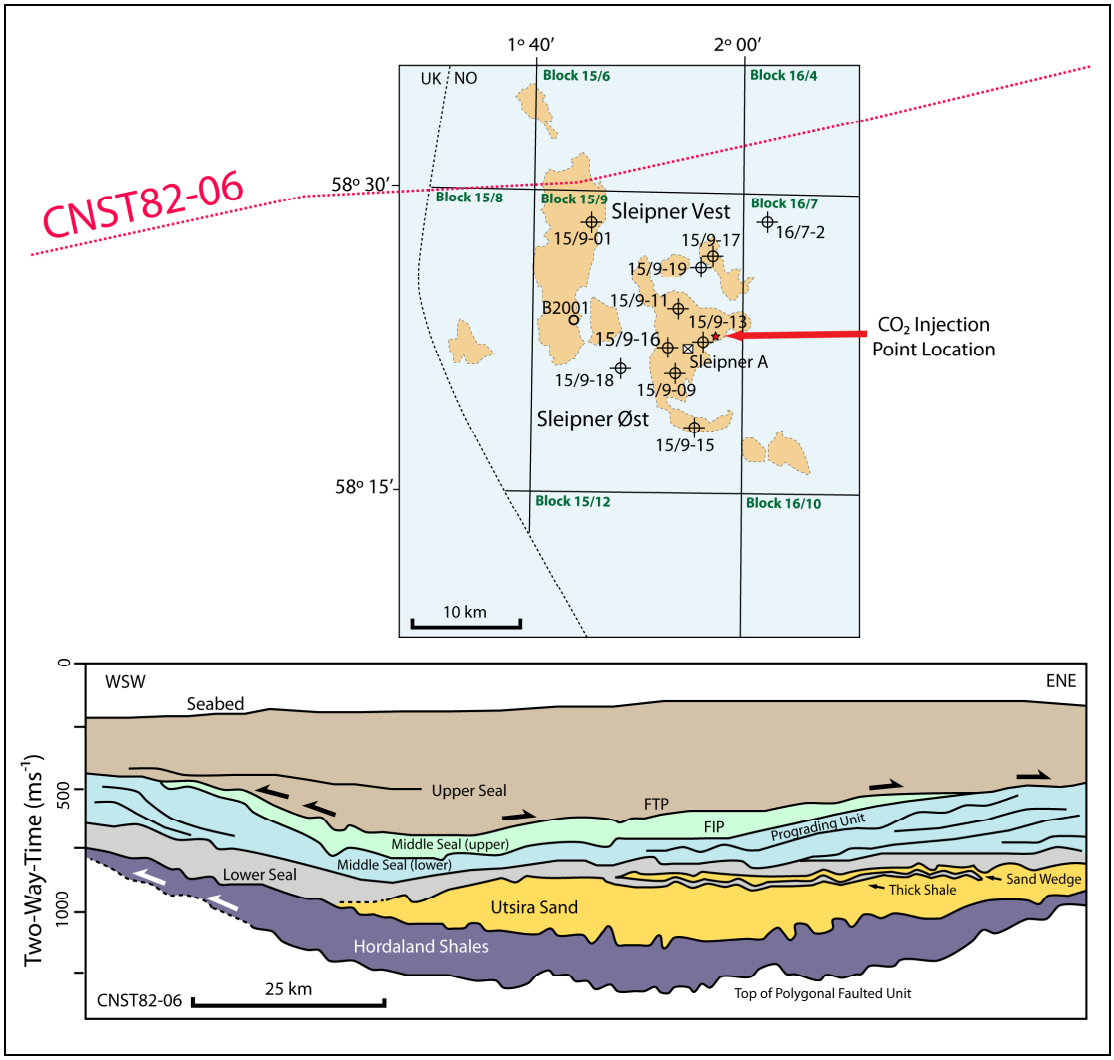

Figure 2.4: 2D seismic cross-section from survey CNST82-06 (lower), illustrating the regional disposition of the Utsira Sand and Nordland Group overburden. The abbreviations FIP = former intra-Pliocene and FTP = former top Pliocene. Location of the survey line in relation to wells and underlying hydrocarbon fields is displayed in the upper inset (modified after Bøe & Zweigel, 2001 and Zweigel et al., 2000).

2.3 Seismic Data:

The 3D seismic data used for this research pre-dates the CO_2 injection at Sleipner and is a post-stack, 4 byte (32-bit) time to depth converted volume generated from the ST 9407 survey (ED50, UTM Zone 31V) covering an area of 16.5 x 5.7 km and a depth range of 0-1500 metres. All seismic data images used in this chapter are SEG normal polarity, zero-phase (i.e. black or red peak represents an increase in acoustic impedance or "hard" event and a grey or blue trough represents an decrease in acoustic impedance or "soft" event). Frequency bandwidth is 10-70 Hz, with a dominant frequency of 40 Hz (Arts, 2000). Sample value format is IBM floating point, 501 samples per trace and 3 ms two-way time sample interval. Inline and crossline interval spacing are identical at 12.5 metres, with a clockwise rotation from North of 0.85 degrees for the survey grid.

Data was initially processed by Joe Bulat at the BGS (Edinburgh) using a velocity function between two-way time and average velocity to depth convert using Landmark's TDQ (Time Depth Quick) software (Table 2.1). The function was derived using a regression fit of the velocity/time pairs in three wells (i.e. 15/9-11, 15/9-13 and 15/9-20) from the survey area, within the two-way time range of 200-1500 ms (pers. comm. Joe Bulat, 2010).

Two-Way Time (milliseconds)	**Average Velocity (metres/second)**
0.0000	1695.0957
230.0000	1695.0957
532.0000	1837.1278
727.0710	1873.5802
812.0000	1885.6060
1022.0000	1910.1407
1325.0710	1938.3744
1507.0710	1953.1354
1599.9999	1960.2650

Table 2.1: Time-Velocity Function used to depth convert 3D seismic dataset

Although this function is comparable with similar time to depth conversion functions used by Arts (2000) and Zweigel & Hamborg (2002), these authors used different combinations of wells in their calculations. During the initial data quality control process our correlation with well logs and published horizon depths from Lothe & Zweigel (1999), revealed that although the horizons for the Top Utsira Sand and Top Hordaland Formation appeared to be located approximately at the correct depths, some of the key overburden horizons (e.g. FIP and FTP) were located at the wrong depth. Thus, further depth-depth corrections were applied in Petrel® using a two-stage workflow incorporating correction surfaces and well tops to ensure each key horizon was located at the correct depth, with the correct orientation. This two-stage process is described as follows:

- Key horizons (i.e. Seabed, FTP, FIP, Top Sand Wedge, Top Utsira Sand and Top Hordaland Formation) were interpreted and extracted from the original depth converted 3D seismic data using a combination of auto-picking and manual picking on a line by line basis. These surfaces were copied and the copies were manually adjusted to approximately the correct well top depths described in Lothe & Zweigel (1999). A new seismic cube was then generated using a depth-depth correction and (original) surface to (copied) surface velocity model (without well correction). Minor surface to well mis-ties in the order of a few metres +/- were noted in the new cube.
- A second velocity model was then applied to the new seismic cube to remove these minor well mis-ties. In this case, the velocity model used a surface to well top correction to generate the final seismic cube. Again, well tops were derived from surface depths published by Lothe & Zweigel (1999). This final 3D seismic cube was used as the basis for the final surface interpretations described in this chapter and further modelling work described in Chapter 4.

The final depth converted cube was also used to generate a range of different realised seismic volume attributes for interpretation purposes (as described in Chopra & Marfurt, 2005). The use of these post-processing techniques helped to improve resolution and clean-up stripes of vertical noise (also observed by Borgos *et al*., 2002 within the same dataset). These volumes included:

- Structural smoothing (dip guiding/edge enhancement enabled and filter setting of 1.5). This volume was used for most of the surface interpretation work.
- Chaos and Variance (inline/crossline filter setting 3, vertical filter setting 15). These were particularly useful in timeslice (z-plane) for better visualising the outline and internal structure of mud mounds, pockmarks, chimneys and lineaments.
- Relative Acoustic Impedance, Trace AGC, Graphic Equaliser (high and low band pass) and Second Derivative. These volumes helped with the visualisation of internal structure and interpretation of glacial channels, given the presence of strong seabed and channel multiples within a few hundred metres of seabed.

Based on the velocities in Table 2.1 and a dominant frequency of 40 Hz, vertical resolution for this 3D seismic data should be in the order of 10-12 m, based on the 1/4 of dominant wavelength relationship (Andreassen *et al.*, 2007).

2.4 Well Data:

Well logs were obtained from the Norwegian Petroleum Directorate (NPD, 2010) for exploration wells 15/9-09, 15/9-11, 15/9-13, 15/9-15, 15/9-16, 15/9-17 (no logs or other wellbore documents are currently available from the NPD for well 15/9-19). These wells are all contained within our regional study area (well logs have all been redrawn for clarity and summarised in a lithology/gamma ray format in Appendix 2.1). Drilling reports were also obtained from the NPD for exploration wells 15/9-01, 15/9-11, 15/9-18 and 16/7-02, some of which lie just outside our regional study area, but are still useful for correlation purposes. The nearest geotechnical borehole B2001 is located 12.93 km WNW of the injection point location (Figure 2.5), thus there is no reliable information for constraining the depths of the shallow Quaternary sediments or determining their composition other than by inference from work performed in adjacent areas by Sejrup *et al.* (1987, 1991), Johnson *et al.* (1993), Carr *et al.* (2006) and Graham *et al.* (2007).

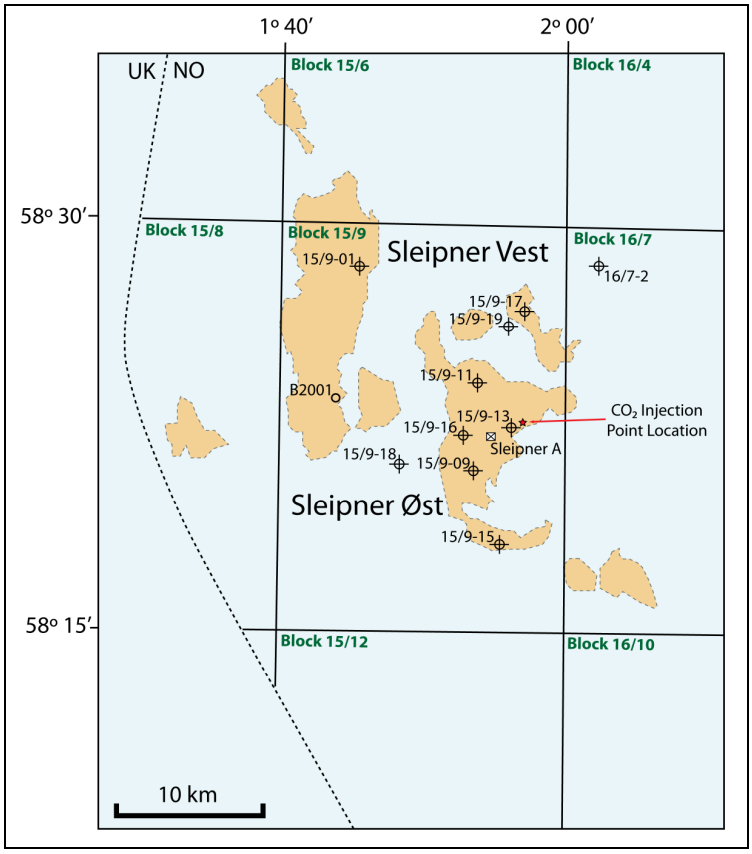

Figure 2.5: Well, borehole and facility locations in Block 15/9 and 16/7 Norwegian Sector, orange shading denotes extent of underlying hydrocarbon fields (modified from Zweigel et al., 2004a).

Surface depths for key wells are presented in Table 2.2. These depths were used to correlate against key reflections in the 3D seismic data and were also used in the additional depth-depth conversion process described in section 2.3. Original data were obtained from well logs and drilling reports available at the NPD (2010) and Appendix A from Lothe & Zweigel (1999):

Well	15/9-01	15/9-09	15/9-11	15/9-13	15/9-14	15/9-15	15/9-16	15/9-17	15/9-18	15/9-19
Seabed	106	83	88	81	102.5	83	85	86	100	85
FTP	520	577	548	566	575	632	575	547	604	N/A
FIP	N/A	660	656	659	N/A	700	655	676	683	N/A
TSW	N/A	818.99	800.02	821.95	N/P	858.54	N/P	809.94	N/P	817.5
BSW TTS	N/A	823	812	836.5	N/P	860	N/P	834.5	N/P	N/A
BTS TUS	798.99	830.5	818	844	900.98	867	817.85	840	842.37	N/A
BUS TH	1039.97	1066.98	1073.99	1028.95	1052.98	1111.54	1064.85	1022.93	1082.35	1034.21

Table 2.2: Well depths to key surfaces in the Sleipner area (NPD, 2010; Lothe & Zweigel, 1999).

Notes: *Abbreviations in table are described as follows, FTP = Former Top Pliocene; FIP = Former Intra-Pliocene; TSW = Top Sand Wedge; BSW/TTS = Base Sand Wedge/Top Thick Shale; BTS/TUS = Base Thick Shale/Top Utsira Sand; BUS/TH = Base Utsira Sand/Top Hordaland.*
N/P = Not Present; N/A = Not Available.

The drilling reports for wells 15/9-01, 15/9-18 and 16/7-02 provide detailed information about lithology derived from drill cuttings returned to surface and the presence of gas detected during drilling operations. Figures 2.6 to 2.8 show that for these wells, the highest amounts of gas (all methane) were recorded in the overburden sediments overlying the Utsira Formation. No gas was recorded in the drilling report for well 15/9-11 (within our regional study area).

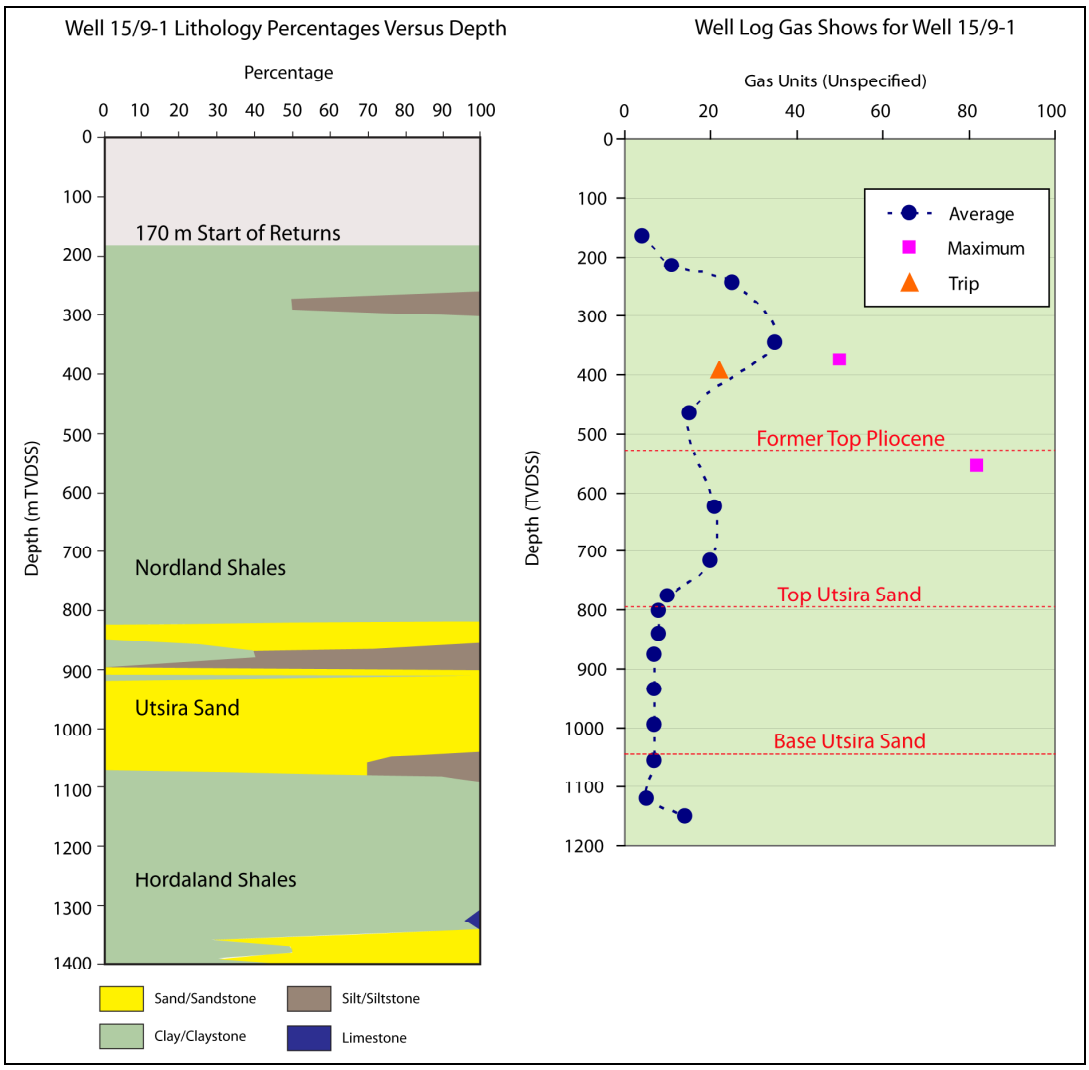

Figure 2.6: Lithology percentages and well log gas shows for well 15/9-01 (NPD, 2010)

(refer to Figure 2.5 for well location)

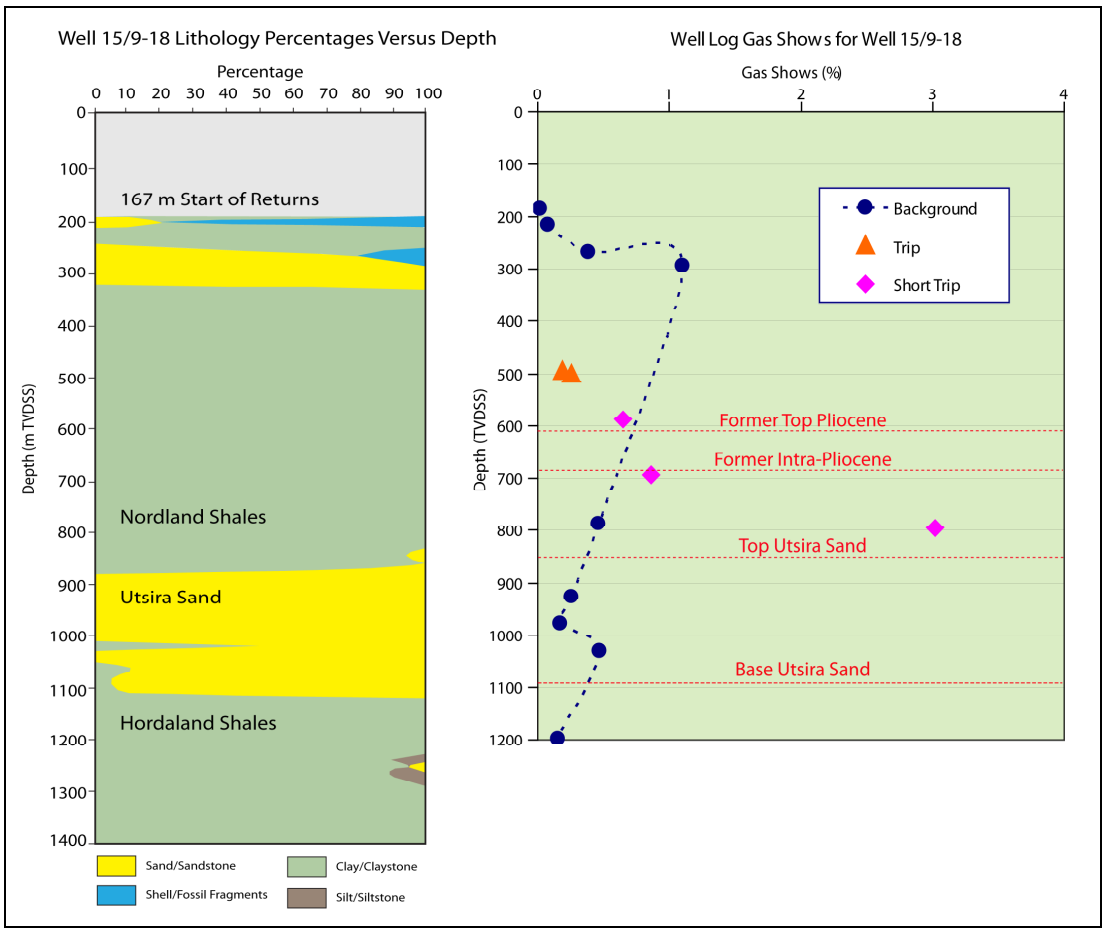

Figure 2.7: Lithology percentages and well log gas shows for well 15/9-18 (NPD, 2010)

(refer to Figure 2.5 for well location)

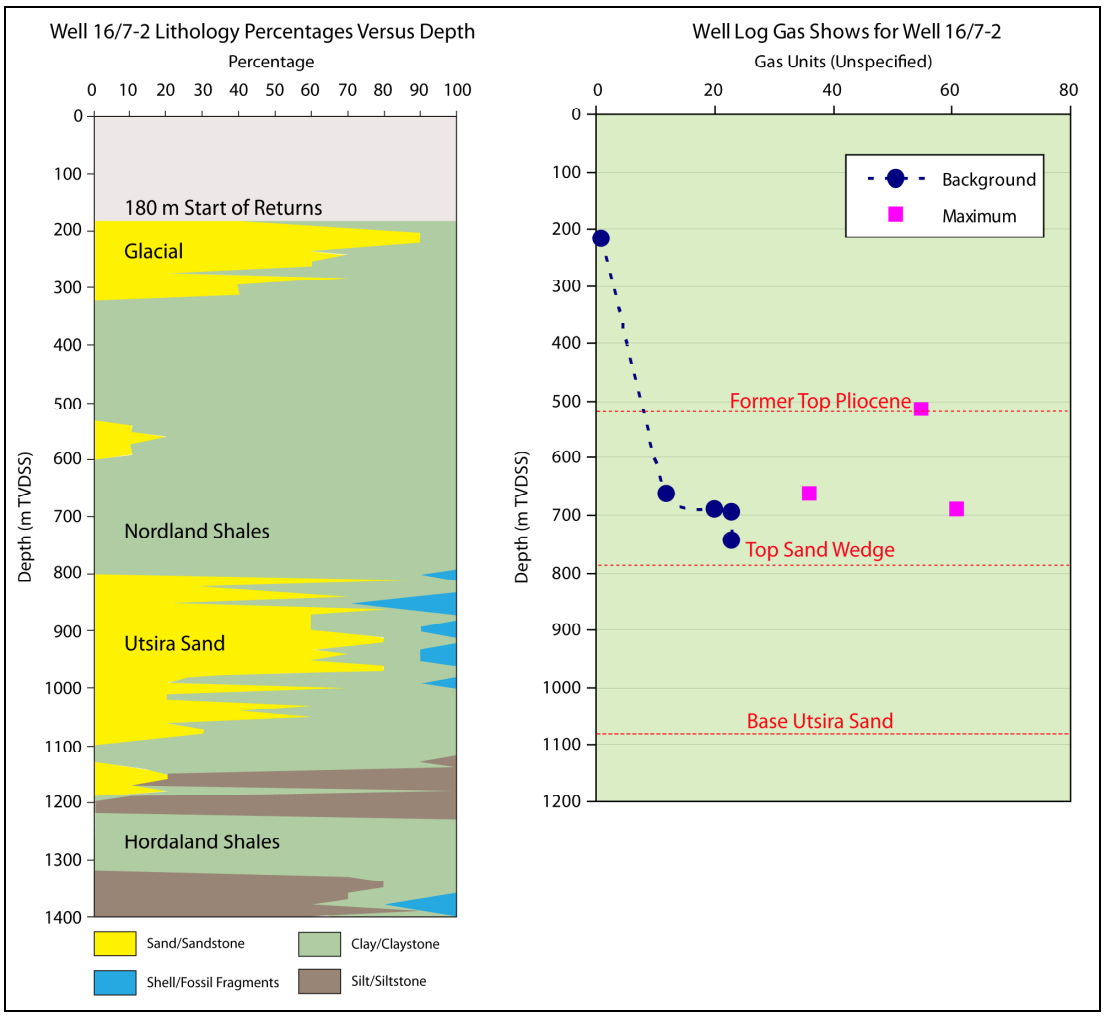

Figure 2.8: Lithology percentages and well log gas shows for well 16/7-02 (NPD, 2010) (refer to Figure 2.5 for well location)

Notes: *Drilling report states that the degasser was not fully operational until ~500m TVDSS*

Figure 2.9 demonstrates how well logs were correlated to seismic data, with key seismic horizons corresponding to strong peaks or troughs as indicated by coloured dashes on the seismic section. Well 15/9-11 penetrates the edge of a glacial channel as is evident from the lithology percentage diagram which shows a high percentage of sand, with secondary lithic fragments, lignite and minor shell/fossil fragments. The remainder of the overburden is predominantly clay-rich with the exception of an acoustically noisy interval between the FTP and FIP horizons that is silt-dominated, with secondary clays and sands. Note also the high percentage of shell/fossil fragments in the Utsira Sand for this particular well.

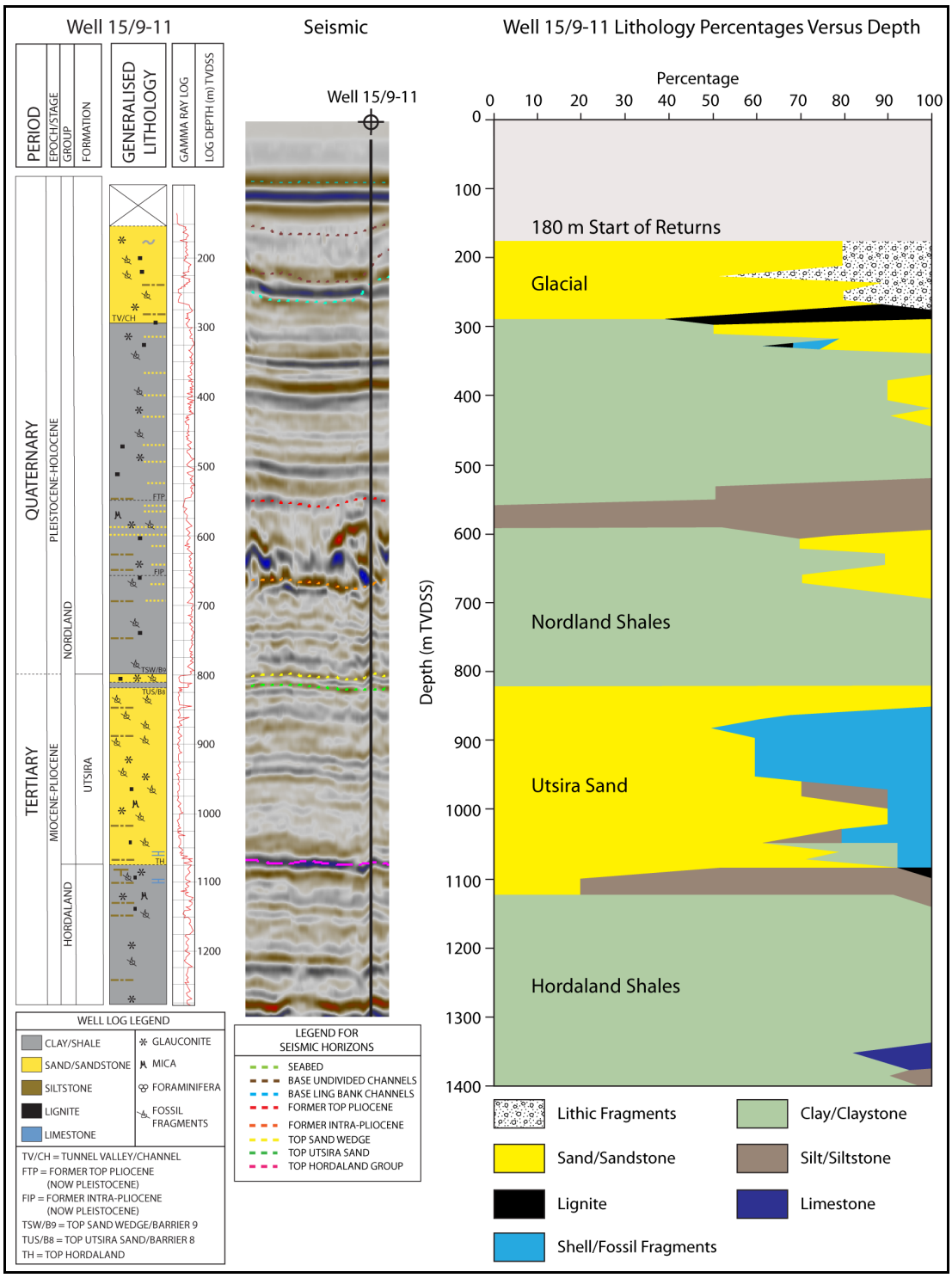

Figure 2.9: Well log data for well 15/9-11 (modified from NPD, 2010) scaled and correlated with an extract of seismic data from inline 1591 (7.5x vertical exaggeration) and lithology percentages (refer to Figure 2.5 for well location)

Notes: *Gamma ray log scale is 1-100 (100-200 wrapped) API and seismic section is ~1.2 km wide*

Another useful source of information obtained from the well reports is drilling mud weight and leak-off point test data that provide an indication of formation strength. These data are plotted on Figure 2.10 for all the wells in our regional survey area (except for well 15/9-19 since this data is currently unavailable at the NPD).

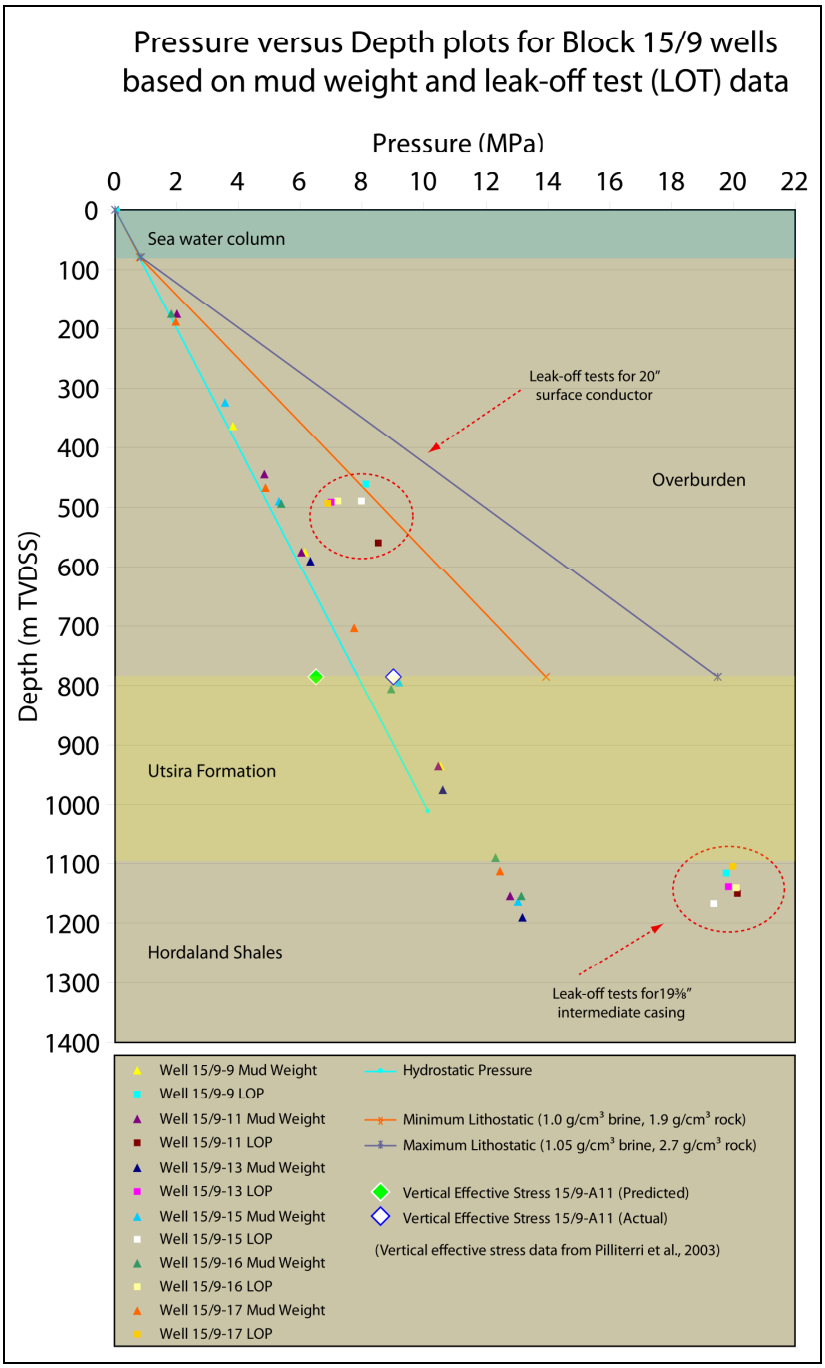

Figure 2.10: Pressure versus Depth plots for Block 15/9 wells within the regional survey area (data sourced from well completion reports NPD, 2010). Vertical effective stress measurements for a caprock sample from well 15/9-A-11 are also shown (data sourced from Pilliterri et al., 2003).

Mud weights on Figure 2.10 indicate that these wells were drilled with a slight overpressure (i.e. mud weight close to or slightly higher than hydrostatic). Two end point lithostatic gradients were calculated and plotted for comparison based on the methodology described in Pilliterri *et al.* (2003), using the range of brine and bulk rock densities described for the Nordland Mudstones in Pilliterri *et al.* (2003), Zweigel & Heill (2003) and Springer & Lindgren (2006). The leak-off test data for the overburden plots closer to the minimum gradient, suggesting weak consolidation and a low fracture gradient. Also overlaid are two effective stress measurements from Pilliterri *et al.* (2003), based on caprock samples (785 m TVDSS) from well 15/9-A11; these indicate that the actual effective vertical stress (determined by rock mechanical tests) is ~2-3 MPa higher than predicted by calculations for a range of comparable water/rock samples at this depth.

Only a single core sample of the Nordland Mudstone from well 15/9-A11 (drilled from the Sleipner A facility) has been obtained from the Sleipner area for biostratigraphic analysis (Head *et al.*, 2004), rock mechanical testing (Pilliterri *et al.*, 2003) and capillary entry pressure core flooding experiments (Springer & Lindgren, 2006; Harrington *et al.*, 2009). Other related analyses have either relied on this core sample or drill cuttings samples from other wells in the Sleipner area to determine mineralogy and estimate capillary entry pressures (Lothe & Zweigel, 1999; Bøe & Zweigel, 2001; Kemp *et al.*, 2002; Lindgren *et al.*, 2002).

2.5 Interpretation Methodology:

The 3D seismic data were interpreted using Petrel® version 2007/2008 software and seventeen surfaces were interpreted (mostly on a line by line basis) using a combination of auto and manual picking of seismic reflections from inlines and crosslines (Table 2.3). As previously described in sections 2.2 to 2.4, six of these surfaces (highlighted orange in Table 2.3) were selected on the basis of established regional stratigraphic correlations with well logs (e.g. Lothe & Zweigel, 1999). Additional surfaces were selected on the basis of reflection amplitude strength, morphology and to account for multiple glacial channelling episodes.

Surface Name	Polarity	Surface Depth Range (m TVDSS)
Seabed	Peak	70 to 99
Phase 3 Channels	Peak	118 to 178
Phase 2 Channels	Peak	127 to 246
Phase 1 Channels	Peak	187 to 297
400 m strong	Peak	363 to 401
Top Quaternary Siltstone	Peak	439 to 497
Quaternary Anomaly	Peak	501 to 565
Former Top Pliocene	Trough	530 to 584
Former Pliocene strong	Peak	552 to 692
Former Intra-Pliocene	Peak	598 to 764
700 m strong	Peak	700 to 783
Supra-Caprock Anomaly	Peak	753 to 826
Top Sand Wedge	Peak	788 to 853
Top Utsira	Peak	810 to 872
Top Hordaland	Trough	953 to 1162
Sand Injectites	Peak	1040 to 1316
Polygonal Faults	Peak	1235 to 1324

Table 2.3: Interpretation surface names, reflection polarity and depth ranges (local area)

Surfaces were created from the interpretation data at seismic grid resolution (12.5 x 12.5 m increment) using the Kriging algorithm (these surfaces were subsequently exported from Petrel® in Irap Classic Grid (ASCII) format as individual *.gri files to create a geo-cellular model using MPath® software as described in Chapter 4).

In addition to surface interpretation, the 3D seismic data was used to investigate the presence of faults, shallow gas and palaeo-gas migration indicators in the overburden (e.g. high-amplitude seismic anomalies, pockmarks and gas chimneys), using a range of interpretation and classification techniques as described by Heggland, 1997, 1998, 2005; Berndt *et al.*, 2003; Ligtenberg, 2005; Andreassen *et al.*, 2007; Cartwright *et al.*, 2007; Evans *et al.*, 2007; Andresen *et al.*, 2008 and Løseth *et al*, 2009. Based on these guidelines, the following interpretation strategy was adopted:

- High amplitude seismic anomalies in the overburden were extracted as geobodies from the 3D volume, categorised into groups between key surfaces, then analysed for connectivity, distribution and morphology,
- Faults and areas of vertical acoustic disturbance (e.g. reflection pull-up and pull-down, zones of chaotic reflections, columns of signal weakness and reflection discontinuity) were mapped on inlines and crosslines using polygons to determine their 3D extent. Each vertical expression was assigned an ID number and documented in an Excel spreadsheet (refer to Appendix 2.8) in terms of UTM location, inline/crossline intersection, root depth, termination depth, height, diameter, morphological description and any obvious association with other related seismic anomalies (e.g. reflection terminations, bright spots, lineaments, faults, polarity reversals, faults/diapirism in the underlying Hordaland Group),
- Time slices (Z) were also examined using a range of different attribute cubes for signs of pockmarks and lineations; these were also mapped using polygons.

Having completed this interpretation work, any spatial association between these mapped features and a potential fluid source was investigated. Results are reported in the following sections.

2.6 Seismic Anomalies:

Two categories of anomaly were identified and mapped within the regional and local study areas outlined on Figure 2.1: a) high-amplitude anomalies and b) seismic discontinuities.

Category a) anomalies are indicative of large acoustic impedance contrasts (bright spots) across sub-surface interfaces. These are characterised by either a "hard" reflection (a positive or red to yellow brightening for this 3D seismic data) indicating a transition into a zone of higher acoustic impedance (e.g. shale into carbonate-cemented horizon), or a "soft" reflection (a negative or dark to pale blue brightening for this 3D seismic data) indicating a transition into a zone of lower acoustic impedance (e.g. shale into gas-charged sandstone). In terms of reflection response, "hard" reflections create a pull-up effect, due to a faster two-way travel time, whereas "soft" reflections create a pull-down effect, due to a slower two-way travel time. Significant localised transitions (e.g. gas accumulations) should also be identified by their reversed polarity reflection characteristics.

The Nordland Group overburden contains four anomaly-rich horizons between 300-700 m depth below seabed (designated as horizons A-D on the left-hand side of Figures 2.11 to 2.13). The deepest horizon (D) is situated just above the Utsira caprock (~775 m), the shallowest horizon (A) is situated in the upper Pleistocene (~400 m), underlying glacial channels. These anomalies exhibit a mixture of convex (pull-up) and concave (pull-down) effects: the former effect may result from the presence of localised diagenetic cementation (e.g. from biodegraded hydrocarbons) or lag deposits (e.g. gravel or shell banks/coquinas), the latter effect is probably due to the presence of shallow gas accumulations. Positive high-amplitude anomalies in the 20-40 k range were extracted as 3D geobodies to assess morphology and connectivity, then assigned a letter/number designation based on the horizon in which they are located (e.g. D40 is the 40th. anomaly mapped in horizon D). Summary details of anomalies mapped within the local survey area are presented in Table 2.4 and anomaly maps for each horizon are presented in Figures 2.14 to 2.19.

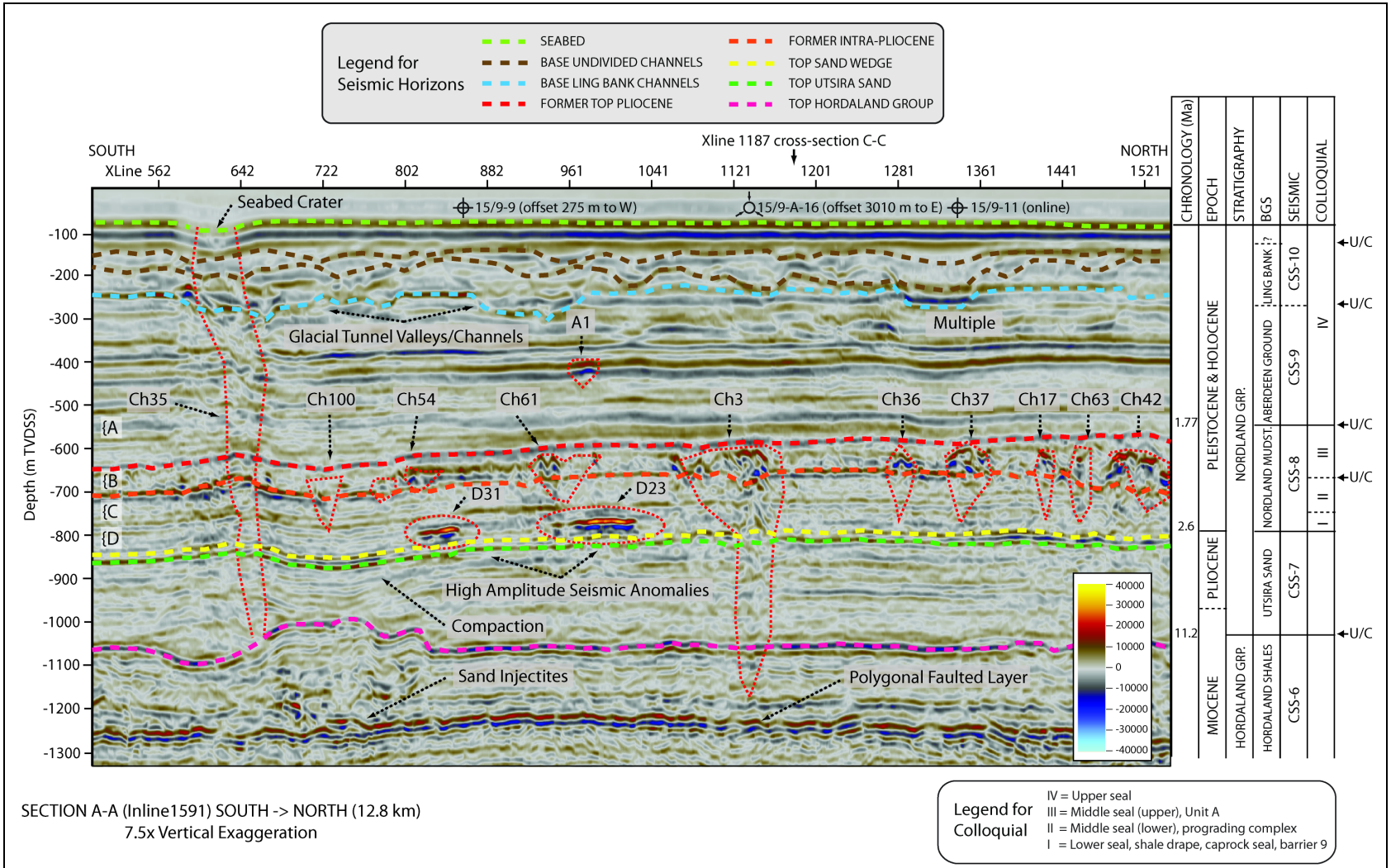

Figure 2.11: Seismic cross-section A-A based on inline 1591 from Figure 2.1 (inset shows range of seismic reflection amplitudes)

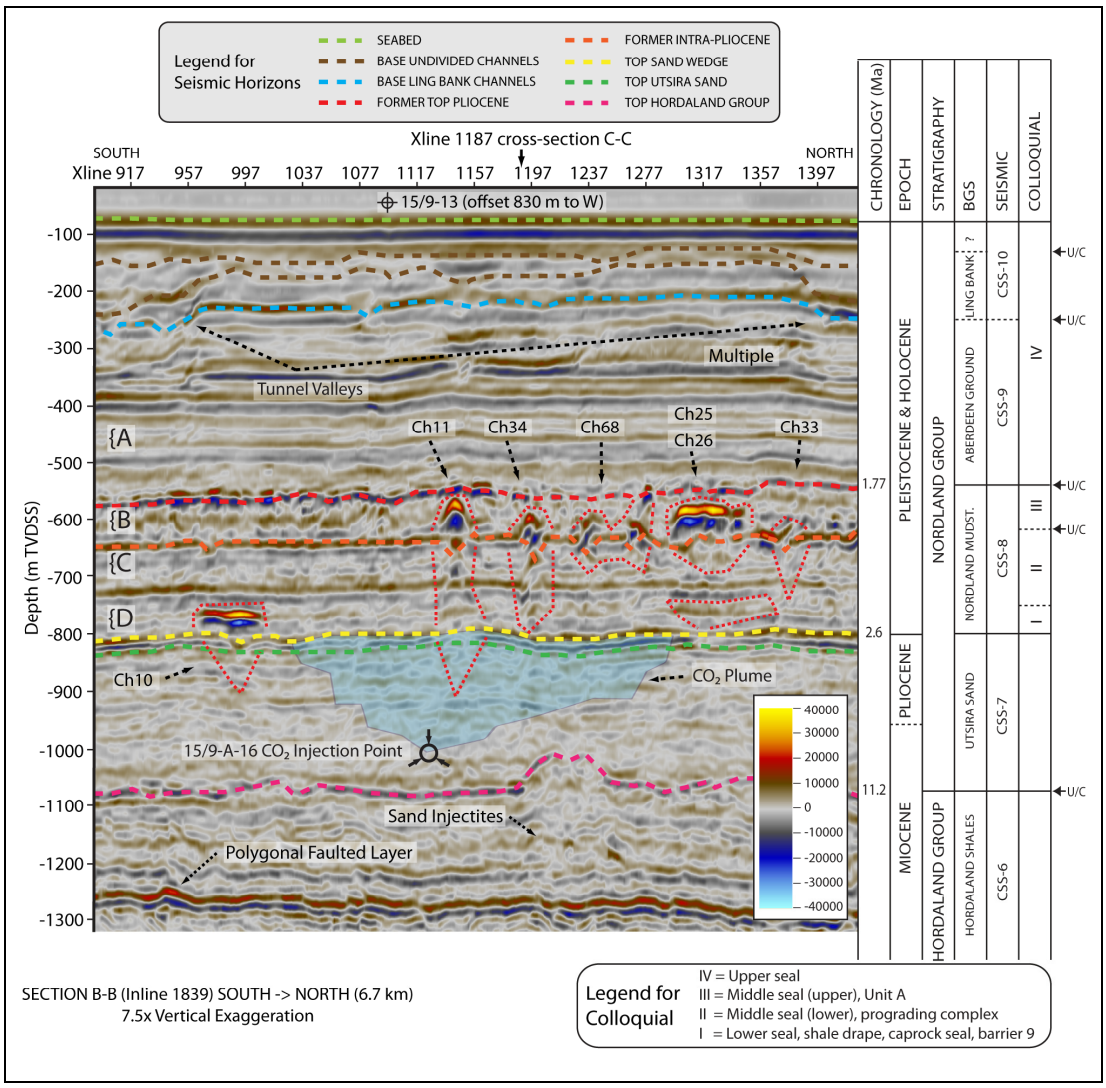

Figure 2.12: Seismic cross-section B-B from Figure 2.1, based on inline 1839

(inset shows range of seismic reflection amplitudes)

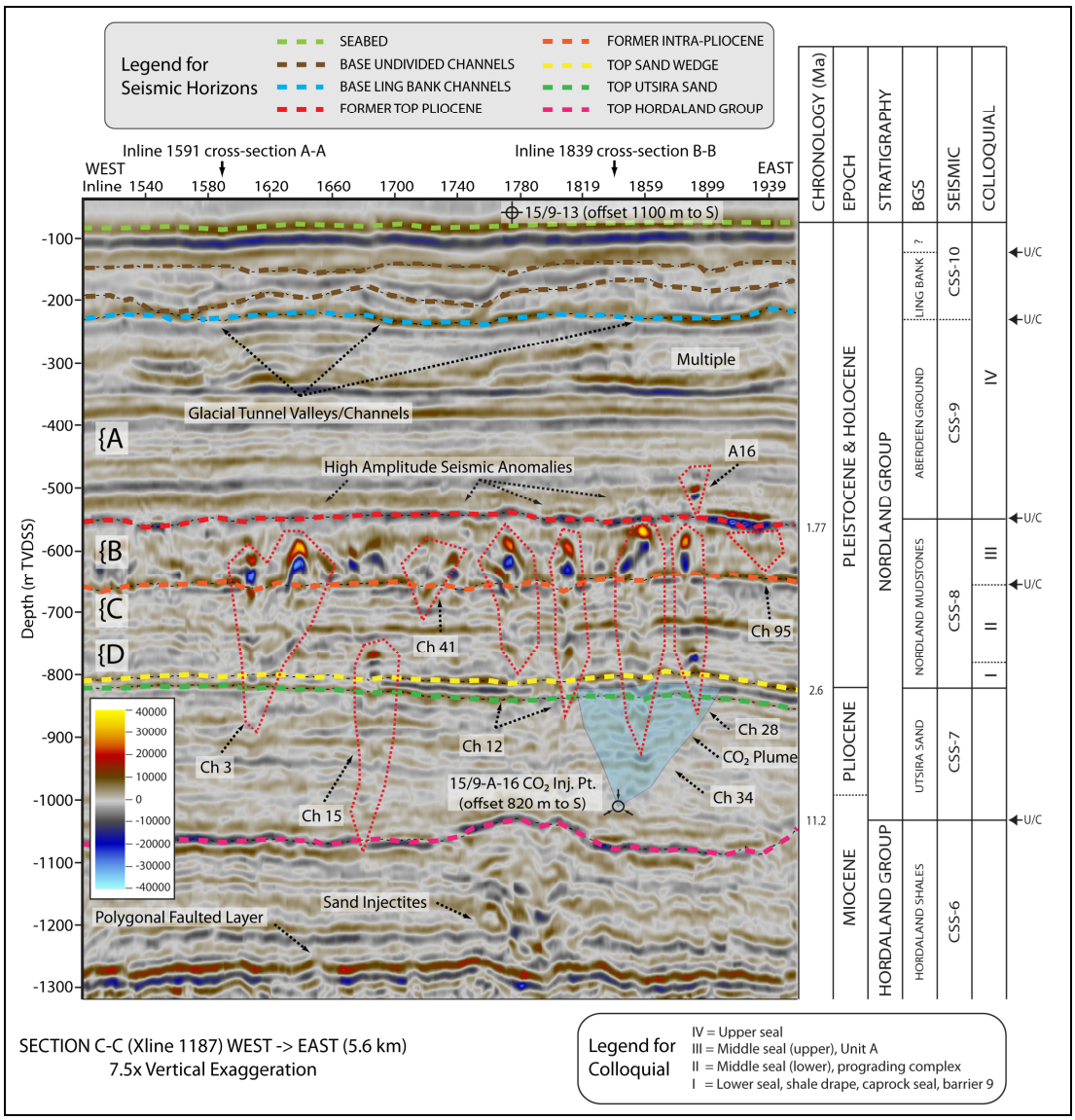

Figure 2.13 Seismic cross-section C-C from Figure 2.1, based on crossline 1187

(inset shows range of seismic reflection amplitudes)

Horizon (no. of anomalies)	Depth Range (m TVDSS)	Description	Notes
A (upper - 13) (refer to Figure 2.19)	~400	Elliptical, linear and circular anomalies 30-500 m long, overlying the 400 m Strong surface, mainly confined to NE corner and S. Weak NE to SW and NW to SE alignment for anomalies at the NE corner.	Low confidence? Possibly multiple enhanced reflections (artefacts) from overlying glacial channels?
A (middle - 24) (refer to Figure 2.18)	~500	Clusters of elliptical and crescent-shaped anomalies 10-150 m long overlying the Quaternary Anomaly surface, mainly confined to E, also appear to overlie the A (lower) anomalies.	Weakly associated with depressions (palaeo-pockmarks?) and channels/lineations on underlying FTP surface?
A (lower - 82) (refer to Figure 2.17)	~550	Confined mainly to E, particularly SE and NE corners, strong NE to SW alignment, interconnected ganglia up to 3.5 km long, also smaller clusters of 10-100 m diameter.	Associated with depressions and channels/lineations on underlying FTP surface?
B (676) (refer to Figure 2.16)	~530-765	Abundant, extensive and large interconnected ganglia up to 2 km wide, with flatter morphology in S, but more convex to N, with NW dipping clinoformal structure evident to the extreme NW. Weak NNE to SSW, NE to SW and NW to SE alignments.	Gas accumulations, diagenetic cements, lag deposits?
C (212) (refer to Figure 2.15)	~600-784	Clusters of elliptical anomalies associated with depressions on the 700 m strong and FIP surfaces, generally smaller, 10-50 m diameter, occasionally up to 100 m diameter. Largely absent in the NW and SE.	Possible escape structures, pull-down artefacts, noise from FIP to FTP horizon?
D (56) (refer to Figure 2.14)	~783-826	Large 100-900 m diameter in SW, central and NE, elsewhere from 10-100 m diameter. Absent in the NW and SE. Weak NE to SW and NW to SE alignment.	Possible relationship with underlying faults/lineations associated with edges of Hordaland mud mound structures?

Table 2.4: Summary description of high-amplitude seismic anomalies in horizons A-D

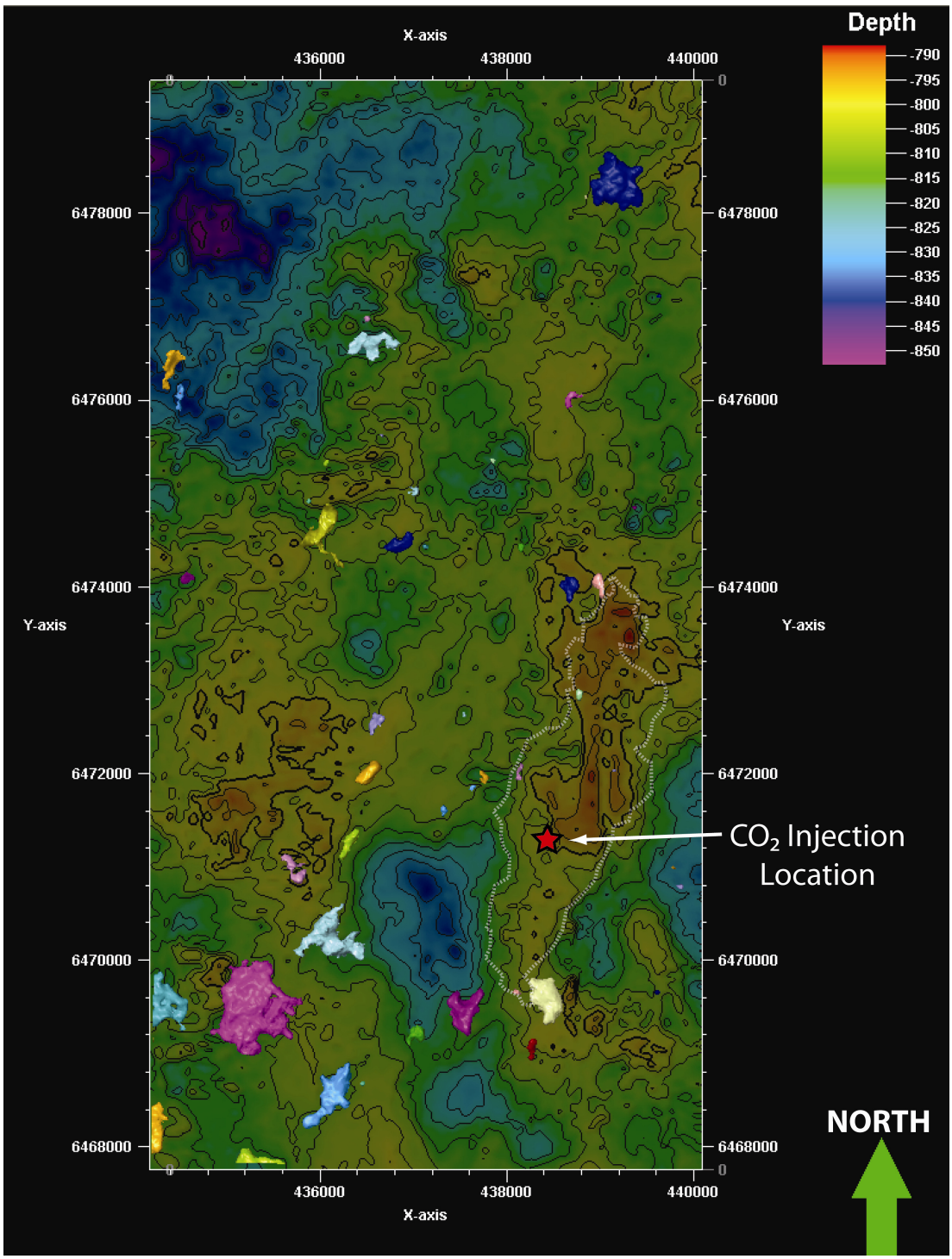

Figure 2.14: Petrel® anomaly distribution map for horizon D, overlaid against the Top Sand Wedge depth surface from Table 2.3. A 2008 CO_2 plume outline is displayed as a white dashed line. UTM 31V grid in 0.4 km increments. Note that individual anomalies are allocated an arbitrary colour scheme in Petrel® to assist with visualisation and interpretation. The Top Sand Wedge surface colour depth scale (top right) and map contours are displayed at 5 m intervals.

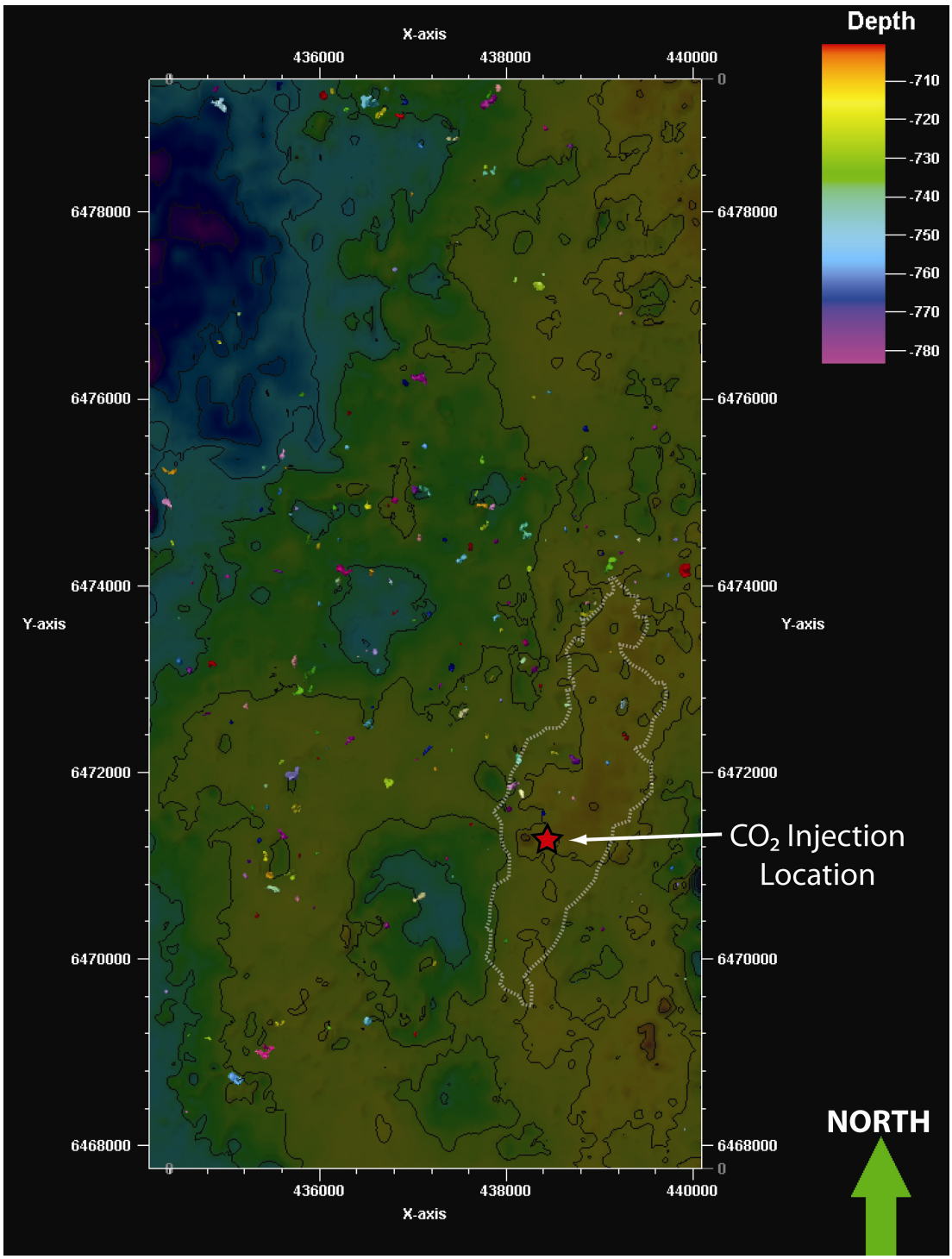

Figure 2.15: Petrel® anomaly distribution map for horizon C, overlaid against the 700 m Strong surface from Table 2.3. A 2008 CO_2 plume outline is displayed as a white dashed line. UTM 31V grid in 0.4 km increments. Note that individual anomalies are allocated an arbitrary colour scheme in Petrel® to assist with visualisation and interpretation. The 700 m Strong surface colour depth scale (top right) and map contours are displayed at 10 m intervals.

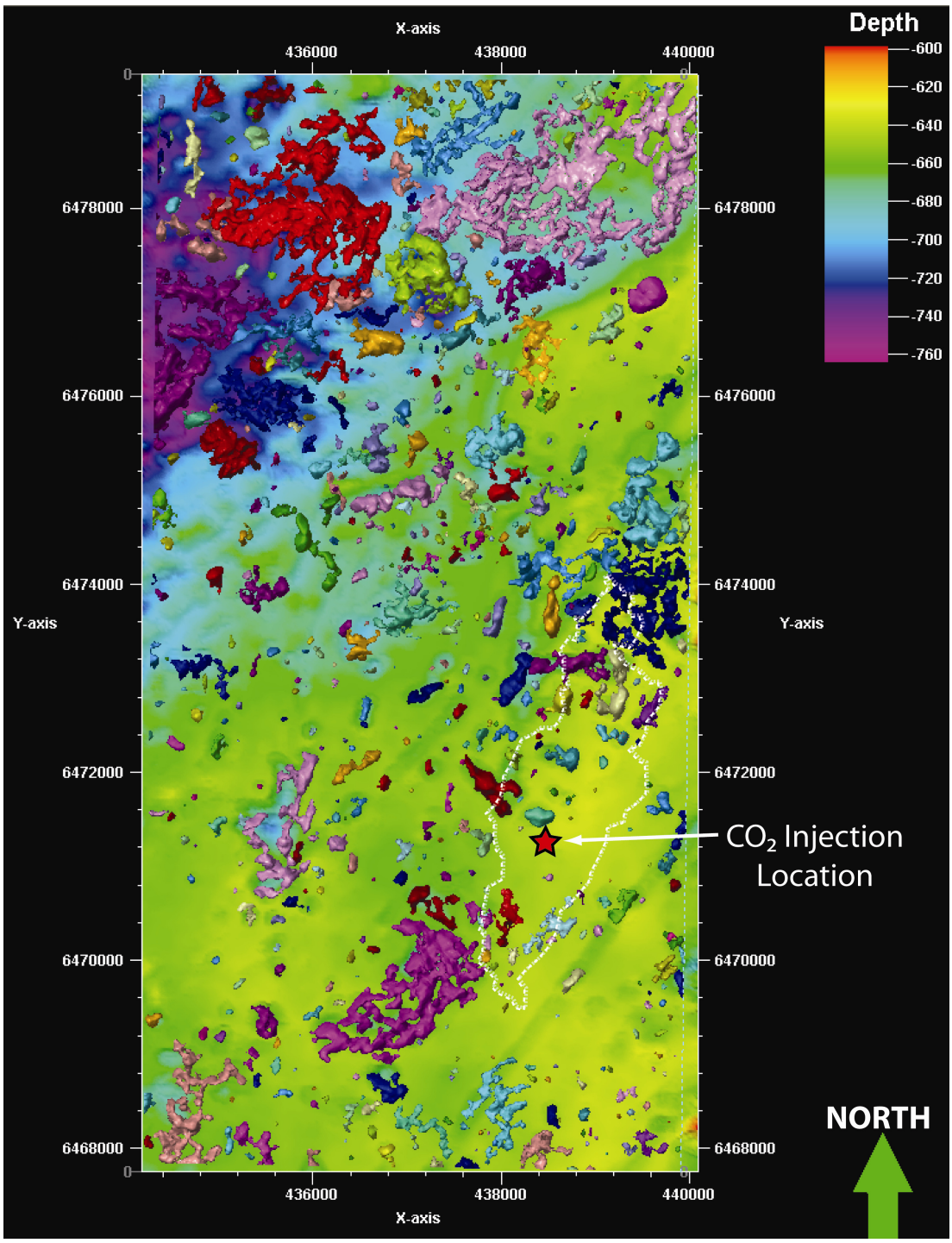

Figure 2.16: Petrel® anomaly distribution map for horizon B, overlaid against the Former Intra-Pliocene surface from Table 2.3. A 2008 CO_2 plume outline is displayed as a white dashed line. Some of these anomalies are partially intersected by wells 15/9-9, 15/9-11 and 15/9-17, which indicate the presence of sands or clays with sandy interbeds on well logs (Appendix 2.1). UTM 31V grid in 0.4 km increments. Note that individual anomalies are allocated an arbitrary colour scheme in Petrel® to assist with visualisation and interpretation. The Former Intra-Pliocene surface colour depth scale (top right) is displayed at 20 m intervals (in this case, contours are omitted for clarity).

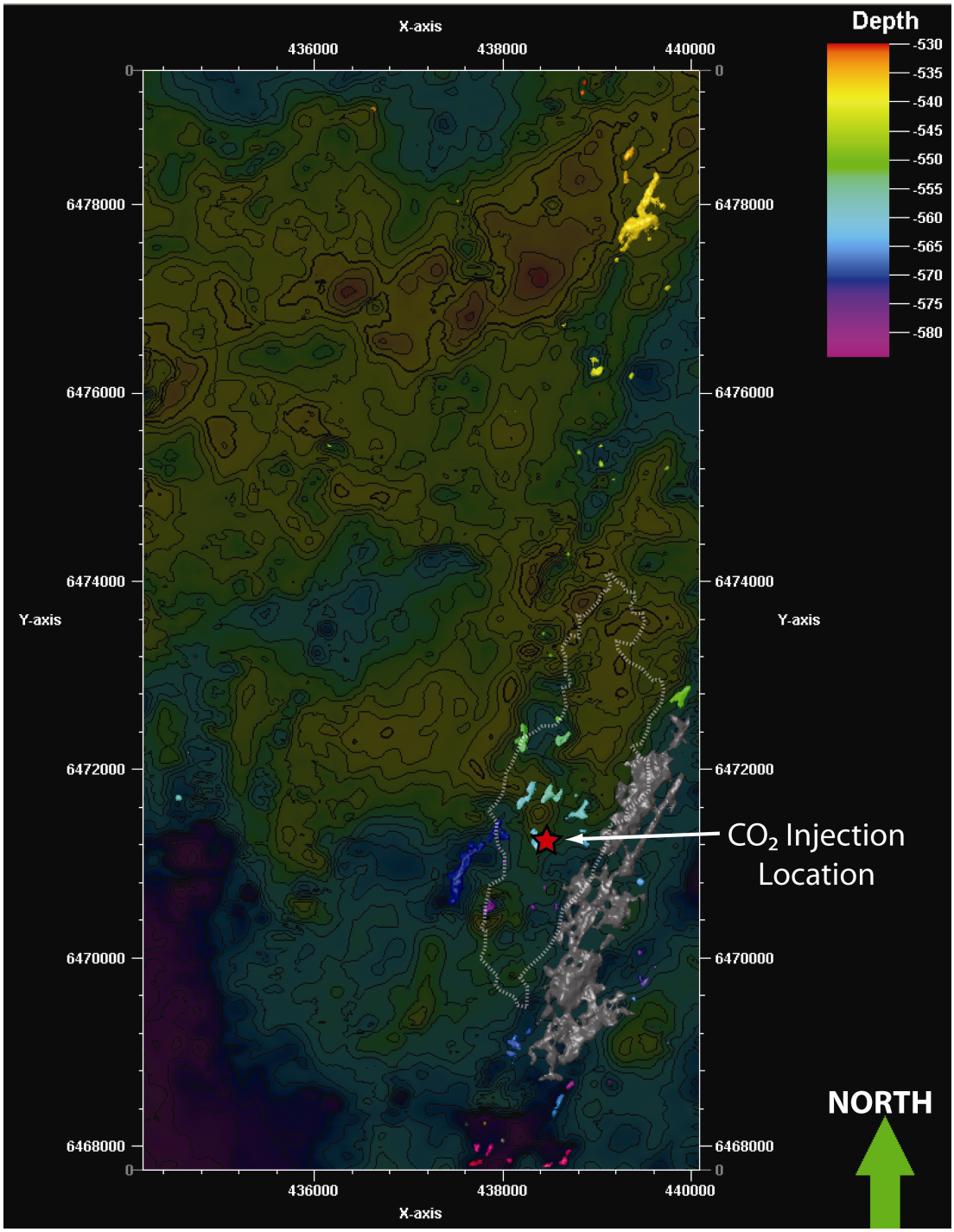

Figure 2.17: Petrel® anomaly distribution map for horizon A (lower), overlaid against the Former Top Pliocene surface from Table 2.3. A 2008 CO_2 plume outline is displayed as a white dashed line. UTM 31V grid in 0.4 km increments. Note that individual anomalies are allocated an arbitrary colour scheme in Petrel® to assist with visualisation and interpretation. The Former Top Pliocene surface colour depth scale (top right) and map contours are displayed at 5 m intervals.

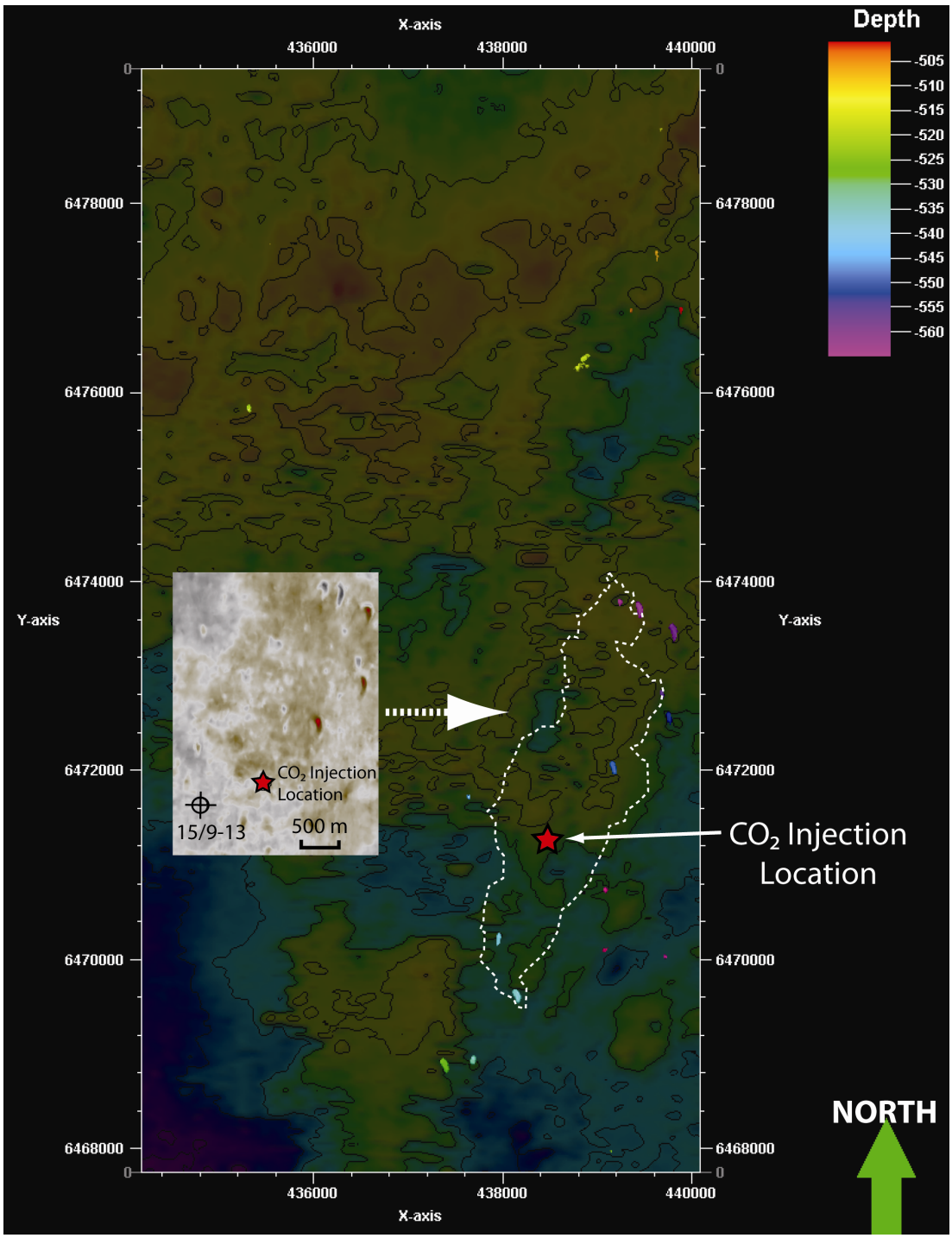

Figure 2.18: Petrel® anomaly distribution map for horizon A (middle), overlaid against the Quaternary Anomaly surface from Table 2.3. A 2008 CO_2 plume outline is displayed as a white dashed line. Inset shows extract from timeslice (Z) at -501 m with crescent-shaped anomalies (palaeo-pockmark remnants?). UTM 31V grid in 0.4 km increments. Note that individual anomalies are allocated an arbitrary colour scheme in Petrel® to assist with visualisation and interpretation. The Quaternary Anomaly surface colour depth scale (top right) and map contours are displayed at 5 m intervals.

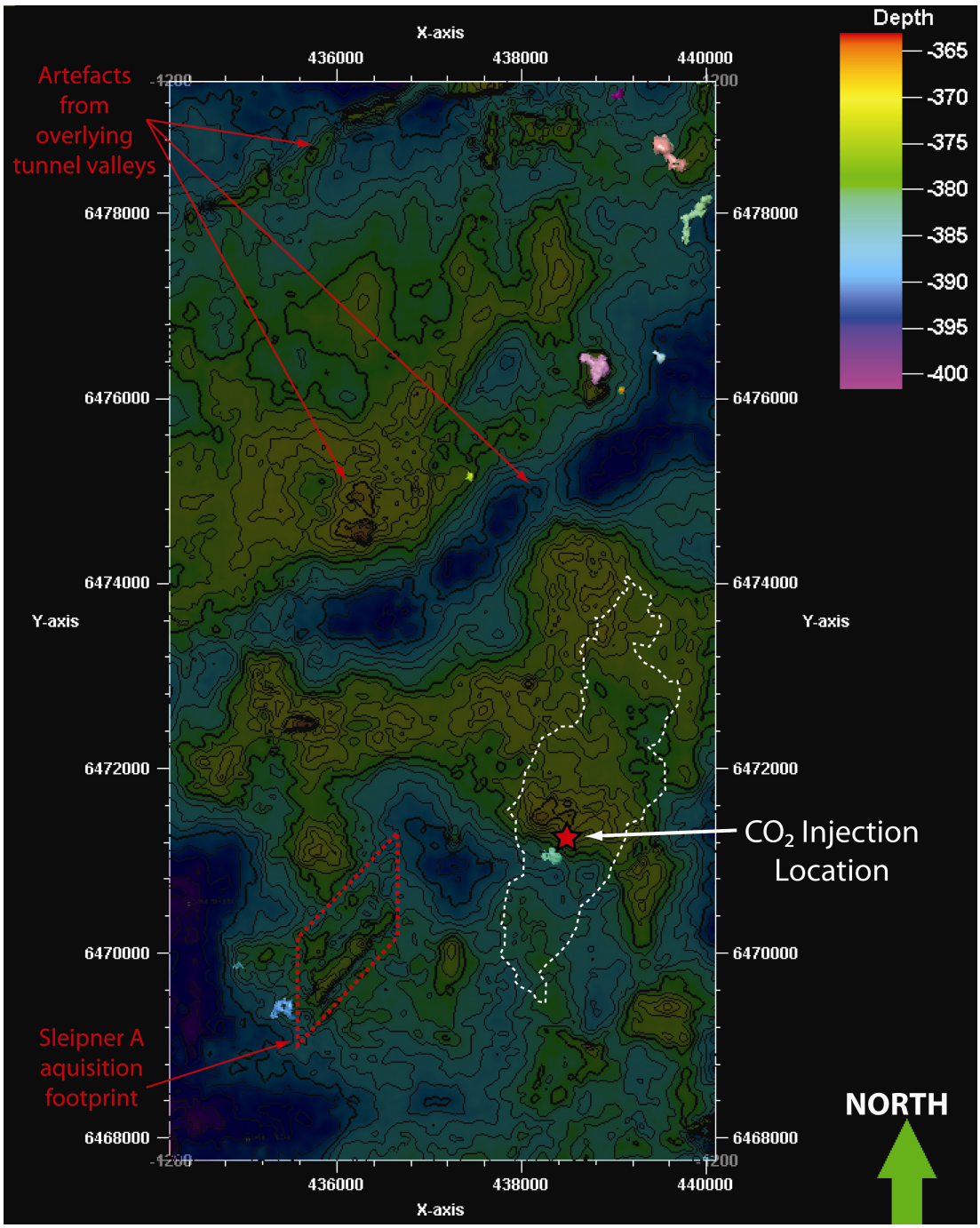

Figure 2.19: Petrel® anomaly distribution map for horizon A (upper), overlaid against the 400 m Strong surface from Table 2.3. A 2008 CO_2 plume outline is displayed as a white dashed line. Note the presence of push-down and pull-up artefacts resulting from overlying tunnel valleys and the Sleipner A drilling and production facility. UTM 31V grid in 0.4 km increments. Note that individual anomalies are allocated an arbitrary colour scheme in Petrel® to assist with visualisation and interpretation. The 400 m Strong surface colour depth scale (top right) and map contours are displayed at 5 m intervals.

From Figures 2.14, 2.16 and 2.17 it is evident that some of these anomalies show a strong alignment along a preferred direction (predominantly NE to SW), in relation to underlying surfaces, suggesting some form of structural (e.g. fault) or stratigraphic (e.g. toplap) control on anomaly distribution. Previous work has inferred a connection between fluid mobilisation in the Hordaland Group mud-rich sediments and subsequent compaction of the Utsira Formation (refer to Figure 2.1), creating faulting in the overburden (Heggland, 1997; Borgos et al., 2002; Jackson & Stoddart, 2005). To investigate such a connection in the local survey area we used the Variance and TraceAGC attribute versions of the interpretation seismic cube and mapped lineations using polygons on a series of seismic time slices (Z) between the Top Utsira and Former Intra-Pliocene surfaces (Figure 2.20).

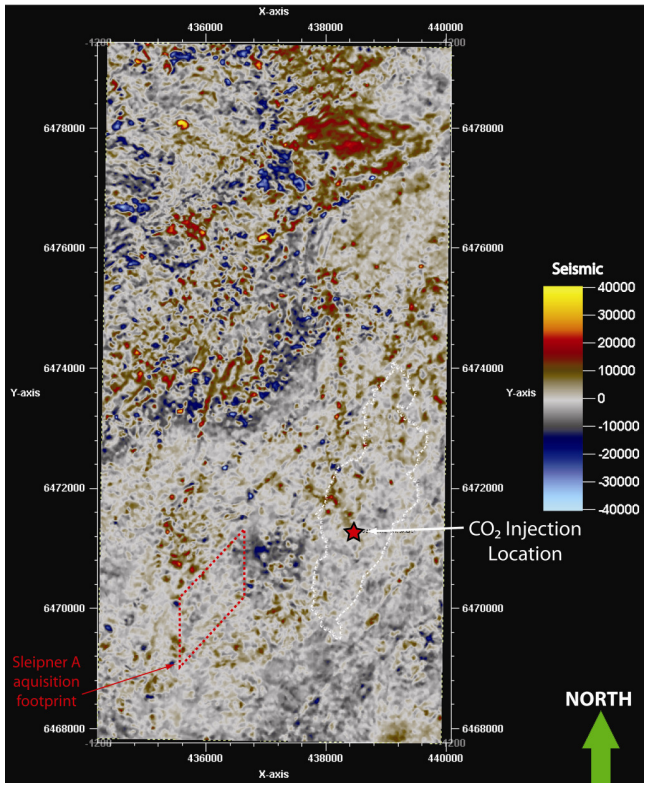

Figure 2.20: Petrel® TraceAGC time slice (Z) from 680 m at approximate depth of Former Intra-Pliocene surface showing distinctive lineations trending NE-SW, NW-SE, N-S and ENE-WSW. A 2008 CO_2 plume outline is displayed as a white dashed line. UTM 31V grid in 0.4 km increments. The colour scale (top right) shows the range of seismic reflection amplitudes.

The lineation map was then overlaid against horizon D anomalies and the surface in which they occur for comparison (Figure 2.21).

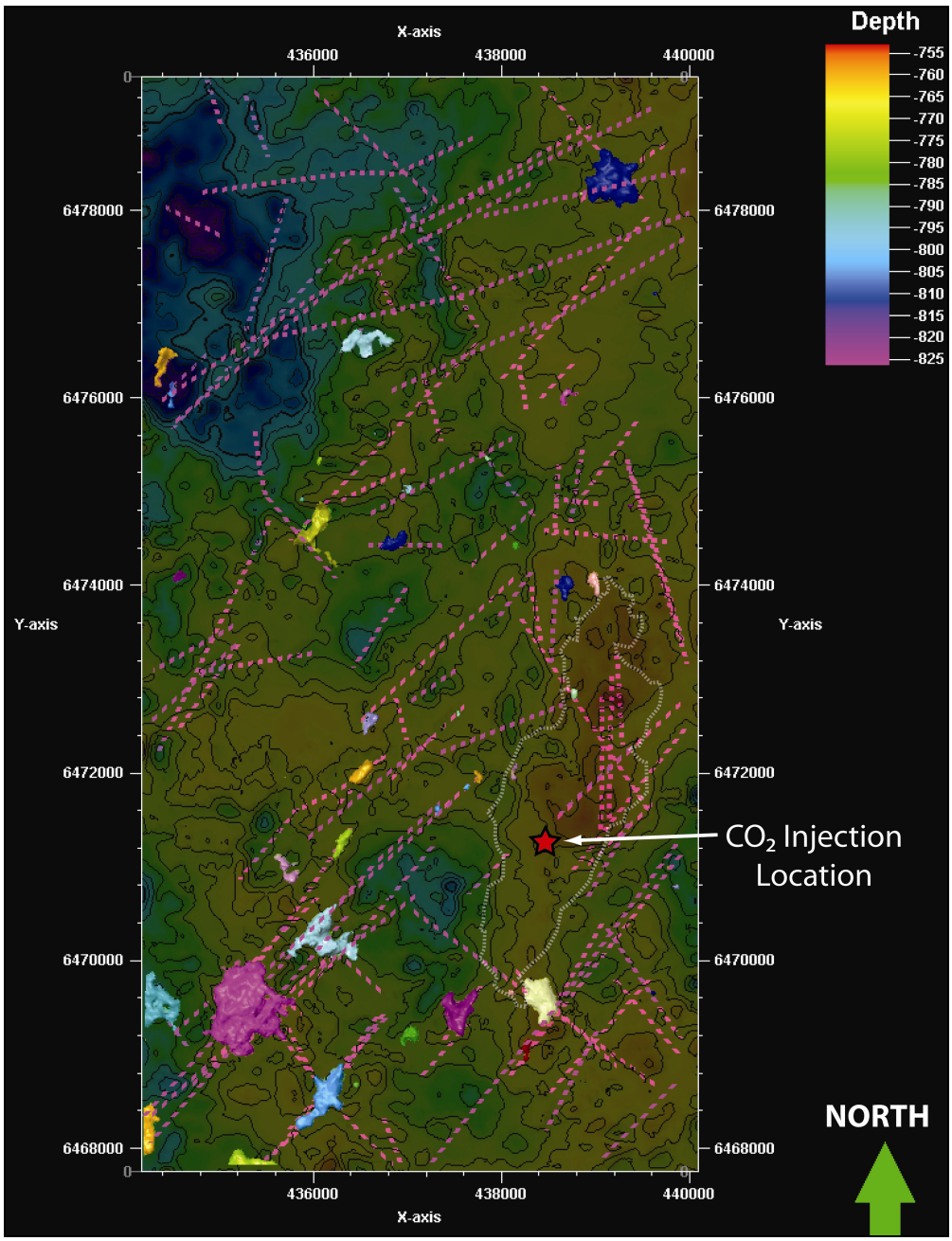

Figure 2.21: Petrel® anomaly distribution map for horizon D overlaid against the surface in which they occur (i.e. Supra-Caprock Anomaly surface from Table 2.3). Lineations mapped between the Top Utsira and Former Intra-Pliocene surfaces are displayed as pink dashed lines. A 2008 CO_2 plume outline is displayed as a white dashed line. UTM 31V grid in 0.4 km increments. Note that individual anomalies are allocated an arbitrary colour scheme in Petrel® to assist with visualisation and interpretation. The Supra-Caprock Anomaly surface colour depth scale (top right) and map contours are displayed at 5 m intervals.

From Figure 2.21 it is evident that a large number of the anomalies in horizon D are intersected by lineations. Most of the larger anomalies in the NE and SW extend along the strike of lineations that may be acting as flow conduits or boundaries.

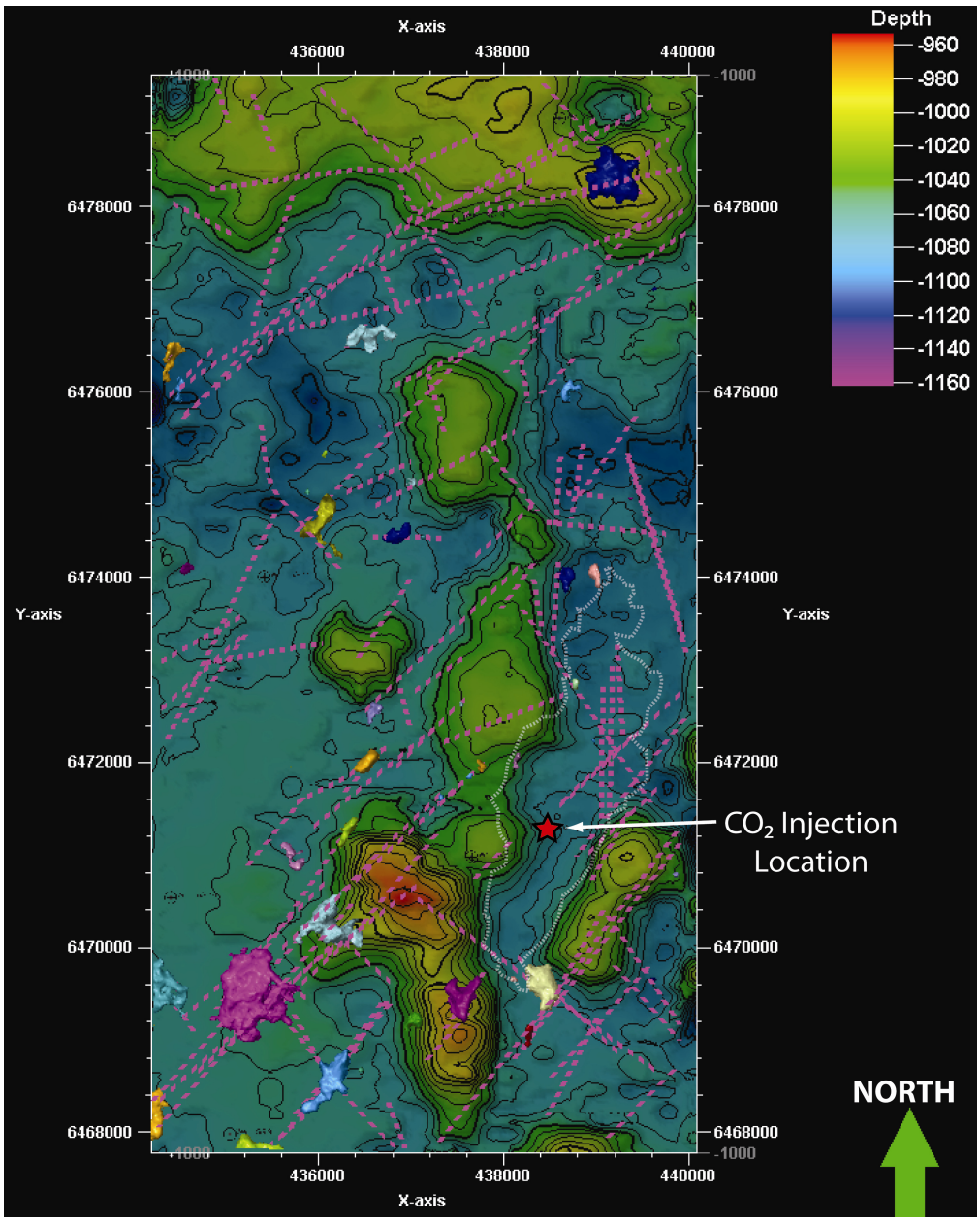

Figure 2.22: Petrel® anomaly distribution map for horizon D overlaid against the Top Hordaland surface. Lineations mapped between the Top Utsira and Former Intra-Pliocene surfaces are displayed as pink dashed lines. A 2008 CO_2 plume outline is displayed as a white dashed line. UTM 31V grid in 0.4 km increments. Note that individual anomalies are allocated an arbitrary colour scheme in Petrel® to assist with visualisation and interpretation. The Top Hordaland surface colour depth scale (top right) and map contours are displayed at 20 m intervals.

Using the same map of horizon D anomalies and TU-FIP lineations from Figure 2.21, but this time overlaying against the Top Hordaland surface, the edges and crests of Hordaland mud mound structures exhibit an alignment coincidence with these overburden features, despite a vertical separation of several hundred metres.

Another lineation map was constructed for the Former Intra-Pliocene to Former Top Pliocene surfaces and overlaid against horizon B anomalies (Figure 2.23) and this shows a similar distribution control as evidenced on Figure 2.21.

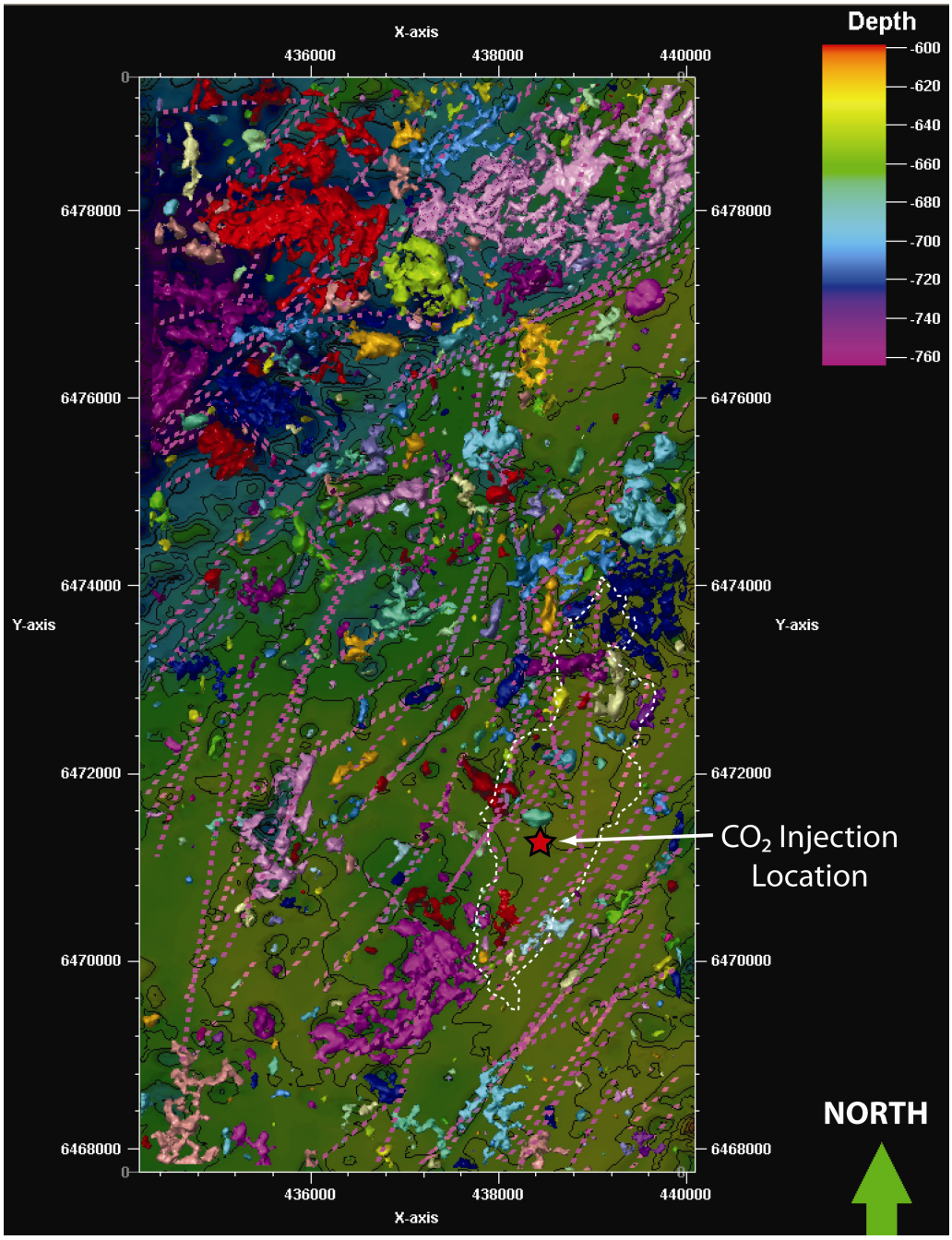

Figure 2.23: Petrel® anomaly distribution map for horizon B overlaid against the Former Intra-Pliocene surface from Table 2.3. Lineations mapped between the Former Intra-Pliocene and Former Top Pliocene surfaces are displayed as pink dashed lines. A 2008 CO_2 plume outline is displayed as a white dashed line. UTM 31V grid in 0.4 km increments. Note that individual anomalies are allocated an arbitrary colour scheme in Petrel® to assist with visualisation and interpretation. The Former Intra-Pliocene surface colour depth scale (top right) and map contours are displayed at 20 m intervals.

A different form of structural control is evident between the Former Intra-Pliocene and Former Top Pliocene surfaces, where the majority of seismic anomalies in horizon B occur as an interconnected network of ganglions situated beneath structural highs, as might be expected for trapping of a buoyant fluid (Figure 2.24).

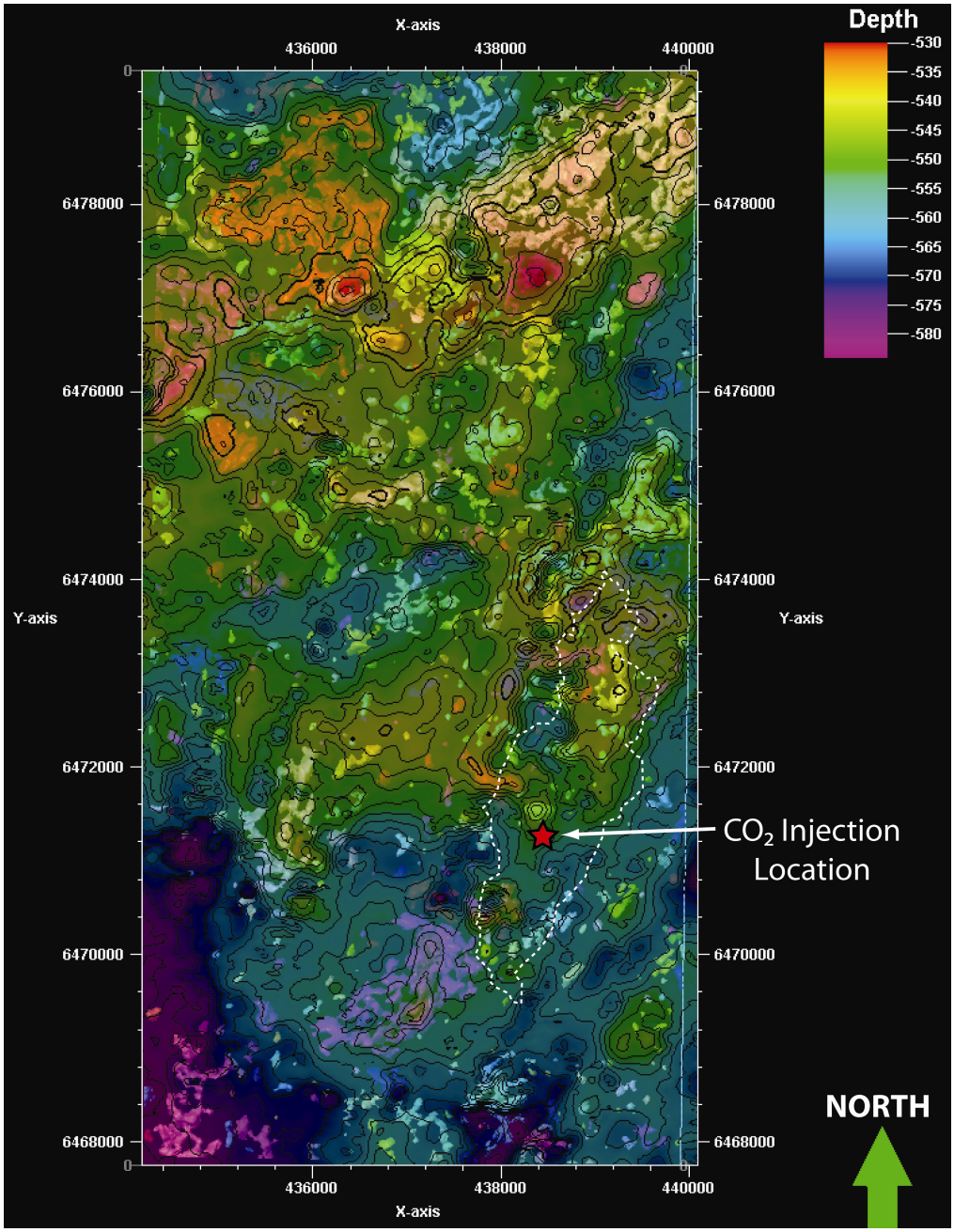

Figure 2.24: Petrel® anomaly distribution map for horizon B displayed below a semi-transparent Former Top Pliocene surface from Table 2.3. A 2008 CO_2 plume outline is displayed as a white dashed line. UTM 31V grid in 0.4 km increments. Note that individual anomalies are allocated an arbitrary colour scheme in Petrel® to assist with visualisation and interpretation. The Former Top Pliocene surface colour depth scale (top right) and map contours are displayed at 5 m intervals.

Category b) anomalies are distinguished by sub-vertical zones of disturbed, discontinuous reflections indicative of injectites, faults, fracture zones and gas chimneys (i.e. features usually associated with the presence of vertical fluid flow conduits). Within our data range of 0-1400 m, the deepest such anomalies are created by the presence of sand injectites in the Hordaland Group. In cross-section, these sand injectites display a v-shaped morphology and emanate from the polygonal-faulted sequence underlying the top Hordaland surface (Figures 2.11 to 2.13). In 3D, these anomalies form clusters of conical (concentric) and elliptical listric faults underlying large mound structures (mud volcanoes) of 100-200 m relief as illustrated on Figures 2.25 to 2.26). Well 15/9-13 penetrates one of these structures within the local survey area, and sands, limestones and silty mudstones of the Marstein Formation occur between 1120-1200 m, underlying the top Hordaland Group and could be a potential source of the injected sands (refer to Appendix 2.1 for a schematic of the 15/9-13 well log).

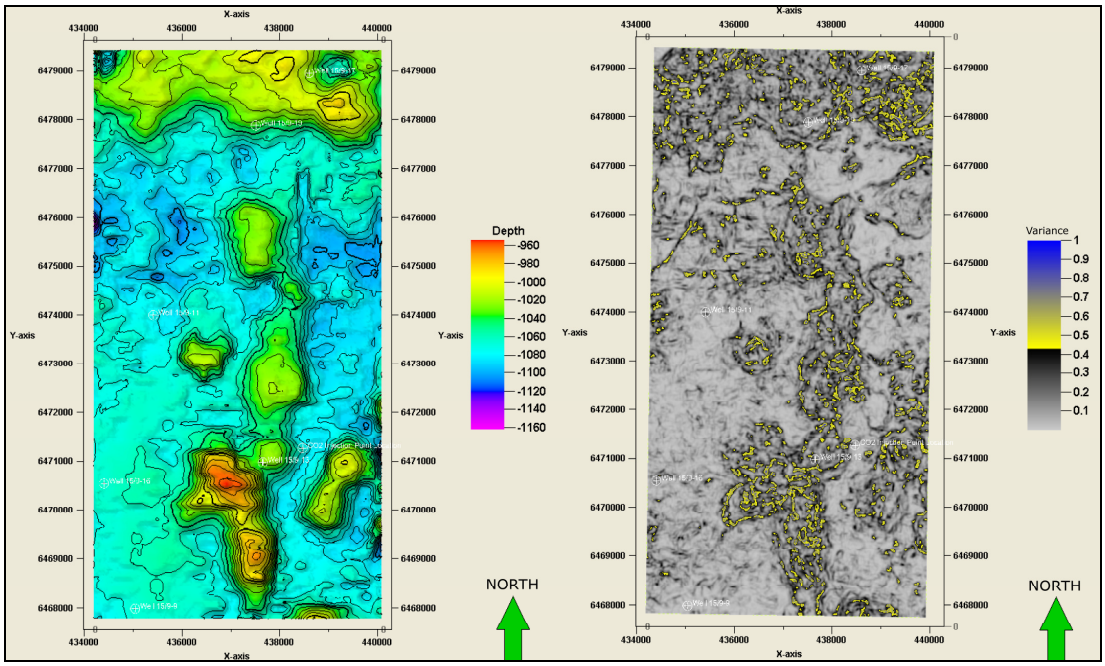

Figure 2.25: Petrel® screenshots showing a comparison between a depth map (20 m contour intervals) for the Top Hordaland surface (left) and the internal structure of the Hordaland mud mounds using a Variance attribute time slice (Z) from -1100 m (right), which just intersects the base of the Top Hordaland (both extracts from the local survey area of Figure 2.1). UTM 31V grid in 1.0 km increments.

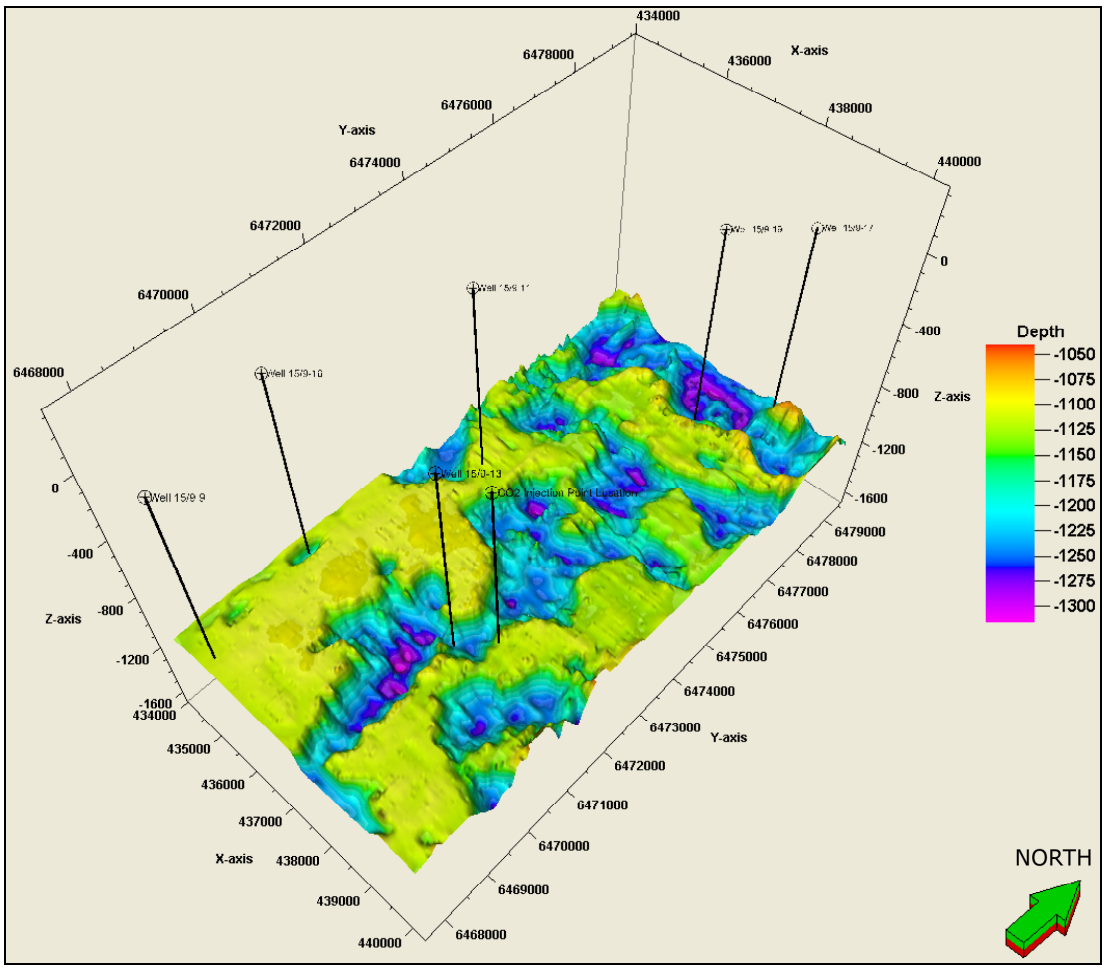

Figure 2.26: Petrel® screenshot showing a 3D view from the SE of the Sand Injectite surface from Table 2.3 extracted from the local survey area of Figure 2.1 (4x vertical exaggeration). UTM 31V grid in 1.0 km increments. The Sand Injectite surface colour depth scale (top right) and map contours are displayed at 25 m intervals.

Above the Hordaland mud mounds subsidence is evident within the Utsira Formation (Figure 2.11), suggesting syn- and/or post-depositional compaction. We mapped sub-vertical chimneys that extend through the Utsira Formation into the overburden and these appear to be sourced from crestal (Figure 2.27) and peripheral (Figure 2.28) regions of the Hordaland Group mounds.

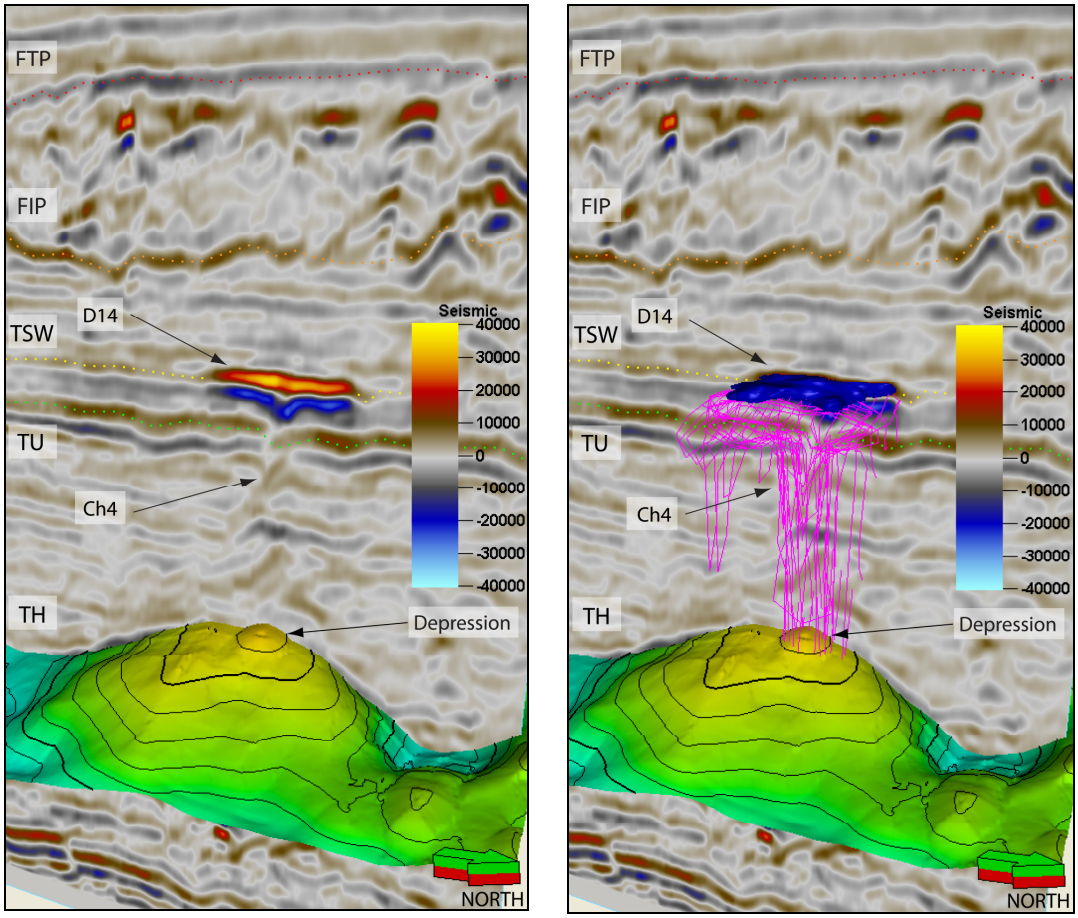

Figure 2.27: Petrel® screenshots of inline 1883 (5x vertical exaggeration). Field of view is 2 km S to N and 800 m vertical for each image. 3D view from ENE of a vertical chimney structure (Ch4) ~292 m high, extending from the crest of a Hordaland mud mound forming a zone of sub-vertical disruption and terminating above the Utsira Formation at a high-amplitude anomaly (D14). Note the weak reflections immediately above the anomaly and down-bending of reflections below it, including the depression on the Top Hordaland surface. The right-hand image demonstrates how chimneys were mapped in 3D using polygons (pink lines) on inlines and cross-lines and high-amplitude seismic anomalies were extracted as 3D geobodies (dark blue object). Refer to Figure 2.14 for the location of D14. The colour scale (centre right) shows the range of seismic reflection amplitudes.

***Note:** FTP = former top Pliocene reflection (red); FIP = former intra-Pliocene reflection (orange); TSW = Top Sand Wedge reflection (yellow); TU = Top Utsira reflection (green) and TH = Top Hordaland surface.*

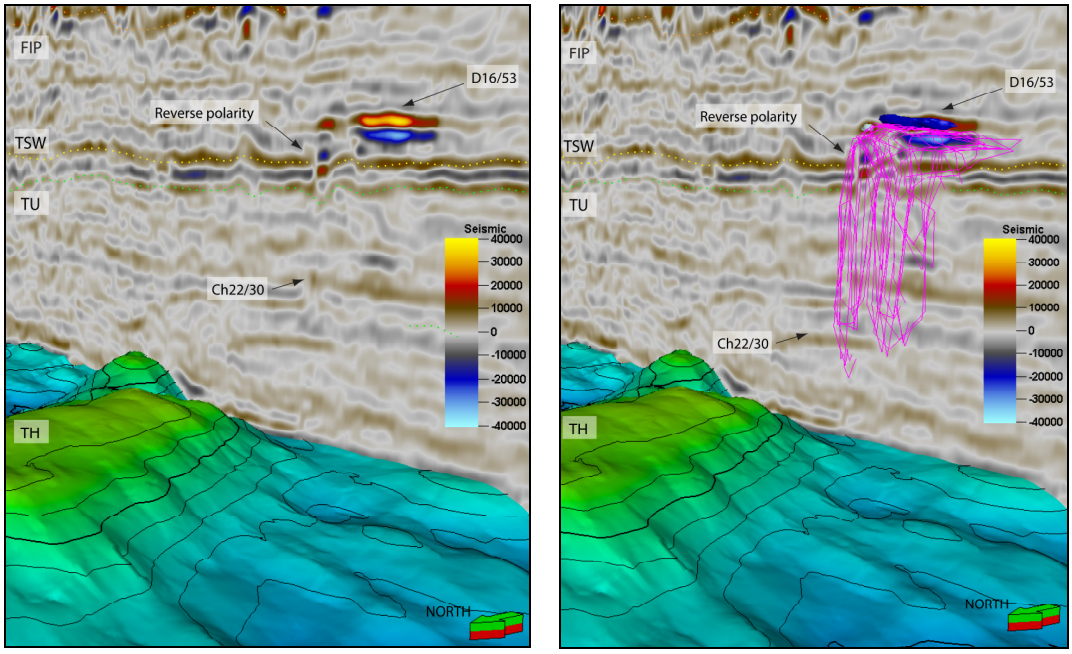

Figure 2.28: Petrel® screenshots of crossline 1374 (5x vertical exaggeration). Field of view is ~3.95 km W to E and ~400 m vertical for each image. 3D view from the NW of a composite vertical chimney structure (Ch22/30) ~240 m high, extending from the W edge of a Hordaland mud mound forming two zones of sub-vertical disruption and terminating above the Utsira Formation at high-amplitude anomalies (D16/53). Again, note the weak reflections immediately above both anomalies and down-bending of reflections below them. Also the reverse polarity anomaly between TSW and TU surfaces associated with D16 (fault and/or gas indicator?). The right-hand image demonstrates how chimneys were mapped in 3D using polygons (pink lines) on inlines and cross-lines and high-amplitude seismic anomalies were extracted as 3D geobodies (dark blue and pale blue objects). Refer to Figure 2.14 for the location of D16/53. The colour scale (centre right) shows the range of seismic reflection amplitudes.

***Note:** FIP = former intra-Pliocene reflection (orange); TSW = Top Sand Wedge reflection (yellow); TU = Top Utsira reflection (green) and TH = Top Hordaland surface.*

Although most chimneys terminate within the anomaly-rich zone bounded by the FIP and FTP surfaces, some chimneys can be mapped from the Hordaland Group to seabed, one example (Ch35) in the regional survey area forms a 500 m^2 seafloor crater, 6.5 km SW of the CO_2 injection point (refer to the seismic cross-section on Figure 2.11 and plan location on Figure 2.29). Another near-vertical structure was mapped in the local survey area, extending from the FIP surface to seabed at the intersection of inline 1742 and crossline 1120 (Figure 2.29). Internally this feature exhibits strong reflection pull-up and forms a structure of positive relief at seabed.

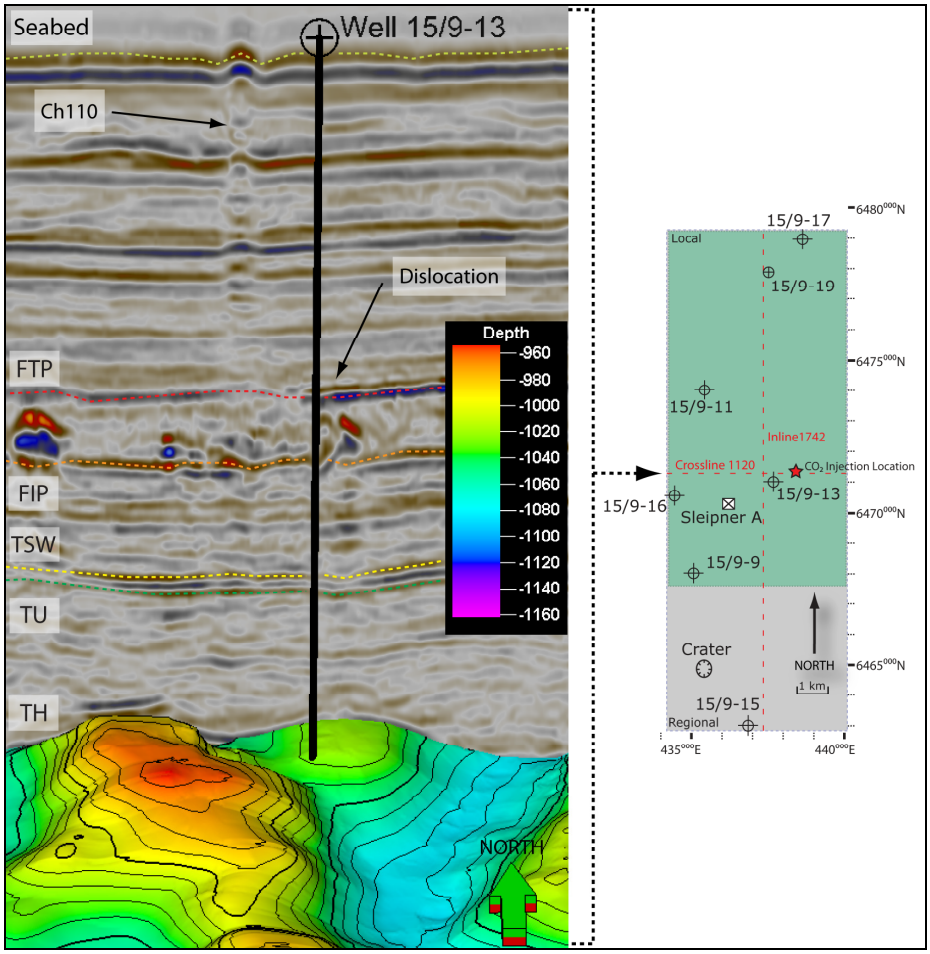

Figure 2.29: Petrel® screenshots of crossline 1120 (5x vertical exaggeration) and location map (right). Field of view for seismic is ~2.8 km W to E and ~1000 m vertical. 3D view from the S of a vertical chimney structure (Ch110) ~560 m high and ~250 m wide, extending from the FTP surface and terminating at seabed forming a structure several metres high. Note the diagonal zone of dislocation to the E of Ch110 bounded by the FTP and FIP surfaces (fault zone?). Colour depth scale and contours for Top Hordaland surface in 20 m intervals.

***Note:** FTP = former top Pliocene reflection; FIP = former intra-Pliocene reflection (orange); TSW = Top Sand Wedge reflection (yellow); TU = Top Utsira reflection (green) and TH = Top Hordaland surface.*

Frequently we observe spatial correlations between both categories of anomaly. By cross-referencing N-S and E-W seismic lines, we mapped 3D structures that indicate processes associated with natural gas migration and accumulation over geological time. In order to further assess the risks these structures may present to future CO_2 containment we focus on chimneys and anomalies in closest proximity to the top seal for the storage site (i.e. TSW surface). A map of these features in conjunction with annotated seismic section extracts is presented in Figures 2.30 to 2.31.

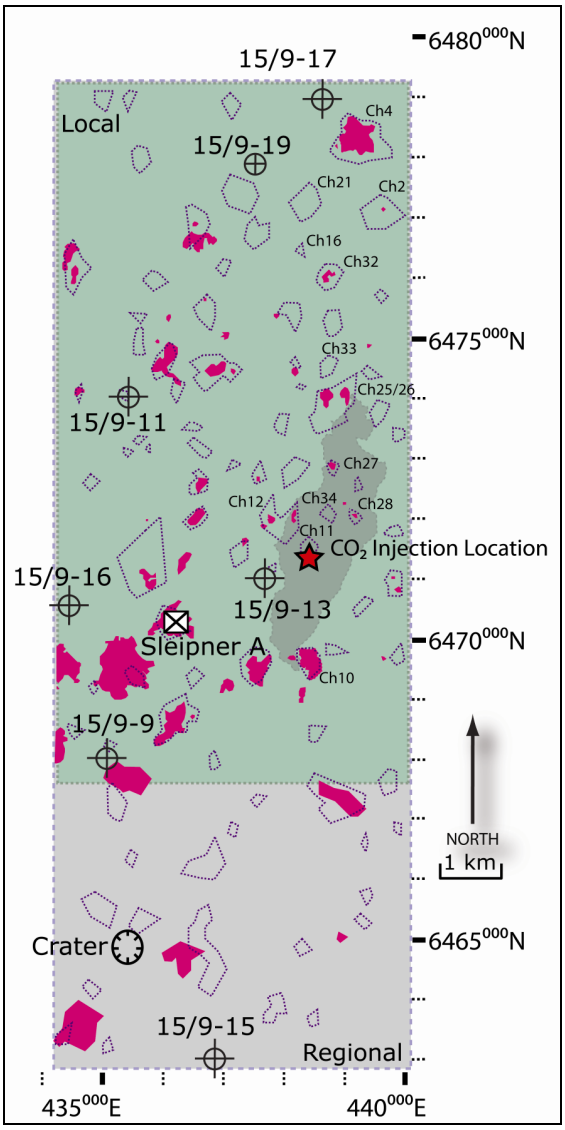

Figure 2.30: High-amplitude seismic anomalies (red) mapped within the regional (green/grey) and local (green) survey areas at horizon D (refer to Figure 2.14). These overlie the top seal for the storage site (i.e. Top Sand Wedge surface). Sub-vertical chimney structures penetrating horizon D are also indicated by purple dashed lines. The CO_2 plume footprint for 2008 (i.e. all layers stacked), is also indicated by grey shading in the local survey area (from Hermanrud et al., 2010) Seismic extracts for numbered chimneys are illustrated in Figure 2.31.

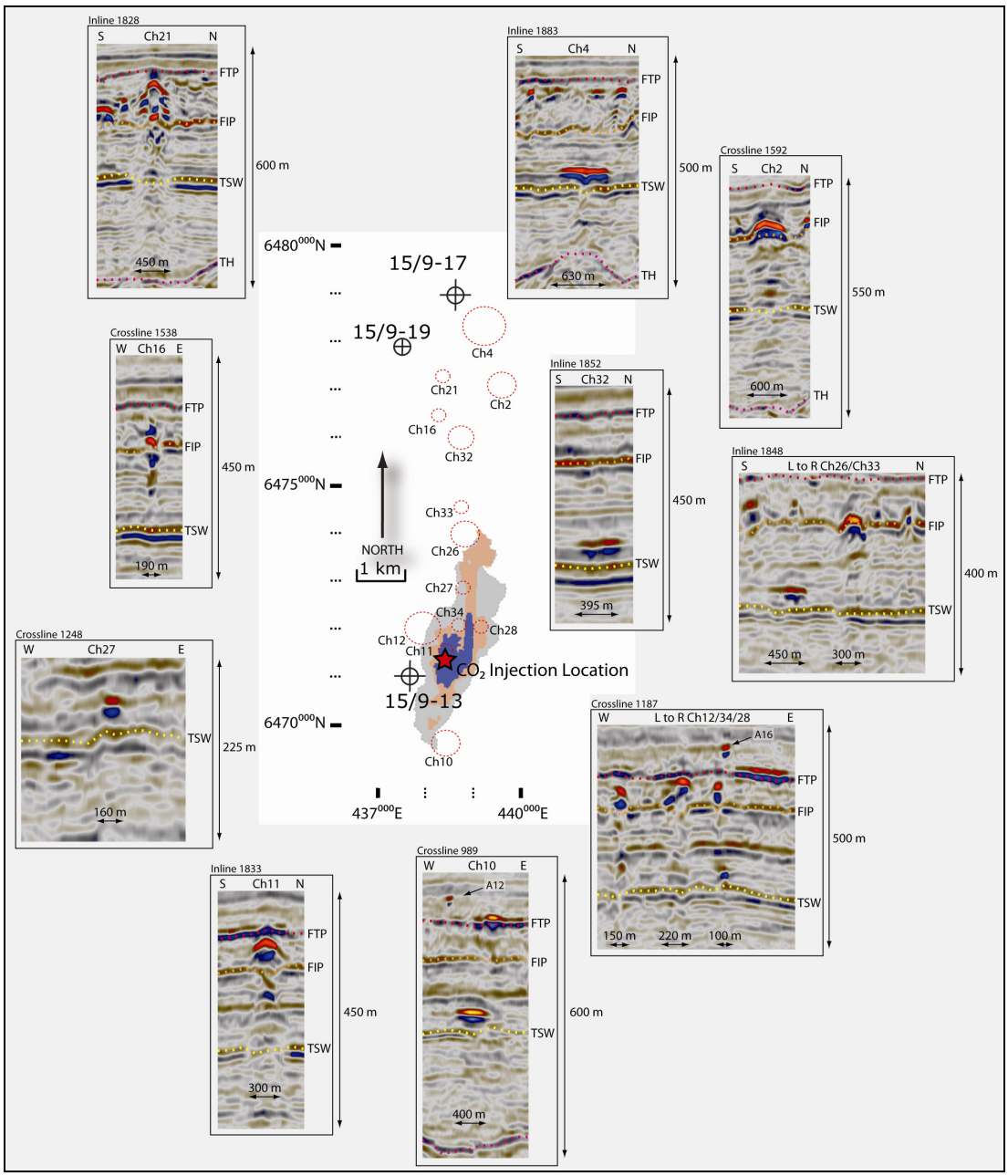

Figure 2.31: Seismic data extracts for numbered chimney structures on Figure 2.30. Also shown are maps indicating the lateral extent of the top layer (layer 9) of CO_2 migrating below the top seal (from Singh et al., 2010). The 2002 (blue) and 2008 (brown) maps are superimposed on the footprint map (from Hermanrud et al., 2010). These indicate that as the top layer of the plume continues to grow post-2008 it is liable to come into contact with several of these chimney structures.

***Note:** FTP = former top Pliocene reflection (red); FIP = former intra-Pliocene reflection (orange); TSW = Top Sand Wedge reflection (yellow) and TH = Top Hordaland reflection (purple).*

With reference to Figure 2.31, although many of the anomalies visible on the extract seismic sections exhibit convexity (pull-up) indicative of a "hard" acoustic impedance contrast, some also show evidence of V-shaped (e.g. Ch16) or M-shaped (e.g. Ch4) pull-down and patches of reverse polarity (e.g. Ch2, Ch12, Ch16 and Ch21), which may indicate the presence of gas. The nearest of these structures to the CO_2 injection point location is Ch11 (60 m offset to NNW) and this is analysed in greater detail using a crossline (1140) and inline (1833) intersection from a TraceAGC attribute seismic volume as shown on Figure 2.32.

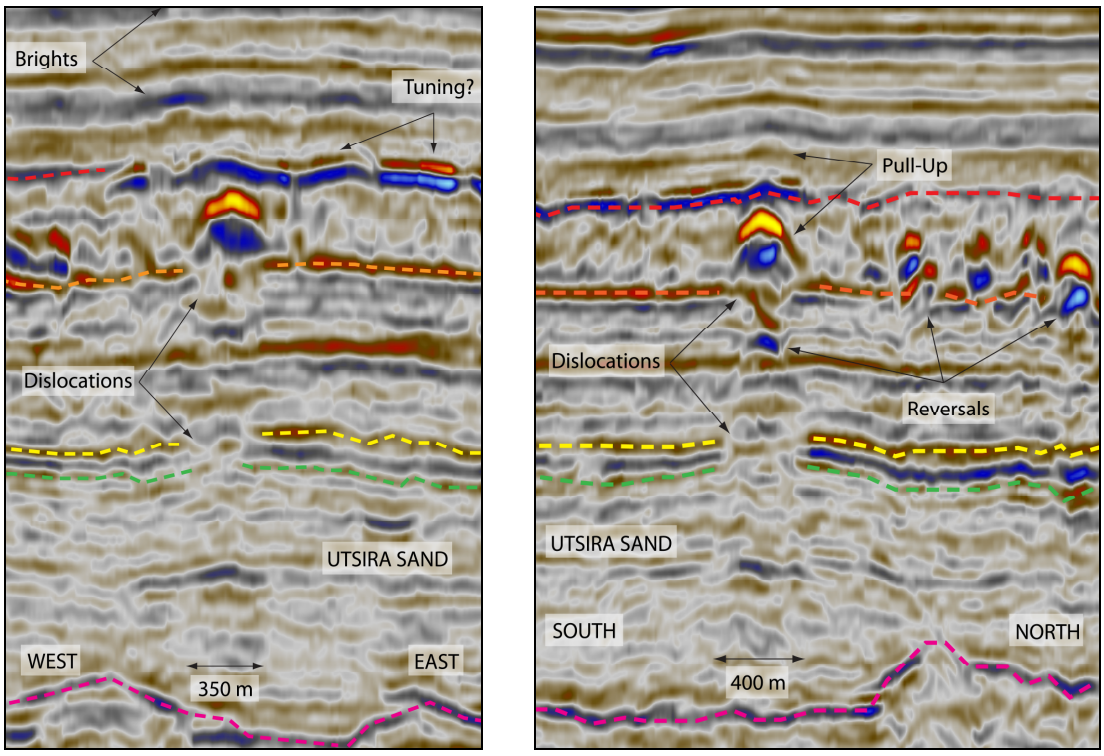

Figure 2.32: Crossline 1140 (left) and inline 1883 (right) which both intersect a zone of vertical disturbance (Ch11) adjacent to the CO_2 injection point location. Vertical distance between FTP and TH reflections in the disturbed zone is ~500 m (4x vertical exaggeration). Note the sub-vertical dislocations at the edge of the chimney and depression of the reflections at the FIP, TSW and TU. High amplitude brights observed above the FTP (left) may result from a tuning response to thin, gas-filled horizons in the overburden (refer also to Figure 2.31).

***Note:** FTP = former top Pliocene reflection (red); FIP = former intra-Pliocene reflection (orange); TSW = Top Sand Wedge reflection (yellow), (TU) = Top Utsira Sand (green) and TH = Top Hordaland reflection (purple).*

Examining this feature in 3D in conjunction with anomalies from horizon A (lower) and Variance time slice (Z), there is some evidence to suggest that chimney feature Ch11, may have served as a migration pathway into this horizon (Figure 2.33).

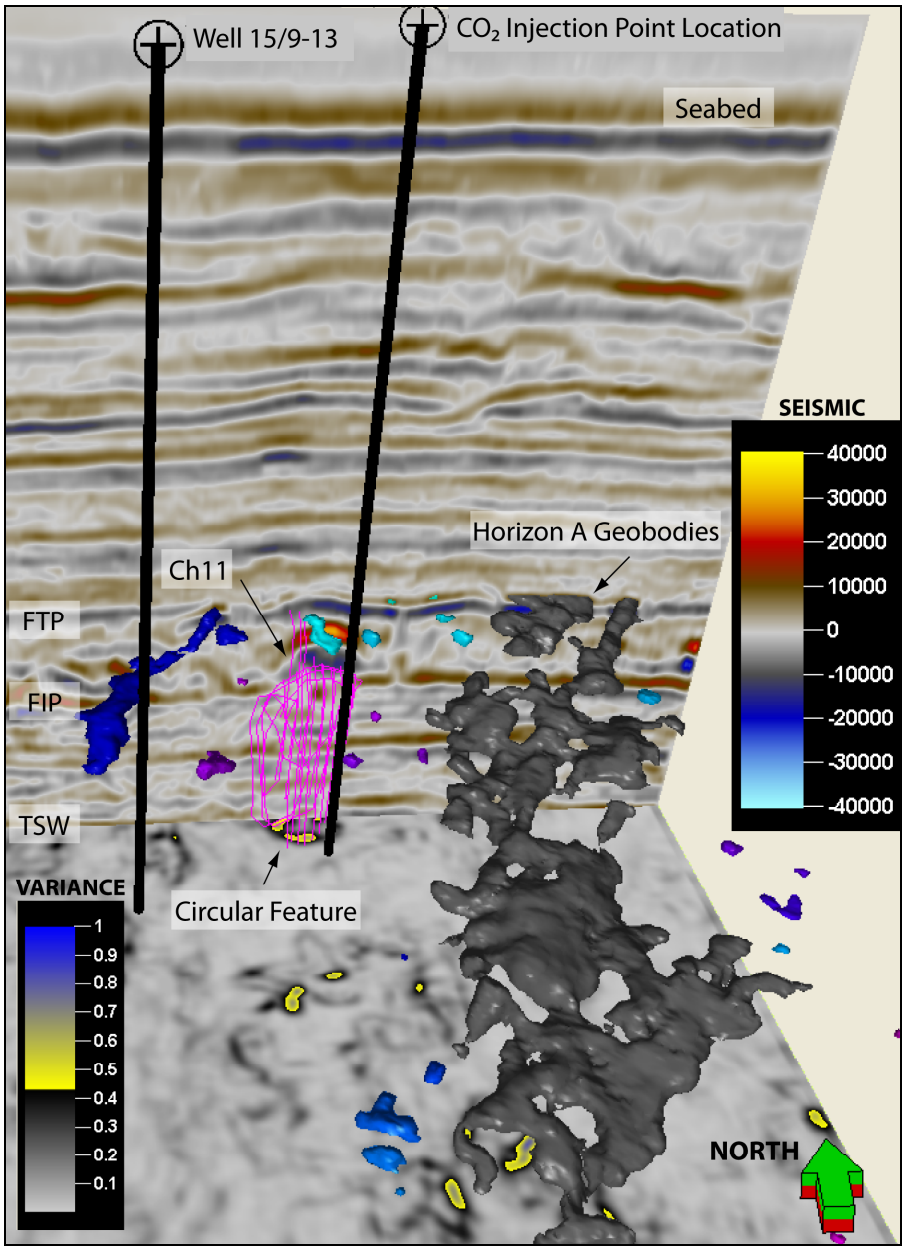

Figure 2.33: 3D view from S of crossline 1140 (seismic section at rear) and Variance time slice (Z) from 810 m (below Top Sand Wedge) which both intersect chimney feature (Ch11) adjacent to the CO_2 injection point location. Vertical distance between FTP and TSW reflections in the disturbed zone is ~265 m (4x vertical exaggeration). Note the circular feature with high variance on the time slice (Z) forming the outline of Ch11. The sub-vertical dislocation zones (faults?) located either side of Ch11, extend from the FIP to FTP surface and appear to feed E and W into the NE to SW aligned high-amplitude anomalies from Horizon A (in this case displayed as 3D geobodies).Colour scales show range of seismic reflection amplitudes for crossline (centre right) and variance for time slice (bottom left). Individual seismic anomalies are are allocated an arbitrary colour scheme in Petrel® to assist with visualisation and interpretation.

***Note:** FTP = former top Pliocene reflection; FIP = former intra-Pliocene reflection; TSW = Top Sand Wedge reflection.*

2.7 Glacial and Marine Sedimentary Features:

Within the Pleistocene overburden in the Sleipner area we also identified and mapped a suite of erosional features and depositional sequences of mixed glacial and marine provenance. The oldest features we observe are on the Former Intra-Pliocene (FIP) surface, which contains a series of sub-parallel linear channels and linked depressions with a predominant NE-SW alignment. These are large-scale features with depths in the 30-50 m range and widths from 300-500 m. To better understand how these channels were formed, we compare the local survey area from this study with results from a larger survey (ST98M11) performed in 1998 and described in Zweigel & Hamborg (2002). On Figure 2.34, the FIP surface from the ST98M11 survey shows a major network of linear channels emanating from a focal point in the NE and fanning outwards through an embayment into a more distal basin region to the WSW and SW. The local survey area FIP surface from this study is located partly on a former shelf area in the SE extent with a transition zone descending ~100 m into the deeper basin area towards the NW.

Although there are no wells located in the NW corner of the local survey area, a comparison of well logs (Appendix 2.1) from 15/9-17 (partly located in the channelled embayment), indicates the presence of a ~40 m thick sand unit above the FIP surface, whereas the other wells located on the shelf, are either clay-dominated (majority) or have thin interbeds of sand/silt or sand/clay (e.g. 15/9-11) at equivalent depths above the FIP surface (refer to Table 2.5).

Well Name	Early Pleistocene Sand Intersections
15/9-9	125 m thick interval of thin sand/clay interbeds, ~610-725 m
15/9-11	75 m thick interval of thin sand/silt/clay interbeds, ~550-625 m
15/9-13	No significant sand intervals
15/9-16	Thin sand interval, ~670 m
15/9-17	40 m thick sand interval, ~620-660 m

Table 2.5: Well intersections of early Pleistocene sand bodies and sandy intervals within the local survey area.

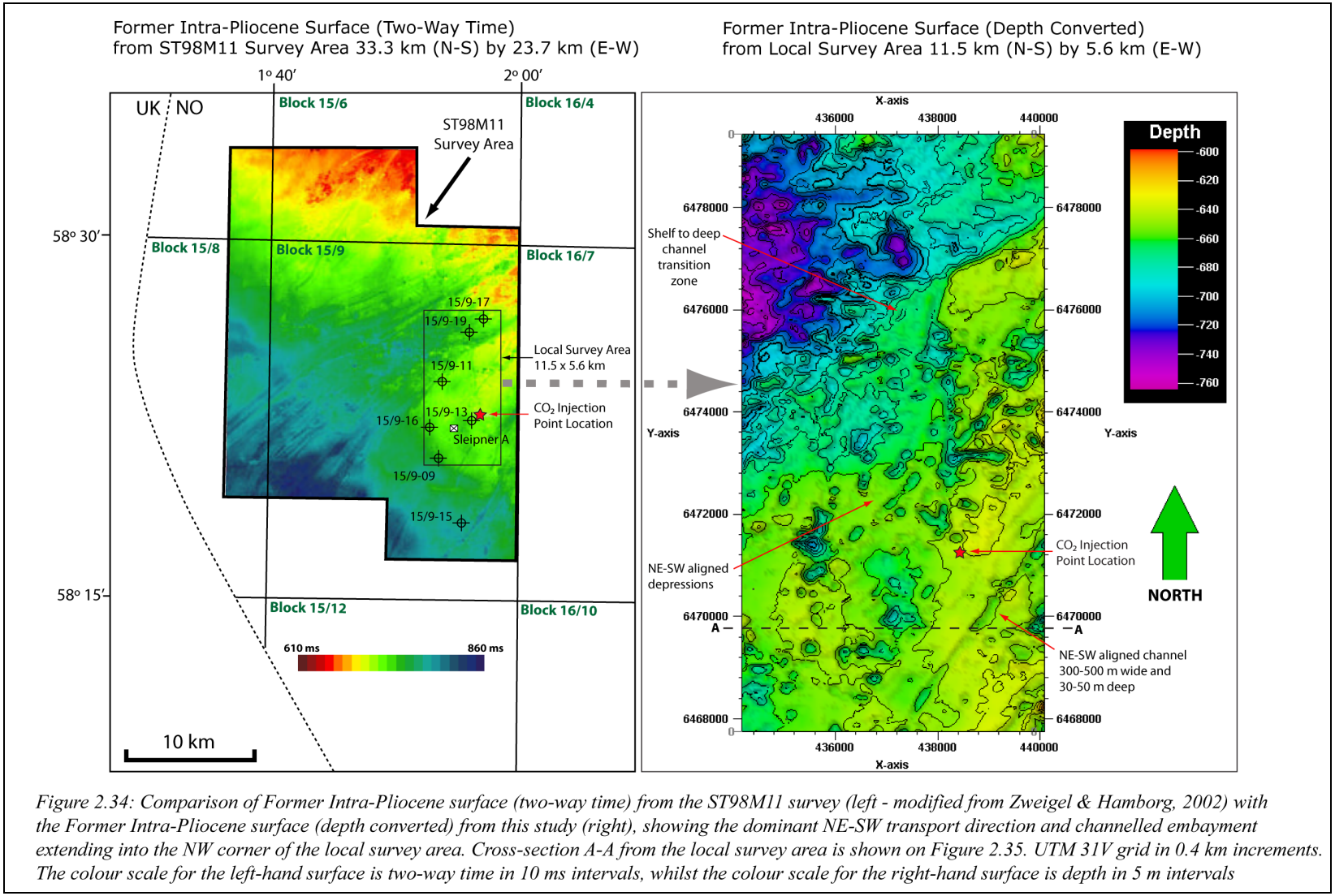

Figure 2.34: Comparison of Former Intra-Pliocene surface (two-way time) from the ST98M11 survey (left - modified from Zweigel & Hamborg, 2002) with the Former Intra-Pliocene surface (depth converted) from this study (right), showing the dominant NE-SW transport direction and channelled embayment extending into the NW corner of the local survey area. Cross-section A-A from the local survey area is shown on Figure 2.35. UTM 31V grid in 0.4 km increments. The colour scale for the left-hand surface is two-way time in 10 ms intervals, whilst the colour scale for the right-hand surface is depth in 5 m intervals

Due to the presence of the embayment the infilling sequence from the FIP surface to the Former Top Pliocene (FTP) surface is also up to ~100 m thicker in the NW. None of the linear channel features are penetrated by wells in the local survey area, so the infill composition of these features can only be inferred on the basis of the 15/9-17 channel fill and comparison with seismic lines that cross-cut these channels as shown on Figure 2.35. As described previously on Figure 2.16, wells that partially intersect anomalies in horizon B (e.g. 15/9-9, 15/9-11 and 15/9-17) either indicate the presence of sands or clays with sandy interbeds (Appendix 2.1).

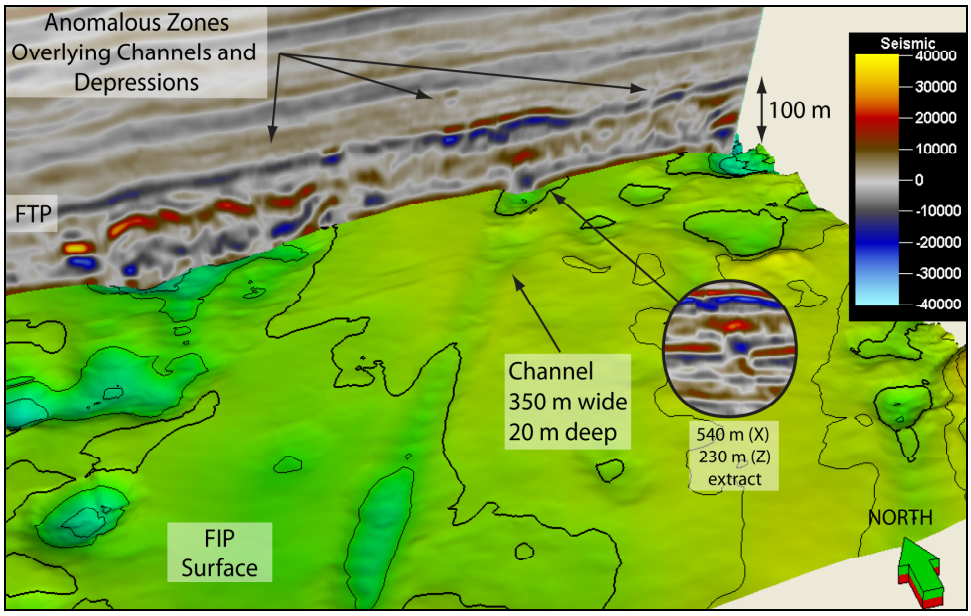

Figure 2.35: Cross-section A-A from Figure 2.34 based on seismic crossline 1013 (4x vertical exaggeration), shows a 3D view from the S of channel and depression intersections with the FIP surface. Each channel and depression is associated with overlying high-amplitude seismic anomalies up to the FTP surface. The seismic extract (circled) shows the rectangular trough-like shape of the channel profile.

The FTP surface is also incised by linear channel features aligned in a NE-SW and NNE-SSW direction (Figure 2.36), which are of similar dimensions to those described for the FIP surface, but appear less well-defined. The shelf part of the FTP surface is also visibly hummocky in appearance compared to the FIP surface (moraine deposits or pull-up artefacts overlying high-amplitude anomalies?). Examination of the FTP surface from the ST98M11 survey shows that sediments have prograded onto the underlying FIP from the NE, infilling the embayment illustrated on Figure 2.34, thus the deepest part of the FTP surface is now at the SW corner of the local survey area and the shelf area has ~10-20 m of relief in the NE.

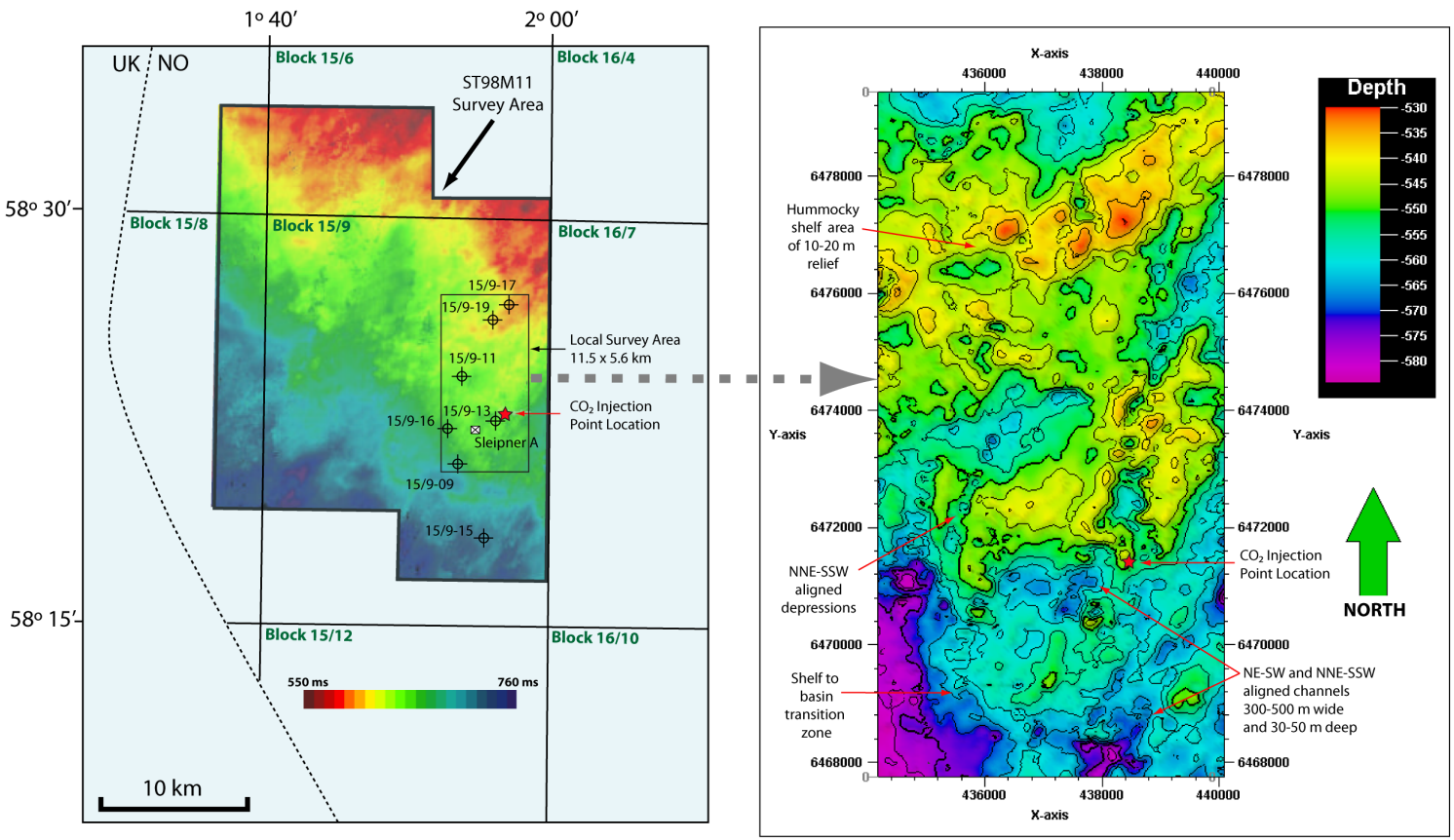

Figure 2.36 Comparison of Former Top Pliocene surface (two-way time) from the ST98M11 survey (left - modified from Zweigel & Hamborg, 2002) with the Former Top Pliocene surface (depth converted) from this study (right), showing the dominant NE-SW and NNE-SSW transport directions and channelled hummocky terrain of 10-20 m relief in the northern half of the local survey area. UTM 31V grid in 0.4 km increments. The colour scale for the left-hand surface is two-way time in 10 ms intervals, whilst the colour scale for the right-hand surface is depth in 5 m intervals.

The more recent Pleistocene overburden above the storage site also contains several large tunnel valleys and smaller channels (Figures 2.11 to 2.13). In contrast to the early Pleistocene features, the earliest phase of channelling in this case (Figure 2.37) has a W-E to WSW-ENE orientation and incises into glacio-marine sediments of the Aberdeen Ground Formation (Sejrup *et al.*, 1987; Bauer & Fichler, 2002; Fichler *et al.*, 2005; Carr *et al.*, 2006; Graham *et al*., 2007). Infill is comprised of Ling Bank and Fisher Formation sediments of Elsterian/Anglian age (~410-380 ka, MIS Stage 12) to Saalian/Wolstonian age (~200-125 ka, MIS Stages 6 and 8). The largest channels range in width from 400-1300 m. The smaller feeder channels range in width from 150-250 m.

In the local survey area exploration well 15/9-13 (adjacent to the CO_2 injection location) drilled through the axis of a feeder channel (Figure 2.37) and sand is recorded on the well log from ~150-265 m. Other wells in near proximity to channel margins also record significant sand content on well logs (refer to Appendix 2.1 and Table 2.6).

Well Name	Late Pleistocene Sand Intersections
15/9-9	100 m thick sand, ~165-265 m (channel margin)
15/9-11	145 m thick sand, ~150-295 m (channel margin)
15/9-13	115 m thick sand, ~150-265 m (channel axis)
15/9-16	150 m thick sand/clay/lignite interbed sequence, with sand recorded at ~150-160 m (channel margin)
15/9-17	110 m thick sand/clay interbed sequence, with sands recorded at ~150-205 m and ~240-260 m (channel margin)

Table 2.6: Well intersections of late Pleistocene sand bodies and sandy intervals within the local survey area.

Note: *Since logging and cuttings return only started at 150 m following the setting of the surface conductor and drilling riser, these sand bodies may extend further towards the seabed (refer also to Figures 2.11 to 2.13).*

Glacial channels are also present within at least 150 m of the seabed (Figures 2.38 and 2.39). These are probably features of Saalian/Wolstonian age (~200-125 ka, MIS Stages 6 and 8) to Weichselian/Devensian age (~110-15 ka, MIS Stages 2-5d), infilled with glacio-marine sediments of the Coal Pit, Tampen, Swatchway and Witch Ground Formations, based on proximal analogue evidence from the UK sector (Graham *et al.,* 2007).

By comparing Figures 2.37-2.39, it is evident that the Ling Bank tunnel valleys are more prominent and deeper structures, with smaller width/depth ratios compared to the younger, nearer seabed structures. In all cases we observe cross-cutting relationships and multiple cut and fill sequences within channels (Figures 2.11-2.13). Similar morphological characteristics are observed in Pleistocene tunnel valleys from other areas of the North Sea (Lonegran *et al.*, 2006; Kristensen *et al.*, 2007; Stewart *et al.*, 2007).

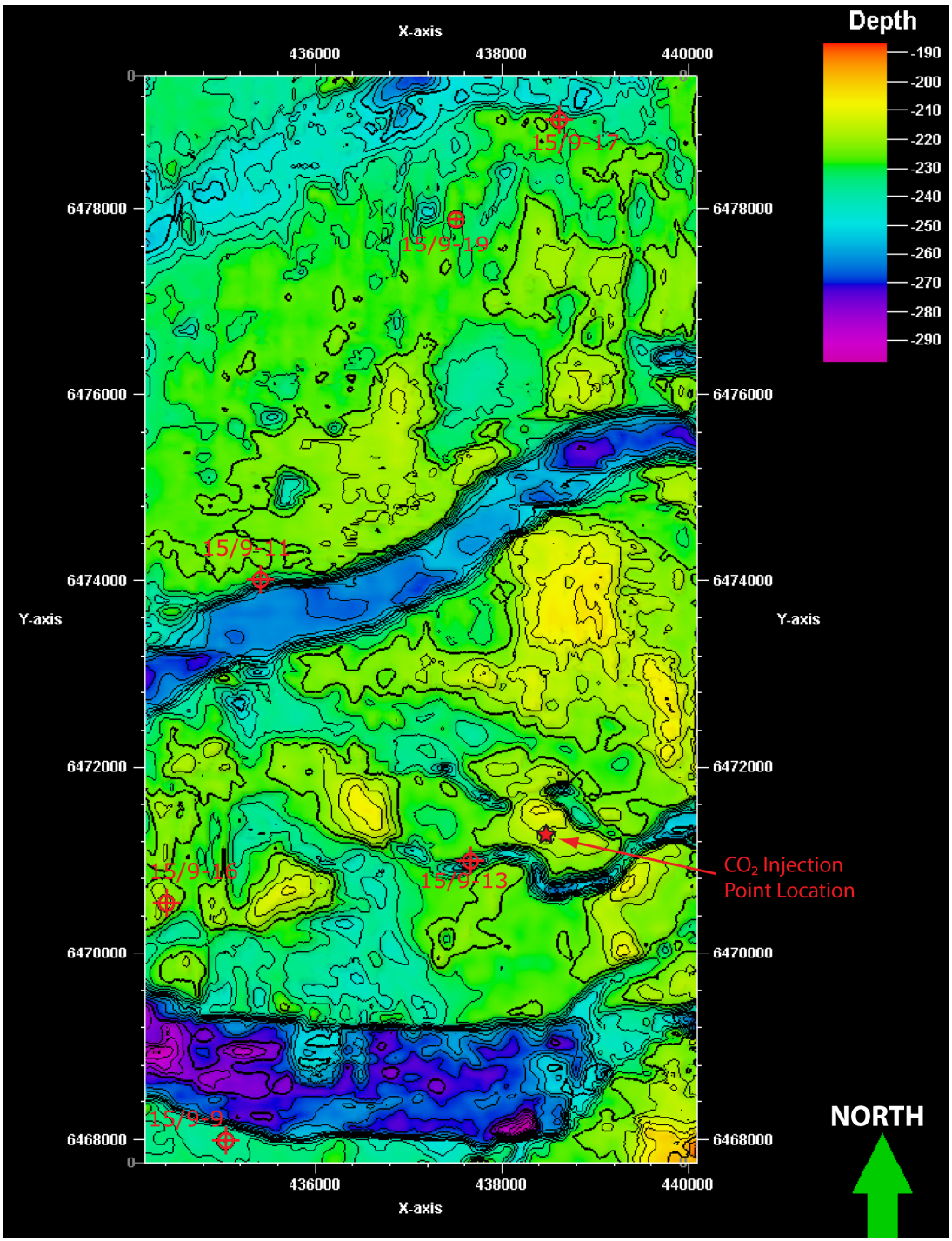

Figure 2.37: First phase of tunnel valley and channel incision observed in the local survey area. Note the square, trough-like shape, over-deepened profile and hanging-wall side branches feeding into the two larger structures. UTM 31V grid in 0.4 km increments.

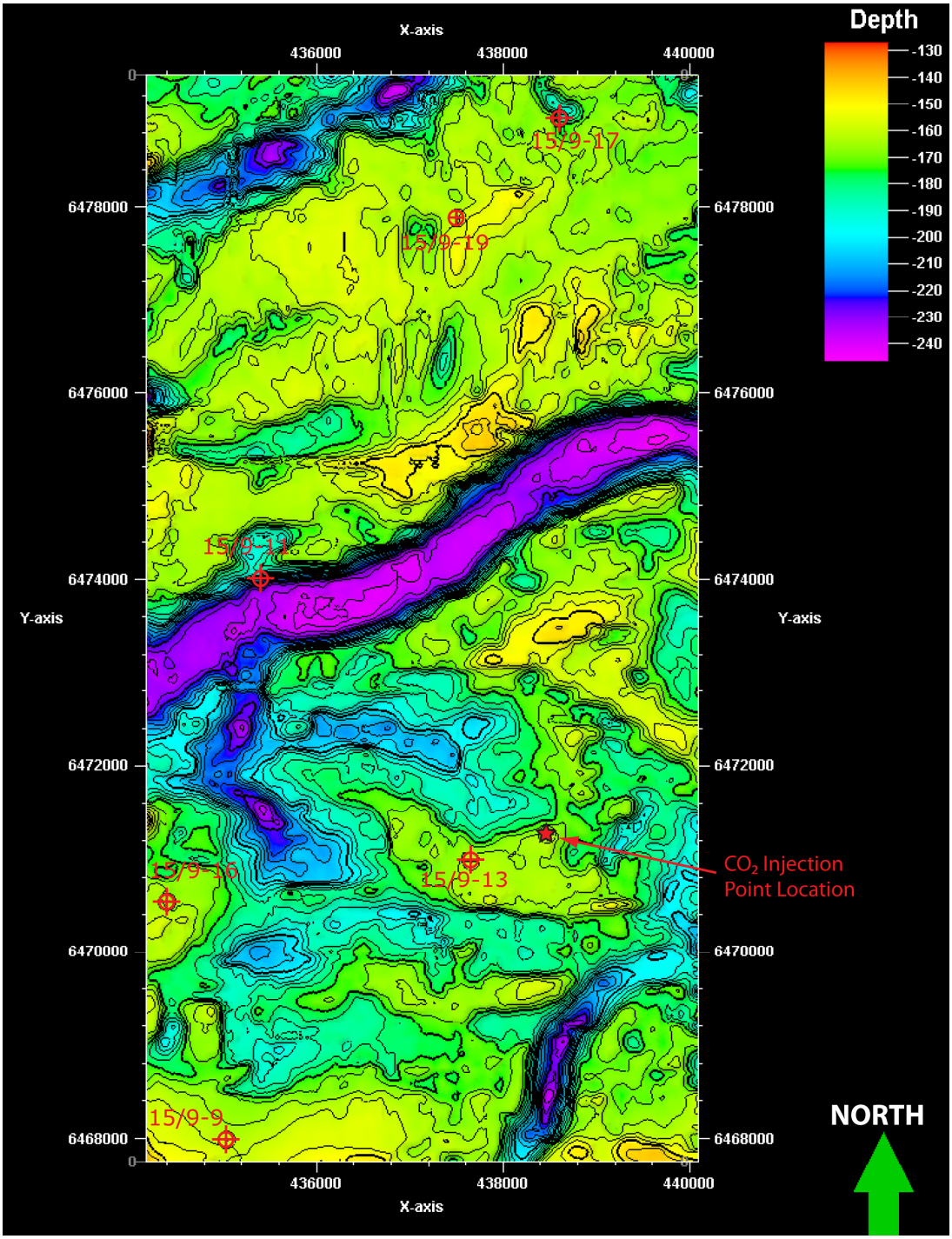

Figure 2.38: Second phase of tunnel valley and channel incision observed in the local survey area. Note the NE-SW and N-S oriented cross-cutting feeder channels and the wider, near seabed channels in the S. UTM 31V grid in 0.4 km increments.

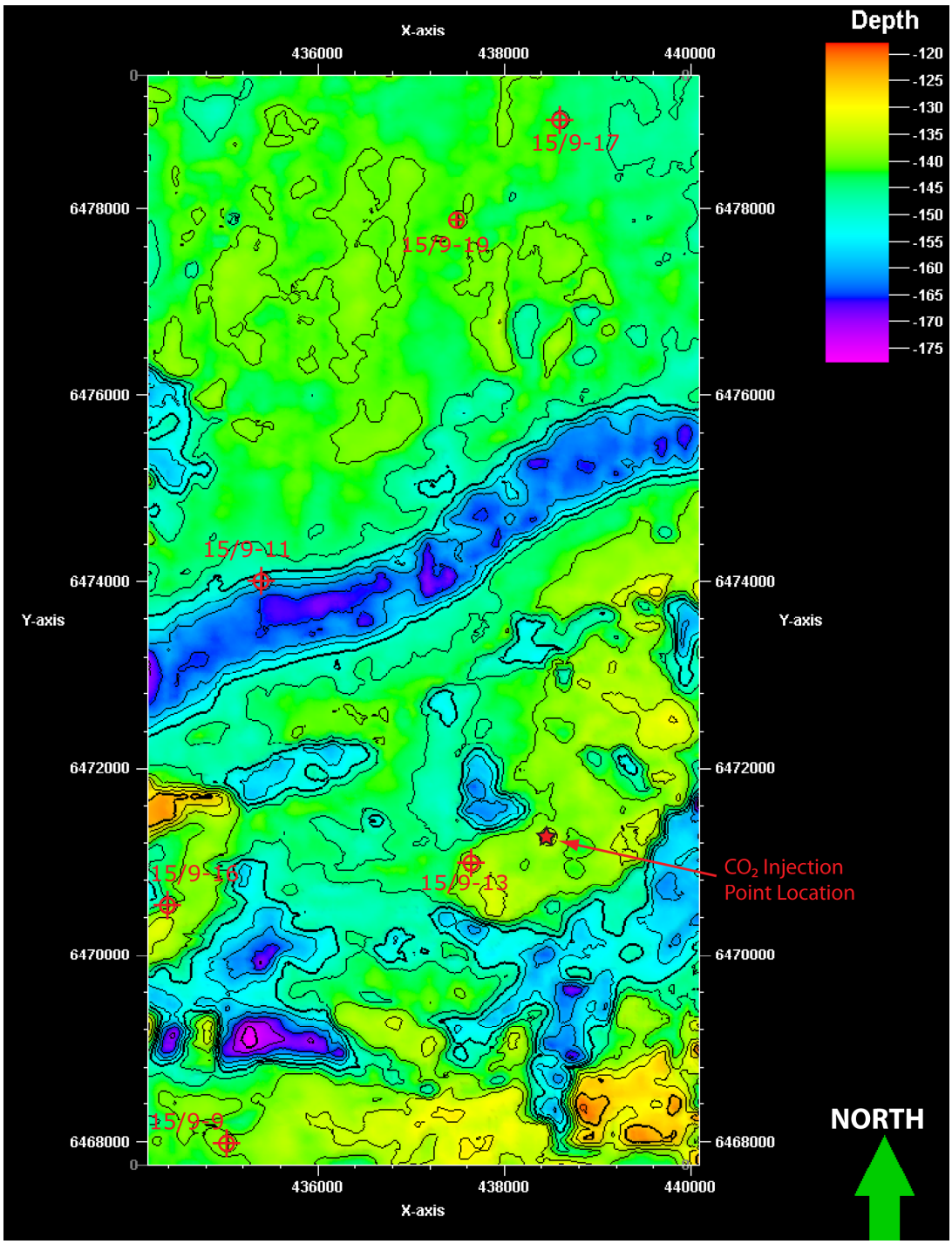

Figure 2.39: Third phase of tunnel valley and channel incision observed in the local survey area. Note the longevity of the central tunnel valley adjacent to well 15/9-11, which is observed throughout all three phases. UTM 31V grid in 0.4 km increments.

2.8 Discussion:

The top layer of the CO_2 plume in contact with the caprock is currently migrating North into areas where we identified the presence of overlying high amplitude anomalies (i.e. gas accumulations and carbonate cemented zones), faults/lineations and chimney structures (Figure 2.31). We also established spatial correlations between apparently isolated anomalies and evident palaeo-fluid migration pathways within the caprock and overburden (refer to Figures 2.11-2.13, 2.21-2.23 and 2.27-2.36). To assess how a migrating CO_2 plume may interact with these mapped structures, we review published literature associated with the Sleipner area.

Prior to CO_2 injection, gas chimneys and high-amplitude seismic anomalies were identified in the overburden above the Sleipner gas fields and attributed to natural gas seepage from underlying hydrocarbon reservoirs or carbonate-cemented horizons (Heggland, 1997). Within Hordaland Group sediments of the North Sea, the concept of vertical fluid migration via polygonal faults, injectite structures, and an association with mud diapirism are well documented (Cartwright *et al.*, 1994, 2003, 2007; Hurst *et al*., 2003; Løseth *et al*., 2003, 2009; Jackson & Stoddart, 2005; Satur & Hurst, 2007). Heggland (1997) suggested that similar links existed between the Hordaland Group underburden and Nordland Group overburden at Sleipner, given a dominant NE-SW alignment for Miocene faulting and high-amplitude seismic anomalies observed in the overburden. Lothe & Zweigel (1999) and Zweigel *et al*. (2000) also noted spatial associations between mud diapirs below the Utsira Sand and overburden anomalies. The latter features were interpreted as shallow natural gas, but no evidence of a preferential NE-SW Miocene fault alignment was documented. In a detailed geophysical analysis of the Utsira Formation and overburden undertaken post-CO_2 injection at Sleipner, Borgos *et al.* (2002) describe the presence of faults/lineaments mapped in a NE-SW, NW-SE, NNW-SSE, N-S, NNE-SSW and WNW-ESE direction within the Nordland Group. These authors propose that these structures act as sealing flow boundaries and non-sealing faults to constrain the growth of the CO_2 plume layers through discrete compartmentalisation, hence the continued extension of certain layers of the plume along an approximate NE-SW axis.

Related studies note an absence of natural gas within the Utsira Formation (Lothe & Zweigel, 1999; Zweigel *et al*., 2000; Borgos *et al*., 2002), which given the presence of overburden anomalies and probable deep source for the underlying Sleipner hydrocarbon reservoirs, implies that natural gas has probably migrated through the formation without accumulating, or accumulated and subsequently breached the caprock in geologically recent times. To date, no samples are available for the seismic anomalies above the Sleipner storage site to conclusively explain their origin. We observe that the anomalies from horizons B and D at Sleipner exhibit a combination of pull-down (gas?) and pull-up (diagenetic carbonate?) effects, which could represent methane from biogenic (in-situ) or thermogenic (migratory) processes, or carbonate cemented zones respectively, as described from other areas of the North Sea with a similar depositional history (e.g. Schroot & Schüttenhelm, 2003; Ligtenberg, 2005; Judd & Hovland, 2007).

An alternative explanation is that these anomalies and chimneys are artefacts: Borgos *et al.* (2002) suggest that anomalies exhibiting central pull-down and marginal pull-up may be pre-processing artefacts resulting from pre-stack time migration; chimney structures directly underlying a "hard" anomaly may represent noise generated by the anomaly itself (Mads Huuse, pers. comm., 2010); some anomalies at depth are believed to be amplitude enhancements created by coincident multiples from shallower events (Zweigel *et al.*, 2000; Andy Chadwick, pers. comm., 2010). In spite of these alternatives, the well log evidence we present (albeit from outside the regional survey area), supports the presence of gas in the overburden between the FIP and FTP surfaces and also at shallower depths (Figures 2.6-2.8). Well log and drilling report data also indicates the presence of silts and sands at these depths where gas could form accumulations (Appendix 2.1). We demonstrate that chimney/anomaly pairs are often offset with reverse polarity effects evident at the connection point (e.g. Figure 2.28), yet even when these pairs are concentrically aligned with no reverse polarity evident, an intersecting lineation and/or underlying mud volcano is usually present (e.g. Figures 2.21, 2.22 and 2.27), suggesting a spatial association rather than just mere coincidence.

If our mapped anomalies and chimneys (Figures 2.11-2.13, 2.14-2.19 and 2.30-2.31) do represent natural gas and their migration expressions respectively, then arguably, the overburden has trapped gas above the storage site as a gas phase or as diagenetic carbonate, despite evidence of seabed expressions from the regional and local survey areas indicating continued upward migration (Figures 2.11 and 2.29). The presence of natural gas in sediments can reduce shear strength (Andreasson *et al*., 2007), which would enable CO_2 to access existing pathways. Conversely, if pull-up anomalies represent carbonate cementation, these features may initially seal but subsequently weaken in the presence of acidic CO_2-saturated water. Cement dissolution may also create preferential migration pathways, as hypothesised for the 'chimney' progression of CO_2 within the Utsira Formation (Hermanrud *et al*., 2007, 2010). We have previously described the presence and abundance of CO_2 reactive elements within the Utsira Sand (shell fragments) and Nordland overburden (calcareous muds and lignite) from well log and drilling report data (Section 2.4 and Appendix 2.1).

Supercritical CO_2 has a lower density contrast with respect to pore water than natural gas, necessitating higher capillary entry pressures to overcome the threshold pressures of water-wet mud rocks. Laboratory experiments show that both natural gas and supercritical CO_2 require the presence of fractures or faults to ingress shales at low capillary entry pressures (Harrington & Horseman, 1999; Springer & Lindgren, 2006; Harrington *et al.*, 2009). But only three years after CO_2 injection commenced at Sleipner, CO_2 was detected in the Sand Wedge underlying the caprock, having breached or bypassed eight internal mudstone barriers, including the ~5-7 m thick barrier immediately underlying the Sand Wedge. Various seal bypass mechanisms are proposed for these barriers within the Utsira Formation, including micro-fractures, injectites, carbonate cement dissolution, sub-seismic faults, lateral discontinuities, erosive holes created by high-energy deposition of overlying sands and chimney excavation (Zweigel *et al*., 2004a; Hermanrud *et al*., 2007, 2010). Similar mechanisms may also affect the overburden.

Past Ice Age events have exerted considerable influence on North Sea geology during the Cenozoic. We have described how the caprock sample acquired from well 15/9-A11 proximal to the storage site returned a 2-3 MPa discrepancy between calculated values (6-7 MPa) and actual values (9 MPa) for the vertical effective stress component (Pillitteri *et al.*, 2003), which is attributed to loading from a 200 m thick ice sheet (Figure 2.10). Basin scale effects of ice loading/unloading on pore pressure, temperature and stress fluctuations are documented for Northern Europe during glacial and inter-glacial events of the Oligocene to Miocene and Pliocene to Pleistocene (Grollimund & Zoback, 2000; Cavanagh *et al.*, 2006). Overpressure and micro-fracturing associated with these episodes may have provided a mechanism for natural gas seepage in the geological past (Cavanagh *et al.*, 2006). During gradual ice-related loading of clay-rich sediments, de-watering can occur directly or indirectly via silt or sand interbeds, resulting in pore collapse and porosity-permeability reduction. In this scenario sediments become overconsolidated and brittle. This makes the overburden susceptible to dilatent shearing if placed under additional stress (Nygård *et al.*, 2006). Alternatively, clay-rich sediments unable to de-water due to rapid ice sheet loading or permafrost become overpressured. The release of natural gas, or destabilisation of gas hydrates trapped in the substrate may occur with the subsequent removal of the ice sheet load and associated temperature change, creating fluid escape structures (Fichler *et al.,* 2005; Judd & Hovland, 2007), as illustrated by the conceptual model shown in Figure 2.40.

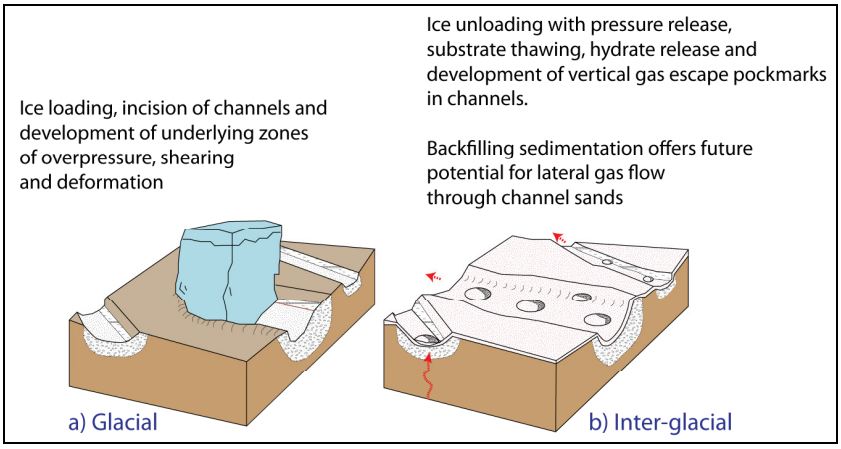

Figure 2.40: Conceptual model of a) glacial ice loading illustrating channel base deformation processes and b) inter-glacial unloading illustrating thawing of entrained hydrates and gas escape processes (modified after Judd & Hovland, 2007).

Compaction of the Hordaland mud mounds and subsequent fluid escape due to loading from the overlying Utsira Formation and Quaternary succession are proposed as potential causal mechanisms for faults induced in the Nordland Group (Borgos et al., 2002; Jackson & Stoddart, 2005) and these faults would also be susceptible to reactivation during ice loading/unloading events. Yet, it is debated whether the Nordland Group overburden behaves in a ductile manner with fracturing unlikely to occur (Zweigel *et al*., 2000; Pillitteri *et al*., 2003), or if high strain rates caused by increasing pore fluid pressure have triggered brittle deformation in soft sediments (e.g. Ingram & Urai, 1991; Løseth *et al*., 2009). Seal lithology, thickness and uniformity are critical parameters affecting ductility as Downey (1984) describes for a range of seal lithologies (Table 2.7). The drilling reports and well logs from the Sleipner area suggest there are significant lateral variation in seal lithology (refer to Section 2.4 and Appendix 2.1), varying from clay shales to very calcareous silty shales, thus seal ductility may be expected to possess a similar lateral variability.

Seal Lithology	**Ductility**
Salt	Highest
Anhydrite	
Kerogen-rich shales	
Clay shales	
Silty shales	
Carbonate mudstones	
Cherts	Lowest

Table 2.7: Range of ductility for different seal lithologies (modified from Downey, 1984).

Shallow marine, arctic conditions prevailed in the North Sea during the late Pliocene to early Pleistocene, as evidenced by an increase in ice-rafted debris and preserved linear seabed scouring and (Jansen & Sjøholm, 1991; Jansen et al., 2000; Kuhlman *et al.*, 2004; Kuhlmann & Wong, 2008; Knies *et al*., 2009; Ottesen *et al.*, 2009). Nordland Mudstone cuttings samples analysed from well 15/9-9 for the Pleistocene interval immediately overlying the Utsira Formation at Sleipner (590-820 m) may

provide further evidence of an early Pleistocene glacial intensification. Bøe & Zweigel (2001) report a distinct upward transition from the Former Intra-Pliocene surface for well log signature and mineralogy of early Pleistocene sediments, with lithic fragments up to 5 mm diameter, indicating possible IRD (ice-rafted debris) and a reduced smectite content in the upper horizon between 590-670 m. Smectite reduction is attributed to an intensification of glaciation (Knies *et al*., 2009). This appears to contradict evidence from Head *et al.* (2004), who found no trace of IRD in Nordland Mudstone samples from well 15/9-A11 (drilled from Sleipner A, NE of the well 15/9-9 location). However, samples in this study were obtained from a deeper core collected ~20 m above the caprock (784-790 m) and dated at 1.8-2.4 Ma (Gelasian). Head *et al.* (2004) suggest a deposition rate of 25 cm/1000 yrs for the Nordland Mudstones, thus assuming the interval sampled by Bøe & Zweigel (2001) is ~114 m shallower in the succession, it will be ~0.46 Ma younger at 1.34-1.94 (Calabrian), which accords with the onset of widespread glaciation and distribution of IRD in NW Europe (Jansen & Sjøholm, 1991; Jansen *et al*., 2000; Ottesen *et al.*, 2009). Palynological evidence from Head *et al.* (2004) also suggests a shift from a warmer to cooler climate during the early Pleistocene; the shallowest samples obtained from 784 m were mainly comprised of species tolerant to cold water temperature conditions.

The Former Intra-Pliocene surface above the storage site displays a series of parallel channels and aligned depressions with a prominent NE-SW and ENE-WSW orientation. During a glacial intensification, these deep, straight features are conventionally associated with high flow velocities encountered in marine turbidity currents and fast flowing ice streams, or attributed to the ploughing action of iceberg keels (Dowdeswell & Bamber, 2007; Ottesen *et al.*, 2009; Laberg *et al.,* 2010). Borgos *et al.* (2002) also report the presence of moraine deposits within the embayment shown on Figure 2.34, at the juncture where these linear channel features deviate from ENE-WSW to NE-SW. Based on the morphology of modern analogues (Clark *et al.,* 2003 and O'Cofaigh *et al.,* 2005) and the presence of similar structures within younger Pleistocene sediments to the W of the Sleipner area (Graham *et al.,* 2007), we suggest these features may record the presence of an ice sheet to the NE,

extending into the marine environment, with an ice stream or strong currents transporting glacially-derived terrestrial and re-worked marine sediments across the shelf area to the SW and WSW. Borgos *et al.* (2002) favour iceberg plough marks as the mechanism for channel incision based on the trough-like character of the channel base, but other research suggests that iceberg plough marks of this length (10-20 km) should display a more sinuous morphology and shallower incision depths (Dowdeswell & Bamber, 2007; Ottesen *et al.*, 2009). The thicker sediment package to the N reflects the gradual infill of an embayment during the early Pleistocene (Figure 2.36) with silt and sands as evidenced from the well log for 15/9-17 (Appendix 2.1). Seismic evidence for the early Pleistocene, suggests NE-SW and ENE-WSW dominant transport directions for prograding sediments derived from the Norwegian coast (Huuse & Clausen, 2001; Ottesen *et al.*, 2009). The Norwegian Channel ice stream is believed to have initiated ~1.1 Ma, proximal to the W coast of Norway (Sejrup et al., 2003; Ottesen *et al.*, 2009) and this must have strongly influenced sub-glacial drainage alignment in the Sleipner area during subsequent phases of glaciation.

Presence of a continuous ice-sheet between the UK and Norway during a later phase of the Pleistocene was recently confirmed (Bradwell *et al*., 2008; Sejrup *et al*., 2009). The Sleipner area was probably ice covered from 32-25 ka BP and 17-14 ka BP (Sejrup *et al*., 2009). Four stadials are recorded in the Witch Ground area of the North Sea (Lonergan *et al*., 2006) and new evidence suggests six to ten stadials for the offshore UK Sector of the Central North Sea (Stewart *et al*., 2007). This suggests the Sleipner area was affected by more than the three known glacial episodes in Northern Europe during the last 500 ka (Elsterian, Saalian, and Weichselian) and multiple cycles of ice sheet advance/retreat during the Pleistocene.
In these younger Pleistocene sequences, glacial tunnel valleys and channel systems are reported from the Sleipner area (Bauer & Fichler, 2002; Fichler *et al.,* 2005). There is still a great deal of debate over their origin and method of infill (Huuse & Lykke Anderson, 2000; Lonergan *et al.*, 2006), but a consensus of opinion favours a sub-glacial origin, with possible initiation along lines of seafloor or glacier weakness (Bauer & Fichler, 2002), and sub-glacial hydraulic excavation occurring through a

combination of steady-state or catastrophic processes (Huuse & Lykke Anderson, 2000). These are large-scale features: widths up to 2-3 km, depths up to 300 meters and lengths up to, and exceeding a hundred kilometres are reported from the Central North Sea (Lonergan *et al*., 2006). Studies in the UK Sector, west of Sleipner (Graham *et al*., 2007 and Stewart *et al*., 2007) suggest that North Sea tunnel valleys contain a multi-stage, fining-up sequence of basal till, fluvio-glacial gravels and bar sands, capped by glacio-marine/lacustrine silts and muds. Studies from the central North Sea and Denmark suggest that tunnel valley infilling may involve a combination of glacio-marine, fluvio-glacial and marine processes during the transition between glacial and inter-glacial periods (Huuse & Lykke Anderson, 2000; Lonergan *et al.*, 2006). In our local study area, the only well penetrating a glacial channel axis (Well 15/9-13), records 115 m of sand on well logs at 150-265 m depth (Appendix 2.1), although we also note sand-rich lithologies at similar depths from four other wells in close proximity to channel margins (Appendix 2.1 and Table 2.6).

Tunnel valley analogues of those present in the Nordland Group overburden have also been studied onshore by Le Heron *et al*. (2005), who describe sub-glacial deformation and shearing effects associated with the degree of coupling between ice sheet and substrate. Deformation and fluid escape structures, micro-fracturing and faulting are also described by Judd & Hovland (2007) from the North Sea in connection with ice sheet loading and transport processes as depicted in the conceptual model from Figure 2.40. We expect similar deformation/shear structures to be present below glacial tunnel valleys in the vicinity of the Sleipner storage site.

2.9 Conclusions:

The Nordland Group overburden in the Sleipner vicinity appears to be a more complex depositional and latent fluid flow environment than previous models suggest. Our detailed evaluation of 3D seismic data and well logs has revealed the presence of faults/lineations, chimney structures, high-amplitude anomalies, unconformities, tunnel valleys, channels, palaeo-pockmarks and seabed craters. Some of these features appear to be spatially connected with structures in the Hordaland Group underburden including polygonal faults, sand injectites and mud volcanoes. The elements of this complex network have served to transport or accumulate natural gas over geological time and result from processes that may operate individually or collectively to compromise seal integrity. These same structures may also be predictable pathways for CO_2 migration within the overburden at Sleipner.

Glacial and inter-glacial cycles affecting the Nordland Group overburden began during the early Pleistocene ~2 Ma, culminating in ice loading and unloading events that may have reduced sediment ductility and created fluid migration pathways via faults, micro-fractures and dilatent shear zones. Well log evidence reveals the presence of sand and gravel within Pleistocene tunnel valleys and channels; these facies may be used as pathways or secondary storage by migrating CO_2 (albeit at the expense of reduced storage capacity if CO_2 is in a low density gas-phase).

Evidence from well logs is insufficient to prove whether seismic anomalies in the Nordland Group overburden represent natural gas deposits of thermogenic/biogenic origin or carbonate cemented zones, although seismic and mineralogical evidence suggests diagenetic carbonate may be present between the Former Intra-Pliocene and Former Top Pliocene surfaces. Drilling reports from the Sleipner area also confirm the presence of shallow gas; therefore pull-down anomalies and zones of reverse polarity probably represent natural gas accumulations. We have also highlighted the presence of reactive minerals in the Utsira Sand and the overburden (i.e. lignite, shell fragments and other carbonate rich minerals) that may react with stored or migrating CO_2 in a positive or negative manner.

A stringent and holistic approach is required for 21st. century CO_2 storage site selection and modelling that extends the rigour of reservoir characterisation and simulation to the overburden and secondary storage containment. This is an essential requisite for areas affected by ice loading and glacial channelling, such as the North Sea. We need to understand how overburden structures relate to migration pathways in case of seal failure and leakage, since identifying and monitoring potential CO_2 escape routes through sub-seismic faults, micro-fractures and thin, isolated carrier beds requires a more discriminatory approach, as highlighted by Cartwright *et al.* (2007) and Løseth *et al.* (2009). The traditional hydrocarbon industry approach is focussed on the reservoir and caprock seal. By contrast, the carbon capture and storage industry has highlighted the importance of the overburden as a contingency seal, secondary repository or potential migration pathway to surface.

Chapter 3:

Could CO_2 storage site performance be compromised by palaeo-gas migration conduits in the overburden?

Grant Nicoll[1], Mark Naylor[1], Andrew Cavanagh[2], Sebastian Geiger[3] and Stuart Haszeldine[1]

[1]The University of Edinburgh, Edinburgh, Scotland.
[2]The Permedia Research Group Inc., Ottawa, Canada,
[3]Heriot-Watt University, Riccarton, Edinburgh, Scotland.

"Baby, can't you see I'm calling
A guy like you should wear a warning
It's dangerous, I'm fallin'

There's no escape I can't wait
I need a hit baby, give me it
You're dangerous I'm lovin' it
Too high can't come down
It's in the air and it's all around
Can you feel me now

With a taste of your lips I'm on a ride
You're toxic I'm slipping under
With a taste of a poison paradise
I'm addicted to you
Don't you know that you're toxic
And I love what you do
Don't you know that you're toxic…"

Extract from "Toxic" (Britney Spears, 2004)

3.1 Introduction:

In an attempt to mitigate climate change, depleted hydrocarbon fields and saline aquifers situated beneath the offshore continental shelf of NW Europe are increasingly being proposed as suitable repositories for anthropogenic CO_2 (Odenberger, *et al*., 2008; Chadwick *et al*., 2009a; Haszeldine, 2009). Typical strategies involve extracting CO_2 from the flue gases of industrial point source emitters such as refineries and coal-burning power stations in the UK and mainland Europe, then transporting the separated CO_2 offshore via dedicated pipelines for sub-surface disposal. Two small-scale storage sites are already operating successfully offshore Norway (Korbøl & Kaddour; 1995; Baklid *et al.*, 1996; Maldal & Tappel, 2004; Arts *et al*., 2008), removing CO_2 from produced natural gas and re-injecting the unwanted by-product back into the sub-surface, rather than venting to atmosphere. The Sleipner CO_2 storage site, situated adjacent to the Sleipner Vest (West) and Øst (East) gas fields in the North Sea, has been operational since 1996. The Snøhvit storage site, situated in the Barents Sea, has been operational since 2007 (Figure 3.1). Collectively these facilities inject several million tonnes (Mt) of CO_2/year into deep, sub-seabed saline aquifers. Since Sleipner and Snøhvit are the first offshore CO_2 storage experiments conducted on a large-scale, experience gained at these sites is invaluable and will guide future site planning (e.g. through the development of more stringent appraisal, risking and monitoring techniques).

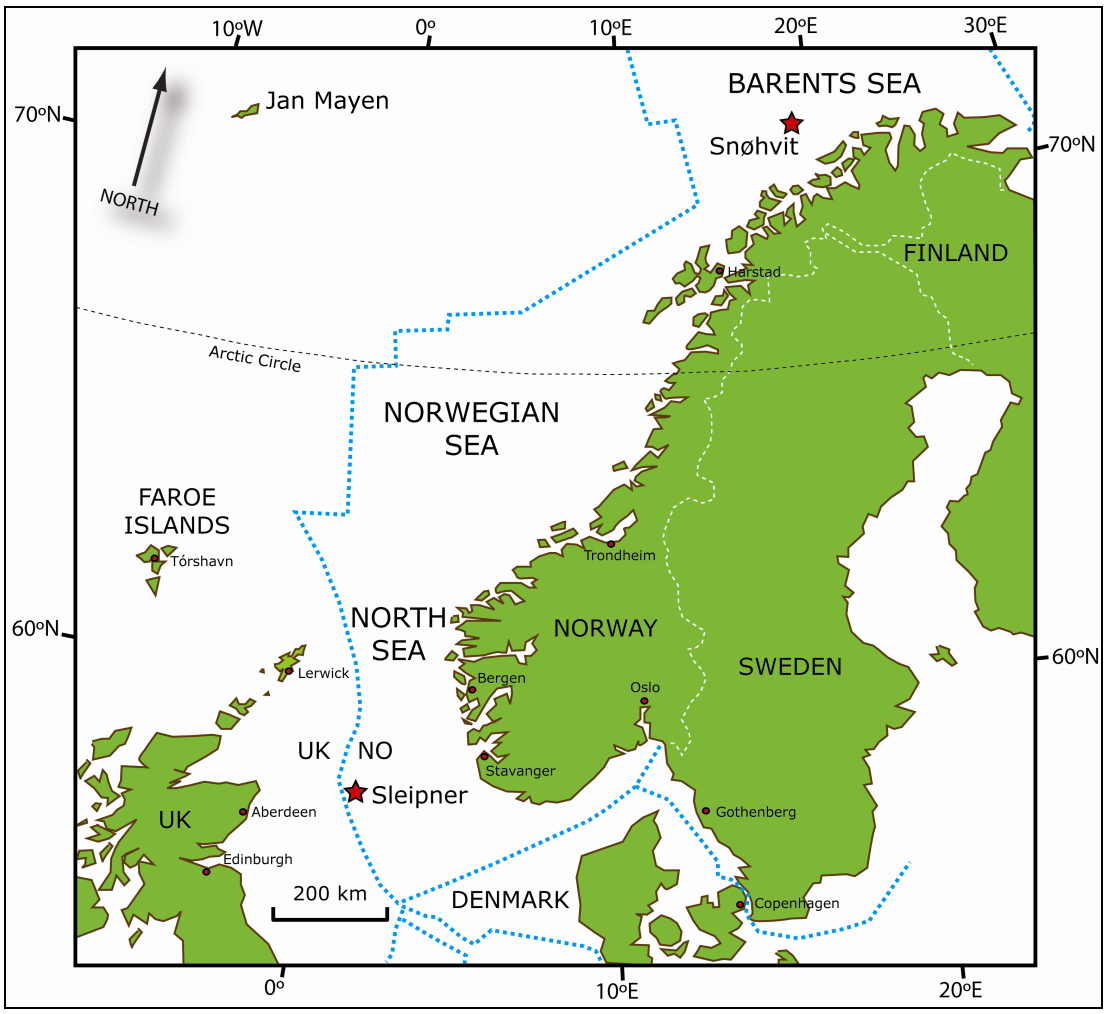

Figure 3.1: Location map for Sleipner and Snøhvit gas fields. CO_2 is extracted from produced gas via an amine capture process and re-injected into the Utsira Formation and Tubåen Formation respectively; both are saline aquifers. Blue dashed lines represent offshore hydrocarbon licence boundaries for different countries.

During the past fifty years of hydrocarbon field development in the North Sea, a wealth of marine geophysical information has been amassed from exploration and site development surveys (Evans *et al.*, 2003). Detailed analysis of this data has revealed that certain seabed and sub-seabed areas of the North Sea contain indicators of natural gas migration through geological time to the present day (Judd & Hovland, 2007). These include features such as seabed depressions or pockmarks (detected on bathymetric and sonar surveys) and gas seepage pathways (detected on seismic and sub-bottom profiling surveys). Such indicators are frequently located in overburden sediments deposited above underlying hydrocarbon reservoirs (e.g. Witch Ground Graben), and can be used as an exploration tool to delineate prospective areas.

Conversely, from a CO_2 storage perspective, the presence of gas migration structures in the overburden could increase the risk of site compromise, since migration pathways have been associated with intersecting lines of weakness such as shear zones and fault planes (Ligtenberg, 2005, Gay *et al*., 2006). Planning of future offshore storage sites in NW Europe will require a rigorous assessment of the potential risk for CO_2 leakage and migration via the overburden. In some cases, it may be necessary to avoid known areas of palaeo-gas migration for proposed CO_2 storage locations (Figure 3.2). The key to understanding whether these features presently constitute a risk for CO_2 leakage is to evaluate the pressure and temperature conditions under which natural gas may have initially leaked, thus allowing the capillary breakthrough properties of critical formations such as caprocks and internal barriers to be constrained. For example, at Tordis (Figure 3.2), overpressure from water-injection operations induced fractures in the overburden (Kvalheim, 2009); demonstrating that failure to acquire such detailed geological and petrophysical information on the overburden may lead to a site being operated beyond safe limits.

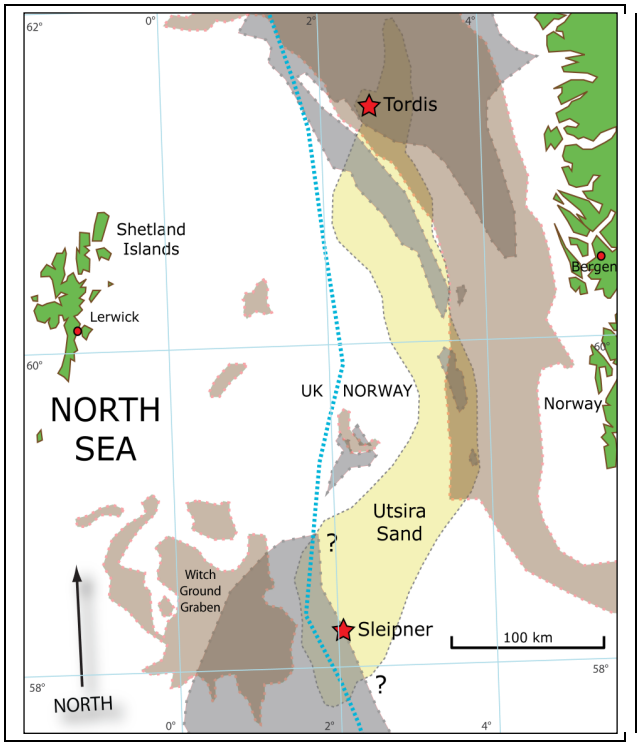

Figure 3.2: North Sea location map of major shallow gas anomalies (grey) and seabed pockmark areas (brown), with areas of uncertainty for shallow gas indicated by question marks (modified from Judd & Hovland, 2007). Yellow areas show the lateral extent of the Utsira Sand. Blue dashed line shows the UK/Norway median line. Red stars show respective locations of the Sleipner and Tordis developments.

In our regional and local studies of the Sleipner area (Chapter 2), we performed detailed sub-seabed mapping using a 3D seismic dataset from 1994 (i.e. acquired before CO_2 injection commenced in 1996), to assess whether this area contained indicators of palaeo-gas migration. Our interpretation identified a large seabed crater (500m^2 area), several chimney structures, lineations/faults and high-amplitude seismic anomalies present at four distinct horizons within the Nordland Group overburden sediments deposited above the Sleipner CO_2 storage site. Some features are laterally offset by several kilometres, but some critically lie within the current CO_2 plume footprint. Given the supporting evidence of shallow gas inventory reported in drilling reports from the Sleipner area (NPD, 2010), we conclude these features are indicators of thermogenic or biogenic gas migration and accumulation over geological time. Vertical palaeo-gas migration pathways have penetrated the caprock seal above the Utsira Sand and it is possible that one or more may be encountered by the top layer of the CO_2 plume as it ascends and migrates laterally beneath the caprock.

Assuming these pathways either contain methane (CH_4) or natural gas with a high (i.e. 80-90%) methane content (Judd & Hovland, 2007), we now consider whether migrating CO_2 (in supercritical, liquid or gas phase) could enter and re-use these pathways as preferential bypass routes through the caprock and overburden using the Sleipner model as a case study. In order to develop a robust methodology that can be applied to Sleipner and other CO_2 storage sites operating under similar storage conditions, we first need to identify the range of significant parameters and physical conditions likely to be encountered at Sleipner and highlight any uncertainties in the data requirements. We use the following methodology to achieve our objectives:

- First, clearly define palaeo-gas migration conduits and explain why these structures influence the CO_2 storage site selection process,
- Critically review modelling parameters and site conditions at Sleipner,
- Assess which key elements present the greatest uncertainty and risk if migrating CO_2 encounters a palaeo-gas migration conduit and test these key elements via end-point members,

- Test the conditions under which palaeo-gas migration conduits (CH_4 proxy) can be re-used by migrating CO_2 to compute a range of critical column heights,
- Evaluate the effects of CO_2 entry into a palaeo-gas migration conduit filled with CH_4.

3.2 Palaeo-Gas Migration Conduits:

We define a palaeo-gas migration conduit as a sub-surface structure that at some point has had (or may still have) a higher permeability than the rock formations surrounding it. Thus the structure has formed (or may still form) a preferential flow path or conduit for fluid migration over geological time, driven by buoyancy effects or a differential pressure gradient (Figure 3.3). Examples of such structures in relation to their fluid flow potential are extensively documented in the North Sea and many other areas of the world and include:

- Faults, fractures, shear zones and joints (Brown, 2000; Nunn & Muelbroek, 2002; Berndt *et al*., 2003; Gudmundsson, *et al*., 2003; Bjørlykke *et al*., 2005; Le Heron *et al*., 2005; Cartwright *et al*., 2007)
- Gas chimneys (Heggland, 1997 and 2005; Bauer & Fichler, 2002; Ligtenberg, 2005; Gay *et al*., 2006; Andreassen *et al*., 2007; Judd & Hovland, 2007; Cartwright *et al*., 2007; Løseth *et al*., 2009)
- Sand injectites (Hurst *et al*., 2003; Mazzini *et al*., 2003; Huuse & Mickelson, 2004; Judd & Hovland, 2007; Cartwright *et al*., 2007; Satur & Hurst, 2007; Løseth *et al*., 2009; Cartwright, 2010)
- Clinoforms (Roberts & Fillon, 2004; Howell *et al*., 2008)
- Unconformities (Hurst *et al*., 2003)
- Glacial tunnel valleys/channels and sub-glacial clastic dykes (Huuse & Lykke-Andersen, 2000; Bauer & Fichler, 2002; Sandersen & Jørgensen, 2003; Fichler *et al*., 2005; Le Heron & Etienne, 2005; Lonergan *et al*., 2006; Graham *et al*., 2007).

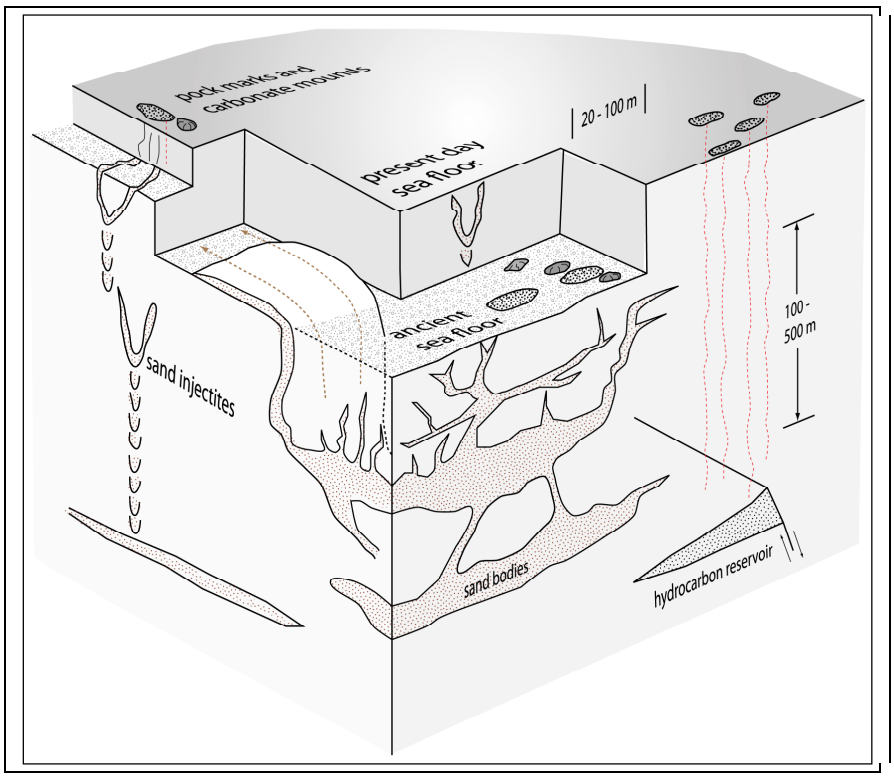

Figure 3.3: Schematic cross-section showing typical examples of fluid migration conduits and their escape expressions at sea floor (modified from Hurst et al., 2003)

Some of these structures may occur at different stratigraphic levels (e.g. due to different depositional/erosional processes, rock properties or stress field orientation) and can be active over a range of geological time periods as a result of ongoing or sudden tectonic processes (e.g. subduction, rifting, glaciation or seismicity). Open conduits may eventually become sealed or cemented due to a loss of fluid supply or a combination of tectonic and diagenetic processes (Judd & Hovland, 2007). But if flow pathways remain open or are reactivated, individually or collectively these structures may create a leakage network that has a significant impact on present day CO_2 storage site security (Figure 3.4).

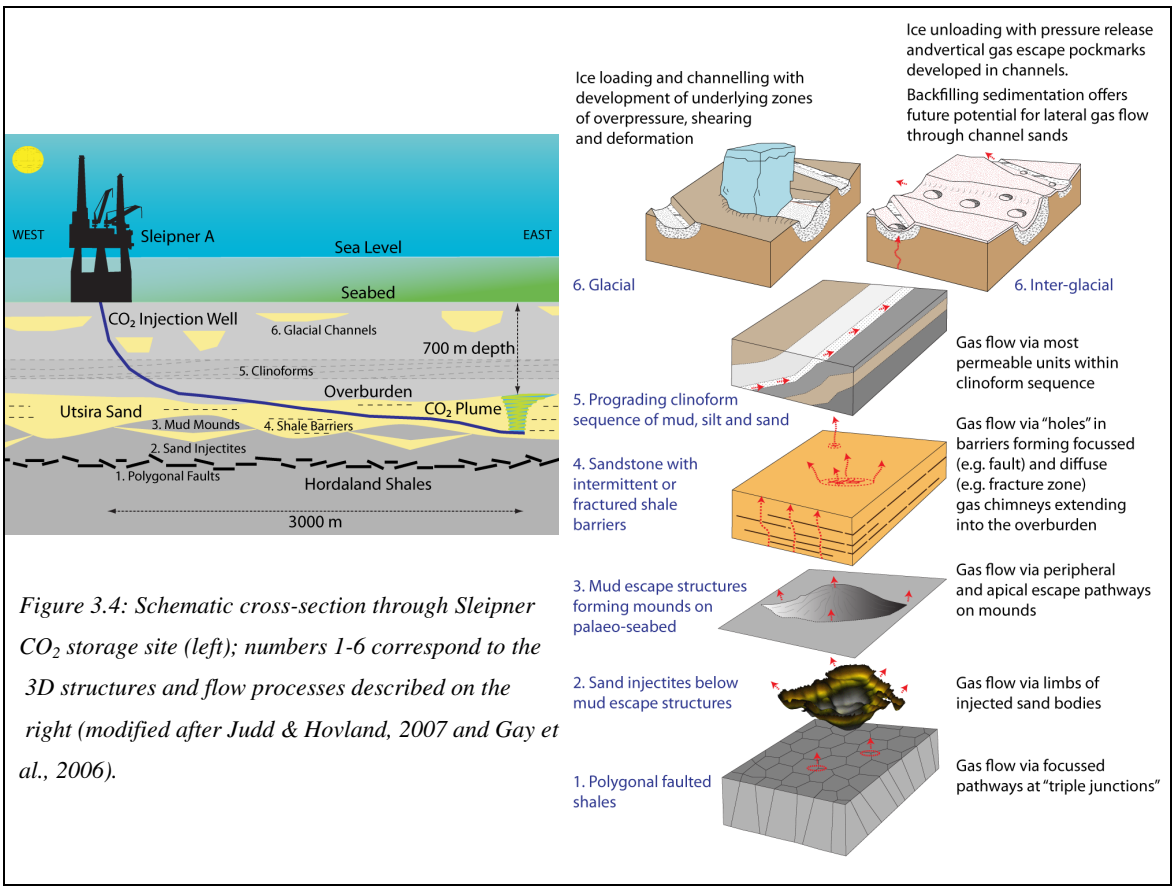

Figure 3.4: Schematic cross-section through Sleipner CO_2 storage site (left); numbers 1-6 correspond to the 3D structures and flow processes described on the right (modified after Judd & Hovland, 2007 and Gay et al., 2006).

Natural gas generation, migration and accumulation are probably, but not necessarily all intermittent and slow processes (Roberts & Nunn, 1995), whereas for a CO_2 storage site, the CO_2 must be injected continuously at higher rates, so the equivalent "generation", migration and accumulation processes are orders of magnitude faster. This may lead to an undesirable disequilibrium within the storage site, such as mineral dissolution or precipitation, pressure/temperature increase in the near wellbore region (Nooner *et al.*, 2007) or Joule-Thomson cooling effects (Pruess, 2008). If migrating CO_2 does encounter an open palaeo-gas migration network, this could lead to site compromise, thus identification of such networks and a critical assessment of the risk they present to storage site security are essential precursors to the selection process. If the risk perception is high, a change of site or injection point location may be required. In some cases, relocation to a more suitable area may be impractical for economic or technical reasons, thus site intervention may be needed to undertake remedial work, such as pre-conditioning or sealing vulnerable parts of the site prior to CO_2 injection (Benson & Hepple, 2005, Levine *et al.*, 2009).

3.3 Review of Sleipner Site Conditions:

Due to its significance as the world's first CO_2 storage site, Sleipner has been the focus for numerous scientific modelling and monitoring studies. We briefly review some of the most influential studies in order to determine the source of critical modelling parameters and ensure that our subsequent analysis is valid for the prevailing site conditions at Sleipner.

3.3.1 Injection Rate:

Injection rate is usually reported in the literature as being ~1 Mt/yr over the proposed 20 year lifespan for the project (e.g. Zweigel *et al.*, 2004a). More recent published data for the injected CO_2 mass (Arts *et al.*, 2008), suggests that the actual injection rate during the first 10 years of the project is rounded-up from 0.84 Mt/yr (Figure 3.5), thus by the end of the proposed 20 year injection period, the site should actually contain ~17 Mt of CO_2, assuming there are no radical changes in injection rate during the remaining years of the project.

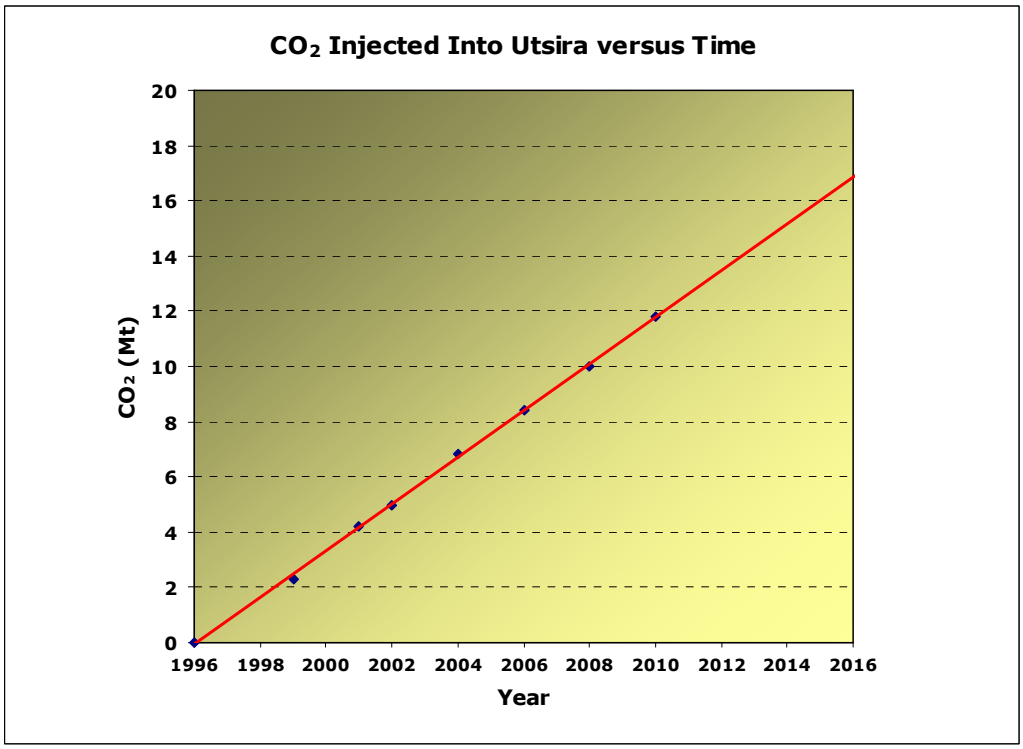

Figure 3.5: Graph of CO_2 mass injected into the Utsira Formation from 1996-2006 (data from Arts et al., 2008 and pers. comm. Ola Eiken, 2010), with projection to 2016, assuming a 20-year injection period for CO_2.

3.3.2 Geothermal Temperature Gradients:

A wide range of temperature models has been used for Sleipner (Table 3.1). Earlier models are based on seabed temperatures of 5-7°C and a single, sub-surface measurement of 37°C at 1058 metres TVDSS, acquired during the CO_2 injection well development process (Zweigel *et al*., 2004a; Bickle *et al*., 2007; Nooner *et al*., 2007). More recent versions consider thermal modelling, to account for temperature fluctuations caused by past glacial events and different thermal conductivities for sandstones and shales. Some models have also been calibrated against proxy temperature measurements from wells in the Sleipner vicinity (Nooner *et al*., 2007; Lindeberg *et al*., 2009; Alnes *et al.,* 2011). Yet there is still much speculation over temperature variations within the CO_2-invaded region arising from CO_2 compression and the effects of elevated temperatures around the wellbore region on CO_2 migration behaviour, since there are no downhole gauges installed within the injection well to accurately constrain the in-situ pressure and temperature conditions (Alnes *et al*., 2011). The injected warm, low-density supercritical CO_2 will probably be surrounded by an envelope of cooler, high-density supercritical CO_2 as it migrates away from the injection point (Nooner *et al*., 2007). Over time, the central core of the CO_2 plume is also expected to attain a temperature approximately 10ºC higher than initial aquifer conditions due to thermal convection (Alnes *et al.*, 2011). The effects of heat transfer via thermal convection within the high poro-perm Utsira Sand have not been thoroughly investigated, nor have the effects of overburden lithology variations (e.g. sand-filled glacial tunnel valleys and channels) or CO_2 replacement of brine on thermal conductivity (Hurter *et al*., 2007a).

Source Publication	Temperatures (°C)	Depth (metres TVDSS)	Location	Comments
Korbøl & Kaddour, 1995	25 - 28	N/A	Unspecified	Caprock?
Baklid *et al*., 1996	37	N/A	Unspecified	Average or from 1058 m reference depth?
Zweigel *et al*., 2004a	4.8 28 37 41	80 810 1058[6] 1083	Seabed Caprock Unspecified Base Utsira	Linear geothermal gradient of 33°C/km
Chadwick *et al*., 2005	29 36	825 1012	Caprock[1] Injection Point[1]	No seabed temperature specified
Nooner *et al*., 2007	4.8 37	80 1058[6]	Seabed Unspecified	Linear geothermal gradient of 33°C/km
Nooner *et al*., 2007	5 36.2 42.5 101.7	80 810 1058[6] 2600	Seabed Caprock[2] Unspecified[2] Unspecified[3]	Dual, non-linear geothermal gradients of 38°C/km in shales and 26°C/km in sands
Bickle *et al*., 2007	7 35 40	80 800 1083	Seabed Caprock Base Utsira	Intermediate temperatures above and below caprock based on different thermal conductivity models
Alnes *et al*., 2008	28-38	870[4]	Caprock?	Gravity data gives CO_2 density best fit of 760 kg/m^3 and (caprock?) temperature of 29°C
Lindeberg *et al*., 2009	5 27.55 37 101.7	80 769 1058[6] 2600	Seabed Caprock Proxy[5] Unspecified[6] Unspecified[3]	Low temperature caprock attributed to glacial temperature fluctuations and geothermal gradient reduction
Alnes *et al*., 2011	48 35.5 36.6 +/- 0.1	1012 1012 Not specified[7]	Injection Point (well) Injection Point (formation) Caprock	Gravity data and temperature modelling suggest average CO_2 density of 675 +/- 20 kg/m^3

Notes:

[1]Temperatures calculated from well logs?

[2]Intermediate values derived from thermal conductivity modelling in BasinMod 1D using different values for shales (1.2 - 2.0 W/m^{-1}/°C^{-1}) and sandstones (2.4 - 4.0 W/m^{-1}/°C^{-1}).

[3]From drill stem tests in Sleipner gas field, top of Ty Formation.

[4]Depth misprint? Most other publications use 800 m or 810 m for caprock depth.

[5]Based on measurement from water production well 15/9-F-7, 8.0 km NW of CO_2 injection point location.

[6]Although the location of this measurement is not explicitly specified in the source publications, it appears to have been acquired from the CO_2 injection well during drilling and completion operations.

[7]Caprock temperature in central (warmer) core of CO_2 plume, assuming expansion from injection point with no heat loss to surrounding formation.

Table 3.1: Range of temperature models used for Sleipner

3.3.3 Brine Density:

Brine density defines the hydrostatic and buoyancy gradients acting within the sub-surface. The density of seawater varies between 1020-1029 kg/m^3. A typical seawater density for the North Sea, based on 3.5 Wt% salt content and 5°C fluid temperature at atmospheric pressure is 1028 kg/m^3. Brine density increases with increasing pressure and salinity, but decreases with increasing temperature (Driesner & Heinrich, 2007; Bennion & Bachu, 2008). Due to the uncertainty of the aquifer temperature in the region of the Sleipner storage site, a wide range of brine densities is thought to prevail (Table 3.2).

Source Publication	Brine Density for Sleipner Modelling (kg/m^3)
Zweigel *et al*., 2004a[1]	1022
Chadwick *et al*., 2005[2]	1040
Springer & Lindgren, 2006[2]	1013
Bickle *et al*., 2007[3]	1020

Notes:

[1]Calculated from wireline density logs run in Utsira Sand at 906-909 metres TVDSS

[2]Brine density calculated from well logs?

[3]Brine density calculated from TOUGH2

Table 3.2: Range of brine density values used for Sleipner

It is also necessary to consider the post-injection increase in brine density due to the dissolution of injected CO_2. Brine saturated with CO_2 is ~10 kg/m^3 more dense than brine containing no dissolved CO_2 (Enick & Klara, 1990; Lindeberg & Bergmo, 2002; Bachu & Adams, 2003). This density difference will eventually lead to a convective overturn process in the long term, creating further mixing and enhancing dissolution (Lindeberg & Bergmo, 2002 and Riaz *et al*., 2006). However, these studies do not consider how geological heterogeneity (e.g. presence of intra-formational shale barriers) may affect the convection process (Simmons *et al.*, 2001; Ghanbari *et al.*, 2006), nor do they consider the effect of impurities (e.g. methane), on CO_2 dissolution. The dissolution rate of the CO_2 plume into the resident brine adds a further uncertainty since dissolved CO_2 cannot be imaged on seismic data, although recent estimates based on time-lapse gravity data (Alnes *et al.,* 2011) suggest an upper bound of 1.8% per year.

3.3.4 Pressure Gradients:

A normal hydrostatic pressure gradient (10 kPa/m) is conventionally used for Sleipner site conditions, based on a 3.5 Wt% salt content and fluid density of 1022 kg/m^3, calculated from wireline logs run in Utsira Sand at 906-909 m (Zweigel *et al.*, 2004a). The following values are generally accepted hydrostatic pressures for the injection point and caprock (Table 3.3). The local pressure field may be ~1-2 MPa higher in the vicinity of the injection point (Baklid *et al.*, 1996), but it is considered that a significant pressure gradient increase is unlikely, given that the Utsira Sand has a high porosity and permeability, in addition to being laterally extensive (Figure 3.2) and several hundred metres thick at the CO_2 injection location (van der Meer & van Wees, 2006).

Source Publication	Location (m TVDSS)	Pressure (MPa)
Bickle *et al.*, 2007	Caprock (800)	8
Bickle *et al.*, 2007	Injection Point (1012)	10

Table 3.3: Range of hydrostatic pressure values used for Sleipner

3.3.5 CO_2 Density:

Since pressure and temperature have a major influence on CO_2 density, a wide range of temperature models are used for Sleipner and different modelling approaches have been used to account for density stratification within the storage site. Either an average aquifer temperature and CO_2 density are used, or more rigorously, a range of values is applied between the injection point and caprock as described in Table 3.4.

Source Publication	Location (m TVDSS)	Density (kg/m^3)
Chadwick *et al.*, 2005	Top Utsira (825) Injection Point (1012) Average	744 718 700
Nooner *et al.*, 2007	Average Average	700 (low aquifer temperature 35°C) 550 (high aquifer temperature 45°C)
Bickle *et al.*, 2007	Caprock (800) Layer 1 (962)	426 607
Alnes *et al.*, 2008, 2011	Average	640 - 770 (lower - upper bound, 2008) 675 +/- 20 (average, 2011)
Lindeberg *et al.*, 2009	Caprock (800) Injection Point (1012)	725 700

Table 3.4: Range of CO_2 density values used for Sleipner

CO_2 density is likely to increase as the buoyant plume ascends, since the effect of temperature reduction is believed to offset any density reduction due to the lower pressure prevailing at the caprock (Zweigel *et al*., 2004a; Nooner *et al*., 2007; Lindeberg *et al*., 2009). Hence CO_2 should remain as a dense, supercritical fluid rather than passing through a phase transition to low-density gas. However, this assumes that the temperature at the aquifer/caprock interface is well constrained and laterally uniform, yet more recent evidence suggests that lateral temperature and density variations are likely to exist (Alnes *et al.*, 2011). Caprock pressure and temperature conditions at the Sleipner storage site are very close to the critical point for CO_2 (i.e. 7.4 MPa and 31.1°C), thus the ability to maintain CO_2 in the optimum (supercritical) storage condition is marginal.

The effect of impurities derived from the CO_2 capture and separation process on injected CO_2 density has also been considered (Zweigel *et al*., 2004a; Nooner *et al*., 2007; Arts *et al*., 2008) and these effects are summarised in Table 3.5.

Source Publication	Impurity	Effects
Zweigel *et al*., 2004a	Methane BTX (butane/toluene/xylene)	Reduced CO_2 density Increased CO_2 density
Nooner *et al*., 2007	0.063% nitrogen, 0.9% methane, 0.123% ethane 0.667% BTX (butane/toluene/xylene)	Reduced CO_2 density Increased CO_2 density
Arts *et al*., 2008	1.5-2.0% methane and heavier hydrocarbons	Reduced CO_2 density

Table 3.5: Effect of capture and separation process impurities on injected CO_2

Zweigel *et al*. (2004a), suggest that the opposing density effects of methane and BTX will cancel each other out, thus CO_2 density is largely unaffected and can be modelled in thermodynamic terms as a pure substance. To the best of our knowledge, this assertion has not been substantiated by published experimental work for such a range of fluid compositions under typical storage conditions.

3.3.6 CO_2 Solubility and pH:

The amount and rate of CO_2 dissolution into pore fluids are important parameters for calibrating geochemical and mass balance models, whilst fluid pH is a major control on mineral reaction kinetics. Solubility is complicated by the interplay between pH, temperature, pressure and salinity, since the introduction of CO_2 into a saline aquifer will initially reduce pH and eventually increase salinity. Generally, high CO_2 solubility is dependent on a high pH, high pressure, low temperature and low salinity.

Rochelle & Moore (2002), performed experimental studies to determine the solubility of pure CO_2 into deionised water and a synthetic Utsira Formation pore fluid. No samples were available from Sleipner, so synthetic pore water was used as a proxy, based on Utsira Formation water samples from the Oseberg field, 200 km north of Sleipner (Gregersen *et al*., 1998). Experiments covered the predicted range of Utsira Formation pressures of 8-12 MPa and temperatures of 18-80°C (Table 3.6). No sensitivity tests were performed to assess the effects of dissolved natural gases (e.g. CH_4, H_2S) on CO_2 solubility (Taggart, 2009), or the influence of injected CO_2 on microbial activity and fluid geochemistry (Morozova *et al.,* 2010).

Source Publication	CO_2 Solubility	Notes
Rochelle & Moore, 2002	4.0 g CO_2/100 g solution	Synthetic Utsira pore water, 37°C and 8 MPa
	4.3 g CO_2/100 g solution	Deionised water, 37°C and 8 MPa
	4.5 g CO_2/100 g solution	Synthetic Utsira pore water, 37°C and 10 MPa
	5.1 g CO_2/100 g solution	Deionised water, 37°C and 10 MPa

Table 3.6: Experimental results for CO_2 solubility at Sleipner

Reactive transport simulations for the Utsira Formation indicate that injected supercritical CO_2 will initially reduce pH from 7.1 to ~3.4 over days to weeks during the initial phase of CO_2/pore water interaction, then pH will increase to over 4.5 after ~9 years due to buffering from the dissolution of calcite and silicate mineral components (Johnson *et al*., 2004; Gaus *et al*., 2005). In the short term (i.e. injection period 20-25 years), calcite dissolution is predicted to be more pronounced within the sandstone rather than the shale inter-beds and calcite precipitation is also predicted beneath shale layers where CO_2-saturated and under-saturated formation waters mix (Audigane *et al*., 2006).

3.3.7 Capillary Entry Pressures at the Caprock:

To determine properties for a cap rock analogue, representative Nordland Mudstone samples from wells in the Sleipner area (Figure 3.6), were tested for mineralogy, mechanical properties and capillary entry pressures, using cuttings acquired from eight wells (Lothe & Zweigel, 1999; Bøe & Zweigel, 2001; Kemp *et al*., 2002; Lindgren *et al*., 2002) and a single core sample acquired from deviated development well 15/9-A-11, drilled from the Sleipner A facility during 2002 (Pillitteri *et al*., 2003; Head *et al*., 2004; Springer & Lindgren, 2006; Harrington *et al*., 2009).

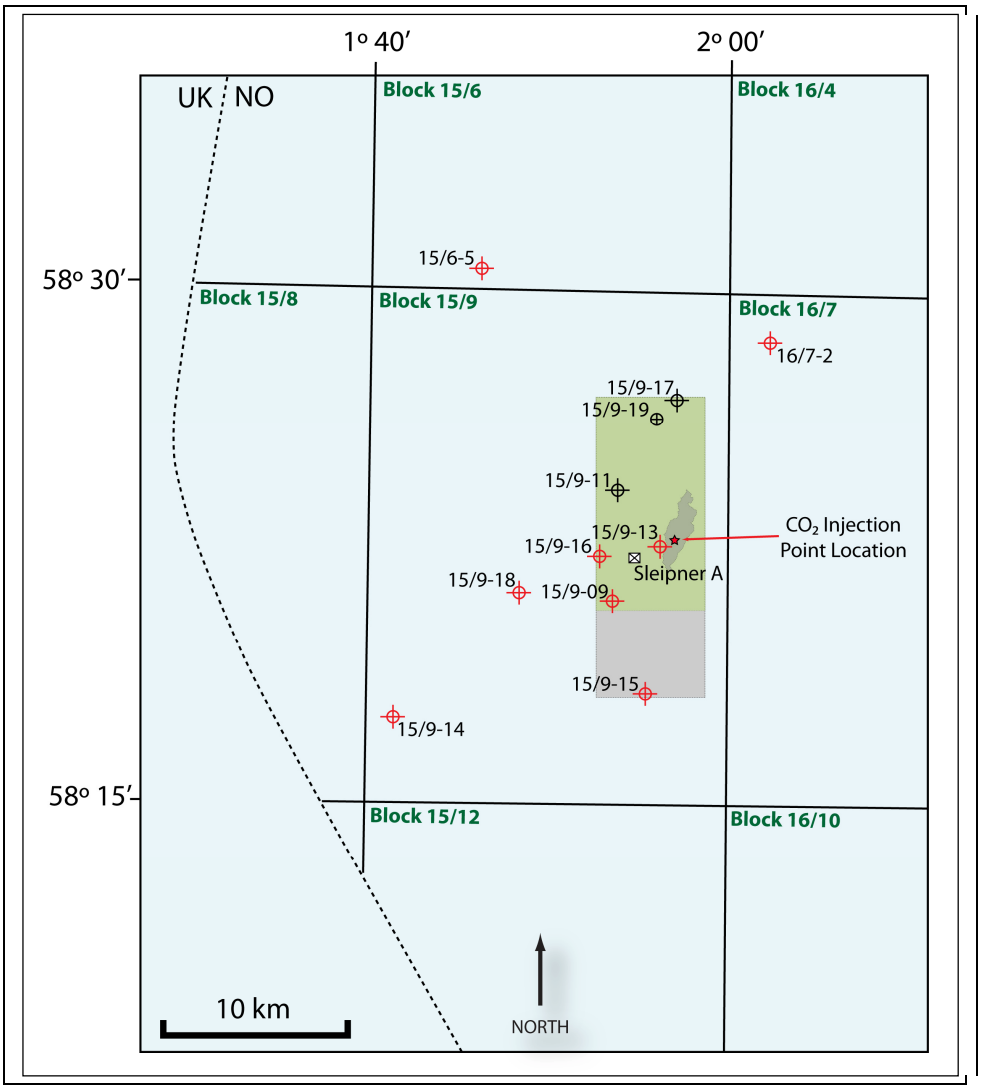

Figure 3.6: Location map for wells in the Sleipner storage site vicinity, co-ordinate system UTM 31V. The 16.5 x 5.7 km regional (green and grey) and 11.5 x 5.6 km local (green only) study areas described in Chapter 2. The CO_2 plume is currently contained within the local area as indicated by the grey outline that represents the CO_2 plume footprint for 2008 (Hermanrud et al, 2010). The eight wells marked in red provided cuttings samples for analysis (Lothe & Zweigel, 1999; Bøe & Zweigel, 2001; Kemp et al., 2002; Lindgren et al., 2002). Well 15/9-A-11 is a directional well drilled from Sleipner A and is not shown.

The majority of cuttings samples were acquired from wells located around the SW periphery of the Sleipner storage site (Figure 3.6), which is a more distal depositional setting for the Nordland Mudstones. Tests performed on cuttings samples used methods described by Krushin (1997), for non-smectite, consolidated shales. Results from these studies are summarised in Table 3.7. It is questionable whether the Krushin (1997) test is valid for shallow, unconsolidated sediments or even if it was applied correctly (Bøe & Zweigel, 2001; pers. comm. J.T. Krushin, 2008). Nordland Shale samples from well 15/9-13 (i.e. nearest to the injection point) have a smectite content ~27% (Marcussen *et al*., 2009), which is considerably higher than the values of 2.2 and 9.0% reported by Bøe & Zweigel (2001) for the same well. More importantly, cuttings samples are prone to contamination and reveal nothing about any localised structural or lithological heterogeneities that may be present within the Nordland Mudstones (e.g. faults, fracture networks, sand injectites, etc.).

Source Publication	Predicted Pore Throat Size From Krushin (1997) Test (nm)	Capillary Entry Pressure Predicted for IFT of 20 mN/m and 100% Water-Wet Formation (MPa)
Bøe & Zweigel, 2001	15 (maximum)	1.3 (radius) or 2.6 (diameter)[1]
Kemp *et al*., 2002	1.1, 11.7 and 10.5	36.7, 3.4 and 3.8 (radii)

Notes:

[1]There was doubt over whether the Krushin (1997) test used a diameter or radius measurement for "pore throat size", hence values were calculated for both.

Table 3.7: Capillary entry pressures derived from caprock cuttings samples acquired in the Sleipner vicinity

Results from CO_2 core flood tests performed at in-situ conditions on samples from deviated well 15/9-A-11 indicate that capillary entry pressures for the caprock sample at Sleipner are ~1.7 MPa for supercritical CO_2 and ~3.0-3.5 MPa for gaseous CO_2; sufficient to hold a column of supercritical CO_2 several hundred metres high (Springer & Lindgren, 2006). A more recent study on similar core material used long-term nitrogen (inert gas) core flooding under in-situ conditions of pressure, temperature and effective stress; results indicate a nitrogen capillary entry pressure of ~3.0 MPa with an "apparent threshold capillary pressure" of 1.6-1.9 MPa (Harrington *et al*., 2009).

The experimental core flood work suggests that CO_2 can be successfully contained within the Utsira Formation, given that confined column heights within structural traps in the Sleipner area are unlikely to exceed 26 metres (Bøe & Zweigel, 2001). This assumes that CO_2 is more likely to spill laterally before it can form large columns capable of breaching vertically. It also assumes uniform properties for the caprock with no faults, fractures or other heterogeneities present above the CO_2 plume footprint. However, the plume is currently migrating NE (Hermanrud *et al.*, 2010) into areas with poor sample coverage.

3.3.8 Summary:

Our review of key storage parameters at the Sleipner storage site suggests that major uncertainties still exist over the following:

- Vertical temperature gradients prevailing between the caprock and injection point and lateral (radial) temperature variations from the plume core to peripheral regions at the CO_2/brine reaction front,
- Vertical and (radial) lateral CO_2 density, particularly at the Utsira Formation/caprock interface (resulting mainly from the previous uncertainty),
- Effects of impurities (including any remnant natural gas saturation present in the Utsira aquifer) and CO_2-induced microbial activity on CO_2 density, solubility, pH, interfacial tension and wettability,
- Range of likely capillary entry pressures for the Nordland Shale caprock above the storage site, given the paucity of samples.

3.3.9 Risking Matrix:

Having identified the key areas of parameter uncertainty at the Sleipner storage site, it is necessary to consider what the critical drivers are for these parameters and examine the effects of end point values. If we consider that one of the main objectives of CO_2 storage is to safely maximise storage capacity within a given formation by maintaining CO_2 at the highest possible density for the minimum compression and injection cost, we can create a risking matrix of parameters that influence CO_2 storage objectives (Table 3.8); grey highlighted rows indicate the areas of uncertainty at the Sleipner storage site on which we will concentrate in subsequent sections. It is evident that although many of the desirable parameters for safe storage coincide at a given storage depth, the optimum values for some parameters are difficult to achieve at similar depths (e.g. high pressure and low temperature to enhance CO_2 dissolution), so there is likely to be a degree of mutual exclusivity in many instances.

Parameter	Critical Drivers	Effect of High Parameter Values	Effect of Low Parameter Values
Temperature in storage site and overburden	Depth of burial, geothermal gradient, heat flux from underlying formations, convection, thermal conductivity of rock/fluid system, temperature of injected CO_2	CO_2 and brine density/viscosity reduction, lower dissolution of CO_2, higher probability of gas phase CO_2 at caprock	CO_2 and brine density/viscosity increase, higher dissolution of CO_2, lower probability of gas phase CO_2 at caprock
Pressure in storage site and overburden	Depth of burial, hydrostatic gradient, brine density, glaciation and ice loading events, CO_2 injection pressure and rate, aquifer response	CO_2 and brine density increase, higher dissolution of CO_2, increased risk of hydro-fracture development	CO_2 and brine density reduction, lower dissolution of CO_2, reduced risk of hydro-fracture development
(IFT) Interfacial Tension (σ) of CO_2/brine system	Pressure, temperature, salinity, amount of dissolved CO_2 in aqueous phase	Increased capillary entry pressure, higher column heights supported	Reduced capillary entry pressure, lower column heights supported
Wettability ($\cos\theta$) of CO_2/rock system	Pressure, temperature, substrate type (e.g. quartz, mica, etc.), fluid interactions, pH	Increased capillary entry pressure, higher column heights supported	Reduced capillary entry pressure, lower column heights supported
Pore/fracture radius in sealing formations	Quartz content, pressure, temperature, fluid viscosity	Reduced capillary entry pressure, lower column heights supported	Increased capillary entry pressure, higher column heights supported
Density of CO_2	Pressure, temperature, salinity, impurities (from hydrocarbons and amine extraction processing)	Reduced buoyancy contrast with brine, increased viscosity, reduced mobility of CO_2	Increased buoyancy contrast with brine, reduced viscosity (markedly so, if CO_2 changes phase from supercritical liquid to gas), increased mobility of CO_2
Density of formation brine	Pressure, temperature, salinity, impurities (dissolved minerals)	Reduced CO_2 dissolution, increased buoyancy contrast with CO_2	Increased CO_2 dissolution, reduced buoyancy contrast with CO_2
Capillary entry pressures for internal barriers and sealing formations	IFT, wettability, pore/fracture radius, buoyancy contrast	Good sealing properties, reduced probability of leakage, higher column heights supported	Poorer sealing properties, increased probability of leakage, lower column heights supported
Fracture density	Rock mechanics, regional stress field, glaciation and ice loading events	Reduced capillary entry pressure, lower column heights supported	Increased capillary entry pressure, higher column heights supported
Dissolution of CO_2	Pressure, temperature, salinity, pH, presence of impurities	Increased brine density, reduced buoyancy contrast – enhanced by higher pressure, lower temperature, lower salinity and higher pH	Negligible increase in brine density, continued buoyancy contrast between CO_2 and brine – enhanced by lower pressure, higher temperature, higher salinity and lower pH

Table 3.8: Risking matrix for key CO_2 storage parameters

Worst-case storage scenario? High (warm) geothermal gradient, low pressure storage, low CO_2/brine IFT, low wettability (<1), large pore throat/fracture radius, low CO_2 density, high brine density, low caprock capillary entry pressure, high fracture density, low CO_2 dissolution rate into brine, low pH.

Best-case storage scenario? Low (cool) geothermal gradient, high pressure storage, high CO_2/brine IFT, high wettability (unity), small pore throat/fracture radius, high CO_2 density, low brine density, high caprock capillary entry pressure, low fracture density, high CO_2 dissolution rate into brine, high pH.

3.4 Parameter Evaluation for a Range of Storage Conditions:

We now focus on parameter uncertainties that may present the greatest risk to storage site security in the event of migrating CO_2 encountering a palaeo-gas migration network. Using software developed at The University of Edinburgh to investigate the density-related buoyancy effects associated with CO_2/brine and natural gas/brine systems (Naylor *et al.*, 2011a, 2011b), we generate a series of density profiles using key parameters previously described for the Sleipner storage site. The effects of different geothermal gradients on CO_2 density are also investigated allowing us to determine the range of depths at which CO_2 can safely be stored in a supercritical state. We then perform a series of risking scenarios, based on phase saturations and pressure, temperature, density, viscosity, interfacial tension and wettability conditions likely to be encountered at depths commensurate with those of the caprock at Sleipner.

The software code uses equations of state developed by the following authors to determine density, viscosity and solubility for the relevant fluids described herein over a range of user-defined input conditions (Naylor *et al.*, 2011a):

- Huang *et al*. (1985), for the calculation of CO_2 density,
- Michels *et al.* (1957) and Jossi *et al.* (1962), for the estimation of CO_2 viscosity,
- Spycher *et al.* (2003) and Spycher & Pruess (2005), for the calculation of CO_2 solubility in formation water,
- García (2001) for the calculation of formation water density (both unsaturated and CO_2-saturated),
- Danesh (1998) for natural gas density.

3.4.1 Density Profiles for an Uncertain Geothermal Gradient:

From Figure 3.7, it is apparent that the predicted caprock temperature and pressure conditions at Sleipner (i.e. 8 MPA and 28-29°C) may be very close to the critical point conditions for CO_2. Significant uncertainty in pressure or temperature conditions makes it very difficult to accurately predict the phase conditions for CO_2 and thus the potential storage efficiency of the site.

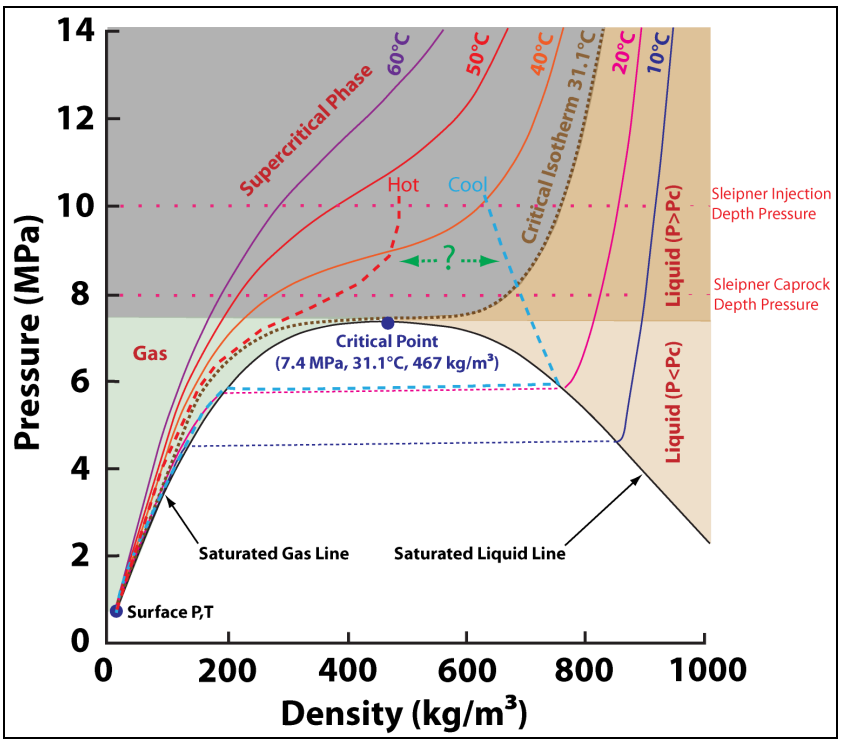

Figure 3.7: Pressure versus density plot for CO_2 with temperature isotherms overlaid. The blue dashed line represents the phase pathway for CO_2 migrating upwards from the injection point through the Sleipner storage site under conditions associated with a cool geothermal gradient. Similarly, the red dashed line represents the phase pathway associated with a hot geothermal gradient (modified from Goto et al., 2008).

The following CO_2 density profiles have been derived for published seabed conditions in the Sleipner area (Nooner *et al.*, 2007), with a constant hydrostatic pressure gradient, but different geothermal gradients. The blue dashed horizontal line in Figure 3.8 highlights the depth that corresponds to the critical pressure; above this line a change from light to dense phase CO_2 is via a rapid phase transition, below it there is no phase transition. This figure clearly indicates that if parts of a storage site are close to critical point conditions, even small changes in pressure and temperature can lead to large changes in the physical properties of CO_2 (i.e. density, viscosity and volume).

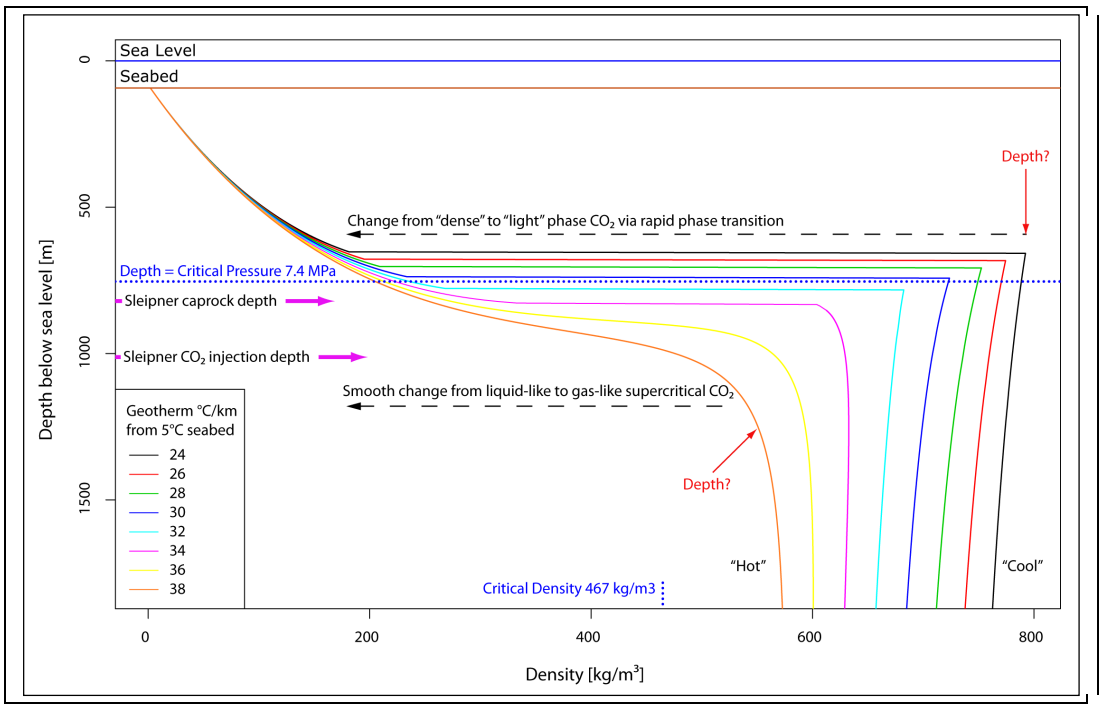

Figure 3.8: Profiles for different CO_2 densities versus depth below sea level. Each curve represents a different geothermal gradient in °C/km. Critical conditions for CO_2 are indicated in blue text.

In the shallow subsurface, CO_2 exists in the gas phase and the density increases with depth from ~20 kg/m^3 at seabed, to ~200 kg/m^3 at a depth of ~600-700 m for all geothermal gradients; the region down to 600 m is well constrained. Now consider the two end-member geothermal gradients; the upper black line represents the cool model ($\delta T/\delta z$ = 24°C/km) and the lower orange line represents the hot model ($\delta T/\delta z$ = 38°C/km). The cool model is such that the pressure-temperature pairs as a function of depth cross the vapour pressure curve implying a rapid phase transition from gas to liquid (refer to Figure 3.7). The density of the liquid is ~800 kg/m^3 at ~700 m depth. With increasing depth the effects of increasing temperature prevail over increasing pressure and the density reduces gradually. The hot model shows fundamentally different behaviour; the pressure-temperature pairs miss the critical point such that a gas-like supercritical phase changes gradually into a liquid-like supercritical phase producing a smooth and continuous change in density tending to a value near 600 kg/m^3, which is a lower density than a pure liquid supercritical phase (refer to Figure 3.7). The precise controls on this behaviour will be explored in greater detail in the next section.

3.4.2 Cool Versus Hot Density Profiles for Sleipner:

The previous section demonstrates why it is important to include an analysis of uncertainty in the thermal regime when assessing CO_2 densities, but without highlighting the origin of the density trends by reference to phase diagrams. In this section we provide this information and highlight useful graphs for being able to critically assess this behaviour. We consider two end members for geothermal gradient: a "cool" model (linear 32.72°C/km from 5°C seabed temperature, as proposed by Lindeberg *et al*., 2009) and "hot" model (linear 38°C/km from 5°C seabed temperature, as proposed by Nooner *et al*., 2007) for the Sleipner storage site (Figure 3.9). These two studies produced fundamentally different predictions of storage efficiency and CO_2 density.

Profiles a) and b) in Figure 3.9 show vapour pressure (VP) curves for CO_2 (solid black lines). These lines indicate where a phase change occurs between gas and liquid CO_2 as a function of pressure and temperature. The end of this line represents the critical point (intersection point of the blue dotted lines); at temperatures and pressures beyond the right-hand end of this line CO_2 is in the supercritical (SC) phase. Blue dotted lines correspond to the critical pressure (CP) and critical temperature (CT) for CO_2. The coloured dashed lines represent density contours. Below the VP curve densities are low and correspond to the gas phase. Above the VP curve, densities are high and correspond to the liquid phase. Density is discontinuous across the VP curve reflecting phase changes. The closely spaced contours occurring within the SC region highlight the rapid change of density that can occur therein for relatively small changes in pressure and temperature. Superimposed on this phase diagram is a solid red line that indicates all of the pressure-temperature pairs as a function of depth below seabed. The line starts at the pressure and temperature corresponding to seabed conditions. Where the geothermal gradient increases more slowly in the cool model, this line is steeper and intersects the VP curve indicating that a sharp phase transition should be expected in the density profile. Conversely, the pressure-temperature pairs have a shallower gradient in the hot model where the red line just misses the critical point and smoothly enters the region of narrowly spaced contours.

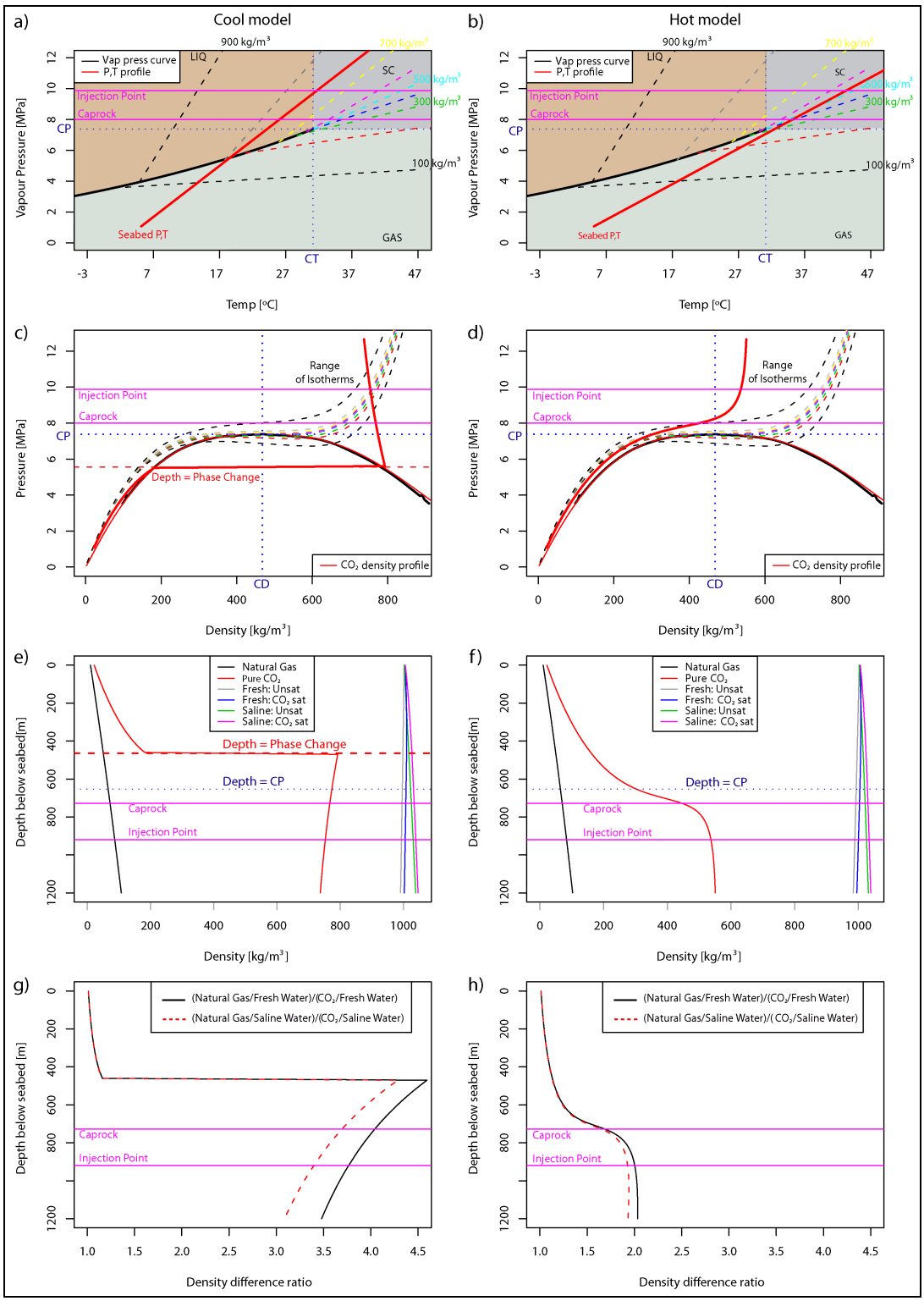

Figure 3.9: Density profiles (a-f) for different CO_2 properties under a "cool" geothermal gradient of 32.72°/km (left-hand series) and "hot" geothermal gradient of 38°/km (right-hand series). Blue dotted lines represent CO_2 critical point conditions for temperature (CT - vertical), pressure (CP - horizontal) and density (CD - vertical). The lower pair of profiles (g-h) illustrate the density difference ratio versus depth for (natural gas/fresh water)/(CO_2/fresh water), represented by a solid black line and (natural gas/saline water)/(CO_2/saline water), represented by a dashed red line. Pink horizontal lines in all cases represent the caprock and injection point pressure and depth conditions for the Sleipner CO_2 storage site.

Profiles c) and d) in Figure 3.9 are pressure-density phase plots. The vertical blue dashed line is now the critical density (CD) and we define the "light" phase of CO_2 being all densities less than the critical density and the "dense", thermodynamically liquid-like phase of CO_2 to be all densities greater than the critical density. The dashed coloured lines in this case indicate a range of reference isotherms generated from a quadratic equation of state to cover the critical point region. Where the isotherms cross the solid black line this indicates a pressure-temperature pair where a phase change occurs (i.e. the VP curve). These pressure-density phase diagrams demonstrate why CO_2 density decreases rapidly once the phase transition has occurred in the cool model and why CO_2 density changes more gradually in the hot model. Consider the initial CO_2 injection point conditions and the manner in which isotherms are crossed. For the cool model the injection point is situated within a region of lower temperature isotherms (right-hand side) and as CO_2 ascends through the storage site, successively colder isotherms are crossed, pushing the density profile further to the right. For the hot model the injection point is situated within a region of higher temperature isotherms (left-hand side), does not encounter the same low temperature isotherms and tends towards some limiting density. Note also the sharp contrast in predicted densities for the hot and cool models at the injection point and caprock depths.

Profiles e) and f) in Figure 3.9 translate the CO_2 density information into (below seabed) depth-density plots (solid red lines). The densities of natural gas (solid black lines), fresh water and brine (both unsaturated and CO_2 saturated), under the same pressure and temperature conditions are also included for reference. These reference densities exhibit significantly less variability than CO_2 density. It should be noted that CO_2 and natural gas densities tend to converge at the shallowest depths, but always remain distinct. The densities of the gas, liquid and supercritical phases of CO_2 are all clearly distinguished and have notably different depth distributions for the cool and hot models; this has implications for the design of the best geophysical monitoring survey. At the caprock depth, for the hot model the CO_2 is marginally in the dense phase, whereas in the cool model the CO_2 is safely in the dense phase.

These calculations have been performed at initial reservoir conditions. However, assuming a CO_2 injection rate of 1 Mt/yr, pressure could increase in the near wellbore region by ~1-2 MPa (Baklid *et al*., 1996). Any long-term pressure build-up will depend on a range of reservoir characteristics (e.g. CO_2-induced diagenetic changes, degree of compartmentalisation, presence of heterogeneities and porosity-permeability characteristics). A large, laterally extensive, high porosity-permeability aquifer like the Utsira Sand should be able to efficiently dissipate pressure unless significant boundaries are encountered (van der Meer & van Wees, 2006). The effect on the cool model is likely to be insignificant since the density contours are widely spaced at the injection and caprock depths (Figure 3.9a). However there is considerable potential to increase the density of the hot model, since the density contours are more closely spaced at these same depths (Figure 3.9b).

Profiles g) and h) in Figure 3.9 illustrate (below seabed) depth-density difference ratios between (natural gas/fresh water)/(CO_2/fresh water) represented by solid black lines) and (natural gas/saline water)/(CO_2/saline water) represented by dashed red lines. Buoyancy is driven by the depth integrated density difference between the dense formation fluid (brine) and the lighter fluid or gas phase. When CO_2 is in a gas phase, the density is similar to that of natural gas resulting in a similar buoyancy force. However, when CO_2 is a dense phase, the buoyancy drive is between a factor of 2 (hot model) and ~4 (cool model) lower than natural gas under the same pressure and temperature conditions. Note that for dense phase CO_2, the ratio for density difference always exceeds ~2 and is at a maximum where pressure and temperature conditions are conducive to a phase change (Naylor et al., 2011a). Therefore, when comparing the performance of a capillary seal, it is important to assess the difference in the buoyancy if natural gas is used as a reference and to account for differences in the thermal regime.

3.4.3 Risking CO_2 Storage Conditions for Cool and Hot Models at Different Depths:
The previous section showed how CO_2 depth-density curves are derived from phase diagrams given a known surface pressure, temperature information and assuming a reasonable hydrostatic pressure gradient and geothermal gradient. In this section, we take the analysis of density uncertainty further by performing a Monte-Carlo estimation of densities based upon uncertainties in the pressure and temperature at the injection point and caprock.

The potential near wellbore pressure increase of ~1-2 MPa caused by CO_2 injection was previously described (Baklid *et al*., 1996), and in their estimation of caprock temperature, Lindeberg *et al*., (2009) quote potential palaeo-temperature fluctuations of +/- 6°C within the overburden sediments during previous glacial and inter-glacial periods. Based on this published information, one thousand Monte-Carlo simulations were performed, varying the injection point and caprock pressure and temperature conditions within these bounds (i.e. temperature +/- 6°C and pressure +/- 2 MPa).

A set of similar profiles was generated as described for Figure 3.9 (profiles a-f), but with the simulation points and frequency distributions added for caprock and injection point depths (Figure 3.10 profiles a-j). Red and green data points represent caprock and injection point conditions respectively. Key points to note from Figure 3.10 are:

- As the geothermal gradient tends towards the hot model, the spread of values is wider and density uncertainty increases, particularly at the caprock, where a bimodal distribution is evident. This indicates that either "light phase" gas or "dense phase" supercritical CO_2 could be present. Use of an average CO_2 density (indicated by vertical red lines on Figures 3.10 profiles g-j) with this type of geothermal gradient could be grossly misleading,
- For the cool model there is less density uncertainty at the injection point and caprock,
- Injection point densities are well constrained for both cool and hot models, although the hot model still exhibits a slight tendency towards bimodality.

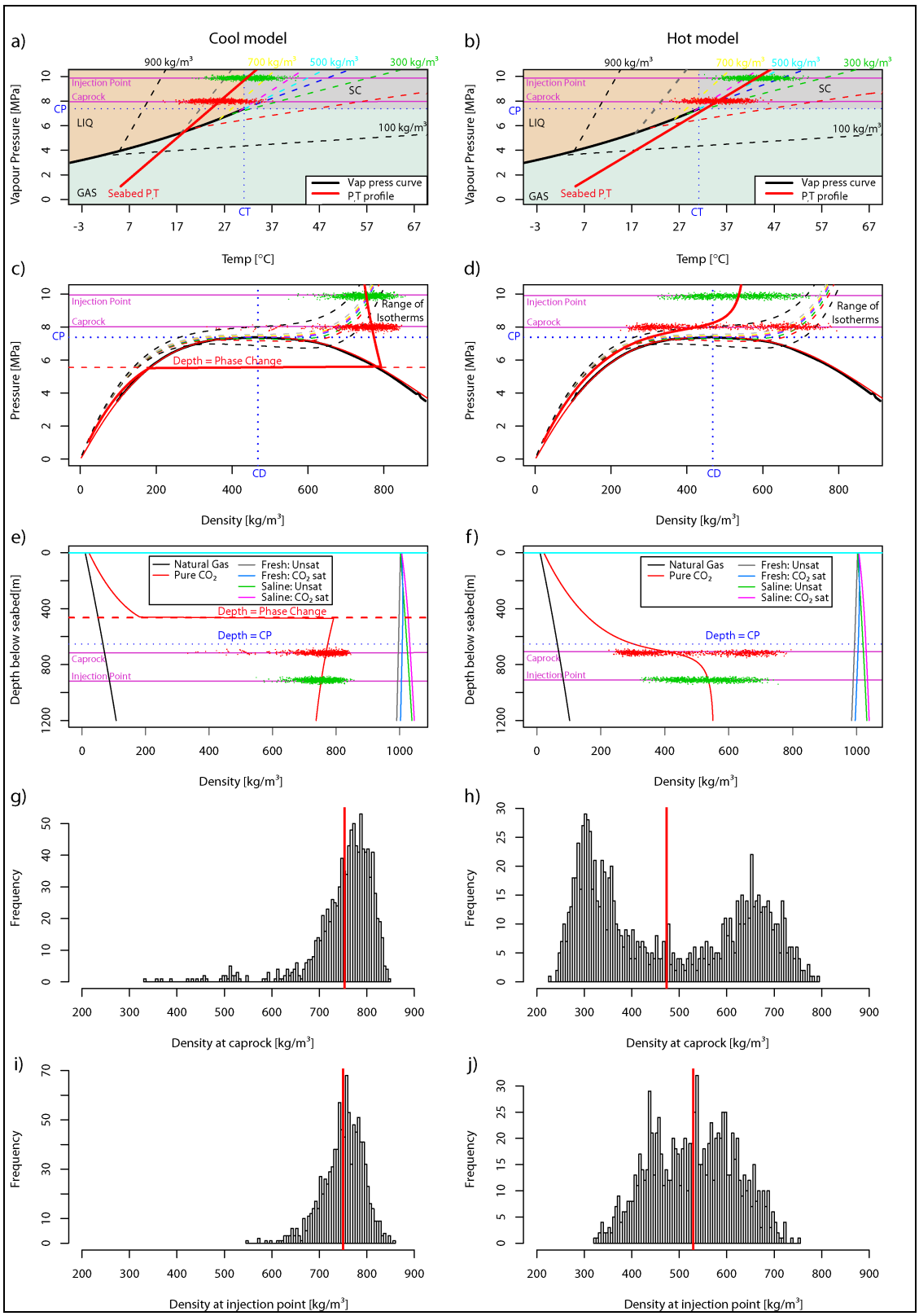

Figure 3.10: Density risking profiles (a-j) for variable CO_2 properties under a "cool" geothermal gradient of 32.72°/km (left-hand series) and "hot" geothermal gradient of 38°/km (right-hand series). The top three rows of profiles are identical to those previously described for Figure3. 9. Individual points represent pressure-temperature risking at the caprock depth (red) and injection point depth (green). The lowest two rows of profiles are frequency distributions for the caprock densities (profiles g-h) and injection point densities (profiles i –j), derived from the Monte-Carlo pressure-temperature simulations.

3.4.4 Comparison of Light to Dense Phase CO_2 Transition for Submarine and Subaerial Storage Cases:

In the previous section we investigated the density uncertainty at two particular depths. In this section we investigate the depth range over which CO_2 is likely to change from "light" to "dense" phase (as previously defined in Section 3.4.2). On the vapour pressure curve, this partitioning corresponds to the vapour pressure curve and an extension of it along the critical density contour.

Figure 3.11 shows the vapour pressure (VP) curve with the vertical axis reversed so that it reflects depth (on the right-hand y-axis). The VP curve is the divide between the light and dense phases. The solid blue and red lines represent the cool and hot geothermal gradient models described previously. In this case the submarine Sleipner case is displayed on the left-hand diagram and compared to a generic subaerial case displayed on the right-hand diagram. The subaerial case uses the same gradients but these are offset to typical surface pressure and temperature conditions rather than seabed conditions (i.e. lower surface pressure and higher surface temperature). Figure 3.11 clearly illustrates that under typical submarine conditions dense phase CO_2 can exist at shallower depths than under subaerial conditions, where the lower pressure and higher temperature conditions cause the pressure-temperature curves to project much deeper before the VP curve is intersected. To summarise:

- For a submarine case and ~80 m water depth (i.e. Sleipner conditions), CO_2 can be stored in dense phase conditions below ~500 m depth for a cool geothermal gradient and ~800 m for a hot geothermal gradient,
- For a subaerial case, CO_2 can be stored in dense phase conditions below ~800 m depth for a cool geothermal gradient and ~1500 m for a hot geothermal gradient.

Obviously, for global carbon storage applications these dense phase CO_2 storage depths will vary according to site-specific conditions such as water depth, seabed temperatures, geothermal gradients and ambient surface temperatures.

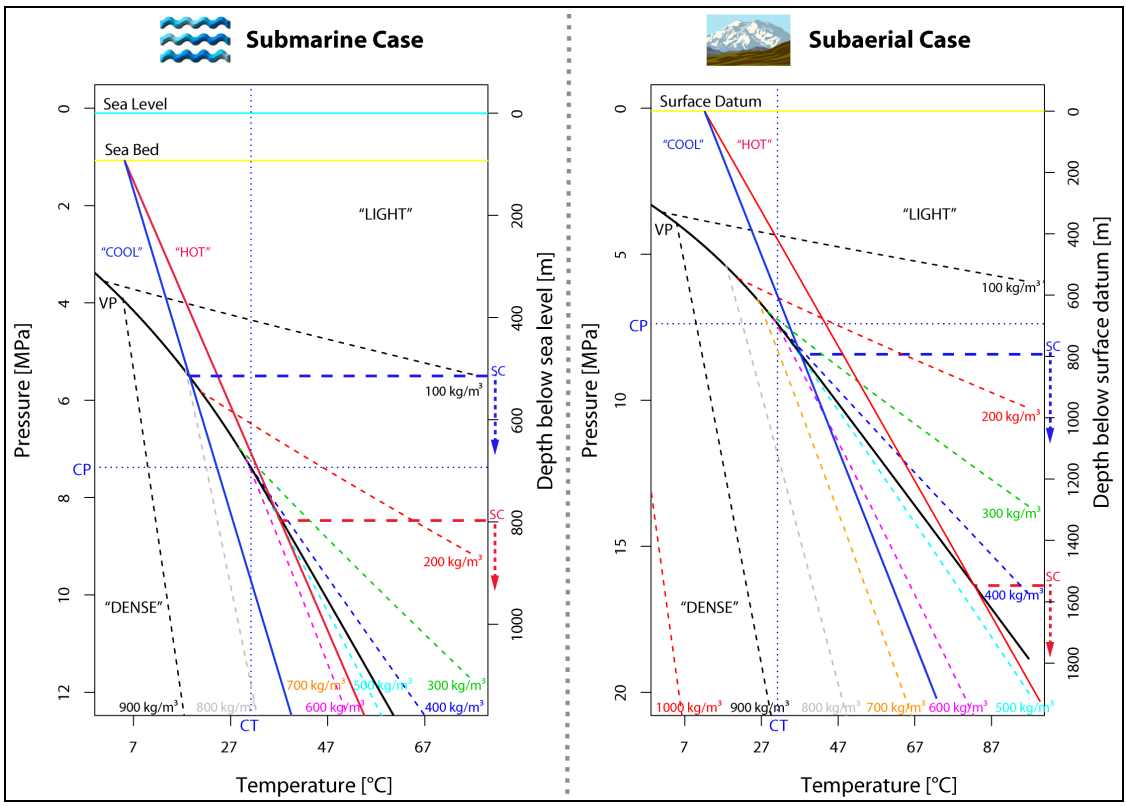

Figure 3.11: Profiles of CO_2 density for the range of pressures, temperatures and depths likely to be encountered under typical storage conditions. The submarine case (based on Sleipner conditions) is illustrated at left and a comparable subaerial case at right. The thick black line is the vapour pressure (VP) curve and thin blue dashed lines are the critical temperature (CT – vertical) and critical pressure (CP – horizontal) conditions for CO_2. Solid blue lines represent a "cool" geothermal gradient of 32.72°C/km and solid red lines a "hot" geothermal gradient of 38°C/km. The thick horizontal blue and red dashed lines with associated vertical arrows on the right-hand axis represent the depths below which CO_2 can be stored in a supercritical phase for "cool" and "hot" geothermal gradients respectively.

3.5 Comparison of Critical Column Heights for CH_4 and CO_2:

In this section, we evaluate the range of critical column heights required for entry into a palaeo-migration pathway under a range of comparable storage conditions for CH_4/brine and CO_2/brine systems. We assume that these pathways and accumulations contain the minimum gas saturation capable of being resolved on seismic data; at least 4% is required in available pore space to create a significant velocity contrast (Andreassen *et al*., 2007).

3.5.1 Capillary Entry Pressures for CH_4 versus CO_2 Based on Column Height:

A significant density contrast exists between CH_4 or CO_2 and water/brine at typical storage conditions, thus fluid migration will be mainly driven by buoyancy forces that can be calculated from the following equation (Schowalter, 1979):

$$P_b = \rho_w - \rho_{nw}\, gH \qquad \text{- Equation 3.1}$$

Where: P_b = Differential pressure due to buoyancy forces (MPa), ρ_w = Density of wetting fluid (kg/m^3), ρ_{nw} = Density of non-wetting fluid (kg/m^3), g = Gravitational constant (9.81 ms^{-2}) and H = Vertical column height of the non-wetting fluid (m).

Buoyancy force will be greatest when the density contrast between CH_4 or CO_2 and water/brine and the vertical height of the CH_4 or CO_2 column are at a maximum. Assuming the reservoir is water-wet and resident pore fluids are either water or brine, CH_4 or CO_2 will only migrate into the reservoir pore spaces (or a fracture network) if P_b is greater than the capillary entry pressure (P_c) of the system; this pressure is equivalent to the absolute pressure difference between the non-wetting and wetting phases (Schowalter, 1979):

$$P_c = \frac{2\sigma \cos\theta}{R} \qquad \text{- Equation 3.2}$$

Equations 3.1 and 3.2 can be combined to derive the maximum CH_4 or CO_2 column height that a sealing formation can withstand (Schowalter, 1979).

$$H = \frac{2\sigma \cos\theta}{\rho_w - \rho_{nw}\ gR}$$ *- Equation 3.3*

Where: σ = Interfacial tension (IFT) between wetting and non-wetting fluids (mN/m^{-1}), θ = Formation wettability represented by the contact angle between wetting and non-wetting fluids (degrees - °) and R = Radius of largest connected pore throats or fracture half-width (nanometres - nm).

From Equations 3.2 and 3.3, it is apparent that anything that reduces IFT and/or increases the contact angle between the wetting and non-wetting phases for a given pore or fracture size will result in a lower capillary entry pressure and reduced column height. Similarly, any increase in phase density contrast will further reduce the column height that can be supported. However, there is also a dichotomy between caprock entry pressure and CO_2 phase as we highlighted in Section 3.3.7; despite having a higher density contrast with brine, the capillary entry pressure value for gaseous CO_2 entry into a caprock seal is almost twice that of supercritical CO_2 (Springer & Lindgren, 2006). Thus, supercritical CO_2 can leak more easily than gaseous CO_2, even though its buoyancy contrast is smaller. This also has implications for CO_2 storage in depleted gas fields, where critical column heights for CH_4/brine and CO_2/brine systems can be similar, depending on the CO_2 phase and density conditions prevailing at the caprock seal (Naylor *et al*., 2011a).

3.5.2 Expected Column Heights at Sleipner:

Regionally mapped structural traps in the Sleipner area appear unlikely to contain column heights exceeding 26 m and the main structural traps at the Sleipner storage site are described as having 12-15 m maximum relief (Zweigel *et al*., 2000; Bøe & Zweigel, 2001 and Chadwick *et al*., 2005). As part of their analytical modelling exercise, Bickle *et al*. (2007) performed a CO_2 layer thickness evaluation for several layers within the Utsira Formation; if we only consider the data for the highest layer (Layer 9A) situated below the caprock seal and project to 2016 (Figure 3.12), this suggests that the injected CO_2 will form a layer 13.5 m thick below the caprock after a 20 year injection period (i.e. structural traps will either be at or close to spill-point).

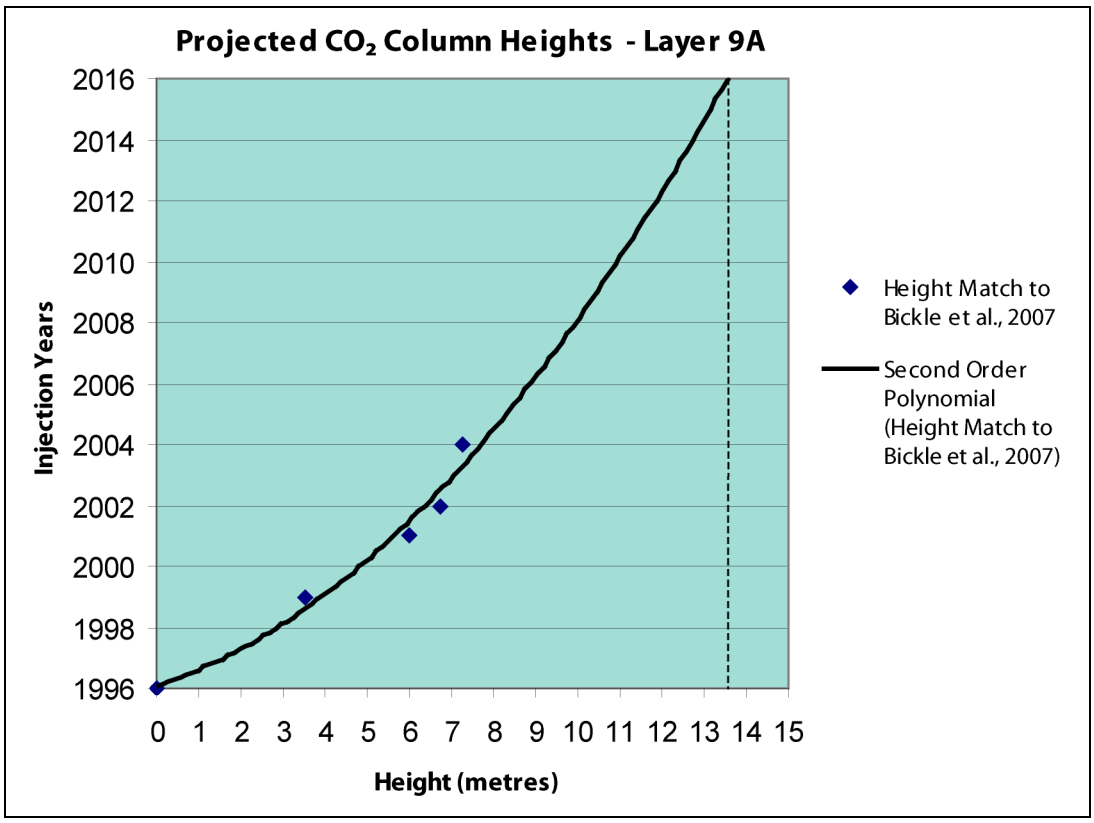

Figure 3.12: Projection of CO_2 column heights/layer thickness for Layer 9A at the Sleipner storage site (based on 1996-2004 data from Bickle et al., 2007).

Two scenarios are now considered for a simple sensitivity analysis, assuming that brine densities and, most importantly, pore radii have not changed significantly over geological time (i.e. no diagenetic cementation of pores or dissolution of pore cements has occurred).

Firstly, if we assume that the largest traps in the Sleipner area (i.e. 26 m relief) had to be filled to spill-point with CH_4 before they leaked and formed palaeo-migration pathways, then using Equations 3.1-3.2 for a range of storage site parameters, we can derive the minimum capillary entry pressures and pore throat radii required to compromise the seal for a CH_4/brine system. By using the same pore radii (and assuming no change in pore radius over time) we then derive an equivalent set of capillary entry pressures and minimum column heights for a CO_2/brine system. Secondly, we consider the main traps at the Sleipner storage site at the lowest end of the spill-point range (i.e. ~12 m relief) following the same procedure.

We used a range of parameters for Sleipner as previously described in Section 3.3, combined with densities for pure CO_2, CH_4 and a range of CO_2/CH_4 mixtures. The latter were calculated from the Lawrence Berkeley National Laboratories WebGasEOS online calculator (http://lnx.lbl.gov/GasEOS using the Peng-Robinson EoS). It should be noted that this calculates slightly lower density values for pure CO_2 with the predicted Sleipner caprock conditions described in Section 3.3.5, thus we extend the range of density values for pure CO_2 accordingly. Values for all other parameters are derived from literature sources noted in Table 3.9.

Range of Parameters used for Sleipner Column Height Sensitivity Analysis	
Depth to caprock (m TVDSS)	800
Pressure at caprock (MPa)	8
Temperature at caprock (°C)	28-36
Brine density (kg/m^3)	1022
Range of column heights considered for CH_4/CO_2 (m)	4-26
CH_4 density (kg/m^3) – 100% pure	55-75
CH_4 density (kg/m^3) – 5% C_2H_6/C_3H_8 (2.5% each)	62-65
CH_4 density (kg/m^3) – 10% C_2H_6/C_3H_8 (5% each)	68-72
Interfacial tension (IFT) CH_4/brine (mNm^{-1})	55-65 [1, 2, 4]
Wettability CH_4/brine (fraction)	1 (100% water-wet)
CO_2 density (kg/m^3) – 100% pure	300-750
CO_2 density (kg/m^3) – 1% CH_4	323-638
CO_2 density (kg/m^3) – 2% CH_4	303-604
Interfacial tension (IFT) CO_2/brine (mNm^{-1})	20-35 [1, 2, 3, 4, 6]
Wettability CO_2/brine (fraction)	0.5, 0.8, 1 (100% water-wet) [5, 7]

Notes:

[1]From Li *et al*., 2006; [2]from Hildenbrand *et al*., 2004; [3]from Chalbaud *et al*., 2006 and 2009; [4]from Shah *et al*., 2008; [5]from Chiquet *et al.*, 2007a; [6]from Chiquet *et al.*, 2007b; [7]from Bikkina, 2011

Table 3.9: Range of Parameters used for Column Height Sensitivity Analysis

Figure 3.13 shows the buoyancy force exerted on the Sleipner caprock by 12 m and 26 m column heights of CO_2 and CH_4; this illustrates the range of buoyancy forces considered for the two scenarios under investigation. End-point density ranges are used for CO_2 and CH_4 with a fixed brine density as specified in Table 3.9.

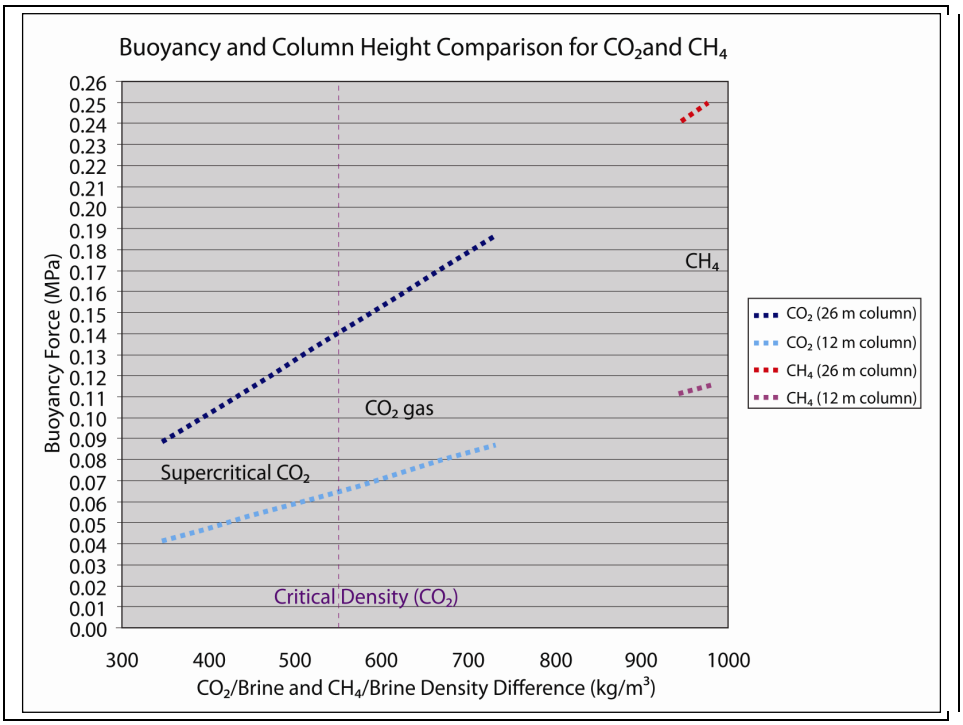

Figure 3.13: Buoyancy force exerted on the Sleipner caprock for end-point CO_2 and CH_4 column heights.

Figure 3.13 illustrates that within the specified range of density differences, a CH_4 column height of 26 m exerts a buoyancy force of 0.24 to 0.25 MPa. The 12 m column height exerts a smaller buoyancy force of 0.11 MPa to 0.12 MPa. Buoyancy forces for the equivalent CO_2 column heights are clearly much smaller, but cover a wider range due to phase/density changes either side of the critical point for CO_2.

We now consider the range of pore radii required for the buoyancy force (P_b) to exceed the capillary entry pressure (P_c) for each column height and allow ingress of CH_4 into the overburden (Figure 3.14). In this case, end-point CH_4 values in Table 3.9 for IFT are used with wettability set to unity (i.e. 100% water-wet).

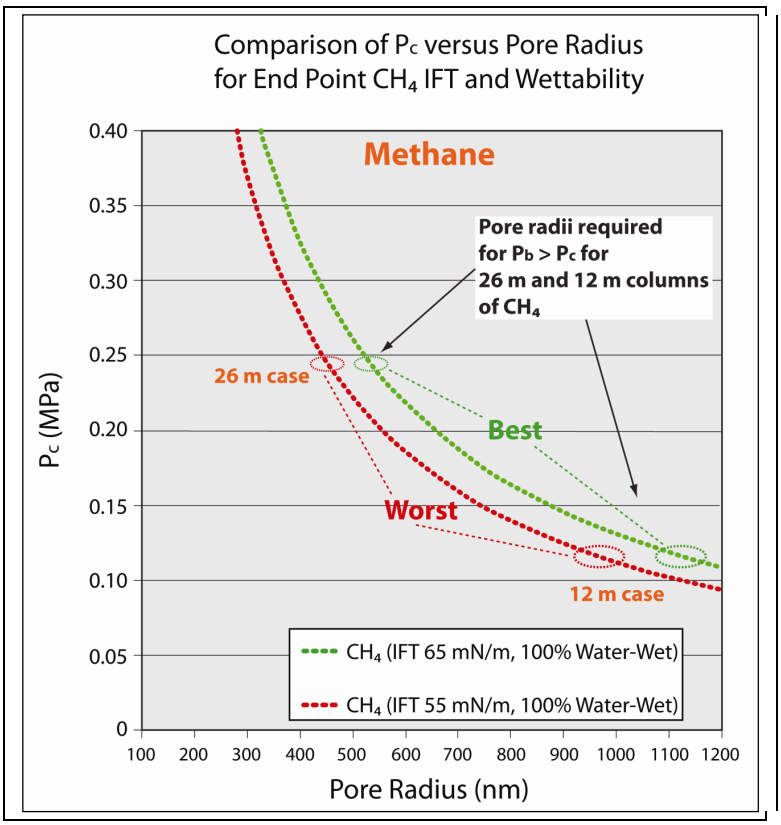

Figure 3.14: Pore radii required for Pb > Pc for 26 m and 12 m columns of CH_4.

From Figure 3.14, end-point pore radii can be derived for best and worst case scenarios in terms of CH_4 buoyancy (P_b) required to overcome capillary entry pressure (P_c) for a given set of CH_4 IFT values. Results are presented in Table 3.10, with the ranges of pore radii highlighted in green (best case) and red (worst case).

Scenario	**26 m column (0.24 MPa P_b)**	**26 m column (0.25 MPa P_b)**	**12 m column (0.11 MPa P_b)**	**12 m column (0.12 MPa P_b)**
	Pore Radius (nm)	**Pore Radius (nm)**	**Pore Radius (nm)**	**Pore Radius (nm)**
IFT 65 (high)	550	530	1190	1090
IFT 55 (low)	460	450	1000	920

Table 3.10: Range of pore radii required for Pb > Pc for different column heights and IFT values.

If these pore radii values are now applied to a CO_2 leakage scenario (Figure 3.15), using the end-point CO_2 values in Table 3.9 for IFT and wettability, it is apparent that the reduction in both parameters (particularly IFT) allows CO_2 to leak more easily than CH_4.

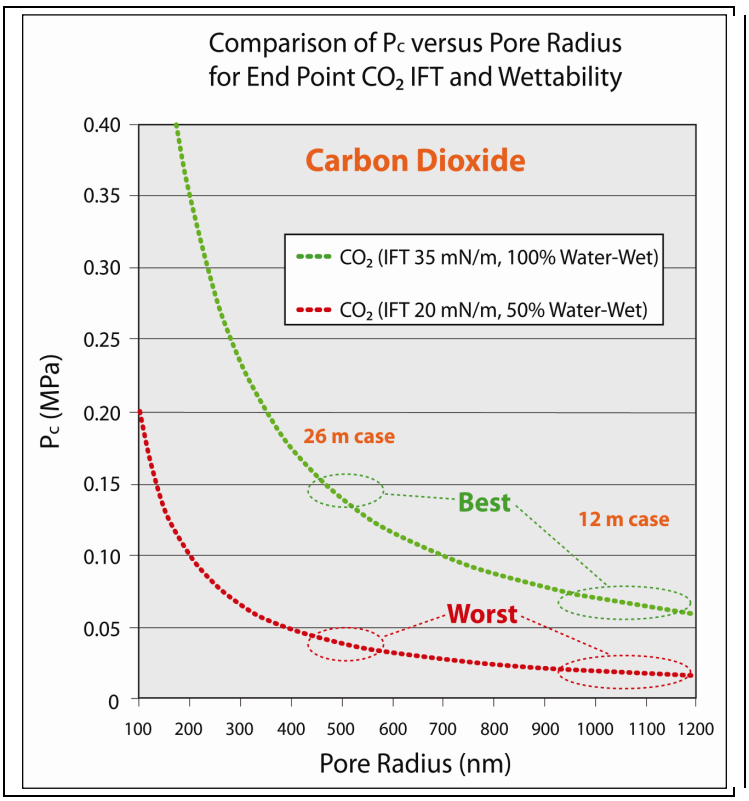

Figure 3.15: Capillary entry pressures for CO_2, using pore radii previously derived from Figure 3.14.

The CO_2 capillary entry pressures for both scenarios and range of pore radii under end-point IFT and wettability conditions are presented in Table 3.11.

Column Height Scenario	**Pore Radii (nm)**	**P_c (MPa) Best case (IFT 35 mN/m^{-1}, 100% water-wet)**	**P_c (MPa) Worst case (IFT 20 mN/m^{-1}, 50% water-wet)**
	Low ranges (Best case scenario – smaller pore radii)		
26 m case	450	0.1555	0.0444
26 m case	460	0.1521	0.0434
12 m case	920	0.0760	0.02
12 m case	1000	0.0700	0.0200
	High ranges (Worst case scenario – larger pore radii)		
26 m case	530	0.1320	0.0377
26 m case	550	0.1272	0.0363
12 m case	1090	0.0642	0.0183
12 m case	1190	0.0588	0.0168

Table 3.11: CO_2 capillary entry pressures for range of pore radii and end-point IFT/wettability conditions.

Having established the capillary entry pressures for CO_2 using these pore radii ranges, the final step involves calculating the critical column heights of CO_2 for buoyancy pressures to exceed these entry pressures.

Results are presented in Table 3.12 for the 26 m column case and Table 3.13 for the 12 m column case using the values of IFT and wettability listed in Table 3.9 and ranges of pore radii and corresponding CO_2 capillary entry pressures listed in Table 3.11. Three sets of CO_2 column height results are presented for comparison, with all assuming a fixed brine density of 1020 kg/m^3:

- **Case 1:** Absolute minimum column height at which P_b exceeds P_c (i.e. gas-like, low CO_2 density, with a high buoyancy),
- **Case 2:** Minimum column height for P_b to exceed P_c with a CO_2/brine density contrast lower than 600 kg/m^3. This corresponds to the critical point region at which CO_2 just becomes a supercritical phase. If the density contrast exceeds this value, CO_2 is tending more to gas-like behaviour and the CO_2/brine IFT shows a significant increase as illustrated in Figure 3.16 (Chalbaud *et al.*, 2006 and 2009),
- **Case 3:** Minimum column height for P_b to exceed P_c with a CO_2/brine density contrast lower than 350 kg/m^3 (i.e. supercritical CO_2 density of 670 kg/m^3 or greater, with a lower buoyancy contrast).

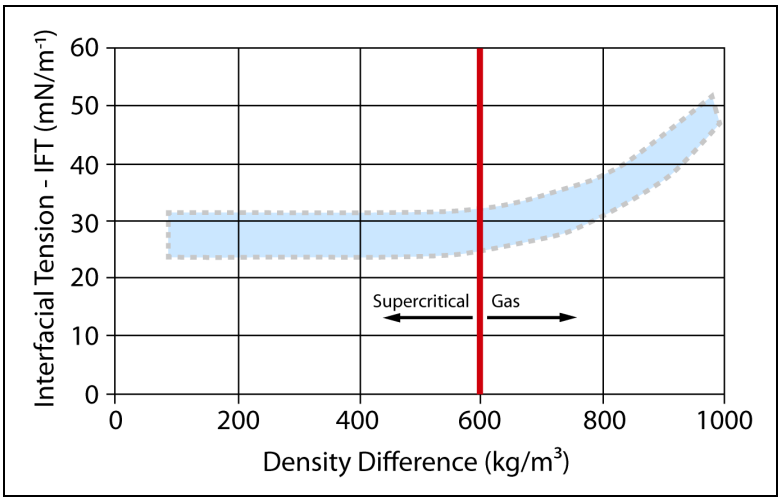

Figure 3.16: Variation of IFT versus density difference for a brine/CO_2 system – range of experimental values represented by the blue shaded area (modified after Chalbaud et al., 2006 and 2009).

26 m column height scenario for leakage				Absolute	(Case 1)	< 600 kg/m^3 density difference	(Case 2)	<350 kg/m^3 density difference	(Case 3)
Pore Radii (nm)	Pc (MPa)	IFT (mN/m^{-1})	Wettability	Column Height (m)	Density Difference (kg/m^3)	Column Height (m)	Density Difference (kg/m^3)	Column Height (m)	Density Difference (kg/m^3)
450	0.0444	20	50%	7	650	8	568	13	350
450	0.0555	25	50%	8	708	10	568	17	334
450	0.0666	30	50%	10	680	12	568	20	340
450	0.0777	35	50%	11	722	14	568	23	346
450	0.0711	20	80%	11	662	13	560	21	348
450	0.0888	25	80%	13	698	16	568	26	350
450	0.1066	30	80%	16	680	19	574	26	420
450	0.1244	35	80%	18	706	22	578	26	490
450	0.0888	20	100%	13	698	16	568	26	350
450	0.1111	25	100%	16	710	19	598	26	436
450	0.1333	30	100%	19	716	23	592	26	524
450	0.1555	35	100%	22	722	26	612	26	612
Pore Radii (nm)	Pc (MPa)	IFT (mN/m^{-1})	Wettability	Column Height (m)	Density Difference (kg/m^3)	Column Height (m)	Density Difference (kg/m^3)	Column Height (m)	Density Difference (kg/m^3)
460	0.0434	20	50%	7	634	8	556	12	370
460	0.0543	25	50%	8	694	10	556	16	348
460	0.0652	30	50%	10	666	12	556	20	334
460	0.076	35	50%	11	714	14	562	23	342
460	0.0695	20	80%	10	710	12	592	21	338
460	0.0869	25	80%	13	684	15	592	26	342
460	0.1043	30	80%	15	710	18	592	26	410
460	0.1217	35	80%	18	690	21	592	26	478
460	0.0869	20	100%	13	684	15	592	26	342
460	0.1086	25	100%	16	694	19	584	26	428
460	0.1304	30	100%	19	702	23	580	26	512
460	0.1521	35	100%	22	706	26	598	26	598
Pore Radii (nm)	Pc (MPa)	IFT (mN/m^{-1})	Wettability	Column Height (m)	Density Difference (kg/m^3)	Column Height (m)	Density Difference (kg/m^3)	Column Height (m)	Density Difference (kg/m^3)
530	0.0377	20	50%	6	644	7	552	12	322
530	0.0471	25	50%	7	688	9	536	14	344
530	0.0566	30	50%	9	644	10	578	17	340
530	0.066	35	50%	10	674	12	562	20	338
530	0.0603	20	80%	9	686	11	560	18	344
530	0.0754	25	80%	11	700	13	594	22	350
530	0.0905	30	80%	13	712	16	578	26	356
530	0.1056	35	80%	15	720	19	568	26	416
530	0.0754	20	100%	11	700	13	594	22	350
530	0.0943	25	100%	14	688	17	568	26	372
530	0.1132	30	100%	16	722	20	578	26	446
530	0.132	35	100%	19	710	23	586	26	520
Pore Radii (nm)	Pc (MPa)	IFT (mN/m^{-1})	Wettability	Column Height (m)	Density Difference (kg/m^3)	Column Height (m)	Density Difference (kg/m^3)	Column Height (m)	Density Difference (kg/m^3)
550	0.0363	20	50%	6	620	7	532	11	338
550	0.0454	25	50%	7	664	8	580	14	332
550	0.0543	30	50%	8	694	10	556	16	348
550	0.0636	35	50%	9	722	11	592	19	342
550	0.0581	20	80%	9	660	10	594	17	350
550	0.0727	25	80%	11	676	13	572	22	338
550	0.0872	30	80%	13	686	15	594	26	344
550	0.1018	35	80%	15	694	18	578	26	400
550	0.0727	20	100%	11	676	13	572	22	338
550	0.0909	25	100%	13	714	16	580	26	358
550	0.109	30	100%	16	696	19	586	26	428
550	0.1272	35	100%	18	722	22	592	26	500

Table 3.12: Critical column height results for 26 m column height leakage scenario – black cells indicate mutual exclusivity (e.g. $\Delta\rho$ > 600 kg/m^3 and low IFT), green cells indicate failure to satisfy leakage criteria (i.e. best-case scenario).

12 m column height scenario for leakage				Absolute	(Case 1)	< 600 kg/m³ density difference	(Case 2)	<350 kg/m³ density difference	(Case 3)
Pore Radii (nm)	Pc (MPa)	IFT (mN/m¹)	Wettability	Column Height (m)	Density Difference (kg/m³)	Column Height (m)	Density Difference (kg/m³)	Column Height (m)	Density Difference (kg/m³)
920	0.0217	20	50%	4	556	4	556	7	318
920	0.0271	25	50%	4	694	5	556	8	348
920	0.0326	30	50%	5	668	6	556	10	334
920	0.038	35	50%	6	664	7	568	12	332
920	0.0347	20	80%	5	710	6	592	11	324
920	0.0434	25	80%	7	634	8	556	12	370
920	0.0521	30	80%	8	666	9	592	12	444
920	0.0608	35	80%	9	690	11	566	12	518
920	0.0434	20	100%	7	634	8	556	12	370
920	0.0543	25	100%	8	694	10	556	12	464
920	0.0652	30	100%	10	666	12	556	12	556
920	0.076	35	100%	11	714	12	656	12	656
Pore Radii (nm)	Pc (MPa)	IFT (mN/m¹)	Wettability	Column Height (m)	Density Difference (kg/m³)	Column Height (m)	Density Difference (kg/m³)	Column Height (m)	Density Difference (kg/m³)
1000	0.02	20	50%	3	714	4	536	7	306
1000	0.025	25	50%	4	664	5	532	8	332
1000	0.03	30	50%	5	632	6	528	10	316
1000	0.035	35	50%	6	612	7	526	11	334
1000	0.032	20	80%	5	674	6	562	10	338
1000	0.04	25	80%	6	698	7	598	12	350
1000	0.048	30	80%	7	714	9	556	12	418
1000	0.056	35	80%	9	646	10	582	12	486
1000	0.04	20	100%	6	698	7	598	12	350
1000	0.05	25	100%	8	650	9	578	12	434
1000	0.06	30	100%	9	692	11	566	12	520
1000	0.07	35	100%	11	658	12	604	12	604
Pore Radii (nm)	Pc (MPa)	IFT (mN/m¹)	Wettability	Column Height (m)	Density Difference (kg/m³)	Column Height (m)	Density Difference (kg/m³)	Column Height (m)	Density Difference (kg/m³)
1090	0.0183	20	50%	3	626	4	470	6	314
1090	0.0229	25	50%	4	588	4	588	7	336
1090	0.0275	30	50%	4	704	5	564	9	314
1090	0.0321	35	50%	5	658	6	548	10	330
1090	0.0293	20	80%	5	600	6	500	9	334
1090	0.0366	25	80%	6	624	7	536	11	342
1090	0.044	30	80%	7	656	8	574	12	384
1090	0.0513	35	80%	8	656	9	584	12	438
1090	0.0366	20	100%	6	624	7	536	11	342
1090	0.0458	25	100%	7	670	8	586	12	390
1090	0.055	30	100%	8	714	10	572	12	476
1090	0.0642	35	100%	10	656	11	596	12	548
Pore Radii (nm)	Pc (MPa)	IFT (mN/m¹)	Wettability	Column Height (m)	Density Difference (kg/m³)	Column Height (m)	Density Difference (kg/m³)	Column Height (m)	Density Difference (kg/m³)
1190	0.0168	20	50%	3	576	3	576	5	346
1190	0.021	25	50%	4	562	4	562	7	322
1190	0.0252	30	50%	4	646	5	516	8	324
1190	0.0294	35	50%	5	602	6	504	9	336
1190	0.0268	20	80%	4	686	5	550	8	344
1190	0.0336	25	80%	5	688	6	574	10	344
1190	0.0403	30	80%	6	688	7	590	12	344
1190	0.047	35	80%	7	700	9	544	12	408
1190	0.0336	20	100%	5	688	6	574	10	344
1190	0.042	25	100%	7	628	8	548	12	370
1190	0.0504	30	100%	8	646	9	572	12	430
1190	0.0588	35	100%	9	670	11	546	12	502

Table 3.13: Critical column height results for 12 m column height leakage scenario – black cells indicate mutual exclusivity (e.g. $\Delta\rho > 600$ kg/m^3 and low IFT), green cells indicate failure to satisfy leakage criteria (i.e. best-case scenario).

It is important to note that some of the combinations displayed in Tables 3.12 and 3.13 are mutually exclusive (black shaded cells). For example, some of the retention favourable cases that require high IFT values of 35 mN/m^{-1} also have a CO_2/brine density contrast lower than 600 kg/m^3, thus the IFT is more likely to lie within the 25-30 mN/m^{-1} range. Similarly, for leakage favourable cases, low IFT values of 20-25 mN/m^{-1} are only attainable with supercritical CO_2 and a CO_2/brine density contrast lower than 600 kg/m^3 (Chalbaud *et al*., 2006 and 2009).

From Tables 3.12 and 3.13, it is apparent that CO_2 can breach the caprock seal for both of the equivalent CH_4 leakage scenarios before the structures are filled to spill point, although capillary leakage of dense phase CO_2 requires higher column heights to compensate for a lower CO_2/brine density contrast, combined with low IFT and 50-80% wettability values. If we assume that the lowest values of IFT and wettability for a CO_2/brine system are unlikely to occur based on results from the most recent experimental work (Chalbaud *et al*. 2009; Tonnet *et al.,* 2010; Aggelopolous *et al.,* 2011), then the most likely worst-case scenarios for leakage require IFT values between 25-30 mN/m^{-1} combined with wettability values between 80-100%. The best-case scenarios for retention require IFT values exceeding 30 mN/m^{-1} combined with wettability values close to 100%, which implies that the CO_2 requires more gas-like rather than supercritical properties.

For each scenario considered here, it appears that if the in-situ storage conditions (e.g. CO_2 density, rock/fluid interactions, etc.) favour a lower IFT and wettability, there is no "comfortable" safety margin for retention. Using the data from Tables 3.12 and 3.13, Figures 3.17-3.18 and Figures 3.19-3.20 are used to illustrate the extreme end-point leakage and retention conditions for the 26 m and 12 m column height scenarios respectively, The worst-case leakage scenarios (highlighted in red within the legend), assume that the lowest IFT (20 mN/m^{-1}) and wettability (50%) conditions are unattainable (the full range of plots for all scenarios are available in Appendix 3).

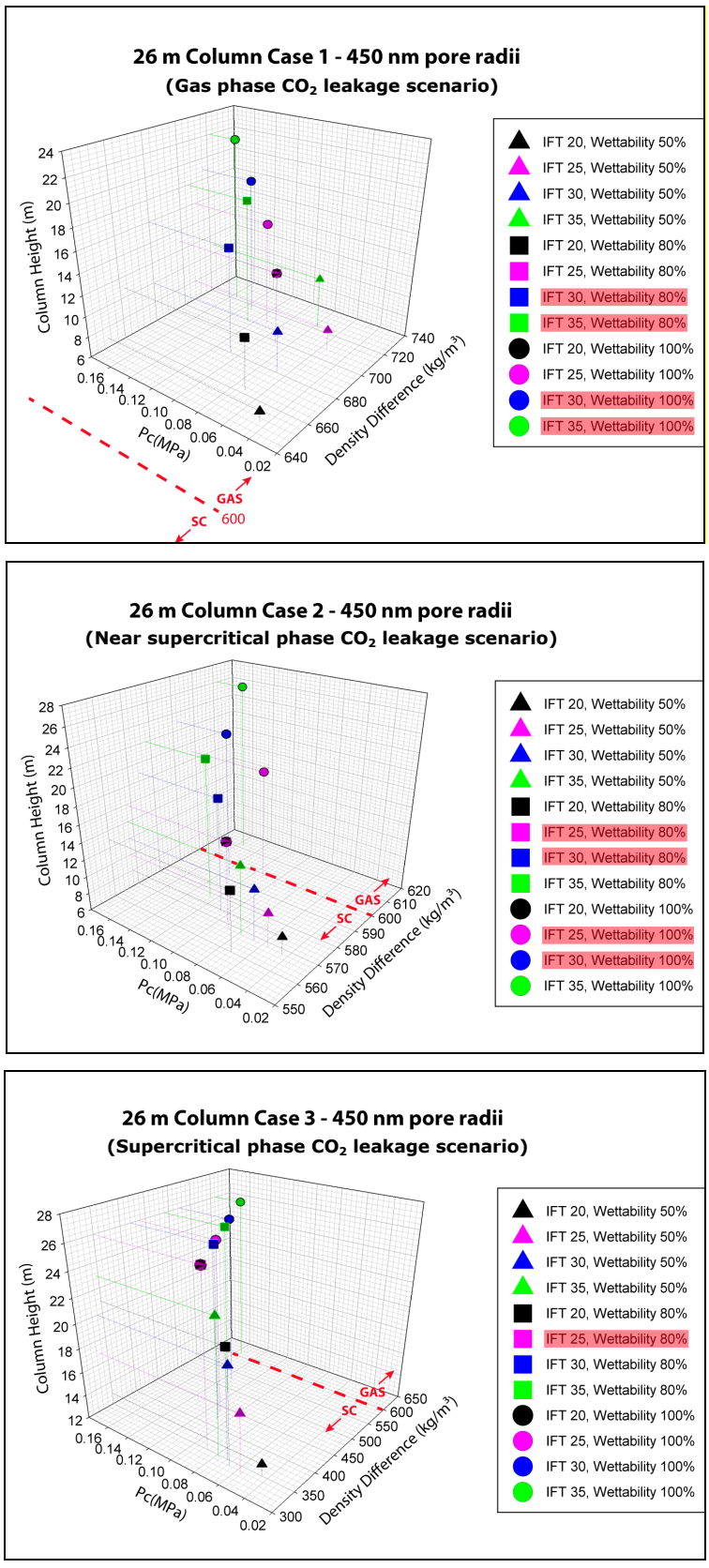

Figure 3.17: Critical column heights for the (low) end-point 450 nm pore radii and 26 m column height scenario over range of IFT, Wettability and Pc conditions, for cases 1-3 described on page 123. Data is from Table 3.12. Entries satisfying leakage criteria are highlighted red within the legend. CO_2 supercritical to gas phase transition zone is marked in red on the plot.

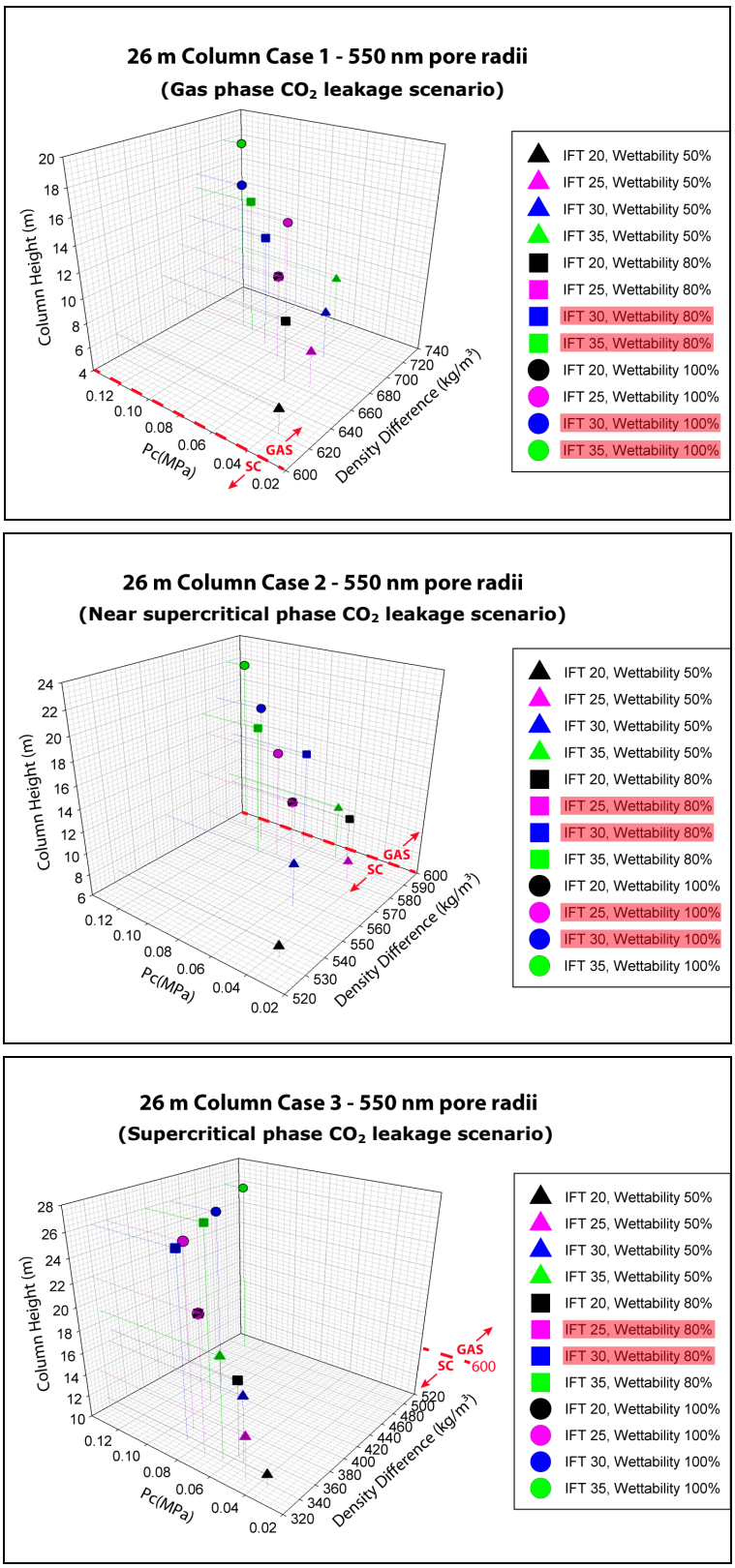

Figure 3.18: Critical column heights for the (high) end-point 550 nm pore radii and 26 m column height scenario over range of IFT, Wettability and Pc conditions, for cases 1-3 described on page 123. Data is from Table 3.12. Entries satisfying leakage criteria are highlighted red within the legend. CO_2 supercritical to gas phase transition zone is marked in red on the plot.

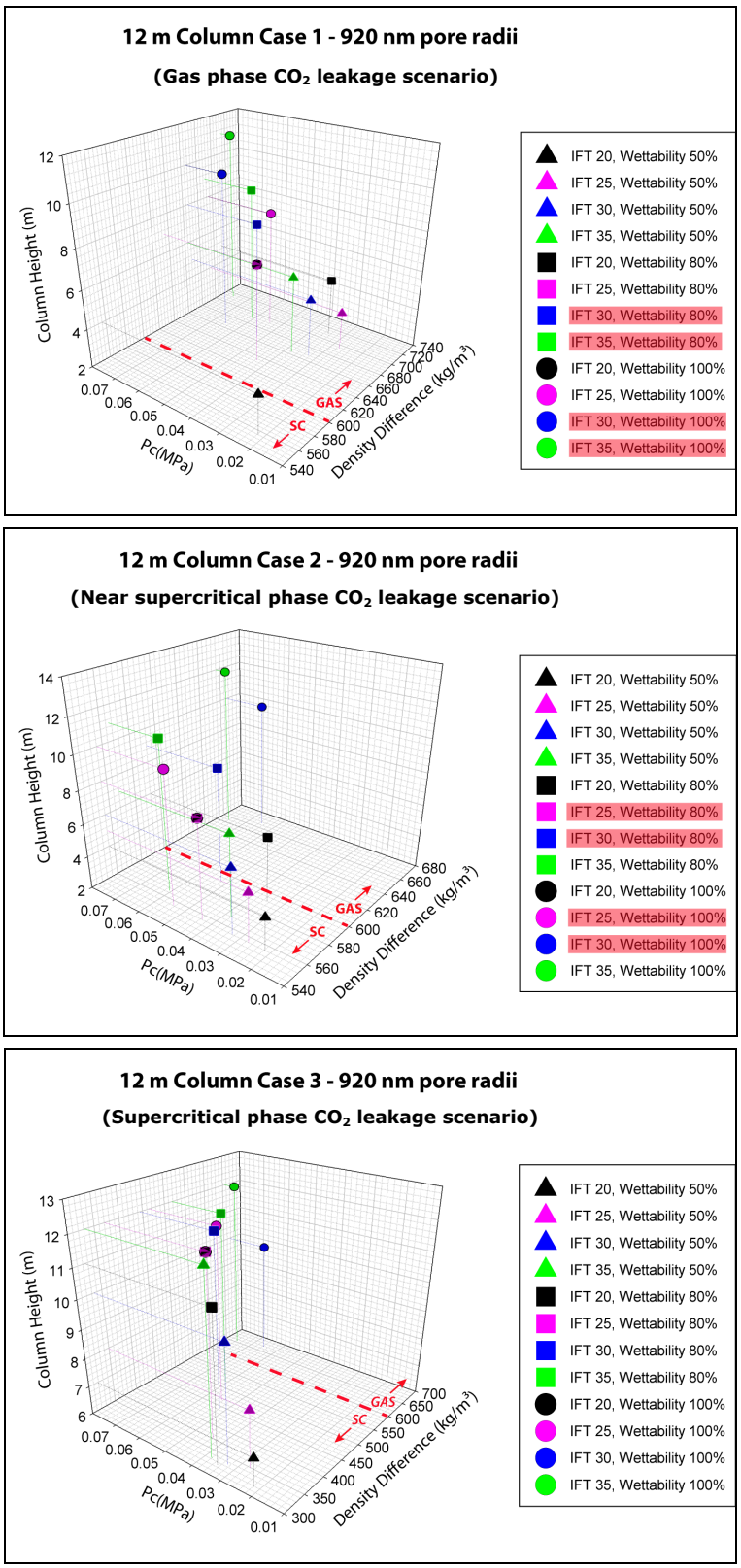

Figure 3.19: Critical column heights for the (low) end-point 920 nm pore radii and 12 m column height scenario over range of IFT, Wettability and Pc conditions, for cases 1-3 described on page 123. Data is from Table 3.13. Entries satisfying leakage criteria are highlighted red within the legend. CO_2 supercritical to gas phase transition zone is marked in red on the plot.

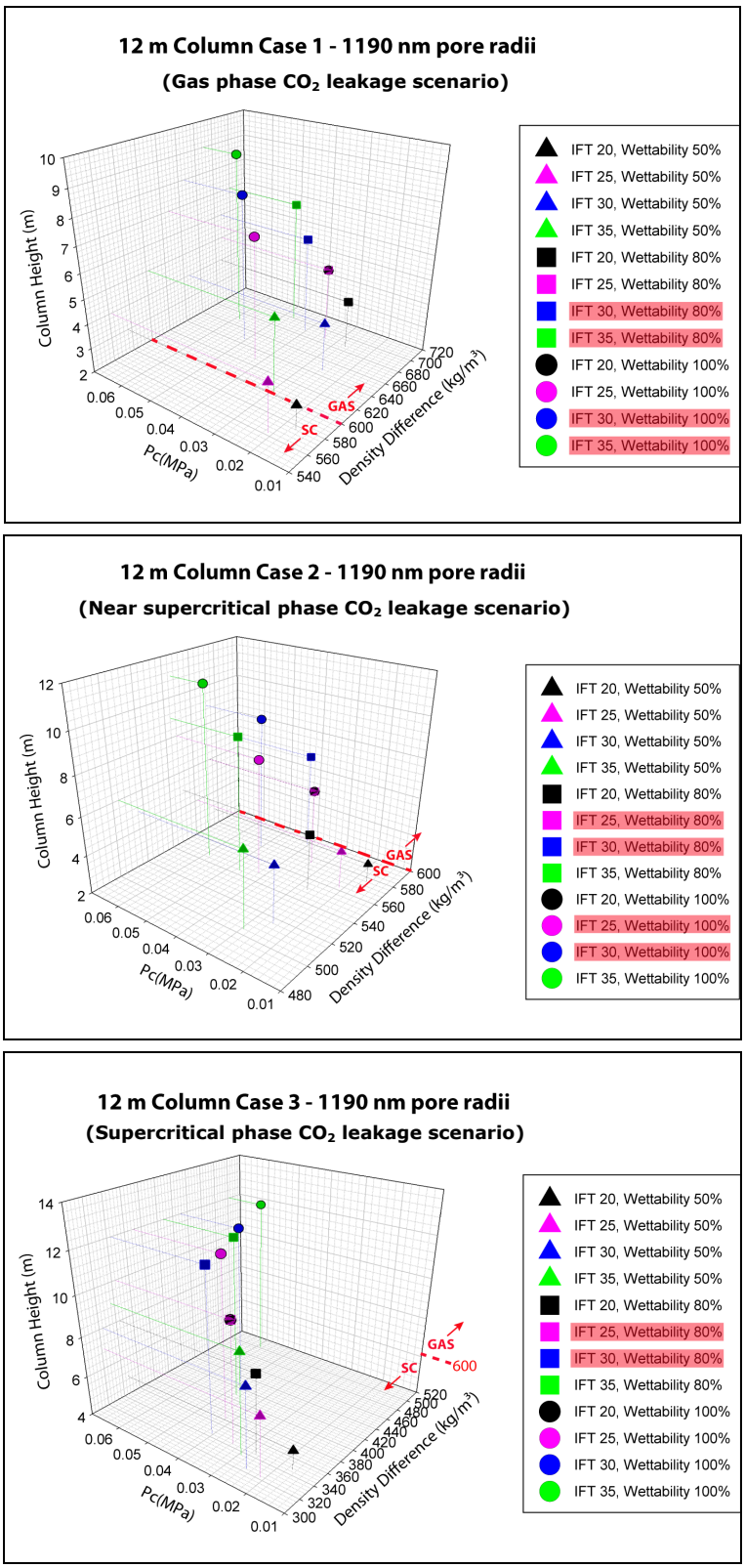

Figure 3.20: Critical column heights for the (high) end-point 1190 nm pore radii and 12 m column height scenario over range of IFT, Wettability and Pc conditions, for cases 1-3 described on page 123. Data is from Table 3.13. Entries satisfying leakage criteria are highlighted red within the legend. CO_2 supercritical to gas phase transition zone is marked in red on the plot.

3.6 Discussion:

This section concentrates on the uncertainties we have identified at Sleipner for three critical storage parameters and their influence on the ability of CO_2 to migrate via palaeo-migration conduits.

3.6.1 Geothermal Gradient and Caprock Temperature:

The Sleipner CO_2 storage site is situated in the South Viking Graben between 58-59°N and as illustrated in Figure 3.21, there have been several conflicting geothermal models proposed for this area over the past 40 years. The North Sea area south of 59°N was studied by Harper (1971) and Evans & Coleman (1974), who concluded that higher geothermal gradients were located in the deeper graben axes with cooler gradients situated on the flanks (structural highs) of the graben systems. Subsequent work by Carstens & Finstad (1981) for the northern North Sea sector from 59-62°N, disputed these findings, suggesting the geothermal relationship was reversed, with cooler gradients being observed in the grabens and higher gradients on the flanks. The latter authors attributed this phenomenon to the convective migration of hot fluids from the graben axis to the margins via fault zones, combined with the insulating effects of unconsolidated, clay-rich Cenozoic sediments (i.e. Hordaland and Nordland Shales) forming a blanket of low thermal conductivity.

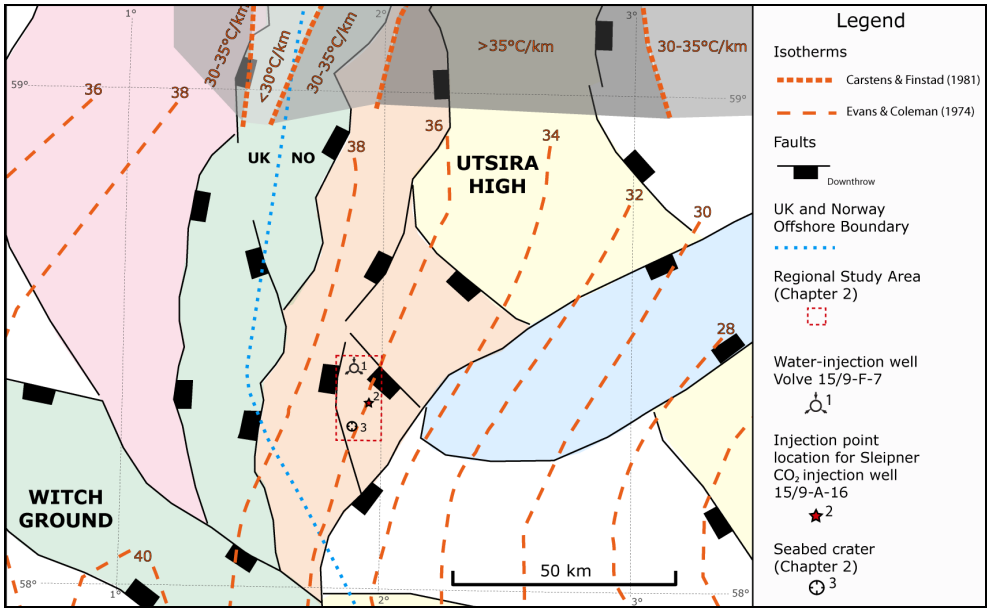

Figure 3.21: Structural map for South Viking Graben (SVG) and Sleipner area (modified after Faleide et al., 2002), with two geothermal gradients superimposed (orange dashed lines). North of 59° geotherms are derived from Carstens & Finstad (1981). South of 59° geotherms are derived from Evans & Coleman (1974).

Cenozoic heat flow mapping performed by Justwan *et al*. (2006) for the South Viking Graben area supports the findings of Carstens & Finstad (1981), in that heat flow appears to increase from the Viking Graben axis onto the Utsira High. Justwan *et al*. (2006), cite a number of other sources (e.g. Eggen, 1984; Brigaud *et al*., 1992 and Burley, 1993), who also suggest geothermal gradients in this part of the Norwegian Sector are driven by hot fluid transfer (initiated during the early Tertiary) in a west to east (graben axis to flank) direction. Similar examples of this heat transfer mechanism are reported by Ritter *et al*. (2004) and Parnell (2010) from the North Sea for passive margins offshore Norway and UK respectively.

Investigating the effects of Cenozoic sedimentation rates on geothermal gradient, Ritter *et al*. (2004) concluded that high accumulation rates correlate with lower geothermal gradients. According to Head *et al*. (2004) the Nordland Shales (~770 m average thickness in the Sleipner vicinity) were deposited between 1.8-2.4 Ma, thus sedimentation rates were approximately 390-292 m/Ma. This equates to a reduction of less than 5°C/km according to the methodology described by Ritter *et al*. (2004), although periods of non-deposition result in a gradient increase, so any unconformity surfaces in the overburden deposited at Sleipner should represent periods of geothermal gradient recovery.

A further complication arises from the addition of ice during periods of glaciation. The typical freezing point for seawater is minus 2°C although this is decreased through ice loading by 0.072°C/MPa (Benn & Evans, 1998). It is suggested by Pilliterri *et al*. (2003) that a 200-300 m thick ice sheet was responsible for imposing a 2-3 MPa overpressure on the overburden at Sleipner; this would result in a range of sub-glacial pressure melting point temperatures between minus 0.144-0.216°C (freshwater) to minus 2.144-2.216°C (seawater). The additional effects of sub-glacial frictional heating or low heat conductivity associated with thick glaciers also have to be considered.

Citing evidence from Carr *et al*. (2006), Lindeberg *et al*. (2009) suggest that the Sleipner area experienced loss of ice cover and subaerial exposure to cold air temperatures during the last glacial maximum (LGM), thus a surface temperature fluctuation of +/- 6°C has served to lower the prevailing geothermal gradient over geological time. This is incorrect on two counts, since Carr *et al*. (2006) actually refer to areas south of 56°N as being "dry land" during the LGM, Sleipner is situated north of 58°N and probably had similar water depths to present day conditions during Pliocene-Pleistocene inter-glacial periods (Faleide *et al*., 2002). Recent evidence from Bradwell *et al*. (2008) and Sejrup *et al*. (2009) also suggests that the British and Scandinavian ice sheets were still confluent during the LGM and for some time after. Allowing for the insulating effects of a thick ice sheet during glacial periods, low thermal conductivity of the Nordland Shale overburden at Sleipner and sub-ice hydraulic excavation of tunnel valleys and channels, it is more likely that any geothermal gradient reduction due to the effects of glaciation would be minimal and relatively short-lived over geological time. There is also evidence of IRD (ice-rafted debris) within early Pleistocene sediments deposited at Sleipner (Bøe & Zweigel, 2001). Jansen & Sjoholm (1991) and Jansen *et al*. (2000) report the first prominent IRD input offshore Norway from ~2.74 Ma, with further IRD peaks occurring on a 41 kyr cyclicity until 0.9 Ma, after which there was a transition to a 100 kyr cyclicity. As these IRD peaks are believed to signal the termination of a glacial episode (Jansen *et al*., 2000), it can be inferred that during the Pliocene-Pleistocene the Sleipner area was either covered by several hundred metres of ice with sub-ice erosional activity occurring during glacial periods or was subject to glacio-marine depositional processes during inter-glacials (Head *et al*., 2004; Carr *et al*., 2006; Graham *et al*., 2007).

Lindeberg *et al*. (2009), also propose that a cooler than expected geothermal gradient in the Sleipner area is confirmed by a 27.55°C temperature measurement acquired at a depth of 769 m (it is not stated explicitly whether this is TVDSS or sub-seabed, although a more recent publication by Alnes *et al.* (2011) confirms that the measurement point is located 768 m below mean sea level). This measurement was obtained from water production well 15/9-F-7 at Volve, which is situated ~8 km NW of the CO_2 injection point location (Figure 3.21). This value was used to calibrate Sleipner temperature models and derive a caprock temperature above the storage site of ~28-29°C (i.e. a linear gradient of 32.72°C from a 5°C seabed temperature). This suggests that the Sleipner area has a lower geothermal gradient than proposed by the research of Evans and Coleman (1974) and Justwan *et al*. (2006), that indicates a general WNW to ESE lateral geothermal gradient variation (Figure 3.21). In their analysis of hydrocarbon migration in the South Viking Graben, Isaksen *et al*. (2002) describe lateral differences in hydrocarbon composition and natural CO_2 concentration between the Sleipner West, East and Volve fields related to the orientation of structural migration paths, degree of compartmentalisation and fractionation effects. The Volve field contains black oil in contrast to the other Sleipner fields that are gas condensate reservoirs, implying a different thermal regime, hydrocarbon source or fluid migration route for Volve. Allowing for the presence of vertical fluid migration pathways in this area described by Løseth *et al*. (2009) for Mesozoic-Cenozoic sequences, could thermal convection effects imprint a similar vertical and lateral variation in geothermal gradient on the Utsira Formation? If so, then the temperature measurement from Volve (where there is negligible CO_2 present in the pore water) may not be a reliable indicator of caprock temperatures above the Sleipner CO_2 storage site ~8 km to the SE.

Once CO_2 has been injected into the storage formation, it will affect the temperature profile within the formation due to large differences in thermal conductivity between the original brine-filled pore space and pore space invaded by CO_2 (Hurter *et al*., 2007a; Bielinski *et al*., 2008). Thermal conductivities for a representative range of rock and fluid types that may be expected in a typical CO_2 storage context are presented in Table 3.14 (modified after Hurter *et al.*, 2007a and references therein).

Fluid/Rock Type	Thermal Conductivity ($W/m^{-1}/°K^{-1}$)	Notes
Air	0.025	
CO_2	**0.04424**	**supercritical**
CH_4	0.042067	
Oil	0.12-0.17	
Coal	0.30	
Water	0.62668	
Clay (Illite)	1.85	
Shale	1.93	water-saturated
K-Feldspar	2.31	
Calcite	3.59	
Sandstone	3.94	water-saturated
Dolomite	5.51	
Halite	6.50	
Quartz	7.69	

Table 3.14: Thermal conductivities for a range of rock and fluid types at ~55°C and ~7.5 MPa in ascending order (modified after Hurter et al., 2007a and references therein).

The thermal conductivity of CO_2 varies with pressure and temperature conditions as illustrated in Figure 3.22:

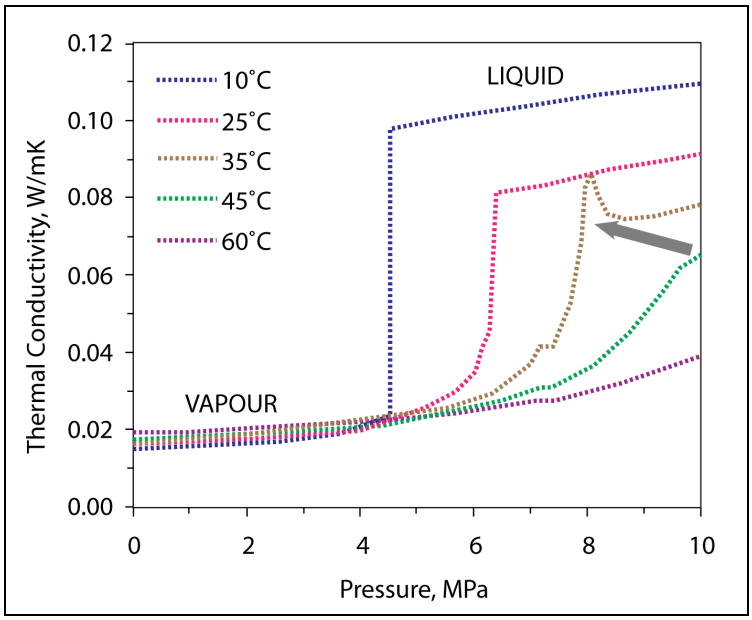

Figure 3.22: Plot of CO_2 thermal conductivity versus pressure for a range of temperatures (modified from Hurter et al., (2007a) after Vesovic et al., (1990)). Grey arrow indicates the range of pressure and temperature conditions from Sleipner injection point to caprock.

If we assume a CO_2 injection temperature between 35-45°C, it appears that the reduction in temperature and pressure from the CO_2 injection point to the caprock will tend to slightly increase the thermal conductivity to ~ 0.07 $W/m^{-1}/°K^{-1}$, followed by a rapid reduction to ~0.02 $W/m^{-1}/°K^{-1}$ as CO_2 passes through a phase transition between 6-8 MPa (actual transition pressure is dependant on caprock temperature). This implies that warm CO_2 injected at high rates into a storage formation may not be able to conduct heat to the surrounding rock fast enough, thus thermal convection and advection processes will tend to dominate (depending on the k_v/k_h ratio), potentially increasing the core temperature of an ascending plume and reducing the CO_2 density (Alnes *et al.,* 2011). Hurter *et al*. (2007a) further demonstrate that at a given depth, any temperature increase is proportional to layer thickness, porosity and CO_2 saturation; this increase may amount to a few °C in sandstone reservoirs.

Naturally, a homogeneous system that allows convective mixing will tend to ameliorate any localised temperature increase and a rapid ascent of the CO_2 plume should result in Joule-Thomson cooling (Pruess, 2008). Yet although the Utsira Formation has a high porosity and permeability it is also vertically heterogeneous and contains multiple horizontal shale barriers (many being sub-seismic), thus vertical convective mixing and rapid ascent (other than through localised high-permeability pathways) will be retarded. High porosity and permeability characteristics may also allow CO_2 to displace brine more effectively, particularly in a lateral direction when the k_v/k_h ratio is low, thereby reducing thermal conductivity more efficiently within such a layer.

The effects of lithological variations on thermal conductivity were considered to a certain extent by Nooner *et al*. (2007), who used different thermal conductivities for the clay-rich Nordland Shale overburden and sand-rich Utsira Formation to calibrate their dual geothermal gradient model and derive a predicted caprock temperature of 36.2°C (described previously in Section 3.3.2 and Table 3.1), which is more in agreement with the earlier work performed by Carstens & Finstad (1981); Eggen (1984); Brigaud *et al*. (1992); Burley (1993) and Justwan *et al*. (2006), that suggests a much warmer geothermal gradient exists above the Sleipner site than proposed by Lindeberg *et al*. (2009).

As we illustrated in Sections 3.3 and 3.4, warmer geothermal gradients can reduce storage efficiency and increase the buoyancy force on the caprock via CO_2 density reduction. In addition, the supercritical to gas phase transition for CO_2 can occur at increasingly greater depths.

3.6.2 CO_2 Density:

We have considered how CO_2 density has been determined at Sleipner for fluid flow modelling purposes (Section 3.3.5) and described the close association between temperature gradients and CO_2 density within a known pressure range (Section 3.4). The use of an average CO_2 density for the entire plume is inadequate since this approach cannot accurately constrain the CO_2 density variations that prevail between the injection point and caprock, nor can it provide a quantitative estimate of the partitioning between high saturation layers of CO_2 in the core of the plume and diffuse volumes of low saturation CO_2 at the periphery (Nooner *et al*., 2007). Such uncertainties will introduce errors into volume calculations based on average density estimates. There is probably a vertical and lateral CO_2 density stratification within the plume, resulting mainly from the temperature effects described in Section 3.6.1. Gravity studies have been used to better constrain CO_2 density within Sleipner (Nooner *et al*., 2007; Arts *et al*., 2008; Alnes *et al.*, 2008 and 2011), but results show a high variability (Table 3.4), again depending on whether a hot or cool geothermal gradient is assumed. It is also doubtful whether gravity measurements are sensitive enough to account for subtle multi-phase effects such as the presence of dense phase CO_2 and gas phase CO_2 simultaneously at the caprock (e.g. gas phase overlying dense phase or lateral phase changes at near critical point conditions associated with lateral temperature variations).

The presence of minor natural gas accumulations within “attic” areas of the Utsira Formation has been described by Zweigel *et al*. (2000) and given our evidence for natural gas migration into the overburden at Sleipner (described in Chapter 2), this suggests there is a high probability of dissolved CH_4 in the Utsira Formation porewater, particularly at the interface between the Utsira Formation and the caprock. The presence and significance of dissolved natural gas should be considered

by seismic and gravity monitoring programmes. Dissolution of CH_4 reduces brine density whilst dissolution of CO_2 has the opposite effect, thus if the presence of dissolved CH_4 is not accounted for, this could result in an underestimated change in brine density within the storage formation following CO_2 injection (Taggart, 2009). If regions containing dissolved natural gas are contacted by migrating CO_2 mutual solubility in this type of multi-phase system could lead to chromatographic separation and exsolution of the least soluble components (i.e. CH_4), as described by Bachu & Bennion (2009) and Taggart (2009), forming a bank of CH_4 ahead of the invading CO_2. This process will affect the fluid density distribution at the peripheral edge of the plume and may also explain why migrating CO_2 appears to move faster beneath the caprock than predicted by history matched, fluid flow modelling simulations (Chadwick *et al*., 2009b, Singh *et al.,* 2010).

3.6.3 Capillary Entry Pressures:

Where palaeo-gas migration conduits overlie a CO_2 storage site and there is a risk of contact with a migrating CO_2 plume, it is essential to understand how these two systems will interact. With the situation illustrated in Figure 3.23, if the highest CO_2 accumulation spills into and fills the adjacent structure it will contact the palaeo-gas migration pathway. However, as we described in Section 3.5, the CO_2 column underlying the relict pathway needs to develop a sufficient column height and buoyancy pressure to overcome the capillary entry pressure of the natural gas and brine filled pores.

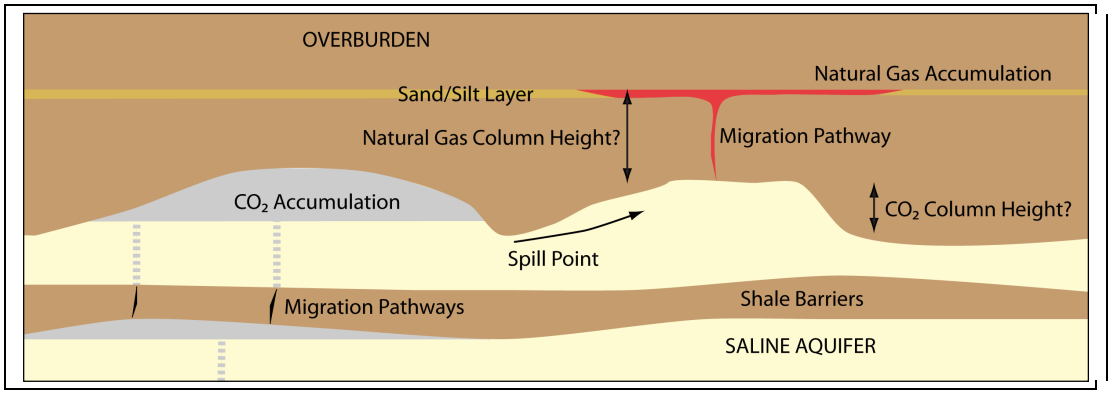

Figure 3.23: Schematic cross-section of CO_2 storage site with an adjacent structure containing a palaeo-migration pathway filled with natural gas.

In terms of how these two fluid systems may interact, research has already been undertaken for two-phase CO_2/brine and CH_4/brine systems (Oldenberg *et al*, 2001, 2004; Shi *et al*., 2008; Bachu & Bennion, 2009; Sidiq & Amin, 2009; Taggart, 2009). Much of this work has been performed to model CO_2 injection for enhanced oil recovery (EOR), enhanced coal bed methane (ECBM) and more recently, carbon sequestration with enhanced gas recovery (CSEGR). Less attention has been focussed on the impact of three-phase saturations, mutual solubility, wettability and IFT for CO_2/CH_4/brine systems (with and without impurities) over a range of typical storage conditions. Most three-phase research has considered CO_2/CH_4/H_2O systems (Ren *et al*., 2000; La Force *et al*., 2008; Qin *et al*., 2008) or CO_2/CH_4(hydrate)/H_2O-brine systems (Austegard *et al*., 2006; Kvamme *et al*., 2009). Some core flood experiments have also been performed using supercritical CO_2 to displace CH_4 from carbonate cores (Mamora & Seo, 2002; Seo & Mamora, 2005) and CH_4/brine from sandstone cores (Sidiq & Amin, 2009). These experiments all indicate that the process of immiscible CH_4 displacement by pure CO_2 (in gas, liquid or supercritical form), is extremely efficient, with high recovery factors recorded for CH_4 in all cases. None of the experiments considered contamination of the CO_2 by impurities (e.g. H_2S, CH_4, C_2H_6, etc.), or dissolution of CH_4 in the resident brine (Taggart, 2009), although experimental work performed on water/H_2S systems by Shah *et al*., (2008) demonstrated the ability of certain impurities such as H_2S to reduce IFT.

The CO_2 phase conditions at the caprock (in turn determined by the prevailing pressure and temperature conditions) will have a major influence on the displacement process. Research suggests that because supercritical CO_2 density and viscosity are greater than CH_4 under equivalent storage conditions, the situation depicted in Figure 3.18 will be a miscible displacement with limited mixing at the CO_2/CH_4 interface (Oldenberg *et al*., 2001). But if CO_2 forms a free gas phase at the caprock, the buoyancy contrast between CO_2/brine is greater and diffusion processes may be more significant, thus we need to consider the positive and negative impacts of having supercritical CO_2 or gas CO_2 at the caprock from a displacement perspective.

A supercritical CO_2/brine system has a lower buoyancy contrast and high density CO_2 also offers optimum storage volumetrics, but reduced CO_2/brine IFT (Chalbaud *et al*., 2006 and 2009) combined with a possible wettability reduction (Chiquet *et al*., 2007a; Yang *et al*., 2008) provides supercritical CO_2 with a higher mobility than CH_4 and promotes easier migration through equivalent pore radii (Li *et al*., 2006; Springer & Lindgren, 2006; Harrington *et al*., 2009). In contrast, a gaseous CO_2/brine system has a higher buoyancy contrast and low density CO_2 offers poorer storage volumetrics. However, gas phases are traditionally non-wetting and gaseous CO_2/brine IFT values are considerably higher, particularly when the CO_2/brine density contrast exceeds 600 kg/m^3 (Chalbaud *et al*., 2006 and 2009). Thus, the capillary entry pressures for gas CO_2/brine are almost double that of a supercritical CO_2/brine system (Springer & Lindgren, 2006) and larger column heights are then required to induce capillary leakage. If gas phase CO_2 does migrate through the overburden via palaeo-migration conduits, density, viscosity and interfacial tension values will gradually tend towards those for CH_4 as the CO_2 ascends to shallower depths (as illustrated on Figures 3.9 and 3.10), which may contribute to diffusive and dispersive mixing of the two gases; it has been observed that this process leads to a strong CO_2 density reduction and consequent pressure increase (Oldenberg *et al*., 2004), particularly within a confined system (e.g. fault or fracture network), where fluid expansion and pressure dissipation are restricted.

Quantitative evaluation of the CO_2/CH_4/brine system depicted here will be extremely challenging, considering the complex multi-phase behaviour of ascending CO_2 in the shallow sub-surface combined with the presence of two additional and potentially mobile phases. For the submarine case depicted in Figure 3.11, the supercritical to gas phase transition for CO_2 will occur between ~500-800 m depending on the prevailing geothermal gradient, at which point interference effects are liable to occur between migrating CO_2 phases, CH_4 and brine (Pruess, 2008; Tsang *et al*., 2008). Reactive transport and microbial processes also need to be considered for this type of migration scenario, since these can promote both positive (e.g. calcite cement dissolution) and negative (e.g. mineral precipitation) feedback effects within a migration conduit (Bildstein *et al*., 2010; Fleury *et al*., 2010; Morozova *et al.,* 2010).

In monitoring terms it may be very difficult to detect such a discrete vertical leakage process via palaeo-gas migration conduits since we cannot accurately quantify the prevailing residual gas saturation within the conduit. The initial stage of CO_2 ingress may be an immiscible sweep process that increases the natural gas saturation at the distal end of the pathway as the ascending CO_2 displaces CH_4 upwards. Since there is no appreciable change in seismic P-wave velocity (V_p) as CO_2 saturation increases beyond ~20% (Nooner *et al*., 2007; Vanorio *et al*., 2010), this re-mobilisation process may only be detected if CO_2 or CH_4 migrates into "virgin" zones of extremely low or zero gas saturation. In the case of monitoring methods that employ time-lapse seismic difference cubes, CO_2 saturation can only be detected in regions which originally contained little or no CO_2 and thereafter become saturated with migrating CO_2 until seismic visibility ensues at the appropriate tuning thickness (Andreassen *et al.*, 2007; Arts *et al*., 2008). In effect, there may be no discernible seismic difference between a vertical conduit in the overburden containing natural gas (pre-CO_2 injection) and the same conduit (post-CO_2 injection) filled with a CO_2/CH_4 mixture until the capillary pressure for the system is exceeded and the CO_2/CH_4 within the conduit is mobilised vertically or laterally to invade areas previously unsaturated by gas.

In our assessment of the two CH_4/CO_2 capillary leakage scenarios described in Section 3.5, we essentially modelled best-case situations (i.e. structures that required to be filled to spill-point before leakage). Yet, palaeo-migration of natural gas may have occurred with column heights of only a few metres (e.g. through larger pore throat radii than we have modelled here). The converse (i.e. overfill before leakage) is unlikely to be the case, since the shale barriers present in the Utsira Formation constrain the capillary continuum in the sandstones to column heights of tens of metres at most. More recent research suggests that our low end-point values for brine/CO_2 IFT and wettability (derived from Hildenbrand *et al.*, 2004; Chiquet e*t al*., 2007a and 2007b) may be too conservative. Increasing salinity and the amount of dissolved CO_2 in the aqueous phase can induce an IFT increase (Chalbaud *et al.,* 2009). Similarly, rock/fluid water-wettability reductions to 50% in the presence of CO_2 reported by the experimental work of Chiquet e*t al.,* (2007a) have not been

confirmed by subsequent work (Shah *et al.*, 2008; Fleury *et al.*, 2010; Tonnet *et al.*, 2010). Thus, we suggest that our results using brine/CO_2 values of 25-30 mNm^{-1} for IFT and 80-100% for water-wettability from Tables 3.12 and 3.13 are probably more reliable for the two column height scenarios considered.

It is argued that early evidence of any CO_2 leakage from Sleipner into the overburden should be detected by a slow down in predicted growth of the highest plume layer (Neufeld *et al.*, 2009), but the latest monitoring results indicate that the highest layer of CO_2 is growing faster than fluid flow models predict (Chadwick *et al.*, 2009b). The 2D laboratory experiments of Neufeld *et al.* (2009), designed to simulate a gravity-driven leakage analogy were not performed at in-situ conditions, so temperature and pressure effects on density, phase changes, IFT and wettability for a multi-phase CO_2/brine/CH_4 system were not addressed. The position of the leakage pathway was also offset from the supply, which served to accentuate layer growth asymmetry, but no sensitivities were performed to assess the impact of a leakage pathway directly above/below the supply (i.e. structural crest leakage). We have described two mechanisms which could help explain faster growth of the highest plume layer than current models predict: a higher geothermal gradient, with a more mobile, low density (or density-stratified) layer of CO_2 (also considered as an option by Chadwick *et al.*, 2009b) and/or a bank of exsolved CH_4 being driven ahead of the migrating CO_2 plume.

3.7 Conclusions:

Geological formations below the North Sea are being proposed as storage locations for anthropogenic CO_2, particularly saline aquifers and depleted oil and gas fields. Two sites are already operational offshore Norway (Sleipner and Snøhvit). We have described specific North Sea areas associated with palaeo-gas migration conduits that are indicators of natural gas leakage from the subsurface to seabed over geological time. We have identified similar conduits and shallow gas anomalies within the Nordland Group overburden sediments deposited above the Sleipner CO_2 storage site. These features were present before CO_2 injection commenced in 1996 and may serve to compromise site integrity if contacted by a migrating CO_2 plume.

After reviewing the critical storage parameters at Sleipner, we conclude that there are still major uncertainties regarding spatial temperature gradients at the storage site, caprock capillary entry pressures and the presence of dissolved natural gas in Utsira Formation porewater. The caprock conditions at Sleipner are very close to the critical point pressure and temperature conditions for CO_2. Since density measurements are strongly reliant on temperature and porewater composition, this can lead to measurement inaccuracies of CO_2 density.

Using published data for Sleipner we have established a range of critical CO_2 column heights based on the range of predicted conditions at the Utsira Formation/caprock interface for two scenarios based on a CH_4 leakage analogy (assuming that caprock pore-throat radii are unchanged over geological time). Our results suggest that if the CO_2/brine/rock system is 100% water-wet, with an IFT ~30 mNm^{-1} and optimum supercritical CO_2 density ~700 kg/m^3, leakage is unlikely to occur even if the closure is filled to spill-point. However, if supercritical CO_2 exists at the caprock in near critical point conditions (i.e. ~500-600 kg/m^3), such that IFT is ~25-30 mNm^{-1}, leakage is possible before the caprock closure is filled to spill-point if the CO_2/brine/rock system has a low to intermediate water-wettability ~80-100%. Recent experimental evidence (Shah *et al.*, 2008; Chalbaud *et al.,* 2009; Fleury *et al.*, 2010; Tonnet *et al.*, 2010) suggests that a CO_2/brine system with a very low IFT (20 mNm^{-1}) and low water-wettability (50%) is unlikely to prevail at the Sleipner caprock depth for the range of pressure, temperature and salinity conditions considered here.

We have described the ingress of CO_2 into a natural gas-filled fracture system and although much work has already been done on two-phase CO_2/brine systems and CH_4/brine systems, it is apparent that more experimental work is required to assess the impact of three-phase saturations, mutual solubility, wettability and IFT for CO_2/CH_4/brine systems (with and without impurities in the CO_2 and brine phases) for a range of typical storage conditions. In terms of seismic monitoring, it may be difficult to discern any difference between a migration conduit filled with CH_4/brine (pre-CO_2 injection) and the same conduit filled with CO_2/CH_4/brine (post-CO_2 injection), given the insensitivity of seismic P-wave velocity to gas saturations above 20%. This implies that "virgin" overburden formation needs to be invaded to form a horizontal accumulation before leakage can be detected by time-lapse seismic methods. It is suggested that a CH_4 efflux may precede a CO_2 leak, providing an early warning, but CH_4 is a more potent greenhouse gas than CO_2, so this is also an undesirable outcome.

In summary, we present a number of observations from our evaluation of Sleipner storage conditions that may help to reduce similar uncertainties during the planning stages for future CO_2 storage sites:

- Detailed overburden mapping is an essential pre-requisite for proposed CO_2 storage sites located near areas of known palaeo-gas migration. Areas of known seepage may need to be avoided. Mitigation strategies may include defining whether the critical CO_2 column height is within an acceptable safety margin for prevailing storage conditions or intervention to pre-emptively seal migration conduits. Risking of the overburden should be performed to minimise uncertainty. Predictive seismic tools such as chimney cubes and fault cubes should be used as a first approach (e.g. Meldahl *et al.,* 2001; Ligtenberg & Connolly, 2003)
- Critical chimney heights need to be established for equivalent CH_4/CO_2 columns (Naylor *et al.,* 2011a). This is particularly relevant for depleted gas field CO_2 storage applications, but a similar methodology can also be extended to depleted oil fields,

- Given the particular sensitivity of CO_2 physical properties to temperature effects, we recommend that the acquisition of accurate pre-injection temperature data is a priority. The initial (undisturbed) geothermal profile of the site should be ascertained. Thermal conductivity of the storage reservoir and overburden should be assessed by core flooding experiments. Real-time temperature acquisition should be employed to monitor the plume movement and potential for unexpected phase changes (Bielinski *et al*., (2008) describe such a fibre-optic system),
- Since most CO_2 injection wells are likely to be new, dedicated disposal wells, this offers the best opportunity to acquire temperature and pressure survey data, drill core and porewater samples. With Sleipner, no pore fluid samples were acquired at the storage site, yet this is a crucial requirement for assessing the degree of dissolved gases present in the resident brine (particularly CH_4), assessing the potential impact of CO_2-induced microbial reactions (Morozova *et al.,* 2010) and accurately calibrating core flood and geochemical experiments to further investigate rock/fluid interactions.

Chapter 4:
Beyond the seal: stochastic flow modelling of CO_2 migration at Sleipner

Grant Nicoll[1], Andrew Cavanagh[2], Sebastian Geiger[3] and Stuart Haszeldine[1]

1. The University of Edinburgh, Edinburgh, Scotland.
2. The Permedia Research Group Inc., Ottawa, Canada.
3. Heriot-Watt University, Riccarton, Edinburgh, Scotland.

"The sciences do not try to explain, they hardly even try to interpret, they mainly make models. By a model is meant a mathematical construct, which with the addition of certain verbal interpretations describes observed phenomena. The justification of such a mathematical construct is solely and precisely that it is expected to work."

Quotation by John von Neumann (1903-1957)

"You can't always get what you want,
You can't always get what you want,
You can't always get what you want,
But if you try sometimes you might find,
You get what you need…"

Extract from "You Can't Always Get What You Want" (The Rolling Stones),
© Universal Music Group

4.1 Introduction:

The Sleipner CO_2 storage site situated offshore Norway (Figure 4.1) is the world's first saline aquifer, carbon capture and storage (CCS) project, designed to sequester industrial CO_2 within the sub-surface. The project was initiated in 1996, partly in response to Norwegian environmental legislation, but also to help reduce CO_2 emissions, because increasing levels of atmospheric CO_2 are currently believed to be responsible for detrimental climatic changes and ocean acidification on a global scale. Sleipner is currently the longest running, and arguably the most successful "CCS experiment" designed to prove the concept of engineered CO_2 storage in saline aquifers.

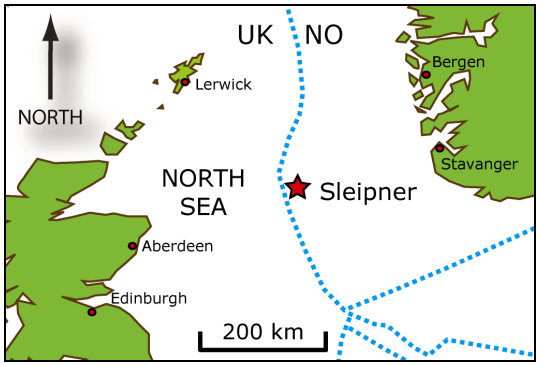

Figure 4.1: Location map for the Sleipner CO_2 storage site, offshore Norway.

The CO_2 is extracted from the Sleipner Vest (West) natural gas operation and injected via a highly deviated well into the Utsira Formation at a depth of 1012 m. Since 1996, over 12 Mt of CO_2 has been injected at a rate of less than ~1 Mt/yr. The Utsira Formation is a saline aquifer comprised of high permeability sandstone (1-5 Darcies) with thin, low permeability inter-bedded shales, and is sealed by a low permeability caprock at a depth of ~800 m (Zweigel *et al.,* 2004a). The Sleipner storage site has been subject to an ongoing monitoring programme since 1996, using time-lapse seismic (Figure 4.2) and other geophysical techniques. No leakage has been detected at the resolution of these geophysical methods and the CO_2 is observed to trap as a multi-layer plume beneath the caprock, which is comprised of a ~700 m thick sequence of Nordland Group shales (Arts *et al.,* 2008).

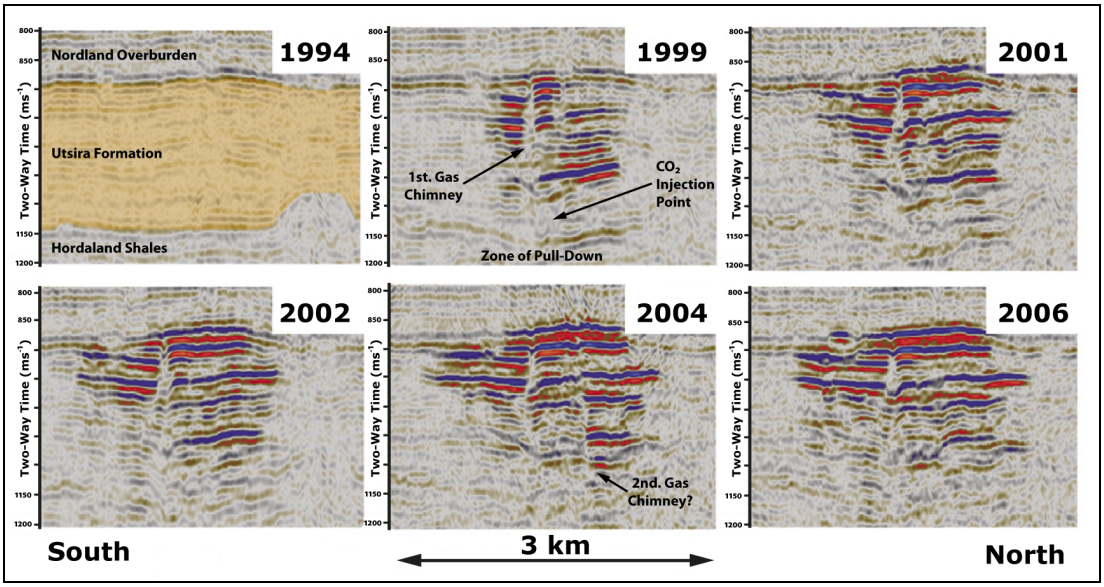

Figure 4.2: Seismic cross-sections showing CO_2 plume development (modified from Arts et al., 2008)

Since this is a high profile, prototype project, there is considerable scientific interest in the ability of this site and other saline aquifers to safely contain CO_2 for millennia (i.e. the timescale required for successful sequestration). The injected CO_2 at Sleipner is observed to have breached at least seven thin shale barriers (with less than 1.5 m thickness) and a 5-7 m thick barrier (Thick Shale) in less than three years (Zweigel *et al.,* 2004a). The Thick Shale (barrier 8) is also inferred to have a similar composition to the overlying caprock shale (Figure 4.3) and this has raised concerns about the caprock response to CO_2 and how effective its retention capability might be in the longer term (Bøe & Zweigel, 2001; Hamborg *et al.*, 2003).

Storage factors affecting seal integrity need to be considered in a geological context, including the presence and influence of palaeo-gas migration pathways and other heterogeneities such as fractures and common lithological variations. As Figure 4.2 illustrates, chimney structures are visible on the seismic cross-sections and these appear to be acting as high permeability conduits, transporting CO_2 to the top of the storage formation. It is debatable whether these chimney features represent existing fracture/fault networks, high-permeability lithological heterogeneities (e.g. sand injectites) or whether an acidic CO_2-brine mixture has self-excavated or enhanced existing migration pathways through the Utsira Formation by dissolution of carbonate matrix (i.e. shell fragments) and pore cements (Hermanrud *et al.,* 2007, 2010).

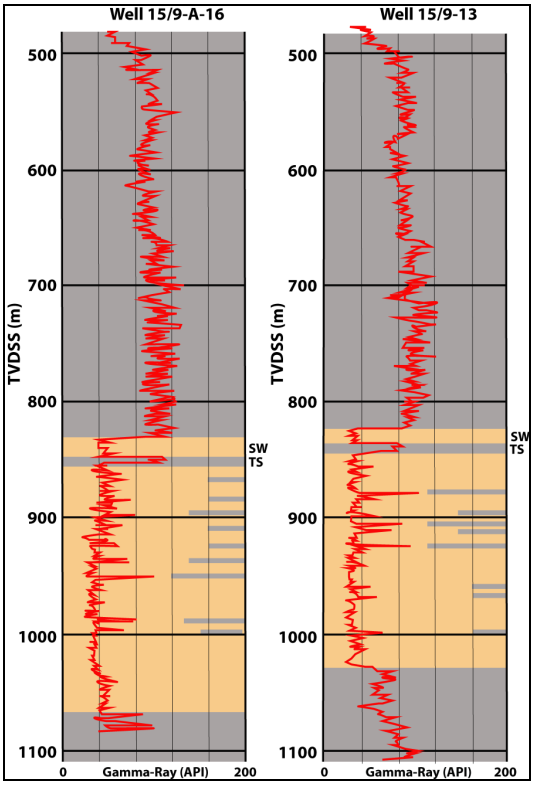

Figure 4.3: Stylised gamma-ray logs for the CO_2 injection well 15/9-A-16 and the closest exploration well 15/9-13 (refer to Chapter 3, Figure 3.6 for well locations), showing the log responses for Nordland Shale overburden (uppermost grey), Utsira Formation (orange) and Hordaland Shale underburden (lowermost grey). The Sand Wedge (SW) and Thick Shale (TS) are also identified along with internal discontinuous shale barriers within the Utsira Formation, represented by gamma-ray spikes (modified from Arts et al., 2008)

As previously described in Chapter 2, we have mapped sand-filled glacial channels and tunnel valleys within the overburden above the storage area and we have also mapped a number of lineations, chimneys and high amplitude seismic anomalies in close proximity to the storage site. Our interpretation is based on a 3D seismic survey that predates the storage of CO_2. We attribute the mapped anomalous zones to geological natural gas seepage, gas accumulation indicators and authigenic carbonate deposits found within four prominent intervals of the Nordland Group shales overlying the storage formation. The absence of similar anomalies within the storage formation prior to injection may indicate that:

1) Palaeo-gas migration pathways and gas accumulations are only detectable within the Nordland Group shales at the resolution of seismic data (this assertion also applies to the CO_2 currently stored at Sleipner within the Utsira Formation),
2) The Utsira Formation has not retained natural gas on a geological timescale,
3) There has been no recent natural gas migration from the petroleum systems underlying the Utsira Formation.

To further understand the significance of these lineations, chimneys, channels and tunnel valleys, we constructed a series of high-resolution 3D models of the storage site and overburden with MPath® software (*see underlying note), using the surfaces extracted from seismic (as described in Chapter 2, Section 2.5). These range in complexity from simple "layer cake" models, to heterogeneous lithological models populated with geological, stratigraphic and structural information derived from our seismic interpretations. The invasion percolation flow simulations (also performed in MPath®) were calibrated to match published data (Chadwick *et al.,* 2005, 2009b; Bickle *et al.,* 2007; Arts, 2008, 2009; Singh *et al.,* 2010) and history-matched to the present-day plume distribution. This provides a base case scenario for modelling the following:

1) The likely migration direction for a given column height of CO_2 as it accumulates beneath the caprock in structural highs and eventually spills laterally,
2) The effect of seismically-induced topographic uncertainty on CO_2 migration behaviour,
3) Capillary entry pressures (CO_2-brine equivalent) for each barrier,
4) Most likely temperature conditions prevailing at the Nordland Shale caprock depth,
5) The density of CO_2 contained in the Utsira Formation beneath each individual barrier,
6) Whether the CO_2 plume is likely to encounter the identified palaeo-gas migration pathways (described in Chapter 2) as it migrates beneath the caprock,
7) The effect on the CO_2 plume distribution and potential for flow along these palaeo-gas migration pathways as we vary some of the key modelling parameters within realistic bounds (e.g. geothermal gradient and capillary entry pressures), since there are still considerable uncertainties about such parameters (as discussed in Chapter 3),
8) The effect of increasing the geological complexity of the models on CO_2 migration and flow dynamics.

**Note:* for all the simulation work described in this chapter a series of nightly MPath® development builds from 2007-2011 were used in conjunction with a beta version of the Permedia CO_2 PVT package. Final simulations were all performed (or re-run) on version 4.19.20110824 of the software, downloaded on 24th. August 2011.*

4.2: Selection of Appropriate Modelling Methodology:

To ensure that the most appropriate flow modelling application was selected for this study, we appraised a range of techniques. A review presented by Welte *et al.* (2000), suggested that modelling should initially be considered on two levels:

- *Temporal:* This involves using either a static approach, where nothing changes over time (i.e. the model uses geometry, fluid properties, etc., from the present day), or a dynamic approach, where the model takes account of changes over time (i.e. back stripping to account for evolving geometries, subsidence, thermal history, PVT evolution, etc.),
- *Scale:* This relates to model resolution at the cell or grid level, up scaling processes and the ability of a particular numerical modelling method to provide the most accurate information within a reasonable timeframe. Scale is normally dealt with on two levels:
    - *Reservoir:* Small scale, cell sizes from 1-10 m upwards,
    - *Basin:* Large scale, cell sizes from 100 m upwards.

Welte *et al.,* (2000) also considered four different modelling methods:

- *Darcy Flow:* The classical method based on Darcy's Law for multi-phase flow through porous media. Used by most of the major basin modelling and reservoir engineering software companies (e.g. Eclipse® and Petromod®). Fluid flux is controlled primarily by permeability and viscosity. It satisfies the requirements of the dynamic approach and is very accurate at describing complex phase behaviour, dissolution and multi-phase flow processes. However, inter-cell calculations can incur extremely high computer processing overheads for large or high-resolution models; this may require a processing compromise between scaling and resolution, creating up scaling and numerical dispersion problems,

- *Ray-Tracing or Flow Path:* This is a high-resolution method that employs mapped grids populated with rock and fluid properties to model fluid migration using the buoyancy concepts described previously in Chapter 3, Section 3.5.1. Although relatively fast compared to Darcy-based simulators and better at honouring scaling, the dynamic and multi-phase capabilities are lacking. Several commercial applications are available (e.g. SEMI® and IES®),
- *Invasion Percolation (IP):* This high-resolution method considers fluid flux to be controlled by gravity and capillary forces during the secondary migration stage. This method is particularly useful for modelling flux through low permeability media (shales) and/or at low flow rates where viscous forces are minimal. This method is computationally faster for large models, since fluid migration can be explained by more simple mathematical assumptions. As with the previous method, it is not limited by scale issues, but still lacks the dynamics and mathematical rigour of Darcy Flow methods,
- *Hybrid:* These methods are designed to employ the best aspects of those previously described (i.e. mathematical rigour of Darcy Flow with the high-resolution and speed of IP or Ray-Tracing). Such a method is described by Carruthers & Van Wijngaarden (2000), where a modified IP method has been combined with an algorithm to account for flow regimes dominated by viscous forces; in essence, a more simple approximation of the Darcy Flow equations. One of these hybrid methods has subsequently been developed and commercialised as MPath®.

Statistical analysis is another important part of the modelling process, particularly when uncertainties exist in modelling parameters (e.g. reservoir pressure and temperature). Two statistical approaches are normally employed:

- **Stochastic:** Allows for random variation in a series of simulations using a probability distribution with a range of estimates for parameters (e.g. Monte Carlo method),
- **Deterministic:** Uses best estimates for parameters. No range is used and no probability is derived.

Based on this preliminary review, MPath® was short-listed as the most suitable flow modelling tool for the purposes of this study, since we needed to construct a reservoir scale model and this software offered the combined advantages of Darcy Flow and IP techniques; mathematical rigour with high resolution modelling. Stochastic modelling was also available within the software package, allowing us to perform risked evaluations for a wide range of operating parameters. However, to reaffirm that this software was appropriate for modelling the fluid properties and range of flow rates under consideration at Sleipner, a further review of capillary-dominated and viscous-dominated systems was also performed.

4.2.1 Capillary Entry Pressure Conversion Between Mercury-Air to CO_2-Brine

Capillary pressure measurements are usually performed as laboratory mercury-air displacement tests, then converted to hydrocarbon-water or CO_2-brine using an appropriate scaling factor (Schowalter, 1979):

$$P_{c(CO2-Brine)} = \frac{\sigma_{(CO2-brine)} \cos\theta_{(CO2-brine)}}{\sigma_{(mercury-air)} \cos\theta_{(mercury-air)}} \bullet P_{c(mercury-air)} \qquad \textit{- Equation 4.1}$$

Where: Pc = Capillary pressure for a given wetting and non-wetting fluid system (MPa),

σ = Interfacial tension (IFT) between wetting and non-wetting fluids (mN/m^{-1}) and

$cos\theta$ = Formation wettability represented by the contact angle between wetting and non-wetting fluids (degrees °)

Once the scaling factor has been calculated, it can be multiplied with an experimentally derived laboratory mercury-air value (or analogue data) to obtain the equivalent capillary entry pressure (P_c) for a CO_2-brine system at typical storage conditions. For example, if the values in Table 4.1 (derived from Daniel & Kaldi, 2008 and Chapter 3, Table 3.9) are used in Equation 4.1:

Fluid System	Interfacial Tension (mNm^{-1})	Contact Angle (degrees°)	Wettability (fraction)
Mercury-Air (Laboratory conditions, STP)	481	140	0.766
CO_2-Brine (Sleipner caprock, 8 MPa, 28-36ºC)	20 - 35	0 - 60	1 - 0.5

Table 4.1: Capillary pressure parameters for fluid systems under consideration.

Scaling factors for CO_2/brine systems may range from 0.027 (for IFT of 20 mNm^{-1} and wettability of 0.5), 0.058 (for IFT of 27 mNm^{-1} and wettability of 0.8) to 0.093 (for IFT of 35 mNm^{-1} and wettability of 1), thus if a caprock seal was laboratory tested with mercury-air and found to have a Pc = 30 MPa, the equivalent P_c for CO_2-brine at storage conditions, would range from 0.027 x 30 = 810 kPa (worst-case) to 0.058 x 30 = 1.74 MPa (intermediate case) to 0.093 x 30 = 2.79 MPa (best-case).

Alternatively, the capillary entry pressure (P_c) for a CO_2-brine system can also be measured directly on core samples under simulated reservoir pressure and temperature conditions (Springer & Lindgren, 2006; Harrington *et al.,* 2009).

Equation 4.1 can also be modified to compare equivalent capillary pressures for different gas-water systems. Hildenbrand *et al.,* (2004) describe the drainage process of a non-wetting gas phase entering water-wet mudrocks in terms of the capillary pressure relationship (Figure 4.4):

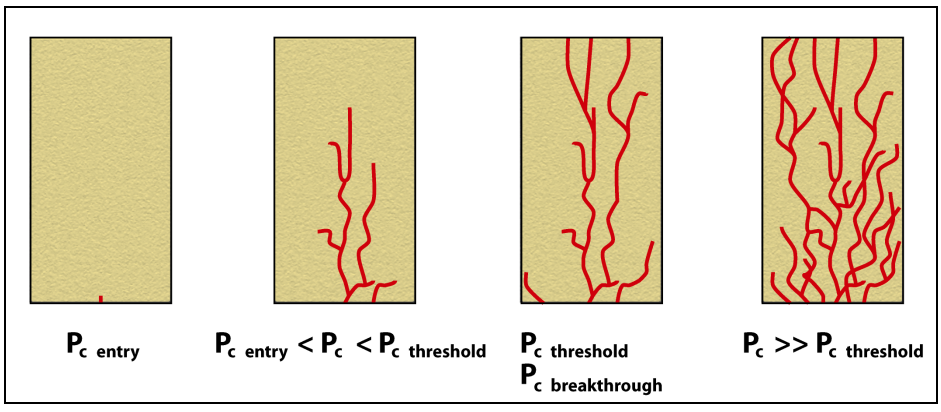

Figure 4.4: Stages of (red) non-wetting fluid breakthrough across porous media during a capillary drainage process (modified from Hildenbrand et al., 2004)

Once ganglia of non-wetting fluid have spanned across the sealing formation, the capillary threshold has been reached and fluid breakthrough is established. Subsequently, viscous forces dominate the system rather than capillary forces (refer to Figure 4.5). This situation will persist and the non-wetting phase saturation will increase up to a maximum value as constrained by the irreducible wetting phase saturation (S_{wirr}), provided the pressure differential is maintained. If the pressure differential falls (e.g. due to cessation of non-wetting phase injection), the original wetting phase will re-imbibe into the pores, unless pore dry-out (Hurter *et al.,* 2007b) has occurred, in which case there may be insufficient wetting phase available to refill the pores by imbibition (Hildenbrand *et al.,* 2004).

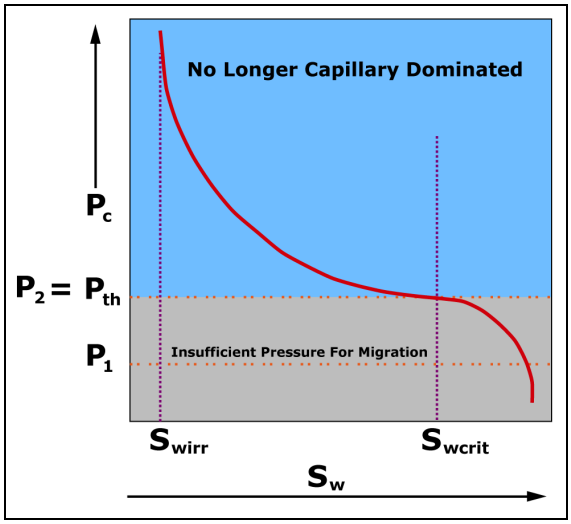

Figure 4.5: Relationship between capillary pressure and wetting phase saturation (modified from Permedia Presentation, 2006)

Tsimpanogiannis & Yortsos (2004) and Or (2008), describe how the dimensionless Capillary Number *(Ca)* can be used to determine the significance of viscous/capillary forces:

$$Ca = \frac{q\mu}{\sigma}$$ - *Equation 4.2*

Where: q = Flowing liquid velocity (ms^{-1}), μ = Viscosity of wetting phase (mPas) and σ = Interfacial tension (IFT) between wetting and non-wetting fluids (mN/m^{-1}).

Capillary forces will dominate the system for critical Capillary Numbers that represent a low flow rate/viscosity regime; Hilfer & Øren (1996) suggest this equates to values less than 10^{-4} for unconsolidated sands (also refer to Figure 4.6).

In this regime, the flow path is determined by pore/fracture throat size variations, with larger pores entered first. Fluid migration can then be described by a few controlling variables, without resorting to more complex solutions based on Darcy's Law.

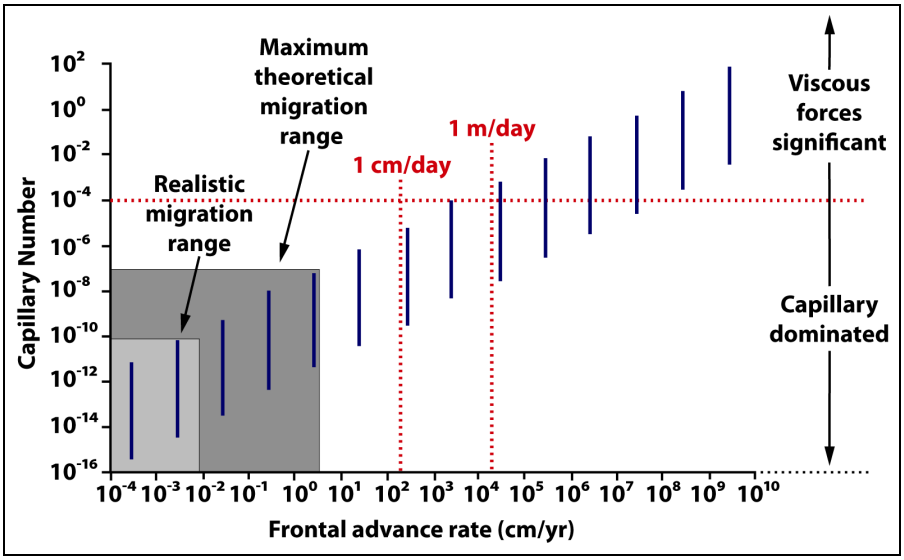

Figure 4.6: Capillary Dominated Regime Governed by Capillary Number (modified from Permedia Presentation, 2006)

Once breakthrough has been established, Darcy flow becomes the controlling influence on leakage. Rates of leakage for CO_2-brine systems have been considered by a number of authors. Zweigel *et al.,* (2004b) presented the following formula for estimating leakage rate from a storage reservoir under multi-phase flow conditions:

$$Q_{leak} = \frac{k_{seal} \cdot k_{rCO_2} \cdot A \cdot \Delta p}{\mu_{CO_2} \cdot \Delta z_{seal}} = \frac{k_{seal} \cdot k_{rCO_2} \cdot A \cdot \Delta \rho \cdot g \cdot h_{CO_2}}{\mu_{CO_2} \cdot \Delta z_{seal}} \qquad \text{- Equation 4.3}$$

Where: Q_{leak} = Leakage rate (m^{-3}/sec), k_{seal} = Seal permeability (single phase - ms^{-1}), k_{rCO2} = CO_2 relative permeability in CO_2-brine system (ms^{-1}), A = Area containing fluid flow (m^{-2}), Δp = Pressure differential across the sealing formation (Pa), $\Delta \rho$ = CO_2-brine density difference (kg/m^{-3}), Δz_{seal} = Seal thickness (m), g = Gravitational constant (ms^{-2}), h_{CO2} = CO_2 column height (m), μ_{CO2} = CO_2 viscosity (Pa.s).

The authors noted that integral reformulation would be necessary to account for vertical and spatial variability in the equation parameters (e.g. permeability variations due to lithological heterogeneities and depth of burial, CO_2 phase changes and viscosity/saturation gradients).

Saripalli & McGrail (2002) also considered the situation of CO_2 leaking through vertically fractured porous media with an aperture of *2d* (where presumably, *d* = radius?) and developed the following formula:

$$q_f = \frac{\Delta\rho g w d^3}{12\mu}\left(\frac{dH_c}{dz}\right) \qquad \text{- Equation 4.4}$$

Where: q_f = CO_2 (single-phase) flow rate through fracture (m^3/sec), $\Delta\rho$ = CO_2-brine density difference (kg/m^{-3}), w = Fracture width (m), d = Fracture radius? (µm), μ = Viscosity (Pa.s), H_c = Head or column of CO_2 driving vertical flow in z-direction (m) - if the fracture is continuous to surface, then the gradient term = $h_c/(h_c + l_f)$ and l_f = Fracture length (m)

As noted by Zweigel *et al.,* (2004b) any formulation designed to quantify CO_2 migration and leakage processes needs to accurately account for the effects of pressure, volume and temperature (PVT) thermodynamics on a temporal basis. In a CO_2 storage situation, vertical and lateral gradients will be present for pressure, volume and temperature, which in turn affect pH, IFT, viscosity, density, salinity, solubility (of the CO_2-brine-rock system), relative permeability to the different phases, phase saturations and the number of phases present (Pruess, 2008). From a numerical modelling perspective, these dynamic changes require CO_2–brine properties to be calculated at reservoir conditions over a wide range of storage conditions using PVT correlations and/or equations of state (e.g. Huang *et al.,* 1985; Span & Wagner, 1996; Duan & Sun, 2003). Many of the critical in-situ geological and thermodynamic properties required to model migration and leakage will also be unknown if there is no representative pressure/temperature data or core material available (e.g. fracture width, fracture length, pore radii and therefore the area or volume containing fluid flow), thus requiring the application of deterministic or stochastic modelling techniques.

4.3 Review of Previous Modelling Work Performed on Sleipner:

A substantial number of analytical and numerical modelling studies have already been performed for the Sleipner CO_2 injection site, both as an integral part of the ongoing monitoring programme (i.e. 4D seismic, gravity, electromagnetic and seabed bathymetry), and as analogues for future CO_2 storage sites, situated in a similar type of saline aquifer. Previous Sleipner modelling studies have concentrated on the following areas:

- Predicting the likely migration direction and lateral extent for the upper layers of the CO_2 plume over time; essentially a fill-spill type of analysis (Zweigel *et al.,* 2000; Zweigel & Hamborg, 2002; Hamborg *et al.,* 2003),
- Predicting individual CO_2 layer thicknesses and growth rates over time using analytical methods (Bickle *et al*., 2007),
- History matching injected CO_2 volumes with resident volumes by attempting to accurately model in-situ CO_2 saturation and density using a combination of seismic and gravity data processing techniques (Arts *et al*. 2004, 2008; Chadwick *et al*., 2004, 2005, 2008, 2009a, 2009b, 2010; Chadwick & Noy, 2010; Nooner *et al*., 2007; Alnes *et al.* 2008, 2011; Zumberge *et al.*, 2008; Dubos-Sallée & Rasolofosaon, 2010; Rubino *et al,* 2011; Rabben & Ursin, 2011),
- History matching the CO_2 plume distribution using reservoir models calibrated against well and seismic data, then forward modelling (with and without coupled reactive transport) over decadal to millennial timescales to investigate long term CO_2 plume migration and (where applicable) dissolution behaviour (Lindeberg & Bergmo, 2002; Johnson & Nitao, 2003; Arts *et al*., 2004; Khattri *et al.,* 2006),
- Modelling potential leakage scenarios, indicators and rates (Lindeberg, 1997; Zweigel & Heill, 2003; Grimstad *et al.,* 2009; Neufeld *et al.,* 2009; Teige *et al.,* 2011),
- Comparison of different fluid flow modelling techniques and their ability to accurately model CO_2 migration beneath the caprock (e.g. Darcy flow versus invasion percolation (IP) simulation), when calibrated against time-lapse monitoring data (Singh *et al.,* 2010).

Early Sleipner reservoir models (pre-CO_2 injection) were based on a homogeneous aquifer with no internal barriers and given the high porosity and permeability characteristics of the Utsira Formation, simulations indicated that injected CO_2 would reach the top of the aquifer within a few months (Zweigel *et al*., 2004a). Subsequent models were revised to account for the presence of thin, laterally impersistent shale barriers identified on wireline logs from the Sleipner area (refer to Figure 4.3). These barriers served to delay buoyant CO_2 migration and distribute the plume into a series of discrete, thin layers, which it was believed might enhance the CO_2 dispersion and dissolution process (Lothe & Zweigel, 1999; Lindeberg, 2001, Zweigel *et al.*, 2004a). Revised reservoir models initially used five vertically equidistant barriers within the storage aquifer, broken by apertures set at 500 m intervals to account for lack of shale continuity (Lindeberg, 2001). After the first post-injection 3D seismic survey was performed in 1999 and analysed, it became apparent that injected CO_2 had already migrated to the shallowest layer of the Utsira Formation, either bypassing or penetrating the internal shale barriers via holes, fractures or zones of higher permeability as predicted. Plume and layer morphologies were also deemed to be consistent with the revised model predictions (Zweigel *et al.*, 2004a).

These conclusions were presumably based on the assumption that CO_2 had only just reached the top of the Utsira Formation during 1999 (i.e. confirmed by the first post-injection survey). Thus, if we assume that the distance between the injection point (~1012 m) and the caprock (~800 m) was travelled in exactly three years, this is equivalent to an average CO_2 migration rate of ~71 m/yr (2.25×10^{-6} m/s). Since no monitoring surveys were performed during 1996-99, there is a distinct possibility that CO_2 may have reached the caprock much earlier. Chadwick *et al*., (2004) suggested that CO_2 may have breached the thick shale layer overlying the main Utsira Formation reservoir and entered the overlying Sand Wedge by 1999. Recent modelling work by Singh *et al.* (2010) suggests a slightly faster CO_2 migration rate of ~90 m/yr (2.85×10^{-6} m/s). In either case, if Equation 4.2 is applied to these rates to calculate the Capillary Number (*Ca*) using an IFT range of 20 to 35 mNm^{-1} (Table 4.1) and wetting-phase viscosity of 0.6 to 0.8 mPas (Singh *et al.,* 2010), a range of 6.5 to 8.6 $^{e-8}$ is obtained for *Ca*. This is significantly lower than the critical threshold of $Ca = 10^{-4}$ (Figure 4.6), suggesting that capillary forces should dominate the CO_2 fluid migration processes being observed at Sleipner.

Post-injection 3D seismic surveys from 1999, 2001 and 2002 provide a much better visualisation of the CO_2 plume within the Utsira Formation and most current simulation models now use nine shale barrier layers (Figure 4.7) as described by Arts *et al*., (2004, 2008); Bickle *et al*., (2007); Chadwick *et al*., (2005, 2008, 2009a, 2009b, 2010) and Nooner *et al*., (2007).

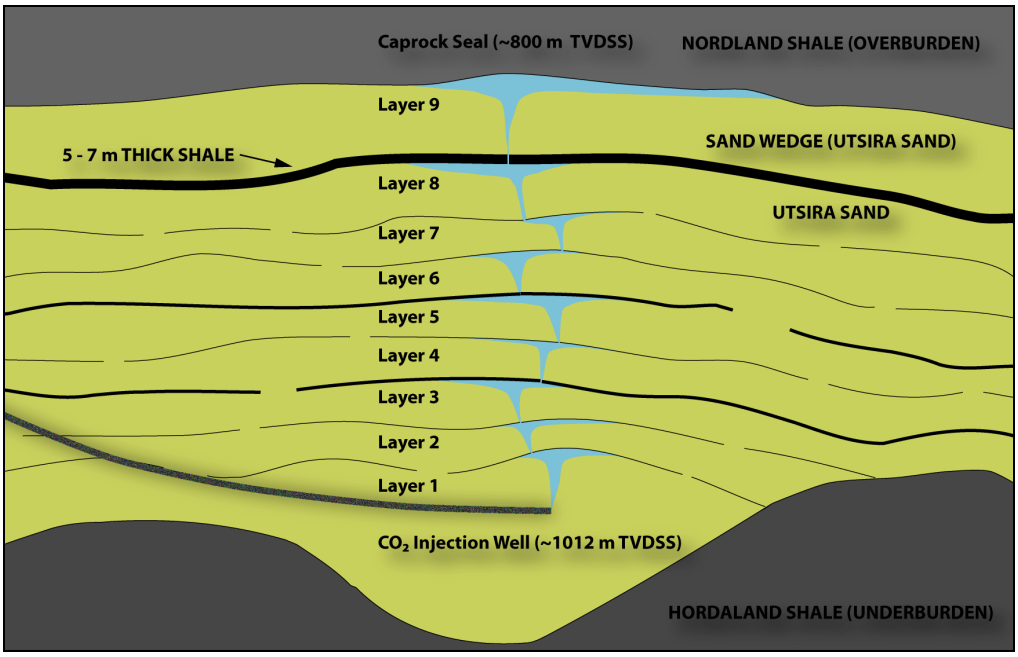

Figure 4.7: Cross-sectional cartoon (not to scale) of the Sleipner storage site depicting nine layers of CO_2 and eight semi-permeable barriers, including the Thick Shale (modified after Bickle et al., 2007).

In the baseline seismic data, only the upper two barriers can be accurately resolved on seismic (i.e. barriers 8 and 9), since the presence of strong seabed and inter-bed multiples, combined with the thin, intermittent nature of barriers 1-7 preclude a reliable interpretation being performed. However, in the seismic datasets collected after CO_2 injection, the remaining barriers currently trapping CO_2 can be resolved with greater confidence due to reflection amplitude enhancement created by thin-bed tuning effects (Chadwick *et al.,* 2005; Andreassen *et al.,* 2007). Although this means that individual CO_2 layers can be monitored more easily in terms of migration direction and layer spreading rates, the seismic reflection surfaces are more distorted due to velocity push-down effects resulting from the presence of lower density CO_2 (this effect is visible on the cross-sections illustrated in Figure 4.2).

Aside from the formation brine/CO_2 buoyancy contrast and presence of discontinuous barriers, a number of proposals have been advanced to explain other control mechanisms that may influence CO_2 migration within the storage reservoir. The inter-layer topography within the Utsira Formation is very flat with less than 1° of dip to the S (Bickle *et al.,* 2007). Thus, to investigate the presence of any hydrodynamic drive, Kristensen & Bidstrup (2001) considered the influence of an active aquifer in the Utsira Formation. Four scenarios were modelled in Petromod®, simulating flow velocities adjacent to the injection well in the range 2 to 4 m/yr, increasing up dip to 10 m/yr at the structurally higher NNW end of the model, where permeability is higher and structural pinch-out affects the fluid hydraulics and flow velocities. In a similar exercise, Lindeberg (2001) required an up dip (N) aquifer flow of 3 m/yr to shift and match simulated CO_2 accumulation positions with actual seismic observations.

Other research suggests the presence of flow barriers is a significant factor, with compartmentalisation either created by a series of pervasive fault networks (Borgos *et al.,* 2002) or a combination of structural and stratigraphic flow barriers (Chadwick *et al.,* 2004, 2009a). To test this hypothesis, we compared our seismic interpretation work from Chapter 2 with the work of Borgos *et al.* (2002) and Chadwick et al. (2004), and then overlaid a sample of our mapped lineations onto the published maps of Chadwick *et al.* (2008) to determine whether the faults/flow barriers may be pervasive through all nine layers (Figure 4.8). From a visual perspective, some form of vertical fault compartmentalisation does appear to be present and merits further investigation, particularly if these features also extend upwards into the overburden.

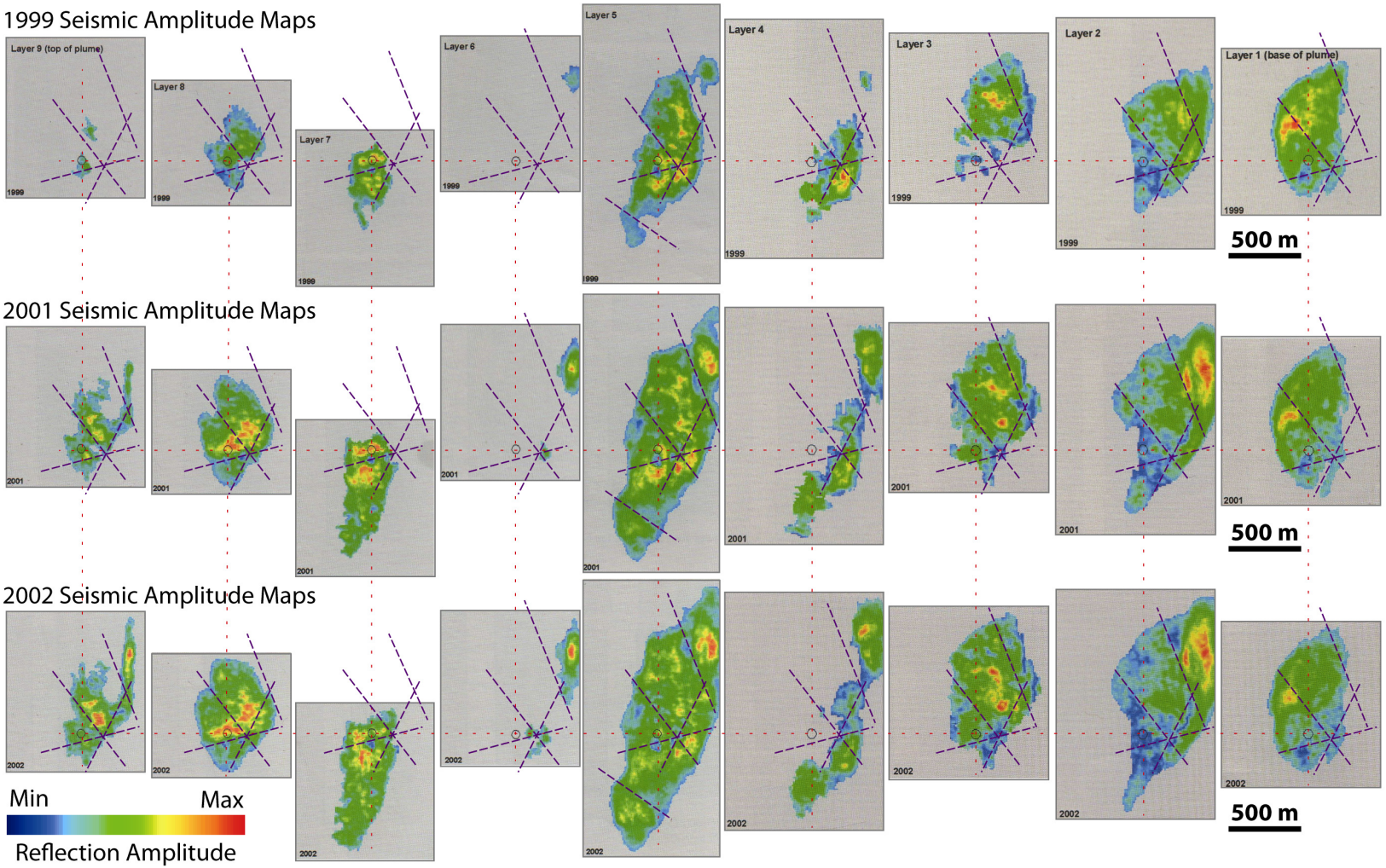

Figure 4.8: Aligned reflection amplitude maps of CO_2 Layers 9 (shallowest on extreme left) to Layer 1 (deepest on extreme right) from 1999 (top) to 2002 (bottom), showing how plume development both within and between layers appears to be controlled by a series of pervasive linear flow barriers (purple dashed lines). The injection point position is shown as a black circle intersected by the horizontal and vertical dashed red lines (maps modified after Chadwick et al., 2008; flow barriers modified after Burgos et al., 2002).

With increasing volumes of CO_2 presently migrating to the top of the Utsira Formation (Chadwick *et al.,* 2009b), it would seem prudent to assess the most likely migration pathways for CO_2 filling and laterally spilling from trapping structures disposed beneath the upper barriers (i.e. Thick Shale/barrier 8 and caprock/barrier 9), to eliminate migration uncertainties and ensure that CO_2 will not encounter any potential leakage paths. Similar work was performed 3 to 4 years after CO_2 injection operations commenced (Zweigel *et al.,* 2000). Two potential migration scenarios were investigated and modelled using the SINTEF in-house simulator SEMI® (secondary hydrocarbon migration tool):

1. The Thick Shale (barrier 8) acts as main seal and CO_2 migrates predominantly to the NW, up to 12 km from the injection location, assuming a net-gross ratio of 0.85 (Zweigel *et al*., 2000, 2004a),
2. The Thick Shale leaks or is bypassed, in which case CO_2 enters the Sand Wedge underlying the caprock/barrier 9 and CO_2 migrates predominantly to the N and NE. This scenario was deemed undesirable, since CO_2 could eventually migrate out of the area of existing 3D seismic coverage available at that time ~7 to 10 km NNE of the injection location, making further migration predictions impossible unless additional seismic coverage was obtained (Hamborg *et al*., 2003).

Considering that CO_2 breached the Thick Shale and entered the Sand Wedge within a few years after starting injection, some migration elements of both scenarios appear likely, although quantifying the degree of partitioning is a difficult task. In either case, there is a significant probability of encountering existing development and appraisal wellbores in the Sleipner area (for Scenario 2, Hamborg *et al*. (2003), suggested that well 16/7-2 to the NE (refer to Chapter 3, Figure 3.6 for the well location) should be risk assessed for leakage potential).

In a subsequent approach using different seismic cubes and time to depth conversion methodologies it was also noted that even minute regional dip differences of ~0.3° (introduced by the method of seismic time to depth conversion used) could result in markedly different migration behaviour (Zweigel & Hamborg, 2002). A series of simulations for migration beneath the caprock/barrier 9 using two different seismic surveys are illustrated in Figure 4.9.

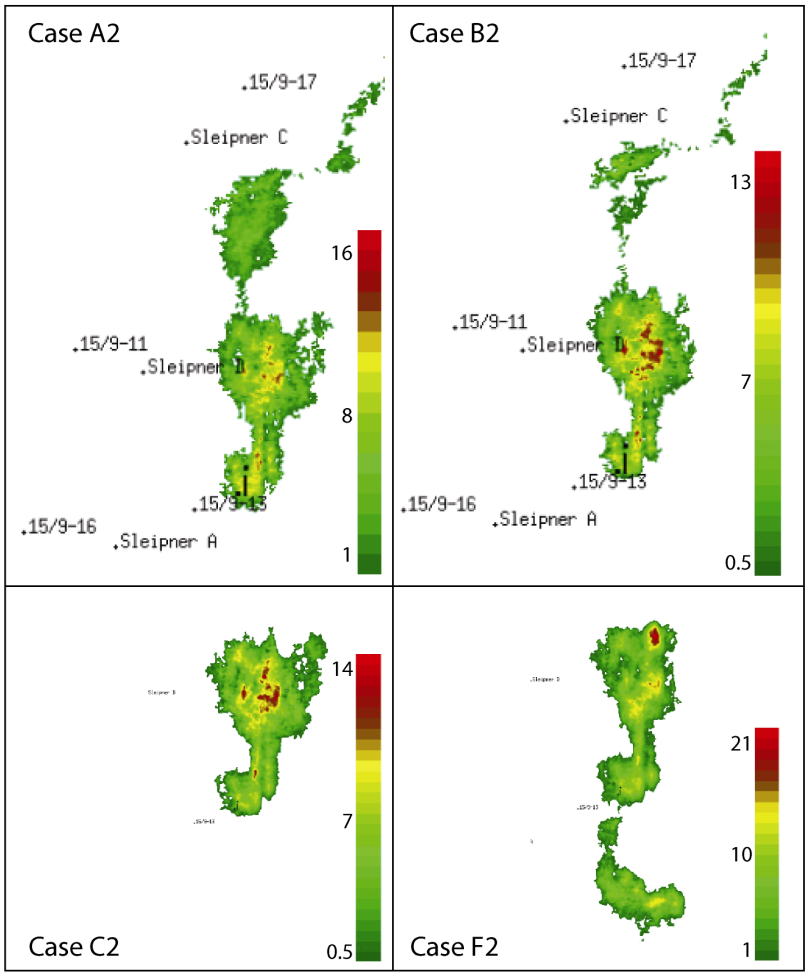

Figure 4.9: CO_2 migration maps for caprock/barrier 9 (not to scale), illustrating three different fill and spill scenarios using the SEMI® simulator. Cases A2 and B2 (both using 1998 survey data) spill to the N and NE, Case C2 (using 1999 survey data) spills to the E and Case F2 (also using 1999 survey data) spills to the S. Graduated colour bars to the right-hand edge of each panel represent column height in metres using 1 metre or 0.5 metre increments (modified from Zweigel & Hamborg, 2002).

Seismic monitoring data from 2008 suggests that the layer of CO_2 underlying the caprock/barrier 9 has developed in line with the migration pattern shown in cases A2-C2 (Figure 4.9), although there is also some development of the S extension visible on case F2 (Arts, 2009). This may indicate that many of the subtle topographic features controlling spillage are still not being adequately resolved by seismic monitoring surveys, due to low topographic relief and the influence of high-amplitude anomalies and lithological heterogeneities within the overburden on seismic velocities (Figure 4.10). Chadwick & Noy (2010) propose that this may also indicate the presence of a complex CO_2 migration network with multiple supply points.

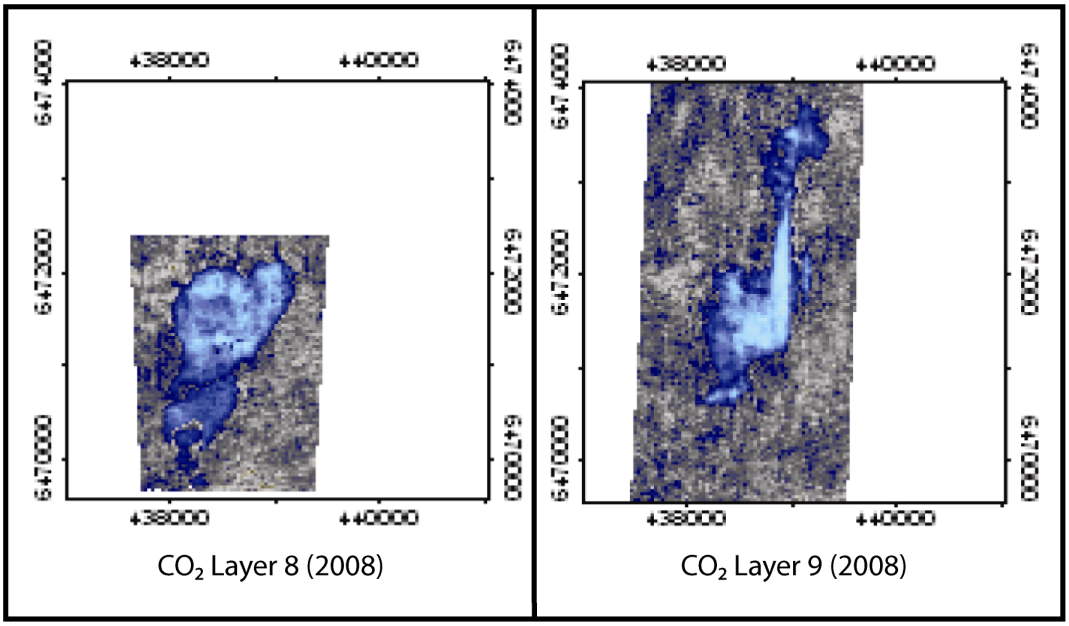

Figure 4.10: CO_2 plume morphology for 2008 visualised below the Thick Shale/barrier 8 (left) and the Top Sand Wedge/barrier 9 (right), illustrating the subtle extension to the S for both surfaces (modified from Arts, 2009).

Simulation work has also been performed to try and resolve the strong N and weaker S migration components of the uppermost CO_2 layer (Singh *et al.,* 2010; Chadwick & Noy, 2010), using different modelling methodologies (i.e. Darcy flow versus invasion percolation). Both studies assigned a high permeability anisotropy to the Top Sand Wedge (i.e. kx/ky = 0.1). Chadwick & Noy (2010) also tried varying the caprock temperature between the expected value of 29ºC up to 36ºC (the higher of which actually provides a better match to the observed seismic data). Although none of these models managed to exactly history match against the seismic data, it was argued by Chadwick & Noy (2010) that the use of higher than expected caprock temperatures is an acceptable technique for modelling purposes since it simulates the presence of 2% CH_4 (i.e. density of pure CO_2 at 31.5ºC being equivalent to the density of a CO_2 (98%) and CH_4 (2%) mixture at 29ºC).

Ongoing monitoring activities at Sleipner are still centred on 4D seismic and gravity surveying (Nooner *et al*, 2007; Arts *et al*, 2008; Arts, 2009; Alnes *et al.,* 2011) to observe differences and quantify CO_2 plume migration, particularly for the uppermost layer 9 disposed beneath the caprock. Future research is also focussed on improving the history matching process through the application of advanced seismic processing and inversion techniques (Chadwick *et al.* 2010; Vanorio *et al.,* 2010).

Future geophysical monitoring programmes and associated modelling studies will also be looking for any evidence of leakage, such as:

- Failure of the uppermost layers of the plume to spread laterally as predicted since the previous geophysical surveys or to reduce in size,

- The presence of any gravity anomalies that suggest localised gravity reductions outside predicted values,

- High amplitude seismic anomalies and/or gas chimneys appearing in the Nordland Group overburden caused by any CO_2 breaching the caprock/barrier 9 and migrating laterally and/or upwards.

Monitoring survey operations still continue every 2 years, but there are as yet no published results from the 2010 survey and the 2012 survey is due to be performed next year, thus there is a lack of more recent public domain data to inform our modelling and history matching.

4.4 Single Map Migration Sensitivity Analysis for the Caprock (Barrier 9):

To compare a simple fill-spill analysis of our barrier 9 surface against previous work (e.g. Zweigel & Hamborg, 2002; Singh *et al.* 2010) and assess the impact of time-depth conversion processes (previously described in Chapter 2 and Section 4.2.) on structural distortion and fluid migration direction beneath the caprock, we performed sensitivity analyses on two versions of the barrier 9 surface map from the local survey area (described in Chapter 2) using the Single Map Migration facility in MPath® and a series of CO_2 column heights up to the maximum 18 m structural height believed to be present in the Sleipner storage site vicinity (Zweigel et al., 2000; Zweigel & Hamborg, 2002). Structural dip of this surface is less than 1° (Bickle *et al.* 2007), thus it is expected to be extremely sensitive to any artificial surface distortions imposed by an erroneous time-depth conversion, poor well calibration or any other travel-time distorting influence present in the overburden (e.g. velocity push-down / pull-up effects caused by gas anomalies and carbonate horizons respectively).

A series of fill-spill analyses were run using a single injection point with CO_2 column height varied in 1 m increments from 3 to 18 m (+/- 2 m uncertainty), using 100 stochastic simulation runs to generate each map (Figures 4.11 and 4.12). Case 1 simulations (Figure 4.11) use a time-depth converted horizon extracted from the seismic cube as supplied by the BGS (described in Chapter 2, Section 2.3). Case 2 simulations (Figure 4.12) use a horizon extracted from the same cube after it has undergone a further two-stage depth-depth correction process to match the horizon to well log depths within the local survey area (also described in Chapter 2, Section 2.3). After a similar migration pattern up to 10-11 m column heights, both sets of simulations diverge and terminate with completely different migration patterns:

- For Case 1 (Figure 4.11), a narrow finger gradually backfills a dome structure to the N, then spills through a narrow saddle to the N with a CO_2 column height between 15 to 16 m. As the column height increases from 16 to 18 m, CO_2 eventually backfills a patchy structure to the W, before finally exiting from the survey area and model bounds to the SW and W
- For Case 2 (Figure 4.12), backfilling initially follows a similar pattern to the N, but as the column height increases from 10 to 11 m, CO_2 begins to spill to the E and completely exits from the survey area and model bounds.

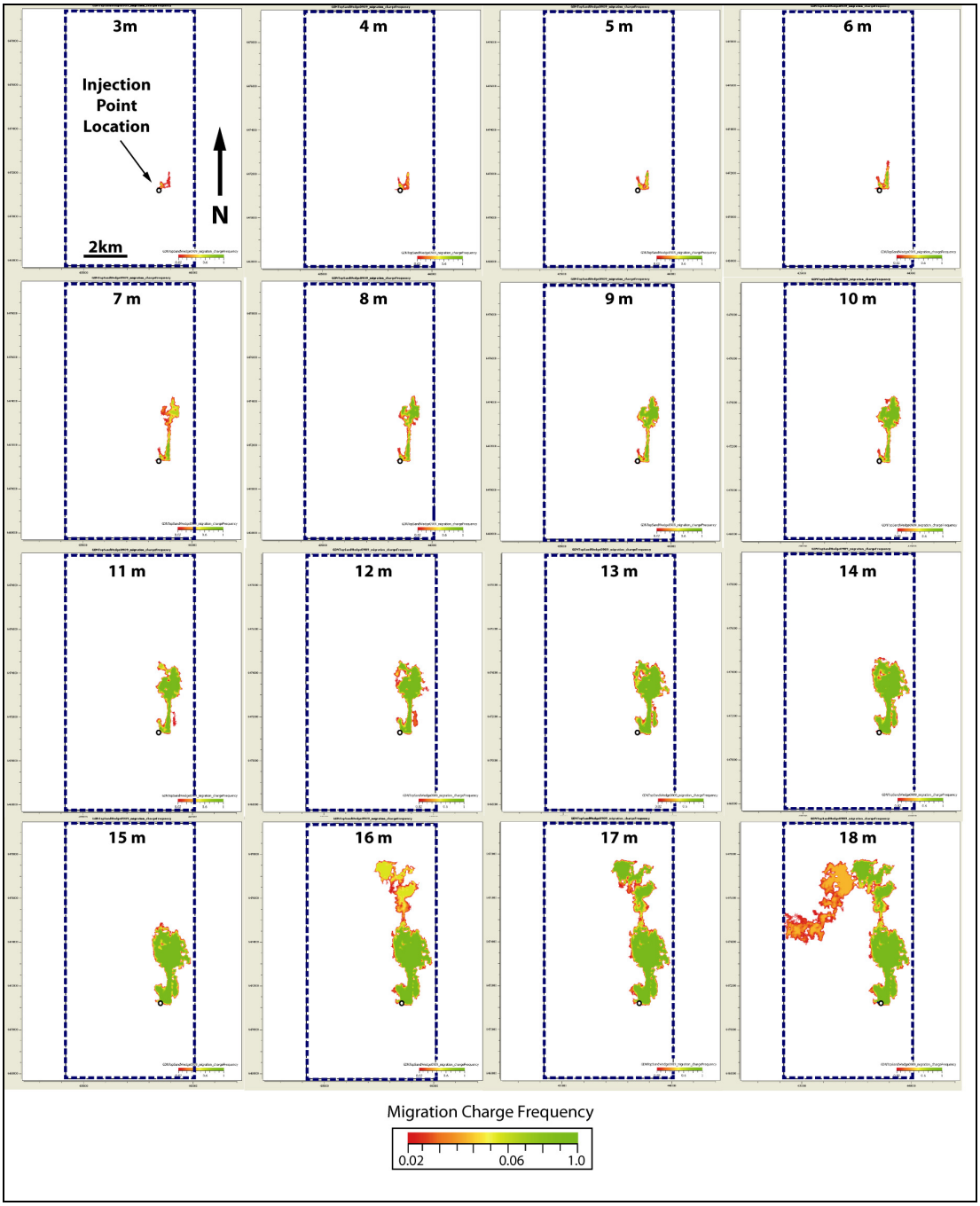

Figure 4.11: Series of single map migration (fill-spill) analyses for a simple depth converted barrier 9 surface (caprock) at Sleipner (i.e. uncalibrated to well log data). Each map was stochastically generated from 100 simulations using the CO_2 column height specified at the top of each image +/- 2 m. The dashed blue box is the local (11.5 km x 5.6 km) survey area previously described in Chapter 2. In this case, the CO_2 plume initially migrates to the N, but once a column height of 15 to 16 m is attained, the CO_2 spills through a narrow saddle to fill a series of separate structures further to the N, before migrating to the SW then spilling out from the model bounds to the W once a column height in excess of 18 m has been attained.

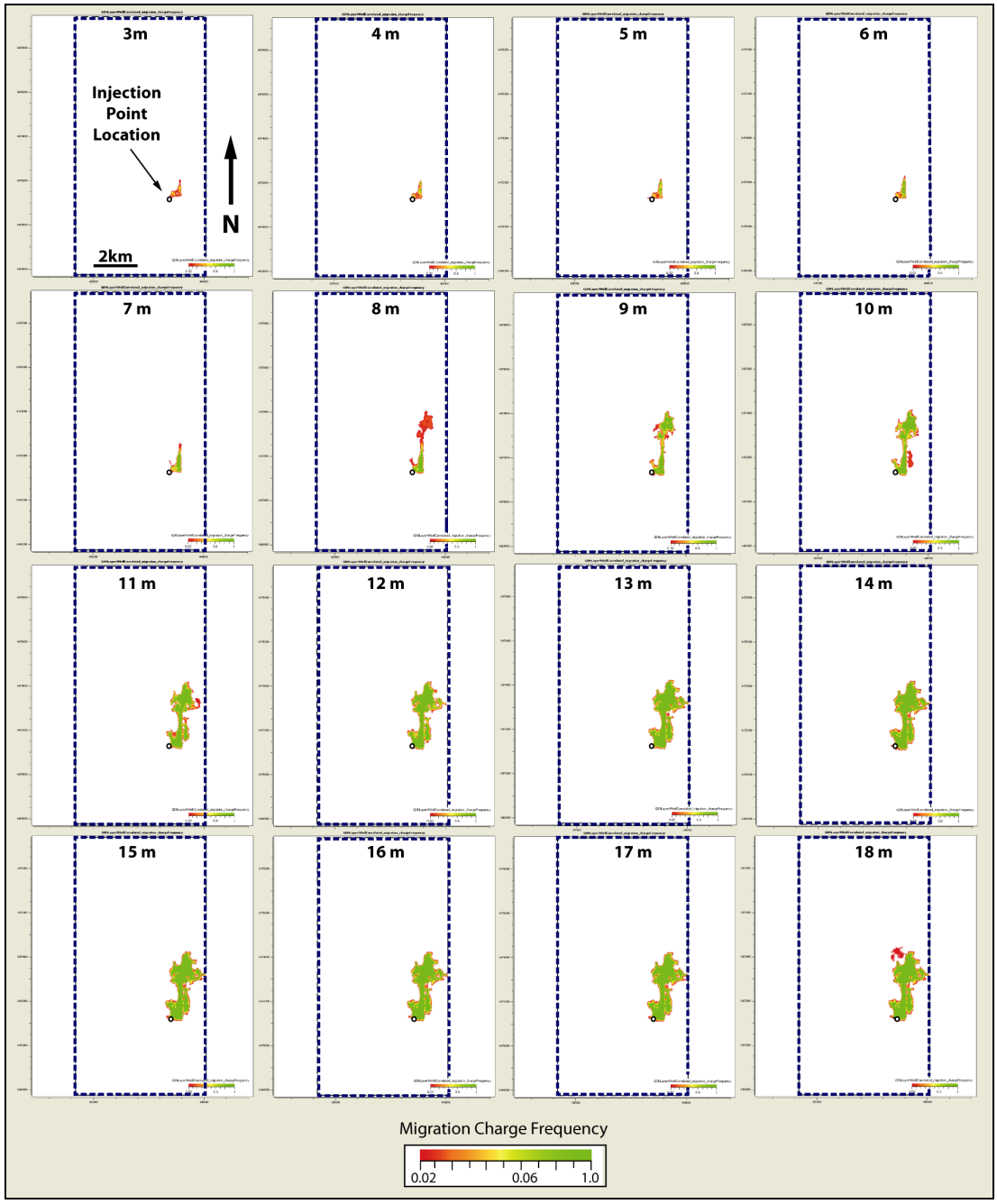

Figure 4.12: Series of single map migration (fill-spill) analyses for a depth converted and multi-well calibrated barrier 9 surface (caprock) at Sleipner. Each map was stochastically generated from 100 simulations using the CO_2 column height specified at the top of each image +/- 2 m. The dashed blue box is the local (11.5 km x 5.6 km) survey area previously described in Chapter 2. In this case, the CO_2 also migrates to the N, but once a column height in excess of 10 to 11 m is attained, the CO_2 spills out of the model bounds to the E.

In comparison with previous work, the migration for the uncorrected barrier surface (Figure 4.11) appears to follow a similar pattern to the Cases A2 and B2 (Zweigel & Hamborg, 2002), as depicted in Figure 4.9, whereas the migration for our corrected surface (Figure 4.12) appears to be a better match to Case C2 (Zweigel & Hamborg, 2002), as also shown in Figure 4.9. On closer inspection it is worth noting the following:

- The reduction in trap capacity for the corrected surface, where the process of correlating the surface to well ties, has not only tilted the surface to the ESE, changing the migration direction, but has also "lost" between 5 m +/- 2 m of structural closure. Naturally, the loss from this trap is presumably a gain for another trap lying to the E, but without the data coverage for this area there is no way of determining this from the current dataset or assessing any loss in storage efficiency,

- The number of wells involved and their disposition in relation to the surface. In this case, the majority are in the central portion and western margins of the local survey area (refer to Chapter 3, Figure 3.6), so even though there are sufficient data available for well triangulation there may still be a slight bias imposed overall by the Petrel® depth to depth conversion algorithms, since the wells are not evenly distributed,

- Several different methods were used to process the data used in Zweigel & Hamborg (2002), including layer cake for case A2, uniform overburden velocity correlated to a range of wells for case B2, uniform overburden velocity correlated to well 15/9-13 only (closest well to the CO_2 injection point location) for C2 and stacking velocity correlated to well 15/9-13 for F2. The data in this case was interpreted every 100^{th} line, refined to every 10^{th} line then auto-tracked with manual quality control applied,

- The surfaces used for our model were picked with the minimum of auto-tracking and any spurious depressions or bumps that were obviously being created by an overlying anomaly were manually edited out, by picking across the artefact zone.

Visual assessment and manual interpretation helps to eliminate errors by avoiding artefacts as illustrated in Figure 4.13 for the upper (orange) horizon.
When auto-tracking of horizons is used indiscriminately, errors may be introduced into a horizon underlying pull-down and pull-up features (as shown for the lower (red) horizon in Figure 4.13). This will result in an incorrect (bumpy) surface topography being generated for modelling purposes. This is particularly relevant for areas with shallow gas, sand channels or localised hard cemented features in the overburden, where depth conversion errors introduced by these features may produce entirely different migration simulations, particularly for low relief structures and/or surfaces with a very low structural dip. A complex velocity analysis in XYZ space will be required to eliminate such errors.

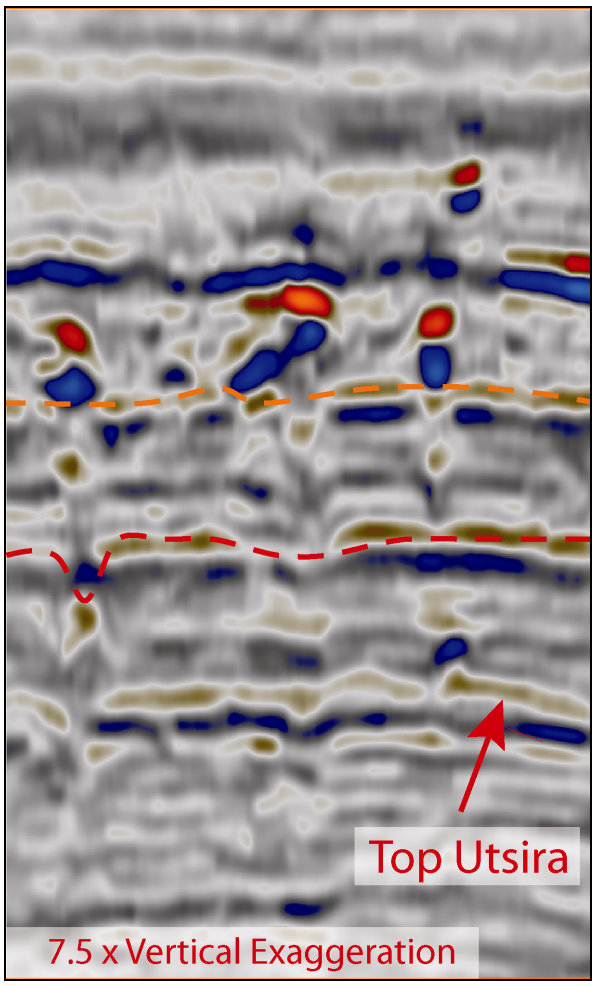

Figure 4.13: Seismic crossline 1187 from an area N of the CO_2 injection point location, illustrating the problems associated with auto-tracking reflections in an area with overlying high amplitude anomalies and vertical perturbations in the data (refer to Chapter 2, Figure 2.31 for map location).

4.5 Geocellular 3D Model Construction Methodology:

After performing the fill-spill analyses on the caprock/barrier 9 map to gain an understanding of migration behaviour below the caprock, the next stage was to combine all the surface maps extracted from our Petrel® interpretation into a 3D model and calibrate CO_2 flow within the model. This process involved the following three main stages:

- Pre-processing missing surface maps for barriers 1 to 7 using proxy surfaces,
- Creating an Earth Model containing all the surface maps tied to an appropriate lithological description (i.e. porosity-depth and porosity-capillary threshold pressure curves describing each lithology in the model),
- Creating the final 3D Mesh geo-cellular model for use in simulations.

4.5.1: Creating Missing Barrier Maps:

The surfaces used to build the MPath® geo-cellular mesh model were derived from our Petrel® seismic interpretation work previously described in Section 2.5 and Table 2.3. The baseline seismic data from 1994 used to extract these surfaces was targeted at a deeper hydrocarbon-bearing zone several thousand metres deeper than the CO_2 storage aquifer, thus the noise present in the shallow section, lack of continuity for intra-formational barriers, presence of strong seabed and inter-bed multiples resulting from the thin shale layers within the Utsira Formation, precluded us performing a seismic interpretation of individual barriers 1-7. Only the top two barriers (i.e. barriers 8 and 9) can be adequately constrained by nature of their strong seismic amplitude response and reliable correlation with well logs (Lothe & Zweigel, 1999). The lowest shale, barrier 1 is described as being 50 m above the injection point (Chadwick *et al.,* 2005), thus given the two end points, the following procedure was then adopted to create the remaining barriers as proxies for modelling purposes:

1. Wireline logs were used (particularly the log for well 15/9-13, nearest the injection point location), to constrain approximate shale barrier depths and a relative thickness for each barrier (refer to Appendix 2.3),

2. The nine barrier tops were constructed starting with the seismic interpretation maps for barrier 9 and barrier 8 (refer to Chapter 2, Table 2.3) loaded into the MPath® Map Viewer. The map for barrier 8 was then cloned to create the underlying barriers 1-7 using the Create/Intermaps (Split) facility from the Tools menu (Figure 4.14), which allows barriers to be spaced out at regular or user-specified intervals from barrier 8 down to the Top Hordaland Formation. Further adjustment was then be applied to readjust and space-out the map stack to a point 50 m above the injection point location for barrier 1 (Chadwick *et al.,* 2005),

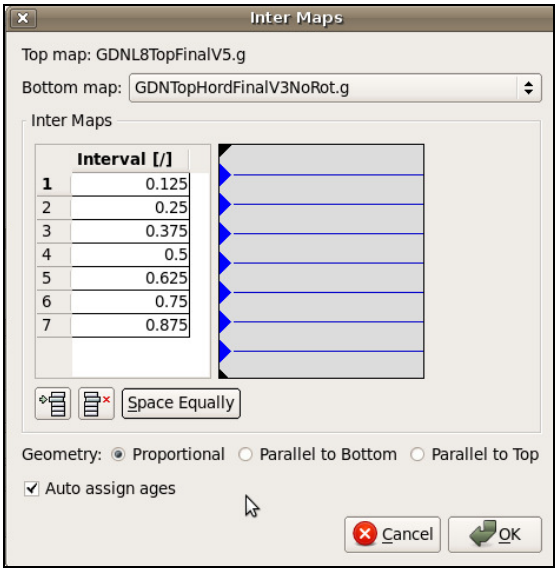

Figure 4.14: Screenshot of the Inter Maps facility in MPath® used to create proxy maps for barriers 1-7.

3. Layer overlay maps for each of the nine CO_2-filled structures were then created from high-resolution copies of seismic amplitude colour maps (Figure 4.15) derived from technical papers and presentations in the public domain (Chadwick *et al.,* 2005, 2008, 2009b; Bickle *et al.,* 2007; Arts *et al.,* 2008, Arts, 2009). These maps were originally created by extracting amplitude data from monitoring seismic surveys performed after the start of CO_2 injection then analysing the tuning response to correlate amplitude with thickness (Chadwick *et al.,* 2005).

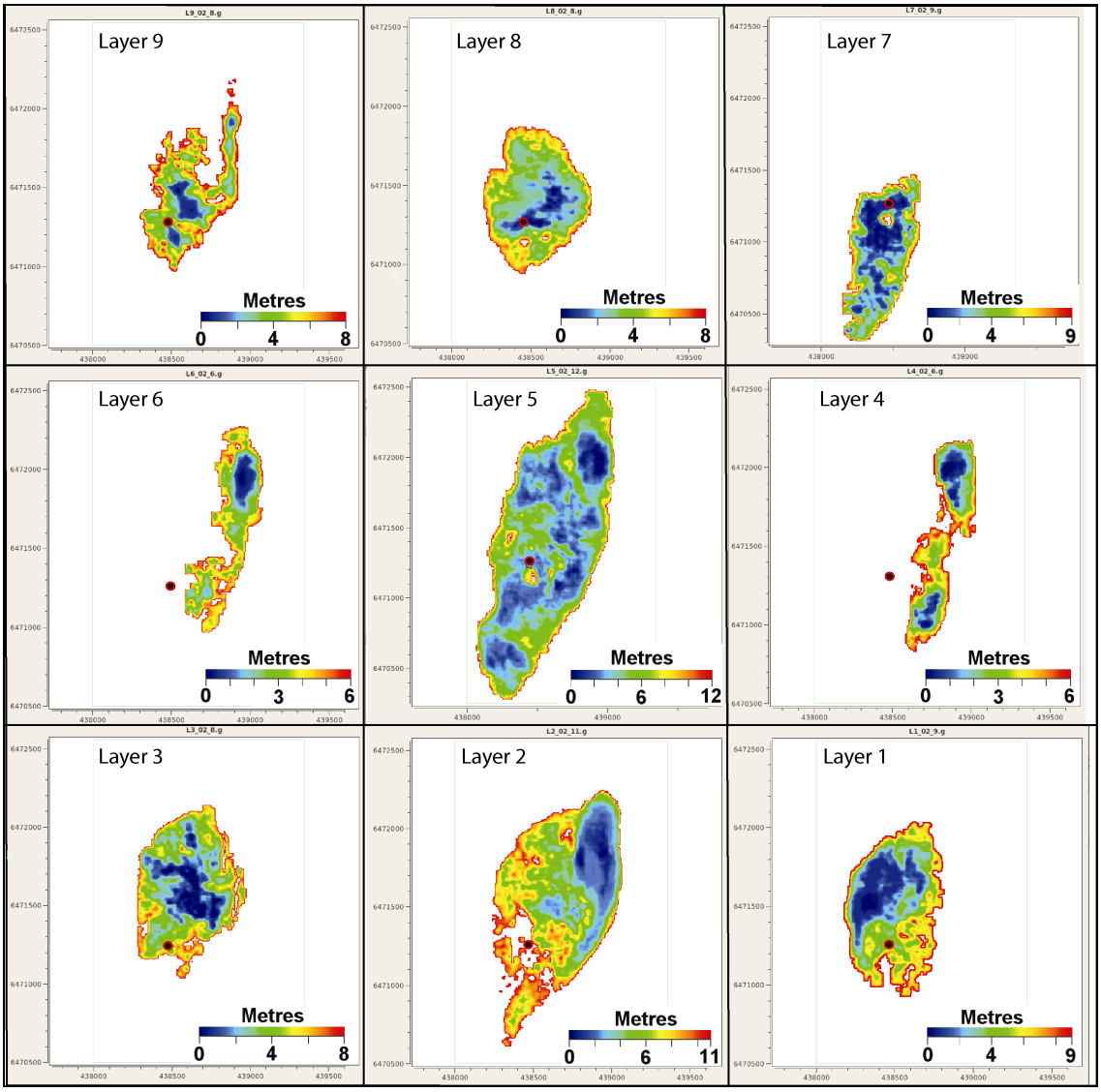

Figure 4.15: Screenshot of the nine high-resolution CO_2 layer maps from 2002, created from public domain data (modified from Chadwick et al., 2005, 2008; Bickle et al., 2007). Note that these maps have already been modified with the Colour Viewer facility in MPath® to assign a structural relief range based on colour scale. The black dot with red surround indicates the approximate injection point location in relation to each layer. Only the maps from layer 1 (bottom right) to layer 7 (top right) were used as overlays.

Related research has used analytical methods to extract CO_2 layer thickness information based on flux rates and layer growth radius (Bickle *et al.,* 2007). This thickness information for 2002 (summarised in Table 4.2) was used to help constrain our maps. Complete sets of these seismic amplitude maps for are only available in the public domain for 1999, 2001 and 2002 (as illustrated in Figure 4.8), although one publication (Arts, 2009) contains detailed UTM-located data for layers 5, 8 and 9 from 2004, 2006 and 2008 (layers 8 and 9 are illustrated in Figure 4.10), and these were subsequently used to assist in correlating our simulations.

Approximate Thickness (metres) of Individual CO_2 Layers Based on 2002 Plume Maps		
CO_2 Layer Number	**As derived from: Chadwick *et al.,* 2005**	**As derived from: Bickle *et al.,* 2007**
9	7	5
8	8	6
7	7	5
6	6	4
5	11	8
4	6	4
3	7	5
2	8	6
1	10	7

Table 4.2: Approximate thickness of individual CO_2 layers for 2002

4. Each amplitude map was digitised and converted to a high-resolution greyscale image, imported to MPath® via the Image Browser facility, then each map was converted into a colour scale overlay map using the Map Viewer (Figure 4.15), with an appropriate structural relief/colour scale range applied to each overlay map (refer to Table 4.2 for details of layer thickness used for guidance),
5. Each overlay map was then opened in the 3D Viewer in conjunction with the barrier map to which it was to be merged and migrated to the correct merge depth by adding an appropriate depth increment to give a good visual fit (Figure 4.16),

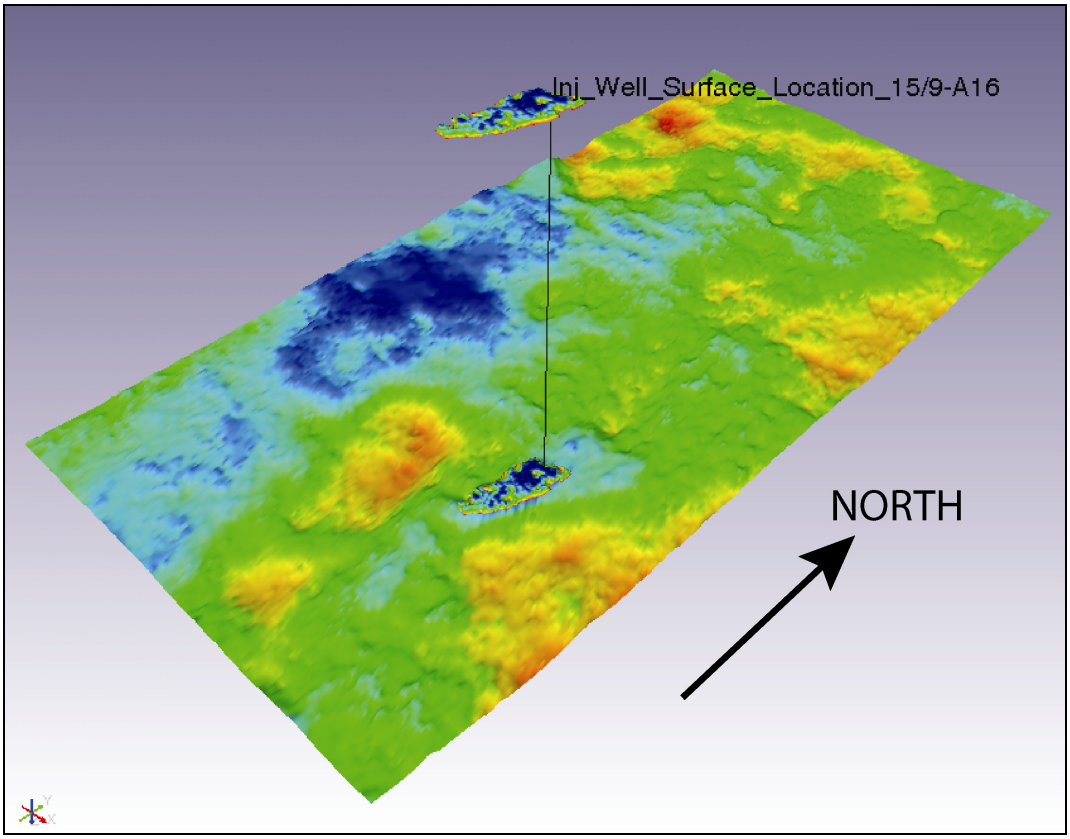

Figure 4.16: MPath® screenshot of the overlay map fitting process, showing the layer 7 map (from Figure 4.13) at top with ~9 metres relief being migrated to the correct depth and fitted to a proxy barrier 7 map in the 3D viewer facility. The black vertical line represents the CO_2 injection point location projected to surface. Vertical exaggeration 5x.

The final step involved returning to the Map Viewer to apply the depth increment to the overlay map via the Calculator facility, then merging the overlay map with the appropriate cloned barrier map using the Edit/Merge facility from the Tools menu,

6. Steps 5 and 6 were repeated for the other overlay/proxy map pairs until a complete set of merged barrier maps were created for barriers 1 to 7, then checked by performing a fill-spill analysis for each merged surface,
7. Barrier top/base pairs were constructed from the merged maps by duplicating each map and adding an appropriate depth increment for individual layers (e.g. based on well log data, a 7 m spacing for barrier 8, a 3 m spacing for barriers 6 and 3, and a 2 m spacing for all remaining barriers),
8. Some of the composite barrier maps ended up within a few metres of each other or had significant overlaps, so each layer was checked by first using 2D cross-sections to check additional space-out requirements, then applying an appropriate vertical up/down shift and reiterating until all layer interference was removed (Figure 4.17),

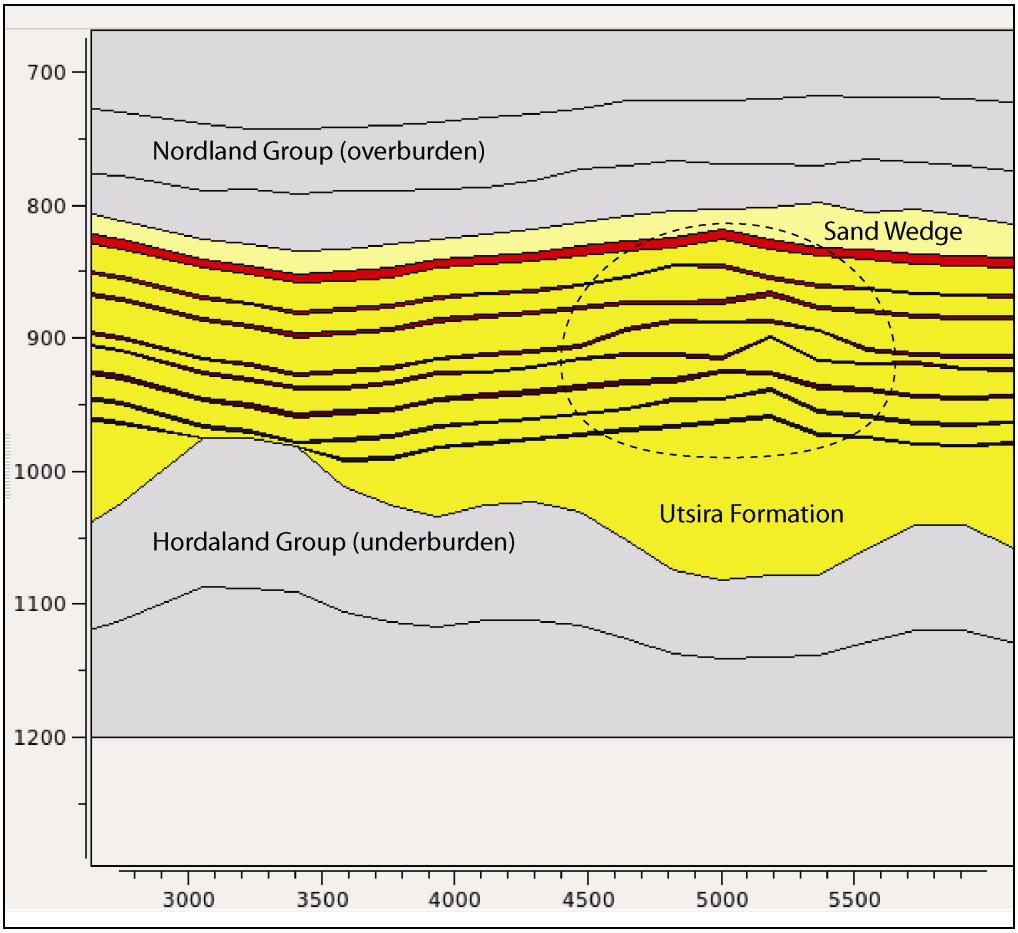

Figure 4.17: MPath® screenshot of a 2D cross-section from W (left) to E (right) through the Sleipner CO_2 storage site model. The improved structural relief of the merged overlay/proxy map pairs is visible within the sub-circular area enclosed by dashed lines. At this stage all the overlaps between barriers (red) have been corrected by adjusting the vertical spacing between barrier top/bottom maps. Vertical scale is in metres TVDSS and horizontal scale represents distance along the cross-section in metres.

9. With all maps completed and corrected for overlaps, the model was then ready to be constructed as an Earth Model, then converted into a Mesh Sequence for fluid flow simulation purposes (surface files use to construct the Earth Models are fully described in Appendix 4.1).

4.5.2: Creating Earth Models:

The Earth Model is essentially a stacked collection of maps that can nominally be assigned lithologies and ages (i.e. precise ages can be applied to a 3D basin model for back stripping purposes through geological time, but in this case, no back stripping was required, so only approximate age values were applied to each surface based on chronostratigraphic ages from Figure 2.2 in Chapter 2). Lithologies are applied to the maps via a lithology (or *.plith) file. For the models described here, the demo.plith file from the MPath® library of generic lithology files was use to assign a specific lithology to each surface (e.g. assigning a sandstone lithology to the base of a barrier map will populate the intervening cells in the subsequent 3D model down to the top of the next barrier with the specified lithology). The stages required to build an Earth Model ready for 3D meshing are described as follows:

1. Load the complete map stack into the Map Viewer and for each map assign an age, ensuring that the maps are always increasing in age with depth,
2. Create an Earth Model, assign an appropriate lithology (*.plith) file to the model, optionally assign pressure and temperature curve (*.xy) files, supply a name/description and save the model (Figure 4.18),

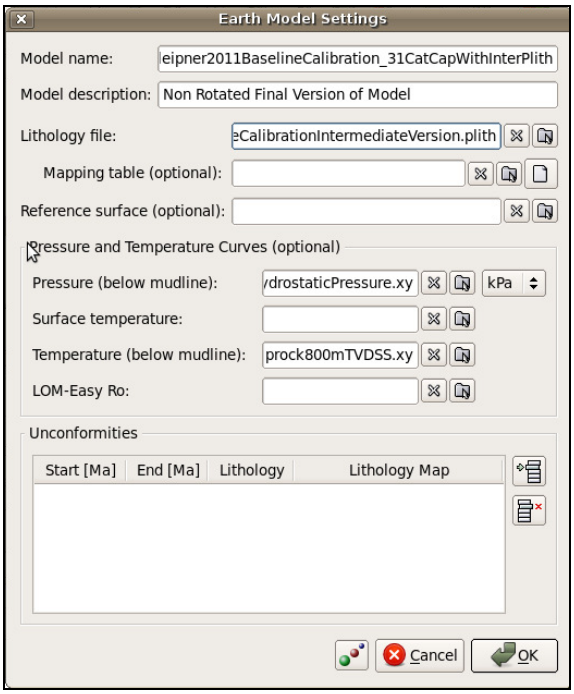

Figure 4.18: Earth Model Settings dialogue from MPath® with Lithology File (.plith file) and Pressure/Temperature Curves (*.xy files) pre-assigned.*

3. Assign a lithology to each surface map. In this case, we used modified versions of the demo.plith file, by creating a range of new lithologies appropriate to the observed porosity and permeability conditions at reference depths previously described for Sleipner in Chapter 3 (e.g. overburden and barrier shale lithologies used modified shale curves from demo.plith and the Utsira Formation used modified high net to gross sandstone curves from demo.plith). Again, these modifications are fully described in Appendix 4.2.
4. Assign a lithology map to the surface map. This is normally only required if the surface map exhibits spatial lithological variations across its surface (e.g. if a predominantly shaly lithology is cross-cut by a sandy channel). For the models described here, no lithology maps were required from the Top Hordaland to the Top Sand Wedge, but due to the complex nature of the overburden, lithology maps were applied to several of the Nordland Group overburden surfaces, to describe different lithological variations (e.g. glacial channel sequences illustrated in Figure 4.19),

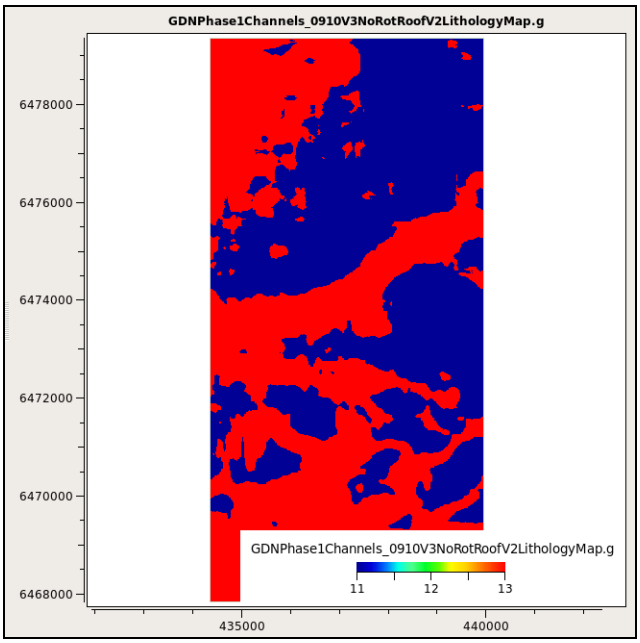

Figure 4.19: Screenshot from the MPath® Map Viewer with a dual lithology map displayed for a glacial channel sequence. The blue colour (11) represents the surrounding Nordland Group mudstones and the red colour (13) represents the channel sand lithology. These maps are used to apply lithological contrast to the topographic surface maps in the Earth Model.

5. Ensure all the maps are added to the Earth Model, save the model and perform a final overlap check before running the Create Mesh Sequence command.

4.5.3: Creating Mesh Sequences:

Two Earth Models were created in MPath® for converting into a Mesh Sequence:

- GDNSleipner2011BaselineCalibration (essentially a basic model created for plume calibration purposes with a simple overburden comprised of four Nordland Group shale sequences and no lithological heterogeneities). This model was used to calibrate the CO_2 plume within the Utsira Formation to published data (Chadwick *et al*., 2005, 2008, 2009b; Bickle *et al.,* 2007; Arts *et al*., 2008, Arts, 2009),
- GDNSleipner2011ComplexModel_OverburdenChannels_Chimneys (a complex model with all the overburden complexity included from Chapter 2, including glacial channels, tunnel valleys and palaeo-gas chimney features). This model was used to assess the effects of lithological heterogeneity on CO_2 migration via the overburden and simulate leakage scenarios.

The Mesh Sequence is created from the Map Viewer facility using the Create Mesh Sequence command from the Model menu (Figure 4.20). Basic run settings are described as follows:

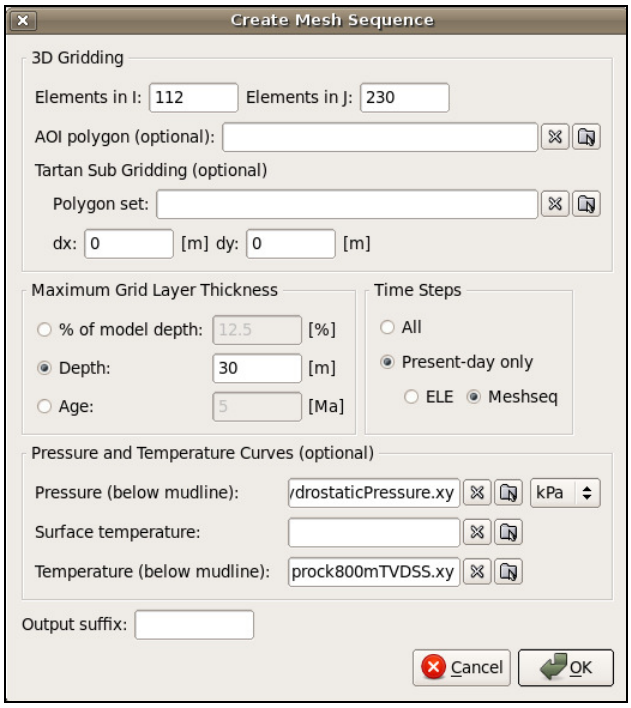

Figure 4.20: Screenshot from the MPath® Map Viewer showing the Create Mesh Sequence dialogue.

1. Enter the cell dimensions required for the mesh in the i (X) and j (Y) directions,
2. Optionally assign any temperature or pressure curves required for the mesh,
3. Select a grid layer thickness – this can either be specified as a percentage of the model depth, maximum layer thickness (depth) or based on geological age,
4. Select whether the mesh will use present day or geological ages (e.g. for back stripping purposes as previously described in Section 4.4.2),
5. Select OK to build the Mesh Sequence.

The run parameters used for the two models herein described are presented in Tables 4.3 (baseline) and 4.4 (complex) respectively.

Mesh Information for Baseline Calibration Model	
Elements in i (X) direction	112
Elements in j (Y) direction	230
Elements in k (Z) direction	98
Total number of elements	2,009,280
Number of lithological properties	16
X origin (SW corner)	434361 m
X maximum (NE corner)	440013 m
X distance	5651.66 m
Y origin (SW corner)	6.4784e+06 m
Y maximum (NE corner)	6.47935e+06 m
Y distance	11512.5 m
Z distance	1200 m
Approximate grid cell size (X, Y)	50 x 50 m
Maximum grid layer thickness	30 m

Table 4.3: Mesh settings for the Baseline Model

Mesh Information for Complex Model	
Elements in i (X) direction	112
Elements in j (Y) direction	230
Elements in k (Z) direction	98
Total number of elements	2,524,480
Number of lithological properties	19
X origin (SW corner)	434361 m
X maximum (NE corner)	440013 m
X distance	5651.66 m
Y origin (SW corner)	6.4784e+06 m
Y maximum (NE corner)	6.47935e+06 m
Y distance	11512.5 m
Z distance	1200 m
Approximate grid cell size (X, Y)	50 x 50 m
Maximum grid layer thickness	30 m

Table 4.4: Mesh settings for the Complex Model

Ideally, a higher resolution mesh with a smaller grid cell size (e.g. 12.5 x 12.5 m seismic resolution) would have been preferred but this resolution was as high as our computing facilities would tolerate in terms of computer memory and graphics card requirements. The two final mesh models are illustrated in Figures 4.21 (for Baseline Calibration) and 4.22 (for Complex Model).

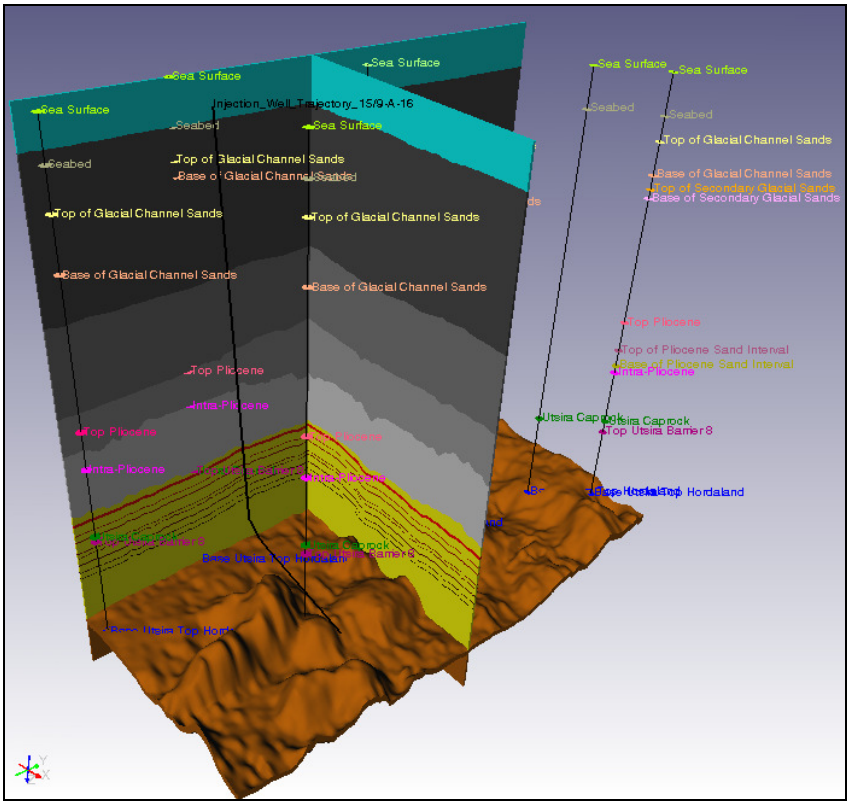

Figure 4.21: Baseline Calibration mesh model viewed from SE-NW with deviated CO_2 injection well and additional block 15/9 wells with stratigraphic tops displayed (10 x vertical exaggeration)

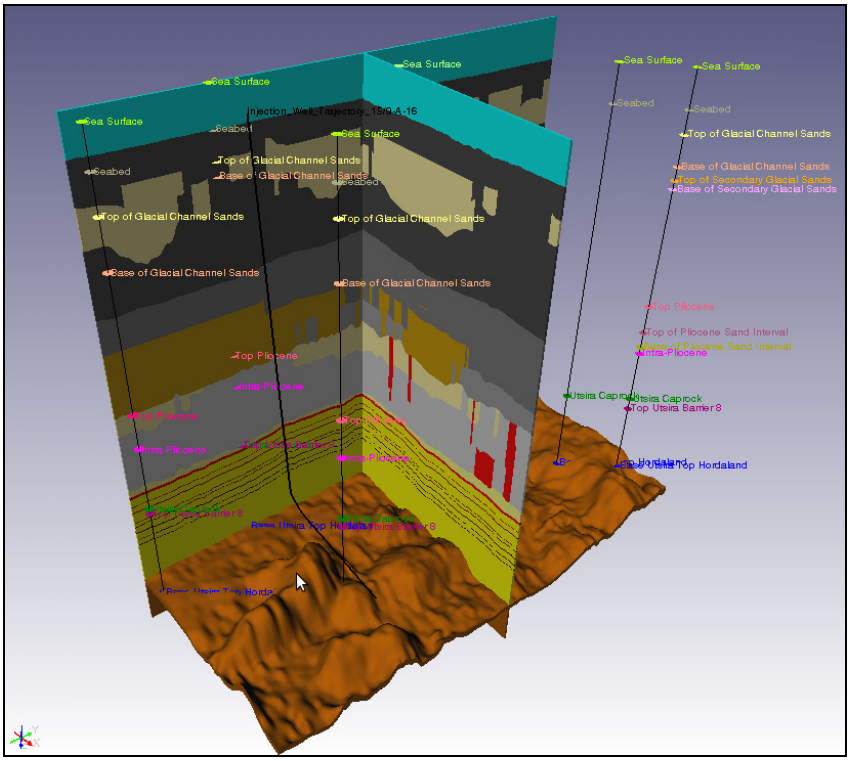

Figure 4.22: Complex mesh model viewed from SE-NW with deviated CO_2 injection well and additional block 15/9 wells with stratigraphic tops displayed (10 x vertical exaggeration)

4.6 Calibration Methodology for CO_2 Flow Simulations:

The CO_2 plume calibration for the Baseline models used the following procedure:

- Three mesh models were constructed and run in the Reservoir Filling simulator in MPath® to match the 2002 set of seismic amplitude maps presented in Chadwick *et al.,* (2005, 2008) and Bickle *et al.,* (2007). These maps were originally used to derive an estimated CO_2 layer thickness based on amplitude response (Table 4.2). Each calibration mesh model used one of three geothermal gradients (i.e. cool, intermediate or hot), represented by MPath® temperature curves giving 28ºC, 32ºC and 36ºC at caprock respectively. The capillary threshold entry pressure/porosity curves were then tuned in an iterative process for individual barriers 1 to 8 in the model (using the Lithology Editor in MPath®) by re-meshing and re-running short 6 year simulations injecting 0.84 Mt/yr CO_2 from 1996 to 2002 until an acceptable match was achieved for each model (refer to Appendix 4.1 for details of temperature/pressure curve files used for the mesh models and Appendix 4.2 for details of lithological parameter values used for the cool, intermediate and hot lithology files).
- Nine models were then run with different geothermal gradients and caprock temperatures, varying in 2ºC increments from 28ºC to 36ºC (Table 4.5). These models used the most appropriate set of capillary threshold entry/porosity curves from the previous stage (i.e. cool, intermediate or hot) to simulate 6 years of injection from 1996 to 2002. By applying a scalar to increase the anisotropy of Pthz (capillary threshold pressure in the z or vertical direction) and re-running, the models could be fine-tuned to improve the match to seismic observations. Comparing the layer morphologies and CO_2 densities observed within each layer of the model against the most recent gravity data obtained at Sleipner (Alnes *et al*., 2008; 2011), it is possible to determine the most likely geothermal gradient prevailing at Sleipner, and so better constrain temperature at the caprock depth (refer to Appendix 4.3 for tabulated simulation results for each run, including CO_2 densities within each layer). Summary results with the range of densities obtained for each run are presented in Table 4.6.
- For this first set of runs a comparison was made against the observed density estimates based on gravity observations at Sleipner (Alnes *et al.* 2008, 2011), previously discussed in Chapter 3 (Section 3.3.5, Table 3.3.4), to constrain the caprock temperature for further simulation runs (Figure 4.23).

Lithology file used (*.plith)	Caprock Temperature (ºC)	Reservoir Filling Pthz anisotropy scalar used
Hot	36	1.108
Hot	35	1.003
Intermediate	34	1.225
Intermediate	33	1.13
Intermediate	32	1.055
Intermediate	31	1.015
Cold	30	1.078
Cold	29	1.05
Cold	28	1.01

Table 4.5: Lithology files and Pthz anisotropy scalars used for each 6-year calibration simulation.

Temperature at Caprock (ºC)	Average CO_2 Density (kg/m^3)	Lowest CO_2 Density (kg/m^3)	Depth (m TVDSS)	Highest CO_2 Density (kg/m^3)	Depth (m TVDSS)
36	512.9	445	789.07	552.08	1002.7
35	589.03	504.26	789.07	578.46	973.73
34	626.92	583.34	806.61	612.36	973.76
33	661.06	637.68	1002.7	642.42	872.57
32	692.57	661.21	1002.7	670.7	789.07
31	711.31	682.51	1002.7	694.78	789.07
30	730.49	701.75	1002.7	714.38	788.21
29	750.39	719.25	1002.7	731.52	789.07
28	764.7	735.42	1002.7	746.44	789.07

Table 4.6: Density averages and ranges for 9 different calibration runs and 6 years of CO_2 injection. Note the switch in depth locations for the lowest and highest densities once caprock temperatures exceed 33ºC.

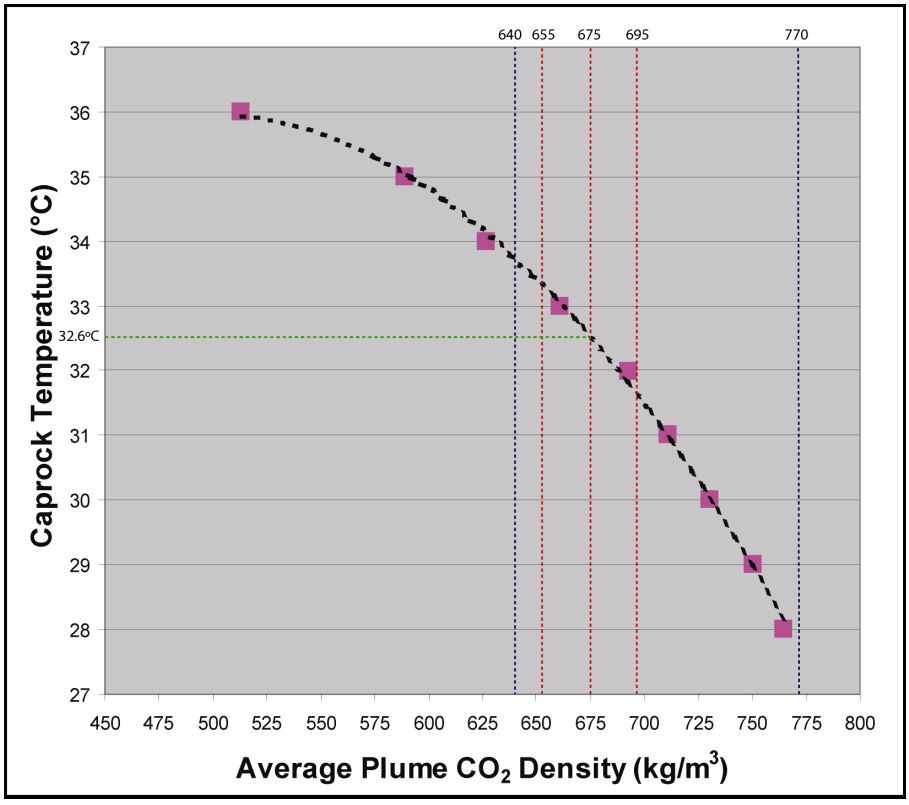

Figure 4.23: Average CO_2 density values plotted against temperature values from Table 4.6. Dashed vertical lines represent density ranges from Alnes et al., 2008 (blue) and Alnes et al., 2011 (red).

The earlier publication (Alnes *et al.,* 2008) stated that gravity measurements indicated a CO_2 density range of 640 to 770 kg/m^3 prevailed at Sleipner (blue vertical dashed lines on Figure 4.20), but in the most recent publication (Alnes et al., 2011), this has been revised to an average value of 675 +/- 20 kg.m^3, a much narrower range of values and a higher density (red vertical dashed lines on Figure 4.20). Based on the earlier set of gravity data, the Sleipner caprock temperature could be in the range of 27.8 to 33.7ºC. The most recent data implies a temperature in the range of 32 to 33ºC, with the average value of 675 kg/m^3 correlating with a caprock temperature of ~32.6ºC.

In Table 4.6, the most recent range of CO_2 density values can only be achieved with a temperature range of 31 to 33ºC at the caprock (yellow highlighted cells), thus for our subsequent calibration runs and forward modelling of CO_2 injection, the value of 32.6ºC was used for the caprock temperature. This is slightly higher than the 31.5ºC temperature used by Chadwick & Noy, (2010) and slightly lower than the 32.8ºC temperature used by Singh *et al*., (2010) in their recent Sleipner modelling work.

4.6.1 Comparison of Calibration Simulations with Seismic Data:

A second phase of calibration runs were performed with the 32.6ºC at caprock model to history match against seismic amplitude maps from 1999 to 2008 available in the public domain (Bickle *et al.*, 2007; Chadwick *et al.,* 2008; Hermanrud *et al.,* 2010). We ran simulations for CO_2 injection into the calibration model at an average injection rate of 0.84 Mt/yr using the MPath® Reservoir Filling simulator and CO_2 PVT module. The Reservoir Filling run parameters are detailed in Table 4.7, injection volumes (kg) are detailed in Appendix 4.4. Note that the lithology file used for the 32.6ºC at caprock model (i.e. Intermediate) was originally calibrated to 2002 plume maps, so the simulation match to the 1999 seismic data is not as good as the simulation matches for the 2001-2008 data, where Pthz Anisotropy Scalars have been used to fine tune the simulations (only scalars greater than 1 could be applied in the version of MPath® used for this study). Calibration runs were performed for 3, 5, 6, 8, 10 and 12 years of CO_2 injection. A combined stack of invasion charge sequence maps (i.e. layers 1-9 overlaid upon each other) from our simulations are illustrated in Figures 4.24 and can be compared against equivalent map stacks of cumulative total seismic reflection strength for CO_2 layers 1-9 up to 2008 (Figure 4.25) derived from Hermanrud *et al.,* (2010).

Simulation Run Time (Years)	**Reservoir Filling Pthz anisotropy scalar used**	**Shallowest Plume in Simulation**	**CO_2 Mass in Layer 9 (kg)**	**Percentage of Total Injected Mass in Layer 9**	**CO_2 Column Height in Layer 9 (m)**	**Notes**
3 (1999)	1 (none)	Layer 6	0	0	0	Overfilling Layer 5
5 (2001)	1.05	Layer 9	5.64002e+07	1.34%	3.83	Slightly underfilling Layer 9
6 (2002)	1.1	Layer 9	5.66058e+07	1.12%	5.66	Reasonably good match
8 (2004)	1.22	Layer 9	1.35903e+08	2.022%	5.87	Reasonably good match
10 (2006)	1.315	Layer 9	2.78305e+08	3.13%	6.65	Reasonably good match, thirteen accumulations in Layer 9 after spill, eight with less than 0.5 m column, five with columns between 1.74 to 6.65 m (maximum)
12 (2008)	1.326	Layer 9	1.41844e+09 (plus spill)	16.8%	10.36	Slightly overfilling Layer 9, no S migration component for Layer 9 and spill of 2.75% of injected volume to E (2.77392e+08 kg)

Table 4.7: Reservoir Filling simulation run parameters for the Baseline Calibration model and layer, column height and stored CO_2 mass information for layer 9 underlying the caprock seal.

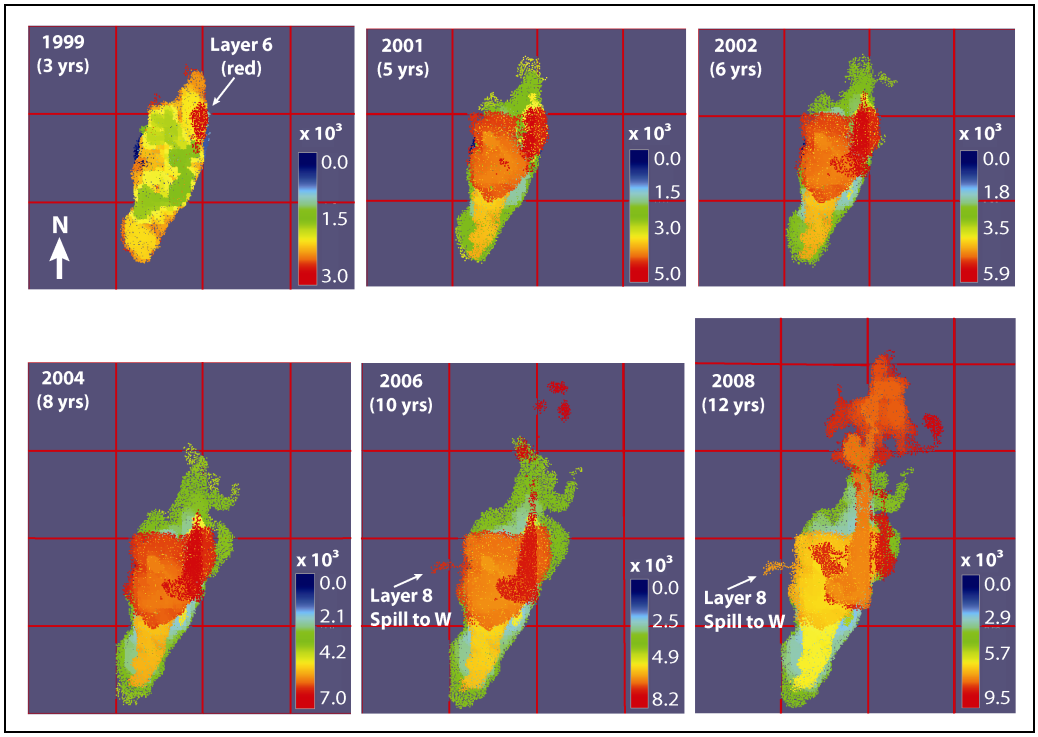

Figure 4.24: Combined map stack for layers 1-9 of MPath® Reservoir Filling simulation results for 3-12 years of CO_2 injection at 0.84 Mt/yr. Colours represent CO_2 invasion charge sequence based on time steps (colour scale), with orange/red representing the most recent charge (i.e. Layers 8 and 9). Grid squares (red lines) are 1 km in extent. Note the initiation of a W spill point from Layer 8 after 2006.

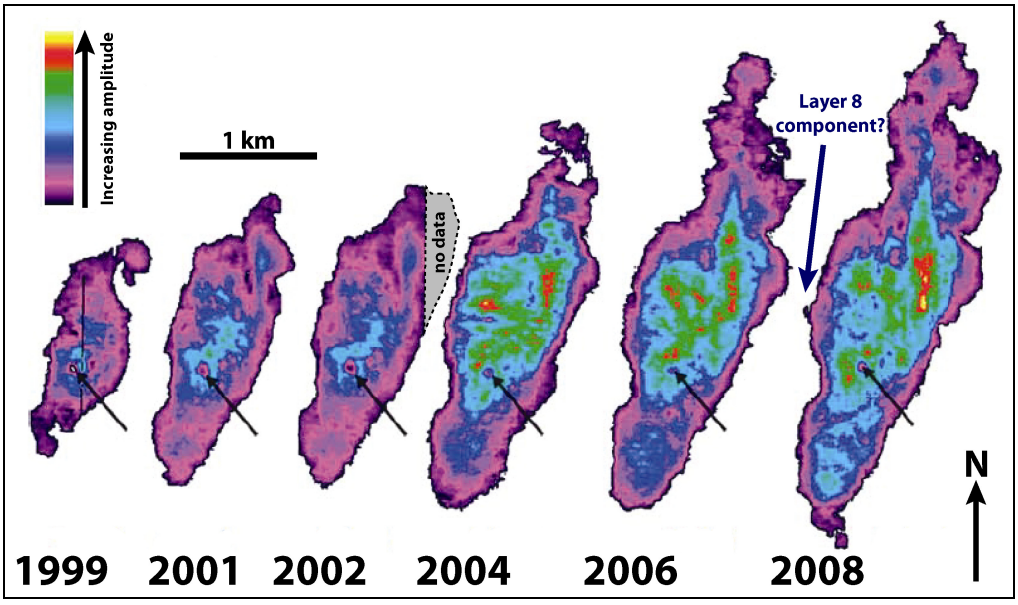

Figure 4.25: Combined map stacks of cumulative total seismic reflection strength for CO_2 layers 1-9 from seismic data acquired between 1999-2008, illustrating the areal extent of the CO_2 plume. Location of the main feeder chimney (visible on cross-section illustrated in Figure 4.2) is indicated by black arrows. Layers 5 (purple) and 9 (green/red) provide the main components of the plume expansion depicted here. A potential spill to the W from Layer 8 is indicated on the 2008 map (modified from Hermanrud et al. 2010).

To obtain an acceptable history match to seismic data it was necessary to increase the vertical capillary threshold entry pressure (Pthz) anisotropy for each successive simulation, by applying a global scalar otherwise the deeper layers (e.g. layer 5) would remain unchanged in terms of lateral spread and overfilling of the shallowest layers occurred. The scalars displayed an asymptotic behaviour and by the 2008 (12 years injection) simulation, the Pthz scalar became so sensitive that even fine adjustment resulted in either no migration into layer 9 and over spilling in layer 8 (Figure 4.26), or over filling of layer 9 (Figure 4.24).

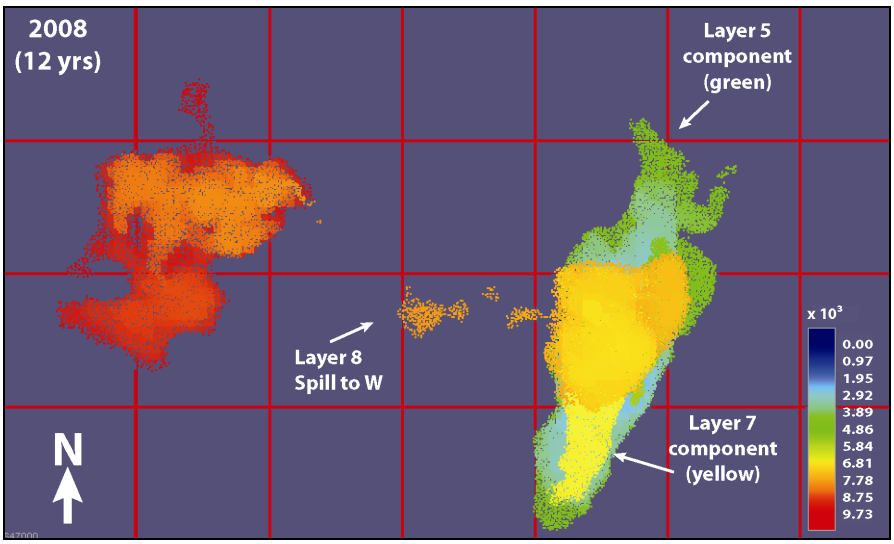

Figure 4.26: Stacked maps of MPath® Reservoir Filling simulation results for 12 years of CO_2 injection at 0.84 Mt/yr with a Pthz anisotropy of 1.327, resulting in the accumulation of an 11-12 m column of CO_2 in layer 8. Colours represent CO_2 invasion charge sequence based on time steps (colour scale). Grid squares (red lines) are 1 km in extent. In this case, a slight increase in Pthz compared to the 2008 simulation depicted in Figure 4.24 has prevented migration into layer 9 and created an over spill to the W in layer 8.

Although no such layer 8 over spill has been detected on the seismic monitoring data up to 2008, a small extension to the W is visible on the 2008 plume map generated from seismic data (indicated with dark blue arrow on Figure 4.25), which may indicate that CO_2 layer 8 was just on the point of over spilling at that time. The general filling behaviour of our Baseline Calibration model (including the apparent increasing CO_2 flux into layer 9, despite incremental increases in Pthz as shown in Table 4.7) and implications for the Sleipner storage site will be further discussed in Section 4.7.

4.6.2 Complex Model Simulations:

Having obtained an acceptable history match to observed seismic data, we used the Baseline Calibration model settings and the Intermediate lithology file as a starting point for the Complex Model, but instead of using a global anisotropy scalar to calibrate Pthz (i.e. incrementing the vertical threshold entry pressure settings for all layers by a specified amount), we used the Reservoir Mesh Overrides facility in MPath® to apply anisotropy to Pthz on an individual layer basis. This allowed us to apply a finer control on capillary entry pressures for the migration process and introduce a more realistic Pth heterogeneity into the Complex Model. This final set of simulations were also used to assess the likelihood of migrating CO_2 at Sleipner contacting any of the palaeo-migration structures we identified and described earlier in Chapter 2. Chimney features were incorporated into the model as a series of lithology maps in a similar manner to the channel and tunnel valley lithologies described in Section 4.5.2 (chimney lithology map construction is described in Appendix 4.4).

For the Nordland Group overburden, the Calibration Model uses default shale threshold entry pressure values derived from the demo.plith lithology file supplied with MPath®. In the Complex Model, threshold entry pressure values for the Nordland Shale are derived from measured values described in Springer & Lindgren (2006) and applied as follows:

- Average caprock porosity of 35% is assumed,
- Average caprock permeability of 0.001 milliDarcy is assumed,
- kv/kh anisotropy of 1/10 is assumed for shale (and applied to threshold entry pressures via the Reservoir Mesh Overrides facility),
- Average kv is therefore 0.0001 milliDarcy,
- This equates to a mercury-air caprock threshold entry pressure (Pthz) value of approximately 11700 kPa for shale of low-moderate permeability (Sperrevik *et al.,* 2002; Cavanagh & Wildegust, 2011), which converts to a CO_2-brine equivalent of 680 to 1088 kPa for an 80 to 100% water-wet case respectively (using the conversion criteria described in Section 4.2). It should be noted that these CO_2-brine values are lower than experimental values obtained by Springer & Lindgren (2006) and Harrington *et al.,* (2009) from Sleipner caprock samples; reasons for this discrepancy will be discussed further in Section 4.7.

Based on observations from the fill-spill and baseline calibration simulations it is apparent that CO_2 column heights within our Sleipner models will not exceed 12 m below the caprock before trap spilling occurs and/or CO_2 exits from our model boundaries. If the caprock is homogeneous over a wide area and the Pthz value is consistent at 11700 kPa, then CO_2 leakage is unlikely to occur through the Nordland Shale lithology, given such a high Pthz and CO_2 column heights less than 12 m. Thus, to model a potential leakage scenario using criteria previously described in Chapter 3, Section 3.5.2, the following assumptions have to be applied to the Complex Model:

- Leakage is only possible from the Utsira Formation via the chimney lithology, since this is suggested to represent the weakest parts of the caprock through which leakage has previously occurred during the past few million years,
- Parameters from the 12 m leakage scenario described in Chapter 3, Section 3.5.2 are only applied to the chimney lithology (i.e. Pth, IFT and wettability),
- IFT values are unlikely to be as low as 20 to 25 mNm^{-1} at the caprock or within the overburden for the prevailing CO_2 density, pressure and temperature conditions (Chalbaud *et al.,* 2009).

Four new lithology files were constructed by adding a new chimney lithology with different threshold entry pressure parameters to the Intermediate lithology file described in Section 4.6 (refer to Appendices 4.1 and 4.2 for file details). These new files were used to capture the range of most likely chimney leakage scenarios for the 12 m case described in Chapter 3, Section 3.5.2 (Table 3.13) at near critical point conditions (Table 4.8):

Lithology File (*.plith)	**Porosity at 800 m TVDSS**	**Pth (mercury-air) at 800 m TVDSS**	**Capillary Properties Assumed**
Low80	35%	625	80% water-wet, IFT 30 mNm^{-1}
High80	35%	825	80% water-wet, IFT 30 mNm^{-1}
Low100	35%	790	100% water-wet, IFT 30 mNm^{-1}
High100	35%	1050	100% water-wet, IFT 30 mNm^{-1}

Table 4.8: Porosity/threshold entry pressure ranges used for the chimney lithology in the Complex Model.

Earth Models and Mesh Sequences were constructed using these new lithology files and complimentary Reservoir Mesh Override files were also constructed to allow individual layer adjustment of Pthz. Updated scalars and mercury-air Pthz values for internal shale barriers are presented in Table 4.9 (also refer to Appendix 4.2 for comparison against the original Intermediate lithology file parameters used in the Baseline models):

Simulation Run Time (Years and Date)	**Reservoir Mesh Overrides applied to each barrier - scalar and (Pthz equivalent in mercury-air kPa)**							
	Barrier 1	**Barrier 2**	**Barrier 3**	**Barrier 4**	**Barrier 5**	**Barrier 6**	**Barrier 7**	**Barrier 8**
3 (1999)	0.91 (701)	0.91 (625)	0.97 (501)	0.97 (528)	0.8 (603)	0.9 (477)	0.86 (473)	0.97 (622)
5 (2001)	1.05 (809)	1.06 (728)	1.09 (563)	1.09 (593)	1.03 (777)	1.07 (567)	1.05 (577)	1.03 (660)
6 (2002)	1.1 (847)	1.1 (756)	1.17 (605)	1.17 (636)	1.08 (814)	1.08 (572)	1.05 (577)	1.11 (711)
8 (2004)	1.22 (939)	1.22 (838)	1.24 (641)	1.22 (664)	1.20 (905)	1.21 (641)	1.21 (665)	1.22 (782)
10 (2006)	1.315 (1012)	1.315 (903)	1.315 (680)	1.315 (715)	1.315 (991)	1.315 (697)	1.315 (723)	1.315 (843)
12 (2008)	1.326 (1021)	1.326 (911)	1.326 (685)	1.326 (721)	1.326 (1000)	1.326 (703)	1.326 (729)	1.326 (850)
14 (2010)	1.32627 (1021)	1.32627 (911)	1.32627 (686)	1.32627 (721)	1.32627 (1000)	1.32627 (703)	1.32627 (729)	1.32627 (850)
16 (2012)	1.3263 (1021)	1.3263 (911)	1.3263 (686)	1.3263 (721)	1.3263 (1000)	1.3263 (703)	1.3263 (729)	1.3263 (850)
18 (2014)	1.3264 (1021)	1.3264 (911)	1.3264 (686)	1.3264 (721)	1.3264 (1000)	1.3264 (703)	1.3264 (729)	1.3264 (850)
20 (2016)	1.3265 (1021)	1.3265 (911)	1.3265 (686)	1.3265 (722)	1.3265 (1000)	1.3265 (703)	1.3265 (729)	1.3265 (850)

Table 4.9: Reservoir Mesh Override scalars and equivalent mercury-air Pthz threshold entry pressures used for internal shale barriers within the Utsira Formation.

Note the tendency to asymptotic behaviour after 10 years (2006). Barrier settings from Table 4.9 were used for all Complex Model simulations. Sensitivity runs at this stage were focussed on varying the chimney lithology Pthz using Reservoir Mesh Overrides.

Reservoir Filling simulations were initially performed for 3, 5, 6, 8, 10 and 12 years of CO_2 injection to check the plume history match. The four new mesh versions of the Complex Model were used (i.e. Low80, High80, Low100 and High100). The sequence of CO_2 pore saturation maps from these simulations for CO_2 layers 1 to 9 up to 2006 are illustrated in Figures 4.27 and can be compared favourably against the seismic amplitude maps from 1999, 2001 and 2002 illustrated in Figure 4.8 (after Chadwick *et al.*, 2008). From 1999 to 2004, the Pthz scalar requires individual layer tuning (Table 4.9) to match the published seismic data sets (Bickle *et al,* 2007; Chadwick *et al.,* 2005, 2008), presumably as a result of unsteady-state behaviour. From 2006 onwards a uniform Pthz scalar can be applied to all layers to obtain a reasonable match to the published plume data, suggesting a tendency towards steady-state behaviour as preferential migration pathways become established and gradually stabilise over time. Migration behaviour for all four Complex Model versions is identical to 2006, since:

- Porosity and Pth conditions within the Utsira Formation are unchanged for all four models (only the Pthz for the overburden chimney lithology is different),
- CO_2 columns underlying the caprock have not yet developed sufficient height to exceed the chimney lithology Pthz, even for the Low80 version of the Complex Model (refer to Appendix 4.5 for simulation statistics).

By 2008 the latter situation has changed, as the CO_2 pore saturation maps from two separate 12-year simulations illustrate. Figure 4.28 shows the simulation plume maps for the High80 and Low80 versions of the Complex Model. The High80 Complex Model manages to retain CO_2 beneath the caprock and the accumulation spills to the E once a column height of 10.363 m has been attained (the same applies to both the Low100 and High100 versions). The Low80 Complex Model with a lower Pthz for the chimney lithology leaks at a CO_2 column height of 8.934 m via one of the chimney lithology pathways (chimney #77 – refer to Appendix 2.9 for details). This migration pathway situated above the NE tip of layer 9, promotes the formation of an accumulation below the Former Top Pliocene (FTP) surface at ~488 m, then leaks vertically to seabed as illustrated in Figure 4.29 (for this series of simulations the Nordland Group is assigned isotropic Pth properties in x, y and z directions, thus a vertical migration and leakage pathway has developed with no lateral component).

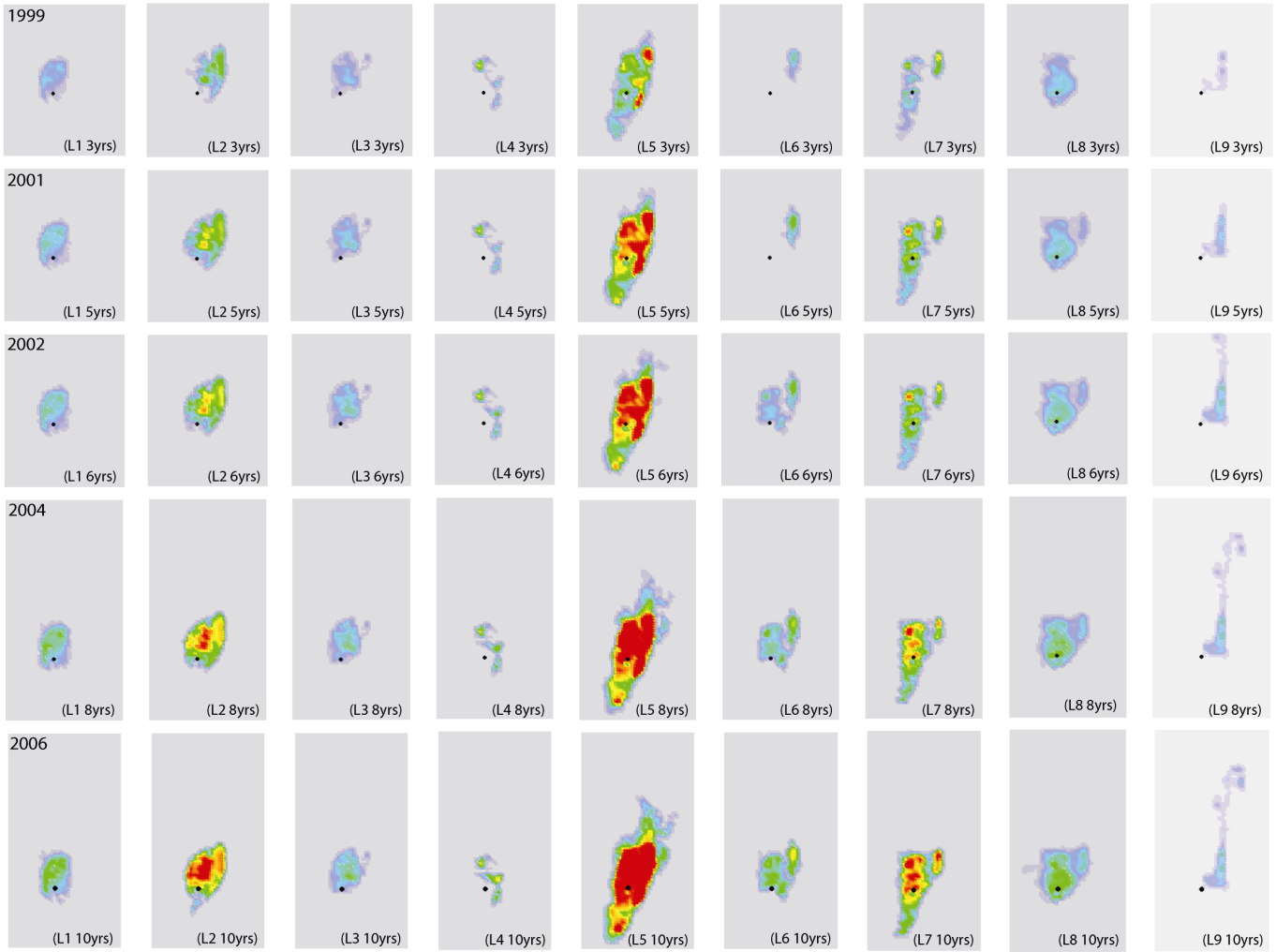

Figure 4.27: Second set of calibration simulations (plume layer maps) from 1999-2006 using the Complex Model and individual layer Pthz anisotropy applied using the Reservoir Mesh Overrides facility. The dimensions of the 1999-2002 maps are 3.0 x 2.1 km and the dimensions of the 2004-2006 maps are 4.5 x 2.1 km. The black dots represent the CO_2 injection point location.

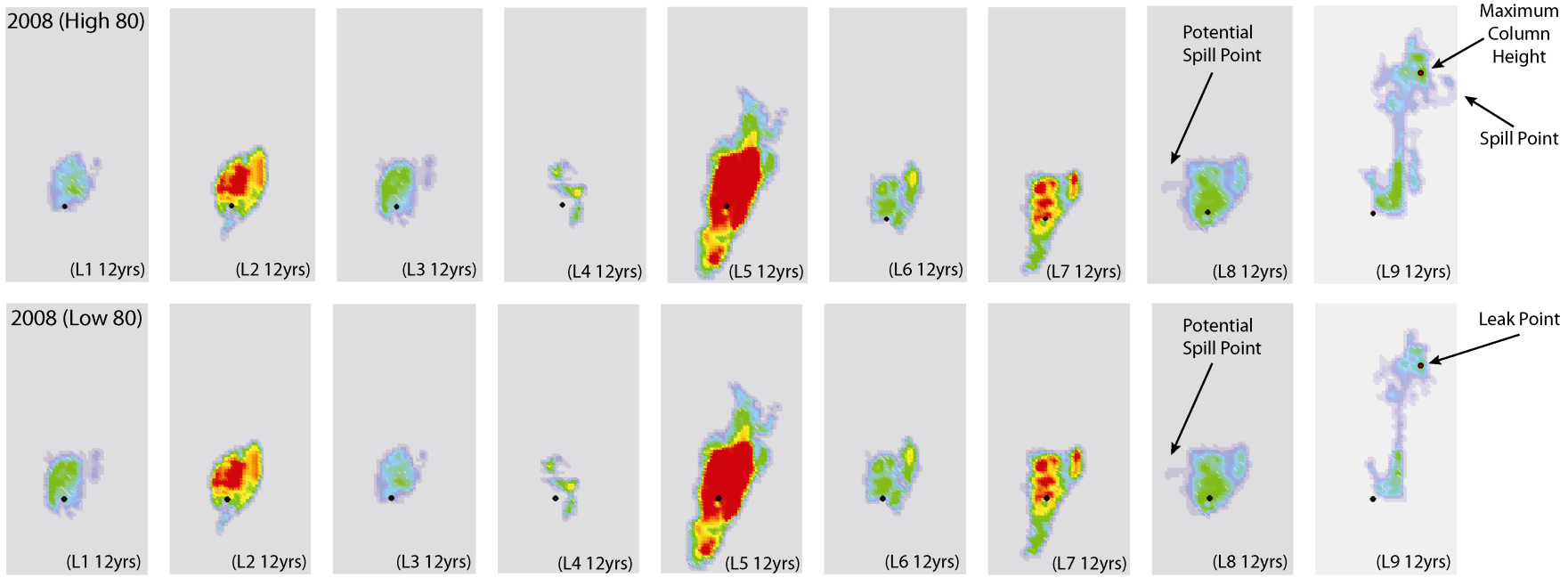

Figure 4.28: Two sets of calibration simulations (plume layer maps) from 2008 using the Complex Model and individual layer Pthz anisotropy applied using the Reservoir Mesh Overrides facility. The dimensions of these 2008 maps are 4.5 x 2.1 km. The black dots represent the CO_2 injection point location. The upper set of maps uses the High80 Lithology file from Table 4.8 (high Pthz for the Chimney lithology) - in this case there is no leakage into the overburden but CO_2 spills to the E beyond the model boundary in layer 9 at the point indicated by the arrow. The lower set of maps uses the Low80 Lithology file from Table 4.8 (low Pthz for the Chimney lithology) - in this case there is leakage into the overburden via the chimney lithology. In both sets of maps note the development of a potential spill point to the W in layer 8. The black dot with the red centre marks the position of the maximum CO_2 column height in layer 9 (same for both sets of simulations and also leak point for Low80).

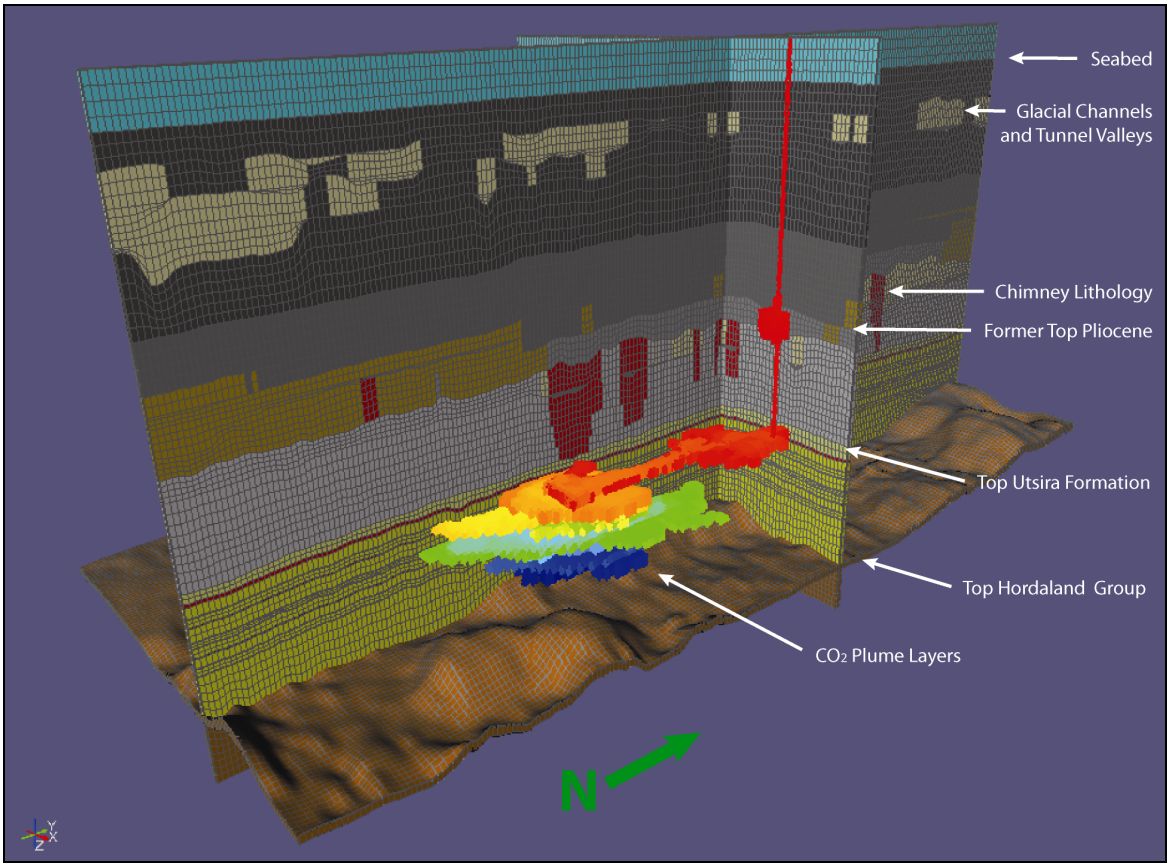

Figure 4.29: 3D view (5x vertical exaggeration) from SE of MPath® Reservoir Filling simulation results after 12 years of CO_2 injection at 0.84 Mt/yr using the Low80 Complex Model (as depicted in map format in Figure 4.28). The CO_2 plume layer colours represent the CO_2 invasion charge sequence based on time steps. Note the vertical migration pathway from layer 9 to seabed via the chimney lithology and the development of an accumulation at the Former Top Pliocene (FTP) level.

This is a hypothetical leakage scenario based on the set of assumptions described earlier within this section (i.e. leakage only occurs via the low Pthz chimney lithology and isotropic 1/1 Pthz/Pthx = 1170 kPa for the Nordland Shale at 800 m TVDSS) and no leakage of this nature was observed or reported in the Sleipner 2008 seismic dataset. In a real leakage situation, fluid migration should also reflect the overburden anisotropy (i.e. shale kv/kh permeability anisotropy of 1/10 described earlier), thus we performed further 12 year sensitivity runs on the Low80 Complex Model using Pthz/Pthx anisotropies of 10/1, 5/1, 2.5/1 and 1.25/1 applied to all the Nordland Shale lithologies via Reservoir Mesh Overrides, to assess the effects of varying degrees of vertical/horizontal shale anisotropy (e.g. 10/1 representing an excellent seal down to 1.25/1 representing a poor/fractured seal). These simulations are shown in Figure 4.30.

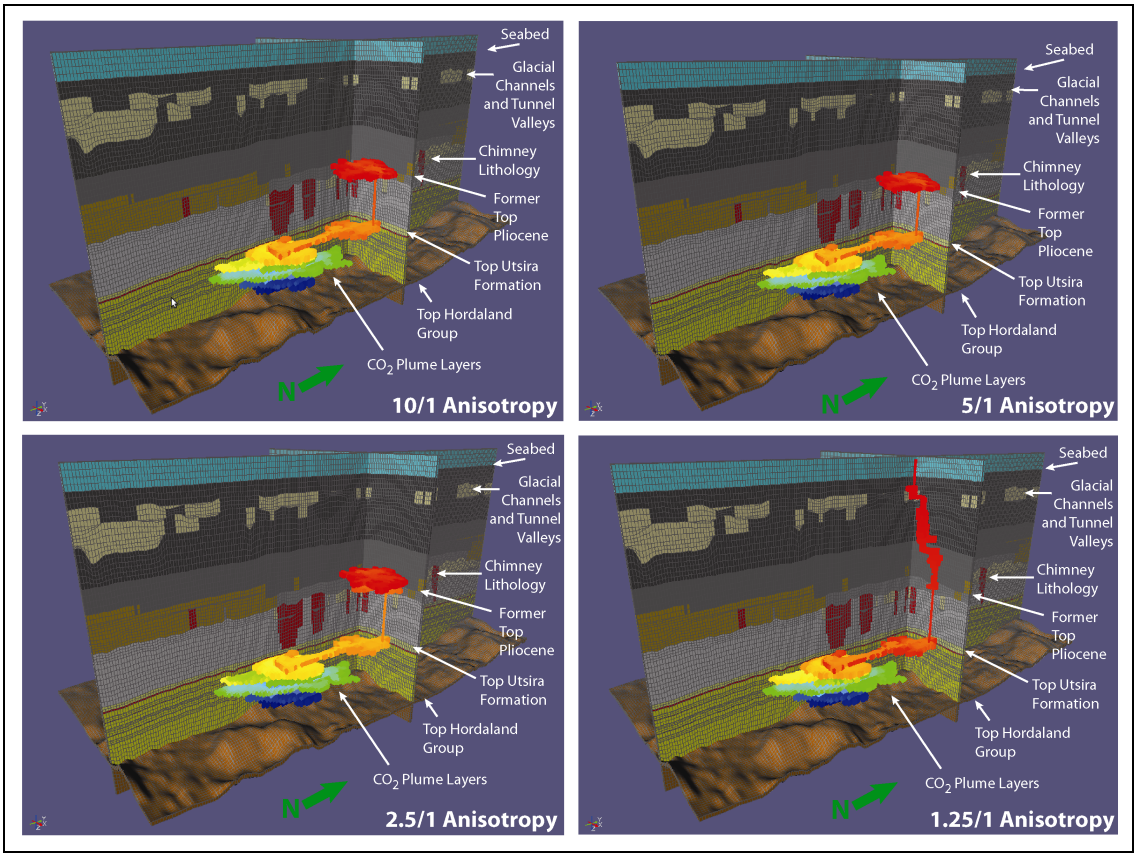

Figure 4.30: 3D view (5x vertical exaggeration) from SE of MPath® Reservoir Filling simulation results after 12 years of CO_2 injection at 0.84 Mt/yr using the Low80 Complex Model (as depicted in map format in Figure 4.28). The CO_2 plume layer colours represent the CO_2 invasion charge sequence based on time steps. In this case, different Pthz/Pthx anisotropy has been applied to simulate a range of vertical retention capacities. The 1.25/1 (Pthz/Pthx) version of the Complex Model is the only one that exhibits migration above the Former Top Pliocene (FTP) surface. The other three versions form accumulations at the FTP surface and spill to the E (refer to Table 4.10 for run parameters).

As Figure 4.30 illustrates, with increasing Pthz/Pthx anisotropy, CO_2 migration is eventually arrested at the Former Top Pliocene (FTP), forming accumulations and spilling to the E out of the model boundary. This suggests that for our models, leakage to seabed is only possible under the following conditions:

- Initial leakage from the Utsira Formation occurs from the crest above the largest CO_2 column height in layer 9 with upward migration via the low Pthz chimney lithology,
- Continued migration above the FTP level requires a low Pthz/Pthx anisotropy for the Nordland Shales, which is only possible if open vertical fractures or some form of connected high permeability lithology (e.g. sand injectites) are present.

The run parameters for each level of anisotropy are presented in Table 4.10:

Complex Model Variant	**Pthz (kPa) at 800 m TVDSS**	**Pthz (kPa) at 500 m TVDSS**	**Pthx (kPa) at 800 m TVDSS**	**Pthx (kPa) at 500m TVDSS**	**CO_2 Leaks, Spills and Accumulations (kg and % of injected volume)**
Nordaland Shale Isotropic (1/1)	1170	884	1170	884	**CO_2 leaked out of model:** 8.89874e+08 (8.83%) **CO_2 in overburden:** 4.0937e+06 accumulations (0.04%) 3.5036e+06 pathway (0.03%) **CO_2 in layer 9:** 8.46481e+08 (8.40%)
Nordland Shale Anisotropic 1.25/1	1463	995	1170	884	**CO_2 leaked:** 8.63417e+08 (8.57%) **CO_2 in overburden:** 3.07576e+07 accumulation (0.3%) 3.29714e+06 pathway (0.03%) **CO_2 in layer 9:** 8.46481e+06 (8.40%)
Nordland Shale Anisotropic 2.5/1	2925	2210	1170	884	**CO_2 spilled:** 7.11372e+08 (7.06%) **CO_2 in overburden:** 1.83461e+08 accumulation (1.82%) 2.6376e+06 pathway (0.02%) **CO_2 in layer 9:** 8.46481e+06 (8.40%)
Nordland Shale Anisotropic 5/1	5850	4420	1170	884	**CO_2 spilled:** 7.48692e+08 (7.43%) **CO_2 in overburden:** 1.46241e+08 accumulation (1.45%) 2.53821e+06 pathway (0.02%) **CO_2 in layer 9:** 8.46481e+06 (8.40%)
Nordland Shale Anisotropic 10/1	11700	8840	1170	884	**CO_2 spilled:** 7.48692e+08 (7.43%) **CO_2 in overburden:** 1.46241e+08 accumulation (1.45%) 2.53821e+06 pathway (0.02%) **CO_2 in layer 9:** 8.46481e+06 (8.40%)

Table 4.10: Run parameters from Low80 Complex Model simulations to 2008 (12 years injection at 0.84 Mt/year) performed with a range of different Pthz/Pthx anisotropy settings for the Nordland Shale (refer also to Figure 4.30).

From the previous simulation results it is clear that nothing further can be gained from forecasting our Complex Model beyond 2008 (12 years). With the Pthz/Pthx anisotropy set to 2.5/1 or higher, any additional CO_2 will simply spill from the model after 2008, following the same established pathways and providing no additional information about the plume extent or column heights within the model. No significant fluid migration will occur at Pth settings in excess of 1000 kPa (mercury-air). Setting the Pthz/Pthx anisotropy lower than 2.5/1 implies that the overburden must be fractured and there is no hard evidence for this at present, thus there is no point in "forcing" the model to migrate via specific lithologies by further altering Pthz and Pthx settings. As illustrated in Figures 4.29 and 4.30, when the anisotropy is low, the migration direction is vertically upwards, significantly avoiding all off the low Pth overburden heterogeneities (e.g. larger tunnel valleys). However, these simulations have raised some interesting points for further discussion:

- The Low80 version of the Complex Model is the only simulation model to exhibit overburden leakage before spilling,
- A supercritical to gas phase change occurs in the overburden at ~670 m TVDSS +/- 20 m, as CO_2 migrates upwards via the chimney lithology and all the accumulations at the FTP level (~500 m TVDSS) are gas phase with a density of 125 to 160 kg/m^3. Average pore saturation is also significantly lower at 46% for the FTP level compared to over 80% for CO_2 contained within the Utsira Formation,
- Despite the addition of significant heterogeneities to the Complex Model (e.g. tunnel valleys, channels, siltstone and chimney lithologies), the Nordland Shale lithology is still too homogeneous, particularly between ~300 to 500 m TVDSS to generate useful and realistic overburden migration simulations,
- This form of simulation relies on pathways already being present and open for migration, it does not account for the gradual development of pathways (e.g. through dissolution and sudden breakthrough), nor does it account for CO_2 dissolution. Another criticism of this simulation technique (Andy Aplin, pers. comm., 2008) is that injected CO_2 will simply migrate via cells with the lowest entry pressure (e.g. chimney lithology or structural crests in this case), thus to a large extent the modeller pre-determines the answer.

4.7 Discussion:

In this chapter we described some of the controlling influences on CO_2 migration below the low relief Nordland Group caprock and the potential for interaction with migration pathways that may allow CO_2 to leak into the overburden. Our modelling highlighted advantages and disadvantages associated with a caprock seal of relatively low relief:

- Large CO_2 columns cannot be established before spillage occurs, resulting in the development of numerous inter-connected accumulations with smaller column heights and consequently a lower buoyancy force acting on the caprock seal,
- More extensive lateral spreading is promoted allowing CO_2 to contact fresh undersaturated brine, thus enhancing the mixing and dissolution processes,
- However, as we demonstrated in Section 4.4, modelling the fill/spill migration process is more unpredictable, particularly if there doubts over the time to depth conversion accuracy (~5 to 10 m discrepancy according to Singh *et al.,* 2010) and the presence of significant overburden heterogeneities has created surface relief distortions during the time-depth conversion process,
- Thin layers or narrow columns of CO_2 at a low saturation may be more difficult to resolve on seismic unless they are extensive enough (or in the case of layers, of sufficient thickness and spaced close enough together to produce a tuned response).

The fill-spill simulations described in this chapter are controlled by surface topography and the reliability of this is dependent on the accuracy of the well log depths and precision of the time-depth conversion process. In previous fill-spill modelling work (Zweigel *et al.,* 2000; Chadwick *et al.,* 2002; Hamborg *et al.,* 2003), the overburden was time-depth converted in simple "layer-cake" fashion, with different velocities applied to each layer. However, as we have described earlier in Chapter 2, the presence of large-scale lithological changes (e.g. tunnel valleys and channels) and anomalous horizons (e.g. shallow gas and authigenic carbonate) will locally distort seismic reflections and 3D surfaces extracted from the seismic inline and crossline data (i.e. gas will increase (pull-down) and carbonate will reduce (pull-up) two-way travel time). It has also been demonstrated that the velocity response for reservoir rocks during CO_2 injection is markedly different, depending on whether the CO_2 has a uniform or patchy saturation distribution and/or whether the rock framework has been dissolved (Vanorio *et al.,* 2010).

Thus, in the Sleipner case where the trap structures are relatively flat and structural dip is low, if these variations are not accounted for by accurate velocity mapping in 3D space before a time-depth conversion is applied, topographic errors will be introduced into the extracted surfaces. These errors will then be introduced into any 3D models constructed with these surfaces, introducing further uncertainty into migration simulations. Many Sleipner fluid flow simulations also assume a single supply point, predominantly vertical transfer (implying a high degree of horizontal and vertical homogeneity) and a flat base for each CO_2 layer. In reality, the Utsira Formation probably contains a few high permeability supply conduits cross-cutting each layer as is evident from Figure 4.2, and possibly a number of smaller, more tortuous conduits between each successive CO_2 layer (Chadwick *et al.,* 2009b; Hermanrud *et al.,* 2010). Migration directions may also be influenced by the presence of heterogeneities and permeability anisotropy (Chadwick and Noy, 2010; Singh *et al.,* 2010), thus the base of each CO_2 accumulation may not be flat, but slightly angled, allowing CO_2 to access much deeper spill points than modelling would suggest (Hamborg *et al.,* 2003). This would certainly help to explain why none of the flow simulations to date have managed to accurately history match the observed plume footprint in its entirety. The filling behaviour of our simulations differs slightly from published seismic for the Sleipner storage site (Arts *et al.,* 2009; Hermanrud *et al.,* 2010), but the history match obtained is reasonably good, except for the S extension to layers 8 and 9; this problem is also reported by Chadwick & Noy (2010) and is only partially resolved by Singh *et al.,* (2010) with their Eclipse® simulations. Our observations suggest that the S extension of layers 8 and 9 may be derived from a secondary pervasive pathway that extends from layer 4 through layers 5, 7, 8 and 9, rather than intra-layer migration to the S within layers 8 and 9. Comparison of the 2002 seismic data (Figure 4.8) against the 2008 seismic data (Figure 4.10), shows that layers 4, 5 and 7 all extend SSW from the injection point location in 2002 and this pattern is repeated for layers 8 and 9 in the 2008 dataset, despite a predominant NNE (i.e. up dip) migration direction for layer 9. To verify whether multiple supply points could be responsible for the S extension, we ran a series of fill-spill analyses on layers 8 and 9 (Figure 4.31), to compare a single supply point against two, with the additional supply point situated 50 m S of the main CO_2 injection location and a 10 m column height varied +/- 1 m over 100 simulations. These results can be compared against the actual seismic data for 2008 (Figure 4.10).

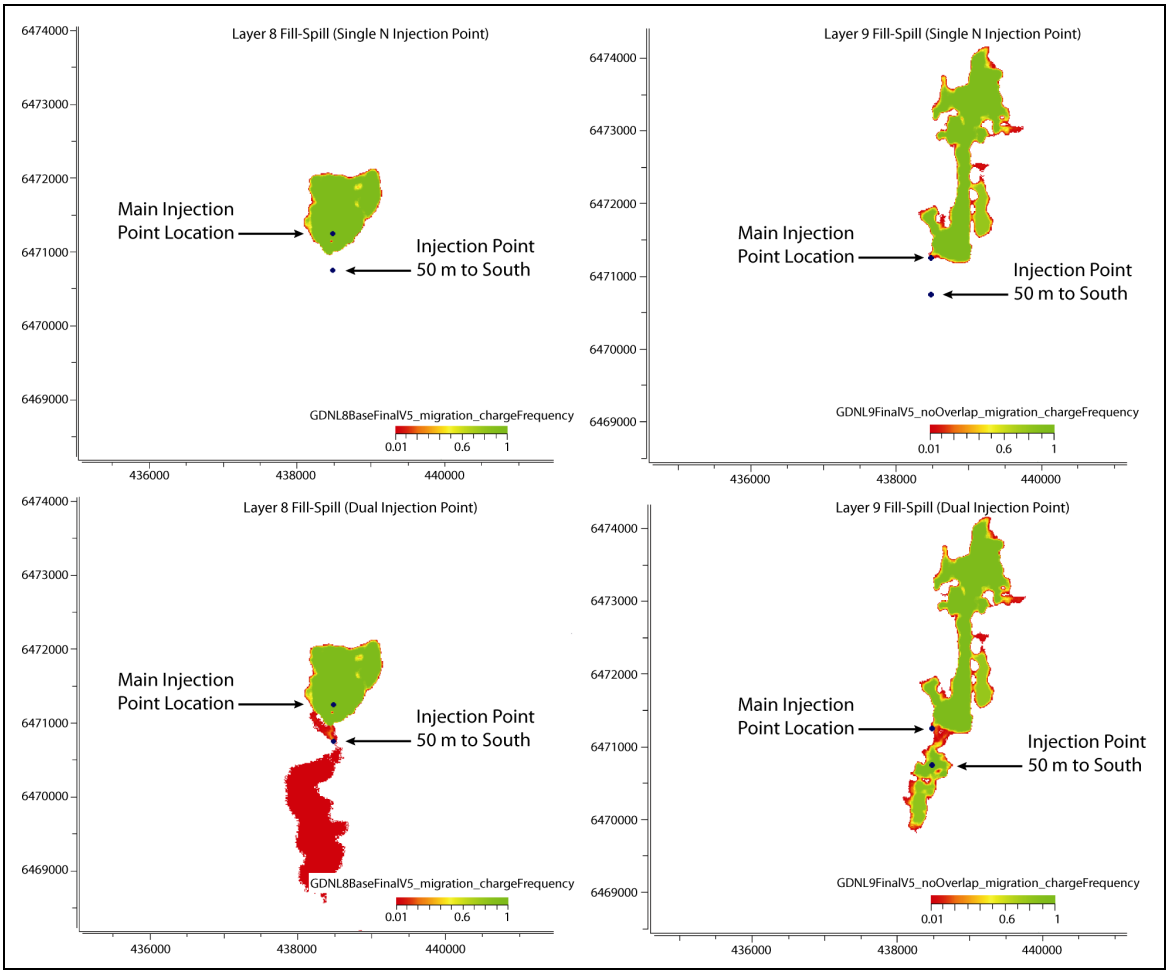

Figure 4.31: MPath® fill-spill analyses performed on layer 8 (left) and layer 9 (right) to assess whether the S extension of plume may result from a secondary CO_2 supply point. Each map was stochastically generated from 100 simulations using a 10 m CO_2 column height varied +/- 1 m.

MPath® allocates the fill-spill injection equally between the two supply points, thus the match to layer 8 with two injection points is overfilling to the S compared to the seismic response. Layer 9 similarly shows a slight overfilling to the S, but overall, the dual supply case is a better match to the 2008 seismic data (Figure 4.10) than the single supply case, thus we propose that future history match simulations for Sleipner should use multiple supply points as a sensitivity, but with a lower supply volume for the S point than used here. Another observation from our simulations was the possibility of W migration occurring in layer 8 from 2008 onwards (Figure 4.26). This was originally expected to be the case if CO_2 did not penetrate the Thick Shale to enter the Sand Wedge to form layer 9 (Zweigel & Hamborg, 2002). With the Complex Model this only occurs for the single supply point case with column heights exceeding ~11 to12 m.

Certain studies (e.g. Harrington *et al.,* 2009, Hermanrud *et al.,* 2010), propose that pathways are being excavated by CO_2 through dissolution, thus porosities and permeabilities should be increasing and capillary entry pressures should be decreasing for the affected lithologies. Other experimental studies (described in Chadwick *et al*., 2008), suggest that shales should become less porous and permeable due to mineralogical changes (e.g. clay mineral alteration and salt precipitation) caused by exposure to CO_2 (and in theory should also develop a higher capillary entry pressure over time). Seismic evidence appears to favour the former explanation (Chadwick *et al.,* 2009b) and combined with a reduction in residual brine saturation as CO_2 dominates the migration network through brine displacement and evaporation processes, a high permeability conduit should develop over time, with most of the CO_2 gradually being advanced to the shallowest point of the containment structure (i.e. barrier 9/caprock). Deeper barriers may gradually become bypassed due to increasingly favourable relative permeability and fluid mobility conditions within the conduits. Consequently, deeper accumulations with a longer residence time should then shrink as they are either drained into the conduit by counter current flow and/or dissolved into the brine underlying each CO_2 layer.

Layer shrinkage represented by dimming of the seismic amplitude response over time has been reported for some of the lower CO_2 layers at Sleipner (Boait *et al.,* 2011) and attributed to real events rather than artefacts created by seismic signal attenuation through overlying layers of CO_2 (Bickle *et al.,* 2007). Yet it is noticeable that between 1999 to 2002 all of the layers continued to grow (Figure 4.8), despite the fact that leakage to overlying layers was occurring simultaneously (Chadwick *et al.*, 2005, 2008; Bickle *et al.,* 2007), contradictory to the (2D) behaviour proposed by Neufeld *et al.,* (2009) and Chadwick & Noy (2010), where a layer is predicted to show retarded development or shrink adjacent to a leakage point. Some of the deeper layers are still growing up to 2008, particularly layer 5, which combined with layer 9 provides almost all of the plume extent visible on plume maps created from stacked layer maps (Hermanrud *et al.,* 2010). This suggests that for certain layers, rather than conditions becoming increasingly favourable to buoyant CO_2 migration to the shallower layers, they are actually becoming more unfavourable and there may be several plausible explanations for this behaviour:

- Flow interference resulting from "bottlenecking" with the injected CO_2 finding it increasingly harder to force its way up the migration network and displace resident brine, resulting in continued backfilling within certain layers. As CO_2 at the periphery of the invaded zone dissolves and forms a denser, less mobile brine phase, this may itself retard the invasion of newly injected CO_2 and slow the rate of lateral spreading (Figure 4.32),
- Multiple supply conduits are visible on the seismic cross-sections (Figure 4.2) and some may be directly feeding the shallowest layer underlying barrier 9/caprock, whilst others may be expanding in number and/or capacity, feeding deeper layers faster than they can leak, so these layers continue to backfill and spread laterally (at least whilst the injected CO_2 supply still continues),
- Salt precipitation, localised mineralogical changes or formation pore collapse in the migration network, increasing the capillary entry pressure for certain layers and resulting in continued backfilling and larger column heights that can be supported,
- Presence of thicker, more heterogeneous shale barriers and/or flow barriers in certain layers, with a higher capillary entry pressure,
- Initial unsteady-state, tending eventually towards steady-state flow behaviour as pathways are eventually established and the system attempts to equilibrate.

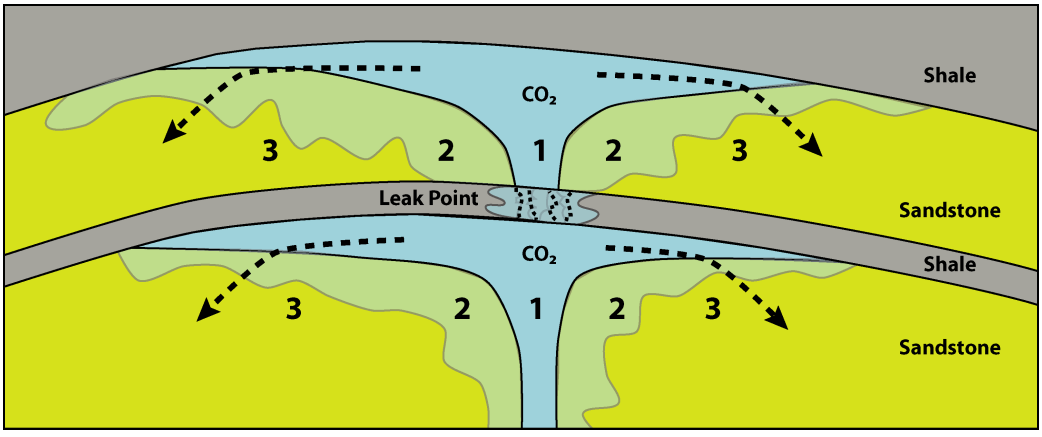

Figure 4.32: Cartoon cross-section depicting upward CO_2 plume migration and lateral spread in thin layers. Zone 1 represents the core of the plume where CO_2 is high density (supercritical), with a high saturation over 80% and negligible residual water saturation. Zone 2 represents a transitional zone where CO_2 is dissolving into the brine, increasing the brine density and reducing its mobility. Zone 3 represents undersaturated, lower density brine not yet contacted by CO_2. This situation results in a complex lateral density gradient, with Zone 2 having the highest density, followed by Zone 3, then Zone 1. Deeper layers with a longer residence time should have a larger Zone 2; this may retard lateral migration and promote higher CO_2 flux vertically upwards within the core (Zone 1) to shallower layers.

The Sleipner simulations described in this chapter required the use of incremental Pthz scalars to prevent the model overfilling (Tables 4.5, 4.7 and 4.9), which suggests the influence of one or more of these mechanisms as CO_2 migrates upwards through the Utsira Formation.

Through the use of 3D computer simulations and 2D models it has been proposed by Lindeberg & Bergmo (2002) and Riaz *et al.,* (2006) that the situation depicted in Figure 4.32 will eventually lead to complete CO_2 dissolution into the brine over thousands of years, enhanced by convective density overturn, particularly after CO_2 injection ceases. Yet, natural analogues provide little evidence for this theoretical "total CO_2 dissolution", even after millions of year's residence time (e.g. Colorado Plateau - Moore *et al.,* 2005 and Southern North Sea – Wilkinson *et al.,* 2009). The 3D simulations performed by Lindeberg & Bergmo (2002) use much higher vertical (kv) permeabilities (i.e. 0.2 to 200 milliDarcies) for the internal barriers within the Utsira Formation than laboratory measurements suggest for the shallower caprock seal at Sleipner (i.e. 0.00075 to 0.0015 milliDarcies – Springer & Lindgren, 2006). Complete dissolution is only possible in the Lindeberg & Bergmo (2002) model at the highest kv of 200 milliDarcies; at the lowest kv of 0.2 milliDarcies, ~80% of the injected CO_2 is still in a free phase after 7,000 years. Additionally, unless the high-density brine with dissolved CO_2 is able to return back down through the same migration conduits the CO_2 ascended, the nascent processes are more likely to involve localised stagnation and diffusion within individual plume layers.

In Chapter 3 and in Section 4.6.2, we described best- and worst-case natural gas leakage scenarios for the Sleipner caprock seal, with capillary entry pressures (Pc) and pore radii converted to CO_2-brine equivalents. For the 12 m column leakage scenario, we used a pore radii range of 920 to 1190 nanometres for a CO_2-brine system and the worst-case Pc for this range of pore radii is between 40 to 50 kPa for an IFT of 30 mNm^{-1} and wettability of 80% as described earlier in this chapter (Section 4.2.1). If this is converted to a mercury-air equivalent using an IFT multiplier of 15.67 (for an IFT of 30 mNm^{-1} and wettability of 80%) this equates to a Pc range of 625 to 825 kPa (as used in our MPath® simulations for the four chimney lithology variants).

Compare these values against the pore radii range of 2.2 to 23.5 nanometres (Bøe & Zweigel, 2001; Kemp *et al.,* 2002 and Table 4.11) and the range of CO_2-brine Pc values of 1700 kPa (1.7 MPa) to 3500 kPa (3.5 MPa) for the Sleipner caprock seal, suggested by Springer & Lindgren (2006) and Harrington *et al.* (2009). If the Pc values are then converted using the same mercury-air equivalent (i.e. 15.67), this gives a Pc equal to 26.63 to 54.84 MPa (refer also to Appendix 4.6). This implies that the Sleipner caprock seal, despite an in-situ porosity of 34 to 36% (Springer & Lindgren, 2006), has very small pore radii and an excessively high capillary entry pressure for such a relatively shallow burial depth (~700 to 800 m TVDSS). In a study of 22 mudstone samples from the North Sea obtained at depths of 1515 to 4781 m (including samples from Block 16/7 adjacent to Sleipner), results from Okiongbo (2011) suggest that pore radii in the range of 2 to 35 nm are associated with porosities in the 3 to 24% range with permeabilities in the 0.05 to 9 nanoDarcy range, yet Springer & Lindgren (2006) report permeabilities in the 750 to 1500 nanoDarcy range for the Sleipner caprock seal, which accords with porosity/permeability relationships based on clay content as illustrated in Figure 4.33 (after Yang & Aplin, 2010).

Sample Depths (m TVDSS and m MD)	**Quartz Content of Sample (%)**	**Total Clay Content of Sample (%)**	**Estimated Pore Radii Based on Krushin (1997) Test (nanometres)**	**Reference Source**	**Notes**
575 to 855 m from Former Top Pliocene FTP) to Top Utsira Formation	15.9 – 29.9	39.75 – 63.1	4 – 15	Bøe & Zweigel (2001)	Based on cuttings analyses from wells 15/9-9 and 15/9-13
From 4 m core sample acquired between 906 to 910 m MD (deviated well)	16.2 – 31.4	50.3 – 70.1	2.2 – 23.5	Kemp et al., (2002)	Based on core samples from well 15/9-A11

Table 4.11: Pore radii estimates calculated by Bøe & Zweigel (2001) and Kemp et al., (2002) for the Sleipner caprock seal using the Krushin (1997) test, based on quartz content of samples. Total clay content is also included for comparison. Note that the Krushin (1997) test was originally developed using well-indurated, non-smectite shale samples of Pre-Cambrian to Jurassic age.

Graphs of clay and calcite percentages for the lower Nordland Shale in the vicinity of the Sleipner CO_2 storage site (i.e. Former Top Pliocene to Top Utsira Formation) are presented in Figure 4.34 (as derived from Bøe & Zweigel, 2001).

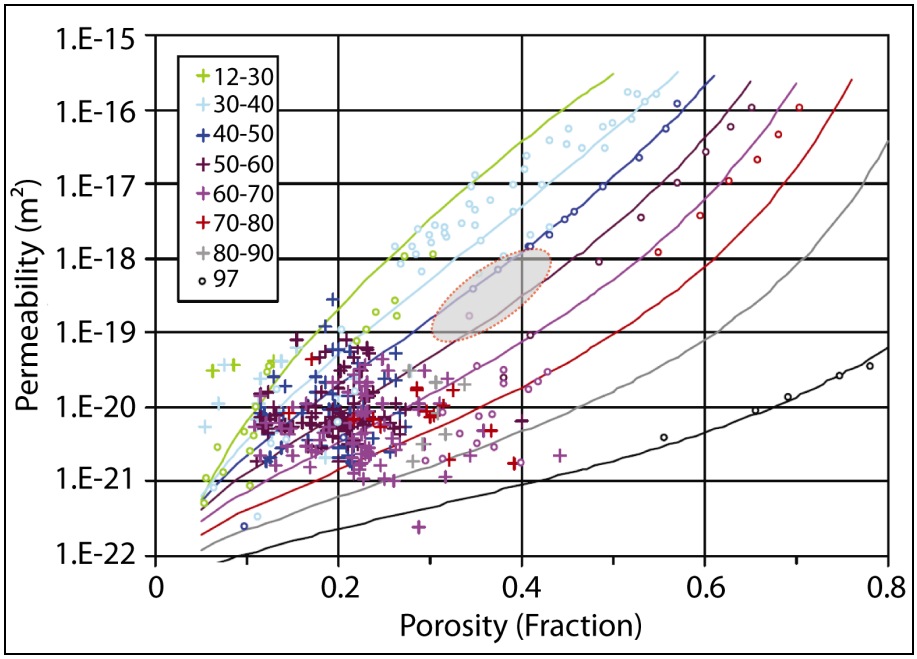

Figure 4.33: Cross-comparisons between measured and modelled permeability using a relationship derived from Yang & Aplin (2010). The curves represent a constrained porosity-permeability relationship based on clay content. The clay content for each band is displayed in the legend. Open circles and crosses are data points of measured or modelled permeability respectively. Each curve represents the relationship at the middle value of clay contents of the band with the same colour (modified from Yang & Aplin, 2010). The grey ellipse covers the range of expected permeability for the Nordland Shale overburden at Sleipner between 575 to 855 m TVDSS, commensurate with measured in-situ porosity and percentage clay content from Bøe & Zweigel (2001) and Springer & Lindgren (2006).

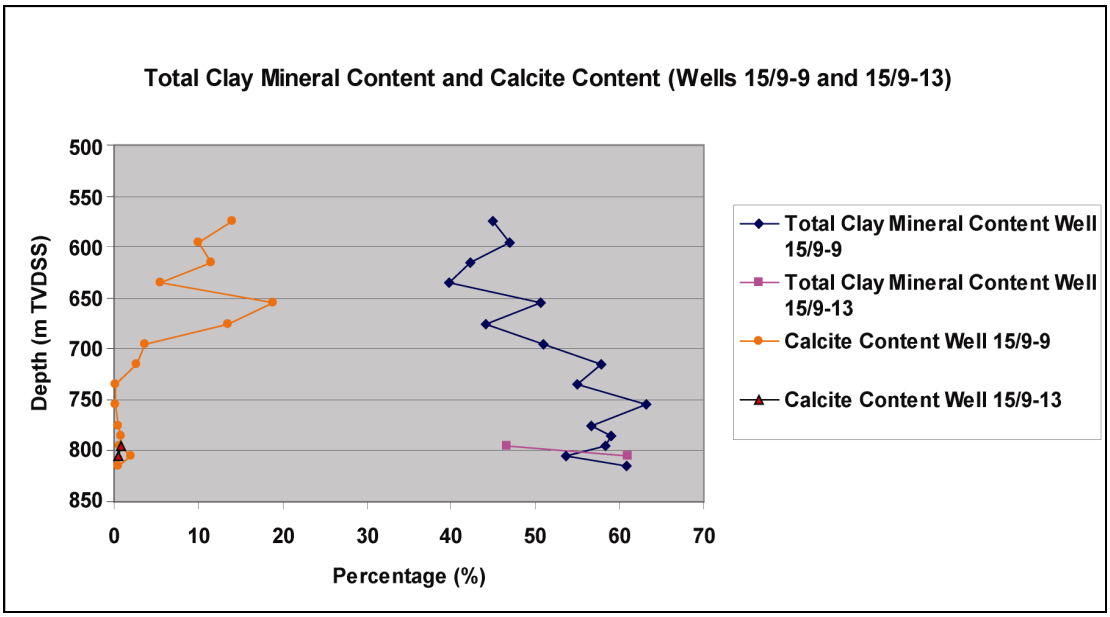

Figure 4.34: Total clay mineral and calcite content for two wells within the vicinity of the Sleipner CO_2 storage site. Note the gradual increase in clay content from 40-60% with depth and the calcite peak between 575 to 675 m TVDSS (data from Bøe & Zweigel, 2001). There are only two data points for well 15/9-13, closest to the CO_2 injection point.

In the two Sleipner studies that derived pore radii for the Sleipner caprock seal (i.e. Bøe & Zweigel, 2001 and Kemp *et al.,* 2002), the Krushin (1997) test based on percentage quartz content was used in both cases (refer to Table 4.11), with the quartz content being obtained from X-ray diffraction (XRD) measurements on cuttings and core samples. We have previously questioned whether this test is entirely appropriate for the reasons described in Chapter 3, Section 3.3.7. Despite other types of more appropriate non-invasive and non-destructive laboratory testing methods being available for characterising shales, such as Computer Tomographic (CT) scanning and Nuclear Magnetic Resonance (NMR) spectroscopy (both described in Clennel *et al.,* 2010), only the former appears to have been used for studying core samples of the Sleipner caprock seal (Springer & Lindgren, 2006). Similarly, for fluid flow tests performed on caprock seal core samples from Sleipner well 15/9-A11 (i.e. Springer & Lindgren, 2006; Harrington *et al.,* 2009), most tests were performed with unreactive nitrogen; only the tests performed by Springer & Lindgren used CO_2 (supercritical and gas phase) and the test performed with CO_2 for the longest period (20 days), exhibited the lowest entry pressure of 1.7 MPa. Experimental methods employed for modelling fluid flow through shales using CO_2-brine systems have shown a high variability (Busch & Müller, 2011) and time-dependent rock-fluid interactions also appear to have a significant effect on fluid flow (Busch *et al.,* 2009). This suggests that the laboratory tests employed to date on Sleipner caprock seal samples may not accurately represent in-situ conditions at the caprock depth (i.e. in terms of being able to derive precise measurements for pore radii and capillary entry pressure to CO_2 under rock-fluid interactive conditions). Errors may also be incorporated during the acquisition, handling, preservation and treatment of shale core samples prior to laboratory testing, particularly if the original pore fluids are lost and/or test pore fluids are not matched correctly to the original pore fluids in terms of salinity and ionic composition or the core has been subjected to cycles of expansion and contraction that may introduce irreversible changes into the sample (Chenevert & Amanullah, 2001; Clennel *et al.,* 2010). It could be argued that the high capillary entry pressures described by Bøe & Zweigel (2001), Kemp *et al.,* (2002), Springer & Lindgren (2006) and Harrington *et al.,* (2009) may result from overconsolidation of the Nordland Shale due to ice loading during glacial episodes (e.g. Pilliterri *et al.,* 2003), but an element of isostatic rebound and trapped gas escape may also be expected upon removal of the ice during inter-glacials (Fichler *et al.*, 2005; Judd & Hovland, 2007).

Previous modelling work has tended to concentrate on history matching and forecasting CO_2 migration within the Utsira Formation (Arts *et al*. 2004, 2008; Bickle *et al.,* 2007; Chadwick *et al*., 2004, 2005, 2008, 2009a; Dubos-Sallée & Rasolofosaon, 2010; Nooner *et al*., 2007), but increasingly the focus has shifted to modelling CO_2 filling behaviour and migration below the caprock seal/barrier 9 (Chadwick *et al*., 2009b, 2010; Chadwick & Noy, 2010; Hermanrud et al., 2010; Singh *et al.,* 2010). Chadwick *et al.,* (2009b) explain that the volume and thickness of the uppermost layer can be more accurately quantified since there are no overlying layers of CO_2 to attenuate the seismic signal and the growth of this layer also provides a reliable time-lapse flux estimate for upward CO_2 migration (Figure 4.35). With the exception of Chadwick & Noy (2010) most of these studies all assume that the caprock seal is laterally homogeneous, it can retain vertical CO_2 columns hundreds of metres in extent and is therefore unlikely to leak. Nevertheless as we have previously described, these assumptions are based on a handful of fluid flow experiments performed on one core sample (15/9-A11) from the Sleipner area (Springer & Lindgren, 2006; Harrington *et al.,* 2009). Earlier experiments performed on shale cuttings samples (Lothe & Zweigel, 1999; Bøe & Zweigel, 2001; Kemp *et al.,* 2002) can only be expected to provide reliable information on mineralogy and very little else (Clennell *et al.,* 2010).

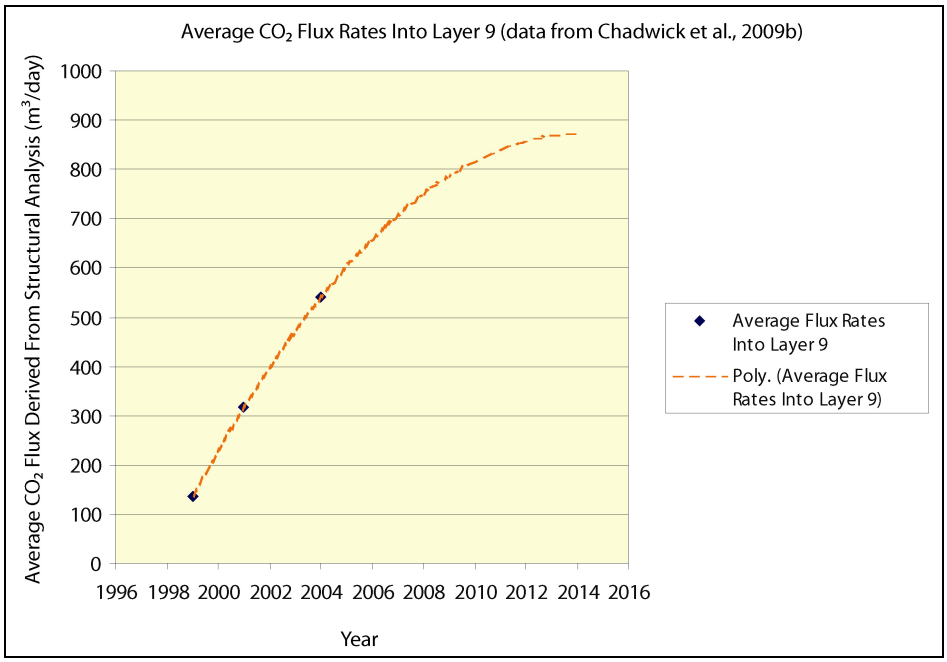

Figure 4.35: Average CO_2 flux rates into layer 9 at Sleipner, based on data derived from a structural analysis of layer thickness (from Chadwick et al., 2009b).

Several modelling studies of Sleipner (e.g. Lindeberg, 1997; Chadwick *et al.,* 2005, 2009a) refer to a CO_2 injection rate of ~1 Mt/year, which is incorrect as Figure 4.36 illustrates (based on official government statistics from Sandmo, 2011). An injection rate of 1 Mt/yr was only achieved briefly in 2001 and the CO_2 injection rate also appears to be gradually declining, as would be expected with declining hydrocarbon production rates and/or an inability to maintain a constant injection rate due to various operational considerations (e.g. maintenance).

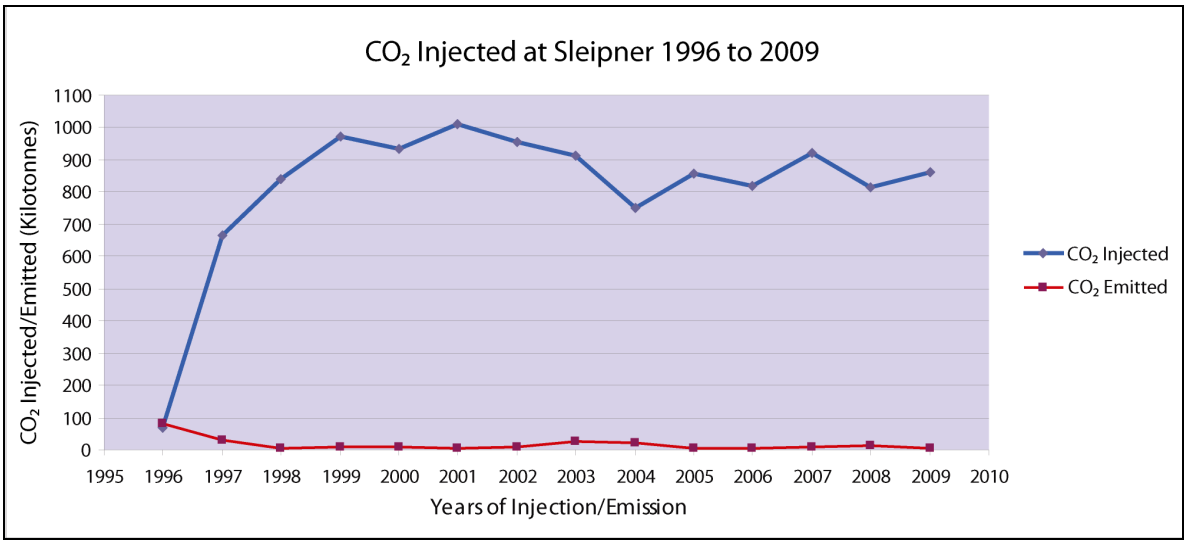

Figure 4.36: Kilotonnes of CO_2 injected into the subsurface and emitted into the atmosphere at Sleipner between 1996 to 2009 (data from Sandmo, 2011).

To illustrate the modelling discrepancies this can cause, consider our simulations that used an average injection rate of 0.84 Mt/year (which is the running average for injection from 1996 to 2009 based on Sandmo, 2011). In our modelling results from the Baseline Calibration illustrated in Table 4.7, the percentage of injected CO_2 in layer 9 appears to be lower than those reported by Chadwick *et al.,* (2009b), both for their amplitude and structural derived volumes as shown below in Table 4.12. For our simulations, an injection rate of 0.84 Mt/year slightly overestimates the injected volumes reported by Sandmo (2011). In the simulations performed by Chadwick *et al.,* (2009b), the injected volumes are all lower than reported by Sandmo (2011) due to the low rates reported for the first three years, thus the results are not comparable as becomes evident from Table 4.13.

Year	Percentage of cumulative CO_2 mass injected in Layer 9 using average CO_2 density of 675 kg/m^3 (after Alnes et al., 2011) and structural derived volume data from Chadwick et al., (2009b)	Percentage of cumulative CO_2 mass injected in Layer 9 using average CO_2 density of 675 kg/m^3 (after Alnes et al., 2011) and amplitude derived volume data from Chadwick et al., (2009b)	Percentage of cumulative CO_2 mass injected in Layer 9 using an average CO_2 density of 675 kg/m^3 (after Alnes et al., 2011) and Baseline Calibration results from Table 4.7
2001	**1.61**	**1.00**	**1.34**
2004	**4.07**	**3.04**	**2.02**
2006	**6.18**	**4.73**	**3.13**

Table 4.12: Comparison of cumulative CO_2 mass in layer 9 as a percentage of injected volume from Chadwick et al., (2009b) and the Baseline Calibration results described in this work (Table 4.7).

Year	Injected CO_2 mass (Mt) used by Chadwick et al., (2009b)	Average injected CO_2 mass (Mt) used in this work (0.84 Mt/yr)	Actual injected CO_2 mass (Mt) reported by Sandmo (2011)
2001	**4.26**	**5.04**	**4.49**
2004	**6.84**	**7.56**	**7.1**
2006	**8.4**	**9.24**	**8.78**

Table 4.13: Comparison of cumulative injected CO_2 mass in the Utsira Formation used for modelling purposes with officially reported mass from Sandmo (2011).

The implications of these discrepancies from a modelling perspective are:

- Larger CO_2 mass in layer 9 implies increased lateral spread and/or higher column heights with increased buoyancy force acting on the caprock seal,
- Smaller CO_2 mass in layer 9 implies reduced lateral spread and/or lower column heights with reduced buoyancy force acting on the caprock seal,
- Inability to accurately history match or forecast CO_2 plume development and to accurately constrain timing of capillary breakthrough in sealing formations.

Of the simulation studies that actually consider CO_2 leakage into the Nordland Overburden from the Utsira Formation, these either involved:

- Upward migration and lateral spreading below the caprock seal with substantial CO_2 dissolution occurring before a leakage pathway is reached (e.g. Lindeberg, 1997). In this study it was not explained why CO_2 had to migrate up to 8 km from the injection location before the leakage point was reached,
- Overburden leakage and migration via synthetically generated sand lobes/channels (Grimstad *et al*., 2009). This model used realistic Utsira Formation parameters and a vertical to horizontal permeability anisotropy of 0.1 (just as we used for the overburden Pth). However, some aspects of this model were not compatible with the Sleipner overburden, such as:
    - Lobes/channels being situated immediately above the caprock (in fact, channels and tunnel valleys at Sleipner are situated between seabed and 600 m TVDSS as we have described in Chapter 2, 150 to 200 m above the caprock),
    - Average channel width/depth at 100m/10m respectively, is an order of magnitude smaller than tunnel valleys and channels observed at Sleipner,
    - Many of the channels have dead-ends and are therefore unconnected pathways that simply trap CO_2, (unlike the inter-connected, multi-level channel and tunnel valleys systems described in Chapter 2),
    - No vertical pathways were included in the model (e.g. faults, fractures or gas chimneys),
    - Overburden sediments are given very low porosities and in some cases zero permeability (shale).
- Molecular diffusion through the caprock seal and overburden versus varying levels of dissolution (Lindeberg & Bergmo, 2002). This study ignores any form of pathway flow into the overburden and assumes a homogeneous shale overburden, which we have shown in Chapter 2 to be an erroneous assumption.

Only one study (i.e. Chadwick & Noy, 2010) actually considered direct buoyancy-driven leakage at Sleipner via a vertical migration pathway, although this study used very low capillary entry pressures (17 to 40 kPa, presumably CO_2-brine values?) and permeabilities (9×10^{-14} m^2) to induce caprock seal leakage (compare this value to the Sleipner region depicted in Figure 4.33).

This is similar to the type of leakage we have investigated during our study, and also appears to be the more likely form of leakage to occur at Sleipner, considering the presence of the overburden structures mapped and described in Chapter 2, which we have incorporated into our simulation models. In comparison, the Chadwick & Noy (2010) model appears to be a simple two layer model and no mention is made of supply versus leakage rates for the simulation, thus their contention that: *"migration into the caprock would significantly retard lateral migration"* cannot be verified and is somewhat at odds with an increasing flux rate into layer 9 (Chadwick *et al.,* 2009b), which may conceal such a leakage indicator, particularly if flux rates into the overburden are low.

Pruess (2008) has performed one of the most useful overburden leakage studies and although not directly related to Sleipner, it provides a very useful indicator of what may happen if CO_2 does migrate into the overburden to form a secondary accumulation and multi-level leakage pathway (Figure 4.37). As our simulations indicate, if leakage and migration occurs via a reactivated relict pathway, there is considerable scope for gas-phase accumulations to develop at several levels within the model such as the channels contained within the Former Top Pliocene (FTP) to Former Intra-Pliocene (FIP) sequences and shallower Quaternary tunnel valleys and channels (Figure 4.30). If this type of situation develops, the Pruess (2008) model suggests that:

- There is a higher potential of maintaining high discharge rates to surface since leakage at moderate rates into a shallow reservoir allows the CO_2 to equilibrate to surrounding temperatures more gradually, thus avoiding cooling effects associated with a rapid migration and expansion from depth directly to surface,
- There is also likely to be a complex interplay between the permeability of the leakage pathway and multi-phase flow conditions occurring therein (i.e. low permeability pathway → higher fluid pressures → three-phase flow and lower fluid mobility → lower flow rates and delayed maximum discharge at surface, whereas a high permeability pathway → two-phase flow and constant discharge), as illustrated in Figure 4.38.

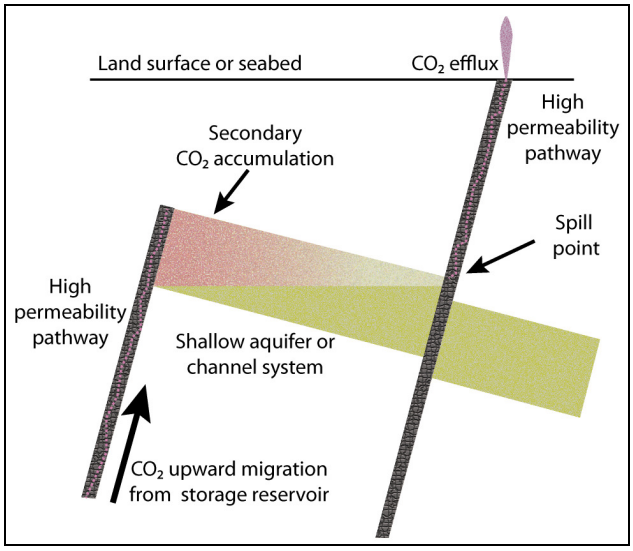

Figure 4.37: Cartoon of multi-stage leakage via shallow accumulation (modified after Pruess, 2008).

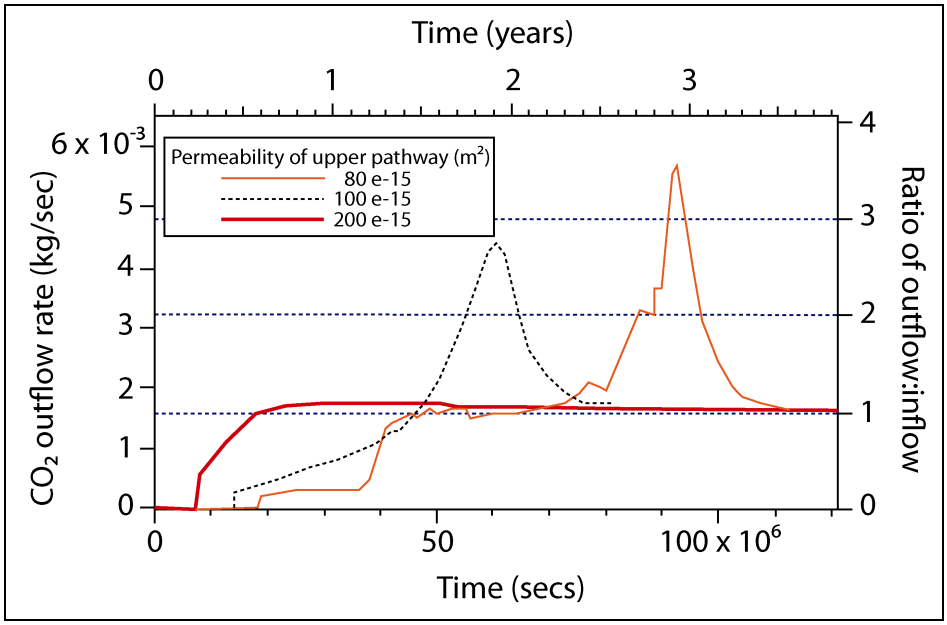

Figure 4.38: Effects of different permeability within the upper pathway illustrated in Figure 4.37. Lower permeability pathways delay the onset of outflow and maximum discharge due to multi-phase flow effects and pressure build-up, but the efflux is more pronounced. The high permeability pathway reaches maximum discharge at an early stage and maintains a constant outflow without developing multi-phase flow conditions (modified after Pruess, 2008).

Cartwright *et al.,* (2007), also describe a direct hydrofracturing mechanism by which CO_2 could also escape from the Utsira Formation if a supercritical to gas phase transition were to occur, although the variable Nordland Group overburden lithology may serve to arrest any fracture tips (e.g. Gudmundsson *et al.,* 2003) at an unconformity or major lithology change such as the Former Intra-Pliocene (FIP).

4.8 Conclusions:

Overall, the results from the MPath® Reservoir Filling simulations were disappointing and this may result from the way in which the models were constructed (e.g. too low a resolution), lack of complexity within certain layers of the model (e.g. Nordland Shales between 350 to 550 m TVDSS), simulation problems with the particular development build of the software used or a combination of these factors. Some of the leakage simulations also showed a tendency to form accumulations below high Pthz lithologies in the overburden and spill, rather than migrate laterally into lithologies with a lower Pthx (e.g. tunnel valleys and channels). This was particularly noticeable in overburden layers that used complex lithology maps with two or more different lithologies (mesh/lithology class overlap conflict?); this behaviour obviously requires further investigation by the software developer. The Reservoir Filling simulations were also unable to supply any quantitative information on dissolution rates, leakage rates or subsequent plume migration behaviour following the termination of injection. Thus, in hindsight it may have been more appropriate to use a geostatistical approach and/or different software for modelling the overburden processes. Although our models were also constrained by the lack of data to the E, the fill-spill and Reservoir Filling simulations we performed did manage to achieve some of the desired objectives and these are summarised as follows:

- For the uncorrected model (Figure 4.11), our fill-spill simulations for layer 9 suggest that CO_2 will fill the four-way dip closure to the NE end of layer 9, spilling further to the N once a 15 to 16 metre CO_2 column has accumulated, gradually filling a series of linked structures, then finally spilling and migrating laterally to the W,
- For the corrected models (Baseline and Complex) with no leakage (Figure 4.12), the structural closure to the NE end of layer 9 will spill to the E following 12 years of CO_2 injection. This assumes that our structural closure height is around 10.363 metres and the topography for the caprock seal is accurate. If this is not the case and the closure is higher or the caprock seal topography has not been mapped accurately enough, then spill may occur later or a different migration scenario may apply,

- For the corrected models (Complex) with leakage (Figures 4.29 and 4.30), the highest structural closure to the NE end of layer 9 fills to a column height of 8.934 metres, then leakage occurs via the palaeo-gas chimney #77 identified and mapped during our seismic interpretation work (described in Chapter 2 and Appendix 2.9). For this scenario to occur, it was necessary to adjust the mercury-air capillary entry pressure for the chimney lithology to 625 kPa at 800 m TVDSS in the Low80 version of the MPath® lithology file (to simulate a CO_2-brine IFT of 30 mNm^{-1} and water wettability reduction to 80% at the caprock seal). If the IFT and water wettability conditions are further reduced over time (e.g. due to the presence of contaminants or if different physical conditions prevail at the caprock than we have used in this work), then it is possible that leakage may occur at smaller column heights under the same capillary entry conditions as described in Chapter 3. Again, all of this assumes that our structural closure height and the topography for the caprock seal are accurate. If this is not the case and the closure is higher or the caprock seal topography has not been mapped accurately enough, then leakage may either not occur, may occur at a different time or a different migration scenario may apply. Notably, leakage could not be achieved before spillage with any of the other three Complex Model variants (i.e. models using the High80, Low100 and High100 lithology files); for these cases the trapped column heights were unable to overcome the (higher) capillary entry pressures for the caprock seal,
- The presence of significant heterogeneities in the overburden (i.e. tunnel valleys, channels, carbonate horizons and natural gas accumulations) can all affect time-depth conversions to a varying degree, creating distortions in the deeper Utsira Formation surfaces (particularly auto-tracked surfaces) extracted from the seismic. These distortions will be transmitted to models and the subsequent simulations performed with them. To address this issue some form of 3D velocity mapping will be required to remove localised pull-up and pull-down artefacts (e.g. using Velocity Manager IMR II®, Vista®, etc.),
- In order to history match the developing CO_2 plume over time, mercury-air capillary entry pressure values for the internal shale barriers in the Utsira Formation required to be increased from 473 to 701 kPa at the early stages of simulation (1999) up to 686 to 1021 kPa for the present day (Table 4.9). We have suggested a range of explanations for this time-dependent “bottlenecking” effect,

- Our observations also suggest that there may be inconsistencies in the laboratory test methods used to calculate capillary entry pressures for a CO_2-brine system. The Nordland Shale core samples tested by Springer & Lindgren (2006) and Harrington *et al.,* (2009), recorded entry pressures in the range 1.6 to 3.5 MPa (equivalent to mercury-air values of 26 to 55 MPa), which is more typical of a shale buried to several thousand metres rather than a shale at ~800 m maximum burial depth. There is lack of documented procedures in the available literature (e.g. Kemp *et al.,* 2002) to confirm whether the core samples acquired from well 15/9-A11 were treated in accordance with recommended handling procedures for shale cores (e.g. Chenevert & Amanullah, 2001; Clennel *et al.,* 2010). There is also no mention of the original pore fluids being retained in these core samples and since no pore fluid samples have been obtained directly from the Utsira Formation (Rochelle & Moore, 2002), it is difficult to see how any reliable information can be obtained from core flooding experiments performed under such circumstances. We have previously addressed the problems associated with the use of shale cuttings samples to derive pore radii and capillary entry pressures in Chapter 2, Section 3.3.7.
- Our modelling results calibrated against the gravity results from Alnes *et al.,* (2011), suggest that the geothermal temperature gradient must be 35.65°C/km from seabed assuming a seabed temperature of 7°C, with a consequent caprock temperature ~32.6°C (above critical point temperature), to history match against the observed plume spatial distribution. Although other research maintains that the caprock seal temperature is below critical point temperature at 29°C (Lindeberg *et al.,* 2009; Chadwick & Noy, 2010), we assert that this would result in a much higher CO_2 density than observed (Figure 4.23) and there is also insufficient local temperature monitoring data available to provide support for such claims of a low caprock temperature(refer also to Chapter 3, Sections 3.3.2 and 3.6.1 for further details),
- With a caprock temperature of ~32. 6°C, the CO_2 density at the caprock matches the 675 kg/m^3 average observed from Sleipner gravity data by Alnes *et al.,* 2011 (Figure 4.23). Given these conditions at the caprock seal our modelling predicts that if CO_2 leaks into the overburden, the supercritical to gas phase transition will occur at ~670 metres TVDSS +/- 20 metres.

- Our simulations have confirmed that migrating CO_2 in layer 9 will contact several of the palaeo-gas migration features previously described in Chapter 2 (and illustrated in Figures 2.30 and 2.31), but in most cases the CO_2 column heights will be too small (~1 to 6 metres) to exert sufficient buoyancy force. We have of course assumed that structural traps must be filled to spill before breach occurs, which is in effect a best case scenario. For the simulations performed, only chimney #77 was observed to leak and the migration was arrested at ~500 m TVDSS at the Former Top Pliocene (FTP) level, where most of the palaeo-gas chimneys terminate (Figure 4.30). The high Pthz of the overlying Nordland Shale lithology prevents further vertical migration into the Pleistocene tunnel valleys and channels unless the Pthz/Pthx anisotropy is reduced from 10/1 to 1.25/1, which in reality would require the presence of additional high permeability pathways or vertical fractures. There is insufficient evidence from this study to support the presence of either mechanism, although some form of developing pathway flow has been agreed by Harrington *et al.,* (2009), Chadwick & Noy, (2010), and Hermanrud *et al.,* (2010) for long-term exposure of the Sleipner caprock seal to CO_2. We have demonstrated what may happen if such pathways are open to the extent that they allow upward CO_2 migration to occur.
- Finally we conclude that the overburden heterogeneity is significant but that the possible storage response is difficult to quantify. The presence of palaeo-gas migration pathways and high permeability channels and tunnel valleys may become potential migration routes or provide secondary storage containment for CO_2 as the plume continues to spread laterally over the coming decades. However, the transitional phase conditions of the plume at or near the caprock require accurate pressure and temperature modelling. The absence of in-situ observational pressure and temperature data introduces significant uncertainty to model outcomes with respect to CO_2 density and column height estimates (Alnes *et al.,* 2011). A first approximation can be arrived at by assuming that any potential pathway response is similar to the thick shale response, which is what we have attempted here. If the CO_2 plume encounters an open migration pathway, the prevailing CO_2 density in addition to the CO_2-brine IFT and wettability, will be critical factors in determining whether the structure breaches vertically or spills laterally.

Chapter 5:
Summary, Conclusions and Future Work

"When a thing was in my reach, I no longer wanted it; my delight lay in the desire. Everything, which my mind could consistently wish for, was attainable, as with all the ambitions of all sane men, and when a desire gained head, I used to strive until I had just to open my hand and take it. Then I would turn away, content that it had been within my strength."

Extract from the Seven Pillars of Wisdom (T.E. Lawrence, 1888 - 1935)

"Just as the sand made everything round,
Just as the tar seeps up from the ground,
Bitter dancer, ever turning,
So was the day you came to town,
You took a room and you settled in,
Washed off the chalk from your weathered skin,
Daylight sleeper, bloody reaper,
You took a room and you settled in,
I should have known one day you would come,
All of us walk so blind in the sun,
Midnight feeder, beggar, pleader,
I should have known one day you would come,
Tell me again, my only son?
Tell me again, what have you done?"

Extract from "The Plains/Bitter Dancer" (Fleet Foxes),
© Bella Union

5.1 Summary:

5.1.1 Debating Climate Change and Carbon Storage:

In Chapter 1 we outlined the ongoing debate between those who believe elevated levels of CO_2 are responsible for climate change and those who are sceptical of such a connection. Recently the Berkeley Earth Project (an independent statistical study set-up in 2010 to investigate the claims of both parties) published its preliminary findings on land-based temperatures (Berkeley Earth Surface Temperature, 2011) and intends to publish its research into changing ocean temperatures in the near future. Hopefully this research will provide a fresh insight into the evidence for or against global climate change resulting from anthropogenic CO_2 emissions from an unbiased viewpoint.

The various methods through which carbon capture and storage (CCS) can be achieved were also described, including CO_2 storage in depleted hydrocarbon fields and saline aquifers such as the Utsira Formation underlying the Sleipner development (the main subject of this thesis). Assuming that there is a CO_2 problem that needs to be addressed, it appears that thousands of CCS projects on the scale of Sleipner or larger will be required in the very near future to reduce current CO_2 emissions (GCCSI, 2011), but is this really a feasible or realistic proposition in economic and technical terms? Aside from the debate on climate change, there is also a related debate on the viability of CCS as a panacea for rising atmospheric CO_2 levels (Table 5.1); amply demonstrated by the recent cancellation of the Longannet-Goldeneye CCS project by the UK Government (Gersmann & Harvey, 2011), and marked public resistance to onshore-based CCS projects in Germany and the Netherlands (Tindale, 2011).

For CCS projects to be feasible, it seems there must be strong financial drivers. The environmental taxation savings enjoyed by the Sleipner and Snøhvit projects in Norway and the revenue benefits derived from CO_2-enhanced oil recovery at the Weyburn-Midale project in Canada being prime examples. As illustrated in Chapter 1 (Figure 1.1), the largest emitters of anthropogenic CO_2 are hydrocarbon-burning power stations (primarily coal) and cement production, yet at present there are no major projects in operation that offer an economically viable CO_2 source to sink solution for such emissions. Imposition of a carbon or energy tax to fund such projects (partly or wholly) would be deeply unpopular, given the current global financial crisis.

Arguments for CO_2 Storage:	Arguments against CO_2 Storage:
• Reduces emissions to environment and helps to reduce the effects of CO_2-induced climate change; • Mitigates environmental taxes (Norway); • Complies with international regulations to reduce greenhouse gas emissions; • Creates new CCS-related jobs and also additional jobs for research, design, technical, professional, construction and maintenance sectors for public and private sector (i.e. government, academia and private companies); • Extends the life of existing hydrocarbon production and processing facilities, preserving existing jobs associated with same in hydrocarbon sector and defers platform abandonment costs which is an attractive benefit for operators, especially if they can obtain this type of benefit from a minimum expenditure perspective (e.g. well recompletion and re-use of existing facilities as envisaged for the Longannet/Goldeneye project); • Prospect of economic and technical spin-offs from CCS research that can be used in other applications (e.g. better understanding of CO_2 fluid flow processes, rock-fluid interactions, phase transitions and fluid mixing for CO_2-EOR operations, development of better seismic processing and monitoring techniques or more efficient industrial absorbents and membrane materials that can be used for CO_2-hydrocarbon separation and other CO_2-related industrial processes); • May attract Clean Development Mechanism (CDM) investment into other developing countries that have little or no storage capacity or the technical capabilities to implement storage.	• Still have CO_2 emissions from injection compressors, geophysical survey vessels and energy consumed in capture, dehydration and scrubbing process in addition to carbon footprint from activities described at left; • For schemes where CO_2 is captured from hydrocarbons (e.g. EOR at Weyburn-Midale, Sleipner, Snøhvit and In Salah), the produced hydrocarbons are still being used for fuel or consumed in some shape or form, so the end result is still grossly in favour of greenhouse gas emissions; • Schemes are not being implemented fast enough since there are poor economic drivers - no useful end product or economically favourable outcome - simply a hazardous waste disposal issue without the upside option of recycling and re-use; • Diverts investment and focus away from other critical clean energy research with a useful end-product (e.g. development of fusion reactors, hydrogen fuel cells, microbial-produced fuels); • Risks and uncertainties associated with leakage. Future time bomb? Those who planned and implemented CCS schemes may be retired or dead when leakage occurs, so they will not be around to answer for the consequences of failure; • Someone has to pay for the capture, transport and storage process. Governments, industrial concerns and ultimately all consumers by direct or indirect taxation; • Not all the pore space can be utilised for storage and sites will ultimately be filled-up, requiring additional infrastructure and a continual search for new capacity.

Table 5.1: Arguments for and against CO_2 storage (modified after Lenstra & van Engelenburg, 2003).

5.1.2 Storage Viability and Liability Issues:

Focussing on the reported statistics (GCCSI, 2011) for CCS projects already in operation is also an illuminating experience (Table 5.2):

Name	**Location**	**Capture Type**	**Storage Type**	**Date of Operational Start-Up**	**CO_2 Volume (Mt/year)**	***Cumulative CO_2 Volume Stored (Mt)**
Val Verde Natural Gas Plant	USA	Pre-combustion (gas processing)	EOR	1972	1.3	50.7
Enid Fertiliser Plant	USA	Pre-combustion (fertiliser)	EOR	1982	0.7	20.3
Shute Creek Gas Processing Facility	USA	Pre-combustion (gas processing)	EOR	1986	7	175
Sleipner CO_2 Storage	Norway	Pre-combustion (gas processing)	Saline Aquifer Storage	1996	1	15
Great Plains Synfuel Plant and Weyburn-Midale Project	USA/Canada	Pre-combustion (synfuels)	EOR with MMV	2000	3	33
In Salah CO_2 Storage	Algeria	Pre-combustion (gas processing)	Saline Aquifer Storage	2004	1	7
Snøhvit CO_2 Storage	Norway	Pre-combustion (gas processing)	Saline Aquifer Storage	2008	0.7	2.1
Century Plant	USA	Pre-combustion (gas processing)	EOR	2010	5	5
Total CO_2 stored between 1972-2011 (Mt)						**308.1**

*Table 5.2: Operational CO_2 storage projects up to 2011. *Note that the cumulatives are simply calculated from years of operation multiplied by the reported CO_2 volumes per year (modified from GCCSI, 2011).*

As Table 5.2 demonstrates, all of these CCS projects are involved with some form of hydrocarbon production operation, so in effect they are storing nothing, since it was already stored in the sub-surface; there is also the issue of the produced hydrocarbons that will add considerably to CO_2 emissions. These projects are merely a recycling and disposal operation, albeit not emitting as much CO_2 to the atmosphere as they would under normal circumstances. It is also worth noting the following points:

- As we have already described in Chapter 4, Section 4.7 (Figure 4.36), injection statistics have a tendency to be rounded-up and it is also unlikely that CO_2 is being injected at a constant rate. Thus, stored volumes are probably not as high as Table 5.2 might suggest,
- Some of the other projects not listed in Table 5.2 that still are, or have been operational during this period (e.g. Otway in Australia, Ketzin in Germany, Nagaoka in Japan and Frio in the USA, all described in GCCSI, 2011) are pilot experimental projects injecting relatively small amounts of CO_2 into the sub-surface over a short time period of a few years (Figure 5.1),
- The highest contributors in Table 5.2 are EOR projects (mainly in the USA). Some of this CO_2 has been extracted and supplied from natural volcanic storage sites such as the Colorado Plateau, thus it is not contributing to the reduction of anthropogenic emissions; quite the opposite in fact (Dooley *et al.,* 2010). Additionally, a proportion of this injected CO_2 will eventually be produced back to surface with the hydrocarbons the CO_2 was intended to mobilise. Some CO_2 may be lost to the atmosphere during the separation and recycling process and there is also a high risk of "double accounting" for any re-injected volumes,
- There are only three saline aquifer storage projects (highlighted in yellow in Table 5.2) and they contribute about 7.8% of the cumulative stored CO_2 volume,
- None of the projects listed in Table 5.2 have tackled the real issue of capturing and storing large quantities of power station CO_2 emissions or removing existing CO_2 from the atmosphere and oceans,
- Finally, if we consider that ~900 Gt (i.e. ~900,000 Mt) of CO_2 has been emitted globally between 1972-2010 (data source Boden *et al.,* 2010), then to date these projects have stored ~0.00034% of these emissions, which is fairly insignificant.

The GCCSI (2011), list 74 large-scale injection projects either in stages of operation (8), construction (6) or planning (60) during 2011, but just how many of these planned projects that will actually reach the operational stage is open to question.

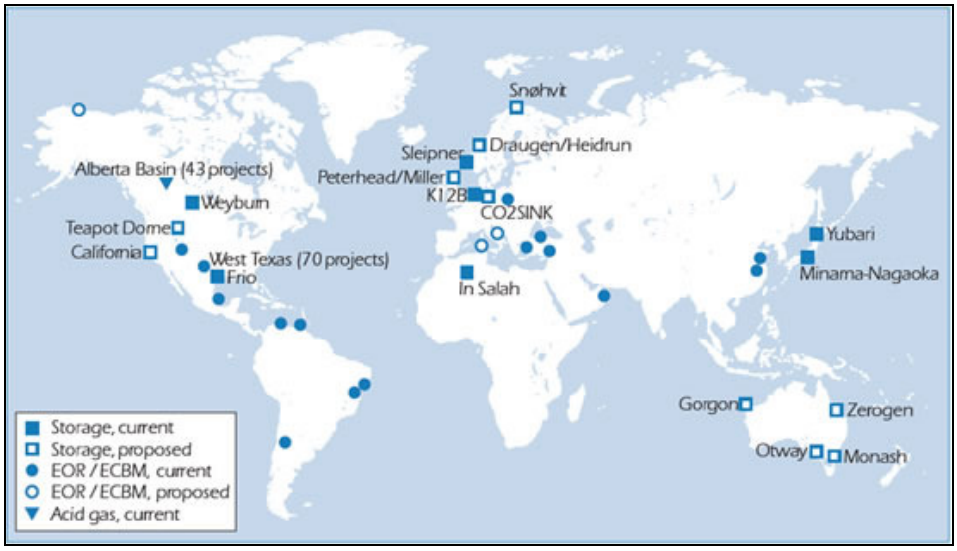

Figure 5.1: Current status of global CCS projects (IEA, 2011)

Shifting the focus to existing saline aquifer projects, many like Sleipner are now approaching the mature or end of life stage (Sleipner was planned for 20 years of injection from 1996-2016 according to Zweigel *et al.,* 2004a) and during the course of CO_2 injection operations many of these projects have been unable to maintain a continuous injection rate for the following reasons:

- Sleipner encountered early injection problems caused by formation collapse and sand production in the near wellbore region and required to be recompleted with finer sand screens (Hansen *et al.,* 2005 also refer to Figure 4.36 and Appendix 5.1). The Tordis incident (Kvalheim, 2009) also raised further concerns about the integrity of the Utsira Formation for CO_2 storage (refer to Appendix 5.2),
- In Salah suffered a minor CO_2 leakage problem from a legacy well that was in contact with an open fracture system containing CO_2 (Ringrose *et al.,* 2009) and is currently the subject of an ongoing geomechanical modelling study to investigate whether CO_2 injection has created or reactivated fractures in the overburden, allowing CO_2 gas chimneys to develop (David Roberts, pers. comm. and presentation at the EAGE Conference, Barcelona 2010),

- Snøhvit has been unable to maintain a continuous injection rate, since there is a high risk that the formation and caprock seal may be fractured by the end of 2011 (Tore Torp, presentation at the EAGE Conference, Barcelona 2010). The operators are currently considering the use of an alternative storage formation (refer to Appendix 5.3 for further details).

It should be stated that these are essentially prototype projects and most prototypes expect to encounter problems at some stage, and although most of the materials and techniques employed for CCS have been developed from existing and field-proven hydrocarbon industry techniques, there are clearly still some problems to be resolved in the translation and application of these techniques to an emergent CCS industry.

As the world's first application of CO_2 storage in a saline aquifer, the Sleipner project has come under intense scrutiny and is the subject of hundreds of scientific papers and technical reports (many of which have been described and referenced in this thesis). Due to the fact that Sleipner is also the longest running storage project (since 1996) and still shows no signs of leakage, the site operators and others associated with the original Saline Aquifer CO_2 Storage (SACS) project consortium, tend to promote this site with an element of hubris as a "best practice" example of how to develop a CO_2 storage complex (e.g. Chadwick *et al.,* 2008). As a result, many subsequent CCS projects have used Sleipner as a role model. Yet, as we have demonstrated during this thesis, this is a somewhat uncertain foundation on which to rest the future hopes and aspirations of the CCS industry. Considering the publicity and kudos it has received as a first class storage site, if Sleipner does eventually leak over the next few decades, this may have a detrimental impact on public confidence towards the CCS concept and may also jeopardise the financing and implementation of future CCS projects.

Another consequence of site failure relates to liability for any CO_2 leakage. Clearly the operators of a site must assume full responsibility if leakage occurs during the operational phase, but if the site leaks during the post-injection phase after the transfer of responsibility has occurred (i.e. ongoing site monitoring has passed into third party control), there is also the possibility that the original operators may be subjected to the terms of Article 18(7) of the EU Directive 2009/31/EC, where it states:

"In cases where there has been fault on the part of the operator, including cases of deficient data, concealment of relevant information, negligence, wilful deceit or a failure to exercise due diligence, the competent authority shall recover from the former operator the costs incurred after the transfer of responsibility has taken place. Without prejudice to Article 20, there shall be no further recovery of costs after the transfer of responsibility."

Again, because Sleipner is a prototype project established in 1996, 13 years prior to this EU Directive coming into force, there may be difficulty establishing what exactly constitutes negligence or simply a lack of regulatory guidance when the site was established. Additionally, although Norway has formally adopted the EU guidelines it is not a member state of the EU.

5.1.3 Site Characterisation at Sleipner:

In Chapter 2 we described the regional geology, stratigraphy and our seismic interpretation of the Sleipner area and stressed the importance of performing a rigorous site characterisation, not just for the storage formation to determine storage capacity and injectivity, but also for the overburden sequences to determine seal capacity and site integrity. Site characterisation and screening are now viewed as essential pre-requisites for CO_2 storage site selection (DNV, 2010) and hopefully this thesis has accentuated some of the deficiencies in the procedures adopted at Sleipner.

Heggland (1997) was the first to describe the presence and significance of high-amplitude anomalies, gas chimneys and seabed pockmarks in the overburden at Sleipner and infer a spatial (fault) connection with deeper (Hordaland Group) structures and underlying hydrocarbon reservoirs. Subsequent studies by Lothe & Zweigel (1999), Zweigel *et al*., (2000) and Borgos *et al.,* (2002) also considered the risk of CO_2 migration via these potential migration pathways into the overburden. However, by the time these latter studies were performed, CO_2 had already reached and was migrating below the caprock seal, after being detected by the first post-injection survey acquired in 1999 (Chadwick *et al.,* 2008). The timing of these events is significant in the context of the site characterisation and development process (refer to Appendix 5.1 for details) since they raise some interesting questions:

- The paper by Heggland (1997) was originally submitted in 1994 (the same year the baseline seismic survey was also acquired) and presented substantial evidence of recent fluid migration from the Hordaland Formation to the seabed within the Sleipner development area. Sleipner also lies within an area known for shallow gas accumulations and seabed pockmarks (Figure 3.2 after Judd & Hovland, 2007), suggesting that any CO_2 storage sites located in this area should be monitored more frequently during the early stages of injection, yet no subsequent seismic monitoring survey was performed at Sleipner until 1999?
- Why was an Utsira Formation core sample from the CO_2 storage site area only acquired for testing immediately before CO_2 injection operations started in 1996 (Lothe & Zweigel 1999; Pearce *et al.,* 2000)?
- Considering the overburden complexity we have described in Chapter 2 (using the same baseline 1994 seismic data), why were no overburden core samples acquired from the proposed CO_2 storage site and tested for geomechanical, palynological and fluid flow properties until 2002 onwards (Kemp *et al*., 2002; Pilliterri *et al*., 2003; Zweigel & Heill, 2003; Head *et al.,* 2004; Springer & Lindgren, 2006)?
- Why was the CO_2 injection well not cored through the caprock or reservoir interval during drilling operations in line with conventional hydrocarbon development practices?
- Why was no detailed overburden mapping and analysis (such as we describe in Chapter 2) performed as part of the site characterisation process prior to site development?

Two vertical subsea well options were originally planned in conjunction with a comprehensive logging and sampling program, but these options were subsequently rejected on cost grounds. Additionally, no monitoring wells could be drilled from the Sleipner A platform, since this was purported to interfere with daily hydrocarbon production operations (Carlsen *et al.,* 2001). This would suggest that a prime opportunity to obtain in-situ, time-lapse monitoring information on CO_2 injection and migration processes was compromised on the basis of economic drivers (i.e. incentives to minimise the cost of CO_2 site development and maximise profits by avoiding potential disruption to hydrocarbon extraction activities).

In Chapters 2 and 3 we performed a detailed examination of sub-surface structures observed on seismic and mapped between the Miocene Hordaland Group sedimentary sequences to the present day seabed at Sleipner. We also highlighted the importance of these structures from a CO_2 storage perspective, suggesting that collectively they could provide a connected migration pathway for CO_2 from storage depths to the seabed and/or act as a dispersal (dissolution) network and secondary storage containment. Previous research has also explored the importance of gas and fluid injection structures and gas chimneys as seal bypass mechanisms, particularly in a Norwegian North Sea context (e.g. Heggland, 1997; Berndt *et al.,* 2003; Løseth *et al.,* 2003, 2009; Cartwright *et al.,* 2007; Judd & Hovland, 2007). Most of this research was directed primarily at hydrocarbon migration processes, whereas our approach considers the wider implications for long-term CO_2 storage and site integrity (Appendix 1.1). Sæther *et al.,* (2008) also describe the requirement to map discrete leakage pathways as part of the CO_2 storage site characterisation process and incorporate these features into computer models and simulations, but the results of this research are intended for a generic application rather than specifically targeted at Sleipner and also consider each mechanism as a discrete entity rather than as part of an integrated system. Similarly, Bauer & Fichler, (2002) and Fichler *et al.,* (2005), describe the presence of shallow gas anomalies and glacial tunnel valleys in the overburden and seabed pockmarks around the Sleipner area and propose that the onset of glaciation trapped migrating natural gas in clathrate form, then released it during inter-glacials, but again, no connection is made between the ability of CO_2 to re-use these relict pathways and migrate out of the storage containment area at Sleipner. Aside from hydraulic fractures that may be created by melting and expanding clathrates, evidence from analogous glacial tunnel valleys and channels exposed onshore (e.g. Le Heron *et al.,* 2005; Le Heron & Etienne, 2005) suggests that the hydraulic forces and sub-glacial sediment deformation generated by ice-loading and shearing can be considerable, with the influence zone extending tens of metres into sediments underlying the ice base. The effects of ice-loading were noted by Pillitteri *et al.,* (2003) during their rock mechanical tests performed on Sleipner caprock core samples (acquired at ~785 metres TVDSS in well 15/9-A11), yet the nearest glacial sedimentary sequences are ~100 to 400 metres shallower (Figures 2.11 to 2.13).

We also described our mapping of the glacial tunnel valley and channel systems in Chapter 2 and our correlation with well logs from the Sleipner area demonstrates that these features contain a substantial sand component in the middle to lower channel sequences (Figures 2.6 to 2.9). In accordance with similar work performed in adjacent North Sea areas on tunnel valleys (i.e. Huuse & Lykke-Andersen, 2000; Lonergan *et al.*, 2006; Graham *et al.,* 2007; Stewart *et al.,* 2007), we also observe multiple phases of cut and fill and cross-cutting behaviour, resulting in the development of inter-connected branches at different stratigraphic levels. This has a number of implications for the distribution of CO_2 (which will be a gas phase at the depth of these systems) if it eventually migrates into such a channel network:

- Tunnel valley and channel intersection points will allow CO_2 to access multiple channel networks and contact additional volumes of under saturated brine. This should prevent the development of large CO_2 columns and provide secondary containment and further dissolution potential,
- If CO_2 does enter and manage to migrate from deeper to shallower tunnel valley and channel sequences, it may eventually reach the seabed,
- The tunnel valley and channel sequences are predominantly aligned ENE to WSW, Sleipner is also relatively close (~25 to 30 km) to the UK/Norway median line and North Sea tunnel valley networks can extend for hundreds of kilometres, thus there is a slim possibility that CO_2 could be transported across this boundary, creating an international liability issue (sub-surface trespass). The likelihood of this scenario occurring would have to be assessed by performing further mapping to the W and/or integrating adjacent studies to determine network connectivity and orientation, since our present data does not extend to the UK/Norway median line.

The presence of seismic anomalies in the Nordland Group overburden has generated wide debate over whether these anomalies represent multiple artefacts (Zweigel *et al.,* 2000), shallow gas accumulations (Heggland, 1997; Bauer & Fichler, 2002), diagenetic carbonate deposits (Løseth *et al.,* 2009) or a combination of all three. We tend to favour the latter explanation based on our observations of mixed seismic character (e.g. polarity reversal, pull-up and pull-down effects) as described and illustrated in Chapter 2.

Our examination of drilling reports and well logs from the Sleipner area (Figures 2.6 to 2.9 and Appendices 2.1 to 2.7) indicates the presence of gas and carbonate-rich lithologies in the overburden, although in the absence of detailed well logs and gas analysis data, it was not possible to make the distinction between biogenic gas generated in-situ and thermogenic gas generated at depth that may have migrated and leaked during the geological past through the Utsira Formation and into the overburden. The fact that there are no significant gas accumulations trapped in the Utsira Formation (despite the presence of extensive hydrocarbon reservoirs underlying the Utsira Formation at depth), either suggests that gas has never migrated into the Utsira Formation or else it has escaped over geological time. Either way, the efficacy of the Nordland Group overburden at Sleipner as a geological seal is unproven.

The most significant overburden seismic anomalies are contained within four zones disposed between ~400 to 800 metres TVDSS (Figures 2.11 to 2.13). The majority of these amplitude anomalies appear to be either hard (diagenetic carbonate?) or variable hard/soft (diagenetic carbonate and free gas mixture?), with an associated chimney or vertical zone of acoustic disturbance either directly underlying or slightly offset. In many cases, we have demonstrated a spatial association with the underlying polygonal faults and mud volcanoes of the Hordaland Group underlying the Utsira Formation (e.g. Figure 2.27). Within our local study area, most of the chimney structures terminate at the Former Top Pliocene (FTP) level, the only exception being chimney #110 (situated ~1.2 km W of the injection point location), which extends to seabed (Figure 2.29). Our regional study area also contains an extensive chimney #35 extending from the Hordaland Group to seabed, terminating at a large 500 m^2 seabed crater, situated 6.5 km SW of the CO_2 injection point (Figure 2.11). The reason for this partition between two levels of migration is uncertain, but it may be related to the onset of glaciation during the early Pleistocene ~2 Ma, subsequent glacial and inter-glacial cycles (e.g. the hydrate formation and disassociation mechanism proposed by Fichler *et al.,* 2005) and the hydraulic effects of ice loading and unloading processes we describe within Section 2.8. Regularity of gas supply is clearly another issue and perhaps in the case of the two seabed features described above, this supply was more continuous, the buoyancy force was stronger and thus pathways were conserved.

Aside from the regularity of seabed and shallow multiples (visible below the tunnel valley sequences in Figures 2.11 to 2.13), inter-bed multiples such as those observed within the Utsira Formation are more difficult to distinguish, hence our inability to extract any of the internal shale surface within the Utsira Formation deeper than barrier 8 for our modelling purposes (Chapter 4). Close correlation was also required between well logs and seismic signal strength to avoid picking "ghost" tunnel valleys and channels multiple reflections in the deeper section. For stacked anomalies that may represent multiples of shallower events such as those described by Zweigel *et al.,* (2000), we checked for loss of signal strength and coincidence rather than offset to clarify whether the deeper events were indeed real or multiple artefacts (e.g. chimney #28 and anomaly #A16 on Figure 2.13). A preferential alignment of anomalies along linear trends was also noted at various stratigraphic levels within our baseline (pre-CO_2 injection) seismic data (e.g. Figure 2.22) and subsequently compared against the CO_2 plume evolution from published data (Figure 4.8), suggesting that development of both the original anomalies and the current CO_2 plume are controlled to some degree (i.e. orientation and lateral extent) by these linear structural features, which may represent pervasive faults or fracture zones.

5.1.4 Potential Reuse of Relict Migration Pathways by Injected CO_2:

In Chapters 2 and 3 we established that prior to CO_2 injection at Sleipner there was compelling evidence for natural gas migration over geological time through the sedimentary sequences of the Hordaland Group, Utsira Formation and Nordland Group overburden to the seabed via an interconnected complex of structural and stratigraphic pathways and fluid migration structures. During the subsequent stages of this research we considered the conditions required to allow natural gas leakage through these sequences and also the likelihood of injected CO_2 reusing these palaeo-gas migration pathways (Chapters 3 and 4). This required us to:

- Compare the conditions required for natural gas leakage (assumed to be predominantly methane for the purposes of this research) versus CO_2 leakage using a range of different pressure, temperature and capillary property conditions commensurate with observed and/or estimated Sleipner conditions,

- Establish the prevailing petrophysical and thermodynamic conditions at the Sleipner CO_2 storage site,
- Construct computer models of the Sleipner CO_2 storage site populated with this petrophysical and thermodynamic data, including the structural and stratigraphic complexity described in Chapter 1,
- Perform stochastic fill-spill and history matching simulations to determine the likelihood of CO_2 leakage.

It is well documented that supercritical CO_2 under typical storage conditions (i.e. depths exceeding ~800 metres TVDSS) requires a better capillary seal than methane (CH_4), due primarily to the capillary properties of supercritical CO_2 (Hildenbrand *et al.,* 2004; Li *et al.,* 2006; Chalbaud *et al.,* 2006, 2009; Chiquet *et al.,* 2007a, 2007b; Shah *et al.,* 2008; Fleury *et al.,* 2010). If the storage pressure and temperature conditions are reduced below critical point conditions (7.4 MPa and 31.1°C, as illustrated in Figure 3.7) such that CO_2 experiences a phase transition from supercritical to gas phase, the capillary properties of CO_2 and CH_4 tend towards similarity in terms of their density, IFT and wettability properties (Hildenbrand *et al.,* 2004; Naylor *et al.,* 2011a). The main difference is that CH_4 will always be a gas under typical storage conditions whereas CO_2 may be a supercritical fluid or a gas, depending on the geothermal gradient and the pressure and temperature conditions prevailing at the caprock seal (as illustrated in Figures 3.9 and 3.10), thus any uncertainties relating to pressure and temperature conditions at the caprock seal will propagate further uncertainties about CO_2 phase, density, viscosity and capillary conditions that prevail there. As Figure 5.2 illustrates, if supercritical CO_2 leaks into the overburden and undergoes a phase transition to gas at lower pressure and temperature conditions, the CO_2 density and viscosity will be reduced, but the CO_2/brine IFT and CO_2 buoyancy force and volume will increase. If the volume cannot increase under isothermal conditions, the pressure must increase, which may lead to a hydraulic fracturing situation (as described by Cartwright *et al.,* 2007 and Pruess, 2008). To minimise the risk of this situation developing at CO_2 storage sites, the ability to accurately constrain pressure and temperature conditions at the caprock seal depth is critical as our modelling work in Chapter 3, Section 3.4 illustrates.

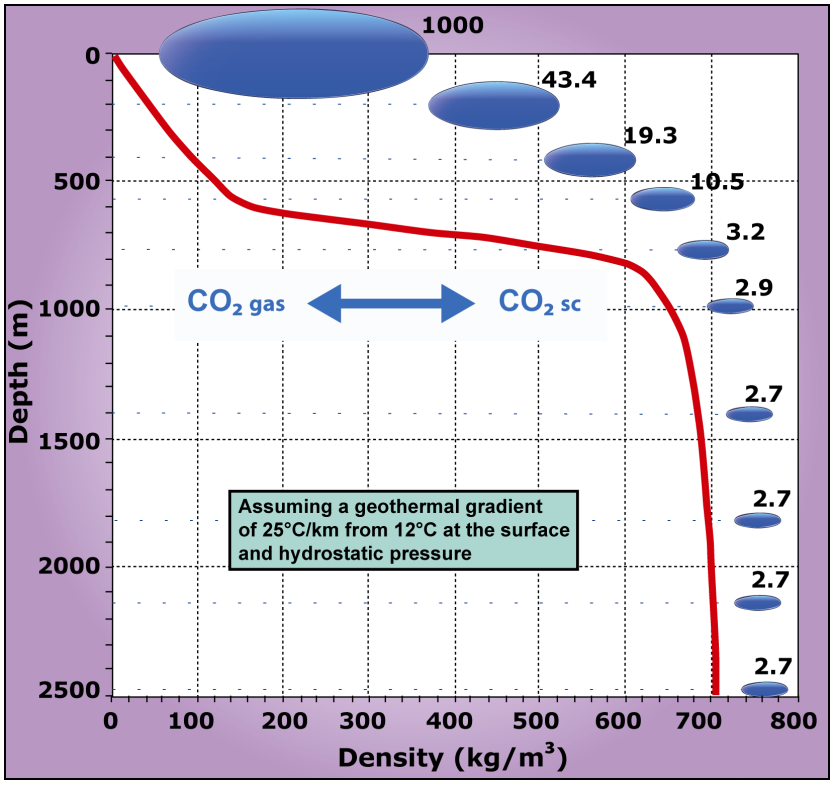

Figure 5.2: CO_2 density variation and relative volume occupied with depth. The density of CO_2 increases rapidly at ~800 m depth, when critical pressure and temperature thresholds are passed and CO_2 enters a supercritical fluid state. Blue ellipses (not to scale) and associated numbers represent the relative volume occupied by the CO_2 at various depths (based on Formation Volume Factors – refer to Appendix 5.4 for details of how these values are calculated). Down to 800 m, this volume can be seen to dramatically decrease with depth as CO_2 deviates from ideal gas behaviour. At depths below 1.4 km, the density and specific volume become nearly constant (corrected and redrawn from the incorrect version displayed on page 198 of IPCC (2005), using calculated data from the Prosper® PVT module – see Appendix.5.4 for details).

Our review of the petrophysical and thermodynamic conditions used for modelling the Sleipner CO_2 storage site (Section 3.3) revealed that most of the major uncertainties associated with this site have resulted from the inability of the operators to acquire fundamental monitoring data in a logical sequence, thus ensuring that the site characterisation is robust for ongoing site monitoring purposes (Figure 5.3). As we outlined in the previous section, the original plans to acquire extensive monitoring and site characterisation data were either not implemented on economic grounds (Carlsen *et al.,* 2001) or were performed at some opportune time as hydrocarbon production conditions dictated (in some cases, some years after injection commenced), then retro-fitted to subsequent studies. Specific deficiencies are outlined as follows:

- No dedicated baseline 3D seismic survey was performed (as is now current practice for most new CO_2 storage sites); a legacy 1994 exploration data set (with a deeper focus) was used instead (Chadwick *et al.,* 2002, 2008),
- Only one temperature measurement was acquired during drilling operations for the CO_2 injection well (Zweigel *et al.,* 2004a; Hansen *et al.,* 2005),
- No dedicated temperature or pressure recording instrumentation was installed in the CO_2 injection well to measure temperature and pressure at the CO_2 injection point or within the storage formation (Alnes *et al.,* 2011) even though there was probably an opportunity to remedy this situation during the sand screen recompletion operations performed during December 1997 (described in Hansen *et al.,* 2005 and Appendix 5.1),
- Temperature at the cap rock is estimated from proxy measurements acquired at Volve water production well 15/9-F-7, situated 8 km NW of the injection point location (Lindeberg *et al.,* 2009; Chadwick & Noy, 2010),
- No pore fluid sampling was performed at Sleipner, thus a proxy (synthetic) sample was used for geochemical and other modelling work (Rochelle & Moore, 2002). This was based on the composition of a Utsira Formation sample obtained at the Oseberg Field, 200 km N of Sleipner, so nothing is known about the actual fluid composition or microbiological content of in-situ pore fluids at Sleipner.

As a result of these oversights, there is a significant uncertainty over the geothermal gradient prevailing at Sleipner and the actual pressure and temperature conditions at the CO_2 injection point and caprock. Lack of temperature and fluid data means that there is no information about thermal conductivity changes induced by the injection of CO_2 and replacement of resident brine (described in Section 3.6.1). Since pressure and temperature conditions directly affect CO_2 density, viscosity and phase conditions, there is also significant uncertainty over the CO_2 phase conditions that may prevail at the cap rock (i.e. supercritical or gas phase). The depth of the caprock seal at Sleipner is also marginal in terms of being deeper than 800 metres TVDSS; the minimum depth suggested for efficiently and safely storing CO_2 as a dense, supercritical phase (IPCC, 2005). Thus, certain regions of the caprock could be very close to, or below the critical point temperature conditions for CO_2 (Alnes *et al.,* 2011).

MMV Technique	1994	1996	1999	2001	2002	2004	2005	2006	2008	2009
3D surface seismic	Yes (legacy)	Utsira Formation (reservoir) core acquired from well 15/9-A23 CO_2 Injection Starts	Yes	Yes	Yes	Yes		Yes	Yes	
2D surface seismic (high-resolution)								Yes		
Seabed imaging (sidescan sonar and multibeam echo sounder)								Yes		
Seabed gravity					Yes		Yes			Yes
Controlled source electro-magnetic (CSEM)									Yes	
Wellhead pressure and temperature			Continuous since injection start							
Pressure, temperature and fluid sampling at injection point			No pressure and temperature monitoring or fluid sampling performed at injection point - only one temperature measurement acquired whilst drilling injection well (Hansen et al., 2005; Alnes et al., 2011)							
Pressure and temperature at cap rock			No pressure or temperature monitoring performed at cap rock - proxy temperature measurement used from Volve water production well 15/9-F-7, approximately 8 km NW of CO_2 injection point location (Lindeberg et al., 2009)							
Cap rock sampling and testing					Cap rock core acquired from well 15/9-A11	Ongoing testing of cap rock sample for mineralogical, geomechanical, petrophysical and long-term flow testing (Kemp et al., 2003; Pillitterri, et al, 2003; Head et al., 2004; Springer and Lindgren, 2006; Harrington et al., 2009)				
Monitoring well			No monitoring wells - two were planned, but rejected on cost basis (Carlsen et al., 2001)							
Cumulative CO_2 injected (Mt)	0	0.07	2.548	4.490	5.445	7.109	7.967	8.787	10.522	11.382
Cumulative CO_2 vented (Mt)	0	0.081	0.123	0.134	0.142	0.187	0.193	0.196	0.216	0.220

Figure 5.3: Monitoring Measurement and Verification (MMV) techniques employed at Sleipner from 1996 to 2009 (modified after Chadwick, 2011 and Sandmo 2011)

In Chapter 3 we also described the potential interaction between injected fluids and resident fluids, given that the injected CO_2 contains impurities and the resident brine may contain small amounts of dissolved natural gas. Typical contaminants from the CO_2 capture process may include a small percentage of nitrogen, methane and heavier hydrocarbons that will reduce CO_2 density, in addition to butane, toluene and xylene (BTX) compounds that will increase CO_2 density (Zweigel *et al.*, 2004a; Nooner *et al.,* 2007; Arts *et al.,* 2008), further complicating the CO_2 plume modelling process from a thermodynamic and capillary pressure perspective (Chadwick & Noy, 2010). It was suggested by Zweigel *et al.,* (2004a) that the effects of these CO_2 density increasing and reducing components should cancel each other out, but we have found no experimental evidence to corroborate such a claim, thus it must be rejected until such research is performed. On seismic data pre-dating CO_2 injection Zweigel *et al.,* (2000) describe the presence of small natural gas accumulations within the attic areas of the Utsira Formation underlying barriers 8 and 9. The CO_2 currently being injected into Sleipner is described as having ~2% methane content (Chadwick *et al.*, 2010), thus it highly probable that any injected CO_2 entering these regions of the storage site (i.e. plume layers 8 and 9) may also encounter relict natural gas that will further reduce the CO_2 density and increase the CO_2 mobility, CO_2/brine IFT and the buoyancy force on the caprock seal. This mechanism may explain why the CO_2 plume in layer 9 is moving faster than several modelling studies predict (e.g. Chadwick et al., 2009b; Chadwick & Noy, 2010). We discussed this type of mixing situation in Section 3.6.2 and suggested it could lead to the type of chromatographic separation and exsolution of least soluble components described by Bachu & Bennion (2009) and Taggart (2009). Since seismic data cannot make the distinction between CO_2 and natural gas, a significant part of the plume currently observed on seismic might actually be composed of swept natural gas from these attic areas.

For modelling the potential of injected CO_2 entering and reusing palaeo-gas migration pathways, we considered two scenarios based on observed structural trap heights at Sleipner (Section 3.5.2). Larger traps are thought unlikely to exceed 26 metres in height and structural traps within the main Sleipner storage site complex are described as having 12 to 15 metres of maximum relief (Zweigel *et al*., 2000; Bøe & Zweigel, 2001; Chadwick *et al*., 2005).

We therefore used the two end points of 12 and 26 metres for a sensitivity analysis, assuming that these traps had to be filled to spill point before leakage could occur (i.e. best-case scenario) and ran a series of leakage scenarios under Sleipner storage conditions for a range of methane (natural gas proxy) density and methane/brine IFT measurements to ascertain the minimum pore radii required for leakage to occur. Having obtained these pore radii, we than ran another series of leakage scenarios with a CO_2/brine system for a range of CO_2 density, CO_2/brine IFT and wettability measurements to determine the equivalent CO_2 column heights that could be supported before leakage could occur. This methodology obviously has a few weaknesses, since it assumes:

- Pore radii are unchanged over geological time and the pathways have remained open to some degree (i.e. no diagenetic changes such as pore cementation or cement/matrix dissolution have occurred),
- Traps all have homogeneous properties and require to be filled to their maximum column height before they leak (i.e. no fractures or other form of heterogeneities are present),
- Brine density has remained unchanged over geological time.

Recent research (Chalbaud *et al.,* 2009) suggests that CO_2/brine IFT and caprock wettability in the presence of CO_2/brine may not be reduced to values in the region of 20 mNm^{-1} and 50% respectively (as previously inferred by Hildenbrand *et al.,* 2004 and Chiquet *et al.,* 2007a, 2007b). Despite this, we determined from our sensitivity modelling results in Chapter 3 that CO_2 leakage before spillage was still possible at fairly conservative values of IFT and wettability for a CO_2/brine system (i.e. 25 to 30 mNm^{-1} and 80 to 100% respectively), for the range of pore radii under consideration. This work also suggested that there is an optimum combination of conditions under which CO_2 is most likely to leak, since:

- Supercritical CO_2 has a low IFT and may reduce rock wettability, but its high density results in a lower buoyancy contrast with resident brine and thus a lower buoyancy force being applied to the seal,

- Gaseous CO_2 has a higher IFT and will probably not reduce rock wettability below 100% water-wet, but its low density results in a higher buoyancy contrast with resident brine and thus a higher buoyancy force being applied to the seal.

The optimum condition for CO_2 leakage needs elements of both scenarios, which can be achieved at near critical point conditions as demonstrated by Figure 3.16 (after Chalbaud *et al.,* 2006, 2009). At near critical point conditions (e.g. ~400 to 600 kg/m^3) CO_2 is still supercritical (with a low IFT and a potential for wettability alteration), but has a lower density and therefore a higher buoyancy contrast. As we have described in Chapter 3, this type of situation is possible at Sleipner if caprock temperatures are higher than predicted by Lindeberg *et al.,* (2009) and/or if the presence of methane in the Utsira Formation and the injected CO_2 stream causes a significant density reduction effect.

The results from our Chapter 3 sensitivity analysis were subsequently applied to a series of high-resolution MPath® 3D models constructed for the Sleipner storage site (Chapter 4). As our workflow methodology explains (Section 4.5), these models range in complexity from simple layer-cake overburden models, to complex lithological models populated with geological, stratigraphic and structural information derived from our seismic interpretations. In all cases, models are calibrated and history-matched against published data (e.g. Zweigel & Hamborg, 2002; Chadwick *et al.,* 2005, 2008; Bickle *et al.,* 2007; Singh *et al.,* 2010) using similar modelling parameters. We also performed a series of stochastic fill-spill and flow simulations to:

- Determine whether the CO_2 stored below the caprock seal (layer 9) is likely to encounter any of the identified palaeo-migration pathways described in Chapter 2 and what the consequences of this contact might be,
- Investigate and evaluate CO_2 migration sensitivity within the overburden to pressure, temperature and capillary entry pressures, in terms of identifying potential leakage points, migration pathways and volumes/percentages leaked.

Unfortunately, during the course of our preliminary fill-spill and calibration modelling work we discovered that the data coverage to the E was insufficient for long term simulations and therefore we were unable to perform any MPath® Reservoir Filling simulations beyond 2008 without CO_2 spilling laterally from the models below the caprock seal in layer 9, thus no valid forecasting simulations could be performed. However, we were able to perform a range of history matching and sensitivity analyses up to 2008 and our modelling work also highlighted a number of significant issues that are of relevance to future CO_2 storage site characterisation and modelling studies:

- The presence of overburden high-amplitude anomalies and large-scale heterogeneities (i.e. tunnel valleys) has a significant effect on the seismic fabric (e.g. locally distorting two-way travel time and time to depth conversion). In a storage site such as Sleipner, which has a relatively low relief and shallow dip, the influence on the fill-spill migration process and migration direction is highly significant and may propagate into model and simulation errors,
- There also appear to be some inconsistencies between the methods used to derive capillary entry pressure values for the Nordland Shale caprock seal at Sleipner. Although the porosity/permeability measurements (Springer & Lindgren, 2006; Harrington *et al.,* 2009) and percentage clay content (Boe & Zweigel, 2001; Kemp *et al.,* 2002) derived for the caprock samples from well 15/9-A11, are consistent with published correlations for North Sea shales (Yang & Aplin, 2010), the CO_2-brine capillary entry pressures derived from laboratory experiments (Springer & Lindgren, 2006; Harrington *et al.,* 2009) on Nordland Shale samples from well 15/9-A11 appear to be exceptionally high for a shale buried to a maximum depth of ~800 m TVDSS and are more consistent with a shale buried to several thousand metres. Although it could be argued that the presence of a 200 metre thick ice sheet during the Pleistocene may have led to overconsolidation of the shale (Pilliterri *et al.,* 2003), the values still appear to be inexplicably high, thus we suspect there may be issues with core sample acquisition, storage and preparation procedures prior to testing and/or the experimental procedures employed for coreflooding shales as we describe in Section 4.7,

- The layer filling behaviour we observe in our modelling of the barriers within the Utsira Formation also suggests that individual layers can still grow laterally as they leak vertically, thus if a similar process occurs in the overburden and CO_2 leaks at relatively low flux rates, whilst layer 9 underlying the caprock is simultaneously supplied with CO_2 at high (or increasing) flux rates (as reported by Chadwick et al., 2009b), it may not be possible to seismically detect diffuse leakage in the overburden and any layer 9 shrinkage would also be insignificant from a seismic detection perspective, contradicting the assertions of Neufeld *et al.,* (2009) and Chadwick & Noy (2010).

Clearly, our overburden modelling and simulation work would have benefited from the use of a more recent seismic dataset (i.e. one of the post-injection monitoring surveys) centred on the CO_2 injection point location, to allow for migration to the E (beyond the current model coverage), but despite extensive inquiries, none of these datasets was made available to us. Nevertheless we have still managed to show that there is strong evidence for hydrocarbon leakage into the overburden at Sleipner within the past 2 Ma to the present day and we have also illustrated that leakage of CO_2 into the overburden could occur at Sleipner under certain circumstances as described in Chapter 4. Within this same context, it should also be emphasised that natural gas generation, migration and accumulation at Sleipner were probably (but not necessarily all) intermittent and slow processes, whereas CO_2 at Sleipner is being injected fairly continuously at a high rate, thus the "generation", migration and accumulation processes are orders of magnitude faster. The effects of this fast track process on the storage site and overburden in terms of thermal conductivity, geochemical and geomechanical response are not yet fully appreciated.

5.2 Conclusions:

The following points summarise the main findings and conclusions drawn from the research work performed for this thesis and described in Chapters 2 to 4:

- The Nordland Group overburden overlying the Sleipner CO_2 storage site appears to be a more complex depositional and latent fluid flow environment than previous models suggest. Our detailed evaluation of 3D seismic data and well logs has revealed the presence of faults/lineations, chimney structures, high-amplitude anomalies, unconformities, tunnel valleys, channels, palaeo-pockmarks and seabed craters. Some of these features appear to be spatially connected with structures in the Hordaland Group underburden including polygonal faults, sand injectites and mud volcanoes. This complex network has served to transport or accumulate natural gas over geological time and results from processes that may operate individually or collectively to compromise seal integrity. These same structures may also be predictable pathways for CO_2 migration within the overburden at Sleipner,
- Glacial and inter-glacial cycles affecting the Nordland Group overburden at Sleipner began during the early Pleistocene ~2 Ma, culminating in ice loading and unloading events that may have reduced sediment ductility and created fluid migration pathways via faults, micro-fractures and dilatent shear zones. Well log evidence reveals the presence of sand and gravel within Pleistocene tunnel valleys and channels; these facies may be used as pathways or secondary storage by migrating CO_2 (albeit at the expense of reduced storage efficiency in gas phase),
- Evidence from well logs is insufficient to prove whether seismic anomalies in the Nordland Group overburden represent natural gas deposits formed by thermogenic or biogenic processes or diagenetic carbonate zones, although seismic and mineralogical evidence suggests diagenetic carbonate may be present between the Former Intra-Pliocene and Former Top Pliocene surfaces. Drilling reports from the Sleipner area also confirm the presence of shallow gas; therefore pull-down anomalies and zones of reverse polarity probably represent natural gas accumulations. We have also highlighted the presence of reactive minerals in the Utsira Sand and the overburden (i.e. lignite and shell fragments) that may react with stored or migrating CO_2 in a positive or negative manner,

- Regions considered for CO_2 storage that are known to contain palaeo-gas migration pathways, faults and/or seismic anomalies in the overburden either need to be avoided or must at the very least be subjected to a rigorous risk assessment during the early stages of site screening. We have already described such a workflow in Chapters 2-4. Other modelling approaches may include the use of different seismic attributes now available for proprietary seismic software and designed to enhance visualisation of seismic discontinuities and the presence of gas, such as neural net training of seismic to produce fault and chimney cubes (Heggland, 2005), the generation of seismic attribute cubes (e.g. chaos, variance, semblance and coherence) and ant tracking (e.g. in Petrel®) to visualise and extract 3D fault/fracture networks (Godfrey & Bachrach, 2008). Some of this software could have been applied at the Sleipner site, albeit a few years after injection started in 1996. Ironically, some of the leading researchers and companies involved in the development and promotion of these techniques were also associated with the site operators (e.g. Meldahl *et al.* 2001; Heggland, 2002; dGB Earth Sciences, 2011), yet to the best of our knowledge, none of these groups appear to have been directly involved with any of the technical publications or reports currently in the public domain relating to overburden risking at Sleipner, using the aforementioned seismic processing techniques. Perhaps data has been generated using these advanced techniques for private or internal consumption, in which case public suspicions may be aroused, since the whole rationale behind the future development of CCS projects is supposed to be one of data transparency, sharing and widespread dissemination to the global CCS community, rather than a selective release of data to favoured institutions (or worse, data censorship),
- The inability of the site operators to acquire temperature data from Sleipner before and during CO_2 injection operations has been particularly problematic (as described in Chapters 2 to 4). Without reliable temperature measurements for the injection point depth or in-situ data acquisition capabilities, there are significant uncertainties over the prevailing geothermal gradient prior to injection, the CO_2 density within the site and the effects of CO_2 on thermal conductivity and the geothermal gradient during injection, given the absence of any monitoring wells.

We recommend that for all future CO_2 storage sites the acquisition of temperature and pressure data at the injection point and the installation of permanent downhole temperature and pressure monitoring equipment should be a **pre-requisite** for storage permit applications. This data can then form an essential part of the ongoing measurement, monitoring and verification (MMV) programme,

- Similarly, the acquisition of fluid samples for all future CO_2 storage sites should be an additional **pre-requisite** for storage permit applications. The use of proxies from a distant location in the same formation reveals nothing about local conditions around the proposed injection site, particularly the presence of microbial species and metal ion concentrations, which may vary spatially and also be significant in terms of geochemical/microbiological reactivity and injectivity as has been amply demonstrated at other CO_2 storage sites such as Ketzin, Germany (Schilling *et al.,* 2009; Morozova *et al.* 2010; Wandrey *et al.,* 2011), Nagaoka, Japan (Mito *et al.,* 2008) and Frio, USA (Kharaka *et al.,* 2009).
- As described in Chapters 3-4, there are large uncertainties involved with accurate leakage predictions at Sleipner (and other sites) based on capillary pressure measurements, particularly when representative core samples acquired from the caprock seal and overburden are lacking. Many key parameters (e.g. pore throat radii) will be unknown and even if limited core data is available, zones containing fault and fracture networks may have been missed by the sampling programme. The dynamic nature of CO_2 in such a shallow storage site (described in Chapter 3), where density, viscosity and relative permeability of CO_2 and brine can vary vertically and laterally over time, due to mutual fluid dissolution, salt precipitation, carbonate rock fabric dissolution (i.e. cement and shell fragments) and subtle CO_2 phase changes at near critical point conditions. We conclude that a more comprehensive sampling and testing programme is necessary for the overburden during the site characterisation phase, with shale samples acquired and handled according to best practice guidelines (e.g. Chenevert & Amanullah, 2001; Clennel *et al.,* 2010),

- If no leakage occurs at Sleipner our depth corrected models (Baseline and Complex), suggest that the structural closure to the NE end of layer 9 will start spilling to the E following 12 years of CO_2 injection (illustrated in Figure 4.12). This assumes that our structural closure height is around 10.363 metres and the topography for the caprock seal is accurate. If this is not the case and the closure is higher or the caprock seal topography has not been mapped accurately enough, then spill may occur later or a different migration scenario may apply,
- Similarly, if leakage does occur at Sleipner, our depth corrected models (Complex) suggest that the highest structural closure to the NE end of layer 9 fills to a column height of 8.934 metres, then leakage is most likely to occur via palaeo-gas chimney #77 (as illustrated in Figures 4.29 and 4.30). For this scenario to occur, it was necessary to adjust the mercury-air capillary entry pressure for the chimney lithology to 625 kPa at 800 m (to simulate a CO_2-brine IFT of 30 mNm^{-1} and water wettability reduction to 80% at the caprock seal). If the IFT and water wettability conditions are further reduced over time (e.g. due to the presence of contaminants or if different physical conditions prevail at the caprock than we have used in this work), then it is possible that leakage may occur at smaller column heights under the same capillary entry conditions (as we described in Chapter 3). Again, all of this assumes that our structural closure height and the topography for the caprock seal are accurate. If this is not the case and the closure is higher or the caprock seal topography has not been mapped accurately enough, then leakage may either not occur, may occur at a different time or a different migration scenario may apply. Notably, leakage could not be achieved before spillage with any of the other three Complex Model variants (i.e. models using the High80, Low100 and High100 lithology files); for these cases the trapped column heights were unable to overcome the (higher) capillary entry pressures for the caprock seal and models simply spilled to the E,

- The presence of significant heterogeneities in the overburden (i.e. tunnel valleys, channels, carbonate horizons and natural gas accumulations) can all affect time-depth conversions to a varying degree, creating distortions in the deeper Utsira Formation surfaces (particularly auto-tracked surfaces) extracted from the seismic. These distortions will be transmitted to models and the subsequent simulations performed with them. To address this issue, some form of 3D velocity mapping should be applied to remove localised pull-up and pull-down artefacts (e.g. using Velocity Manager IMR II®, Vista®, etc.),
- In order to history match the developing CO_2 plume over time, mercury-air capillary entry pressure values for the internal shale barriers in the Utsira Formation required to be increased from 473 to 701 kPa at the early stages of simulation (1999) up to 686 to 1021 kPa for the present day (Table 4.9). We have suggested a range of explanations for this time-dependent "bottlenecking" effect in Chapter 4, Section 4.7,
- Our observations also suggest that there may be inconsistencies in the laboratory test methods used to calculate capillary entry pressures for a CO_2-brine system. The Nordland Shale core samples tested by Springer & Lindgren (2006) and Harrington *et al.,* (2009), recorded entry pressures in the range 1.6 to 3.5 MPa (equivalent to mercury-air values of 26 to 55 MPa), which is more typical of a shale buried to several thousand metres rather than a shale at ~800 m maximum burial depth. There is lack of documented procedures in the available literature (e.g. Kemp *et al.,* 2002) to confirm whether the core samples acquired from well 15/9-A11 were treated in accordance with recommended handling procedures for shale cores (e.g. Chenevert & Amanullah, 2001; Clennel *et al.,* 2010). There is also no mention of the original pore fluids being retained in these core samples and since no pore fluid samples have been obtained directly from the Utsira Formation (Rochelle & Moore, 2002), it is difficult to see how any reliable information can be obtained from core flooding experiments performed under such circumstances. We also conclude that the use of shale cuttings samples and the Krushin (1997) test to derive pore radii and capillary entry pressures (described in Chapter 2, Section 3.3.7) is inappropriate for the Sleipner overburden and should not be used for similar CO_2 storage site characterisation studies unless an independent corroboration of accuracy can be obtained,

- Our modelling results calibrated against the gravity results from Alnes *et al.,* (2011), suggest that the geothermal temperature gradient must be 35.65°C/km from seabed assuming a seabed temperature of 7°C, with a consequent caprock temperature ~32.6°C (above critical point temperature), to history match against the observed plume spatial distribution. Although other research maintains that the caprock seal temperature is below critical point temperature at 29°C (Lindeberg *et al.,* 2009; Chadwick & Noy, 2010), we assert that this would result in a much higher CO_2 density than observed (Figure 4.23) and there is also insufficient local temperature monitoring data available to provide support for these former claims (refer also to Chapter 3, Sections 3.3.2 and 3.6.1 for further details),
- With a caprock temperature of ~32. 6°C, the CO_2 density at the caprock matches the 675 kg/m^3 average observed from Sleipner gravity data by Alnes *et al.,* 2011 (Figure 4.23). Given these conditions at the caprock seal our modelling predicts that if CO_2 leaks into the overburden, the supercritical to gas phase transition will occur at ~670 metres TVDSS +/- 20 metres.
- Our simulations have also confirmed that migrating CO_2 in layer 9 will contact several of the palaeo-gas migration features (described in Chapter 2 and illustrated in Figures 2.30 and 2.31), but in most cases the CO_2 column heights will be too small (~1 to 6 metres) to exert sufficient buoyancy force. We have of course assumed that structural traps must be filled to spill before breach occurs, which is in effect a best-case scenario. For the simulations performed, only chimney #77 was observed to leak and the migration was arrested at ~500 m TVDSS at the Former Top Pliocene (FTP) level, where most of the palaeo-gas chimneys terminate (Figure 4.30). The high Pthz of the overlying Nordland Shale lithology prevents further vertical migration into the Pleistocene tunnel valleys and channels unless the Pthz/Pthx anisotropy is reduced from 10/1 to 1.25/1, which in reality would require the presence of additional high permeability pathways or vertical fractures. There is insufficient evidence from this study to support the presence of either mechanism, although some form of developing pathway flow has been agreed by Harrington *et al.,* (2009), Chadwick & Noy, (2010), and Hermanrud *et al.,* (2010) for long-term exposure of the Sleipner caprock seal to CO_2. We have demonstrated what may happen if such pathways are open to the extent that they allow upward CO_2 migration to occur.

- It would appear that the overburden heterogeneity is significant but that the possible storage response is difficult to quantify. The presence of palaeo-gas migration pathways and high permeability channels and tunnel valleys may become potential migration routes or provide secondary storage containment for CO_2 as the plume continues to spread laterally over the coming decades. However, the transitional phase conditions of the plume at or near the caprock require accurate pressure and temperature modelling. The absence of in-situ observational pressure and temperature data introduces significant uncertainty to model outcomes with respect to CO_2 density and column height estimates (Alnes *et al.,* 2011). A first approximation can be arrived at by assuming that any potential pathway response is similar to the thick shale response, which is what we have attempted here. If the CO_2 plume encounters an open migration pathway, the prevailing CO_2 density in addition to the CO_2-brine IFT and caprock seal wettability, will be critical factors in determining whether the structure breaches vertically or spills laterally.
- If Sleipner does eventually leak it will give the operators an opportunity to implement a remediation plan and test its effectiveness. It will also provide an opportunity to acquire valuable field data on leakage rates and mechanisms, migration pathway development, geochemical changes and multi-phase flow effects, that can subsequently be used to improve future CO_2 storage research,
- Finally, despite being promoted as the first engineered storage site for anthropogenic CO_2 emissions and a prime example of best practice, many data acquisition issues at Sleipner were not addressed as stringently as they should have been (mainly on the grounds of false economy). Too many crucial studies and operations (e.g. core sampling and caprock testing) were performed several years after CO_2 injection operations started and subsequently retrofitted to the project. In this respect, absence of leakage is probably due more to good luck rather than best practice. Hopefully, these oversights will not result in long-term site compromise and valuable lessons will have been gained, allowing future storage sites to be planned with more due diligence.

5.3 Future Work:

During the three phases of work undertaken during this study, key areas of uncertainty have been highlighted in relation to how CO_2 storage sites are characterised and modelled. These areas offer an opportunity for future research that may improve our understanding of CO_2 behaviour in the sub-surface, further reducing those uncertainties and hopefully increasing public confidence in long-term storage security. The following list describes some potential subject areas for future research:

- In Chapters 2 and 4, we described the problems encountered by previous researchers (Zweigel & Hamborg, 2002; Chadwick *et al.*, 2009b) involving time to depth conversions of the Sleipner 3D dataset for accurately constraining surface topography, given the overburden complexity, heterogeneity, presence of gas and diagenetic carbonate at Sleipner. Combined with a low dip, this generates high uncertainty over the eventual CO_2 migration direction, increasing long-term storage risk. Improved seismic processing methods and software are now available to perform high-resolution velocity mapping in 3D (e.g. Velocity Manager IMR II®, Vista®, etc.). Surface maps such as the ones we produced for Sleipner, could be time to depth converted more accurately with this type of software to remove the effects of high-amplitude seismic anomalies, account for large-scale lithological heterogeneities and produce a more reliable topography for 3D model construction and fluid migration modelling,
- In Chapters 2 to 4, the mapping of palaeo-gas migration chimneys and other potential fluid migration structures was described. We adopted a manual approach for our seismic interpretation, but several automated processes are now available within some seismic processing and interpretation packages (e.g. Neural Net Analysis and Ant Tracking workflows described by Godfrey & Bachrach, 2008 and Fault Cube / Chimney Cube processing described by Ligtenberg, 2005 and Connolly & Brouwer, 2008). Some of these techniques involve running interpreter-guided training routines on the seismic data to inform the data extraction. As a result, the extraction processes are highly subjective and dependent on the individual interpreter's experience, yet these automated techniques may prove to be useful validation tools to help confirm or refute manual interpretations such as ours,

- In Chapters 2 and 3, we investigated the potential interactions between CO_2 and natural gas (predominantly CH_4) and considered whether thermogenic or biogenic processes may have generated the natural gas and carbonate horizons detected in the overburden at Sleipner. The process of microbial degradation of hydrocarbons to form diagenetic carbonate is well documented (Curtis, 1987; Hovland *et al.* 1987; Mazzini *et al*., 2003; Ligtenberg, 2005; Judd & Hovland, 2007 and further references therein) and this appears to be an area that clearly merits further research in a CO_2 storage context, to investigate the detrimental and /or beneficial effects of microbially-mediated reactions. Very little research has been performed in this area until relatively recently (e.g. Wigand *et al.,* 2008; Kharaka *et al.,* 2009; Schilling *et al.,* 2009; Morozova *et al.* 2010; Wandrey *et al.,* 2011; Berger & Roy, 2011; Jones *et al.,* 2011); the majority of this research has been performed for the Ketzin CO_2 storage site in Germany. From a geochemical perspective the introduction of anthropogenic CO_2 and associated impurities into a previously undisturbed saline aquifer could prove detrimental or beneficial to certain types of micro-organisms and may instigate further biological and/or geochemical reactions. A mass kill of CO_2 intolerant species could create a biological "sludge" in the pore space reducing injectivity and potential storage capacity (Kharaka *et al.,* 2009). Conversely, population enhancement of CO_2 tolerant species may result in the consumption of desirable/undesirable ions in the pore fluid and production of by-products that may dissolve the rock framework and metal tubular goods and/or form pore-clogging precipitates. In either case, the types of bacteria and reactions involved need to be considered in detail and one of the key objectives during the core and fluid sampling of a prospective storage aquifer should be the collection and identification of the resident microbial populations, so that likely microbial reactions can be assessed in terms of favourable/unfavourable impacts on environmental and storage conditions. Clearly, any reactions that enhance storage security (e.g. conversion of CO_2 to CH_4) will be of great interest.

- As discussed in Chapters 3 and 4, the range of laboratory-derived capillary entry pressure values for CO_2/brine (or equivalent fluid systems) used for modelling the integrity of caprock shales at Sleipner falls within the range of 1.6 – 3.5 MPa (Kemp *et al*., 2002; Springer & Lindgren, 2006; Harrington *et al.*, 2009) appear to be inexplicably high for such shallow, relatively unconsolidated sediments. This suggests that further research is required to investigate whether the tests (e.g. Krushin, 1997), procedures and equipment used were appropriate for determining in-situ capillary entry pressures for a CO_2/brine system infiltrating the shale lithologies of the Nordland Group overburden,
- The simulation work described in Chapter 4 used a CO_2/brine system, but as we discussed in Chapter 3, many CO_2 storage sites (particularly those situated in depleted hydrocarbon reservoirs), will encounter multi-component systems and multi-phase flow conditions; the problems of modelling such systems in a CO_2 storage context have already been described by others (e.g. Oldenberg *et al*., 2004; Seo & Mamora, 2005; Pruess, 2008; Chadwick & Noy, 2010). Many simulation packages use Pressure/Volume/Temperature (PVT) calculations based on pure CO_2, but as explained in Chapter 3, the presence of other impurities such as butane, toluene and xylene (BTX) from the capture process, natural gas (biogenic and thermogenic) and H_2S may all be expected within a CO_2 storage site. Some research has already been performed in this area to determine the effects of such mixtures on interfacial tension reduction (Shah *et al.,* 2008), but this work needs to be expanded to cover a wider range of mixtures and to investigate the effects of complex CO_2 mixtures on fluid miscibility, wettability alteration and the capillary entry pressures of shales,

- Although the seismic data we used for the seismic interpretation and modelling work on Sleipner pre-dated CO_2 injection and was therefore unadulterated and undistorted by the presence of CO_2, our simulation work described in Chapter 4 suggests that there is insufficient coverage to the E with this dataset (ST9407), resulting in long-term simulations overspilling CO_2 from the model and providing no further information about future migration directions or the probability of intersecting vertical migration pathways. Although we managed to obtain an additional seismic dataset in 2009 with overlap along the E margin of the original dataset (ES9401-TVF), the data was poor (noisy) in the top 200 ms^{-1} and the merging process (performed in Petrel®) created too much vertical distortion within the overlap region and would have biased any simulations run with a merged dataset. Therefore, future research could be performed to either investigate a better merge process for the ST9407 and ES9401-TVF datasets and/or obtain one of the monitoring 3D surveys (acquired post-1996) with better overall coverage centred on the plume footprint, so that the models constructed during this study can be extended and simulations re-run over a wider area. Combined with a robust time to depth conversion based on velocity mapping (discussed previously), this would improve the accuracy of migration simulations and confirm or disprove the likelihood of CO_2 migration to the E,
- Adding more complexity to the Sleipner overburden models may also improve the model response and make the simulations more realistic for leakage migration scenarios. This could be achieved through the use of better wireline log and geotechnical borehole data obtained from the site operators, since the NPD data is fairly limited in quality and quantity. More heterogeneity could also be added to the glacio-marine sequences based on natural analogues. It is already known that these sequences have a multi-stage fill (Huuse & Piotrowski, 2003), so high-frequency, high-resolution seismic data (e.g. boomer, sparker, etc.), could be acquired at Sleipner (or may already be available?) to better delineate depositional sequences and determine the seismic response of the channel fill. As we described in Chapter 2, tunnel valley sequences are also accessible at sites in Europe (Huuse & Lykke-Andersen, 2000; Huuse & Piotrowski, 2003; Jørgensen & Sandersen, 2008) and North Africa (Le Heron et al., 2005).

Thus, further research at these sites may provide more specific information on the depth, extent and type of deformation (potential fluid migration pathways?) that might be expected below tunnel valleys, in addition to the usual sedimentological and petrophysical information.

Grant Douglas Nicoll, November 2011

Evaluation of the Nordland Group overburden as an effective seal for the Sleipner CO_2 storage site (offshore Norway) using analytical and stochastic modelling techniques

Grant Douglas Nicoll

Thesis submitted in fulfilment of
the requirements for the degree of
Doctor of Philosophy

(References and Appendices)

School of Geosciences
University of Edinburgh

2011

References:

Note: *SINTEF reports listed in this reference list are available in the public domain via the SINTEF website (http://www.sintef.no). Users should follow the route Environment and Climate/CO_2 Capture and Sequestration/CO_2 storage, navigate via the Projects list to select CO_2 STORE, this provides access to the Saline Aquifers CO_2 Storage (SACS) area where both Formal Reports and Technical Reports can be selected or downloaded (February 2011).*

Aggelopoulos, C.A., Robin, M., & Vizika, O., 2011. Interfacial tension between CO_2 and brine (NaCl + $CaCl_2$) at elevated pressures and temperatures, The additive effect of different salts. Advances in Water Resources, Vol. 34, Iss. 4, pp. 505-511.

Alnes, H., Eiken, O. & Stenvold, T., 2008. Monitoring gas production and CO_2 injection at the Sleipner field using time-lapse gravimetry. Geophysics, Vol. 73, No. 6 (November-December, 2008), pp. 155-161.

Alnes, H., Eiken, O., Nooner, S., Sasagawa, G., Stenvold, T. & Zumberge, M., 2011. Results from Sleipner gravity monitoring: updated density and temperature distribution of the CO_2 plume. Energy Procedia, 4, pp. 5504-5511.

Andreassen, K., Nilssen, E.G. & Ødegaard, C.M., 2007. Analysis of Shallow Gas and Fluid Migration within the Plio-Pleistocene Sedimentary Succession of the SW Barents Sea Continental Margin Using 3D Seismic Data. Geo-Marine Letters 27, Nos. 2-4, June 2007, pp. 155-171.

Andresen, K.J., Huuse, M. & Clausen, O.R., 2008. Morphology and ditribution of Oligocene and Miocene pockmarks in the Danish North Sea – implications for bottom current activity and fluid migration. Basin Research, 20, pp. 445-466.

Arrhenius, S.A., 1896. On the Influence of Carbonic Acid in Air upon the Temperature of the Ground. The London, Edinburgh and Dublin Philosophical Magazine and Journal of Science, Series 5, Vol. 41, pp. 237-276.

Arts, R., 2000. SACS Internal Report - Note on the seismic data. Project Number 005.70205, TNO Report NITG 00-237-B, 18p.

Arts, R., Eiken, O., Chadwick, A., Zweigel, P., Van Der Meer, B. & Kirby, G., 2004. Seismic monitoring at the Sleipner underground CO_2 storage site (North Sea), in: Baines, S. J. & Worden, R. H. (Eds.) 2004. Geological Storage of Carbon Dioxide. Geological Society, London, Special Publications, 233, 181-191.

Arts, R., Chadwick, A., Eiken, O., Thibeau, S. & Nooner, S., 2008. Ten Years' Experience of Monitoring CO_2 Injection in the Utsira Sand at Sleipner, Offshore Norway. First Break, Vol. 26, January 2008, pp. 65-72.

Arts, R., 2009. Portfolio of monitoring technologies. Presentation from the 3rd. International Symposium on the Capture and Geological Storage of CO_2, Paris, November 6th., 36p (Powerpoint pdf).

Audigane, P., Gaus, I., Pruess, K. and Xu, T., 2006. A long term 2D vertical modelling study of CO_2 storage at Sleipner (North Sea) using TOUGHREACT. Proceedings, TOUGH Symposium 2006 Lawrence Berkeley National Laboratory, Berkeley, California, May 15–17, 2006.

Austegard, A., Solbraa, E., De Koeijer, G. & Mølnvik, M.J., 2006. Thermodynamic Models for Calculating Mutual Solubilities in H_2O-CO_2-CH_4 Mixtures. Chemical Engineering Research and Design, 84 (A9), pp. 781-794.

Bachu, S. & Adams, J.J., 2003. Sequestration of CO_2 in geological media in response to climate change: capacity of deep saline aquifers to sequester CO_2 in solution. Energy Conversion and Management, 44, pp. 3151-3175.

Bachu, S. & Rothenburg, L., 2003. Carbon Dioxide Sequestration in Salt Caverns: Capacity and Long Term Fate, in: Proceedings of the Second Annual Conference on Carbon Dioxide Sequestration, Alexandria, VA, May 5-8, 2003, pp. 1-12.

Bachu, S., Bonijoly, D., Bradshaw, J., Burruss, R., Holloway, S., Christensen, N.P. & Maathiassen, O.M., 2007. CO_2 Storage Capacity Estimation: Methodology and Gaps. International Journal of Greenhouse Gas Control, Vol. 1, No. 4, pp. 430-443.

Bachu, S. & Bennion, D.B., 2009. Chromatographic partitioning of impurities contained in a CO_2 stream injected into a deep saline aquifer: Part 1, Effects of gas composition and in situ conditions. International Journal of Greenhouse Gas Control, 3, pp. 458-467.

Baines, S. & Worden, R.H., 2004. The Long-Term Fate of CO_2 in the Subsurface: Natural Analogues for CO_2 Storage, in: Baines, S.J. & Worden, R.H. (Eds.), Geological Storage of Carbon Dioxide. Geological Society, London, Special Publications, 233, pp. 59-85.

Baklid, A., Korbøl, R.& Owren, G., 1996. Sleipner Vest CO_2 disposal, CO_2 injection into a shallow underground aquifer. SPE Annual Technical Conference and Exhibition, Denver, Colorado, USA, SPE paper, 36600, 9p.

Bauer, C. & Fichler, C., 2002. Quaternary lithology and shallow gas from high resolution gravity and seismic data in the central North Sea. Petroleum Geoscience, 8, pp. 229-236.

Benn, D.I. & Evans, D.J.A., 1998. Glaciers and Glaciation, Arnold, London. 734p.

Bennion D.B. & Bachu, S., 2008. A Correlation of the Interfacial Tension between Supercritical Phase CO_2 and Equilibrium Brines as a Function of Salinity, Temperature and Pressure. SPE Paper 114479, presented at the SPE Annual Technical Conference and Exhibition, Denver, Colorado, USA, 21-24th. September 2008, 13p.

Benson, S. & Hepple, R., 2005. Prospects for Early Detection and Options for Remediation of Leakage from CO_2 Storage Projects, in: Thomas, D.C. & Benson, S.M. (Eds.), Carbon Dioxide Capture for Storage in Deep Geologic Formations, Volume 2, Chapter 28, Elsevier Ltd., pp. 1189-1202.

Berger, P.M. & Roy, W.R., 2011. Potential for Iron Oxides to Control Metal Releases in CO_2 Sequestration Scenarios. Energy Procedia 4, pp. 3195-3201.

Berkeley Earth Surface Temperatures, 2011: http://berkeleyearth.org/index.php (November 18th. 2011)

Berndt, C., Bünz, S. & Mienert, J., 2003. Polygonal Fault Systems on the Mid-Norwegian Margin: A Long-Term Source for Fluid Flow, in: Van Rensbergen, P., Hillis, R.R., Maltman, A.J. & Morley, C.K. (Eds.), Subsurface Sediment Mobilisation. Geological Society, London, Special Publication, 216, pp. 283-290.

Bickle, M., Chadwick, A., Huppert, H.E., Hallworth, M. & Lyle, S., 2007. Modelling Carbon Dioxide Accumulation at Sleipner: Implications for Underground Carbon Storage, Earth and Planetary Science Letters, 255, pp. 164-176.

Bielinski, A., Kopp, A., Schütt, H. & Class, H., 2008. Monitoring of CO_2 plumes during storage in geological formations using temperature signals: Numerical investigation. International Journal of Greenhouse Gas Control 2, pp. 319-328.

Bikkina, P.K., 2011. Contact angle measurements of CO_2-water-quartz/calcite systems in the perspective of carbon sequestration. International Journal of Greenhouse Gas Control 5, pp. 1259-1271.

Bildstein, O., Kervévan, C., Lagneau, V., Delaplace, P., Crédoz, A., Audigane, P., Perfetti, E., Jacquemet, N. & Jullien, M., 2010. Integrative Modelling of Caprock Integrity in the Context of CO_2 Storage: Evolution of Transport and Geochemical Properties and Impact on Performance and Safety Assessment. Oil and Gas Science and Technology – Rev. IFP. Dossier – CO_2 Storage in the Struggle against Climate Change. Institut Français du Pétrole, DOI: 10.2516/ogst/2010006, 18 p.

Bjørlykke, K., Høeg, K., Faleide, J.I. & Jahren, J., 2005. When do Faults in Sedimentary Basins Leak? Stress and Deformation in Sedimentary Basins; Examples from the North Sea and Haltenbanken, Offshore Norway. AAPG Bulletin, Vol. 89, No. 8, pp. 1019–1031.

Boait, F., White, N., Chadwick, A., Noy, D. & Bickle, M., 2011. Layer spreading and dimming within the CO_2 plume at the Sleipner Field in the North Sea. Energy Procedia 4 (GHGT-10), pp. 3254-3261.

Boden, T.A., G. Marland, and R.J. Andres. 2010. Global, Regional, and National Fossil-Fuel CO_2 Emissions. Carbon Dioxide Information Analysis Center, Oak Ridge National Laboratory, U.S. Department of Energy, Oak Ridge, Tennessee, U.S.A., DOI 10.3334/CDIAC/00001 V2010 and website link: http://cdiac.ornl.gov/trends/emis/overview_2007.html (August 24th. 2011).

Bøe, R. & Zweigel, P., 2001. Characterisation of the Nordland Shale in the Sleipner area by XRD analysis - A contribution to the Saline Aquifer CO_2 Storage (SACS) project. Confidential SINTEF Report 33.0764.00/01/01.

Borgos, H.G., Dahl, G.V., Halvorsen, K.Å., Iversen, T., Lygren, M., Nickel, M., Randen, T., Skov, T. and Tjøstheim, B.A., 2002. SACS2 Final Report by GECO, WP 8-11 Geophysical Interpretation, MSCO2_rep_Final.doc, 53p.

Bradwell, T., Stoker, M.S., Golledge, N.R., Wilson, C.K., Merritt, J.W., Long, D., Everest, J.D., Hestvik, O.B., Stevenson, A.G., Hubbard, A.L., Finlayson, A.G., & Mathers, H.E., 2008. The northern sector of the last British Ice Sheet: Maximum extent and demise. Earth-Science Reviews, 88, pp. 207-226.

Brigaud, F. Vasseur, G. & Caillet, G., 1992. Thermal state in the North Viking Graben (North Sea) determined from oil exploration well data. Geophysics, 57 (1), pp. 69-88.

British Geological Survey, Map Sheet 58N 00, Fladen (Quaternary), 1988.

Brown, A., 2000. Evaluation of Possible Microseep Mechanisms. AAPG Bulletin, v. 84, No. 11, November 2000, pp. 1775-1789.

Burley, S.D., 1993. Models of burial diagenesis for deep exploration plays in Jurassic fault traps of the central and northern North Sea. *In:* Parker, J.R. (editor), Proceedings of the Fourth Conference Petroleum Geology of Northwest Europe. The Geological Society, London, pp. 1353-1375.

Busch, A., Alles, S., Kroos, B.M., Stanjek, H. & Dewhurst, D., 2009. Effects of physical sorption and chemical reactions of CO_2 in shaly caprocks. Energy Procedia 1 (GHGT-9), pp. 3229-3235.

Busch, A. & Müller, N., 2011. Determining CO_2/brine relative permeability and capillary threshold pressures for reservoir rocks and caprocks: Recommendations for development of standard laboratory protocols. Energy Procedia 4 (GHGT-10), pp. 6053-6060.

Carlsen, I.M., Mjaaland, S. & Nyhavn, F., 2001. SACS - 2, Work Package 4. Monitoring Well Scenarios. SINTEF Petroleum Research, Report No. 32.1021.00/01/01 (Restricted), 45p.

Carr, S.J., Holmes, R., Van Der Meer, J.J.M. & Rose, J., 2006. The Last Glacial Maximum in the North Sea Basin: Micromorphological Evidence of Extensive Glaciation. Journal of Quaternary Science 21 (2), pp. 131-153.

Carruthers, D.J. & van Wijngaarden, 2000. Modelling Viscous-Dominated Fluid Transport Using Modified Invasion Percolation Techniques. Journal of Geochemical Exploration, 69-70, pp. 669-672.

Carstens, H. & Finstad, K.G., 1981. Geothermal Gradients of the Northern North Sea Basin, 59-62°N. Institute of Petroleum (London), Petroleum Geology of the Continental Shelf of North-West Europe, pp. 152-161.

Cartwright, J.A., 1994. Episodic Basin-Wide Fluid Expulsion from Geopressured Shale Sequences in the North Sea Basin. Geology 22, pp. 447-450.

Cartwright, J., James, D. & Bolton, A., 2003. The genesis of polygonal fault systems: a review, in: Van Rensbergen, P., Hillis, R.R., Maltman, A.J. & Morley, C.K. (Eds.), Subsurface Sediment Mobilisation. Geological Society, London, Special Publication, 216, pp. 223-243.

Cartwright, J., Huuse, M. & Aplin, A., 2007. Seal Bypass Systems. AAPG Bulletin, v.91, No.8, pp. 1141-1166.

Cavanagh, A.J., Di Primio, R., Scheck-Wenderoth, M. & Horsfield, B., 2006. Severity and timing of Cenozoic exhumation in the southwestern Barents Sea. Journal of the Geological Society, London, 163, pp. 761-774.

Cavanagh, A. & Wildgust, N., 2011. Pressurisation and Brine Displacement Issues for Deep Saline Formation CO_2 Storage. GHGT-10, Energy Procedia 4, pp. 4814-4821.

Cawley, S.J., Saunders, M.R., Le Gallo, Y., Carpentier, B., Holloway, S., Kirby, G.A., Bennison, T., Wickens, L., Wikramaratna, R., Bidstrup, T., Arkley, S.L.B., Browne, M.A.E. & Ketzer, J.M., 2005. The NGCAS Project - Assessing The Potential For EOR And CO_2 Storage At The Forties Oilfield, Offshore UK, in: Thomas, D.C. & Benson, S.M. (Eds.), Carbon Dioxide Capture for Storage in Deep Geologic Formations - Results from the CO_2 Capture Project, Vol. Two: Geologic Storage of Carbon Dioxide with Monitoring and Verification, Elsevier, pp. 713-750.

Celia, M.A. & Bachu, S., 2003. Geological Sequestration of CO_2: Is Leakage Avoidable and Acceptable?, in: Gale, J. & Kaya, Y. (Eds.), Proceedings of the 6th International Conference on Greenhouse Gas Control Technologies (GHGT-6), 1–4 October, Kyoto Japan, Pergamon, v.1, pp. 477–482.

Celius, H.K. & Ingeberg, K., 1996. The Impact of CO_2 Taxation on Oil and Gas Production in Norway. SPE paper 35961, presented at the International Conference on Health, Safety & Environment, New Orleans, Louisiana, USA, 9-12 June. 10p.

Chadwick, R.A., Holloway, S., Kirby, G.A., Gregersen, U. and Johannesen, P.N., 2000. The Utsira Sand, Central North Sea - An Assessment of its Potential for Regional CO_2 Disposal. In: Proceedings of the 5th. International Conference on Greenhouse Gas Control Technologies. CSIRO Publishing, 6p.

Chadwick, R.A., Kirby, G.A., Holloway, S., Gregersen, U., Johannessen, P.N., Zweigel, P. & Arts, R., 2002. Saline Aquifer CO_2 Storage (SACS 2), Final report: Geological Characterisation of the Utsira Sand reservoir and caprocks (Work Area 1), British Geological Survey Commissioned Report CR/02/153C, p. 30 (minus figures).

Chadwick, R.A., Zweigel, P, Gregersen, U., Kirby, G.A., Holloway, S. & Johannessen, P.N., 2004. Geological Characterisation of a CO_2 Storage Site: The Utsira Sand, Sleipner, Northern North Sea. Energy (29), pp. 1371-1381.

Chadwick, R.A., Arts, R. & Eiken, O. 2005. 4D Seismic Quantification of a Growing CO_2 Plume at Sleipner, North Sea, in: Dore, A.G. & Vining, B.A. (Eds.), 6th Petroleum Geology Conference, Geological Society London, Vol. 6, Geological Society London, pp. 1385–1399.

Chadwick, A., Arts, R., Bernstone, C., May, F., Thibeau, S., & Zweigel, P., 2008. Best practice for the storage of CO_2 in saline aquifers - observations and guidelines from the SACS and CO2STORE projects. Nottingham, UK, British Geological Survey, 267pp. (BGS Occasional Publication, 14).

Chadwick, R.A., Noy, D.J. & Holloway, S., 2009a. Flow processes and pressure evolution in aquifers during the injection of supercritical CO_2 as a greenhouse gas mitigation measure. Petroleum Geoscience, v.15, pp. 59-73.

Chadwick, R.A., Noy, D., Arts, R. & Eiken, O., 2009b. Latest time-lapse seismic data from Sleipner yield new insights into CO_2 plume development. Energy Procedia I, pp. 2103-2110.

Chadwick, A., Williams, G., Delepine, N., Clochard, V., Labat, K., Sturton, S., Buddensiek, M.-L., Dillen, M., Nickel, M., Lima, A.L., Arts, R., Neele, F. & Rossi, G., 2010. Quantitative analysis of time-lapse seismic monitoring data at the Sleipner CO_2 storage operation. The Leading Edge, February, pp. 170-177.

Chadwick, R.A. & Noy, D., 2010. History-matching flow simulations and time-lapse seismic data from the Sleipner CO_2 plume, in: Vining, B.A. & Pickering, S. C. (Eds.) Petroleum Geology: From Mature Basins to New Frontiers – Proceedings of the 7th. Petroleum Geology Conference, 1171–1182.

Chadwick, R.A., 2011. CO_2 storage site monitoring: can we meet the regulatory requirements? Presentation at the CO_2ReMoVe NGO-research dialogue workshop, February 23rd., Brussels, 22p.

Chalbaud, C., Robin, M, & Egermann, P., 2006. Interfacial Tension Data and Correlations of Brine/CO_2 Systems Under Reservoir Conditions. SPE Paper 102918, presented at the SPE Annual Technical Conference and Exhibition, San Antonio, Texas, USA, 24-27th. September 2006, 11p.

Chalbaud, C., Robin, M., Lombard, J-M., Egermann, P. & Bertin, H., 2009. Interfacial Tension Measurements and Wettability Evaluation for Geological CO_2 Storage. Advances in Water Resources, Vol. 32, Issue 1, January 2009, pp. 98-109.

Chenevert, M.E. & Amnullah, M., 2001. Shale Preservation and Testing Techniques for Borehole-Stability Studies. SPE Drilling and Completion, September, pp. 146-149 (also available as SPE paper 73191).

Chiquet, P., Broseta, D. & Thibeau, S., 2007a. Wettability Alteration of Caprock Minerals by Carbon Dioxide. Geofluids, 7, pp. 112-122.

Chiquet, P. Daridon, J.L., Broseta, D. & Thibeau, S., 2007b. CO_2 -Water Interfacial Tensions Under Pressure and Temperature Conditions of CO_2 Geological Storage. Energy Conversion and Management, 48, pp. 736-744.

Chopra S. & Marfurt, K.J., 2005. Seismic attributes - A historical perspective. Geophysics, Vol. 70, No. 5 (September-October), pp. 3SO-28SO.

Clark, C.D., Tulaczyk, S.M., Stokes, C.R. & Canals, M., 2003. A groove-ploughing theory for the production of mega-scale glacial lineations, and implications for ice-stream mechanics. Journal of Glaciology, Vol. 49, No. 165, pp. 240-256.

Clennell, M.B., Josh, M., Dewhurst, D., Esteban, L. & Raven, M., 2010. Shale Petrophysics: Electrical, Dielectric and NMR Methods to Characterise Mudrocks and Discover Relationships to Mechanical Properties and Hydrocarbon Affinity. Paper presented at the AAPG Hedberg Conference, December 5-10, Austin, Texas, USA, 5p.

Connolly, D.L. & Brouwer, F., 2008. Detection Fault Related Hydrocarbon Migration Pathways in Seismic Data: Implications for Fault-Seal Pressure and Charge Prediction. Southeastern Geophysical Society of New Orleans, Reflections, December, pp. 1-5.

Cronin, T.M., Dwyer, G.S, Kamiya, T., Schwede, S. & Willard, D.A., 2003. Medieval Warm Period, Little Ice Age and 20th. Century temperature variability from Chesapeake Bay. Global and Planetary Change, 36, pp. 17-29.

Curtis, C., 1987. Mineralogical Consequences of Organic Matter Degradation in Sediments: Inorganic / Organic Diagenesis, in: Leggett, J.K. & Zuffa, G.G. (Eds.), Marine Clastic Sedimentology, Chapter 6, pp. 108-123.

.

Danesh, A., 1998. PVT and Phase Behaviour of Petroleum Reservoir Fluids, Elsevier, 400p.

Daniel, R.F. & Kaldi, J.G., 2008. Evaluating seal capacity of caprocks and intraformational barriers for the geosequestration of CO_2. Paper presented at the PESA Eastern Australia Basins Symposium III, Sydney, 14-17th. September, pp. 475-484.

dGB Earth Sciences, Seismic Software and Services, website address: http://www2.dgb-group.com/index.php/fluid-migration.html (24th. August 2011).

DNV (Det Norske Veritas), 2010. CO2QUALSTORE: Guideline for selection and Qualification of Sites and Projects for Geological Storage of CO_2. DNV Report No. 2009-1425, 77p.

Doney, S.C., Fabry, V.J., Feely, R.A. & Kleypas, J.A., 2009. Ocean Acidification: The Other CO_2 Problem. Annual Review of Marine Science, 1, pp. 169-192.

Dooley, J.J., Dahowski, R.T & Davidson, C.L., 2010. CO_2-driven Enhanced Oil Recovery as a Stepping Stone to What? Report PNNL-19577 prepared for the US Department of Energy under Contract DE-AC05-76RL01830, 33p.

Dowdeswell, J.A. & Bamber, J.L., 2007. Keel depths of modern Antarctic icebergs and implications for sea-floor scouring in the geological record. Marine Geology, Vol. 243, pp. 120-131.

Downey, M., 1984. Evaluating Seals for Hydrocarbon Accumulations. The American Association of Petroleum Geologists, Vol. 68, No.11, November, pp. 1752-1763.

Driesner, T. & Heinrich, C.A., 2007. The system H_2O-NaCl. Part I: Correlation formulae for phase relations in temperature-pressure-composition space from 0 to 1000°C, 0 to 5000 bar, and 0 to 1 X_{NaCl}. Geochimica et Cosmochimica Acta, 71, pp. 4880-4901.

Duan, Z. & Sun, R., 2003. An Improved Model Calculating CO_2 Solubility in Pure Water and Aqueous NaCl Solutions from 273-533°K and from 0-2000 bar. Chemical Geology 193, pp. 257-271.

Dubos-Sallee, N. & Rasolofosaon, P.N.J., 2010. Data-driven Quantitative Analysis of the CO_2 Plume Extension from 4D Seismic Monitoring in Sleipner. Paper K010 presented at the 72nd EAGE Conference & Exhibition incorporating SPE EUROPEC 2010, Barcelona, Spain, 14 - 17 June, 5p.

Eidvin, T. and Rundberg, Y., 2001. Late Cainozoic stratigraphy of the Tampen area (Snørre and Visund fields) in the northern North Sea, with emphasis on the chronology of early Neogene sands. Norsk Geologisk Tidsskrift, 81, pp. 119–160.

Eidvin, T. and Rundberg, Y., 2007. Post-Eocene strata of the southern Viking Graben, northern North Sea; integrated biostratigraphic, strontium isotopic and lithostratigraphic study. Norwegian Journal of Geology, 87, pp. 391-450.

Eggen, S.S., 1984. Modelling of subsidence, hydrocarbon generation and heat transport in the Norwegian North Sea. In: Durand, B. (editor), Thermal Phenomena in Sedimentary Basins. Edition Techniprint, Paris, pp. 271-286.

Enick, R.M. & Klara, S.M., 1990. CO_2 solubility in water and brine under reservoir conditions. Chemical Engineering Communications, 90, pp. 23-33.

Environment Department – The World Bank, 2007. Growth and CO_2 Emissions: How Do Different Countries Fare? (Lead Author) Bacon, R.W., 38p.

European Union, 2009. Directive 2009/31/EC of the European Parliament and of the Council of 23rd. April 2009 on the geological storage of carbon dioxide and amending Council Directive 85/337/EEC, European Parliament and Council Directives 2000/60/EC, 2001/80/EC, 2004/35/EC, 2006/12/EC, 2008/1/EC and Regulation (EC) No 1013/2006, 22p.

Evans, D., Graham, C., Armour, A. & Bathhurst, P. (Editors), 2003. The Millennium Atlas: Petroleum Geology of the Central & Northern North Sea. The Geological Society of London (Publisher), 390p.

Evans, R.J., Stewart, S.A. and Davies, R.J., 2007. Phase-reversed seabed reflections in seismic data: examples related to mud volcanoes from the South Caspian Sea. Geophysical Marine Letters, 27, pp. 203-212.

Evans, T.R. & Coleman, N.C., 1974. North Sea Geothermal Gradients. Nature, v.247, January 4, pp. 28-30.

Faleide, J.I., Kyrkjebo, R., Kjennerud, T., Gabrielsen, R.H., Jordt, H., Fanavoll, S. & Bjerke, M.D., 2002. Tectonic impact on sedimentary processes during Cenozoic evolution of the northern North Sea and surrounding areas. *From:* Dore, A.G., Cartwright, J.A., Stoker, M.S., Turner, J.P. & White, N. (editors) 2002. Exhumation of the North Atlantic Margin: Timing, Mechanisms and Implications for Petroleum Exploration. Geological Society, London, Special Publications, 196, pp. 235-269.

Fichler, C., Henrikson, S., Rueslaatten, H. & Hovland, M., 2005. North Sea Quaternary morphology from seismic and magnetic data: indications for gas hydrates during glaciation? Petroleum Geoscience, Vol. 11, pp. 331-337.

Fisher, Q.J., Harris, S.D., McAllister, E., Knipe, R.J. & Bolton, A.J., 2001. Hydrocarbon flow across faults by capillary leakage revisited. Marine and Petroleum Geology, 18, pp. 251-257.

Fleury, M., Pironon, J., Le Nindre, Y.M., Bildstein, O., Berne, P., Lagneau, V., Broseta, D., Pichery, T., Fillacier, S., Lescanne, M. & Vidal, O., 2010. Evaluating Sealing Efficiency of Caprocks for CO_2 Storage: an Overview of the Geocarbone-Integrity Program and Results. Oil and Gas Science and Technnology – Rev. IFP. Dossier – CO_2 Storage in the Struggle against Climate Change. Institut Français du Pétrole, DOI: 10.2516/ogst/2010007, 10p.

Fraiser, M.L. & Bottjer, D.J., 2007. Elevated Atmospheric CO_2 and the Delayed Biotic Recovery from the End-Permian Mass Extinction. Palaeogeography, Palaeoclimatology, Palaeoecology, Vol. 252, Iss. 1-2, 20th. August, pp. 164-175.

Gale, J., 2004. Why Do We Need To Consider Geological Storage Of CO_2?, in: Baines, S.J. & Worden, R.H. (Eds.), Geological Storage of Carbon Dioxide. Geological Society, London, Special Publications, 233, pp. 7-15.

Galloway, W.E., 2002. Paleogeographic Setting and Depositional Architecture of a Sand-Dominated Shelf Depositional System, Miocene Utsira Formation, North Sea Basin. Journal of Sedimentary Research, Vol. 72, No. 4, July, pp. 476-490.

García, J.E., 2001. Density of Aqueous Solutions of CO_2, Lawrence Berkeley National Laboratory Report LBNL-49023, Berkeley, CA, 8p.

Gaus, I., Azaroual, M. & Czernichowski-Lauriol, I. 2005. Reactive Transport Modelling of the Impact of CO_2 Injection on the Clayey Cap Rock at Sleipner (North Sea), Chemical Geology, 217, pp. 319-337.

Gay, A., Lopez, M., Cochonat, P., Seranne, M., Levache, D. & Sermondadaz, G., 2006. Isolated Seafloor Pockmarks Linked to BSRs, Fluid Chimneys, Polygonal Faults and Stacked Oligocene-Miocene Turbiditic Palaeochannels in the Lower Congo Basin. Marine Geology 226, pp. 25-40.

GCCSI (Global Carbon Capture and Storage Institute), 2011. The Global Status of CCS: 2011, Canberra, Australia, ISBN 978-0-9871863-0-0, 156p.

Gersmann, H. & Harvey, F., 2011. Longannet Carbon Capture Project Cancelled. The Guardian Newspaper, Wednesday 19th. October (19th. November 2011).

Ghanbari, S., Al-Zaabi, Y., Pickup, G.E., Mackay, E., Gozalpour, F. & Todd, A.C., 2006. Simulation of CO_2 Storage in Saline Aquifers. Chemical Engineering Research and Design, 84 (A9), pp. 764-775.

Gibbard, P.L. & Head, M.J., 2010. The newly-ratified definition of the Quaternary System/Period and redefinition of the Pleistocene Series/Epoch, and comparison of proposals advanced prior to formal ratification. Episodes, 33, pp. 152-158.

Gibbins, J., Haszeldine, R.S., Holloway, S., Pearce, J., Oakey, J., Shackley, S. and Turley, C., 2006. Scope for Future CO_2 Emission Reductions from Electricity Generation through the Deployment of Carbon Capture and Storage Technologies, in: Avoiding Dangerous Climate Change (Ed.), Schellnhuber, H.J., Cambridge University Press, pp. 379-384.

Godfrey, R. & Bachrach, R., 2008. Seismically Guided Fracture Characterisation. CSEG Recorder, March Issue, pp. 30-36.

Goto, M., Sasaki, M., Kiyan, T., Fang, T, Roy, B.C., Namihiri, T., Akiyama, H. and Hara, M., 2008. Reaction in Plasma Generated in Supercritical Carbon Dioxide. Joint 21st. AIRAPT and 45th. EHPRG Int. Conf. on High Pressure Science and Technology, Journal of Physics: Conference Series 121, 082009, 8p.

Graeme-Rowe, D., 2008. Let's Hear it for CO_2. New Scientist, 1st. March, pp. 32-34.

Graham, A.G.C., Lonergan, L. & Stoker, M.S., 2007. Evidence for Late Pleistocene ice stream activity in the Witch Ground Basin, central North Sea, from 3D seismic reflection data. Quaternary Science Reviews, 26, pp. 627-643.

Gregersen, U., Michelsen, O. & Sørensen, J.C., 1997. Stratigraphy and Facies Distribution of the Utsira Formation and the Pliocene Sequences in the Northern North Sea. Marine and Petroleum Geology, (14), 7/8, pp. 893-914.

Gregersen, U., Johannessen, P.N., Moller, J.J., Kristensen, L., Christiansen, N.P., Holloway, S., Chadwick, A., Kirby, G., Lindeberg, E. and Zweigel, P., 1998. Saline Aquifer CO_2 Storage (SACS) Phase Zero. Confidential.

Gregersen, U. & Johannessen, P.N., 2007. Distribution of the Neogene Utsira Sand and the succeeding deposits in the Viking Graben area, North Sea. Marine and Petroleum Geology, 24, pp. 591-606.

Grimstad A.-A., Georgescu, S., Lindeberg, E. & Vuillaume, J.-F., 2009. Modelling and Simulation of Mechanisms for Leakage of CO_2 from Geological Storage. Energy Procedia I, pp. 2511-2518.

Grollimund, B. & Zoback, M.D., 2000. Post glacial lithospheric flexure and induced stresses and pore pressure changes in the northern North Sea. Tectonophysics, 327, pp. 61-81.

Gudmundsson, A., Gjesdal, O., Brenner, S.L. & Fjeldskaar, I., 2003. Effects of linking up of discontinuities on fracture growth and groundwater transport. Hydrogeology Journal, 11, pp. 84-99.

Hamborg, M., Kirby, G., Lothe, A. & Zweigel, P., 2003. Seismic mapping and simulation of CO2 migration in the upper Utsira sand wedge east of the Sleipner injection site - A contribution to the Saline Aquifer CO2 Storage (SACS) project. SINTEF Petroleum Research, Report No. 33.5324.00/03/03 (Confidential), 43p.

Hansen, H., Eiken, O. & Aasum, T.O., 2005. Tracing the path of carbon dioxide from a gas-condensate reservoir, through an amine plant and back into a subsurface aquifer. Case study: The Sleipner area, Norwegian North Sea. SPE paper 96742, presented at Offshore Europe 2005, Aberdeen, Scotland, UK, 6-9 September. 15p.

Harper, M.L., 1971. Approximate Geothermal Gradients in the North Sea Basin. Nature, v.230, March 26, pp. 235-236.

Harrington, J.F. & Horseman, S.T., 1999. Gas transport properties of clays and mudrocks. From: Aplin, A. C., Fleet, A. J. & Macquaker, J. H. S. (eds), Muds and Mudstones: Physical and Fluid Flow Properties. Geological Society, London, Special Publications, 158, pp.107-124.

Harrington, J.F., Noy, D.J., Horseman, S.T., Birchall, D.J. & Chadwick, R.A., 2009. Laboratory Study of gas and water flow in the Nordland Shale, Sleipner, North Sea, *in* Grobe, M., Pashin, J. and Dodge, R. (editors), Carbon dioxide sequestration in geological media – State of the science: AAPG Studies in Geology, 59 (Special Publication of the American Association of Petroleum Geologists), pp. 521-543.

Haszeldine, R.S., 2009. Carbon Capture and Storage: How Green Can Black Be? Science, Vol. 325, pp. 1647-1652.

Head, M.J., Riding, J.B, Eidvin, T. & Chadwick, R.A., 2004. Palynological and foraminaferal biostratigraphy of (Upper Pliocene) Nordland Group mudstones at Sleipner, northern North Sea. Marine and Petroleum Geology, 21, pp. 277-297.

Heggland, R., 1997. Detection of gas migration from a deep source by use of exploration 3D seismic data. Marine Geology, 137, pp. 41-47.

Heggland, R., 1998. Gas seepage as an indicator of deeper prospective reservoirs. A study based on exploration 3D seismic data. Marine and Petroleum Geology, 15, pp. 1-9.

Heggland, R., 2002. Using Detection of Seismic Chimneys In Seal Integrity Analysis; A Discussion Based On Case Histories. Paper presented at the AAPG Hedberg Research Conference, December 1-5, Barossa Valley, South Australia, 4p.

Heggland, R., 2005. Using Gas Chimneys in Seal Integrity Analysis: A Discussion Based on Case Histories, in: Boult, P. & Kaldi, J. (Eds.), Evaluating Fault and Cap Rock Seals: AAPG Hedberg Series, No. 2, pp. 237-245.

Helama, S, Fauria, M.M., Mielikainen, K., Timonen, M. & Eronen, M., 2010. Sub-Milankovich solar forcings of past climates: Mid and late Holocene perspectives. Geological Society of America Bulletin, November/December, Vol. 122, No. 11/12, pp. 1981-1988.

Henderson, C., 2006. Paradise Lost. New Scientist, 5th. August, pp. 29-33.

Hermanrud, C., Zweigel, P., Eiken, O., Lippard, J. & Andresen, T., 2007. CO_2 Flow in the Utsira Formation: Inferences made from 4D seismic analyses of the Sleipner area, presentation at the AAPG European Region Conference, Athens, Greece.

Hermanrud, C., Teige, G.M.G., Iding, M., Eiken, O., Rennan, L. & Østmo, S., 2010. Differences between flow of injected CO_2 and hydrocarbon migration, in: Vining, B.A. & Pickering, S.C. (Eds.) Petroleum Geology: From Mature Basins to New Frontiers – Proceedings of the 7th Petroleum Geology Conference, Published by the Geological Society of London, pp.1183–1188.

Hildenbrand A., Schlömer, S., Krooss, B.M. & Littke, R., 2004. Gas Breakthrough Experiments on Pelitic Rocks: Comparative Study with N_2, CO_2 and CH_4. Geofluids, 4, pp. 61-80.

Hilfer, R. & Øren, P.E., 1996. Dimensional Analysis of Pore Scale and Field Scale Immiscible Displacement. Transport in Porous Media, 22, pp. 53-72.

Holloway, S., 2001. Storage Of Fossil Fuel-Derived Carbon Dioxide Beneath The Surface Of The Earth. Annu. Rev. Energy Environ. Vol. 26, pp. 145-166.

Holloway, S., Bentham M. & Kirk, K., 2006. Chapter 2: Underground Storage Of Carbon Dioxide, in: Shackley, S. & Gough, C. (Eds.), Carbon Capture and its Storage, Ashgate Publishing Ltd.

Hovland, M., Talbot, M.R., Qvale, H., Olaussen, S. & Aasberg, L., 1987. Methane-Related Carbonate Cements in Pockmarks of the North Sea. Journal of Sedimentary Petrology, Vol. 57, No. 5, September, pp. 881-892.

Howell, J., Vassel, Å. & Aune, T., 2008. Modelling of dipping clinoform barriers within deltaic outcrop analogues from the Cretaceous Western Interior Basin, USA. From: Robinson, A., Griffiths, P., Price, S., Hegre, J. & Muggeridge, A. (Eds.). The Future of Geological Modelling in Hydrocarbon Development. The Geological Society, London, Special Publications, 309, pp. 99–121.

Huang, F-H., Li, M-H. Lee, L.L., Starling, K.E. & Chung, F.T.H., 1985. An Accurate Equation of State for Carbon Dioxide. Journal of Chemical Engineering of Japan, Vol. 18, No. 6, pp. 490-496.

Hurst, A., Cartwright, J., Huuse, M., Jonk, R., Schwab, A., Duranti, D. & Cronin, B., 2003. Significance of large-scale sand injectites as long-term fluid conduits: evidence from seismic data. Geofluids, 3, pp. 263-274.

Hurter, S., Garnett, A., Bielinski, A. & Kopp, A., 2007a. Thermal Signature of Free-Phase CO_2 in Porous Rocks: Detectability of CO_2 by Temperature Logging. SPE paper 109007, presented at Offshore Europe 2007, Aberdeen, Scotland, UK, 4-7 September. 12p.

Hurter, S., Labregere, D. & Berge, J., 2007b. Simulations for CO_2 Injection Projects with Compositional Simulator. SPE paper 108540, presented at Offshore Europe 2007, Aberdeen, Scotland, UK, 4-7 September. 7p.

Huuse, M. & Lykke-Andersen, H., 2000. Overdeepened Quaternary valleys in the eastern Danish North Sea: morphology and origin. Quaternary Science Reviews, 19, pp. 1233-1253.

Huuse, M. & Clausen, O.R., 2001. Morphology and origin of major Cenozoic sequence boundaries in the eastern North Sea Basin: top Eocene, near-top Oligocene and the mid-Miocene unconformity. Basin Research, 13, pp. 17-41.

Huuse, M. & Piotrowski, J.A., 2003. Geophysical investigations of buried Quaternary valleys in the formerly glaciated NW European lowland: significance for groundwater exploration. Journal of Applied Geophysics, 53, pp. 153-157.

Huuse, M. & Mickelson, M., 2004. Eocene Sandstone Intrusions in the Tampen Spur Area (Norwegian North Sea Quad 34) Imaged by 3D Seismic Data. Marine and Petroleum Geology 21, pp. 141-155.

IEA (International Energy Agency), 2011. Existing and Planned CCS Projects. http://www.iea.org/subjectqueries/ccs/technology_status.asp (November 19th. 2011).

Ingram, G.M. & Urai, J.L., 1999. Top-seal leakage through faults and fractures: the role of mudrock properties. From: Aplin, A. C., Fleet, A. J. & Macquaker, J. H. S. (eds), Muds and Mudstones: Physical and Fluid Flow Properties. Geological Society, London, Special Publications, 158, pp.125-135.

IPCC, 2001 – Third Assessment Report: Climate Change 2001: Synthesis Report, Summary for Policy Makers, pp. 1-34.

IPCC, 2002: Climate Change and Biodiversity, Technical Paper V, pp. 1-77.

IPCC, 2005: IPCC Special Report on Carbon Dioxide Capture and Storage. Prepared by Working Group III of the Intergovernmental Panel on Climate Change [Metz, B.,O. Davidson, H. C. de Coninck, M. Loos, and L. A. Meyer (eds.)]. Cambridge University Press, Cambridge, United Kingdom and New York, NY, USA, 442 p.

IPCC, 2007: Climate Change 2007: The Physical Science Basis. Contribution of Working Group I to the Fourth Assessment Report of the Intergovernmental Panel on Climate Change [Solomon, S., D. Qin, M. Manning, Z. Chen, M. Marquis, K.B. Averyt, M. Tignor and H.L. Miller (eds.)]. Cambridge University Press, Cambridge, United Kingdom and New York, NY, USA, 996 p.

Isaksen, D. & Tonstad, K. 1989: A revised Cretaceous and Tertiary Lithostratigraphic Nomenclature for the Norwegian North Sea. NPD Bulletin No. 5, ISBN 82-7257-295-8, 59p.

Isaksen, G.H., Patience, R., van Gras, G. & Jenssen, A.I., 2002. Hydrocarbon system analysis in a rift basin with mixed marine and nonmarine source rocks: The South Viking Graben, North Sea. AAPG Bulletin, v.86, No.4, April, pp. 557-591.

Jakobsen, B. & Rosendahl, F., 1994. The Sleipner Platform Accident. Structural Engineering International, 4 (3), August, pp.190-193.

Jackson C. & Stoddart, D., 2005. Temporal constraints on the growth and decay of large-scale mobilised mud masses and implications for fluid flow mapping in sedimentary basins. Terra Nova, 17, pp. 580-585.

Jadhawar, P., Mohammadi, A.H., Yang, J. & Tohidi, B., 2006. Subsurface Carbon Dioxide Storage Through Clathrate Hydrate Formation, in: Lombardi, S., Altunina, L.K. & Beaubien, S.E. (Eds.), Advances in the Geological Storage of Carbon Dioxide. NATO Science Series, IV. Earth and Environmental Sciences - Vol. 65, pp. 111-126.

Jansen, E. & Sjøholm, J., 1991. Reconstruction of glaciation over the past 6 Myr from ice-borne deposits in the Norwegian Sea. Nature, Vol. 349, 14 February, pp. 600-603.

Jansen, E., Fronval, T., Rack, F. & Channell, J.E.T., 2000. Pliocene-Pleistocene ice rafting history and cyclicity in the Nordic Sea during the last 3.5 Myr. Palaeoceanography, Vol. 15, No. 6, pp. 709-721.

Johnson H., Richards P.C., Long D. & Graham C.C., 1993. United Kingdom Offshore Regional Report: The Geology of the Northern North Sea. HMSO, London, 111p.

Johnston, I., 2007. Saudi Arabia of Renewable Energy off Scottish Coast. The Scotsman Newspaper, 23rd. June 2007.

Johnson, J.W. & Nitao, J.J., 2003. Reactive Transport Modelling of Geologic CO_2 Sequestration at Sleipner. Proceedings of the 6th International Conference on Greenhouse Gas Control Technologies 1 – 4 October 2002, Kyoto, Japan, pp. 327-332.

Johnson, J.W., Nitao, J.J. & Knauss, K.G., 2004. Reactive transport modelling of CO_2 storage in saline aquifers to elucidate fundamental processes, trapping mechanisms and sequestration partitioning. *From:* Baines, S.J. & Worden, R.H. (editors) Geological Storage of Carbon Dioxide. The Geological Society, London, Special Publications, 233, pp. 107-128.

Jones, D.G., Lister, T.R., Smith, D.J., West, J.M., Coombs, P., Gadalia, A., Brach, M., Annunziatellis, A. & Lombardi, S., 2011. In Salah Gas CO_2 Storage JIP: Surface gas and biological monitoring. Energy Procedia 4, pp. 3566-3573.

Jordt, H., Faleide, J.I., Bjørlykke, K. & Ibrahim, M.T., 1995. Cenozoic sequence stratigraphy of the central and northern North Sea Basin: tectonic development, sediment distribution and provenance areas. Marine and Petroleum Geology, Vol. 12, No. 8, pp. 845-879.

Jørgensen, F. & Sandersen, P.B.E., 2008. Mapping of buried tunnel valleys in Denmark: new perspectives for the interpretation of the Quaternary succession. Geological Survey of Denmark and Greenland Bulletin, 15, pp. 33-36.

Jossi, J. A., Stiel, L.I. & Thodos, G., 1962. The Viscosity of Pure Substances in the Dense Gaseous and Liquid Phases. AIChE Journal, Vol. 8, Iss. 1, pp. 59-63.

Judd, A. & Hovland, M., 2007. Seabed Fluid Flow: The Impact on Geology, Biology and the Marine Environment. Cambridge University Press, 491p. ISBN-10: 0521114209.

Justwan, H., Meisingset, I., Dahl, B. & Isaksen, G.H., 2006. Geothermal history and petroleum generation in the Norwegian South Viking Graben revealed by pseudo-3D basin modelling. Marine and Petroleum Geology, 23, pp. 791-819.

Kaufman, A.J. & Xiao, S., 2003. High CO_2 levels in the Proterozoic atmosphere estimated from analyses of individual microfossils. Nature, Vol. 425, 18th. September, pp. 279-282.

Kemp, S.J., Pearce, J.M. & Steadman, E.J., 2002. Mineralogical, geochemical and petrographical characterisation of Nordland Shale cores from well 15/9-A-11, Sleipner field, northern North Sea. British Geological Survey Commissioned Report CR/02/313, 40p.

Kharaka, Y.K., Thordsen, J.J., Hovorka, S.D., Seay Nance, H., Cole, D.R., Phelps, T.J. & Knauss, K.G., 2009. Potential environmental issues of CO_2 storage in deep saline aquifers: Geochemical results from the Frio-I Brine Pilot test, Texas, USA. Applied Geochemistry 24, pp.1106-1112.

Khattri, S.K., Hellevang, H., Fladmark, G.E. & Kvamme, B., 2006. Simulation of long-term fate of CO_2 in the sand of Utsira. Submitted to Journal of Transport in Porous Media, 27p.

Klerkx, J., De Batist, M., Poort, J., Hus, R., Van Rensbergen, P., Khylstov, O. & Granin, N., 2006. Tectonically Controlled Methane Escape In Lake Baikal, in: Lombardi, S., Altunina, L.K. & Beaubien, S.E. (Eds.), Advances in the Geological Storage of Carbon Dioxide. NATO Science Series, IV. Earth and Environmental Sciences - Vol. 65, Springer, pp. 203-219.

Knies, J., Matthiessen, J., Vogt, C., Laberg, J.S., Hjelstuen, B.O., Smelror, M., Larsen, E., Andreassen, K, Eidven, T. & Vorren, T.O., 2009. The Plio-Pleistocene glaciation of the Barents Sea-Svalbard region: a new model based on revised chronostratigraphy. Quaternary Science Reviews, 28, pp. 812-829.

Knoll, A.H., Bambach, R.K., Payne, J.L, Pruss, S. & Fischer, W.W., 2007. Palaeophysiology and End-Permian Mass Extinctions. Earth and Planetary Science Letters, Vol. 256, Issue 3-4, 30th. April, pp. 295-313.

Korbøl, R. & Kaddour, A., 1995. Sleipner Vest CO_2 Disposal – Injection Of Removed CO_2 Into The Utsira Formation, Energy Conversion and Management. Vol. 36, No. 6-9, pp. 509-512.

Koschel, D., Coxam, J-Y., Rodier, L. & Majer, V., 2006. Enthalpy and Solubility Data of CO_2 in Water and NaCl (aq) at Conditions of Interest for Geological Sequestration. Fluid Phase Equilibria, Vol. 247, Issues 1-2, 15th. September, pp. 107-120.

Kristensen, L. & Bidstrup, T. 2001. The Natural Fluid Flow in the (Utsira) Storage Reservoir - Basin Modelling. Final Technical Report of SACS Project, Work Area 1: Geology, Task 1.6. GEUS Report 2001/2.

Kristensen, T.B., Huuse, M., Piotrowski, J.A. & Calausen, O.R., 2007. A morphometric analysis of tunnel valleys in the eastern North Sea based on 3D seismic data. Journal of Quaternary Science, 22 (8), pp. 801-815.

Krushin, J.T., 1997. Seal Capacity of Non-Smectite Clays, in: Surdam, R.C. (Editor), Seals, Traps and the Petroleum System, AAPG Memoir 67, pp. 31-47.

Kuhlmann, G., de Boer, P.L., Pedersen, R.B. & Wong, T.E., 2004. Provenance of Pliocene sediments and palaeoenvironmental changes in the southern North Sea region using Samarium-Neodymium (Sm/Nd) provenance ages and clay mineralogy. Sedimentary Geology, 171, pp. 205-226.

Kuhlmann, G. & Wong, T.E., 2008. Pliocene palaeoenvironment evolution as interpreted from 3D-seismic data in the southern North Sea, Dutch offshore sector. Marine and Petroleum Geology, 25, pp. 173-189.

Kvalheim, B., 2009. The Tordis Incident 2008. Presentation at the CO_2 Workshop, Svalbard, August 3rd. to 7th., 17p.

Kvamme, B., Graue, A., Buanes, T., Kuznetsova, T. & Ersland, G., 2009. Effects of solid surfaces on hydrate kinetics and stability. *From:* Long, D., Lovell, M.A., Rees, J.G. & Rochelle, C.A. (editors) Sediment-Hosted Gas Hydrates: New Insights on Natural and Synthetic Systems. The Geological Society, London, Special Publications, 319, pp. 131-144.

Laberg, J.S., Andreassen, K., Knies, J., Vorren, T.O. & Winsborrow, M., 2010. Late Pliocene-Pleistocene development of the Barents Sea Ice Sheet. Geology, Vol. 38, No.2, February, pp. 107-110.

Lackner, K.S., 2002. Carbonate Chemistry For Sequestering Fossil Carbon, Annual Review of Energy and the Environment, Vol. 27, pp. 193-232.

La Force, T., Jessen, K. & Orr Jnr., F.M., 2008. Four-component gas/water/oil displacements in one dimension: part II, example solutions. Transport in Porous Media, 72, pp. 83-96.

Le Heron, D.P. & Etienne, J.L., 2005. A complex subglacial clastic dyke swarm, Solheimajokull, southern Iceland. Sedimentary Geology, 181, pp. 25-37.

Le Heron, D.P., Sutcliffe, O.E., Whittington, R.J. & Craig, J., 2005. The origins of glacially related soft-sediment deformation structures in Upper Ordovician glaciogenic rocks: implication for ice-sheet dynamics. Palaeogeography, Palaeoclimatology, Paleaoecology, 218, pp. 75-103.

Lenstra, W.J. & van Engelenburg, B.C.W., 2003. Climate Policy, CO_2 Storage and Public Perception. In: Williams, D., Durie, B., McMullan, P., Paulson, C. & Smith, A. (Eds.). Proceedings of the 5th. International Conference on Greenhouse Gas Control Technologies. CSIRO, Collingwood, Australia, pp. 31–39.

Levine, J.S., Matter, J.M., Goldberg, D. & Lackner, K.S., 2009. Gravitational trapping of carbon dioxide in deep ocean sediments: hydraulic fracturing and mechanical stability. Energy Procedia I, pp. 3647-3654.

Li, Z., Dong, M., Li, S. & Huang, S., 2006. CO_2 sequestration in depleted oil and gas reservoirs – caprock characterization and storage capacity. Energy Conversion and Management, 47, pp. 1372-1382.

Ligtenberg, H. & Connolly, D., 2003. Chimney detection and interpretation, revealing sealing quality of faults, geohazards, charge of and leakage from reservoirs. Journal of Geochemical Exploration, 78-79, pp. 385-387.

Ligtenberg, J.H., 2005. Detection of fluid migration pathways in seismic data: Implications for fault seal analysis. Basin Research, 17, pp. 141-153.

Lindeberg, E., 1997. Escape of CO_2 from Aquifers. Energy Conversion, Management, Vol. 38, Suppl., pp. S235-S240.

Lindeberg, E., 2001. Simulation of CO_2 Distribution Pattern in an Underground CO_2 Injection Project Calibrated by 3D Seismics. Second Nordic Minisymposium on Carbon Dioxide Capture and Storage, Göteburg, October 26th., 6p.

Lindeberg, E. & Bergmo, P., 2002. The Long Term Fate of CO_2 Injected Into an Aquifer. Paper presented at the 6th. Greenhouse Gas Technologies Conference (GHGT6), Kyoto 2002.

Lindeberg, E., Vuillaume, J.-F., Ghaderi, A., 2009. Determination of the CO_2 storage capacity of the Utsira formation. GHGT-9, Energy Procedia I, pp. 2777-2784.

Lindgren, H., Fries, K. & Springer, N., 2002/03. Saline Aquifer CO_2 Storage Project, SACS, Phase II, Task 1.4: Evaluation of cap rock sealing the reservoir. Clay mineralogical investigation of core and cuttings from the Ekofisk and Sleipner areas. (Confidential Report) GEUS (Geological Survey of Denmark and Greenland), 11p.

Lonergan, L., Maidment, S. & Collier, J., 2006. Pleistocene subglacial tunnel valleys in the central North Sea basin: 3-D morphology and evolution. Journal of Quaternary Science, 21, 8, pp. 891–903.

Løseth, H., Wensaas, L., Arntsen, B. & Hovland, M., 2003. Gas and fluid injection triggering shallow mud mobilisation in the Hordaland Group, North Sea. From: Van Rensbergen, P., Hillis, R.R., Maltman, A.J. & Morley, C.K. (eds) 2003. Subsurface Sediment Mobilisation. Geological Society, London, Special Publications, 216, pp. 139-157.

Løseth, H., Gading, M. & Wensaas, L., 2009. Hydrocarbon leakage interpreted on seismic data. Marine and Petroleum Geology, 26, pp.1304-1319.

Lothe, A.E. & Zweigel, P., 1999. Saline Aquifer CO_2 Storage (SACS). Informal annual report 1999 of SINTEF Petroleum Research's results in work area 1 – 'Reservoir Geology'. SINTEF Report 23.4300.00/03/99, 54p.

MacIntyre, K.J., 1986. Design Considerations for Carbon Dioxide Injection Facilities. Paper JCPT 86-02-09, presented at the Heavy Oil and Tar Sands Technical Symposium, Calgary, Canada, February 1985, 7p.

Maldal, T. & Tappel, I.M., 2004. CO_2 underground storage for Snøhvit gas field development. Energy 29, pp. 1403-1411.

Mamora, D.D. & Seo, J.G., 2002. Enhanced Gas Recovery by Carbon Dioxide Sequestration in Depleted Gas Reservoirs. SPE Paper 77347, presented at the 2002 SPE Annual Technical Conference & Exhibition, San Antonio, Texas, USA, 29 September - 2 October, 9p.

Mann, M.E., Bradley, R.S., & Hughes, M.K., 1998. Global-scale temperature patterns and climate forcing over the past six centuries. Nature, Vol. 392, 23rd. April, pp. 779-787 (refer also to Corrigendum for this article in Nature, Vol. 430, 1st. July, 2004, pp. 105).

Marcussen, Ø, Thyberg, B.I., Peltonen, C., Jahren, J., Bjørlykke, K. & Faleide, J.I., 2009. Physical properties of Cenozoic mudstones from the northern North Sea: Impact of clay mineralogy on compaction trends. AAPG Bulletin, Vol. 93, No. 1 (January 2009), pp. 127-150.

Maslin, M., 2004. Global Warming – A Very Short Introduction, Oxford University Press, 176p. ISBN-10: 0199548242.

Mazzini, A., Duranti, D., Jonk, R., Parnell, J., Cronin, B.T., Hurst, A. & Quine, M., 2003. Palaeo-Carbonate Seep Structures Above an Oil Reservoir, Gryphon Field, Tertiary, North Sea. Geo Marine Letters 23, pp. 323-339.

McIntyre, S. & McKitrick, R., 2003. Corrections to the Mann et al. (1998) proxy data base and Northern Hemisphere average temperature series. Energy & Environment, 14, pp. 751-771.

Meldahl, P., Heggland, R., Bril, B. & De Groot, P., 2001. Identifying faults and gas chimneys using multi-attributes and neural networks. The Leading Edge, May 2001, pp. 474-482.

Michels, A., Botzen, A. & Schuurman, W., 1957. The Viscosity of Carbon Dioxide between 0°C and 75°C and at Pressures up to 2000 Atmospheres. Physica, Vol. 23, Iss. 2, pp. 95-102.

Mito, S., Xue, Z. & Ohsumi, T., 2008. Case study of geochemical reactions at the Nagaoka CO_2 injection site, Japan. International Journal of Greenhouse Gas Control 2, pp. 309-318.

Monnin, E., Indermühle, A., Dällenbach, A., Flückiger, J., Stauffer, B., Stocker, T.F., Raynaud, D. & Barnola, J.-M., 2001. Atmospheric CO_2 concentrations over the last glacial termination. Science 291, pp. 112-114.

Moore, J., Adams, M., Allis, R., Lutz, S., Rauzi, S., 2005. Mineralogical and Geochemical Consequences of the Long-Term Presence of CO_2 in Natural Reservoirs: An Example from the Springerville-St. Johns Field, Arizona and New Mexico, U.S.A. Chemical Geology, 217, pp. 365-385.

Morozova, D., Wandrey, M., Alawi, M., Zimmer, M., Vieth, A., Zettlitzer, M & Würdemann, H., 2010. Monitoring of the microbial community in saline aquifers during CO_2 storage by fluorescence in-situ hybridisation. International Journal of Greenhouse Gas Control, 4, pp. 981-989.

National Aeronautics and Space Administration (NASA), 2011: http://climate.nasa.gov/keyIndicators/ (August 24th. 2011)

National Oceanic and Atmospheric Administration (NOAA), 2011: http://www.esrl.noaa.gov/gmd/ccgg/trends/ (August 24th. 2011).

Naylor, M., Wilkinson, M. & Haszeldine, R.S., 2011a. Calculation of CO_2 column heights in depleted gas fields from known pre-production gas column heights. Marine and Petroleum Geology, Vol. 28, Issue 5, May 2011, pp. 1083-1093.

Naylor, M., Nicoll, G.D. & Heafford, A., 2011b. Derisking CO_2 Phase Uncertainty at Geological Storage Sites Using Well Logs. In prep.

Neufeld, J.A., Vella, D. & Huppert H.E., 2009. The effect of a fissure on storage in a porous medium. Journal of Fluid Mechanics, Vol. 639, pp. 239-259.

Nooner, S.L., Eiken, O., Hermanrud, C., Sasagawa, G.S., Stenvold, T. & Zumberge, M.A., 2007. Constraints on the in-situ density of CO_2 within the Utsira Formation from time-lapse seafloor gravity measurements, International Journal of Greenhouse Gas Control 1, pp. 198-214.

NPD (Norwegian Petroleum Directorate). http://www.npd.no/en/ (August 24th. 2011)

Nunn, J.A. & Meulbroek, P., 2002. Kilometer-Scale Upward Migration of Hydrocarbons in Geopressured Sediments by Buoyancy-Driven Propagation of Methane-Filled Fractures. AAPG Bulletin 86 (5), May, pp. 907-918.

Nygård, R., Gutierrez, M., Bratli, R.K. & Høeg, K., 2006. Brittle-ductile transition, shear failure and leakage in shales and mudrocks. Marine and Petroleum Geology, 23, pp. 201-212.

Ó Cofaigh, C., Dowdeswell, J.A., Allen, C.S., Hiemstra, J.F., Pudsey, C.J., Evans, J. & Evans, D.J.A., 2005. Flow dynamics and till genesis associated with a marine-based Antarctic palaeo-ice stream, Quaternary Science Review, 24, pp. 709–740.

Odenberger, M., Kjärstad, J. & Johnsson, F., 2008. Ramp-up of CO_2 capture and storage within Europe. International Journal of Greenhouse Gas Control 2, pp. 417-438.

Okiongbo, K.S., 2011. Petrophysical Properties of North Sea Shales. Research Journal of Applied Sciences, Engineering and Technology, 3 (1), pp. 46-52.

Oldenberg, C.M., Pruess, K. & Benson, S.M., 2001. Process Modelling of CO_2 Injection into Natural Gas Reservoirs for Carbon Sequestration and Enhanced Gas Recovery. Energy and Fuels, 15, pp. 293-298.

Oldenberg, C.M., Webb, S.W., Pruess, K. & Moridis, G.J., 2004. Mixing of Stably Stratified Gases in Subsurface Reservoirs: A Comparison of Diffusion Models. Transport in Porous Media, 54, pp. 323-334.

Or, D., 2008. Scaling of capillary, gravity and viscous forces affecting flow morphology in unsaturated porous media. Advances in Water Resources, Vol. 31, Iss. 9, pp. 1129-1136.

Ottesen, D., Rise, L., Andersen, E.S., Bugge, T. & Eidvin, T., 2009. Geological evolution of the Norwegian continental shelf between 61°N and 68°N during the last 3 million years. Norwegian Journal of Geology, Vol. 89, pp. 251-265.

Pacala, S. & Socolow, R., 2004. Stabilisation Wedges: Solving the Climate Problem for the Next 50 Years with Current Technologies. Science Vol. 305, 13th. August, pp. 968-972.

Parnell, J., 2010. Potential of palaeofluid analysis for understanding oil charge history. Geofluids, Vol. 10, Issue 1-2, pp. 73-82.

Pearce, F., 1994. Responsible Norway Plans to Bury Greenhouse Gas at Sea. New Scientist, Issue 1950, 5th. November, p. 8.

Pearce, F., 2010. The Climate Files: The Battle For The Truth About Global Warming. Guardian Books, ISBN 978-0-85265-229-9, 266p.

Pearce, J.M., Kemp, S.J. & Wetton, P.D., 2000. Mineralogical and petrographical characterisation of a 1 m core from the Utsira Formation, central North Sea. BGS Technical Report WG/99/24C.

Pillitteri, A., Cerasi, P., Stavrum, J., Zweigel, P. & Bøe, R., 2003. Rock mechanical tests of shale samples from the cap rock of the Utsira Sand in well 15/9-A11 – A contribution to the Saline Aquifer CO_2 Storage (SACS) project. SINTEF Petroleum Research, Report No. 33.5324.00/06/03 (Confidential), 28p.

Pruess, K. 2008. Leakage of CO_2 from Geologic Storage: Role of Secondary Accumulation at Shallow Depth, International Journal of Greenhouse Gas Control, Vol. 2, Iss. 1, January, pp. 37-46.

Qin, J., Rosenbauer, R.J. & Duan, Z., 2008. Experimental Measurements of Vapor-Liquid Equilibria of the $H_2O + CO_2 + CH_4$ Ternary System. Journal of Chemical Engineering Data, 53, pp. 1246-1249.

Rabben, E. & Ursin, B., 2011. AVA inversion of the top Utsira Sand reflection at the Sleipner field. Geophysics, Vol. 76, Iss. 3, C53, doi: 1190/1.3567951.

Ren, Q-Y., Chen, G-J., Yan, W. & Guo, T-M., 2000. Interfacial Tension of (CO_2 + CH_4) + Water from 298 K to 373 K and Pressures up to 30 MPa. Journal of Chemical Engineering Data, 45, pp. 610-612.

Riaz, A., Hesse, M., Tchelepi, H.A. & Orr Jr., F.M., 2006. Onset of convection in a gravitationally unstable diffusive boundary layer in porous media. Journal of Fluid Mechanics, Vol. 548, pp. 87-111.

Ringrose P., Atbi, M., Mason, D., Espinassous, M., Myhrer, Ø., Iding, M., Mathieson, A. & Wright, I., 2009. Plume development around well KB-502 at the In Salah CO_2 storage site. First Break, Volume 27, January, pp. 85-89.

Ritter, U., Zielinski, G.W., Weiss, H.M., Zielinski, R.L.B. & Saettem, J., 2004. Heat flow in the Vøring Basin, Mid-Norwegian Shelf.
Petroleum Geoscience, 10, pp. 353 – 365.

Roberts H.H. & Fillon, R.H., 2004. Deltaic Deposits and Linked Downslope Petroleum Systems. Presented at the AAPG International Conference and Exhibition, Cancun, Mexico, October 24-27th., 4p.

Roberts, S.J. & Nunn, J.A., 1995. Episodic fluid expulsion from geopressured sediments. Marine and Petroleum Geology, 12, pp. 195-204.

Rochelle, C.A. & Moore, Y.A., 2002. The Solubility of CO_2 into Pure Water and Synthetic Utsira Porewater. British Geological Survey Commissioned Report, CR/02/052, 36p.

Rohde, R.A. (graphic artist), 2000, based on information from the Emission Database for Global Atmospheric Research, Version 3.2, Fast Track 2000 Project. http://www.globalwarmingart.com/wiki/Image:Greenhouse_Gas_by_Sector_png (August 24th. 2011).

Rubino, J.G., Velis, D.R. & Sacchi, M.D., 2011. Numerical analysis of wave-induced fluid flow effects on seismic data: Application to monitoring of CO_2 storage at the Sleipner field. Journal of Geophysical Research, Vol. 116, B03306, 16p.

Sæther, O.M., Flach, T., Bøe, R, Beer, H. de, & Rise, L., 2008. NFR CLIMIT Project No. 176004/I30. Deliverable D1.1 Compilation of estimation procedures for discrete leakage paths related to CO_2 geological storage. NGU (Norges Geologiske Undersøkelse) Geological Survey of Norway, 123p.

Sandersen, P.B.E. & Jorgensen, F., 2003. Buried Quaternary valleys in western Denmark – occurrence and inferred implications for groundwater resources and vulnerability. Journal of Applied Geophysics, 53, pp. 229-248.

Sandmo, T. (Ed.), 2011. The Norwegian Emission Inventory 2011. Documentation of methodologies for estimating emissions of greenhouse gases and long-range transboundary air pollutants. Statistics Norway, 267p.

Saripalli, P. & McGrail, P., 2002. Semi-analytical approaches to modelling deep well injection of CO2 for geological sequestration. Energy Conversion and Management, 43, pp. 185-198.

Satur, N. & Hurst, A., 2007. Sand Fluidisation Structures from the Ty Formation (Palaeocene), Sleipner Øst field, Norwegian North Sea, in: Hurst, A. & Cartwright, J. (Eds.), Sand Injectites: Implications for Hydrocarbon Exploration and Production, AAPG Memoir 87, pp. 113-117.

Schilling, F. Borm, G., Würdemann, H., Möller, F., Kühn, M. & CO_2SINK Group, 2009. Status Report on the First European on-shore CO_2 Storage Site at Ketzin (Germany). Energy Procedia 1, pp. 2029-2035.

Schowalter, T.T., 1979. Mechanics of secondary hydrocarbon migration and entrapment. American Association of Petroleum Geologists Bulletin, V.63, No.5, pp. 723-760.

Schroot, B.M. & Schüttenhelm, R.T.E., 2003. Expressions of shallow gas in the Netherlands North Sea. Netherlands Journal of Geosciences / Geologie en Mijnbouw, 82 (1), pp. 91-105.

Sejrup, H.P., Aarseth, I., Ellingsen, K.L., Reither, E., Jansen, E., 1987. Quaternary Stratigraphy of the Fladen Area, Central North Sea: a Multidisciplinary Study. Journal of Quaternary Science 2, pp. 35–58.

Sejrup, H.P., Aarseth, I. & Haflidason, H., 1991. The Quaternary Succession in the Northern North Sea. Marine Geology, 101, pp. 103-111.

Sejrup, H.P., Larsen, E., Haflidason, H., Berstad, I.M., Hjelstuen, B.O., Jonsdottir, H., King, E.L., Landvik, J., Longva, O., Nygard, A., Ottesen, D., Raunholm, S., Rise, L. & Stalsberg, K., 2003. Configuration, history and impact of the Norwegian Channel Ice Stream. Boreas, Vol. 32, pp. 18-36.

Sejrup, H.P., Nygård, A., Hall, A.M. & Haflidason, H., 2009. Middle and Late Weichselian (Devensian) glaciation history of south-western Norway, North Sea and eastern UK. Quaternary Science Reviews, 28, pp.370-380.

Seo, J.G. & Mamora, D.D., 2005. Experimental and Simulation Studies of Sequestration of Supercritical Carbon Dioxide in Depleted Gas Reservoirs. Journal of Energy Resources Technology, March 2005, v.127, pp. 1-6.

Shah, V., Broseta, D., Mouronval, G. & Montel, F., 2008. Water/gas interfacial tensions and their impact on acid gas geological storage. International Journal of Greenhouse Gas Control 2, pp. 594-604.

Shell Exploration & Production Standard Legend, 1995. Shell International Exploration and Production B.V., The Hague, The Netherlands, 212p.

Shi, J-Q., Mazumder, S. Wolf, K-H. & Durucan, S., 2008. Competitive Methane Desorption by Supercritical CO_2 Injection in Coal. Transport in Porous Media, 75, pp. 35-54.

Sidiq, H. & Amin, R., 2009. Mathematical model for calculating the dispersion coefficient of super critical CO_2 from the results of laboratory experiments on enhanced gas recovery. Journal of Natural Gas and Engineering, 1, pp. 177-182.

Simmons, C.T., Fenstemaker, T.R. & Sharp Jr., J.M., 2001. Variable-density groundwater flow and solute transport in heterogeneous porous media: approaches, resolutions and future challenges. Journal of Contaminant Hydrology, 52, pp. 245-275.

Singh, V., Cavanagh, A., Hansen, H., Nazarian, B., Iding, M. & Ringrose, P., 2010. Reservoir Modelling of CO_2 Plume Behaviour Calibrated Against Monitoring Data From Sleipner, Norway. SPE paper 134891, presented at the SPE Annual Technical Conference and Exhibition, Florence, Italy, 19-22 September, 19p.

Soon, W. & Baliunas, S., 2003. Proxy climatic and environmental changes of the past 1000 years. Climate Research, 23, pp. 89-110.

Span, R. & Wagner, W., 1996. A New Equation of State for Carbon Dioxide Covering the Fluid Region from the Triple-Point Temperature to 1100°K at Pressures up to 800 MPa. Jour. Phys. Chem. Ref. Data, 25 (6), pp. 1509–1596.

Sperrevik, S., Gillespie, P.A., Fisher, Q.J., Halvorsen, T. & Knipe, R., 2002. Empirical estimation of fault rock properties. In: Koestler, A.G. & Hunsdale, R. (Eds.) Hydrocarbon Seal Quantification. Norwegian Petroleum Society (NPF), Special Publications, 11, pp. 109–126.

Springer N. & Lindgren, H., 2006. Caprock properties of the Nordland Shale recovered from the 15/9-A-11 well, the Sleipner area. Paper presented at the 8th. International Conference on Greenhouse Gas Control Technologies 2006, Trondheim, Norway, 6p.

Spycher, N., Pruess, K. & Ennis-King, J. 2003. CO_2-H_2O Mixtures in the Geological Sequestration of CO_2. I. Assessment and calculation of mutual solubilities from 12 to 100 °C and up to 600 bar. Geochimica Et Cosmochimica Acta Vol. 67, No. 16, pp. 3015-3031.

Spycher, N. & Pruess, K., 2005. CO_2-H_2O mixtures in the Geological Sequestration of CO_2. II. Partitioning in Chloride Brines at 12-100 °C and up to 600 bar. Geochimica Et Cosmochimica Acta, Vol. 69, No. 13, pp. 3309-3320.

Stewart, M., Lonergan, L. & Hampson, G., 2007. Pleistocene Buried Tunnel Valleys in the North Sea: Fresh Insights from 3D Seismic. Oral Presentation at the BSRG Annual Meeting, University of Birmingham, December 16th.–18th.

Stuevold, L., R. Faerseth, L. Arnsen, J. A. Cartwright, and N. Moller, 2003. Polygonal faults in the Ormen Lange field, offshore Norway, in: Van Rensbergen, P., Hillis, R.R., Maltman, A.J. & Morley, C.K. (Eds.), Subsurface Sediment Mobilisation. Geological Society, London, Special Publication, 216, pp. 263– 282.

Stuiver, M., Burk, R. L. & Quay, P. D., 1984. 13C/12C Ratios and the Transfer of Biospheric Carbon to the Atmosphere, Journal of Geophysical Research, 89, pp. 1731–1748.

Taggart, I., 2009. Extraction of Dissolved Methane in Brines by CO_2 Injection: Implications for CO_2 Sequestration. SPE paper 124630, presented at the 2009 SPE Annual Technical Conference & Exhibition, New Orleans, Louisiana, USA, 4-7 October, 14p.

Teige, G.M.G., Hermanrud, C. & Reuslätten, H.G., 2011. Membrane seal leakage in non-fractured caprocks by the formation of oil-wet flow paths. Journal of Petroleum Geology, Vol. 34, 1, January, pp. 45-52.

Teng, H., Masutanii, S.M., Kinoshita, C.M. & Nihous, G.C., 1996. Solubility Of CO_2 In The Ocean And Its Effect On CO_2 Dissolution, Energy Conversion and Management, Vol. 37, Nos. 6-8, pp. 1029-1038.

Tindale, S., 2011. Carbon capture and storage: EU advancing but not fast enough. Centre for European Reform, TGAE Report, 3rd. June, pp. 36-43.

Tonnet, N., Broseta, D. & Mouronval, G., 2010. Evaluation of the petrophysical properties of a carbonate-rich caprock for CO_2 geological storage purposes. SPE paper 131525, presented at the SPE EUROPEC/EAGE Annual Conference & Exhibition, Barcelona, Spain, 14-17 June, 12p.

Tsang, C-F, Birkholzer, J. & Rutqvist, J., 2008. A comparative review of hydrologic issues involved in geologic storage of CO_2 and injection disposal of liquid waste. Environmental Geology, 54, pp. 1723-1737.

Tsimpanogiannis, I.N. & Yortsos, Y.C., 2004. The critical gas saturation in a porous medium in the presence of gravity. Journal of Colloid and Interface Science, 270, pp. 388-395.

Van der Meer, L.G.H. & van Wees, J.D., 2006. Limitations to Storage Pressure in Finite Saline Aquifers and the Effect of CO_2 Solubility on Storage Pressure. SPE paper 103342, presented at the 2006 SPE Annual Technical Conference & Exhibition, San Antonio, Texas, USA, 24-27 September, 9p.

Vanorio, T., Mavko, G., Vialle, S. & Spratt, K., 2010. The rock physics basis for 4D seismic monitoring of CO_2 fate: Are we there yet? The Leading Edge, February, pp. 156-162.

Vesovic, V., Wakeham, W.A., Olchowy, G.A., Sengers, J.V., Watson, J.T.R. & Millat, J., 1990. The Transport Properties of Carbon Dioxide. Journal of Physical Chemistry Reference Data, 19, pp.763-808.

Vidal, J. & Adam, D., 2007. China Overtakes US as World's Biggest CO_2 Emitter. Guardian Newspaper, 19th. June.

Walraven, D., Connolly, D.L. & Aminzadeh, F., 2005. Determining Migration Pathway in Marco Polo Field Using Chimney Technology. Presented at the EAGE 67th. Conference and Exhibition, Madrid, Spain, 13-16th. June, 2005, pp. 1-6.

Wandrey, M., Pellizari, L., Zettlitzer, M. & Wurdemann, H., 2011. Microbial community and inorganic fluid analysis during CO_2 storage within the frame of CO_2SINK - Long-term experiments under in-situ condition. Energy Procedia 4, pp. 3651-3657.

Welte, D.H., Hantschel, T., Wygrala, B.P., Weissenburger, K.S. & Carruthers, D., 2000. Aspects of Petroleum Migration Modelling. Journal of Geochemical Exploration, 69-70, pp. 711-714.

Wigand, M., Carey, J.W., Schütt, H., Spangenberg, E. & Erzinger, J., 2008. Geochemical effects of CO_2 sequestration in sandstones under simulated in-situ conditions of deep saline aquifers. Applied Geochemistry 23, pp. 2735-2745.

Wilkinson, M., Haszeldine, R.S., Fallick, A.E., Odling, N., Stoker, S.J. & Gatliff, R.W., 2009. CO_2-Mineral Reaction in a Natural Analogue for CO_2 Storage – Implications for Modelling. Journal of Sedimentary Research, v. 79, pp. 486-494.

Wood, F.B., 1988. Comment: On the need for validation of the Jones et al. temperature trends with respect to urban warming. Climatic Change, Vol. 12, No. 3, pp. 297-312.

World Nuclear Association, 22a St James's Square, London, UK, SW1Y 4JH. http://www.world-nuclear.org (24th. August 2011).

Xie, X., Li, S., He, H. & Liu, X., 2003. Seismic Evidence for Fluid Migration Pathways from an Overpressured System in the South China Sea. Geofluids 3, pp. 245-253.

Yang, D., Gu, Y. & Tontiwachwuthikul, P., 2008. Wettability Determination of the Reservoir Brine-Reservoir Rock System with Dissolution of CO_2 at High Pressures and Elevated Temperatures. Energy & Fuels, 22, pp. 504-509.

Yang, Y. & Aplin, A.C., 2010. A permeability-porosity relationship for mudstones. Marine and Petroleum Geology, Vol. 27, Iss. 8, September, pp. 1692-1697.

Zumberge, M., Alnes, H., Eiken, O., Sasagawa, G. & Stenvold, T., 2008. Precision of seafloor gravity and pressure measurements for reservoir monitoring. Geophysics, 73, WA133–WA141.

Zweigel, P., Lothe, A.E., Arts, R. & Hamborg, M., 2000. Reservoir geology of the storage units in the Sleipner CO_2 injection case – A contribution to the Saline Aquifer CO_2 Storage (SACS) project. SINTEF Petroleum Research, Report No. 23.4285.00/02/00 (Confidential), 79p.

Zweigel, P. & Hamborg, M., 2002. The effect of time-depth conversion procedure on key seismic horizons relevant for underground CO_2 storage in the Sleipner field (North Sea) – A contribution to the Saline Aquifer CO_2 Storage (SACS) project. SINTEF Petroleum Research, Report No. 33.5324.00/01/02 (Confidential), 49p.

Zweigel, P. & Heill, L.K., 2003. Studies on the likelihood for caprock fracturing in the Sleipner CO_2 injection case – A contribution to the Saline Aquifer CO2 Storage (SACS) project. SINTEF report no. 33.5324.00/02/03 (Confidential), 28p.

Zweigel, P., Arts, R., Lothe, A.E., & Lindeberg, E.B.G, 2004a. Reservoir geology of the Utsira Formation at the first industrial-scale underground CO_2 storage site (Sleipner area, North Sea). From: Baines, S.J. & Worden, R.H. (eds.) 2004. Geological Storage of Carbon Dioxide. Geological Society, London, Special Publications, 233, pp.165-180.

Zweigel, P., Lindeberg, E., Moen, A. & Wessel-Berg, D., 2004b. Towards a methodology for top seal efficacy assessment for underground CO_2 storage. 7^{th}. Greenhouse Gas Control Technologies Conference (GHGT-7), Vancouver, Canada, 6p.

Appendices:

- UKCCSC Meeting, London, November 2008 - Poster Presentation on St. Johns-Springerville (Contributor):

  Simulation of CO_2 Flow in a Natural System

  G. Pickup[1], H. Al-Waheibi[1], G. D. Nicoll[2], S. Gilfillan[2]

  [1]Institute of Petroleum Engineering, Heriot-Watt University,

  [2]The University of Edinburgh.

- CO_2GeoNet Meeting, Delft, November 2008 - Verbal Presentation on St. Johns-Springerville (Contributor):

  Simulation of CO_2 Flow in a Natural System

  G. Pickup[1], H. Al-Waheibi[1], G. D. Nicoll[2], S. Gilfillan[2]

  [1]Institute of Petroleum Engineering, Heriot-Watt University,

  [2]The University of Edinburgh.

- British Sedimentological Research Group, Annual Conference, Liverpool, December 2008 - Verbal Presentation:

  Modelling CO_2 Flow in Sedimentary Basins: Sleipner Overburden

  G. D. Nicoll[1], R. S. Haszeldine[1], S. Geiger[2], A. J. Cavanagh[3]

  [1]The University of Edinburgh,

  [2]Institute of Petroleum Engineering, Heriot-Watt University,

  [3]Permedia Research Group, Ottawa, Canada.

- North British Student Forum, Aberdeen, February 2009 - Verbal Presentation (2^{nd}. Prize):

  Modelling CO_2 Flow in Sedimentary Basins: Sleipner Overburden

  G. D. Nicoll[1], R. S. Haszeldine[1], S. Geiger[2], A. J. Cavanagh[3]

  [1]The University of Edinburgh,

  [2]Institute of Petroleum Engineering, Heriot-Watt University,

  [3]Permedia Research Group, Ottawa, Canada.

- Svalbard CO_2 Modelling Conference, August 2009 - Poster Presentation:

  Modelling CO_2 Migration in Sedimentary Basins: Utsira Overburden

  G. D. Nicoll[1], A. J. Cavanagh[2], R. S. Haszeldine[1], S. Geiger[3]

  [1]The University of Edinburgh,

  [2]Permedia Research Group, Ottawa, Canada,

  [3]Institute of Petroleum Engineering, Heriot-Watt University.

- British Sedimentological Research Group, Annual Conference, Bangor December 2009 - Verbal Presentation:

  Utsira Overburden: Investigating Existing Fluid Migration Pathways - Implications for Long-Term CO_2 Storage

  G. D. Nicoll[1], A. J. Cavanagh[2], R. S. Haszeldine[1], S. Geiger[3]

  [1]The University of Edinburgh,

  [2]Permedia Research Group, Ottawa, Canada,

  [3]Institute of Petroleum Engineering, Heriot-Watt University.

- North British Student Forum, Edinburgh, February 2010 - Verbal Presentation (Joint 1st. prize):

  Utsira Overburden: Investigating Existing Fluid Migration Pathways - Implications for Long-Term CO_2 Storage

  G. D. Nicoll[1], A. J. Cavanagh[2], R. S. Haszeldine[1], S. Geiger[3]

  [1]The University of Edinburgh,

  [2]Permedia Research Group, Ottawa, Canada,

  [3]Institute of Petroleum Engineering, Heriot-Watt University.

- Geological Society of London Conference - Carbon Storage Opportunities in the North Sea, March 2010 - Verbal Presentation:

  Could CO_2 storage site performance be compromised by palaeo-gas migration conduits in the overburden?

  G. D. Nicoll[1], M. Naylor[1], A. J. Cavanagh[2], S. Geiger[3], R. S. Haszeldine[1]

  [1]The University of Edinburgh,

  [2]Permedia Research Group, Ottawa, Canada,

  [3]Institute of Petroleum Engineering, Heriot-Watt University.

- Geology Magazine, April 2010 - Paper submitted for review and subsequently rejected by Editor August 2010 - not resubmitted:

  Overburden architecture and palaeo-fluid migration indicators above the Sleipner CO_2 storage site

  G. D. Nicoll[1], A. J. Cavanagh[2], S. Geiger[3], R. S. Haszeldine[1]

  [1]The University of Edinburgh,

  [2]Permedia Research Group, Ottawa, Canada,

  [3]Institute of Petroleum Engineering, Heriot-Watt University.

- 72nd EAGE Conference & Exhibition incorporating SPE EUROPEC, Barcelona June 2010 - Poster Presentation:

  Could CO_2 storage site performance be compromised by palaeo-gas migration conduits in the overburden?

  G. D. Nicoll[1], M. Naylor[1], A. J. Cavanagh[2], S. Geiger[3], R. S. Haszeldine[1]

  [1]The University of Edinburgh,

  [2]Permedia Research Group, Ottawa, Canada,

  [3]Institute of Petroleum Engineering, Heriot-Watt University.

- SPE Young Professionals London Section, Inaugural SPE YP European Technical Series: Carbon Capture and Storage - Are We Ready Yet? Geological Society of London, March 2011 - Verbal Presentation:

  Assessment of the Overburden Seal at Sleipner

  G. D. Nicoll[1,4], A. J. Cavanagh[2], S. Geiger[3], M. Naylor[1], R. S. Haszeldine[1]

  [1]The University of Edinburgh,

  [2]Permedia Research Group, Ottawa, Canada,

  [3]Institute of Petroleum Engineering, Heriot-Watt University,

  [4]Senergy (GB), Edinburgh.

- Paper in preparation - 2011 (Contributor)

  Derisking CO_2 Phase Uncertainty at Geological Storage Sites Using Well Logs

  M. Naylor[1], G.D. Nicoll[1,2], A. Heafford[3]

  [1]The University of Edinburgh,

  [2]Senergy (GB), Edinburgh,

  [3]IHS Energy (UK), Epsom.

Appendix 2.1: Well Log and Lithological Description for Well 15/9-09

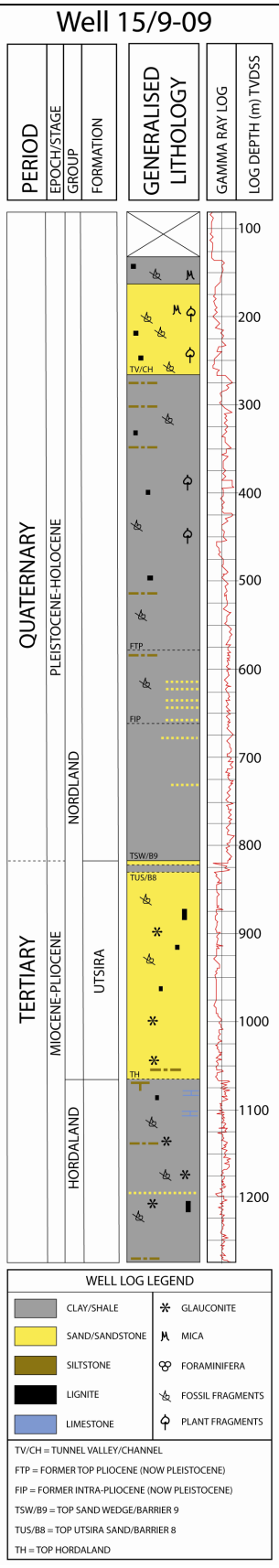

Well 15/9-09 lithological description from well completion log (top down):

- Clay (above TV/CH ~125 m TVDSS): medium grey, soft, calcareous
- Sand (in TV/CH ~160 m TVDSS): clear quartz, very fine, well-rounded, well-sorted, pyrite and peat
- Clay (below TV/CH ~270 m TVDSS): medium grey, soft, calcareous
- Sand (Utsira Formation ~800 m TVDSS): clear, quartz, very fine, occasionally coarse, loose, angular-rounded, well-sorted, glauconite, pyrite, shell fragments, clay streaks
- Claystone (Hordaland Formation ~1060 m TVDSS): light-medium brown, soft, sticky, silty, pyrite, glauconite, peat, limestone streaks, occasional sands

Appendix 2.2: Well Log and Lithological Description for Well 15/9-11

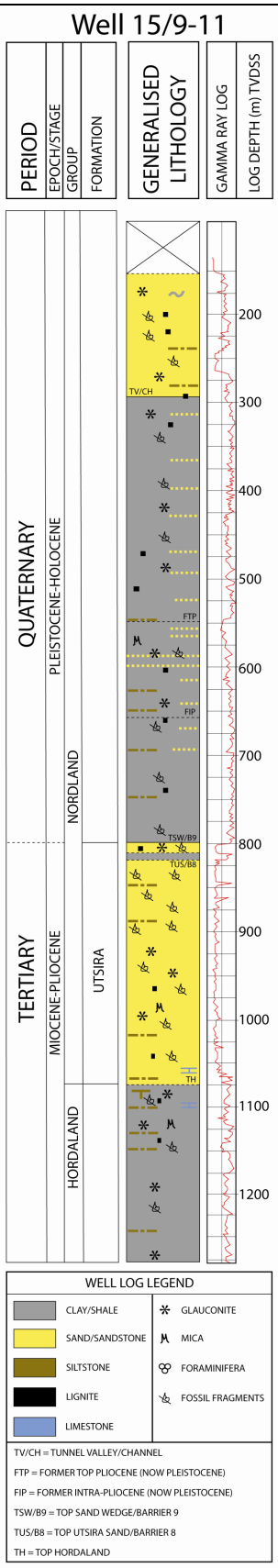

Well 15/9-11 lithological description from well completion log (top down):

- Sand (in TV/CH ~150 m TVDSS): clear quartz, occasionally milky white-opaque, fine-very coarse, well-sorted, angular to sub-angular, sub-rounded to rounded, rock fragments
- Clay (below TV/CH ~290 m TVDSS): light grey to light green grey, silty, micaceous, sticky, pyrite, glauconite
- Clay (above FTP ~550 m TVDSS): light-medium-dark grey, soft, slightly sticky, silty, slightly calcareous
- Sand interbeds (~600 m TVDSS): clear quartz, very fine-medium, loose, sub-rounded-rounded
- Siltstone interbeds (below ~ 600 m TVDSS) - light grey-light green grey, soft, slightly calcareous, pyrite, glauconite
- Clay (~790 m TVDSS): light-medium grey, soft to firm, calcareous
- Sand (Utsira Formation ~800 m TVDSS): clear-milky white quartz, very fine, loose, angular to sub-rounded, well-sorted, micaceous, shell fragments, glauconite
- Sand (~875 m TVDSS): clear quartz, fine-coarse, loose, sub-angular to rounded, well-sorted, with siltstone and claystone streaks
- Claystone (Hordaland Formation ~1075 m TVDSS): medium brown to grey, soft-firm, silty, micaceous, slightly calcareous
- Siltstone: light-medium grey to brown grey, friable-hard, calcite cemented
- Limestone streaks: light grey, hard-crystalline, slightly argillaceous

Appendix 2.3: Well Log and Lithological Description for Well 15/9-13

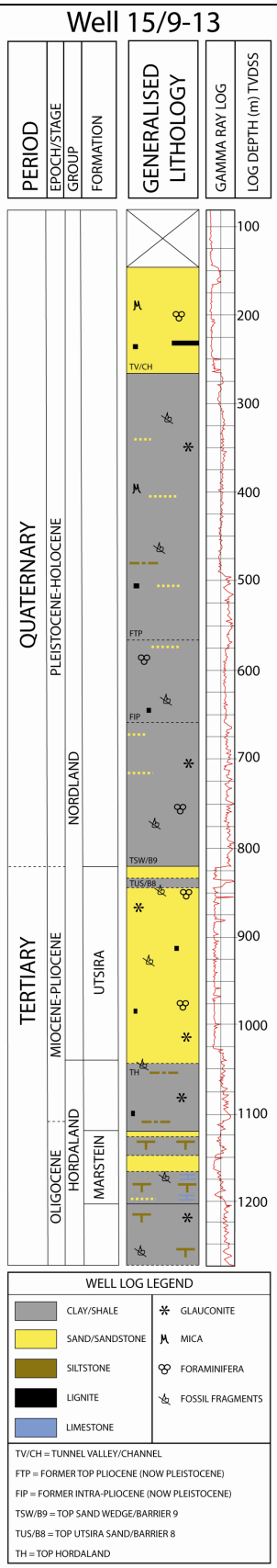

Well 15/9-13 lithological description from well completion log (top down):

- Clay (above TV/CH ~150 m TVDSS): light blue grey-olive grey, very soft, soluble, sticky, calcareous-very calcareous
- Sand (in TV/CH ~180 m TVDSS): clear milky quartz, loose, fine-coarse, poorly sorted, sub-rounded, abundant mica, glauconite and pyrite
- Lignite (in TV/CH ~220 m TVDSS): brown-black, fibrous
- Clay (below TV/CH ~275 m TVDSS): olive grey, soft, sticky, calcareous-very calcareous
- Clay (above FTP ~520 m TVDSS): light grey-grey, soft, sticky, (calcareous), silty, micaceous
- Sand (Utsira Formation ~825 m TVDSS): clear, quartz, occasional lithic fragments, medium-fine, occasionally very fine, sub-angular-sub-rounded, inter-bedded with clay, light grey-grey, soft, sticky, calcareous, abundant shell fragments
- Clay (Hordaland Formation ~1050 m TVDSS): olive grey-grey, soft, sticky, (calcareous), silty, micaceous
- Sand (Top Marstein ~ 1125 m TVDSS): clear quartz, occasional white or brown, loose, medium-coarse, grading to fine-medium, moderately sorted, angular-well rounded
- Claystone/Siltstone (in Marstein ~1160 m TVDSS): medium brown-dark brown grey, very silty in places, soft-firm, slightly calcareous, occasional sub-fiss?, occasional mica
- Claystone (below Marstein ~1220 m TVDSS): light grey, pale green grey, brown grey, firm, calcareous, silty in places

Appendix 2.4: Well Log and Lithological Description for Well 15/9-15

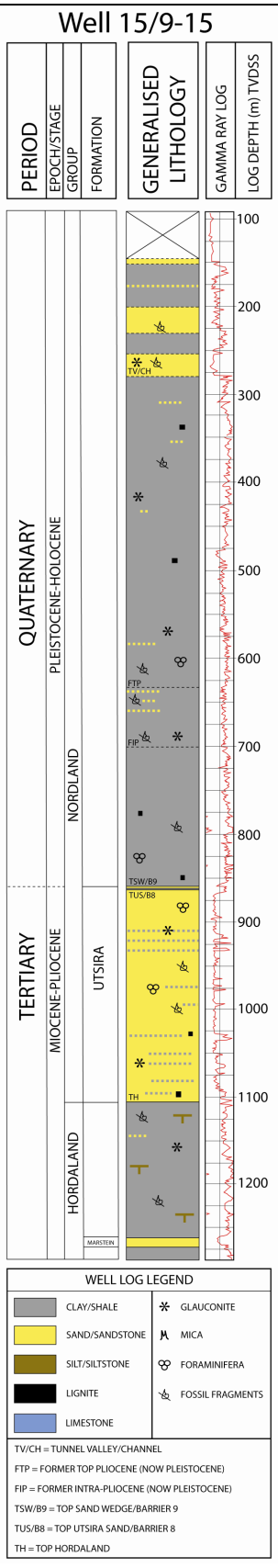

Well 15/9-15 lithological description from well completion log (top down):

- Sand (in TV/CH ~150 m TVDSS): clear to milky, orange, yellow, quartz, loose, very coarse-medium, becoming very fine-medium, poorly sorted, sub-rounded to rounded
- Clay interbeds: light grey-black grey, soft, sticky, soluble, occasionally silty, calcareous
- Lignite: black-brown, soft-firm, fibrous, woody, abundant rock fragments
- Sand (~250 m TVDSS): description as above
- Clay (~400 m TVDSS): light-dark grey to greenish grey, soft, sticky, soluble occasionally silty, occasionally non-calcareous
- Clay (~500 m TVDSS): light brown-grey, soft, sticky, micaceous, carbonate, non-moderately calcareous
- Clay (FTP ~625 m TVDSS): light-medium grey, black green grey, soft-firm, sticky, calcareous-very calcareous, micaceous
- Sand (below FTP ~630 m TVDSS): clear, pink, orange, quartz, very fine-medium, occasionally coarse-very coarse, poorly-moderately sorted, sub-angular to sub-rounded
- Sand (Utsira Formation ~860 m TVDSS): clear-milky quartz, fine-medium, occasional coarse-very coarse, sub-rounded to rounded, poorly-moderately sorted, micaceous, glauconite
- Clay interbeds - light-medium grey, soft, sticky, calcareous, glauconite, silty in places
- Clay/Claystone (Hordaland Formation ~1105 m TVDSS): light-medium grey, becoming light brownish grey, soft-firm, non-moderately calcareous, micaceous, pyrite, glauconite
- Sand interbeds: description as above
- Claystone (below ~1150 m TVDSS): light-medium grey, soft-firm, slightly silty, micaceous, moderate carbonate, calcareous to non-calcareous
- Sand (Top Marstein ~ 1270 m TVDSS): clear quartz, very fine-fine occasionally crystalline, sub-angular to sub-rounded
- Claystone (below Marstein): light-medium grey, medium brownish grey, firm, blocky to sub-fissile, micaceous, moderate carbonate, slightly silty, non-calcareous to calcareous

Appendix 2.5: Well Log and Lithological Description for Well 15/9-16

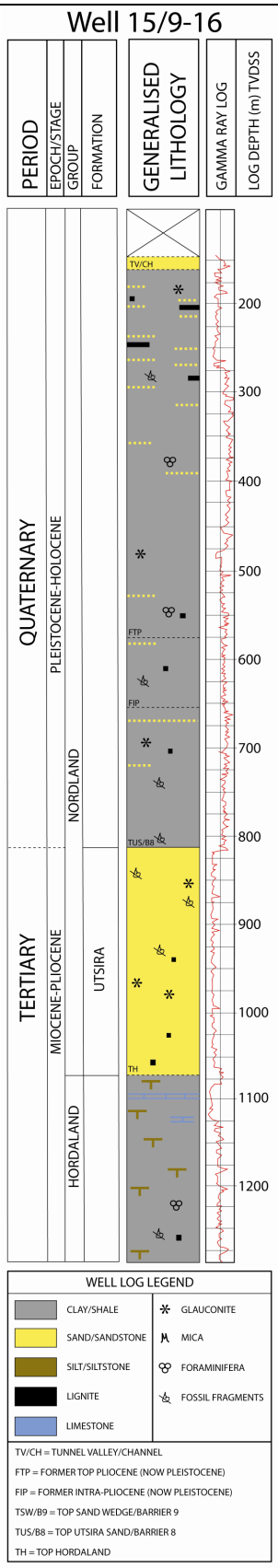

Well 15/9-16 lithological description from well completion log (top down):

- Sand (in TV/CH ~150 m TVDSS): clear milky quartz, very fine-very coarse, poorly-moderately sorted, sub-angular to sub-rounded, loose
- Clay (below TV/CH ~160 m TVDSS): grey, silty, soft, sticky, soluble
- Lignite (below TV/CH ~200 m TVDSS): brown-black, soft, fibrous
- Clay (above FTP ~570 m TVDSS): vari-coloured, soft-moderate, micaceous, silty, non-slightly calcareous, traces of glauconite and pyrite
- Sand (below FIP ~670 m TVDSS): clear quartz, very fine-fine, moderately-poorly sorted, angular to sub-angular, loose
- Sand (Utsira Formation ~810 m TVDSS): clear, white quartz, very fine-fine, well sorted, sub-angular to sub-rounded, micaceous, glauconite
- Clay (~870 m TVDSS): light grey, soft
- Clay (Hordaland Formation ~1070 m TVDSS): light-dark grey, green grey, soft-firm, blocky, micaceous, slightly calcareous
- Limestone (~1100 m TVDSS): light brown grey, hard-firm, crystalline, micaceous
- Siltstone: medium-dark grey, firm, blocky, micaceous, calcareous to very calcareous
- Claystone: brown black-black olive grey, blocky, soft-firm, micaceous, silty, calcareous to very calcareous

Appendix 2.6: Well Log and Lithological Description for Well 15/9-17

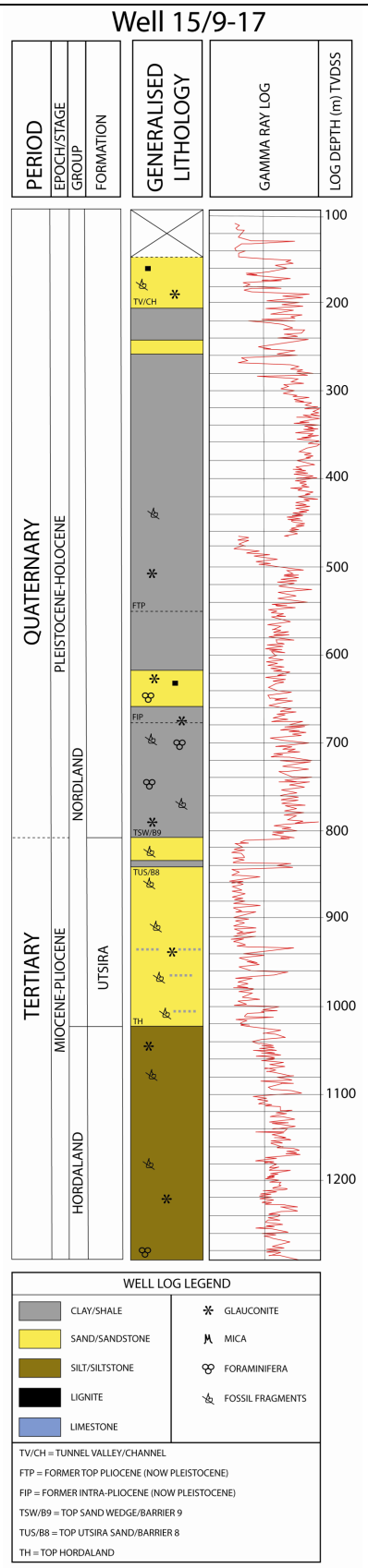

Well 15/9-17 lithological description from well completion log (top down):

- Sand (in TV/CH ~145 m TVDSS): clear to translucent quartz, very fine-coarse, poorly-moderately sorted, sub-angular to sub-rounded
- Clay (below TV/CH ~210 m TVDSS): grey, soft, sticky, non-slightly calcareous
- Sand (~240-260 m TVDSS): clear to translucent quartz, very fine-coarse, poorly-moderately sorted, sub-angular to sub-rounded
- Clay (below ~260 m TVDSS): grey, soft, sticky, non-slightly calcareous
- Sand (~620-660 m TVDSS): predominantly clear to translucent quartz, very fine-coarse, poorly-moderately sorted, sub-angular to sub-rounded, occasionally coarse and angular
- Clay (below ~660 m TVDSS): grey, soft, sticky, non-slightly calcareous
- Sand (Utsira Formation ~810 m TVDSS): clear to translucent quartz, very fine-fine, moderately sorted, sub-angular to sub-rounded
- Claystone/Siltstone/Sandstone (Hordaland Formation below ~1020 m TVDSS): Claystone: grey, brown grey-brown, soft-firm, sticky, moderately micaceous, slightly silty-silty, non-slightly calcareous; Siltstone: grey, brown, firm-moderately hard, calcareous, moderately micaceous, argillaceous; Sandstone: clear-light grey, very fine-fine, moderately sorted, subrounded, calcite cement, moderately hard

Appendix 2.7: Well Log and Lithological Description for Well 16/7-02

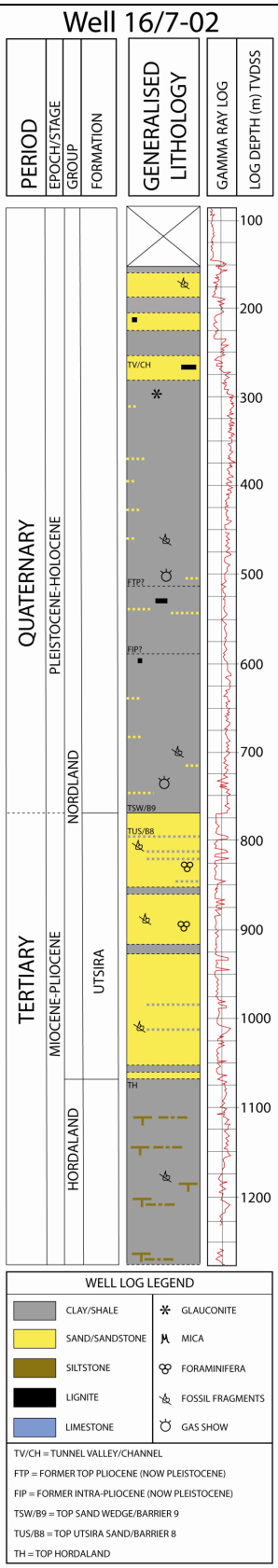

Well 16/7-02 lithological description from well completion log (top down):

- Clay (~150 m TVDSS): grey-grey brown, soft, sticky, calcareous
- Sand (in TV/CH ~155 m TVDSS): clear, white, green, friable-very coarse, poorly sorted, sub-angular to well-rounded
- Clay (below ~575 m TVDSS): light-medium grey, soft, sticky, calcareous
- Clay (below ~700 m TVDSS): light grey-medium brown, soft, sticky, calcareous
- Sand (Utsira Formation ~775 m TVDSS): clear, friable occasionally medium-coarse, well-poorly sorted, sub-rounded-rounded
- Clay (interbeds starting at ~850 m TVDSS): light grey, grey-green, soft, non-sticky
- Clay (Hordaland Formation ~1070 m TVDSS): light grey, grey-green, soft, non-sticky, consolidated
- Claystone/Siltstone (Hordaland Formation below ~1150 m TVDSS): light-medium grey, firm-moderately hard, non-calcareous
- Shale/Siltstone (Hordaland Formation below ~1200 m TVDSS): dark grey-grey, moderately firm-soft, blocky occasionally sub-fissile, silty-very silty, occasional limestone streaks

Appendix 2.8: List of Petrel Project Files Used For Interpretation

The following files were used for Chapter 2 interpretation work loaded into Petrel® 2008.1 (32-bit version) software:

- **depth32.sgy** – This is the original depth converted SEGY file obtained from the BGS (details of the original depth conversion are described in Chapter 2, Section 2.3) and contains two surveys merged together; ST9305 (western) from 1993 and ST9407 from 1994 (eastern), with an obvious N-S join at the overlap between the two surveys (as the following survey maps show). A cropped version of this cube was used for the seismic interpretation work described herein.

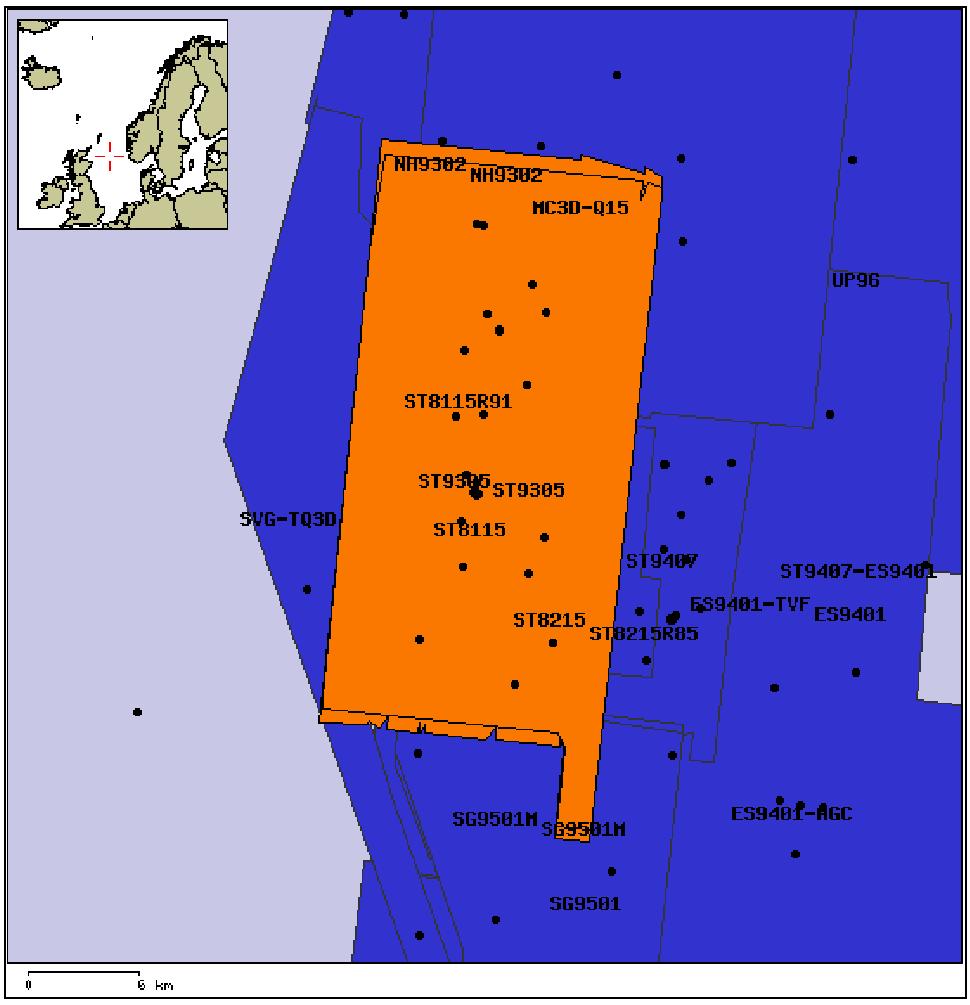

ST9305 survey area map - orange (extracted from the NPD database)

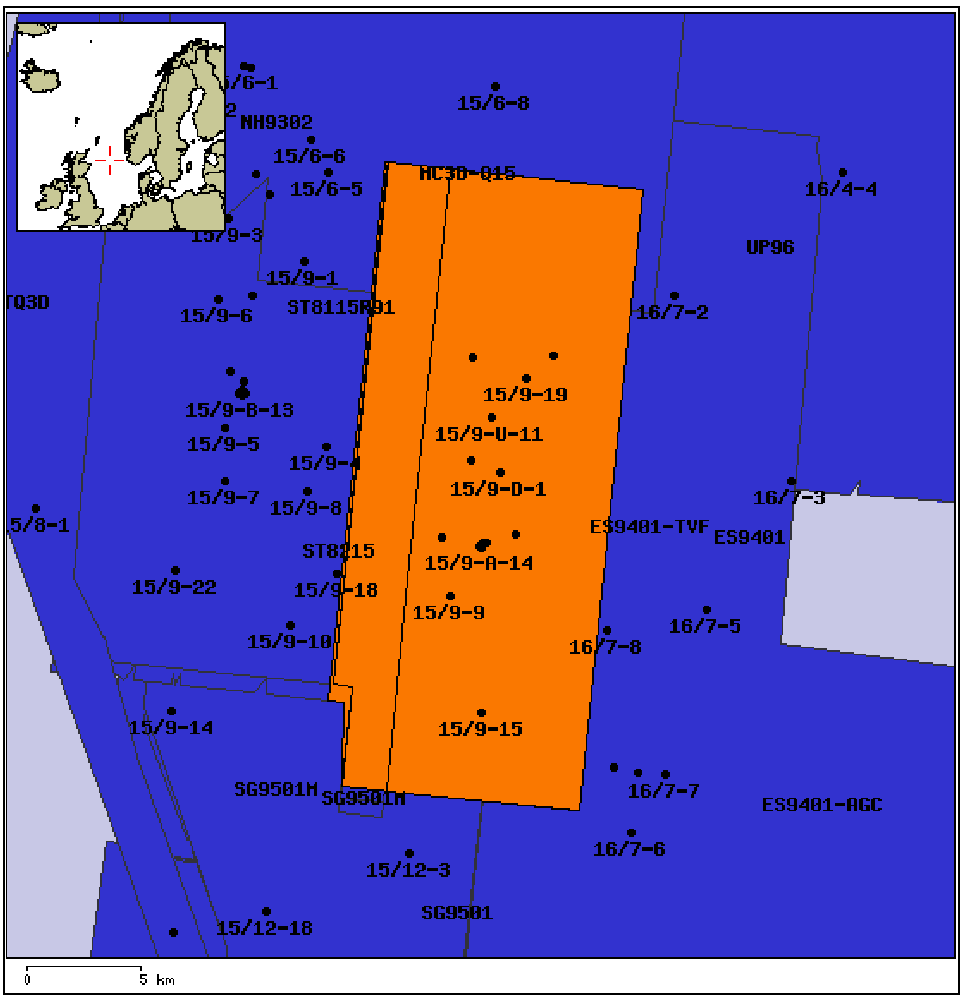

ST9407 survey area map - orange (extracted from the NPD database)

- **UtsiraExtendedProjectAug09** (*.pet file and associated *.ptd folder) – These Petrel® project files contain all the seismic data and interpretations described in Chapter 2. Key file folders within this project include:
  - **Depth32** – the cropped seismic cube used for the regional study,
  - **Depth32[StructSmooth]1[Crop]1[Domain Converted:Depth1]1[Domain Converted:Depth1]1[Realised]1** – the cropped and depth to depth converted seismic cube for the local study - several variations of this file were also generated using different filters and attributes to enhance visualisation and help with interpretation (e.g. Chaos, Variance, etc.),

- **Well Tops -** folder contains all the well tops information for each horizon (based on well log and horizon depth information from Lothe & Zweigel (1999), Appendix A),
- **Wells** - folder contains all the well positional information in UTM co-ordinates as extracted from the Norwegian Petroleum Directorate (NPD) database,
- **Final Surfaces for Depth and Well Converted Cube** - folder contains all the interpreted and generated surfaces used in subsequent MPath® work described in Chapter 4,
- **Linear Traces** - folder contains lineations (polygons) mapped for the local study,
- **Chimneys in Local Cube** - folder contains mapped palaeo-gas chimneys (polygons) for the local study,
- **Anomalies in Local Cube** - contains mapped seismic anomalies (geobodies) for the local study,
- **Chimneys in Regional Cube** - folder contains mapped palaeo-gas chimneys (polygons) for the regional study,
- **Anomalies in Regional Cube** - contains mapped seismic anomalies (geobodies) for the regional study,

Appendix 2.9: Palaeo-Gas Chimney Location/Description Spreadsheet

Formation and Horizon abbreviations used in spreadsheet:
HORD = within Hordaland, HMM = Hordaland Mud Mound, TH = Top Hordaland, UTS = within Utsira Formation, TU = Top Utsira (between barriers 8-9), SCAH = Supra-Caprock Anomalous Horizon, SHMAH = ~700 m Anomalous Horizon, FIP = Former Intra-Pliocene, FTP = Former Top Pliocene, QAH = Quaternary Anomalous Horizon, FHMAH = ~400 m Anomalous Horizon.

Spreadsheet table colour coding for Local Survey Area (based on proximity to migrating CO_2 plume, compared against the 2008 published plume footprint from Hermanrud *et al.*, 2010):
Pale Blue = Not on potential CO_2 migration route, Orange = Marginal – at periphery of potential CO_2 migration route, Pink = Directly on potential CO_2 migration route.

Note: Chimney #35 (no colour shading) is in the Regional Survey Area and is merely included to provide location co-ordinates and morphological description.

Chimney ID	UTM Location	Inline Intersect	Crossline Intersect	Root Depth/Horizon (m TVDSS)	Termination Depth/Horizon (m TVDSS)	Height (m)	Diameter (m)	Morphological Description	On potential CO2 migration route?	Distance/direction from CO2 injection point location	Associated With Underlying Hordaland Mud Mound Structures?	Associated With Overburden Lineaments?
1	x = 439730.17 m y = 6469634.19 m	1941	994	-998 (UTS)	-566 (FTP)	432	100-1500	Tapered (carrot-shaped) vertical discontinuity from periphery of an HMM extending upwards through UTS, TU and mainly terminating in FTP, with minor high amplitude anomalies above FTP	No	2.2 km to SW	Directly above edge of HMM	Yes, ENE-WSW chimney intersection at FIP level
2	x = 439563.26 m y = 6477072.29 m	1916	1592	-975 (UTS)	-537 (FTP)	438	100-630	Cylindrical vertical discontinuity from periphery of an HMM extending upwards through UTS, TU and terminating in FTP, with minor high amplitude anomalies above FTP	Marginal	5.8 km to NNE	Directly above edge of HMM	Yes, multiple ENE-WSW and NE-SW trending chimney intersections at FIP level
3	x = 435763.40 m y = 6471170.67 m	1622	1112	-1183 (HORD)	-579 (FTP)	604	200-1600	Extensive tapered (carrot-shaped) vertical discontinuity emanating from below the periphery of an HMM and extending upwards through UTS, TU and terminating in FTP	No	2.7 km to W	Directly above depression in TH, 300 m away from the edge of an HMM. Root appears to be sourced from the polygonal faulted horizon within the HORD	Yes, NE-SW trending chimney intersection at TU, SHMAH and multiple intersections between FIP and FTP levels
4	x = 439179.98 m y = 6478381.91 m	1887	1691	-1066 (HORD)	-774 (FTP)	292	200-800	Tapered (mushroom-shaped) discontinuity from apex of an HMM and extending upwards through UTS, TU and terminating in extensive bright spot at the SCAH	Marginal	7.1 km to NNE	Directly above a depression situated on the crest of an HMM, internal pull-down structures within the HMM further suggest a chimney source within the HORD	No
6	x = 435925.47 m y = 6474499.52 m	1378	1631	-1020 (UTS)	-535 (FTP)	485	150-1000	Two interconnected cylindrical vertical discontinuities forming a NW-SE aligned feature from lower UTS extending upwards through TU and terminating in FTP	No	3.9 km to NW	Directly above depression in TH, 400-1000 m away from the edge of an HMM	Yes, chimney is aligned along an intersection of multiple NE-SW trending lineaments and a zone of NW-SE trending lineaments between FIP and FTP levels
8	x = 436071.57 m y = 6468525.91 m	1651	901	-962 (UTS)	-768 (SCAH)	194	120-900	Vertical tapered (mushroom-shaped) discontinuity forming a NE-SW aligned feature from lower UTS extending upwards through TU and terminating in extensive bright spot at the SCAH, with some evidence of laterally offset brights also occurring to the E and N at the FTP level (faults?)	No	3.4 km to SW	Directly above depression in TH, 450 m away from the edge of an HMM	Yes, chimney is aligned along a series of multiple NE-SW trending lineaments at SCAH level
10	x = 438426.97 m y = 6469590.38 m	1838	993	-923 (UTS)	-763 (SCAH)	160	250-500	Vertical discontinuity (mushroom-shaped) extending upwards from UTS through TU and terminating in SCAH	Marginal	1.6 km to S	Directly above edge of HMM	Yes, chimney is aligned along a NE-SW trending lineament at TU to SCAH level
11	x = 438381.10 m y = 6471545.70 m	1830	1145	-903 (UTS)	-568 (FTP)	335	200-450	Vertical discontinuity extending upwards from periphery of an HMM through UTS, TU and terminating in FTP	Yes	0.25 km to NNW	Directly above edge of HMM	Yes, chimney is intersected by a NE-SW trending lineament at FTP level
12	x = 437916.36 m y = 6471849.21 m	1793	1169	-940 (UTS)	-564 (FTP)	376	300-1100	Vertical discontinuity extending upwards from col between two HMMs through UTS, TU and terminating in FTP	Marginal	0.8 km to NW	Directly above col between two HMMs	Yes, chimney appears to be "contained" within three lineaments at the FIP to FTP levels NE-SW, NW-SE and WSW-ENE

Chimney ID	UTM Location	Inline Intersect	Crossline Intersect	Root Depth/Horizon (m TVDSS)	Termination Depth/Horizon (m TVDSS)	Height (m)	Diameter (m)	Morphological Description	On potential CO2 migration route?	Distance/direction from CO2 injection point location	Associated With Underlying Hordaland Mud Mound Structures?	Associated With Overburden Lineaments?
14	x = 436572.26 m y = 6472612.76 m	1687	1236	-804 (TU)	-573 (FTP)	231	200-400	Tapered (carrot-shaped) N-S aligned vertical discontinuity extending upwards from TU and terminating in FTP	No	2.3 km to WNW	Directly above edge of HMM	Yes, chimney is intersected by a NE-SW trending lineament at TU-SCAH levels
15	x = 436534.23 m y = 6472007.33 m	1683	1180	-990 (UTS)	-758 (SCAH)	232	180-300	Vertical discontinuity with SW-NE alignment from UTS extending upwards through TU and terminating in SCAH	No	2.0 km to WNW	520 m from edge of HMM	Yes, chimney is intersected by a NE-SW trending lineament at TU-SCAH levels
16	x = 438267.28 m y = 6476490.52 m	1817	1541	-780 (SCAH)	-600 (FTP)	180	75-230	Weak vertical discontinuity extending upwards from SCAH and terminating in FTP	Marginal	5.2 km to N	Directly above edge of HMM	Yes, chimney is intersected by a NE-SW trending lineament at SCAH level and bounded to the NW by an intersection of NE-SW and ENE-WSW trending lineaments at the FIP level
17	x = 435578.07 m y = 6474959.75 m	1414	1602	-887 (UTS)	-568 (FTP)	319	80-210	Two interconnected vertical discontinuities extending upwards from UTS through TU and terminating in FTP	No	4.5 km to NW	Directly above depression in TH	Yes, chimney is intersected by a NNW-SSE trending lineament at SCAH level and bounded by parallel NE-SW and NW-SE trending lineaments at the FIP-FTP levels
18	x = 439835.20 m y = 6470995.81 m	1948	1104	-826 (TU)	-574 (FTP)	252	200-700	Wide zone of vertical discontinuity aligned N-S and extending upwards from TU and terminating in FTP	No	1.4 km to ESE	Directly above flank of HMM	Yes, chimney is intersected by a distinct NE-SW trending lineament that can be tracked from SCAH to FTP levels
19	x = 437690.94 m y = 6471360.34 m	1780	1129	-817 (TU)	-548 (FTP)	269	125-450	Tapered (carrot-shaped) NW-SE aligned vertical discontinuity extending upwards from TU and mainly terminating in FTP, with minor high amplitude anomalies and reverse polarity visible above FTP	No	0.75 to W	Directly above flank of HMM	Yes, chimney is intersected by a NW-SE trending lineament at SCAH to FTP levels and by a further NE-SW intersection at the FIP-FTP levels which gives the associated high-amplitude anomaly an L-shape
21	x = 438353.45 m y = 6477240.92 m	1823	1602	-1070 (HORD)	-539 (FTP)	531	280-700	Wide, cylindrical vertical discontinuity extending upwards from an HMM through UTS, TU and terminating in FTP	Marginal	6.0 km to N	Directly above depression in TH, lying between the edge of two HMMs (200-300 m distant)	Yes, chimney is intersected by a ENE-WSW trending lineament at FIP to FTP levels and bounded to the SE by a parallel ENE-WSW trending lineament, also by a NW-SE trending lineament to the W
22	x = 437149.16 m y = 6474423.97 m	1729	1374	-1005 (UTS)	-765 (SCAH)	240	125-155	Focussed chimney, extending upwards from UTS, through TU and terminating in SCAH, narrow zone of vertical disruption with reflection breaks and negative polarity effects most evident on crossline 1374 at TU (fault zone?)	No	3.4 km to NW	Directly above edge of HMM	No, but very weak E-W component to the associated anomaly
25	x = 438700.22 m y = 6473671.00 m	1854	1319	-800 (TU)	-555 (FTP)	245	200-580	Tapered (mushroom-shaped) vertical discontinuity (with dominant N-S alignment) extending upwards from TU/SCAH and mainly terminating in FIP to FTP, with minor high amplitude anomalies visible above FTP (laterally offset to E)	Yes	2.5 km to N	Directly above N-S aligned edge of HMM	Yes, weak intersection of N-S and NE-SW lineaments associated with anomalies to the NE at the SCAH level (from chimney #26), but much stronger parallel N-S and NE-SW intersections at the FIP to FTP levels, bounding the chimney
26	x = 438753.78 m y = 6473910.65 m	1858	1335	-877 (UTS)	-757 (SCAH)	120	150-650	Short, vertical discontinuity (mushroom-shaped), possibly two chimneys coalesced from UTS extending upwards through TU and terminating in SCAH	Yes	2.5 km to N	Directly above N-S aligned edge of HMM	Yes, weak intersection of N-S lineaments associated with SCAH anomalies
28	x = 439151.07 m y = 6472054.74 m	1892	1186	-802 (TU)	-754 (SCAH)	48	75-150	High amplitude seismic anomaly exhibiting pull-up above the TU, but a discontinuous reflection to the N below the TU level (fault?)	Yes	1.0 km to NE	Mid-way between two HMMs (380 m closest)	Indistinct, but possible weak NE-SW lineament at top UTS to TU level
29	x = 439077.13 m y = 6472094.48 m	1886	1192	-713 (TU)	-570 (FTP)	143	65-190	Narrow, pipe-like vertical discontinuity extending upwards from SHMAH and terminating in FTP, with patchy reverse polarity anomalies present in chimney	Yes	1.1 km to NE	Mid-way between two HMMs (250 m closest)	Weak NE-SW lineament at FIP level

Cell Colour Code: Pale Blue = Not on potential CO_2 migration route, Orange = Marginal – at periphery of potential CO_2 migration route, Pink = Directly on potential CO_2 migration route.

Chimney ID	UTM Location	Inline Intersect	Crossline Intersect	Root Depth/Horizon (m TVDSS)	Termination Depth/Horizon (m TVDSS)	Height (m)	Diameter (m)	Morphological Description	On potential CO2 migration route?	Distance/direction from CO2 injection point location	Associated With Underlying Hordaland Mud Mound Structures?	Associated With Overburden Lineaments?
30	x = 436847.54 m y = 6474453.23 m	1706	1376	-825 (UTS)	-769 (SCAH)	56	200-420	Mushroom-shaped high amplitude seismic anomaly exhibiting weak pull-down and noise below TU	Marginal	3.7 km to NW	NE corner of anomaly directly above the edge of HMM	Weak E-W to NE-SW lineament at SCAH level
31	x = 438003.63 m y = 6473893.39 m	1798	1333	-790 (TU)	-605 (FTP)	185	100-1150	Two interconnected carrot-shaped vertical discontinuities extending upwards from TU and SCAH, terminating in FTP	Yes	2.4 km to NNW	Directly above the crest of an HMM	Chimneys appear to be forming along the limbs of a NE-SW lineament and form an A-shaped intersection with a N-S lineament associated with chimneys #25 and #26
33	x = 438751.55 m y = 6474600.18 m	1857	1391	-794 (TU)	-571 (FTP)	223	200-400	Tapered (carrot-shaped) vertical discontinuity extending upwards from TU and terminating in FTP	Yes	3.4 km to N	Directly above the edges of two adjoining HMMs	At the TU level, the chimney is intersected by an E-W trending lineation and two further lineations with a NNE-SSW component. At the FIP to FTP level the chimney is intersected by a strong NE-SW lineation
34	x = 438665.32 m y = 6472166.92 m	1857	1192	-836 (UTS)	-513 (FTP)	323	130-370	Narrow, tapered (carrot-shaped) vertical discontinuity extending upwards from TU and terminating in FTP	Yes	0.9 km to NNE	Directly above N-S aligned edge of HMM	At the FTP level, the chimney lies along the intersections of three parallel NE-SW trending lineations and one lineation with a NNW-SSE trend
35	x = 435180.35 m y = 6465035.23 m	1590	625	-1100 (HORD)	-108 (Seabed)	992	200-1200	Tapered (mushroom-shaped) vertical discontinuity from periphery of an HMM extending upwards through UTS, TU, Nordland Group overburden and terminating at seabed with 500 m diameter pockmark with raised centre. No significant gas anomalies in main chimney suggesting dominant process is migration rather than accumulation	No	6.5 km to WSW (Check to see if this agrees with text)	Directly above the edges of two adjoining HMMs	Between the FIP and FTP the chimney lies along the axis of prominent NE-SW lineaments - at the UTS to FIP level there also appears to be a prominent WNW-ESE lineament running through the chimney axis (fault?)
36	x = 435392.08 m y = 6473092.20 m	1590	1269	-798 (TU)	-575 (FTP)	223	80-980	Narrow, tapered (carrot-shaped) vertical discontinuity from TU extending laterally to the W and SW at the FIP level and terminating in FTP	No	3.6 km to WNW	Offset 700 m to W of N-S aligned edge of HMM	Chimney is intersected at the TU level by an ENE-WSW trending lineation and bounded on the W by a series of sub-parallel lineations with NE-SW trend
37	x = 435406.33 m y = 6473924.57 m	1591	1332	-807 (TU)	-574 (FTP)	233	70-600	Narrow, tapered (carrot-shaped) vertical discontinuity extending upwards from TU and terminating in FTP	No	4.0 km to WNW	Offset 800 m to NW of N-S aligned edge of HMM	At the TU to FIP level the chimney is intersected by a strong NE-SW lineation and a weaker NW-SE lineation
38	x = 435569.83 m y = 6473278.33 m	1604	1281	-850 (UTS)	-579 (FTP)	271	60-280	Narrow, tapered (carrot-shaped) vertical discontinuity extending upwards from upper UTS and terminating in FTP	No	3.5 km to WNW	Offset 250 m to W of N-S aligned edge of HMM	Weak ENE-WSW lineation intersects at TU level
39	x = 435762.02 m y = 6473178.17 m	1618	1273	-811 (TU)	-602 (FTP)	209	100-340	Narrow, tapered (carrot-shaped) vertical discontinuity extending upwards from TU and terminating in FTP	No	3.3 km to WNW	Offset 80 m to W of N-S aligned edge of HMM	Weak ENE-WSW lineation intersects at TU level, stronger NE-SW lineation intersection at FIP to FTP levels
40	x = 437243.33 m y = 6472889.09 m	1738	1252	-775 (SCAH)	-562 (FTP)	213	120-700	Wedge-shaped region of vertical discontinuity, aligned NE-SW, extending upwards from SCAH and terminating in the FTP	No	2.0 km to NW	Directly above N-S aligned W edge of HMM	Chimney is intersected by strong NE-SW lineation from the TU to FTP, also by a NNE-SSW lineation at FIP level, forming an A-shape bounding the chimney
41	x = 436748.46 m y = 6471855.85 m	1700	1169	-808 (TU)	-584 (FTP)	224	100-560	Narrow, tapered (carrot-shaped) vertical discontinuity extending upwards from TU and terminating in FTP	No	1.8 km to WNW	Directly above depression in TH surrounded by four HMMs, 100 m away from the edge of the nearest HMM	Chimney is intersected by strong NE-SW lineation from the TU to FTP
42	x = 435728.38 m y = 6476007.76 m	1617	1495	-826 (TU)	-561 (FTP)	265	100-1500	Extensive wedge-shaped vertical discontinuity extending upwards from TU and terminating in FTP	No	5.5 km to NW	Directly above depression in TH, 750 m W from the edge of the nearest HMM	Bounded by NW-SE and NE-SW lineations
55	x = 437088.37 m y = 6470673.77 m	1728	1075	-783 (SCAH)	-577 (FTP)	206	90-500	Narrow, tapered (carrot-shaped) vertical discontinuity extending upwards from SCAH and terminating in FTP	No	1.4 km to WSW	Directly above the crest of an HMM	Chimney intersected by a strong NE-SW lineation from TU to FTP, weaker NW-SE lineation also evident between FIP and FTP
57	x = 434930.17 m y = 6479000.81 m	1548	1737	-842 (TU)	-623 (FTP)	219	230-530	Narrow, tapered (carrot-shaped) vertical discontinuity extending upwards from TU and terminating in FTP	No	8.5 km to NNW	Directly above the crest of an HMM	
58	x = 437204.27 m y = 6478911.46 m	1728	1733	-833 (TU)	-610 (FTP)	223	250-901	Asymmetric, tapered (wedge-shaped) vertical discontinuity, possibly two interconnected features forming a N-S aligned feature extending upwards from TU and terminating in FTP	No	7.6 km to NW	Directly above the crest of an HMM	

Cell Colour Code: Pale Blue = Not on potential CO_2 migration route, Orange = Marginal – at periphery of potential CO_2 migration route, Pink = Directly on potential CO_2 migration route.

Note: Chimney #35 (grey row shading) is in the Regional Survey Area and is merely included to provide location co-ordinates and morphological description.

Chimney ID	UTM Location	Inline Intersect	Crossline Intersect	Root Depth/Horizon (m TVDSS)	Termination Depth/Horizon (m TVDSS)	Height (m)	Diameter (m)	Morphological Description	On potential CO2 migration route?	Distance/direction from CO2 injection point location	Associated With Underlying Hordaland Mud Mound Structures?	Associated With Overburden Lineaments?
59	x = 436975.49 m y = 6476189.70 m	1713	1516	- 856 (UTS)	-621 (FTP)	235	200-420	Narrow, tapered (carrot-shaped) vertical discontinuity extending upwards from TU and terminating in FTP	Marginal	5.2 km to NW	Directly above the periphery of an HMM	
60	x = 438144.99 m y = 6474153.61 m	1809	1354	-876 (UTS)	-584 (FTP)	292	313-1645	Asymmetric, tapered (wedge-shaped) vertical discontinuity, formed by two interconnected features coalescing at the FIP level, forming a N-S to NE-SW aligned linear feature from UTS extending upwards and terminating in FTP	Marginal	2.75 km to NNW	Directly above the crestal axis of an HMM	
61	x = 435526.75 m y = 6469284.20 m	1606	963	-833 (UTS)	-589 (FTP)	244	295-745	Asymmetric, tapered (carrot-shaped) vertical discontinuity, possibly forming an approximately N-S aligned feature extending upwards from UTS and terminating in FTP	No	3.5 km to WSW	Situated above level area approximately 275 m SW of the periphery of an HMM	
62	x = 435511.47 m y = 6469360.24 m	1604	967	-540 (QAH)	-382 (FHMAH)	158	50-750	Short, vertical discontinuity (mushroom-shaped), overlying chimney feature #61, extending upwards and terminating at high amplitude anomaly at FHMAH level	No	3.5 km to WSW	Approximately 275 m SW of the periphery of an HMM	
63	x = 435512.06 m y = 6475274.05 m	1597	1439	-796 (TU)	-596 (FTP)	200	180-360	Narrow, tapered (carrot-shaped) vertical discontinuity extending upwards from TU and terminating in FTP	No	5.1 km to NW	Directly above the peripheral junction of two HMMs	
64	x = 434522.55 m y = 6476147.42 m	1517	1508	-985 (UTS)	-595 (FTP)	390	450-970	Wide, slightly tapered vertical discontinuity from UTS, extending upwards and broadening through the TU and terminating in FTP - partly truncated to the W by edge of survey coverage	No	6.3 km to WNW	Directly above crest of an HMM	
65	x = 435443.43 m y = 6478950.19 m	1587	1735	-848 (UTS)	-625 (FTP)	223	150-600	Narrow, tapered (wedge-shaped) vertical discontinuity extending upwards from TU and terminating in FTP, with extension to S between FIP and FTP surfaces	No	8.2 km to NW	Directly above the crest of an HMM	
67	x = 438817.89 m y = 6469823.72 m	1868	1007	-897 (UTS)	-577 (FTP)	320	200-650	Tapered (mushroom-shaped) discontinuity extending upwards from above edge of an HMM through UTS, TU and terminating in a series of high amplitude anomalies at the FTP level	No	1.5 km to SSW	Directly above the periphery of an HMM	
68	x = 438241.46 m y = 6473078.65 m	1817	1269	-797 (TU)	-567 (FTP)	230	250-800	Wide (wedge-shaped) vertical discontinuity from TU, extending upwards and broadening through the FIP - extending along a NE-SW axis and terminating at the FTP in a cluster of high amplitude anomalies	Marginal	4.3 km to NNW	Directly above the crestal axis of an HMM	
69	x = 438089.03 m y = 6475431.17 m	1804	1456	-914 (UTS)	-585 (FTP)	329	230-950	Two tapered (carrot-shaped) interconnected vertical discontinuities, aligned N-S and extending upward from UTS through TU and terminating in a cluster of high amplitude anomalies at the FTP	Marginal	4.2 km to NNW	Directly above the flank of an HMM between the crestal axis and periphery	
70	x = 439264.34 m y = 6476917.81 m	1895	1575	-791 (TU)	-588 (FTP)	203	160-700	Narrow, (wedge-shaped) vertical discontinuity extending upward from TU and terminating in FTP, with weak N-S alignment	Marginal	5.5 km to NNE	Directly above the periphery of an HMM	
71	x = 437545.01 m y = 6476666.57 m	1759	1555	-810 (TU)	-584 (FTP)	226	350-660	Cylindrical vertical discontinuity (possible coalescence with chimney #107 to N?) extending upward from TU and terminating in FTP, with minor high amplitude anomalies above FTP	Marginal	5.5 km to NNW	Directly above the periphery of an HMM	
72	x = 435627.72 m y = 6478004.22 m	1603	1657	-856 (UTS)	-667 (FIP)	189	300-500	Narrow, tapered (carrot-shaped) vertical discontinuity extending upward from UTS and terminating in FIP	No	7.3 km to NW	Directly above the periphery of an HMM	
73	x = 436523.05 m y = 6476860.74 m	1676	1568	-898 (UTS)	-581 (FTP)	317	250-900	Narrow to wide, (wedge-shaped) vertical discontinuity extending upwards from UTS and terminating in FTP, with elongation along a NW-SE axis from FIP to FTP	No	5.9 km to NW	Directly above the periphery of an HMM	
74	x = 437587.24 m y = 6472789.21 m	1766	1244	-800 (TU)	-609 (FTP)	191	280-650	Two tapered (carrot-shaped) interconnected vertical discontinuities, aligned N-S and extending upward from TU and terminating in a cluster of high amplitude anomalies at the FTP	No	1.7 km to NW	Directly above the flank of an HMM between the crestal axis and periphery	
75	x = 434765.73 m y = 6472583.80 m	1541	1224	-870 (UTS)	-601 (FTP)	269	170-350	Narrow, tapered (carrot-shaped) vertical discontinuity extending upwards from UTS and terminating in FTP	No	3.9 km to WNW	Situated above level area approximately 1200 m WSW of the periphery of an HMM	

Cell Colour Code: Pale Blue = Not on potential CO_2 migration route, Orange = Marginal – at periphery of potential CO_2 migration route, Pink = Directly on potential CO_2 migration route.

Chimney ID	UTM Location	Inline Intersect	Crossline Intersect	Root Depth/Horizon (m TVDSS)	Termination Depth/Horizon (m TVDSS)	Height (m)	Diameter (m)	Morphological Description	On potential CO2 migration route?	Distance/direction from CO2 injection point location	Associated With Underlying Hordaland Mud Mound Structures?	Associated With Overburden Lineaments?
77	x = 439588.61 m y = 6473824.77 m	1926	1329	-889 (UTS)	-570 (FIP/FTP)	319	230-960	Two tapered (carrot-shaped) interconnected vertical discontinuities, aligned N-S and extending upward from UTS and terminating in a cluster of high amplitude anomalies between the FIP and FTP surfaces - possible connection at FTP level with chimney # 78 to the SE?	Yes	2.8 km to NNE	Offset approximately 200 m to the S from the periphery of an HMM	Yes, bounded by two NW-SE trending lineaments from UTS to FIP level and from FIP to FTP levels bounded to the NW by a NE-SW trending lineament
78	x = 439916.02 m y = 6473419.80 m	1952	1297	-815 (TU)	-603 (FIP/FTP)	212	240-500	Columnar vertical discontinuity from TU, extending upwards and broadening through the FIP and terminating between the FIP to FTP - partly truncated to the E by edge of survey coverage - possible connection at FTP level with chimney #77 to NW?	Yes	2.6 km to NE	Directly above the periphery of an HMM	Yes, bounded by two NW-SE trending lineaments from UTS to FIP level and from FIP to FTP levels bounded to the NW by a NE-SW trending lineament
79	x = 438797.86 m y = 6475192.16 m	1859	1436	-803 (TU)	-571 (FTP)	232	340-900	Narrow (wedge-shaped) vertical discontinuity, with N-S extension, extending upwards from TU and broadening through FIP to FTP	Marginal	4.1 km to N	Offset approximately 200 -300 m from the periphery of three HMMs	
80	x = 436509.93 m y = 6469266.92 m	1683	960	-943 (UTS)	-607 (FTP)	336	230-2500	Extensive area of diffuse vertical disruption (series of interconnected chimneys?) , aligned NE-SW, extending upwards from UTS emanating from the periphery of HMM through the TU and terminating in a cluster of high amplitude anomalies at the FTP	No	2.0 km to SW	Directly overlying the periphery and crest of a large HMM	
81	x = 435135.06 m y = 6468189.78 m	1576	874	-807 (TU)	-630 (FTP)	177	16-1100	Two tapered (carrot-shaped) interconnected vertical discontinuities, aligned NE-SW and extending upward from TU through FIP and terminating in a cluster of high amplitude anomalies at the FTP - partly truncated to SW by edge of survey coverage	No	4.7 km to SW	No, overlying a level area in the vicinity of well 15/9-9	
82	x = 434610.18 m y = 6468425.83 m	1534	891	-816 (TU)	-628 (FTP)	188	200-510	Narrow, tapered (carrot-shaped) vertical discontinuity extending upwards from TU, broadening through the FIP and terminating in FTP	No	4.8 km to WSW	No, overlying a level area in the vicinity of well 15/9-9	
83	x = 436816.86 m y = 6467802.14 m	1710	844	-792 (TU)	-631 (FTP)	161	200-600	Narrow (wedge-shaped) vertical discontinuity, with N-S alignment, extending upwards from TU and terminating at FTP - partially truncated to S by edge of survey coverage	No	3.9 km to SW	Directly overlying a small HMM and offset 200-300 m SW from the periphery of a large HMM	
84	x = 434832.15 m y = 6469194.52 m	1550	953	-806 (TU)	-623 (FTP)	183	22-815	Narrow (wedge-shaped) vertical discontinuity, with NE-SW alignment, extending upwards from TU and terminating at FTP at cluster of high amplitude anomalies	No	4.0 km to WSW	No, overlying a level area between wells 15/9-9 and 15/9-16	
85	x = 434361.72 m y = 6469539.11 m	1512	980	-850 (UTS)	-630 (FTP)	220	180-600	Narrow (wedge-shaped) vertical discontinuity, extending upwards from UTS and terminating at FTP - partially truncated to W by edge of survey coverage	No	4.4 km to WSW	No, overlying a level area between wells 15/9-9 and 15/9-16	
88	x = 438549.98 m y = 6468388.97 m	1849	895	-802 (TU)	-595 (FTP)	207	180-630	Two tapered (carrot-shaped) interconnected vertical discontinuities, aligned NE-SW and extending upward from TU and terminating in a cluster of high amplitude anomalies between the FIP and FTP surfaces	No	2.7 km to S	Directly above the peripheral junction of two inter-connected HMMs	
91	x = 439262.65 m y = 6472833.27 m	1900	1247	-778 (TU/SCAH)	-569 (FTP)	209	220-830	Narrow (wedge-shaped) vertical discontinuity, with N-S alignment, extending upwards from TU/SCAH, broadening along a N-S axis through the FIP and terminating at the FTP level in a cluster of large (300 m wide) high amplitude anomalies	Yes	1.7 km to NE	Situated between two HMMs with periphery 400 m offset to W and 200 m offset to SW	Yes, bounded by NW-SE and NE-SW lineaments at the UTS level, intersected by N-S lineaments between TU and FIP levels, then bounded by N-S and NE-SW lineaments between FIP to FTP levels
92	x = 439134.41 m y = 6474292.63 m	1889	1363	-777 (TU/SCAH)	-567 (FTP)	210	240-540	Tapered (carrot-shaped) vertical discontinuity, aligned NNE-SSW and extending upward from TU/SCAH and terminating within a cluster of high amplitude anomalies between the FIP and FTP surfaces	Yes	2.9 km to NNE	Directly above periphery of an HMM	Yes, directly intersected by NE-SW trending lineament in UTS, bounded to the N by an E-W lineament between TU and FIP, then intersected by two major lineaments through the FIP to FTP levels
93	x = 439555.42 m y = 6475706.80 m	1922	1479	-806 (TU)	-595 (FTP)	211	100-250	Narrow, columnar vertical discontinuity, extending upwards from TU through the FIP and terminating within a high amplitude anomaly at the FTP level - possible inter-connection with chimney feature #94 to the S	Marginal	4.6 km to NNE	Directly above periphery of an HMM	
94	x = 439506.04 m y = 6474909.00 m	1920	1415	-782 (TU/SCAH)	-570 (FTP)	212	400-1400	Extensive area of diffuse, noisy vertical disruption (series of interconnected chimneys?), broadly aligned NE-SW, extending upwards from TU/SCAH and terminating in a cluster of high amplitude anomalies at the FTP	Marginal	3.7 km to NNE	Directly above a three-way peripheral junction for two HMMs	
95	x = 439735.24 m y = 6471809.62 m	1939	1168	-789 (TU/SCAH)	-571 (FTP/QAH)	218	25-800	Columnar (mushroom-shaped) vertical discontinuity, extending upwards from TU through the FIP, broadening and terminating within a cluster of high amplitude anomalies at the FTP/QAH level	Marginal	1.4 km to ENE	Directly above periphery of an HMM	

Cell Colour Code: Pale Blue = Not on potential CO_2 migration route, Orange = Marginal – at periphery of potential CO_2 migration route, Pink = Directly on potential CO_2 migration route.

Chimney ID	UTM Location	Inline Intersect	Crossline Intersect	Root Depth/Horizon (m TVDSS)	Termination Depth/Horizon (m TVDSS)	Height (m)	Diameter (m)	Morphological Description	On potential CO2 migration route?	Distance/direction from CO2 injection point location	Associated With Underlying Hordaland Mud Mound Structures?	Associated With Overburden Lineaments?
96	x = 438271.42 m y = 6469118.29 m	1825	951	-732 (SCAH)	-615 (FIP/FTP)	117	100-150	Narrow, columnar vertical discontinuity, extending upwards from SCAH through the FIP and terminating between FIP/FTP	No	2.1 km to S	Offset 300 m to E from periphery of large HMM	
102	x = 437575.86 m y = 6469378.71 m	1771	972	-895 (UTS)	-776 (SCAH)	119	195-420	Columnar vertical discontinuity, extending upward from above the apex of an HMM, through UTS and TU and terminating at high amplitude anomaly in SCAH	No	2.0 km to SSW	Directly overlying the crest of a large HMM	
103	x = 436133.19 m y = 6470212.88 m	1651	1036	-929 (UTS)	-706 (SHMAH)	223	250-450	Columnar vertical discontinuity, extending upward from the UTS at the periphery of an HMM and terminating within the SHMAH	No	2.6 km WSW	Directly overlying the crestal extension of a large HMM	
104	x = 439241.27 m y = 6470558.64 m	1902	1068	-817 (TU)	-597 (FTP)	220	200-540	Tapered (carrot-shaped) vertical discontinuity, extending upward from TU and terminating within a cluster of high amplitude anomalies between the FIP and FTP surfaces	No	1.1 km to SE	Directly overlying the crestal axis of a large HMM	
105	x = 437229.42 m y = 6471421.11 m	1134	1736	-809 (TU)	-585 (FTP)	224	300-425	Columnar vertical discontinuity, extending from the TU and terminating in the FTP - possibly associated with chimney #110 extending to seabed with structure of positive relief?	No	1.2 km to W	Directly overlying the peripheral intersection of two offset HMMs	
106	x = 436701.92 m y = 6475443.59 m	1692	1454	-807 (TU)	-557 (FTP)	283	35-635	Columnar vertical discontinuity, elongated N-S, extending upward from the TU and terminating in the FTP	No	4.6 km to NW	Situated 15-200 m W of the edge of an HMM	Yes, chimney is intersected by a NE-SW trending lineament at 700 m Strong level and bounded by ENE-WSW and NE-SW lineations at the FIP level
107	x = 437279.39 m y = 6477460.00 m	1735	1617	-976 (UTS)	-580 (FTP)	396	300-870	Wide topped, tapered (carrot-shaped) vertical discontinuity extending upward from above TH and terminating in FTP - possible coalescence with chimney #71 to SE?	No	6.3 km to NNW	Situated above hollow on the TU, 200 m S of the edge of an HMM	Yes, bounded and intersected by NW-SE trending lineations at TU level and mainly bounded by NW-SE, NE-SW and ENE-WSW trending lineations at FIP to FTP level
108	x = 438718.30 m y = 6471737.24 m	1858	1161	-720 (700 m Strong)	-540 (FTP)	180	230-500	Diagonal wedge-shaped discontinuity extending upward from 700m Strong, shallowing to SE and terminating in the FTP	Yes	0.5 km to NE	Mid-way between two HMMs (220 m closest to SE)	Yes, chimney is intersected by a NE-SW trending lineament at FIP level and NW-SE trending lineament at the FTP level
109	x = 436519.94 m y = 6473295.67 m	1679	1283	-819 (TU)	-554 (FTP)	265	250-600	One wedge-shaped or two interconnected carrot-shaped vertical discontinuities extending from TU and terminating in FTP	No	2.8 km to WNW	Directly above the crest of an HMM	Yes, chimney is intersected by a ENE-WSW trending lineament at FIP to FTP level
110	x = 437252.47 m y = 6471221.45 m	1742	1120	-550 (FTP/QAH)	-75 (Seabed)	475	150-260	Columnar vertical discontinuity, elongated N-S, extending upward from the FTP/QAH and terminating at seabed with structure of positive relief - possibly associated with underlying chimney #105?	No	1.2 km to W	Directly overlying the peripheral intersection of two offset HMMs	

Cell Colour Code: Pale Blue = Not on potential CO_2 migration route, Orange = Marginal – at periphery of potential CO_2 migration route, Pink = Directly on potential CO_2 migration route.

Appendix 3.1: Critical column height plots for12 m column leakage scenario

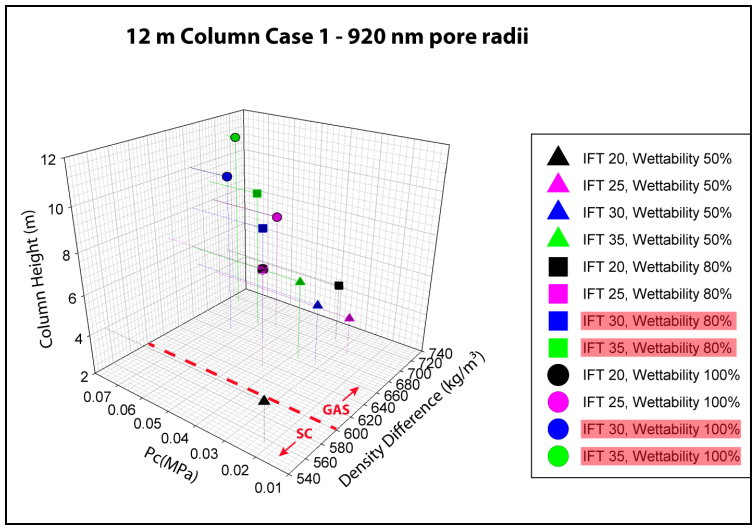

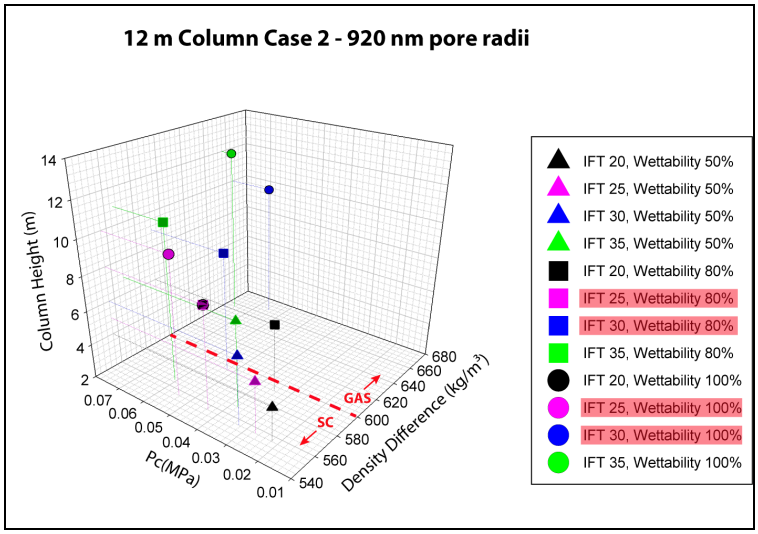

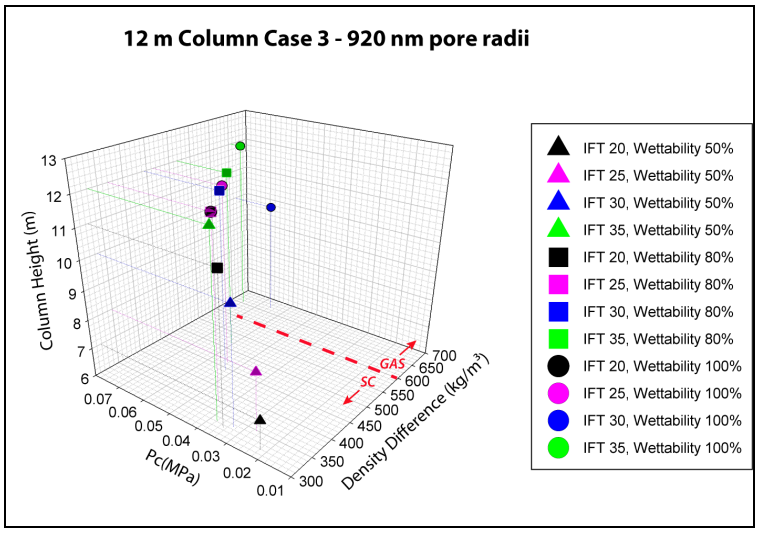

Critical column heights for the (low) end-point 920 nm pore radii and 12 m column height scenario over range of IFT, Wettability and Pc conditions, for cases 1-3 described in Section 3.5.2. Data is from Table 3.13. Entries satisfying leakage criteria are highlighted red within the legend. *CO_2 supercritical to gas phase transition zone is marked in red on the plot.*

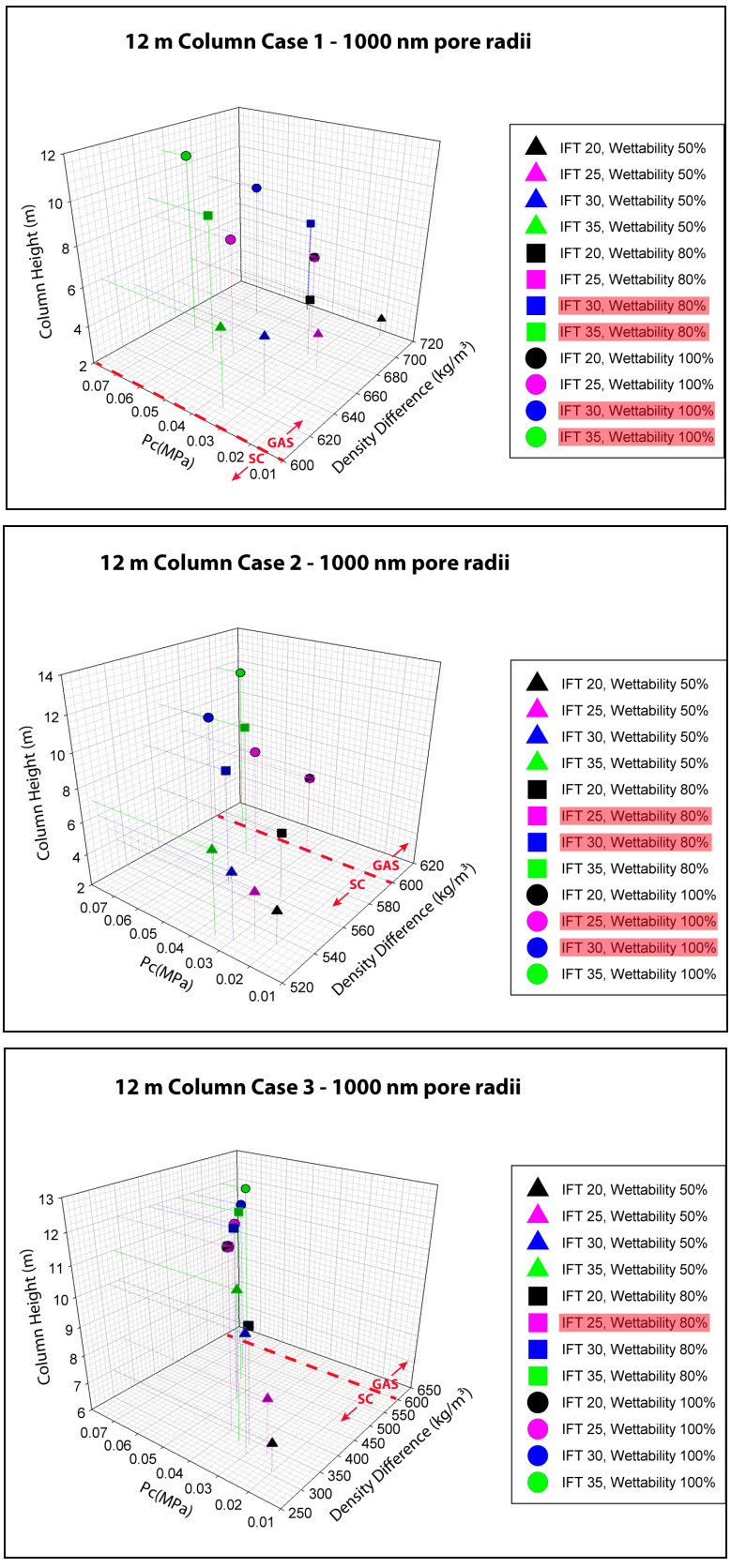

Critical column heights for the (low) end-point 1000 nm pore radii and 12 m column height scenario over range of IFT, Wettability and Pc conditions, for cases 1-3 described in Section 3.5.2. Data is from Table 3.13. Entries satisfying leakage criteria are highlighted red within the legend. *CO_2 supercritical to gas phase transition zone is marked in red on the plot.*

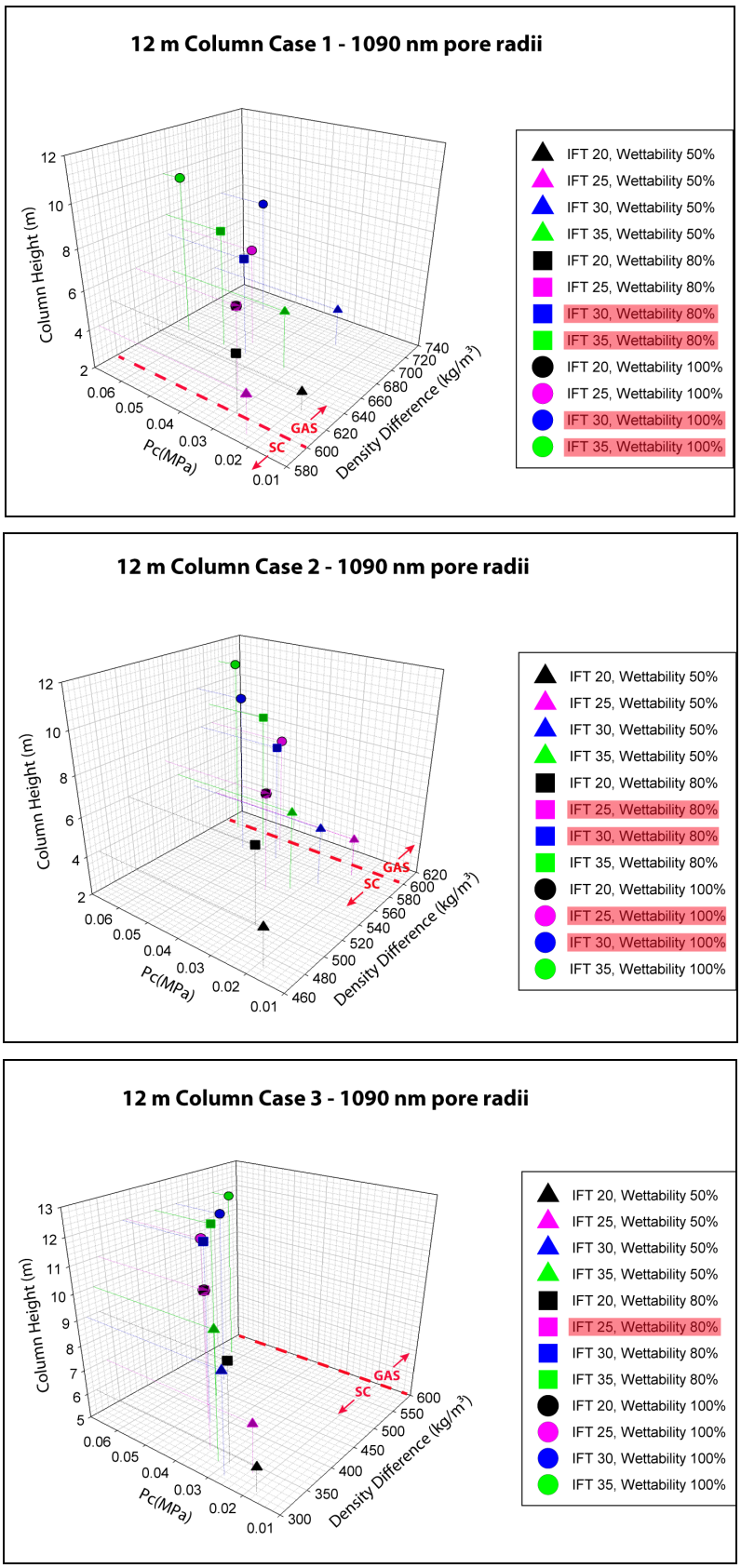

Critical column heights for the (high) end-point 1090 nm pore radii and 12 m column height scenario over range of IFT, Wettability and Pc conditions, for cases 1-3 described in Section 3.5.2. Data is from Table 3.13. Entries satisfying leakage criteria are highlighted red within the legend. *CO_2 supercritical to gas phase transition zone is marked in red on the plot.*

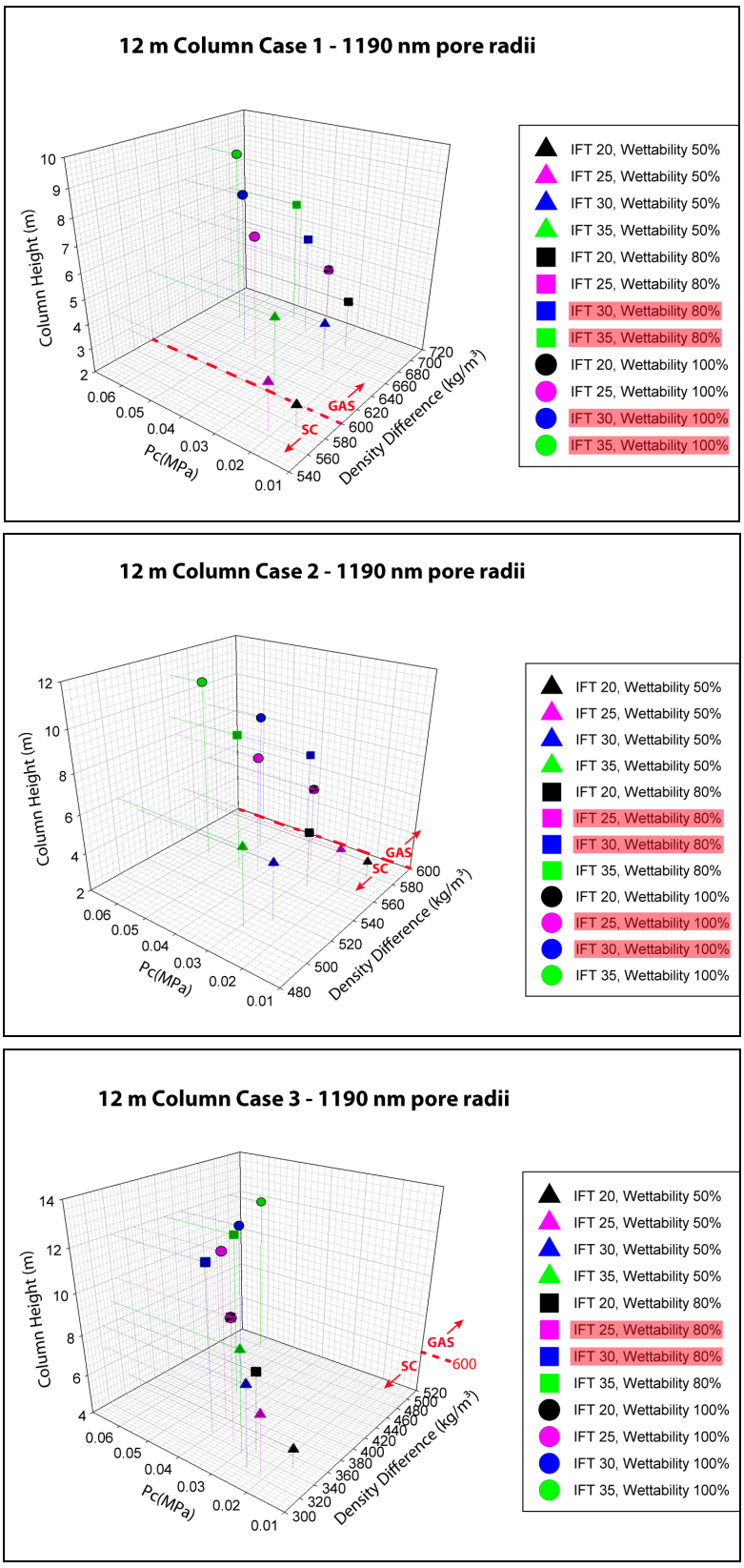

Critical column heights for the (high) end-point 920 nm pore radii and 12 m column height scenario over range of IFT, Wettability and Pc conditions, for cases 1-3 described in Section 3.5.2. Data is from Table 3.13. Entries satisfying leakage criteria are highlighted red within the legend. *CO_2 supercritical to gas phase transition zone is marked in red on the plot.*

Appendix 3.2: Critical column height plots for26 m column leakage scenario

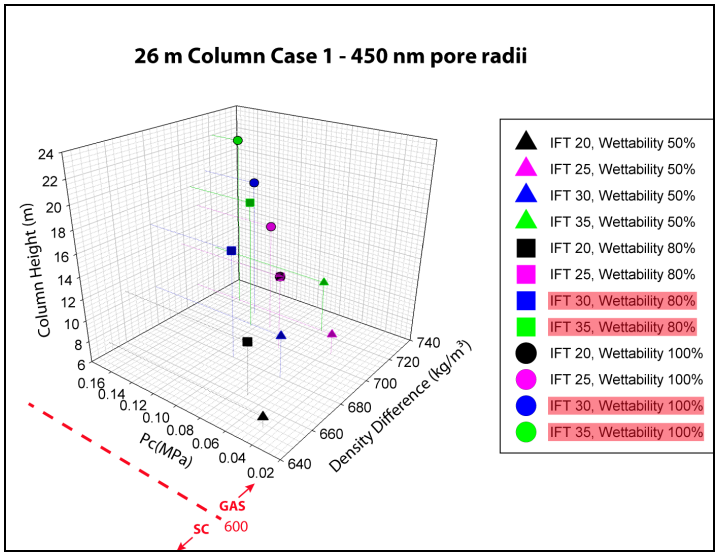

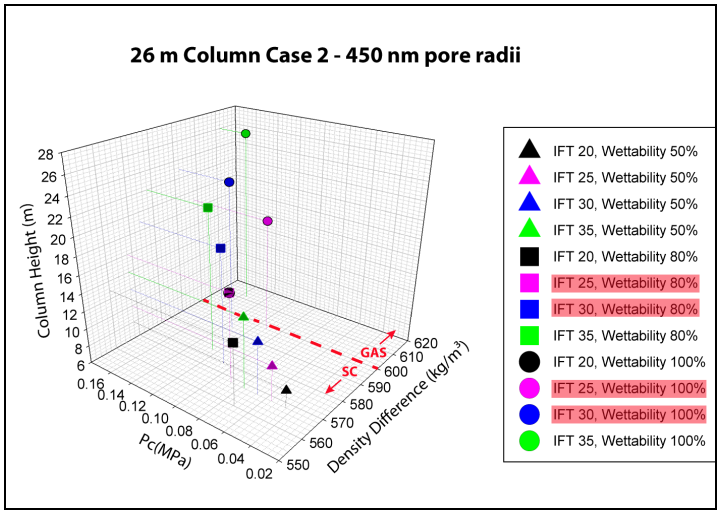

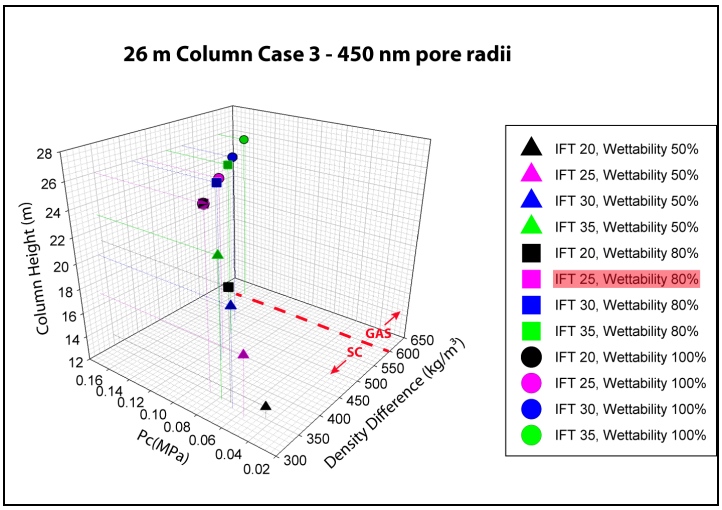

Critical column heights for the (low) end-point 450 nm pore radii and 26 m column height scenario over range of IFT, Wettability and Pc conditions, for cases 1-3 described in Section 3.5.2. Data is from Table 3.12. Entries satisfying leakage criteria are highlighted red within the legend. *CO_2 supercritical to gas phase transition zone is marked in red on the plot.*

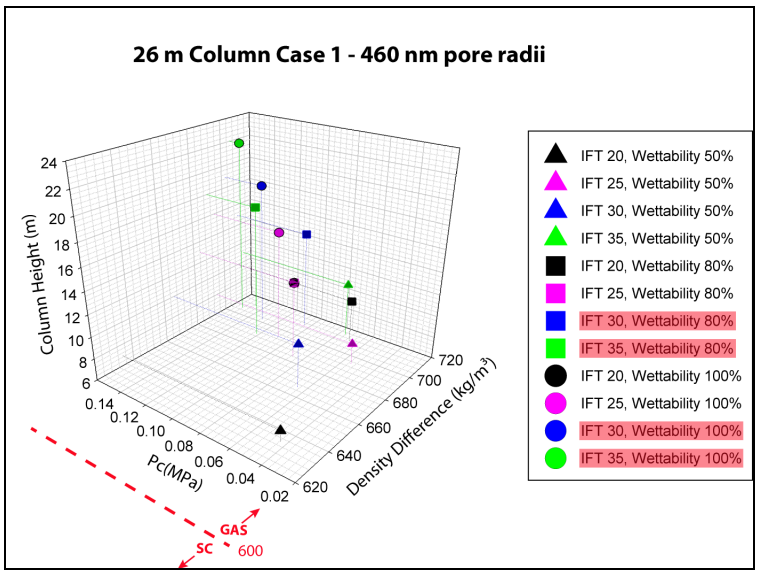

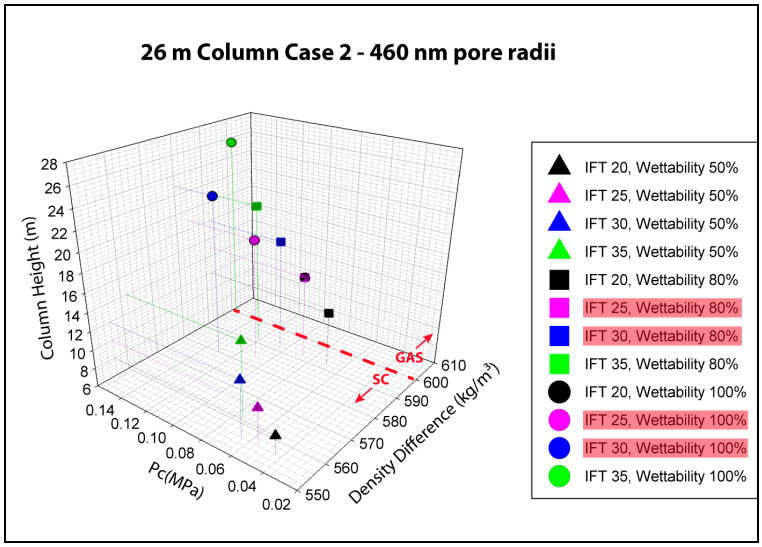

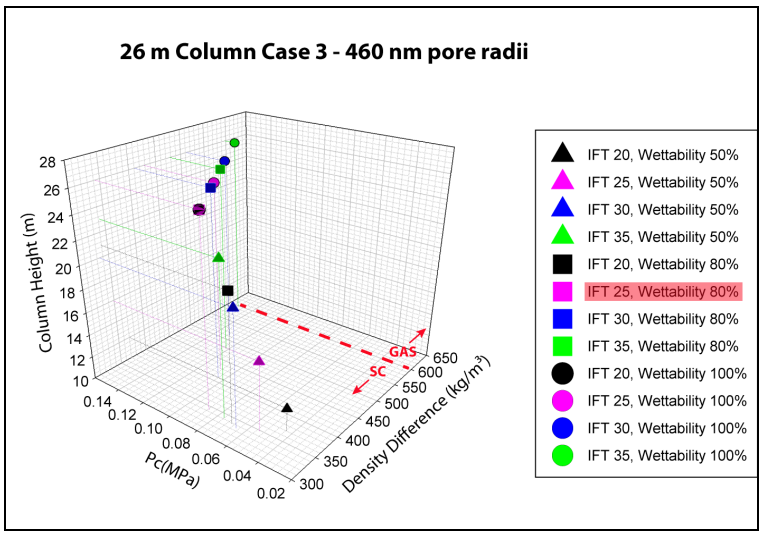

Critical column heights for the (low) end-point 460 nm pore radii and 26 m column height scenario over range of IFT, Wettability and Pc conditions, for cases 1-3 described in Section 3.5.2. Data is from Table 3.12. Entries satisfying leakage criteria are highlighted red within the legend. *CO_2 supercritical to gas phase transition zone is marked in red on the plot.*

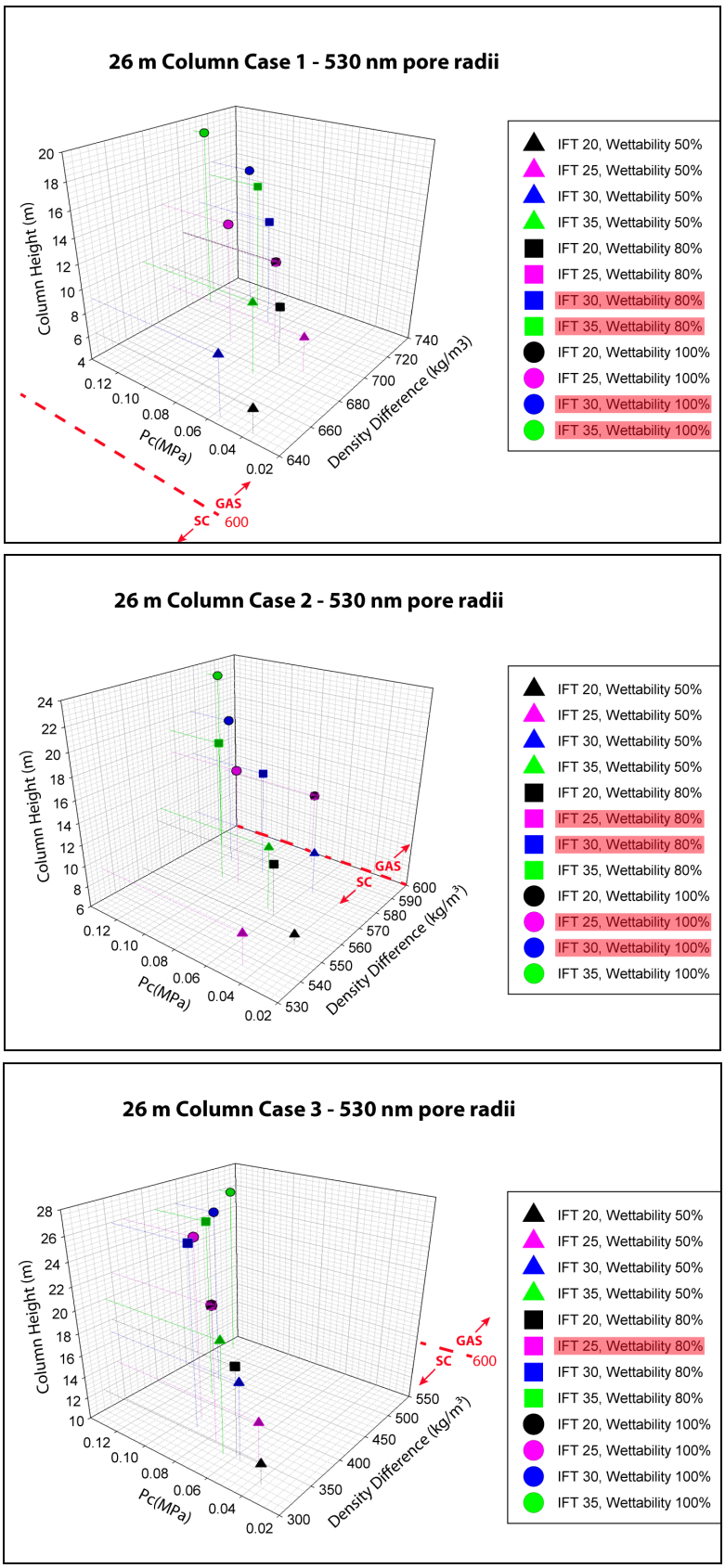

Critical column heights for the (high) end-point 530 nm pore radii and 26 m column height scenario over range of IFT, Wettability and Pc conditions, for cases 1-3 described in Section 3.5.2. Data is from Table 3.12. Entries satisfying leakage criteria are highlighted red within the legend. *CO_2 supercritical to gas phase transition zone is marked in red on the plot.*

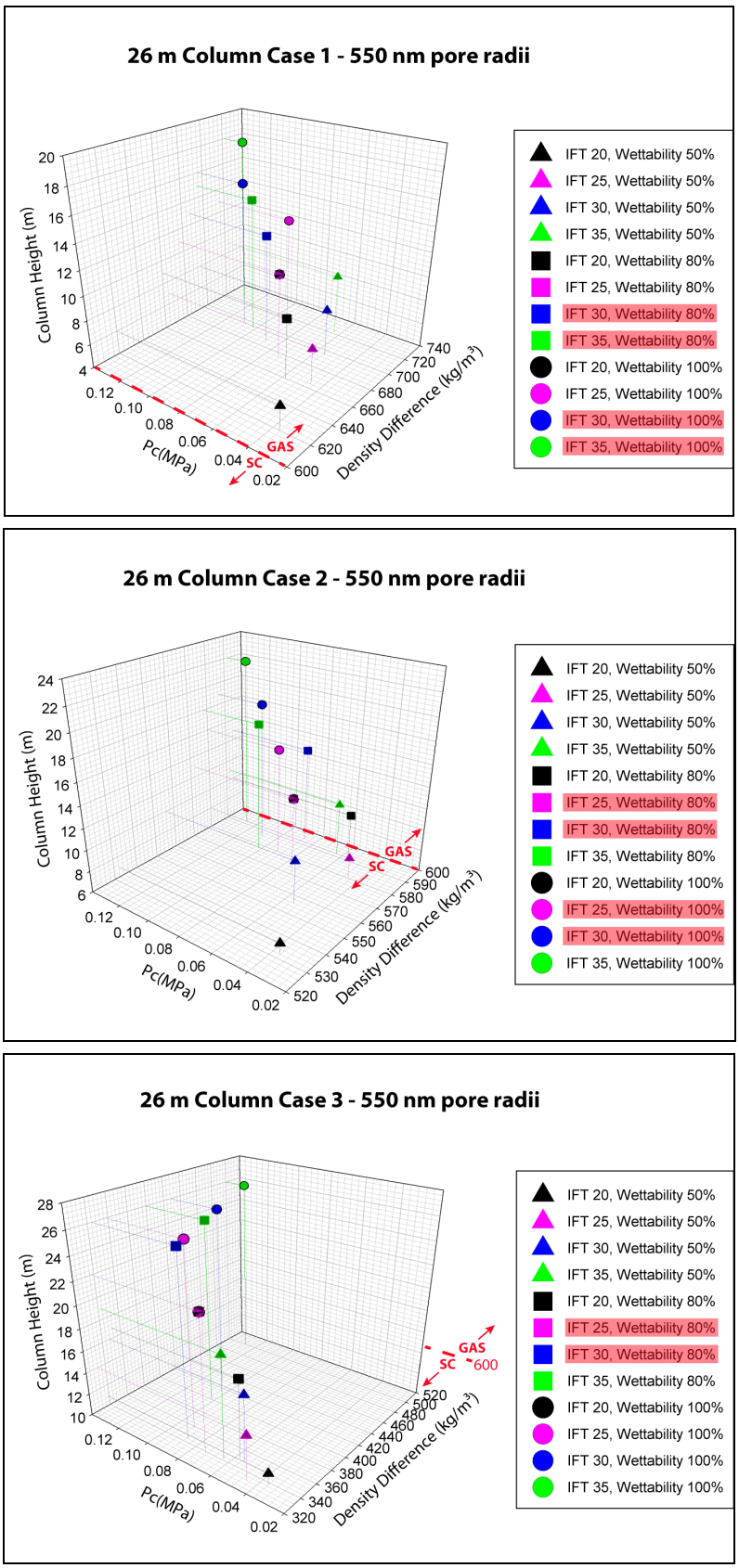

Critical column heights for the (high) end-point 550 nm pore radii and 26 m column height scenario over range of IFT, Wettability and Pc conditions, for cases 1-3 described in Section 3.5.2. Data is from Table 3.12. Entries satisfying leakage criteria are highlighted red within the legend. *CO_2 supercritical to gas phase transition zone is marked in red on the plot.*

Appendix 4.1: List of MPath® Project Files Used For Simulations

The following files were used for Chapter 4 modelling and simulation work:

Final Sleipner 2011 – This is the project file containing:

- All the original map files (*.g, *.dat and *.gri files),
- CO_2 PVT beta file (*.pvt) - **CO2_beta.pvt**
- Lithology Files (*.plith) - starting point is demo.plith (supplied with MPath®), then this file has been edited (see Appendix 4.2 for details) and saved to create:
  GDNFinalBaselineCalibrationHotVersion.plith
  GDNFinalBaselineCalibrationIntermediateVersion.plith
  GDNFinalBaselineCalibrationColdVersion.plith
- Temperature curve files (*.xy) – created in Curve Editor and all designated as:
  XXCatCaprock800mTVDSS.xy
  Where: XX denotes the caprock temperature in ºC,
- Pressure curve file (*.xy) – created in Curve Editor; only one file is used:
  SleipnerHydrostaticPressure.xy
- Earth Model files (*.pmodel) - created in the Map Viewer and all designated as:
  GDNSleipner2011BaselineCalibration_XXCatCapWithYYPlith.pmodel
  Where: XX denotes the temperature in ºC and YY refers to the Hot, Intermediate or Cold plith files described above,
- Meshes files (*.meshseq) - naming convention is same as that for Earth Models, but suffix of **Aol_0.meshseq** follows,
- Simulation files (*.din) – naming convention is same as that for Earth Models, but suffix of **RunZZyrs.din** follows, where ZZ denotes the run time (based on injection volumes) in years,
- Well files (*.**welltk**) – these files contain well tops for each horizon that can be toggled on/off as required,
- Well files (*.**cwell**) – these files contain only positional information (i.e. well sticks for trajectory).

Surface files used in the Earth Models are described in the following tables for the overburden and the Utsira Formation and Hordaland Formation:

Overburden Surfaces:

Map Name (Top Down)	Map Description	Used in Baseline Calibration?	Used in Chimney Model?	Depth Range (m TVDSS)	*Age (Ma)	Lithology Code for Plith File	Notes
GDNRoofFinalV3NoRot	Model Roof	Yes	Yes	0	0	14	
GDNSeabedFinalV3NoRot	Seabed Surface	Yes	Yes	70.9 - 97.5	0.01	29	
GDNPhase3ChannelsMk5_1010_Roof	Phase 3 Tunnel Valley/Channel Roof	No	Yes	119.5 - 147.2	0.1	13	GDNPhase3ChannelsMk5_1010_Lithmap (Lithology Map) used for Channel Model
GDNPhase3ChannelsMk4_1010	Phase 3 Tunnel Valley/Channel Floor	No	Yes	119.5 - 177.5	0.12	13	GDNPhase2ChannelsMk5_1010_Lithmap (Lithology Map) used for Channel Model
GDNPhase2ChannelsMk5_1010_Roof	Phase 2 Tunnel Valley/Channel Roof	No	Yes	156.2 - 187.1	0.15	13	GDNPhase2ChannelsMk5_1010_Lithmap (Lithology Map) used for Channel Model
GDNPhase2ChannelsMk4_1010	Phase 2 Tunnel Valley/Channel Floor	No	Yes	156.2 - 243.2	0.18	13	GDNPhase1ChannelsMk5_1010_Lithmap (Lithology Map) used for Channel Model
GDNPhase1ChannelsMk5_1010_Roof	Phase 1 Tunnel Valley/Channel Roof	No	Yes	213.9 - 243.2	0.2	13	GDNPhase1ChannelsMk5_1010_Lithmap (Lithology Map) used for Channel Model
GDNPhase1ChannelsMk4_1010	Phase 1 Tunnel Valley/Channel Floor	No	Yes	213.9 - 312.2	0.25	11	
GDN400mPeakV3NoRot	400 m Surface	Yes	Yes	363.4 - 399.1	1	28	
GDNTopQuaternarySiltstoneInterval_Roof	Quaternary Siltstone Interval (Upper) Roof	No	Yes	445.2 - 470.9	1.45	4	GDNTopQuaternarySiltstoneInterval_Lithmap (Lithology Map) used for Channel Model
GDNTopQuaternarySiltstoneInterval	Quaternary Siltstone Interval (Upper) Floor	No	Yes	445.2 - 493.1	1.5	4	GDNTopQuaternarySiltstoneInterval_Intermap_Lithmap (Lithology Map) used for Channel Model
GDNTopQuaternarySiltstoneInterval_Intermap_Roof	Quaternary Siltstone Interval (Lower) Roof	No	Yes	479.1 - 505.6	1.55	4	GDNTopQuaternarySiltstoneInterval_Intermap_Lithmap (Lithology Map) used for Channel Model
GDNTopQuaternarySiltstoneInterval_Intermap	Quaternary Siltstone Interval (Lower) Floor	No	Yes	479.1 - 523.2	1.6	4	QuaternaryAnomalySurfaceV3NoRot_Lithmap (Lithology Map) used for Channel Model
QuaternaryAnomalySurfaceV3NoRot_SiltRoof	Quaternary Anomalous Surface (Roof)	No	Yes	501.1 - 525.4	1.65	4	QuaternaryAnomalySurfaceV3NoRot_Lithmap (Lithology Map) used for Channel Model
QuaternaryAnomalySurfaceV3NoRot	Quaternary Anomalous Surface (Floor)	Yes	Yes	501.1 - 561.2	1.7	28	QuaternaryAnomalySurfaceV3NoRot_Lithmap (Lithology Map) used for Channel Model
GDNTopPliocene_0910V3NoRot	Former Top Pliocene Surface	Yes	Yes	529.8 - 584.0	1.77	27 (11)	11 used for complex models
GDNIntraPlioceneBrightSurfaceMk3_Roof	Former Intra Pliocene Channel Roof (Upper)	No	Yes		2	13	
GDNIntraPlioceneBrightSurfaceMk2	Former Intra Pliocene Bright Surface (Floor)	Yes	Yes	551.9 - 659.9	2.5	27 (11)	11 used for complex models
GDNIntraPliocene_0910V3NoRotMk3_Roof	Former Intra Pliocene Channel Roof (Lower)	No	Yes		3	13	
GDNIntraPliocene_0910V3NoRot	Former Intra Pliocene Surface (Floor)	Yes	Yes	628.8 - 758.7	3.58	15 (11)	11 used for complex models
GDN700mPeakV3NoRot	700 m Surface	Yes	Yes	701.1 - 777.9	4	15	
GDNAnomalousHorizonSupraCaprockV3NoRot	Anomalous Surface Above Caprock (Horizon D)	Yes	Yes	753.4 - 823.0	4.75	13	

***Note:** Ages are not precise chronolithostratigraphic, simply approximates for MPath®, which requires ages defined for Earth Model construction, basin modelling and backstripping purposes.

Utsira Formation and Hordaland Formation Surfaces:

Map Name (Top Down)	Map Description	Used in Baseline Calibration?	Used in Chimney Model?	Depth Range (m TVDSS)	*Age (Ma)	Lithology Code for Plith File	Notes
GDNL9FinalV5_NoOverlap	Caprock Seal (Barrier 9)	Yes	Yes	788.0 - 852.7	5	13	
GDNL8TopFinalV5	Top of Thick Shale (Barrier 8)	Yes	Yes	803.4 - 861.1	5.3	26	
GDNL8BaseFinalV5	Base of Thick Shale (Barrier 8)	Yes	Yes	810.4 - 868.1	5.6	13	
GDNL7TopFinalV5	Top of Barrier 7	Yes	Yes	831.5 - 888.8	5.9	25	
GDNL7BaseFinalV5_NoOverlap	Base of Barrier 7	Yes	Yes	833.5 - 890.8	6	13	
GDNL6TopFinalV5	Top of Barrier 6	Yes	Yes	847.7 - 905.4	6.3	24	
GDNL6BaseFinalV5	Base of Barrier 6	Yes	Yes	850.7 - 908.4	6.5	13	
GDNL5TopFinalV5	Top of Barrier 5	Yes	Yes	877.0 - 935.2	6.8	23	
GDNL5BaseFinalV5	Base of Barrier 5	Yes	Yes	879.0 - 937.2	6.9	13	
GDNL4TopFinalV6	Top of Barrier 4	Yes	Yes	883.9 - 947.2	7.2	22	
GDNL4BaseFinalV6	Base of Barrier 4	Yes	Yes	885.9 - 949.2	7.3	13	
GDNL3TopFinalV5_NoOverlap	Top of Barrier 3	Yes	Yes	906.3 - 965.7	7.6	21	
GDNL3BaseFinalV5_NoOverlap	Base of Barrier 3	Yes	Yes	909.3 - 968.7	7.8	13	
GDNL2TopFinalV5	Top of Barrier 2	Yes	Yes	926.2 - 986.4	8.1	20	
GDNL2BaseFinalV5	Base of Barrier 2	Yes	Yes	928.2 - 988.4	8.2	13	
GDNL1TopFinalV5	Top of Barrier 1	Yes	Yes	941.2 - 1002.2	8.5	19	
GDNL1BaseFinalV5	Base of Barrier 1	Yes	Yes	943.2 - 1004.2	8.6	13	
GDNTopHordFinalV3NoRot	Top of the Hordaland Formation	Yes	Yes	953.9 - 1110.8	11	11	
GDNFloorFinalV3NoRot	Model Floor	Yes	Yes	1200	12	11	

Note: Ages are not precise chronolithostratigraphic, simply approximates for MPath®, which requires ages defined for Earth Model construction, basin modelling and backstripping purposes.

Appendix 4.2: Editing MPath Lithology (.plith)Files*

All the lithology files used in this research were created from demo.plith supplied with MPath®. The file was edited to create a new set of lithologies based on existing ones, then curves for the new lithologies were edited and saved. For example, the Utsira Sand lithology was created from the *High Net to Gross Sandstone* lithology in demo.plith and similarly, the Nordland Shale lithology was created from the *Shale* lithology in demo.plith.

In the lithology editor (example screenshot illustrated below), in the Poro-Pth tab, the curves can be edited by right-clicking on the Pth-Porosity drop-down menu at the far right of the dialogue, then selecting the Calculator menu option. The Pth for a given porosity can be reduced by multiplying with a scale factor (as illustrated) or increased by scaling up (e.g. multiplying by 1.1), or using some other form of mathematical manipulation:

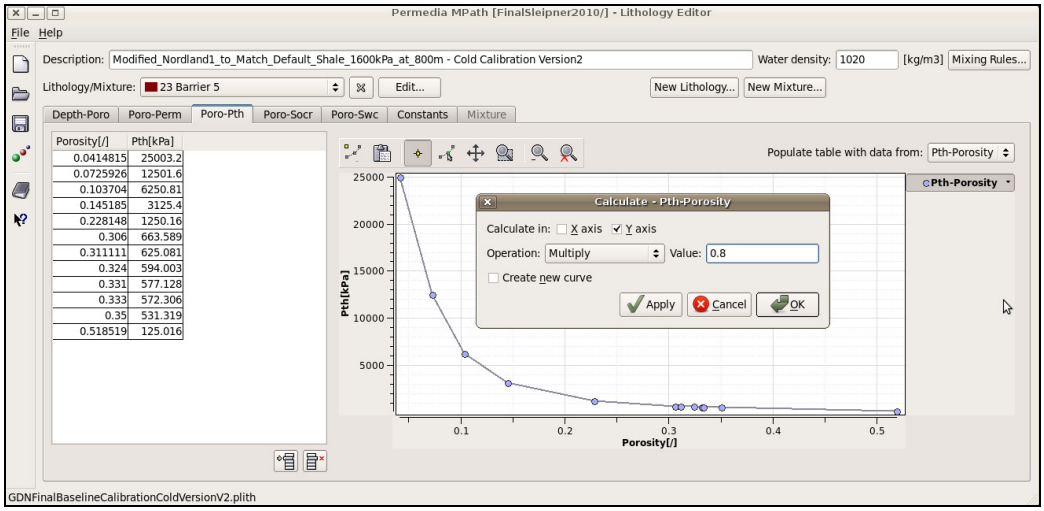

The edited Pth values used for the Cold, Intermediate and Hot calibration models are presented in the following tables. In order to populate the mesh model with porosity and capillary threshold entry pressure data matching observed data from Sleipner, the default Depth-Porosity and Porosity-Threshhold Entry Pressure curves were adjusted to account for an Utsira Sandstone porosity of 38% and Nordland Shale (caprock) porosity of 35% at the injection point caprock depth (~800 m TVDSS), based on results published in Zweigel *et al.,* (2004) and Springer & Lindgren, (2006).

:

Adjustments made to MPath® Demo.Plith High NTG Sandstone Lithology:

	Demo.Plith (default)		Cold Plith		Intermediate Plith		Hot Plith	
Depth (m TVDSS)	**Porosity (fraction)**	***Pth (kPa)**	**Porosity (fraction)**	***Pth (kPa)**	**Porosity (fraction)**	***Pth (kPa)**	**Porosity (fraction)**	***Pth (kPa)**
800	0.42	240	0.36	218	0.36	218	0.36	218
900	0.41	245	0.345	228	0.345	228	0.345	228
1000	0.40	1824	0.33	238	0.33	238	0.33	238

Adjustments made to MPath® Demo.Plith Shale Lithology:

		Demo.Plith (default)		Cold Plith		Intermediate Plith		Hot Plith	
Barrier	**Depth at Injection Point Location (m TVDSS)**	**Porosity (fraction)**	***Pth (kPa)**	**Porosity (fraction)**	***Pth (kPa)**	**Porosity (fraction)**	***Pth (kPa)**	**Porosity (fraction)**	***Pth (kPa)**
9	800	0.34	1680	0.35	1600	0.35	1600	0.35	1600
8	824	0.335	1720	0.345	776	0.345	641	0.345	982
7	847	0.330	1760	0.341	550	0.341	550	0.341	726
6	868	0.326	1792	0.337	400	0.337	530	0.337	634
5	890	0.322	1824	0.305	754	0.305	754	0.305	1086
4	909	0.318	1856	0.329	651	0.329	544	0.329	651
3	920	0.316	1872	0.335	721	0.335	517	0.335	779
2	945	0.311	1912	0.322	549	0.322	687	0.322	825
1	960	0.308	1936	0.32	560	0.32	770	0.32	907

***Note that all Pth values used in MPath® are Mercury-Air values and need to be multiplied by an appropriate interfacial tension factor (e.g. 0.0625, as used in Singh *et al.*, 2010) to obtain equivalent CO_2-Brine values. Although Barrier 9 should have a higher Mercury-Air value in reality, the value of 1600 kPa is sufficiently high to prevent CO_2 capillary entry into the overburden during the Baseline Calibration simulations.**

Appendix 4.3: Lithology Map Construction Workflow

The following workflow was developed to create a channel fill of specified lithology for the MPath® 3D mesh models:

1. Load channel surface map imported from Petrel into the Map Viewer and use the Mapping/Edit/Fill Holes and Mapping/Edit/Fill Null Areas commands to make a "clean" copy of the original map:

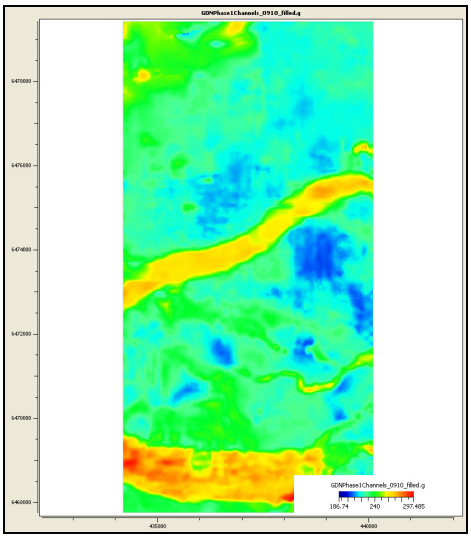

2. Open the Colour Editor for the "clean" map and use the sculpting control to create transparent areas where channels cut the topography. Several attempts may be required to capture the appropriate depths to match well log data (if available):

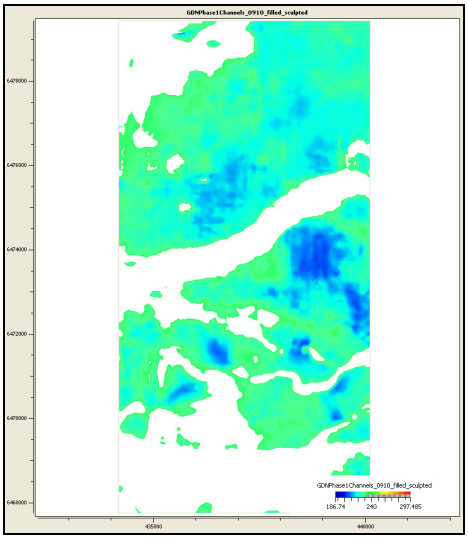

3. The Lithology Map can be created first from the sculpted map, by using the Mapping/Create/Categories/Assign Categories command to open the Category Editor and set-up the Lithology Map. First select an appropriate Lookup Table (in this case one of the edited Lithology *.plith files). Only two lithology categories are required (i.e. low NTG sandstone and Nordland Shale4), so remove the two middle rows of the table and move the triangular sliders to match the histogram to the map (which shows the current sculpting profile and depth ranges) - adjustments can be made "on-the-fly" using the Apply button until the desired map is created, then OK. If required, more categories can be reassigned later (e.g. if users want to create additional lithology categories such as palaeo-gas chimneys). Save the Lithology Map with an appropriate name:

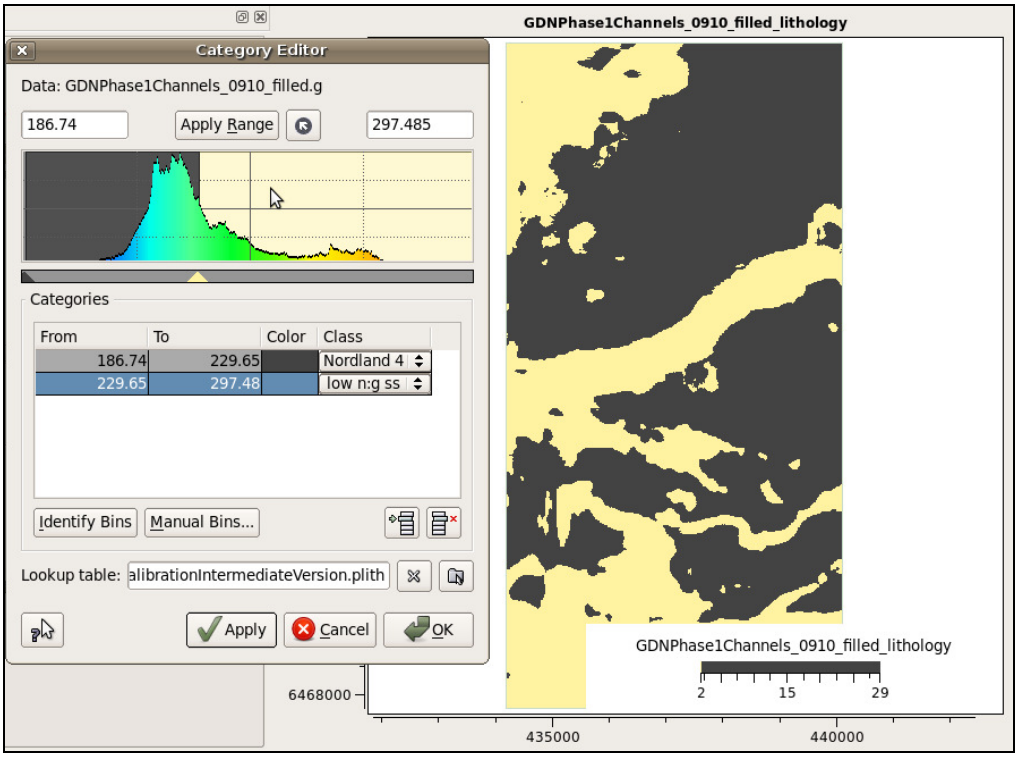

4. There should now be two maps for constructing a channel fill – the "clean" channel surface map created at Step 1 and the “roof” map created at Step 3. When an Earth Model is constructed MPath® will assign the selected lithology from the base of the upper map to the top of the underlying map.

5. Note that when an Earth Model is finally created with these maps, the (upper) Roof map should have the younger age and the Lithology Map should be assigned to it, whilst the (lower) Channel/Floor map has no Lithology Map and is simply assigned a suitable underlying lithology from the *.plith file selected for the Earth Model. However, if there are a series of overlying channels, the assignment is a little more complicated as the underlying table illustrates:

Channel Phase	Map Position	Lithology Map to be Assigned	Notes
3 (Youngest)	Roof	GDNPhase3ChannelsMk5_1010_LithMap	
3	Channel/Floor	GDNPhase2ChannelsMk5_1010_LithMap	
2	Roof	GDNPhase2ChannelsMk5_1010_LithMap	
2	Channel/Floor	GDNPhase1ChannelsMk5_1010_LithMap	
1	Roof	GDNPhase1ChannelsMk5_1010_LithMap	
1 (Oldest)	Channel/Floor	None	Nordland Shale assigned from *.plith file

In essence, the lithology map from the Channel/Floor of the upper map (e.g. Phase 3 Channels) is assigned to the Roof of the underlying map (i.e. Phase 2 Channels).

6. To add the chimney lithology to the overburden surface maps the process is similar, except three or more lithologies are used instead of two. All of the chimney structures (described and mapped in Chapter 2) were either cylindrical or tapered (i.e. carrot-shaped), so by viewing each of the overburden surfaces penetrated by chimney structures from below, it was possible to screen capture and export from Petrel® a UTM located map of each chimney footprint on the affected surfaces. These were subsequently imported into MPath®, flipped the correct way up, converted into a black and white image and used to add additional complexity to the models. Note that the white background must be assigned a null value before the chimney lithology is merged into another map.

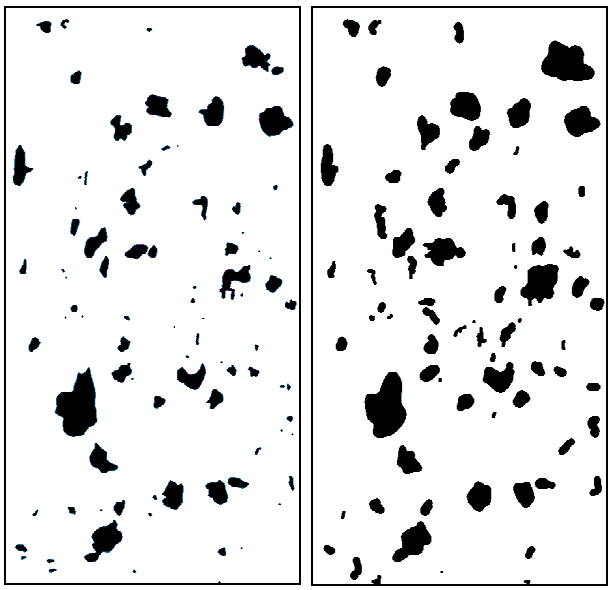

Examples of Chimney Lithology maps (black areas) used in MPath® for the Complex Model:

Top Sand Wedge (left)

Supra Caprock Anomaly (right)

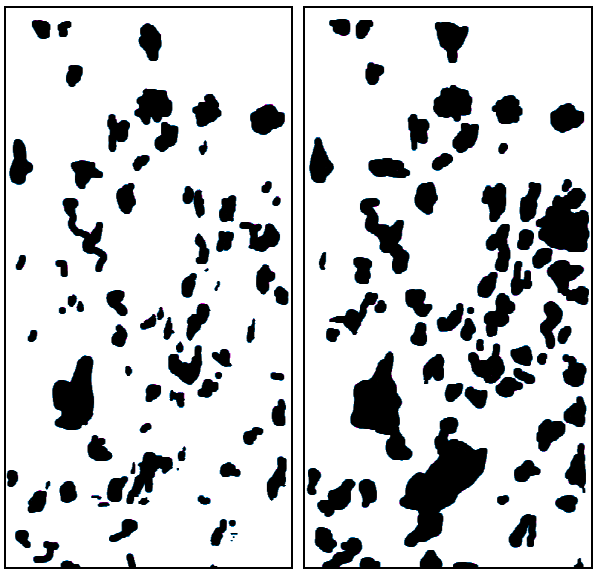

700 m Surface (left)

Former Intra Pliocene (right)

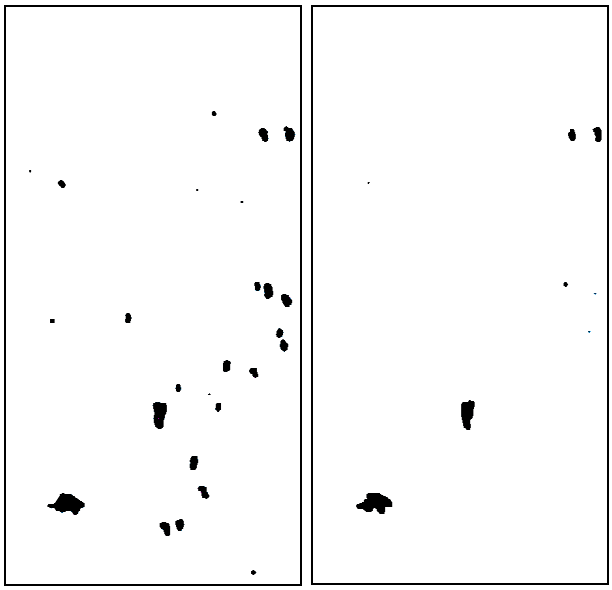

Former Top Pliocene (left)

Quaternary Anomalous (right)

Appendix 4.4: Tabulated Results from Baseline Calibration Model Simulations

Years of Injection	Year	Mt CO_2 Injected	kg of CO_2 Injected
1	1997	0.84	8.4000E+08
2	1998	1.68	1.6800E+09
3	1999	2.52	2.5200E+09
4	2000	3.36	3.3600E+09
5	2001	4.2	4.2000E+09
6	2002	5.04	5.0400E+09
7	2003	5.88	5.8800E+09
8	2004	6.72	6.7200E+09
9	2005	7.56	7.5600E+09
10	2006	8.4	8.4000E+09
11	2007	9.24	9.2400E+09
12	2008	10.08	1.0080E+10
13	2009	10.92	1.0920E+10
14	2010	11.76	1.1760E+10
15	2011	12.6	1.2600E+10
16	2012	13.44	1.3440E+10
17	2013	14.28	1.4280E+10
18	2014	15.12	1.5120E+10
19	2015	15.96	1.5960E+10
20	2016	16.8	1.6800E+10
21	2017	17.64	1.7640E+10
22	2018	18.48	1.8480E+10
23	2019	19.32	1.9320E+10
24	2020	20.16	2.0160E+10
25	2021	21	2.1000E+10
26	2022	21.84	2.1840E+10
27	2023	22.68	2.2680E+10
28	2024	23.52	2.3520E+10
29	2025	24.36	2.4360E+10
30	2026	25.2	2.5200E+10

CO_2 injection volumes used for all Sleipner MPath® simulations

GDNSleipner2011BaselineCalibration_28CatCapWithColdPlith_Run6yrs

Barrier Number	Crest X Location	Crest Y Location	Crest Depth (m TVDSS)	Column Height (m)	Temperature C	Pressure (kPa)	Liquid IFT Multiplier	Average Pore Saturation (Fraction)	Liquid Volume (m3)	Liquid Density (kgm3)
9	**438886**	**6471980**	**789.078**	**4.84314**	**27.9546**	**8193.72**	**0.067842**	**0.865023**	**71980.3**	**746.443**
	438632	6471430	792.805	1.29706	28.0074	8211.78	0.0678113	0.865019	1140.91	746.337
	438768	6471310	793.969	0	28.0003	8209.37	0.0678177	0.865013	2.49809e-05	746.359
	438717	6471310	794.102	0.00262451	27.9996	8209.11	0.0678182	0.865005	0.000166285	746.361
	438566	6471360	794.797	0	28.0148	8214.32	0.0678045	0.864987	7.76168e-05	746.314
	438566	6471310	795.914	0.000366211	28.0495	8226.2	0.0677733	0.864927	4.69336e-09	746.208
	438482	6471280	806.617	0.0269775	28.3411	8325.97	0.0675238	0.864352	0.0563624	745.509
8	**438482**	**6471280**	**822.453**	**9.94482**	**28.9965**	**8550.23**	**0.0670113**	**0.862904**	**1226080**	**744.731**
7	**438381**	**6471730**	**845.312**	**5.39789**	**29.4568**	**8707.75**	**0.0666699**	**0.862015**	**335542**	**743.404**
	438987	6471930	849.156	3.90216	29.5231	8730.41	0.0666233	0.86199	51171.3	743.265
	438734	6471780	850.914	0.00152588	29.6059	8758.76	0.0665656	0.861909	4.04433e-08	743.111
	438987	6471930	853.773	0.0438843	29.6452	8772.22	0.0665383	0.861817	0.132019	743.044
6	**438936**	**6471930**	**860.969**	**5.24756**	**29.9674**	**8882.47**	**0.0663177**	**0.8611**	**101116**	**742.68**
	438936	6471930	872.57	0.0186157	30.307	8998.67	0.066126	0.860551	0.0496644	742.342
5	**438936**	**6471980**	**886.102**	**10.4902**	**30.6182**	**9105.15**	**0.0659653**	**0.859667**	**2281020**	**741.525**
4	**438684**	**6471030**	**897.227**	**6.97778**	**31.1487**	**9286.7**	**0.0656885**	**0.858958**	**57488.7**	**740.49**
	438432	6471830	902.852	4.05035	31.1155	9275.34	0.0657056	0.858949	30940.1	740.56
	438532	6471630	906.117	0.00189209	31.1844	9298.9	0.0656702	0.858887	5.93521e-07	740.419
	438532	6471730	907.18	0	31.1858	9299.38	0.0656694	0.858883	1.25367e-06	740.416
	438583	6471680	910.289	0.0499878	31.2773	9330.68	0.065622	0.858708	1.16504	740.25
3	**438633**	**6471630**	**915.727**	**8.28912**	**31.7014**	**9475.81**	**0.0654006**	**0.857781**	**669089**	**739.807**
	438987	6471730	925.594	0.000854492	31.8012	9509.99	0.0653496	0.857696	5.80916e-06	739.714
	438987	6471930	925.719	1.84851	31.8111	9513.37	0.0653453	0.857572	3955.53	739.69
	439037	6471780	927.141	0	31.8596	9529.96	0.0653241	nan	0	739.575
	439037	6471830	927.32	0.00115967	31.8767	9535.82	0.0653166	0.857576	2.67242e-05	739.536
	438936	6471880	927.734	6.10352e-05	31.8211	9516.8	0.065341	0.857637	8.00905e-07	739.686
	438919	6471860	928.234	0.0010376	31.83	9519.85	0.0653371	0.857646	7.939e-08	739.644
2	**438936**	**6471830**	**934.102**	**7.4563**	**32.1403**	**9626**	**0.0651874**	**0.856955**	**426741**	**738.883**
	438583	6471730	944.312	0.0480957	32.3256	9689.41	0.0650869	0.856687	0.0718379	738.446
1	**438583**	**6471730**	**950.555**	**8.9649**	**32.8297**	**9861.9**	**0.0647965**	**0.85561**	**437783**	**737.671**
	438280	6471230	973.766	0.00415039	33.4109	10060.8	0.0644636	0.854573	6.72728e-05	736.881
	438280	6471230	994.438	0.00341797	33.9968	10261.3	0.0641531	0.853457	0.00172672	735.844
	438432	6471280	1002.07	-6.10352e-05	34.2562	10350	0.0640307	0.853015	2.92188e-05	735.422
									Average Density	764.70459375

28ºC at Caprock Run for 6years With Cold Lithology File

GDNSleipner2011BaselineCalibration_29CatCapWithColdPlith_Run6yrs

Barrier Number	Crest X Location	Crest Y Location	Crest Depth (m TVDSS)	Column Height (m)	Temperature C	Pressure (kPa)	Liquid IFT Multiplier	Average Pore Saturation (Fraction)	Liquid Volume (m3)	Liquid Density (kgm3)
9	**438886**	**6471980**	**789.078**	**5.33319**	**28.9525**	**8193.72**	**0.0673449**	**0.865015**	**99110.2**	**731.352**
	438566	6471360	794.797	0	29.0156	8214.32	0.0673147	0.864987	7.02867e-05	731.205
	438566	6471310	795.914	0.000183105	29.0519	8226.2	0.0672991	0.864927	1.52398e-09	731.078
	438482	6471280	806.617	0.231873	29.3574	8325.97	0.0671583	0.864352	33.7527	730.279
8	**438482**	**6471280**	**822.453**	**9.9743**	**30.0439**	**8550.23**	**0.0668036**	**0.862904**	**1233910**	**729.536**
7	**438381**	**6471730**	**845.312**	**5.51733**	**30.5262**	**8707.75**	**0.06662**	**0.862013**	**355462**	**728.007**
	438987	6471930	849.156	3.90216	30.5956	8730.41	0.0665905	0.861989	51168.4	727.858
	438734	6471780	850.914	0.00152588	30.6824	8758.76	0.0665525	0.861909	4.06515e-08	727.697
	438987	6471930	853.773	0.248962	30.7236	8772.22	0.066534	0.861815	19.2709	727.63
6	**438936**	**6471930**	**860.969**	**5.37872**	**31.0611**	**8882.47**	**0.066376**	**0.861097**	**106613**	**727.224**
	438936	6471930	872.57	0.224609	31.4169	8998.67	0.0662055	0.860548	32.3964	726.891
5	**438936**	**6471980**	**886.102**	**10.5526**	**31.7428**	**9105.15**	**0.0660831**	**0.859667**	**2307750**	**725.93**
4	**438684**	**6471030**	**897.227**	**7.08759**	**32.2987**	**9286.7**	**0.0658544**	**0.858958**	**60710.1**	**724.613**
	438432	6471830	902.852	4.05066	32.2639	9275.34	0.0658694	0.85895	30948.3	724.685
	438532	6471630	906.117	0.00201416	32.336	9298.9	0.0658381	0.858887	6.79936e-07	724.54
	438381	6471780	908.797	0.239014	32.4174	9325.47	0.0658017	0.85871	148.106	724.4
	438683	6471680	910.289	0.196106	32.4333	9330.68	0.0657945	0.858708	71.5808	724.375
3	**438633**	**6471630**	**915.727**	**8.38721**	**32.8776**	**9475.81**	**0.0655731**	**0.85778**	**683727**	**724.056**
	438987	6471730	925.594	0.000915527	32.9823	9509.99	0.0655205	0.857696	6.02149e-06	723.995
	438987	6471930	925.719	1.84821	32.9926	9513.37	0.0655165	0.857572	3952.98	723.969
	439037	6471780	927.141	6.10352e-05	33.0434	9529.96	0.0654995	0.857587	1.32742e-08	723.801
	439037	6471830	927.32	0.00115967	33.0614	9535.82	0.0654935	0.857576	2.37602e-05	723.74
	438936	6471880	927.734	6.10352e-05	33.0031	9516.8	0.0655126	0.857637	7.60793e-07	723.939
	438919	6471860	928.234	0.000610352	33.0125	9519.85	0.0655096	0.857646	1.8736e-08	723.907
2	**438936**	**6471830**	**934.102**	**7.56689**	**33.3375**	**9626**	**0.0653977**	**0.856952**	**442814**	**722.922**
	438583	6471730	944.312	0.253296	33.5316	9689.41	0.0653245	0.856686	14.2077	722.473
1	**438583**	**6471730**	**950.555**	**9.06921**	**34.0597**	**9861.9**	**0.0651013**	**0.855608**	**449791**	**721.717**
	438280	6471230	973.766	0.210266	34.6686	10060.8	0.0648533	0.854552	1.2649	720.884
	438280	6471230	994.438	0.209961	35.2823	10261.3	0.0646157	0.853453	13.4479	719.631
	438432	6471280	1002.07	-6.10352e-05	35.5541	10350	0.0644846	0.853015	2.38538e-05	719.253
									Average Density	750.399551724138

29ºC at Caprock Run for 6years With Cold Lithology File

GDNSleipner2011BaselineCalibration_30CatCapWithColdPlith_Run6yrs

Barrier Number	Crest X Location	Crest Y Location	Crest Depth (m TVDSS)	Column Height (m)	Temperature C	Pressure (kPa)	Liquid IFT Multiplier	Average Pore Saturation (Fraction)	Liquid Volume (m3)	Liquid Density (kgm3)
9	**439289**	**6473480**	**788.211**	**5.76776**	**29.9575**	**8195.99**	**0.0672534**	**0.864945**	**132249**	**714.388**
	438886	6471980	789.078	6.65265	29.9503	8193.72	0.0672572	0.86499	201372	714.402
	438785	6472980	792.445	2.35931	30.0675	8230.34	0.0671962	0.864831	14639.6	714.023
	438987	6473130	794.344	0.289124	30.1374	8252.17	0.06716	0.864766	87.7151	713.764
	439037	6473180	794.633	0.00799561	30.1306	8250.06	0.0671635	0.864775	4.75938e-05	713.787
	438936	6472780	795.008	0.0592041	30.1275	8249.09	0.0671651	0.864765	2.1001	713.798
	438886	6472730	795.289	0	30.124	8247.99	0.0671669	0.864786	6.6089e-07	713.811
	438633	6471380	804.641	0.348083	30.3317	8312.88	0.0670609	0.864414	257.782	713.229
	438532	6471380	805.852	0	30.3766	8326.91	0.0670383	0.864338	5.25376e-07	713.144
	438482	6471280	806.617	0.278137	30.3736	8325.97	0.0670398	0.864352	58.1268	713.149
8	**438482**	**6471280**	**822.453**	**9.79077**	**31.0914**	**8550.23**	**0.0666841**	**0.862907**	**118170**	**712.608**
7	**438381**	**6471730**	**845.312**	**5.46344**	**31.5955**	**8707.75**	**0.0664307**	**0.862013**	**34487**	**710.739**
	438987	6471930	849.156	3.90253	31.6681	8730.41	0.0663949	0.86199	51179.3	710.571
	438987	6471930	853.773	0.371094	31.8019	8772.22	0.0663292	0.861815	62.808	710.327
6	**438936**	**6471930**	**860.969**	**5.32623**	**32.1548**	**8882.47**	**0.0661589**	**0.861098**	104390	709.809
	438936	6471930	872.57	0.345337	32.5267	8998.67	0.0659839	0.860547	97.0453	709.708
5	**438936**	**6471980**	**886.102**	**10.3253**	**32.8675**	**9105.15**	**0.0658241**	**0.859669**	**2211580**	**708.647**
4	**438684**	**6471030**	**897.227**	**6.9693**	**33.4486**	**9286.7**	**0.0655562**	**0.858958**	**57234.6**	**707.1**
	438432	6471830	902.852	4.05078	33.4122	9275.34	0.0655728	0.85895	30948.1	707.166
	438532	6471630	906.117	0.00164795	33.4877	9298.9	0.0655383	0.858887	3.97389e-07	707.035
	438381	6471780	908.797	0.360657	33.5727	9325.47	0.0654993	0.85871	333.228	706.917
	438583	6471680	910.289	0.196594	33.5894	9330.68	0.0654916	0.858708	72.0988	706.898
3	**438633**	**6471630**	**915.727**	**8.23114**	**34.0539**	**9475.81**	**0.0652785**	**0.857781**	**660535**	**706.785**
	438987	6471930	925.719	1.8479	34.1742	9513.37	0.0652256	0.857572	3951.16	706.611
	439037	6471780	927.141	6.10352e-05	34.2272	9529.96	0.0652029	0.857589	5.45087e-08	706.418
	439037	6471830	927.32	0.000915527	34.246	9535.82	0.0651948	0.857576	1.8605e-05	706.352
	438936	6471880	927.734	6.10352e-05	34.1851	9516.8	0.0652209	0.857637	6.54448e-07	706.57
	438919	6471860	928.234	0.000732422	34.1949	9519.85	0.0652167	0.857646	2.40491e-08	706.534
2	**438936**	**6471830**	**934.102**	**7.43304**	**34.5347**	**9626**	**0.0650717**	**0.856955**	**421937**	**705.48**
	438583	6471730	944.312	0.374817	34.7376	9689.41	0.0649852	0.856686	46.9831	705.028
1	**438583**	**6471730**	**950.555**	**8.8772**	**35.2897**	**9861.9**	**0.0647504**	**0.855611**	**427875**	**704.138**
	438280	6471230	973.766	0.333618	35.9263	10060.8	0.0644796	0.854551	5.03077	703.545
	438280	6471230	994.438	0.333557	36.5679	10261.3	0.0642378	0.853454	51.5176	702.069
	438432	6471280	1002.07	-6.10352e-05	36.852	10350	0.064129	0.853015	2.07488e-05	701.755
									Average Density	730.493787878788

30ºC at Caprock Run for 6years With Cold Lithology File

GDNSlejpner2011BaselimeCalibration_31CatCapWithInterPlith_Run6yrs
(Note that the simulation results file is wrongly labelled: WithHotPlith)

Barrier Number	Crest X Location	Crest Y Location	Crest Depth (m TVDSS)	Column Height (m)	Temperature C	Pressure (kPa)	Liquid IFT Multiplier	Average Pore Saturation (Fraction)	Liquid Volume (m3)	Liquid Density (kgm3)
	438886	**6471980**	**789.078**	**3.51532**	**30.9481**	**8193.72**	**0.0670339**	**0.865045**	**25441.8**	**694.783**
	438532	6471430	792.805	1.29718	31.0084	8211.78	0.0670147	0.865019	1141.39	694.639
	438768	6471310	793.969	0	31.0004	8209.37	0.0670154	0.865013	1.39153e-05	694.688
	438717	6471310	794.102	0.00219727	30.9995	8209.11	0.0670156	0.865004	9.91658e-05	694.691
	438566	6471360	794.797	0	31.0169	8214.32	0.0670139	0.864987	5.1873e-05	694.589
	438566	6471310	795.914	0.000366211	31.0566	8226.2	0.0670096	0.864927	3.03179e-09	694.364
	438482	6471280	806.617	0.045105	31.3898	8325.97	0.0669277	0.864352	0.255157	693.178
8	**438482**	**6471280**	**822.453**	**8.79303**	**32.1388**	**8550.23**	**0.0665774**	**0.862923**	**937962**	**693.119**
7	**438381**	**6471730**	**845.312**	**6.86145**	**32.6649**	**8707.75**	**0.0664664**	**0.862**	**608857**	**690.948**
	438987	6471930	849.156	3.90271	32.7406	8730.41	0.066441	0.861989	51176.9	690.783
	438987	6471930	853.773	0.0597534	32.8802	8772.22	0.066388	0.861816	0.300378	690.574
6	**438936**	**6471930**	**860.969**	**6.29706**	**33.2484**	**8882.47**	**0.0662484**	**0.861046**	**358456**	**690.013**
	438936	6471930	872.57	0.0386963	33.6365	8998.67	0.066041	0.86055	0.318489	690.44
5	**438936**	**6471980**	**886.102**	**10.743**	**33.9921**	**9105.15**	**0.0659376**	**0.859661**	**2389840**	**689.318**
4	**438684**	**6471030**	**897.227**	**6.38464**	**34.5985**	**9286.7**	**0.0657569**	**0.858956**	**41995.4**	**687.493**
	438432	6471830	902.852	4.05109	34.5605	9275.34	0.0657718	0.858949	30953.5	687.547
	438532	6471630	906.117	0.00177002	34.6393	9298.9	0.0657404	0.858887	4.80936e-07	687.445
	438532	6471730	907.18	0	34.6408	9299.38	0.0657397	0.858883	4.12442e-07	687.444
	438583	6471680	910.289	0.0652466	34.7454	9330.68	0.065695	0.858708	2.64373	687.365
3	**438633**	**6471630**	**915.727**	**5.84912**	**35.2301**	**9475.81**	**0.0654645**	**0.857808**	**340710**	**687.427**
	438987	6471730	925.594	0.000671387	35.3443	9509.99	0.0654129	0.857696	3.48542e-06	687.39
	438987	6471930	925.719	1.84778	35.3556	9513.37	0.0654099	0.85757	3950.32	687.346
	439037	6471780	927.141	6.10352e-05	35.411	9529.96	0.0653946	0.857585	2.99437e-09	687.138
	439037	6471830	927.32	0.000915527	35.4305	9535.82	0.065369	0.857576	1.58067e-05	687.067
	438936	6471880	927.734	6.10352e-05	35.367	9516.8	0.0654068	0.857637	5.62989e-07	687.302
	438919	6471860	928.234	0.000610352	35.3772	9519.85	0.065404	0.857646	1.09497e-08	687.264
2	**438936**	**6471830**	**934.102**	**9.09003**	**35.7318**	**9626**	**0.0652924**	**0.856936**	**703396**	**686.167**
	438583	6471730	944.312	0.0637817	35.9435	9689.41	0.0652128	0.856686	0.191501	685.746
1	**438583**	**6471730**	**950.555**	**10.698**	**36.5196**	**9861.9**	**0.0649949**	**0.855589**	**651203**	**684.735**
	438280	6471230	973.766	0.0257568	37.1838	10060.8	0.0647057	0.854558	0.00329001	684.312
	438280	6471230	994.438	0.0257568	37.8534	10261.3	0.0644529	0.853455	0.0438494	682.846
	438432	6471280	1002.07	-6.10352e-05	38.1499	10350	0.0643256	0.853015	1.81837e-05	682.517
								Average Density	711.312193548387	

31ºC at Caprock Run for 6years With Intermediate Lithology File

GDNSleipner2011BaselineCalibration_32CatCapWithInterPlith_Run6yrs

Barrier Number	Crest X Location	Crest Y Location	Crest Depth (m TVDSS)	Column Height (m)	Temperature C	Pressure (kPa)	Liquid IFT Multiplier	Average Pore Saturation (Fraction)	Liquid Volume (m3)	Liquid Density (kgm3)
9	**438886**	**6471980**	**789.078**	**6.55066**	**31.946**	**8193.72**	**0.0680228**	**0.864992**	**191998**	**670.705**
	438566	6471310	796.914	0.000306176	32.059	8226.2	0.0679993	0.864927	1.79854e-09	670.109
	438482	6471280	806.617	0.215027	32.406	8325.97	0.0679098	0.864352	26.8536	668.555
8	**438482**	**6471280**	**822.453**	**8.82227**	**33.1863**	**8550.23**	**0.0674163**	**0.862921**	**944803**	**670.213**
7	**438381**	**6471730**	**845.312**	**6.91394**	**33.7343**	**8707.75**	**0.0672754**	0.862	619821	667.687
	438987	6471930	849.156	3.90302	33.8131	8730.41	0.0672424	0.86199	51183.9	667.551
	438987	6471930	853.773	0.230286	33.9586	8772.22	0.0671731	0.861815	15.2029	667.449
6	**438936**	**6471930**	**860.969**	**6.35931**	**34.3421**	**8882.47**	**0.0670067**	**0.861044**	**368411**	**666.864**
	438936	6471930	872.57	0.210327	34.7464	8998.67	0.0667163	0.860548	27.4391	668.37
5	**438936**	**6471980**	**886.102**	**10.7355**	**35.1169**	**9105.15**	**0.0666065**	**0.859663**	**2386440**	**666.845**
4	**438684**	**6471030**	**897.227**	**6.44775**	**35.7485**	**9286.7**	**0.0663718**	**0.858956**	**43447.6**	**665.074**
	438432	6471830	902.852	4.05127	35.709	9275.34	0.0663913	0.85895	30955.7	665.096
	438532	6471630	906.117	0.00164795	35.7909	9298.9	0.0663503	0.858887	3.87117e-07	665.063
	438381	6471780	908.797	0.222412	35.8834	9325.47	0.0663009	0.85871	127.915	665.087
	438583	6471680	910.289	0.197449	35.9015	9330.68	0.0662908	0.858708	73.2397	665.1
3	**438633**	**6471630**	**915.727**	**5.92462**	**36.4064**	**9475.81**	**0.0660057**	**0.857807**	**349631**	**665.543**
	438987	6471930	925.719	1.84747	36.5371	9513.37	0.065933	0.857572	3948.81	665.639
	439037	6471830	927.32	0.000915527	36.6152	9535.82	0.0659075	0.857576	1.46196e-05	665.342
	438936	6471880	927.734	6.10352e-05	36.549	9516.8	0.0659292	0.857637	5.08368e-07	665.592
	438919	6471860	928.234	0.000610352	36.5596	9519.85	0.0659258	0.857646	2.05062e-08	665.55
2	**438936**	**6471830**	**934.102**	**9.11157**	**36.929**	**9626**	**0.0657893**	**0.856935**	**707659**	**664.442**
	438583	6471730	944.312	0.234802	37.1495	9689.41	0.0657068	0.856686	11.3179	663.781
1	**438583**	**6471730**	**950.555**	**10.6877**	**37.7496**	**9861.9**	**0.0654279**	**0.855588**	**649744**	**663.054**
	438280	6471230	973.766	0.198486	38.4415	10060.8	0.0650716	0.854552	1.07416	662.922
	438280	6471230	994.438	0.198242	39.139	10261.3	0.0647694	0.853453	11.261	661.505
	438432	6471280	1002.07	-6.10352e-05	39.4478	10350	0.0646195	0.853015	1.42676e-05	661.21
									Average Density	692.57392

32ºC at Caprock Run for 6years With Intermediate Lithology File

GDNSleipner2011BaselineCalibration_33CatCapWithInterPlith_Run6yrs

Barrier Number	Crest X Location	Crest Y Location	Crest Depth (m TVDSS)	Column Height (m)	Temperature C	Pressure (kPa)	Liquid IFT Multiplier	Average Pore Saturation (Fraction)	Liquid Volume (m3)	Liquid Density (kgm3)
9	**438886**	**6471980**	**789.078**	**6.26154**	**32.9437**	**8193.72**	**0.0679414**	**0.864997**	**166836**	**638.819**
	438633	6471380	804.641	0.483704	33.3749	8312.88	0.0677084	0.864412	620.366	634.742
	438532	6471380	805.852	0	33.4257	8326.91	0.0676836	0.864338	2.58369e-07	634.711
	438482	6471280	806.617	0.278687	33.4222	8325.97	0.0676852	0.864352	58.3376	634.709
8	**438482**	**6471280**	**822.453**	**9.0213**	**34.2337**	**8550.23**	**0.0673221**	**0.862917**	**992843**	**642.089**
7	**438381**	**6471730**	**845.312**	**7.10815**	**34.8036**	**8707.75**	**0.067023**	**0.861997**	**661219**	**639.027**
	438987	6471930	849.156	3.9032	34.8856	8730.41	0.0669822	0.86199	51184.5	638.962
	438987	6471930	853.773	0.512695	35.0369	8772.22	0.066907	0.861815	163.483	638.817
6	**438936**	**6471930**	**860.969**	**6.56464**	**35.4358**	**8882.47**	**0.0667094**	0.861041	402332	638.582
	438936	6471930	872.57	0.496704	35.8562	8998.67	0.0665119	0.860546	241.246	642.422
5	**438936**	**6471980**	**886.102**	**10.9354**	**36.2415**	**9105.15**	**0.0663119**	**0.859656**	**2475040**	**640.29**
4	**438684**	**6471030**	**897.227**	**6.68066**	**36.8984**	**9286.7**	**0.0659856**	**0.858957**	**49262**	**638.825**
	438432	6471830	902.852	4.05151	36.8573	9275.34	0.066006	0.858949	30961.7	638.788
	438532	6471630	906.117	0.00140381	36.9425	9298.9	0.0659636	0.858887	2.47683e-07	638.883
	438381	6471780	908.797	0.507324	37.0387	9325.47	0.0659159	0.85871	658.094	638.932
	438583	6471680	910.289	0.197937	37.0575	9330.68	0.0659066	0.858708	73.8439	638.912
3	**438633**	**6471630**	**915.727**	**6.18335**	**37.5826**	**9475.81**	**0.0656441**	**0.857803**	**380790**	**640.393**
	438987	6471730	925.594	0.000610352	37.7063	9509.99	0.0655828	0.857696	2.29817e-06	640.876
	438987	6471930	925.719	1.84717	37.7185	9513.37	0.0655767	0.857572	3946.43	640.828
	439037	6471780	927.141	6.10352e-05	37.7785	9529.96	0.0655466	0.857584	1.12745e-09	640.605
	439037	6471830	927.32	0.000915527	37.7997	9535.82	0.065536	0.857576	1.17779e-05	640.531
	438936	6471880	927.734	6.10352e-05	37.7309	9516.8	0.0655705	0.857637	3.97325e-07	640.78
	438919	6471860	928.234	0.000488281	37.742	9519.85	0.0655649	0.857646	7.36192e-09	640.738
2	**438936**	**6471830**	**934.102**	**9.35065**	**38.1261**	**9626**	**0.0653764**	**0.856932**	**753919**	**639.387**
	438683	6471730	944.312	0.523865	38.3555	9689.41	0.06527	0.856672	248.084	638.642
1	**438583**	**6471730**	**950.555**	**10.9279**	**38.9796**	**9861.9**	**0.0649714**	**0.855586**	**681757**	**638.599**
	438280	6471230	973.766	0.48822	39.6992	10060.8	0.0646147	0.854551	15.5681	639.065
	438280	6471230	994.438	0.487427	40.4245	10261.3	0.0642911	0.853459	148.066	637.633
	438381	6471280	999.75	0.00744629	40.6748	10330.4	0.0641616	0.853112	6.32099e-07	637.62
	438432	6471280	1002.07	-6.10352e-05	40.7457	10350	0.0641234	0.853015	1.38672e-05	637.681
									Average Density	661.065103448276

33ºC at Caprock Run for 6years With Intermediate Lithology File

GDNSleipner2011BaselineCalibration_34CatCapWithInterPlith_Run6yrs

Barrier Number	Crest X Location	Crest Y Location	Crest Depth (m TVDSS)	Column Height (m)	Temperature C	Pressure (kPa)	Liquid IFT Multiplier	Average Pore Saturation (Fraction)	Liquid Volume (m3)	Liquid Density (kgm3)
	438886	**6471980**	**789.078**	**6.18866**	**33.9417**	**8193.72**	**0.0672447**	**0.864999**	**160843**	**587.571**
	438633	6471380	804.641	0.745361	34.3894	8312.88	0.0669926	0.864406	2011.42	582.962
	438532	6471380	805.852	0	34.4421	8326.91	0.0669761	0.864338	2.09904e-07	583.385
	438482	6471280	806.617	0.279053	34.4386	8325.97	0.0669771	0.864352	58.5145	583.349
8	**438482**	**6471280**	**822.453**	**9.15253**	**35.2812**	**8550.23**	**0.0668212**	**0.862917**	**1025070**	**605.264**
7	**438381**	**6471730**	**845.312**	**7.27441**	**35.8731**	**8707.75**	**0.066585**	**0.861995**	**697600**	**601.504**
	438987	6471930	849.156	3.90338	35.9582	8730.41	0.0665479	0.86199	51191.1	601.622
	438987	6471930	853.773	0.807678	36.1153	8772.22	0.0664841	0.861814	624.151	601.111
6	**438936**	**6471930**	**860.969**	**6.77289**	**36.5296**	**8882.47**	**0.0662972**	**0.861039**	**437802**	**602.743**
	438936	6471930	872.57	0.806641	36.9662	8998.67	0.0660467	0.860544	813.471	611.046
5	**438936**	**6471980**	**886.102**	**11.1714**	**37.3662**	**9105.15**	**0.0658946**	**0.859648**	**2598680**	**608.077**
4	**438684**	**6471030**	**897.227**	**6.96191**	**38.0484**	**9286.7**	**0.0656085**	**0.858958**	**57005.6**	**607.242**
	438432	6471830	902.852	4.05188	38.0057	9275.34	0.0656231	0.858949	30963.8	607.29
	438532	6471630	906.117	0.00128174	38.0942	9298.9	0.0655926	0.858887	1.96002e-07	607.226
	438381	6471780	908.797	0.817139	38.1941	9325.47	0.0655568	0.858706	1647.25	607.321
	438583	6471680	910.289	0.198303	38.2136	9330.68	0.0655496	0.858708	74.3457	607.361
3	**438633**	**6471630**	**915.727**	**6.51239**	**38.7589**	**9475.81**	**0.0653486**	**0.857799**	**421928**	**611.189**
	438987	6471730	925.594	0.000610352	38.8874	9509.99	0.0653068	0.857696	1.94666e-06	612.198
	438987	6471930	925.719	1.84705	38.9001	9513.37	0.0653029	0.857572	3945.85	612.152
	439037	6471780	927.141	6.10352e-05	38.9624	9529.96	0.0652841	0.857588	9.46769e-09	611.944
	439037	6471630	927.32	0.000671387	38.9844	9535.82	0.0652773	0.857576	6.75946e-06	611.877
	438936	6471880	927.734	6.10352e-05	38.9129	9516.8	0.0652991	0.857637	3.47671e-07	612.107
	438919	6471860	928.234	0.000610352	38.9244	9519.85	0.0652956	0.857646	1.59566e-08	612.068
2	**438936**	**6471830**	**934.102**	**9.70465**	**39.3233**	**9626**	**0.0651688**	**0.856928**	**824287**	**610.277**
	438583	6471730	944.312	0.841553	39.5615	9689.41	0.0650893	0.85667	968.067	609.735
1	**438583**	**6471730**	**950.555**	**11.3247**	**40.2096**	**9861.9**	**0.0648349**	**0.855581**	**735758**	**610.338**
	438280	6471230	973.766	0.813477	40.9569	10060.8	0.0644137	0.854551	71.4664	612.361
	438280	6471230	994.438	0.81189	41.7101	10261.3	0.0639937	0.853471	566.679	611.145
	438381	6471280	999.75	0.00720215	41.9701	10330.4	0.0638407	0.853111	6.65356e-07	611.512
									Average Density	626.92775

34ºC at Caprock Run for 6years With Intermediate Lithology File

GDNSleipner2011BaselineCalibration_35CatCapWithHotPlith_Run6yrs

Barrier Number	Crest X Location	Crest Y Location	Crest Depth (m TVDSS)	Column Height (m)	Temperature C	Pressure (kPa)	Liquid IFT Multiplier	Average Pore Saturation (Fraction)	Liquid Volume (m3)	Liquid Density (kgm3)
9	438686	6471980	789.078	6.16882	34.9395	8193.72	0.0675954	0.864999	159208	504.269
	438566	6471310	795.914	0.00012207	35.0661	8226.2	0.0675156	0.864927	2.66876e-10	507.386
	438482	6471280	822.453	11.0023	36.3287	8550.23	0.0663796	0.862891	1514280	554.752
	438381	6471730	845.312	7.24243	36.9424	8707.75	0.0662052	0.861997	690400	551.376
8	438987	6471930	849.156	3.90356	37.0307	8730.41	0.066162	0.861989	51189.2	551.825
7	438987	6471930	853.773	0.00354004	37.1936	8772.22	0.0660781	0.86182	0.000319778	552.854
	438936	6471930	860.969	5.89685	37.6232	8882.47	0.0657777	0.861089	129413	559.387
	438936	6471980	866.102	12.524	38.4909	9105.15	0.0653377	0.859606	3315520	568.77
6	438684	6471030	897.227	6.13525	39.1983	9286.7	0.0650452	0.858931	29921.9	569.406
	438785	6471430	900.977	2.61322	39.085	9257.63	0.065095	0.859059	8759.77	569.022
5	438432	6471830	902.852	4.05212	39.154	9275.34	0.065065	0.85895	30966.3	569.23
4	438532	6471630	906.117	0.00134277	39.2459	9298.9	0.0650235	0.858887	2.00269e-07	569.633
	438532	6471730	907.18	0	39.2477	9299.38	0.0650227	0.858883	1.81445e-07	569.643
	438583	6471680	910.289	0.00720215	39.3697	9330.68	0.064965	0.858707	0.00305739	570.408
	438633	6471630	915.727	8.12946	39.9352	9475.81	0.0646567	0.857783	645526	577.3
	438987	6471730	925.594	0.000610352	40.0684	9509.99	0.0645862	0.857696	1.7101e-06	578.632
3	438987	6471930	925.719	1.8468	40.0816	9513.37	0.0645817	0.857572	3944.01	578.55
	439037	6471780	927.141	6.10352e-05	40.1462	9529.96	0.0645594	0.857576	2.16073e-11	578.176
	439037	6471830	927.32	0.000732422	40.169	9535.82	0.0645514	0.857576	7.34451e-06	578.053
	438936	6471880	927.734	6.10352e-05	40.0949	9516.8	0.0645771	0.857636	2.53999e-07	578.469
	438919	6471860	928.234	0.000610352	40.1068	9519.85	0.064573	0.857646	1.33436e-08	578.399
	438936	6471830	934.102	8.65558	40.5204	9626	0.0644212	0.856941	622170	576.836
	438583	6471730	944.312	0.00628662	40.7675	9689.41	0.0643209	0.856688	2.02009e-05	576.726
2	438583	6471730	950.555	9.89117	41.4396	9861.9	0.0640194	0.855598	548026	578.611
1									Average Density	589.031

35ºC at Caprock Run for 6years With Hot Lithology File

GDNSleipner2011BaselineCalibration_36CatCapWithHotPlith_Run6yrs_SecondPass

Barrier Number	Crest X Location	Crest Y Location	Crest Depth (m TVDSS)	Column Height (m)	Temperature C	Pressure (kPa)	Liquid IFT Multiplier	Average Pore Saturation (Fraction)	Liquid Volume (m3)	Liquid Density (kgm3)
9	439289	6473480	788.211	3.31519	35.9464	8195.99	0.0679647	0.865013	13515.9	445.401
	439239	6473730	789.039	2.51978	35.9744	8202.91	0.0679316	0.864988	10649.7	446.619
	438886	6471980	789.078	6.65063	35.9373	8193.72	0.0679755	0.864989	201117	445.006
	438987	6473480	790.5	1.74274	36.0436	8220.05	0.0678391	0.864925	3625.76	450.172
	438785	6472980	792.445	2.35938	36.0851	8230.34	0.067781	0.864831	14633.4	452.431
	438936	6473430	792.828	0.00177002	36.0953	8232.88	0.0677668	0.86487	2.49339e-06	452.982
	438987	6473380	793.016	0.00335693	36.1059	8235.51	0.0677521	0.864846	0.000475729	453.547
	439088	6473230	793.469	0.00250244	36.1391	8243.73	0.0677067	0.864793	8.01752e-08	455.297
	439020	6473210	793.703	0.00372314	36.1588	8248.62	0.0676799	0.864788	4.56244e-07	456.322
	438987	6473130	794.344	0.289062	36.1732	8252.17	0.0676605	0.864766	88.1957	457.061
	439037	6473180	794.633	0.0043335	36.1647	8250.06	0.067672	0.864775	7.63181e-06	456.624
	438936	6472780	795.008	0.0571899	36.1607	8249.09	0.0676773	0.864765	2.0152	456.421
	438886	6472730	795.289	0	36.1663	8247.99	0.0676833	0.864786	9.91325e-08	456.191
	438633	6471380	804.641	0.276428	36.4182	8312.88	0.0674111	0.864415	137.951	468.76
	438532	6471380	805.852	0	36.4748	8326.91	0.0673613	0.864336	6.37893e-08	471.218
	438482	6471280	806.617	0.279419	36.471	8325.97	0.0673646	0.864352	58.6433	471.056
8	438482	6471280	822.453	11.0872	37.3761	8550.23	0.0668201	0.86289	1538580	492.237
7	438381	6471730	845.312	7.4953	38.0118	8707.75	0.0665555	0.861993	747129	495.916
	438987	6471930	849.156	3.90393	38.1032	8730.41	0.0665043	0.861989	51195.9	497.908
	438987	6471930	853.773	0.309509	38.2719	8772.22	0.0664036	0.861815	36.2542	501.714
6	438936	6471930	860.969	6.25757	38.7169	8882.47	0.0661104	0.861083	146358	512.572
	438936	6471930	872.57	0.306472	39.1858	8998.67	0.0657854	0.860547	71.4445	524.637
5	438936	6471980	886.102	12.9519	39.6155	9105.15	0.0656416	0.859591	3570530	523.418
4	438684	6471030	897.227	6.55609	40.3482	9286.7	0.0653098	0.858957	46052.7	527.854
	438432	6471830	902.852	4.05212	40.3023	9275.34	0.0653332	0.85895	30969.7	527.376
	438532	6471630	906.117	0.00115967	40.3975	9298.9	0.0652842	0.858887	1.30326e-07	528.392
	438381	6471780	908.797	0.322388	40.5047	9325.47	0.0652274	0.85871	265.321	529.652
	438583	6471680	910.289	0.198975	40.5257	9330.68	0.065216	0.858708	75.4404	529.913
3	438633	6471630	915.727	8.62543	41.1114	9475.81	0.0648761	0.857777	719900	538.884
	438987	6471730	925.594	0.000610352	41.2494	9509.99	0.0648012	0.857696	1.49928e-06	540.345
	438987	6471930	925.719	1.84644	41.263	9513.37	0.0647973	0.857572	3942.34	540.297
	439037	6471780	927.141	6.10352e-05	41.3299	9529.96	0.0647771	0.857585	2.28296e-09	540.089
	438936	6471880	927.734	6.10352e-05	41.2768	9516.8	0.0647932	0.857637	1.91024e-07	540.251
	438919	6471860	928.234	0.000488281	41.2691	9519.85	0.0647895	0.857646	9.1112e-09	540.211
2	438936	6471830	934.102	9.18762	41.7175	9626	0.0646378	0.856933	722089	539.751
	438683	6471730	944.312	0.340027	41.9734	9689.41	0.0645306	0.856686	35.0761	540.339
1	438583	6471730	950.555	10.501	42.6695	9861.9	0.0641753	0.855591	625363	544.306
	438280	6471230	973.766	0.316848	43.4721	10060.8	0.0637465	0.854551	4.35775	549.475
	438280	6471230	994.438	0.320679	44.2812	10261.3	0.0634149	0.853453	45.4723	550.552
	438432	6471280	1002.07	-6.10352e-05	44.6395	10350	0.0632417	0.853015	6.6785e-06	552.084
									Average Density	512.904641025641

36ºC at Caprock Run for 6years With Hot Lithology File

Appendix 4.5: Tabulated Results from Complex Model Simulations

Years of Injection	Year	Mt CO_2 Injected	kg of CO_2 Injected
1	1997	0.84	8.4000E+08
2	1998	1.68	1.6800E+09
3	1999	2.52	2.5200E+09
4	2000	3.36	3.3600E+09
5	2001	4.2	4.2000E+09
6	2002	5.04	5.0400E+09
7	2003	5.88	5.8800E+09
8	2004	6.72	6.7200E+09
9	2005	7.56	7.5600E+09
10	2006	8.4	8.4000E+09
11	2007	9.24	9.2400E+09
12	2008	10.08	1.0080E+10
13	2009	10.92	1.0920E+10
14	2010	11.76	1.1760E+10
15	2011	12.6	1.2600E+10
16	2012	13.44	1.3440E+10
17	2013	14.28	1.4280E+10
18	2014	15.12	1.5120E+10
19	2015	15.96	1.5960E+10
20	2016	16.8	1.6800E+10
21	2017	17.64	1.7640E+10
22	2018	18.48	1.8480E+10
23	2019	19.32	1.9320E+10
24	2020	20.16	2.0160E+10
25	2021	21	2.1000E+10
26	2022	21.84	2.1840E+10
27	2023	22.68	2.2680E+10
28	2024	23.52	2.3520E+10
29	2025	24.36	2.4360E+10
30	2026	25.2	2.5200E+10

CO_2 injection volumes used for all Sleipner MPath® simulations

Body Id	Bulk Rock Volume [m3]	Pore Volume [m3]	Average Pore Saturation [/]	CO2 Volume [m3]	CO2 Density [kg/m3]	Crest X Position	Crest Y Position	Crest Depth [m]	Average Horizontal CO2-Water Contact	Approximate CO2 Column Height [m]	Flash Temperature [C]
21	53991.10156	21730.69922	0.833997011	18123.30078	158.0829926	439390	6473580	512.2969971	515.6829834	3.386229992	22.59869957
20	3049820	1097130	0.864899993	948908	651.7050171	439289	6473480	788.2109985	797.1450195	8.933839798	32.55279922
17	4.51757E-05	1.62448E-05	0.864847004	1.40492E-05	651.2449951	438532	6471280	797.7269897	797.7269897	6.10352E-05	32.69840027
13	5656150	2004230	0.862878978	1729410	654.2880249	438482	6471280	822.4530029	834.1640015	11.71109962	33.81480026
15	4430690	1559260	0.86197007	1344030	651.0529785	438381	6471730	845.3120117	854.6799927	9.36730057	34.37590027
18	2729240	953506	0.861012995	820981	651.3259888	438936	6471930	860.9689941	869.6950073	8.72661972	34.99840164
14	14214600	4910910	0.855556973	4221210	651.5100098	438936	6471980	886.1019897	900.1010132	13.99919987	35.79169846
12	434408	149381	0.858951986	128312	649.6450195	438684	6471030	897.2269897	906.0479736	8.821229935	36.43849945
16	104821	36044.39844	0.858949006	30960.30078	649.6890259	438432	6471830	902.8519897	906.9030151	4.051449776	36.39759881
11	2.34242E-06	8.0495E-07	0.858948989	6.91245E-07	649.6119995	438583	6471680	907.1799927	907.1799927	0	36.49440002
10	8.43586E-08	2.89548E-08	0.858946009	2.48934E-08	649.6110229	438633	6471680	907.8519897	907.8540039	0.00274658	36.49739838
9	2255810	768668	0.857782006	659350	651.0889893	438633	6471630	915.7269897	923.9500122	8.223388626	37.11220169
7	9.267E-06	3.15563E-06	0.857695997	2.70657E-06	651.2689819	438987	6471730	925.5939941	925.5939941	0.000671387	37.23400116
5	13530.90039	4603.120117	0.857572019	3947.51001	651.2080078	438987	6471930	925.7189941	927.565979	1.847350001	37.24599838
4	3.78824E-05	1.28977E-05	0.857576013	1.10522E-05	650.8259888	439037	6471830	927.3200073	927.3209839	0.000854492	37.32600021
1	6.60435E-08	2.24905E-08	0.857645988	1.92803E-08	651.0639941	438919	6471860	928.2340088	928.2349854	0.000610352	37.26910019
8	4694970	1598670	0.85689199	1361320	649.6749878	438936	6471830	934.1019897	946.1459961	12.04439967	37.64730072
3	4157940	1391880	0.855531991	1190800	648.5809937	438583	6471730	950.5549927	964.4899902	13.9350096	38.48759842

12 year run with the Complex Low80Plith Pthz/Pthx Isotropic Model

Note: Individual plume layers are denoted by grey shaded rows.

Body Id	Bulk Rock Volume [m3]	Pore Volume [m3]	Average Pore Saturation [/]	CO2 Volume [m3]	CO2 Density [kg/m3]	Crest X Position	Crest Y Position	Crest Depth [m]	Average Horizontal CO2-Water Contact	Approximate CO2 Column Height [m]	Flash Temperature [C]	Flash Pressure [kPa]	CO2 IFT Multiplier
19	2949490	1186090	0.528213978	626510	156.7550049	438886	6473830	509.7229919	519.2000122	9.477359772	22.4951992	5372.830078	0.078168802
20	3049820	1097130	0.864899993	948908	651.7050171	439289	6473480	788.2109985	797.1450195	8.933839798	32.55279922	8195.990234	0.068245202
17	4.51757E-05	1.62448E-05	0.864847004	1.40492E-05	651.2449951	438532	6471280	797.7269897	797.7269897	6.10352E-05	32.68840027	8234.05957	0.068171799
13	5656150	2004230	0.862878978	1729410	654.2880249	438482	6471280	822.4530029	834.1640015	11.71109962	33.81480026	8550.230469	0.067617796
15	4430690	1559260	0.861970007	1344030	651.0529785	438381	6471730	845.3120117	854.6799927	9.36730957	34.37590027	8707.75	0.067306899
18	2729240	953506	0.861012995	820981	651.3259888	438936	6471930	860.9689941	869.6950073	8.72661972	34.99840164	8882.469727	0.066968103
14	14214600	4910910	0.859556973	4221210	651.5100098	438936	6471980	886.1019897	900.1010132	13.99919987	35.79169846	9105.150391	0.0665804
12	434408	149381	0.858951986	128312	649.6450195	438684	6471030	897.2269897	906.0479736	8.821229935	36.43849945	9286.700195	0.066240899
16	104821	36044.39844	0.858949006	30960.30078	649.6890259	438432	6471830	902.8519897	906.9030151	4.051449776	36.39799881	9275.339844	0.066261798
11	2.34242E-06	8.0485E-07	0.858848989	6.91245E-07	649.6119995	438583	6471680	907.1799927	907.1799927	0	36.49440002	9302.389648	0.066212103
10	8.43586E-08	2.89848E-08	0.858846009	2.48934E-08	649.6110229	438633	6471680	907.8519897	907.8540039	0.00274658	36.49739838	9303.230469	0.066210501
9	2255810	768668	0.857782006	659350	651.0889893	438633	6471630	915.7269897	923.9500122	8.223389626	37.11220169	9475.80957	0.065897197
7	9.267E-06	3.15563E-06	0.857695997	2.70657E-06	651.2689819	438987	6471730	925.5939941	925.5939941	0.000671387	37.23400116	9509.990234	0.065834597
5	13530.90039	4603.120117	0.857572019	3947.51001	651.2080078	438987	6471930	925.7189941	927.565979	1.847350001	37.24599838	9513.370117	0.065828301
4	3.78824E-05	1.28877E-05	0.857576013	1.10522E-05	650.8259888	439037	6471830	927.3200073	927.3209839	0.000854492	37.32600021	9535.820313	0.065786399
1	6.60435E-08	2.24805E-08	0.857645988	1.92803E-08	651.0939941	438919	6471860	928.2340088	928.2349854	0.000610352	37.26910019	9519.849609	0.065816201
8	4694970	1598670	0.85689199	1361320	649.6749878	438936	6471830	934.1019897	946.1459961	12.04469967	37.64730072	9626	0.0656197
3	4157940	1391880	0.855531991	1190800	648.5809937	438583	6471730	950.5549927	964.4899902	13.9350996	38.48759842	9861.900391	0.065188497

12 year run with the Complex Low80Plith 10/1 Pthz/Pthx Anisotropic Model

Note: Individual plume layers are denoted by grey shaded rows.

Body Id	Bulk Rock Volume [m3]	Pore Volume [m3]	Average Pore Saturation [/]	CO2 Volume [m3]	CO2 Density [kg/m3]	Crest X Position	Crest Y Position	Crest Depth [m]	Average Horizontal CO2-Water Contact	Approximate CO2 Column Height [m]	Flash Temperature [C]	Flash Pressure [kPa]	CO2 IFT Multiplier
19	2949490	1186090	0.528213978	626510	156.7550049	438886	6473830	509.7229919	519.2000122	9.477359772	22.4951992	5372.830078	0.078168802
20	3049820	1097130	0.864899993	948908	651.7050171	439289	6473480	788.2109985	797.1450195	8.933839798	32.55279922	8195.990234	0.068245202
17	4.51757E-05	1.62448E-05	0.864847004	1.40492E-05	651.2449951	438532	6471280	797.7269897	797.7269897	6.10352E-05	32.68840027	8234.05957	0.068171799
13	5656150	2004230	0.862878978	1729410	654.2880249	438482	6471280	822.4530029	834.1640015	11.71109962	33.81480026	8550.230469	0.067617796
15	4430690	1559260	0.861970007	1344030	651.0529785	438381	6471730	845.3120117	854.6799927	9.36730957	34.37590027	8707.75	0.067306899
18	2729240	953506	0.861012995	820981	651.3259888	438936	6471930	860.9689941	869.6950073	8.72661972	34.99840164	8882.469727	0.066988103
14	14214600	4910910	0.859556973	4221210	651.5100098	438936	6471980	886.1019897	900.1010132	13.99919987	35.79169846	9105.150391	0.0665804
12	434408	149381	0.858951986	128312	649.6450195	438684	6471030	897.2269897	906.0479736	8.821229935	36.43849945	9286.700195	0.066240899
16	104821	36044.39844	0.858949006	30960.30078	649.6890259	438432	6471830	902.8519897	906.9030151	4.051449776	36.39799881	9275.339844	0.066261798
11	2.34242E-06	8.0485E-07	0.858848989	6.91245E-07	649.6119995	438583	6471680	907.1799927	907.1799927	0	36.49440002	9302.389648	0.066212103
10	8.43586E-08	2.89848E-08	0.858846009	2.48934E-08	649.6110229	438633	6471680	907.8519897	907.8540039	0.00274658	36.49739838	9303.230469	0.066210501
9	2255810	768668	0.857782006	659350	651.0889893	438633	6471630	915.7269897	923.9500122	8.223389626	37.11220169	9475.80957	0.065897197
7	9.267E-06	3.15563E-06	0.857695997	2.70657E-06	651.2689819	438987	6471730	925.5939941	925.5939941	0.000671387	37.23400116	9509.990234	0.065834597
5	13530.90039	4603.120117	0.857572019	3947.51001	651.2080078	438987	6471930	925.7189941	927.565979	1.847350001	37.24599838	9513.370117	0.065828301
4	3.78824E-05	1.28877E-05	0.857576013	1.10522E-05	650.8259888	439037	6471830	927.3200073	927.3209839	0.000854492	37.32600021	9535.820313	0.065786399
1	6.60435E-08	2.24805E-08	0.857645988	1.92803E-08	651.0939941	438919	6471860	928.2340088	928.2349854	0.000610352	37.26910019	9519.849609	0.065816201
8	4694970	1598670	0.85689199	1361320	649.6749878	438936	6471830	934.1019897	946.1459961	12.04469967	37.64730072	9626	0.0656197
3	4157940	1391880	0.855531991	1190800	648.5809937	438583	6471730	950.5549927	964.4899902	13.9350996	38.48759842	9861.900391	0.065188497

12 year run with the Complex Low80Plith 5/1 Pthz/Pthx Anisotropic Model

Note: Individual plume layers are denoted by grey shaded rows.

Body Id	Bulk Rock Volume [m3]	Pore Volume [m3]	Average Pore Saturation [/]	CO2 Volume [m3]	CO2 Density [kg/m3]	Crest X Position	Crest Y Position	Crest Depth [m]	Average Horizontal CO2-Water Contact	Approximate CO2 Column Height [m]	Flash Temperature [C]	Flash Pressure [kPa]	CO2 IFT Multiplier
23	1907020	777257	0.469482988	364909	143.4949951	438886	6473830	481.8909912	487.6570129	5.766109943	21.51989937	5099.060059	0.079084
22	1253430	504273	0.5654001018	285116	156.7550049	438886	6473830	509.7229919	517.552002	7.829410076	22.4951992	5372.830078	0.0781688
19	22.27059937	8.807430267	0.588189006	5.180429935	158.397995	438738	6473470	517.1560059	522.1099854	4.953609943	22.62339973	5408.819824	0.0780524
21	16.26129913	6.433440208	0.588252008	3.784490108	158.2590027	438738	6473470	517.1560059	521.4849854	4.329219818	22.61249924	5405.75	0.0780623
20	3049820	1097130	0.864899993	948908	651.7050171	439289	6473480	788.2109985	797.1450195	8.933839798	32.55279922	8195.990234	0.0682452
17	4.51757E-05	1.62448E-05	0.864847004	1.40492E-05	651.2449951	438532	6471280	797.7269897	797.7269897	6.10352E-05	32.68840027	8234.05957	0.0681718
13	5656150	2004230	0.862878978	1729410	654.2880249	438482	6471280	822.4530029	834.1640015	11.71109962	33.81480026	8550.230469	0.0676178
15	4430690	1559260	0.861970007	1344030	651.0529785	438381	6471730	845.3120117	854.6799927	9.36730957	34.37590027	8707.75	0.0673069
18	2729240	953506	0.861012995	820981	651.3259888	438936	6471930	860.9689941	869.6950073	8.72661972	34.99840164	8882.469727	0.0669881
14	14214600	4910910	0.859556973	4221210	651.5100098	438936	6471980	886.1019897	900.1010132	13.99919987	35.79169846	9105.150391	0.0665804
12	434408	149381	0.858951986	128312	649.6450195	438684	6471030	897.2269897	906.0479736	8.821229935	36.43849945	9286.700195	0.0662409
16	104821	36044.39844	0.858949006	30960.30078	649.6890259	438432	6471830	902.8519897	906.9030151	4.051449776	36.39799881	9275.339844	0.0662618
11	2.34242E-06	8.04685E-07	0.858849989	6.91245E-07	649.6119995	438583	6471680	907.1799927	907.1799927	0	36.49440002	9302.389648	0.0662121
10	8.43586E-08	2.89848E-08	0.858846009	2.48934E-08	649.6110229	438633	6471680	907.8519897	907.8540039	0.00274658	36.49739838	9303.230469	0.0662105
9	2255810	768668	0.857782006	659350	651.0889893	438633	6471630	915.7269897	923.9500122	8.223389626	37.11220169	9475.80957	0.0658972
7	9.267E-06	3.15563E-06	0.857695997	2.70657E-06	651.2689819	438987	6471730	925.5939941	925.5939941	0.000671387	37.23400116	9509.990234	0.0658346
5	13530.90039	4603.120117	0.857572019	3947.51001	651.2080078	438987	6471930	925.7189941	927.565979	1.847350001	37.24599838	9513.370117	0.0658283
4	3.78824E-05	1.28877E-05	0.857576013	1.10522E-05	650.8259888	439037	6471830	927.3200073	927.3209839	0.000854492	37.32600021	9535.820313	0.0657864
1	6.60435E-08	2.24805E-08	0.857645988	1.92803E-08	651.0939941	438919	6471860	928.2340088	928.2349854	0.000610352	37.26910019	9519.849609	0.0658162
8	4694970	1598670	0.85689199	1361320	649.6749878	438936	6471830	934.1019897	946.1459961	12.04469967	37.64730072	9626	0.0656197
3	4157940	1391880	0.855531991	1190800	648.5809937	438583	6471730	950.5549927	964.4899902	13.9350996	38.48759842	9861.900391	0.0651885

12 year run with the Complex Low80Plith 2.5/1 Pthz/Pthx Anisotropic Model

Note: Individual plume layers are denoted by grey shaded rows.

Body Id	Bulk Rock Volume [m3]	Pore Volume [m3]	Average Pore Saturation [/]	Total Volume [m3]	CO2 Volume [m3]	CO2 Density [kg/m3]	Crest X Position	Crest Y Position	Crest Depth [m]	Average Horizontal CO2-Water Contact	Approximate CO2 Column Height [m]	Flash Temperature [C]	Flash Pressure [kPa]	CO2 IFT Multiplier
52	2639.319322	1295.4100034	0.508888006	659.2219849	659.2219849	26.36560059	439138	6473080	98.31349945	98.72080231	0.407371998	7.311650181	1279.22998	0.101387002
50	1107.160034	527.427002	0.507009029	267.4100037	267.4100037	30.36520004	439138	6473080	116.4260025	116.8533963	0.428957992	8.56525	1461.920044	0.099327701
51	852.1539917	403.5249939	0.50544339	203.9583996	203.9583996	33.90470123	439138	6473080	134.5370026	135.0160065	0.478036	9.106479645	1614.609985	0.0986415
49	167.6040039	79.24239622	0.505038977	40.02080154	40.02080154	34.79118873	438987	6473280	137.4859324	137.6349945	0.148422003	9.240730286	1652.300049	0.098319501
48	0.00145673	0.000688894	0.505097985	0.000347959	0.000347959	34.75960159	438987	6473230	137.6499939	137.6519928	0.00175476	9.23593398	1650.949951	0.098330997
45	2.76744E-07	1.30771E-07	0.504894018	6.60256E-08	6.60256E-08	35.25939941	439037	6473430	140.5939941	140.5939941	0.000442505	9.31178894	1672.22998	0.098149501
44	1.00662E-08	4.75643E-09	0.504884005	2.40144E-09	2.40144E-09	35.22778946	439037	6473480	141.1799927	141.1799927	0	9.306920052	1670.880005	0.098160937
43	189.3400223	89.1815033	0.50405401	44.95230103	44.95230103	36.96920013	439037	6473530	143.602005	150.173996	0.572510004	9.571579333	1745.170044	0.097528357
42	371.170399	174.4029999	0.503430009	87.79963788	87.79963788	38.73600006	439037	6473530	156.2440033	156.8243963	0.580734015	9.841070175	1820.810059	0.0968858
41	1095.400024	512.2109985	0.502180934	257.2223816	257.2223816	41.77510071	438987	6473530	162.6390051	163.2250061	0.525864005	10.30650043	1951.469971	0.095827737
40	1527.01001	708.8273907	0.500235021	354.4809875	354.4809875	46.19820023	439037	6473530	181.7910004	182.2700043	0.478592008	10.94250011	2129.97998	0.094666801
38	1397.77002	643.7369995	0.498239986	320.7739868	320.7739868	50.63963995	438987	6473580	200.6089935	201.1109924	0.502120972	11.59139992	2309.310059	0.0933448
39	1483.810059	686.0880127	0.498286009	341.8680115	341.8680115	50.73809814	438835	6473580	201.0370026	201.3760071	0.339370996	11.58639893	2310.889893	0.093332398
36	4714.259766	2151.860107	0.496051997	1067.430054	1067.430054	56.31940079	438785	6473780	219.6889954	219.6920013	0.502213001	12.37549973	2532.219971	0.091704302
34	5382.120117	2701.989899	0.483423015	1333.22998	1333.22998	63.18700027	438785	6473730	244.7299957	245.2079926	0.477432013	13.27420044	2784.48999	0.090163497
35	6480.370215	2896.370117	0.490797997	1421.530029	1421.530029	70.09329987	438785	6473730	270.1600037	270.6689922	0.508388002	14.17840004	3038.320068	0.089033097
33	5906.279785	2611.389893	0.488175005	1274.810059	1274.810059	77.53220367	438886	6473680	295.5350037	296.0663861	0.532195985	15.07240009	3289.26001	0.087774701
37	4164.859863	1817.25	0.485958987	882.3839722	882.3839722	85.08119965	438886	6473680	320.8240051	321.3823956	0.558380008	15.97809982	3543.48999	0.086563201
32	135.3329926	59.15593988	0.485394001	28.71990071	28.71990071	85.63980103	439088	6473530	322.3320007	322.5920105	0.259552002	16.03820038	3560.340088	0.086468503
30	556.1519775	240.4060059	0.482746399	116.0550003	116.0550003	93.36160126	439088	6473530	347.7420044	348.32901	0.587127984	16.94939995	3816.123883	0.0851987
31	239.3769989	103.3800003	0.482547998	49.88980103	49.88980103	94.62830353	439390	6473630	351.0549927	351.25	0.195739899	17.02379989	3837.01001	0.0850963
29	47815	2045.680054	0.480307013	382.5543927	382.5543927	101.8089981	439340	6473580	374.6210022	375.1960144	0.575234802	17.79739952	4054.159912	0.084018398
28	7222.25	3063.22998	0.478276014	1465.069946	1465.069946	108.9250031	439390	6473630	394.3200073	395.0239868	0.7041202	18.48830032	4248.100098	0.083021998
27	1600.930054	673.1920166	0.476274997	320.6239929	320.6239929	115.8069992	439390	6473630	413.5660095	414.2900085	0.724059999	19.18099976	4442.540039	0.082038999
26	673.315979	280.6589966	0.474256992	133.1040039	133.1040039	123.6900024	439390	6473630	432.6120117	433.5649927	0.742828012	19.87369919	4636.97998	0.0810607
25	444.5109863	183.8509979	0.472481996	86.86630249	86.86630249	130.7960052	439390	6473630	452.0589905	452.8439941	0.785432003	20.49870006	4809.089824	0.080310002
24	919.334021	377.3400024	0.470957994	177.3940033	177.3940033	136.7149963	439390	6473630	467.1480103	467.9750061	0.826233029	21.02020073	4958.819824	0.079668302
23	2224.189941	946.40802	0.46343301	445.2139893	445.2139893	143.9799957	439390	6473630	482.2420044	483.0849915	0.843078971	21.55639949	5108.560059	0.079051301
22	2370.5	960.7520142	0.467911988	449.5480042	449.5480042	151.326004	439441	6473580	496.380011	497.8389893	0.858856022	22.0848999	5257.649902	0.078548603
19	1017.059998	409.6023968	0.466502994	191.0809937	191.0809937	157.7700043	439441	6473580	511.356011	512.2420044	0.886760024	22.57419968	5394.97998	0.078097001
21	57363.30078	23087.80078	0.833395398	19255.09961	19255.09961	158.0829926	439390	6473580	512.2363971	515.802002	3.505189896	22.59863957	5401.870117	0.078074798
20	3049820	1097100	0.864899993	949808	949808	6517.050171	439289	6473480	788.2109985	797.1450195	8.933839798	32.55279922	8195.980234	0.068245202
17	4.51757E-05	1.62448E-05	0.864847004	1.40493E-05	1.40493E-05	6512.443951	438532	6471280	797.7263897	797.7263897	6.10352E-05	32.63840027	8234.05957	0.068177799
13	5658160	2004230	0.862878978	1729410	1729410	6514.288024	438482	6471280	822.4530029	834.1640015	11.71009982	33.81480026	8550.230469	0.067617796
15	4430690	1559260	0.861970007	1344030	1344030	6510.052979	438381	6471730	845.3120117	854.6739927	9.361730957	34.37590027	8707.75	0.067306899
18	2729240	953506	0.861012995	820981	820981	6513.259888	438936	6471930	860.9683941	863.6950073	8.726691972	34.99840164	8882.469727	0.066988103
14	14214600	4910910	0.859556573	4221210	4221210	6515.000098	438936	6471980	886.1019897	900.1010132	13.99919987	35.79163946	9105.150391	0.0665804
12	434408	149381	0.858951986	128312	128312	6449.645019	438684	6471030	897.2268897	906.0479736	8.821229935	36.43843945	9286.700195	0.066240898
16	104821	36044.39844	0.858949006	30960.30078	30960.30078	6449.689026	438432	6471830	902.9519897	906.9030151	4.051449776	36.39799881	9275.339844	0.066261798
11	2.34242E-06	8.04855E-07	0.858849989	6.91245E-07	6.91245E-07	6449.611999	438583	6471680	907.1799927	907.1799927	0	36.43440002	9302.389648	0.06621203
10	8.43586E-08	2.89846E-08	0.858846009	2.48934E-08	2.48934E-08	6449.611022	438633	6471680	907.8519897	907.8519897	0.00274658	36.43739838	9303.230469	0.066210501
9	2255810	769868	0.857782006	659350	659350	6510.889893	438633	6471630	915.7269897	923.3500122	8.223389626	37.11220169	9475.80957	0.065897797
7	9.267E-06	3.1566E-06	0.857695997	2.70657E-06	2.70657E-06	6512.689819	438987	6471730	925.5939941	925.5939941	0.000671387	37.22440186	9509.390234	0.065834597
5	10530.90039	4603.120117	0.857572019	3947.51001	3947.51001	6512.080078	438987	6471830	925.7939941	927.565979	1.847350001	37.24539838	9513.370117	0.065828301
4	3.78824E-05	1.23877E-05	0.857576013	1.10522E-05	1.10522E-05	650.8258888	439037	6471830	927.3200073	927.3209839	0.000854492	37.32600021	9535.820313	0.065786399
1	6.60435E-08	2.24905E-08	0.857645898	1.92803E-08	1.92803E-08	6510.939941	438819	6471860	928.2340088	928.2349854	0.000610352	37.26910019	9518.849609	0.065816201
8	4694370	1588670	0.85688999	1361320	1361320	6449.674988	438936	6471830	934.1018987	946.1459961	12.04469967	37.64730072	9626	0.0656197
3	4157940	1391880	0.855553991	1190800	1190800	6448.580933	438583	6471730	950.5549927	964.4899902	13.9350586	38.49759842	9861.900391	0.065188437

12 year run with the Complex Low80Plith 1.25/1 Pthz/Pthx Anisotropic Model

Note: Individual plume layers are denoted by grey shaded rows.

Appendix 4.6: MPath® Hg-Air and CO_2-Brine Capillary Pressure Comparison

MPath® Porosity (fraction)	MPath® Horizontal Permeability (milliDarcy)	MPath® Vertical Permeability (milliDarcy)	MPath® Hg-Air Threshold Entry Pressure (kPa)	MPath® CO_2-Brine Equivalent Threshold Entry Pressure (kPa)
0.34	5.44	0.544	1680	80.83 – 121.25
0.36	8.99	0.899	1520	89.34 – 134.01

Notes: Default settings in MPath® for shale - assumes kv/kh of 0.1 - range of CO_2-Brine values based on IFT 25 mNm^{-1} and wettability of 0.8 (lower values) to IFT 30 mNm^{-1} and wettability of 1.0 (higher values).

Porosity (fraction)	Permeability (milliDarcy)	Capillary Entry Pressure to Supercritical CO_2 (kPa)	MPath® Equivalent Porosity for Shale (fraction)	MPath® Equivalent Hg-Air Threshold Entry Pressure (kPa)	MPath® CO_2-Brine Equivalent Threshold Entry Pressure (kPa)
0.34 – 0.36	0.00075 – 0.0015	1700	0.135 – 0.152	9100 - 11250	483.95 – 598.29 (low) 725.93 – 897.44 (high)

Notes: First three columns contain data from Springer & Lindgren (2006) - MPath® equivalent values were obtained by matching permeability values from Springer & Lindgren (2006) to MPath® porosity-permeability and porosity-threshold entry pressure curves for shale, to obtain equivalent porosity and Hg-Air threshold entry pressures. The range of CO_2-Brine values are based on IFT 25 mNm^{-1} and wettability of 0.8 (lower values) to IFT 30 mNm^{-1} and wettability of 1.0 (higher values).

Porosity (fraction)	Permeability (milliDarcy)	Apparent Threshold Capillary Pressure to Nitrogen (kPa)	MPath® Equivalent Porosity for Shale (fraction)	MPath® Equivalent Hg-Air Threshold Entry Pressure (kPa)	MPath® CO_2-Brine Equivalent Threshold Entry Pressure (kPa)
0.32 – 0.38	0.000364 – 0.000466 (axial) 0.00101 – 0.00109 (radial)	1600 - 1900	0.08 – 0.09 0.10 – 0.11	~30000 ~20000	1595.45 (low) 2393.18 (high) 1063.63 (low) 1595.45 (high)

Notes: First three columns contain data from Harrington et al., (2009) - MPath® equivalent values were obtained by matching permeability values from Harrington et al., (2009) to MPath® porosity-permeability and porosity-threshold entry pressure curves for shale, to obtain equivalent porosity and Hg-Air threshold entry pressures. The range of CO_2-Brine values are based on IFT 25 mNm^{-1} and wettability of 0.8 (lower values) to IFT 30 mNm^{-1} and wettability of 1.0 (higher values).

Notes: In each case an IFT scale factor of 0.05361 was used for the IFT 25 mNm^{-1} and wettability of 0.8 cases, and IFT scale factor of 0.0804 was used for the IFT 30 mNm^{-1} and wettability of 1.0 cases MPath®

Appendix 5.1: Timeline for the Sleipner CO_2 Storage Project

In February 1985, K.J. Macintyre presented his paper entitled: "Design Considerations for Carbon Dioxide Injection Facilities" at the Heavy Oil and Oil Sands Technical Symposium, Calgary, Canada.

During 1986, SINTEF researchers Torleif Holt and Erik Lindeberg allegedly "invented" sub-surface CO_2 storage during a holiday break (http://www.eu-norway.org/Climate_change/father_of_ccs/ - last accessed 19/09/2011).

In January 1991, Norwegian government implemented a tax on CO_2 emissions, originally set at 0.6 NOK/Sm^3 for gas flared (or used for energy generation) and 0.6 NOK/litre for diesel fuel combustion. The tax was gradually increased, reaching 0.82 NOK/Sm^3 by 1994. This was reported as the highest CO_2 tax imposed in the world at that time (Celius & Ingeberg, 1996). In 2008, the tax equivalent was 325 NOK/tonne (Chadwick *et al.,* 2008).

From 1991-1996, Statoil investigated the possibility of implementing CO_2 disposal in the Utsira Formation, with the CO_2 being extracted from hydrocarbons produced from the Sleipner Vest (West) field development (Korbøl and Kaddour, 1995).

In August 1991, the original Sleipner A platform, a Condeep-type concrete structure, suffered a catastrophic failure during construction operations and sank to the bottom of a 220 m deep fjord. A replacement platform was constructed following redesign and successfully installed on site during 1993 (Jakobsen & Rosendahl, 1994).

The first technical presentations and publications relating to the Sleipner CO_2 storage project appeared in the public domain (Korbøl & Kaddour, 1994/1995; Baklid *et al.,* 1996).

CO_2 injection well 15/9-A16 was drilled and completed during Q1 of 1996 (wellbore entry date 13/03/1996 - wellbore completion date 16/04/1996 - according to NPD).

CO_2 injection operations started in September 1996 and immediately encountered injection problems. Sand screens (300 micron) were installed during December 1996, but sand production still proved to be a problem and CO_2 had to be vented during Q4. Well intervention was performed during August 1997; the well was re-perforated and gravel packed with finer screens (200 microns) installed (Hansen *et al.,* 2005).

A core sample 9 m long was acquired from the Utsira (Sand) Formation in development well 15/9-A23 (wellbore entry date 25/09/1996 - wellbore completion date 22/11/1996 - according to NPD website) immediately prior to CO_2 injection and subjected to various mineralogical and petrophysical tests (Pearce *et al.,* 2000; Chadwick *et al.,* 2002).

Heggland (1997) published his paper on gas seepage, high-amplitude seismic anomalies and pockmarks detected within the Nordland Group overburden in the Sleipner vicinity.

A series of joint European Union / industry / government projects were initiated in 1998 with SACS Phase Zero, followed by SACS1 (1998-1999), SACS2 (2000-2002) and finally CO2STORE (2003-2006), to promote research and development activities relating to CO_2 storage in saline aquifers, with Sleipner as the primary case study (Chadwick *et al.,* 2008).

The first post-injection monitoring survey was performed during October 1999. Subsequent evaluation of the seismic data revealed that CO_2 had reached the top of the Utsira Formation after only 3 years of injection (Chadwick *et al.,* 2005). Monitoring frequency was increased and a range of studies begun to investigate the caprock sealing integrity and potential for leakage.

Tests were performed on sets of Nordland Shale cuttings samples from Sleipner wells 15/6-5, 15/9-9, 15/9-13, 15/9-14 and 16/7-2 (Bøe & Zweigel, 2001).

A related study also performed similar tests on cuttings samples from wells 15/9-15, 15/9-16, 15/9-18 and a Nordland Shale core sample from proxy well 2/4-C11 (wellbore entry date 16/06/1986 - wellbore completion date 15/10/1986 - according to NPD website) located in the Ekofisk area (Lindgren *et al.,* 2002/3). This latter report suggested that significant smectite content in the Block 15/9 wells (detected by XRD analyses) made the application of the Krushin (1997) test to characterise the caprock capillary properties highly questionable.

To provide a more representative sample, a Nordland Shale (caprock) core was acquired from development well 15/9-A11 in July 2002 (wellbore entry date 01/07/2002 - wellbore completion date 18/08/2002 - according to NPD website), six years after CO_2 injection operations started at Sleipner. Samples were supplied to the BGS in the UK and SINTEF in Norway and subjected to various mineralogical, geomechanical, petrophysical and palynological tests (Kemp *et al*., 2002; Pilliterri *et al*., 2003; Zweigel & Heill, 2003; Head *et al.,* 2004).

Various reservoir modelling studies and flow simulations were also performed from 1999 onwards (Lindeberg, 2001; Zweigel & Hamborg, 2002) to determine the probable CO_2 migration directions beneath the uppermost shale barriers of the Utsira Formation (i.e. barrier 8/Thick Shale and barrier 9/caprock).

Subsequent modelling studies are described in Chapters 2-4 of this thesis.

Appendix 5.2: Translated Press Releases on Tordis from the Stavanger Aftenblad

Tordis article in Stavanger Aftenblad – 21 October 2008 (Camilla Bjørheim):

http://www.aftenbladet.no/energi/olje/Droppet-geolog---Tordis-begynte--lekke-2562305.html (last accessed 20/09/2011)

Dropped the geologist – Tordis started leaking. StatoilHydro wanted to store oily water in the bedrock, but skipped involving geologists in the planning process

On May 14 this year oil was detected on the sea near the Tordis field in the North Sea. Water and oil residue had quite simply burst a hole in the Utsira Formation. Utsira is the geological formation intended to store the water from the Tordis subsea facility. StatoilHydro also stores CO_2 from Sleipner in this formation.

Mistake for the prestigious project

Tordis is one of StatoilHydro's prestigious projects, but the company skipped involving a geologist when the innovative subsea facility was being planned. This had consequences:

"A big mistake. Geologists could have revealed that the Utsira Formation in the relevant area was of poor quality and that the possibility of injection was uncertain," says Anke Wolff, geologist with the Norwegian Petroleum Directorate.

The special feature of the Tordis subsea facility is that it separates water and sand from the oil wells and pumps this directly back to the bedrock through an injection well. The water may contain oil residue and shall therefore not be discharged to sea.

Based on assumptions

StatoilHydro has now investigated the leak. The report states that the Tordis management based its planning on assumptions.

“They assumed that the Utsira Formation was well-suited as a storage facility for produced water,” says Wolff, who has read the report thoroughly.

“The company blundered. The preliminary work was deficient. This is rather surprising,” says Svein Eggen, geologist and head of technology in Gassnova. Øystein Håland, head of StatoilHydro’s subsea technology, totally agrees:

“We approached the work process a bit backwards. The geologist was involved when it was too late,” he says.

StatoilHydro assumed that an evaluation of the formation was unnecessary. The company has stored CO_2 in Utsira in the Sleipner area for many years. The management therefore thought that the formation could also receive water from Tordis. The perception was that Utsira was so large and would “swallow” the water from Tordis.

“When you inject you have to know that the formation can receive. With too high pressure the bedrock will fracture. It is odd that the company did not involve geologists more actively. That would have been natural,” says Eggen.

Lots of water

StatoilHydro has forced a million cubic metres of water into the Utsira Formation since December last year when Tordis started. The company’s investigation report states that the work on the injection well in an early phase was deemed to be “simple and routine”, and the substantial “swallowing capacity” of the Utsira Formation was mentioned. On the basis of documentation and feedback, no geologists were involved to appraise this assumption. The Utsira Formation was largely generalized and comparisons made with CO_2 injection on the Sleipner field.

“The formation has an entirely different and far better quality at Sleipner than at Tordis”, says Wolff.

Misgivings

When the injection well in the Utsira Formation was to be drilled, the management became aware that problems could arise.

"They then discovered that there was uncertainty linked to the characteristics of the formation and that injecting water into the relevant area could be difficult," says Wolff.

Despite the misgivings, StatoilHydro chose to drill an injection well and start injecting produced water in December last year. This was despite the fact that several persons on the project were uncertain about whether the well was correctly located. But there was never sufficient uncertainty so that the project chose to stop.

Several fault indications

StatoilHydro stopped water injection into Utsira several times this spring. The reason was that the company did not manage to inject as much water as anticipated and that pressure fell. Oil was also observed on the sea surface on several occasions, but it was not until 30 May that one discovered water flowed out of a pit on the seabed.

The report states that the management chose to continue several times during the Tordis process, because alternative solutions entailed shutdown or postponement of the project. The company now plans to drill a new injection well on Tordis.

"Following the Tordis incident we have prepared a new and improved well manufacturing process, i.e. a procedure for how we are to drill a well, says Håland in StatoilHydro.

Conclusion soon to come

The Petroleum Safety Authority Norway (PSA) and the Norwegian Petroleum Directorate (NPD) will have a meeting with StatoilHydro this week. The PSA has not yet summarized the Tordis incident.

"It is important for the PSA to evaluate whether this incident may have consequences for similar issues," says press spokesperson Inger Anda.

Follow-up Tordis article in Stavanger Aftenblad – 22 October 2008
(Camilla Bjørheim – Ellen Kongsnes):

http://www.aftenbladet.no/energi/olje/Ingen-garanti-mot-CO2-lekkasjer-2562698.html (last accessed - 20/09/2011)

Photo caption: Sleipner is Norway's and StatoilHydro's showcase. The international press makes pilgrimages to the North Sea to be told how the greenhouse gas CO_2 has been stored in the underground for 12 years. (Photo: Øyvind Hagen/StatoilHydro)

Utsira leaked water: No guarantee against CO_2 leaks
CO_2 storage was to rescue Norway's climate accounts. But is it safe to send greenhouse gas emissions down into the bedrock when water can leak out of the Utsira Formation?

StatoilHydro has stored more than 10 million tonnes of CO_2 in the sandstone formation Utsira under the Sleipner area in the North Sea for 12 years. The company claims CO_2 has not leaked. Three hundred kilometres from Sleipner, however, at Tordis, water leaked from the same formation. Several researchers believe there are no guarantees that CO_2 will not leak from Utsira as well.

No guarantee
"Twelve years is not a long time in terms of storing CO_2," says Asbjørn Torvanger in Cicero, the Center for International Climate and Environmental Research.

He notes that Sleipner is the first project in the world that stores CO_2 in an underground geological formation.

"We can never issue a guarantee that there will be no leaks," says Torvanger.

Peter M. Haugan, Director of the Department of Geophysics at the University of Bergen, agrees.

“It is not possible to prove that all the CO_2 injected still remains there. Seismics do not enable measuring of how much CO_2 is in the formation. All injections into the formation will increase pressure and may destroy the formation,” Haugan believes.

Could be undetected cracks

Seismics show that CO_2 moves upwards in the formation, because gas is lighter than water.

“There may be undetected cracks, for example,” says Torvanger.

The reason is that surveying every part of a geological formation in detail is too expensive, and small areas may be overlooked.

“The general opinion is that we can store CO_2 in the bedrock, but we must then be quite certain that the greenhouse gas will remain there for thousands of years,” says Haugan.

“Would you caution against storage of CO_2 in the bedrock?”

“I would say that we must be more certain about the safety of this than we are today,” says Haugan.

Sceptical EU

This concern is shared in Europe. The EU has been very sceptical to the safety of CO_2 storage for a long time on the basis of environmental concerns,” Paal Frisvold confirms. He is with Bellona (environmental organization) at the Brussels office.

He believes any doubts attributed to the quality of the Utsira Formation are a very serious matter. This is the formation Norway like to use as a showcase for part of the solution to the climate problems.

“Ninety-eight per cent of the EU’s legislation on CO_2 capture is about storage safety,” says Frisvold.

The amendments that will now be considered by the EU Parliament entail a further tightening of the requirements for CO_2 storage safety.

Time is needed

Asbjørn Torvanger in Cicero believes it may be necessary to monitor the Utsira Formation for 100 to 200 years. A legal clarification of the responsibilities concerning storage is therefore very important.

“Placing the responsibility on a company that may no longer exist is not natural. Therefore, the State must be involved,” says Torvanger.

He believes the State must stipulate requirements that the operating companies must fulfil, including insurance schemes. In this manner the State will avoid being left with all the costs should a leak occur in a CO_2 storage facility.

“Quite safe”

Øystein Håland, head of StatoilHydro’s subsea technology, points out that Utsira at Sleipner is of an entirely different quality than at Tordis, and maintains that it is quite safe to store CO_2.

“We have a good monitoring programme and shoot four-dimensional seismics at regular intervals to map the movement of CO_2. We would have detected any cracks in the formation and gas gone astray,” says Håland.

He is backed by Fritjof Riis from IRIS (International Research Institute of Stavanger).

“At Sleipner there is a good roof over Utsira, a seal of thick layers of clay. High pressure will not occur here as was the case with Tordis, because there is good communication in the thick Utsira sand. The CO_2 will thus be spread. It is quite safe to store CO_2 at Sleipner,” says Riis.

The Utsira formation

Utsira covers an enormous area in the North Sea, from Sleipner in the south to Gullfaks in the north. The sand formation is not the same everywhere. The quality is far better at Sleipner than about 300 kilometres away at Tordis, where water burst a hole in the ceiling of the formation. In the thickest areas, Utsira is several hundred metres thick and there are more sand layers in addition to Utsira. At Tordis the formation is not so thick and contains a lot of clay. The sand here is also of a different quality than at Sleipner.

Appendix 5.3: Translated Press Releases on Snøhvit from the Teknisk Ukeblad

Article posted on the Internet site of Teknisk Ukeblad on May 19th. 2011 (Maiken Ree – Ole K. Helgesen):

http://www.tu.no/olje-gass/article286534.ece (last accessed 20/09/2011).

Summary:

The article says that the injection may soon lead to fracturing of the Tubåen reservoir, either because the volume in that formation is not large enough or the communication is too poor in the area surrounding the CO_2 injection well.

"The reservoir will collapse during the year if we continue to inject CO_2 from Snøhvit..."

Statoil had major problems with the injection of CO_2 on Snøhvit since its start up in April 2008. The injected CO_2 is not distributed as expected in the reservoir, and thus the pressure rises rapidly. New calculations show that if the injection continues as today, the pressure will be higher than the formation strength as early as September this year. This means that the formation could fracture.

Action Plan:

" The capacity of the selected reservoir injection, Tubåen, has not been as good as we thought. A more rapid pressure build-up has been observed than expected, and the reservoir is full. We have known this for a while, and have made an action plan which will look at how we take this issue further, to have a long-term and robust solution for injection", said Sverre Kojedal, Head of Statoil's information office.

The company has tried to intervene in the injection well to improve CO_2 flow in the reservoir. Statoil has used the vessel Island Wellserver to make new perforations in the upper parts of the formation. But there are indications that it is necessary to inject CO_2 in the gas reservoir on Snøhvit. At the same time a new injection well is in planning.

Currently, it appears that volumes in Tubåen Formation are not large enough or there is insufficient communication to the area around the injection well. The question is whether the planned perforations in the second sand in Tubåen will solve the problem or whether perforations will have to be placed at the bottom of the Stø Formation in the near future, writes Statoil in a new report on the issues.

Graph of injection pressure from 01/04/2008 to 01/04/2011 with future projected pressure in red

Must Inject in Snøhvit

The report makes it clear that it is likely Statoil will have to shut off the present injection and rather inject CO_2 into the shallower Stø Formation. This is where the Snøhvit gas is located. Statoil estimates that this should be safe, but since this scenario is now likely, several simulations and studies must be performed.

The preliminary results of injection into the Steady Formation, where the group also produces gas, are encouraging.

"It's a completely different reservoir than Tubåen, and is more suited to receive CO_2. The Stø Formation is covering a large area, and we have perforated far from where the gas producers are located. So far, it appears that the injection is going well here", says Kojedal.

(Link to different article - " CO_2 problem at Snøhvit will cost hundreds of millions")

Can Leak

Is there a risk that this could contaminate the natural gas on Snøhvit?

"It is a large area, as I said, and the CO_2 injector is placed a good distance from the gas producers in the same reservoir. But it is true that there is some risk that we after some time may find that CO_2 comes up through the gas producers. But then we're talking years away", says Kojedal.

Why do not you inject into the Steady Formation first?

"Because we wanted to inject CO_2 somewhere else than where we are producing gas. When we discovered that Tubåen could not receive the quantity envisaged, we had to create an action plan for the long-term solution to injection. The first step is to perforate the Stø Formation, then we'll do the analysis to look at the necessary measures".

Kojedal stressed that they did not embark on new interventions without adequate data and mapping available.

(Link to different article - "Shell uses similar model (at Gorgon, Australia)")

Following the Case Closely

Norwegian Petroleum Directorate (NPD) has followed the group's CO_2 injection problems for some time.

"They have had problems with Tubåen formation for a long time, and we follow the case closely. We are confident that Statoil will do a good job of finding new solutions for injection, partly by injecting into the Steady Formation", said Torsten Bertelsen, senior vice president with responsibility for the Norwegian Sea and Barents Sea in the NPD. He says that it currently is not an acute problem that CO_2 will leak out.

"We have no worries that the gas will be contaminated by CO_2, and have no reason to respond to the chosen solution. Not least because the group has focused on alternative solutions all the time. It is also possible to drain parts of the Northern Snøhvit gas reservoir, and thereafter use it for storage", says Bertelsen.

(Link to different article - "Ekofisk can also get a CO_2 (EOR) project")

Will Not Release CO_2

According to Sverre Kojedal, CO_2 from the Melkøya will not be released to the atmosphere.

"We currently have no discharge permit for the amount of CO_2 that comes with the gas from the Snøhvit field to Melkøya, where it is captured and shipped back for injection into the subsurface at sea. The volume we extract from the well stream each year is 700 - 800,000 tons at full production. We have no plans to apply for a discharge permit for the CO_2. It may well be that we have to perform new measures to keep the injection going. All action plans are simulated and evaluated in advance, but sometimes it does not work so well as they originally thought", says Kojedal.

Senior Advisor from Climate and Pollution Control Agency (Klif), Ingrid Bjotveit, told Tech Magazine that they have followed the injection problems on Snøhvit closely.

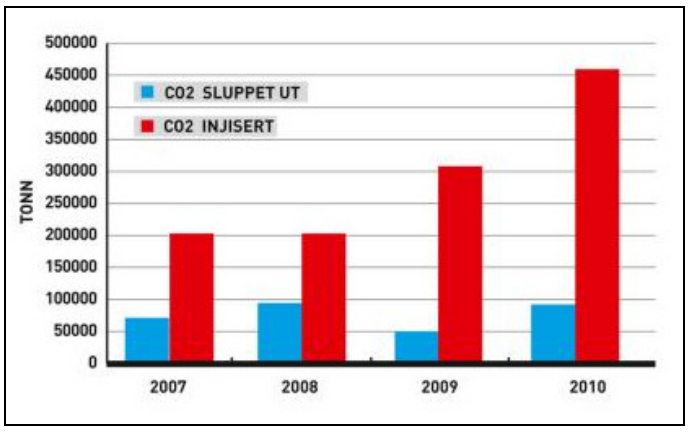

Graph of CO_2 injected (red) and emitted (blue) at Snøhvit between 2007 and 2010

Has Not Received Report:

"We know that there has been some well intervention on Snøhvit, but we have not received a final report from Statoil since they now have workover break at Snøhvit. But we have not received any indications that it will not work with injection in the Snøhvit reservoir", said Bjotveit.

Statoil received extended permission of Klif in January this year for CO_2 emissions of 65,000 tonnes.

"The emissions have somewhat exceeded the original limit, and we follow the injection of Snøhvit very carefully", said Bjotveit.

Klif have not yet decided whether they are going to tighten the requirements for injection of CO_2.

"There is a strict national regulation drawn-up for injection. We have not yet reviewed whether we are going to tighten the requirements. We must in this case, learn more about how things work on Snøhvit with the new injection well", said Bjotveit.

Temperature	Pressure	Depth	Gas Density	Gas Viscosity	Gas FVF	Expansion Factor	Relative Volume *1000	Z-Factor	Water Density	Water Viscosity	Water FVF	Water Compressbility
(deg C)	(psig)	(m)	(Kg/m3)	(centipoise)	(ft3/scf)				(Kg/m3)	(centipoise)	(RB/STB)	(1/psi)
15	0	0	1.87566	0.0077846	0.99146	1.0	**1,000.0**	0.99356	1000.08	1.23904	0.99995	3.26E-06
20	290	200	43.2069	0.0089208	0.04304	23.2	**43.4**	0.87816	1000.01	1.10314	1.00003	4.68E-06
25	580	400	96.9999	0.011091	0.019171	52.2	**19.3**	0.75066	999.2	0.98812	1.00084	4.65E-06
30	870	600	179.151	0.016084	0.01038	96.3	**10.5**	0.59466	998.155	0.88994	1.00188	4.62E-06
35	1160	800	585.474	0.15537	0.0031763	314.8	**3.2**	0.23769	996.889	0.80549	1.00316	4.61E-06
40	1450	1000	652.915	0.23702	0.0028482	351.1	**2.9**	0.26151	995.416	0.73234	1.00464	4.59E-06
50	2030	1400	682.298	0.28321	0.0027255	366.9	**2.7**	0.33853	991.907	0.61267	1.00819	4.59E-06
60	2610	1800	694.764	0.30389	0.0026766	373.6	**2.7**	0.41396	987.734	0.51974	1.01245	4.63E-06
70	3190	2200	702.188	0.31604	0.0026483	377.6	**2.7**	0.48551	982.975	0.44618	1.01736	4.69E-06
77.5	3625	2500	706.148	0.32237	0.0026335	379.7	**2.7**	0.5366	979.064	0.40066	1.02142	4.75E-06

Relative Volume (red text in Column 8) is calculated by dividing all the Gas FVF values (Column 6) by the surface value (i.e. 0.99146), then multiplying by 1000. The Expansion Factor (Column 7) is calculated by dividing all the Gas FVF values (Column 6) by 1 (surface conditions) and represents the amount of expansion that might be expected if a volume of CO_2 stored at a particular depth were allowed to escape and migrate to surface conditions.